

AD-A119 664

PALISADES INST FOR RESEARCH SERVICES INC NEW YORK
IEEE CONFERENCE RECORD OF 1982 FIFTEENTH POWER MODULATOR SYMPOS--ETC(U)
1982

F/6 9/5

UNCLASSIFIED

82-CH-1785-5

NL

1 x 4

3 x 3

4 x 4

5 x 5

6 x 6

7 x 7

8 x 8

9 x 9

10 x 10

11 x 11

12 x 12

13 x 13

14 x 14

15 x 15

16 x 16

17 x 17

18 x 18

19 x 19

20 x 20

21 x 21

22 x 22

23 x 23

24 x 24

25 x 25

26 x 26

27 x 27

28 x 28

29 x 29

30 x 30

31 x 31

32 x 32

33 x 33

34 x 34

35 x 35

36 x 36

37 x 37

38 x 38

39 x 39

40 x 40

41 x 41

42 x 42

43 x 43

44 x 44

45 x 45

46 x 46

47 x 47

48 x 48

AD A119664

~~SECRET~~
82 CH1786-5



IEEE

CONFERENCE RECORD OF

1982 FIFTEENTH POWER
MODULATOR SYMPOSIUM

June 14-16, 1982

DTIC FILE COPY

Sponsored by the
IEEE Electron Devices Society
In cooperation with the
Advisory Group on Electron Devices
and under the management of
Alliades Institute for Research Services, Inc.

DTIC
ELECTE
SEP 28 1982

D

DISTRIBUTION STATEMENT A

Approved for public release
Distribution Unlimited

82 09 27 072



IEEE

CONFERENCE RECORD OF

1982 FIFTEENTH POWER MODULATOR SYMPOSIUM

Sponsored by the
IEEE Electron Devices Society
In cooperation with the
Advisory Group on Electron Devices
and under the management of
Palisades Institute for Research Services, Inc.



Accession For	
NTIS GRA&I	<input checked="" type="checkbox"/>
DTIC TAB	<input type="checkbox"/>
Unannounced	<input type="checkbox"/>
Justification	
By <i>Per Ltr (Aug 22-1967)</i>	
Distribution/ <i>ch 6 Aug 82</i>	
Availability Codes	
Dist	Avail and/or Special
<i>A</i>	

Library of Congress Catalog Card No.: 82-819-90

Printed in USA

Available from
IEEE Single Copy Sales
445 Wood Lane
Piscataway, N.J. 08854

Copyright © 1982 by The Institute of Electrical and Electronics Engineers, Inc.
345 East 47th Street, New York, N.Y. 10017

FOREWORD

The 1982 Fifteenth Power Modulator Symposium is the latest in a series beginning with the Hydrogen Thyratron Symposium in 1950. These conferences have provided early views of the evolution of devices and technologies in the modulator field. As part of the Symposium, information is presented on recent trends associated with repetition-rated pulsed modulators, including switches, auxiliary devices, energy storage, power conditioning, RF systems, accelerators, lasers and low-frequency generators.

We wish to express our appreciation to the following for their talks at the Symposium banquet:

Dr. Leo Young
Director for Research and Technical Information
Office of the Under Secretary of Defense for
Research and Engineering

and

Mr. James E. Colvard
Deputy Chief of Naval Material
Department of the Navy

Appreciation is also expressed to the IEEE, Advisory Group on Electron Devices, Palisades Institute for Research Services, Inc., the committee members, session chairmen, banquet chairman, authors, and attendees for their contributions to the Symposium.

Ken Baile
Symposium Chairman

1982 EXECUTIVE COMMITTEE

K. Baile, Conference Chairman
Naval Surface Weapons Center

S. Schneider, Honorary Chairman
SCEEE

R. Pollard, Program Co-Chairman
Naval Surface Weapons Center

J. Carter, Program Co-Chairman
U.S. Army ET&D Lab (ERADCOM)

L. H. Klein, Secretary and Treasurer
Palisades Institute for Research Services, Inc.

TECHNICAL ADVISORY COMMITTEE

T. R. Burkes
Consultant

R. Caristi
EG&G

W. Crewson
Physics International

R. A. Gardenghi
Westinghouse Electric Corporation

A. S. Gilmour, Jr.
SUNYAB

B. Gray
RADC

P. C. Herren, Jr.
AFWAL

J. Jensen
Los Alamos Scientific Laboratory

S. Levy
U.S. Army ET&D Lab (ERADCOM)

L. H. Luessen
Naval Surface Weapons Center

P. N. Mace
Los Alamos Scientific Laboratory

H. Menown
English Electric Valve Co.

J. J. Moriarty
Raytheon Co.

N. S. Nicholls
Royal Signals and Radar Establishment

J. C. O'Connell
U.S. Army ET&D Lab (ERADCOM)

J. O'Laughlin
AFWL

L. Reginato
Lawrence Livermore Laboratory

J. Rohwein
Sandia Laboratories

W. J. Sarjeant
SUNYAB

G. Simcox
Consultant

J. Stover
Hughes Aircraft Co.

TABLE OF CONTENTS

ANNOUNCEMENT	PAGE
Computerized Bibliography of Pulsed Power <i>R. L. Druce and A. H. Guenther, Air Force Weapons Laboratory (CA) Kirtland AFB M. Kristiansen, Texas Tech University</i>	1
 SESSION I: MAGNETICS	
An Investigation into the Repetition Rate Limitations of Magnetic Switches <i>D. L. Bix, L. L. Reginato, and J. A. Schmidt, Lawrence Livermore National Laboratory</i>	4
The Application of Magnetic Pulse Compression to the Grid System of the ETA/ATA Accelerator <i>D. L. Bix, E. G. Cook, L. L. Reginato, J. A. Schmidt, and M. W. Smith, Lawrence Livermore National Laboratory</i>	10
Regulation and Drive System for High Rep-Rate Magnetic Pulse Compressors <i>D. L. Bix, E. G. Cook, S. Hawkins, A. Meyers, L. L. Reginato, J. A. Schmidt, and M. W. Smith, Lawrence Livermore National Laboratory</i>	15
Metallic Glasses for Magnetic Switches <i>C. H. Smith, Allied Corporation</i>	22
Development of Stripline Magnetic Modulators <i>W. C. Nunnally, J. Power, T. E. Springer, A. Litton, P. N. Mace, and K. W. Hanks, Los Alamos National Laboratory</i>	28
Magnetic Modulator for Low-Impedance Discharge Lasers <i>E. Y. Chu, G. Hofmann, H. Kent, and T. Bernhardt, Maxwell Laboratories, Inc.</i>	32
Pulse Sharpening with a Series Ferrite Magnetic Switch in Line-Type and Blumlein Modulators <i>S. Schneider, Southeastern Center for Electrical Engineering Education</i>	37
Tests of a Low-Pressure Switch Protected by a Saturating Inductor <i>E. J. Lauer and D. L. Bix, Lawrence Livermore National Laboratory</i>	47
An Improved 50 KV Pulser Design <i>J. A. Oicles and E. S. Fulkerson, Lawrence Livermore National Laboratory</i>	51
High Voltage High Power Pulse Transformer <i>R. L. Haumesser and Dr. D. L. Lockwood, Clarence Controls, Inc., Dr. A. S. Gilmour, Jr., State University of New York at Buffalo Dr. J. O'Connell, ERADCOM</i>	55
 SESSION II: HIGH PRESSURE SWITCHING	
Analysis of a High Power, Preionized Gas Switch with Low Inductance and Long Life <i>A. Ramrus and N. R. Pereira, Maxwell Laboratories, Inc.</i>	67
High Power Spark Gap Test Result <i>R. Limpoecher, Avco Everett Research Laboratory R. Schneider, Physics International Company</i>	75
UV-Laser Triggering of Multi-Megavolt Gas Switches <i>R. G. Adams, J. R. Woodworth, and C. A. Frost, Sandia National Laboratories</i>	79
Electrode Erosion in High Power Spark Gaps <i>A. L. Donaldson, R. Ness, M. O. Hagler, and M. Kristiansen, Texas Tech University</i>	84
Spark Erosion Characteristics of Graphite and CO Gas <i>K. J. Bickford, K. W. Hanks, and W. L. Willis, Los Alamos National Laboratory</i>	89
Long-Life Triggered Spark Gap for a CO ₂ Tea Laser Power Conditioner <i>J. N. Elkins, United Technologies Research Center S. Friedman, EG&G M. Weiner, US Army Electronics Technology and Device Laboratory</i>	93
Recovery of Electric Strength in Pressurized Spark Gaps <i>S. L. Moran, L. F. Rinehart, and R. N. DeWitt, Naval Surface Weapons Center</i>	99
Flow Visualization in a Gas Blown Spark Gap <i>R. J. Pederson and H. J. Carper, Texas Tech University</i>	105
Spark-Gap Switches Illuminated by KrF Laser Through UV Optical Fibers <i>K. Kunitomo, Y. Itoh, M. Obara, and T. Fujioka, Keio University</i>	110

TABLE OF CONTENTS

	PAGE
UV Radiation Triggered Rail-Gap Switches <i>R. S. Taylor and K. E. Leopold, National Research Council of Canada</i>	113
SESSION III: LOW-PRESSURE SWITCHING	
Fundamental Processes in Hydrogen Thyratrons <i>S. Guha, J. Kunc, H. Cole, and M. A. Gundersen, University of Southern California</i>	119
A High Power, Triple Grid Thyatron and Its Test Circuit <i>H. Mengown and B. Newton, English Electric Valve Co. Ltd.</i> <i>R. F. Lambiase, Brookhaven National Laboratory</i>	123
Instant-Start Cathodes for High Average Power Hydrogen Thyratrons <i>S. Friedman, EG&G Inc.</i> <i>R. Petr, Math Sciences Northwest, Inc.</i> <i>J. McGowan and J. O'Connell, ERADCOM</i>	127
Thyatron Switch Generation of Multi-Kilovolt Pulses in the Nanoseconds Region for Linac Electron Gun Drive <i>H. D. Kitchin, Cardon Instrument Co.</i> <i>J. M. Salome, Central Bureau for Nuclear Measurements</i>	133
High DI/DT Operation of Multi-Gap Thyratrons <i>Wm. H. Wright, Jr.</i>	141
SESSION IV: GENERAL SWITCHING	
Multiple Pulse Electron-Beam Controlled Switch <i>V. E. Scherrer, R. J. Commisso, R. F. Fernsler, and I. M. Vitkovitsky, Naval Research Laboratory</i>	146
A Preliminary Study of the Breakdown Mechanism of Surface Discharge Switches <i>S. T. Pai and J. P. Marton, Opto-Electronics Ltd.</i>	153
Tests of a Dielectric-Vacuum Surface Flashover Switch <i>J. Smith, Pulse Sciences Inc.</i> <i>G. Lauer, Lawrence Livermore National Laboratory</i> <i>M. Levine, Lawrence Berkeley Laboratory</i>	160
Optically Activated Switch for Nanosecond Pulsers <i>M. Weiner, J. Carter, R. Youmans, ERADCOM</i> <i>T. Burke, Rutgers College of Engineering</i>	164
SESSION V: COMPONENTS	
Area Effects in the Breakdown of Water Subjected to Long-Term ($\sim 100\mu s$) Stress <i>M. T. Buttram, Sandia National Laboratories</i>	168
Water/Glycol Mixtures as Dielectric for Pulse Forming Lines in Pulse Power Modulators <i>R. J. Gripshover and D. B. Fenneman, Naval Surface Weapons Center</i>	174
High Repetition Rate, Long Life Capacitors Developed for Laser Isotope Separation Modulators <i>V. Valencia, D. K. Haskell, and R. A. Cooper, Maxwell Laboratories, Inc.</i>	181
Miniaturized Pulse Forming Lines <i>J. Carter, ERADCOM</i>	186
Pulse Characteristics of Xenon Flashlamps <i>J. P. O'Loughlin, Air Force Weapons Laboratory</i>	189
Broad-Area Dispenser Cathodes for High Power Gas Lasers <i>H. W. Friedman, J. E. Eninger, and L. N. Litzenberger, Avco Everett Research Laboratory, Inc.</i>	193
SESSION VI: MODULATORS/DIAGNOSTICS	
Thyatron Switched Marx Generator <i>C. L. Kimberlin, HQ Defense Nuclear Agency</i> <i>R. L. Lundberg, Lawrence Livermore National Laboratories</i> <i>W. H. Wright, Jr., ET&D Laboratory, U.S. Army ERADCOM</i>	196
Line Type Modulator with Pulsewidth Agility <i>E. M. Plechawiek, E. H. Hooper, and E. C. Ferkas, Westinghouse Electric Corporation</i> <i>M. Lipka, Naval Research Laboratories</i>	200

TABLE OF CONTENTS

	PAGE
Precision Pulse Regulator for Radar Modulators C. A. Corson, Westinghouse Electric Corporation	210
An Evaluation of Charging Techniques for Line Type Modulators E. H. Hooper, Westinghouse Electric Corporation	214
Development and Evaluation of Systems for Controlling Parallel High di/dt Thyatrons A. Litton and G. McDuff, Los Alamos National Laboratory	220
A Novel Voltage Multiplication Scheme Using Transmission Lines I. D. Smith, Pulse Sciences Inc.	223
Fast, High-Powered Triode Pulse Amplifiers S. J. Davis, Pico Second Enterprises, Inc.	227
A Low Power Modulator for a High Power Pulsed E-Beam R. Limpacher and R. Litte, Avco Everett Research Laboratory	231
Multimegawatt Modulator Designs for Minimum Weight and Volume J. J. Moriarty, A. M. Herling, P. A. Corbiere, and G. K. Simcox, Raytheon Company	237
Pulse Power Circuit Diagnostics for the Nova Laser D. J. Christie, G. E. Dallum, D. G. Gritton, B. T. Merritt, and K. Whitham, Lawrence Livermore National Laboratory	246
SESSION VII: RF SYSTEMS	
Magnetron Filament Control P. Nocella, Sperry Corporation	249
A 95 GHz Gridded Eio Transmitter with Nanosecond Pulse Widths J. Bajda, and S. Brody, Norden Systems, Inc.	260
Impact of Electron Guns on Modulators for High Frequency, Mobile Platform Radar Systems B. Smith, US Army Electronics T&D Laboratory (ERADCOM)	265
Gridded Traveling-Wave Tube Modulator Tradeoffs A. S. Zinkin, R. S. Boiles, R. F. McClanahan, and R. D. Washburn, Hughes Aircraft Company	269
Universal Modulator for Gridded Traveling Wave Tubes A. W. Mimms, Space Microwave Laboratories, Inc. S. Meppalli, Electronics and Radar Development Establishment	275
750 KW Power System for a Solid State Pulsed RF Transmitter C. A. Corson and H. S. Ginsberg, Westinghouse Electric Corporation	282
Universal Electron Tube Control Grid Modulator D. C. Miller, Westinghouse Electric Corporation	286
SESSION VIII: KICKERS/ACCELERATORS	
Fast Pulsed Magnet Systems for Proton and Antiproton Injection into the Cern 400 GeV Proton Synchrotron E. Frick, H. Kuhn, M. Mayer, V. Rödel, G. H. Schröder, and E. Vossenberg, CERN	290
H5 Fast Kicker Magnet Pulser W. Frey, S. Ghoshroy and J. G. Cottingham, Brookhaven National Laboratory	299
Design of a Fast-Rise Slow-Fall Magnet Modulator R. F. Lambiase, Brookhaven National Laboratory	303
Initial Performance Parameters on FXR* B. Kulke, T. Innes, R. Kihara, and R. Scarpetti, Lawrence Livermore National Laboratory	307
SESSION IX: POWER CONDITIONING	
Variable Frequency Inverters for HT Supply for Pulsed Radar Transmitters J. McCafferty, Marconi Radar Systems Ltd. N. S. Nicholls, Royal Signals and Radar Establishment	312
The Tap Converter—An Alternative VSCF Converter M. Sandler and M. Wrzesniewski, The Cooper Union	317

TABLE OF CONTENTS

	PAGE
The Rotary Flux Compressor—A New High Power Compact Energy Store <i>B. Carder and D. Eimerl</i> , Lawrence Livermore National Laboratory <i>W. Bird</i> , The University of Texas at Austin.	323
A Compact Semi-Conductor AC Switch with High Interrupting Capacity <i>D. E. Crees</i> , Marconi Electronic Devices Ltd. <i>P. R. Pearson and N. S. Nicholls</i> , Royal Signals and Radar Establishment	327
The Power Conditioning System for the Advanced Test Accelerator <i>M. A. Newton, M. E. Smith, D. L. Bix, D. R. Branum, E. G. Cook, R. L. Copp, F. D. Lee, L. L. Reginato, D. Rogers, and G. C. Speckert</i> , Lawrence Livermore National Laboratory	333
Solving the Low-First-Pulse Problem <i>W. H. Wright, Jr.</i> , US Army Electronics T&D Laboratory, ERADCOM	338
List of Attendees	343
Author Index	351

COMPUTERIZED BIBLIOGRAPHY OF PULSED POWER

R. L. Druce and A. H. Guenther
Air Force Weapons Laboratory (CA) Kirtland AFB
Albuquerque, NM 87117

M. Kristiansen
Department of Electrical Engineering
Texas Tech University, Lubbock, TX 79409

Summary

As a vibrant and growing field of endeavor, pulsed power has a need at this time for an organized collection of literature pertinent to the field. For this reason, a comprehensive bibliography of pulsed power is being compiled to provide researchers and students in this field a guide to the literature. The bibliography will consist of citations pertaining to energy storage, switching, particle beam generation, power conditioning and transmission, breakdown, and diagnostics. The bibliography will contain four indices organized by subject category, title, author, and corporate affiliation. In addition, there will be a listing of conferences relevant to the pulsed power field. Each citation will include title, author(s) and affiliation(s), abstract, and key words. Citations not generally available will include a source for the document when possible. Two bibliographies, one unrestricted and one restricted circulation, will be printed automatically from a computerized data base. Publication of the first edition is planned for September - December 1982. The philosophy of the bibliography, as well as the computer facility used to utilize the data base, will be discussed.

Introduction

With pulsed power and high-voltage technologies playing a greater role in weapons research, nuclear weapons' effects simulation, fusion power research, power distribution, materials processing, and even medical research; the past two decades have seen a rapid expansion of these two technologies from a novelty to a growing and vital part of the research establishment. This rapid growth has, of course, produced an attendant growth in associated published literature. However, the fact that pulsed power is a young technology and is of an applied engineering nature, has resulted in the occurrence of several adverse conditions. Since there is no journal dedicated to publishing pulsed power articles, research relevant to pulsed power must be published when and where possible. This haphazard publishing policy results in many hours spent in literature searches that could otherwise be avoided, or work may be repeated unnecessarily because a paper was not found at all. In addition, much work has been published only in report form, which may be difficult to find at best. This paper is reporting an effort by the Air Force Weapons Laboratory (AFWL) to fill the need for an organized listing of the literature by compiling a comprehensive bibliography of pulsed power. It is planned that this bibliography will provide not only a quick reference to the available literature, but also a guide to direct the reader to obscure and hard to find documents that relate to pulsed power.

Material to be Included

The AFWL pulsed power bibliography will reference documents in the following areas:

Breakdown Studies
Diagnostics and Instrumentation
Energy Storage
Insulation
Particle Beam Generation
Power Conditioning
Switching (Including Electrode and Insulation Degradation)

with each of the above serving as the main heading. In addition, each main heading will include several subheadings (such as Thyratrons, Spark Gaps, etc. under Switching) to provide additional categorization. A section entitled Reviews and Conferences will also be included. All review articles and conference proceedings, in addition to being included in the appropriate subject category, will be placed in this section for easy reference. Types of documents to be referenced will include, but not be limited to, journal articles, research reports, contractor reports, books, and lecture notes. Any other type of document will be considered for inclusion if it has been published and is available. No attempt will be made to editorialize the quality of citations that are included in the bibliography. There will be an effort made, however, to weed out very poor quality papers.

Publication Format

The pulsed power bibliography will be published as two documents, one open circulation and one restricted. Each will be published in loose leaf form as four cross referenced sections ordered by title, subject, author, and author's affiliation. The section indexed by title will include the following information:

1. Accession number
2. Title
3. Authors and their affiliations
4. Type of document (including volume number for journal articles and report number for reports and lectures)
5. Availability of all non-journal citations when possible
6. Abstract with number of references
7. Key Words
8. Copyright
9. Security record on all classified documents

as in Fig. 1.

TITLE (DE)

250
DETAILED DESIGN, FABRICATION AND TESTING OF AN
ENGINEERING PROTOTYPE COMPENSATED PULSED
ALTERNATOR

W. L. Bird and H. H. Woodson
 University of Texas, Austin, TX 78712
 LLL Report No. UCRL 15213 (03/1980)
 The design, fabrication, and test results of a prototype compensated pulsed alternator are discussed. The prototype compulsator is a verticle shaft single phase alternator with a rotating armature and salient pole stator. The machine is designed for low rep rate pulsed duty and is sized to drive a modified 10 cm Beta amplifier. The load consists of sixteen 15 mm x 20 mm x 112 cm long xenon flashlamps connected in parallel. The prototype compulsator generates an open circuit voltage of 6 kV, 180 Hertz, at a maximum design speed of 5400 rpm. At a maximum speed, the inertial energy stored in the compulsator rotor is 3.4 MJ. 1 Ref.
 Primary Keywords: Compulsator; High Power; Laminated Rotor; Compensating Windings; High Average Flux Density; Time Varying Armature Circuit
 Secondary Keywords: Pulse Shaping; Simulation; Magnetic Field Mapping; Design Notes

Fig. 1. Sample Bibliography Citation, Indexed by Title

In the interest of brevity, the sections grouped by subject, author, and author's affiliations will include:

1. Accession number
2. Title
3. Authors and their affiliations
4. Type of Document
5. Keywords

as in Fig. 2.

SWITCHES, CLOSING

Thyratrons

716
 HIGH VOLTAGE, LOW INDUCTANCE HYDROGEN THYRATRON STUDY PROGRAM
 R. F. Caristi and D. V. Turnquist
 E. G. & G., Salem, MA 01970
 ERADCOM Report No. DELET-TR-78-2977-F (01/1981)
 Primary Keywords: Thyratrons; Switches; Pulse Generators; Blumleins; Pulse Modulators; Nanosecond Pulsers; High voltage Components

1296
 INSTANT START THYRATRON SWITCH
 S. Merz and D. Turnquist
 E. G. & G. Inc., Salem, MA 01970
 ERADCOM Report No. DELET-TR-79-0270-1 (01/1981)
 Primary Keywords: Thyratron; Hydrogen Thyratron; Cold Cathode
 Secondary Keywords: Gas Filled Device; Switch Tube

1283
 LECTURES ON HIGH-VOLTAGE AND PULSE POWER TECHNOLOGY; LECTURE 7: THYRATRONS AND IGNITRONS
 W. J. Sarjeant
 Los Alamos Scientific Laboratory, Los Alamos, NM 87544
 LASL Report No. LA-UR-80-517 (10/1981)
 Primary Keywords: Thyratron; Ignitron; Theory Application; State-of-the art; Devices Under Development; Trigger Circuit; Recovery Time
 Secondary Keywords: Charging Circuit; Delay Recovering Mechanism

Thyristors

1260
 LIGHT-FIRED THYRISTOR DEVELOPMENT
 D. K. Page, L. L. Lowry, and P. Rai-Choudhury
 Westinghouse Electric Corporation, Pittsburgh, PA 15235
 EPRI Report No. EL-776 (04/1978)
 Primary Keywords: Thyristor; Power Electronics; Optical Triggering System

Fig. 2. Sample Bibliography Citation, Indexed by Subject

The subject, author, and author's affiliation indices will be cross referenced to the title index by title and accession number.

Implementation

The bibliography is being implemented as a computerized data base to facilitate efficient and error-free handling of the data. The System 2000 data base manager was chosen for its ease of data manipulation and its availability. To facilitate on-line use, each component of a citation (subject, title, author, etc.) may be searched individually or several components may be searched simultaneously. All or part of each citation found may then be printed to the user's terminal or to a high-speed line printer for future reference. In addition, the data base is structured to provide automatic printing of all indices to be included in the printed version. This automatic printing reduces the probability of errors in format and content in the printed document. Combining this automatic printing with structured and computer prompted input will reduce the time needed to proofread the bibliography. The ability to cross-check citations from many sources for duplication quickly and easily has also been very effective.

Contributions and Availability

All contributions to the bibliography from outside sources will be most welcome. Obviously, the more complete the bibliography is, the more useful it will be. Due to the extensive literature search performed at the AFWL technical library, it is probable that a large portion of the open literature documents have already been obtained. However, any articles published in journals or other periodicals not generally devoted to physics or engineering will gladly be accepted if they are of a technical nature.

A copy of all documents submitted for inclusion in the bibliography will be required for permanent retention by the AFWL. Documents to be submitted for inclusion should be forwarded to:

AFWL/CA
Kirtland AFB
Albuquerque, NM 87117
ATTN: R. L. Druce (or A. H. Guenther)

with the permanent retention copy included. Also,

Dr. Druce is visiting installations with libraries too voluminous to be copied and transported to the AFWL. Invitations for a visit should be forwarded to the above address. The bibliography will be made available to the public for a nominal fee to cover printing and handling. The proposed publication date is flexible but is slated for September - December 1982. In addition, it is intended that all organizations making a significant contribution to the pulsed power bibliography will receive a complimentary copy of the published document.

AN INVESTIGATION INTO THE REPETITION RATE LIMITATIONS OF MAGNETIC SWITCHES*

D. L. Birx, L. L. Reginato, and J. A. Schmidt
Lawrence Livermore National Laboratory, University of California
Livermore, California 94550

Summary

The use of magnetic switches to generate high power pulses has opened up a whole new spectrum of possibilities. Here we describe an investigation into the maximum repetition rates possible with these devices.

Introduction

The use of saturable reactors for high power pulse generation was first described by Melville¹ in 1951, but the use of these devices as the power sources for electron accelerators has only recently been considered.

Our investigation into magnetic switching was motivated by the pulse power requirements of the ETA/ATA induction accelerators.

ETA (a 10 kA, 5 MeV Linac) now operating and ATA (a 10 kA, 50 MeV Linac) under construction are essentially ferrite core transformers with an electron beam as a secondary. A series of simultaneously triggered high pressure gas switches transfer the energy stored in water-filled Blumlein lines to the multiple single turn primaries. ATA is designed to generate a burst of up to 10 pulses each pulse 50 ns in duration with a pulse repetition rate of up to 1 kHz.

This 1 kHz repetition rate is achieved by circulating gas through the spark gaps at high velocity. Operation at 1 kHz requires 15 hp worth of blower per spark gap. Although for some applications it is desirable to operate at ten times this value, an order of magnitude increase in rep rate would up the blower requirement to 15,000 hp per gap and this would have been a cause of concern for other people using power in this country.

Research into alternative switching schemes resulted in the development of high power magnetic switches. To date, five of the 33 spark gap switches on ETA (comprising the original trigger system and grid drive) have been replaced with magnetic switches. These devices were installed to both gain operating experience with magnetic switches and to obtain a side by side comparison with spark gaps.

Our current experiments in this area are directed at understanding more about magnetic switches in the hopes of generating further improvements of this technology. This paper outlines our recent attempts to document the maximum repetition rate at which a magnetic switch can be operated. While we have failed to achieve this goal, we feel that the reader might be interested in how hard we tried.

Operation

The theory of operation of magnetic modulators and the conditions for optimum operation have been described in several reports.¹⁻¹⁰ It is briefly repeated here for continuity.

The basic principle behind magnetic switching is to use the large changes in permeabilities exhibited by saturating ferri- (ferro-) magnetic material to produce large changes in impedance. The standard technique for capitalizing on this behavior is illustrated in Fig. 1. By using multiple stages as shown, it is possible to achieve an effective change in impedance much larger than can be obtained from a single stage. The operating of this circuit can be described as follows.

Fig. 1a Multistage Saturable Reactor

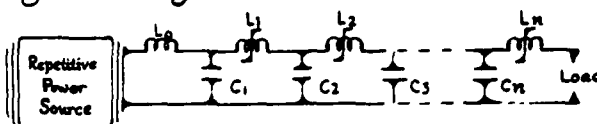


Fig. 1b Waveforms

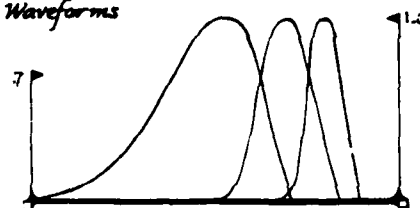


Fig. 1. Magnetic switch.

Capacitor C_1 is charged through L_0 until L_1 saturates; L_1 is chosen to have a saturated inductance much less than L_0 . Once L_1 saturates, C_2 will begin to charge from C_1 through L_1 , but because $L_{1sat} \ll L_0$, C_2 charges much more rapidly than C_1 did. The process continues through the successive stages until C_n discharges into the load. Each successive saturable reactor is designed so that saturation occurs at the peak of the voltage waveform.

Before the switch can be used again, the inductor cores must be reset. The time for the pulse energy to propagate through the switch and the time required to reset the saturable inductors determines the maximum repetition rate.

The magnetic switches employed on ETA are reset by charging C_1 to an opposite polarity between pulses. This reverse polarity pulse cascades through the switch and resets all the successive stages. For the sake of maintaining high efficiency, this reset pulse is at lower voltage than the main pulse because the energy is simply discarded at the load after the switch is reset. Typically, the propagation time of the forward pulse is 5 μ s while the 1/4 voltage reset pulse requires 20 μ s to reach the load. This allows a pulse to be produced every 25 μ s. This performance is better than adequate for our purposes, but it was of interest to see if a different resetting scheme might produce higher repetition rates without sacrificing efficiency.

The design of a magnetic switch which employs a different resetting method is schematically depicted in Fig. 2. We will attempt to describe its operation in the following section, but the reader is warned that to really understand this circuit may require actually building it. We were aided by a discovery that these devices are totally scalable. This operation of a large device can be precisely predicted from the operation of a scale model. The scaling laws are as follows:

- Power gain per stage is independent of scaling factor
- Efficiency is independent of scaling factor
- Pulse energy varies as the scaling factor to the third power
- All times vary linearly with scaling factor (including minimum construction time)

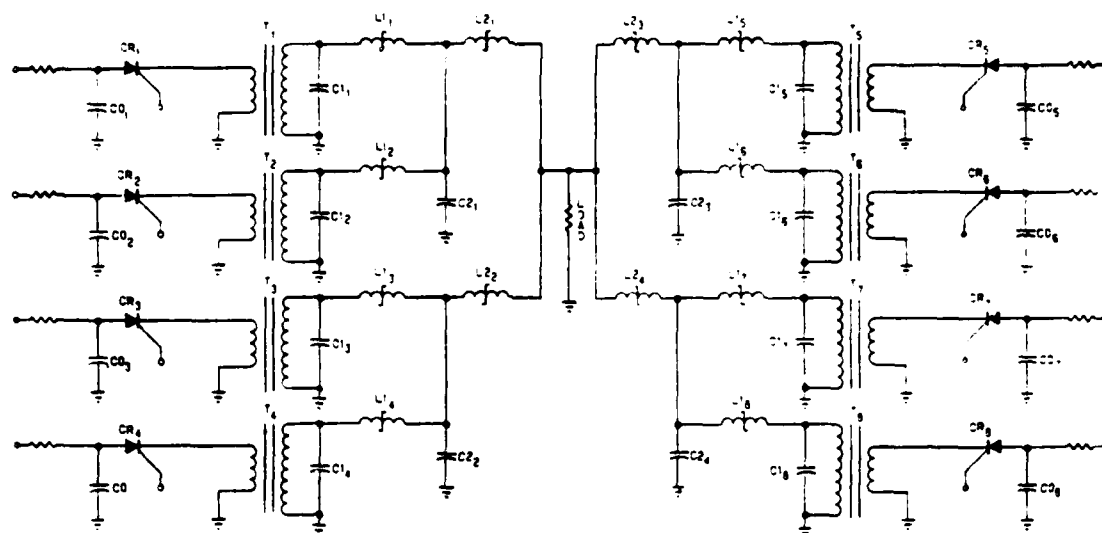


Fig. 2. Eight pulse burst generator.

- Power levels vary as the scaling factor to the second power
- Voltages vary linearly with scaling factor
- Currents vary linearly with scaling factor
- Finally, and always of the greatest importance,
- Cost varies as the scaling factor to the third power

Self-Resetting Magnetic Switches

The circuit for a magnetic burst generator which does not require resetting between pulses is illustrated in Fig. 2. Here portions of the eight forward-pulses are used to reset the saturable inductors in the circuit. This eight pulse burst generator is essentially a two stage magnetic compressor with eight first-stages and four second-stages all feeding into one output load.

When SCR S_1 is triggered, capacitor C_{11} is charged from C_{01} through T_1 until inductor L_{11} saturates. Once L_{11} saturates capacitor C_{11} begins to both charge C_{21} and reset L_{12} . When L_{21} saturates the energy stored in capacitor C_{21} is transferred to the load. This voltage appearing across the output terminals partially resets L_{23} , L_{24} , and L_{25} . Capacitor C_{11} is chosen to have a slightly smaller capacitance than C_{21} , resulting in a small negative voltage remaining on C_{11} after discharging into C_{21} . This negative voltage will begin the job of resetting L_{11} , a job that the discharge of C_{12} into C_{21} will mostly finish.

The actual firing sequence is S_1 , S_3 , S_5 , S_7 , S_2 , S_4 , S_6 , and finally S_8 . The timing between the output pulses is simply determined by the time delay between triggering the successive SCR's.

Small-Scale Model Operation

This idea sounded almost sane enough to work, so the authors decided to build a small scale model and see what really would happen. A description of the components used is provided in Fig. 3. With exception of C_{2n} , the components were assembled on a printed circuit board. The cable lengths which comprised C_{2n} ($n = 1$ to 4) lay in a neatly tangled pile on the floor. The time delays between the triggering of the SCR's was determined by cable lengths. These cable lengths added greatly to the confusion on the floor.

The first person to make it all the way to the scope obtained the data from the resistor dividers shown in Fig. 4. Here 120-ns cable lengths separated the SCR firing times. The first stage capacitor can be seen to only charge once, while the 4-s stage capacitors are each charged twice from two of the eight first stages. Finally, all eight pulses are summed together at the output terminal. The result of reducing the time delay between successive triggers from 120 ns to 60 ns is illustrated in Fig. 5.

At this point, it was decided to change the PFL used for C_{2n} from 2 parallel 15-ns lengths of RG58 to 3 parallel 10-ns lengths of RG58. This was done to avoid overlapping pulses when proceeding to higher repetition rates. These results are provided in Fig. 6. Here an attempt to get to 40 MHz resulted in the return to a single pulse generator.

Finally, all the capacitances were reduced by a factor of two. This allowed a substitution of 5-ns cables for the 10-ns lengths in the PFL. These results are presented in Fig. 7.

It was then decided the search for the repetition rate limitations of magnetic switches should be abandoned.

Conclusion

It appears possible to build high power pulse generators which operate at repetition rates determined only by the pulse lengths. This paper described an eight pulse burst generator which could be operated at repetition rates exceeding 10^7 /Hz. The authors feel that a greater number of pulses, high power levels, shorter pulses, and/or higher repetition rates is certainly achievable. However, until a use for such a device becomes apparent, we will continue to look at the other properties of magnetic switches, and untangle a few remaining problems associated with this experiment.

Acknowledgment

We would like to thank George Butner for his time spent in drawing the illustrations for this paper. Also, we would like to thank W. S. Melville for inventing the magnetic switch. It appears to be a very useful device.

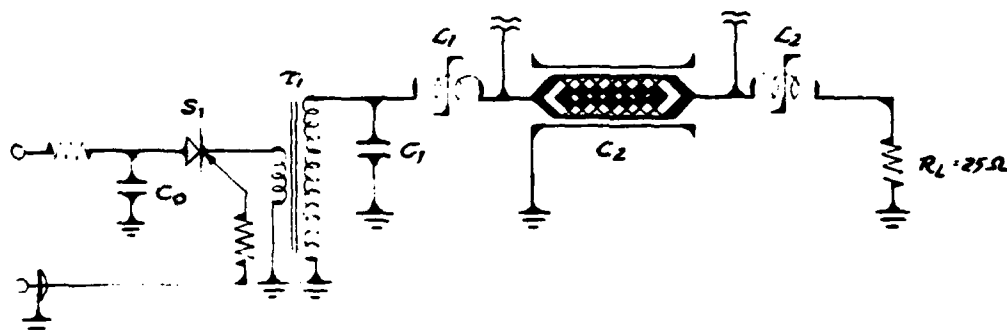
As a final note, we would like to thank Ian Smith who was the first person to believe this idea would work.

References

- ¹W. S. Melville, "The Use of Saturable Reactors as Discharge Devices for Pulse Generators", Proceedings Institute of Electrical Engineers, (London) Vol. 98, Part 3 (Radio and Communication), No. 53, 1951, p. 185.
- ²R. A. Mathias and E. M. Williams, "Economic Design of Saturating Reactor Magnetic Pulsers", Transactions of the American Institute of Electrical Engineers, Vol. 74, Part I (1955).
- ³D. L. Bix, Basic Principles Governing the Design of Magnetic Switches, Lawrence Livermore National Laboratory, Livermore, Ca, UCID 18831, (1980).
- ⁴M. F. Thompson, R. R. Trautwein and E. R. Ingersoll, "Magnetic Pulse Generator Practical Design Limitations", Communication and Electronics, No. 28, January 1957, p.789.
- ⁵E. J. Smith, "Design and Performance of Pulse Magnetic Modulators", Proceedings of Fifth Symposium of Hydrogen Thyratrons and Modulators, May 1958, p. 112.
- ⁶F. M. Lassiter, P. R. Johannessen and R. H. Spencer, "High Power Pulse Generation Using Semiconductors and Magnetic Cores", Proceedings Special Technical Conference on Nonlinear Magnetics and Magnetic Amplifiers, September 1959, p. 215.
- ⁷E. W. Manteuffel and R. E. Cooper, "Direct Current Charged Magnetic Pulse Modulator", Proceedings Special Technical Conference on Nonlinear Magnetics and Magnetic Modulators, September 1959, p. 234.
- ⁸E. M. Goldfarb, "Performance of 9.6 MW Magnetic Pulse Modulator Prototype", Proceedings of the Sixth Symposium on Hydrogen Thyratrons and Modulators, May 1960, p. 235.
- ⁹L. Bix, E. J. Lauer, L. L. Reginato, D. Rogers Jr., M. W. Smith, T. Zimmerman, "Experiments in Magnetic Switching", Lawrence Livermore National Laboratory, Livermore, CA, UCRL-85738 Preprint, (1981). Presented at the Third IEEE International Pulsed Power Conference, Albuquerque, NM, June 1-3, 1981.
- ¹⁰D. L. Bix, et al., Non-Linear Magnetics and the First 80kV of ETA, a 5 MeV, 10kA Induction Linac, Lawrence Livermore National Laboratory, Livermore, CA, UCRL-87142, (1982).
- ¹¹J. P. Van Devenor, Third IEEE International Pulsed Power Conference, Albuquerque, NM, June 1-3, 1981.

*Lawrence Livermore National Laboratory (LLNL) is operated by the University of California for the U.S. Department of Energy under Contract No. W-7405-Eng-48.

This work is performed by LLNL for the U.S. Department of Defense under DARPA (DOD) ARPA Order No. 3717, Amendment 41, monitored by NSWC under Contract No. #N60921-81-LT-W0043, and DARPA (DOD) ARPA Order No. 4395 A#1.

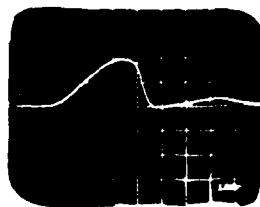


- T_1 : 30:1 Transformer wound on 1.0" O.D. x .75" I.D. x .5" W. MnZn Ferrite core
 L_1 : 30 Turns wound on 1.00" O.D. x .75" I.D. x .250" W. MnZn Ferrite core
 L_2 : 5 Turns wound on .375" O.D. x .20" I.D. x .5" W. MnZn Ferrite core
 S_1 : 2xGR-201 Unitrode
 C_0 : .4 μ fd capacitor
 C_1 : .0005 μ fd capacitor
 C_2 : 2 Parallel 15 nsec lengths RG 58

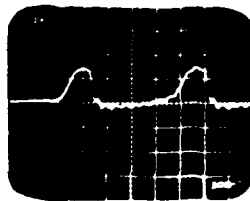
Fig. 3. Single section of eight pulse burst generator.

Typical Waveforms

10 volt charge of C_{on}
 120 nsec delays between SCR triggers
 Firing sequence 1-3-5-7-2-4-6-8



Voltage on C_{1n}
 1kv/d 100ns/d



Voltage on C_{2n}
 (2x15 nsec RG-58)
 1kv/d 100ns/d

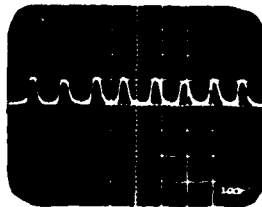


Output pulse @ R_L
 $R_L = 25 \Omega$
 625V/d 100ns/d

Fig. 4. Eight pulse burst generator stages.

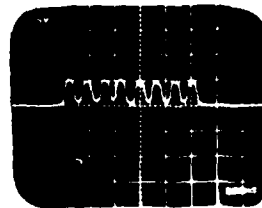
$C_2 : 2 \times 15 \text{ nsec} \cdot \text{RG-58 PFL} , R_L : 25 \Omega$

8MHz

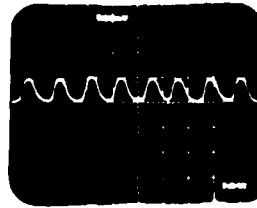


625V/d 100ns/d

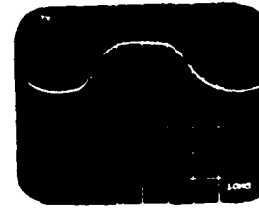
16MHz



625V/d 100ns/d



50ns/d



250V/d 10ns/d

Fig. 5. Output pulse sequence at various repetition rates.

$C_2 = 3 \times 10 \text{ nsec} \cdot R_G 58 \quad R_L = 16 \Omega \quad \text{Data at } R_{\text{Load}}$

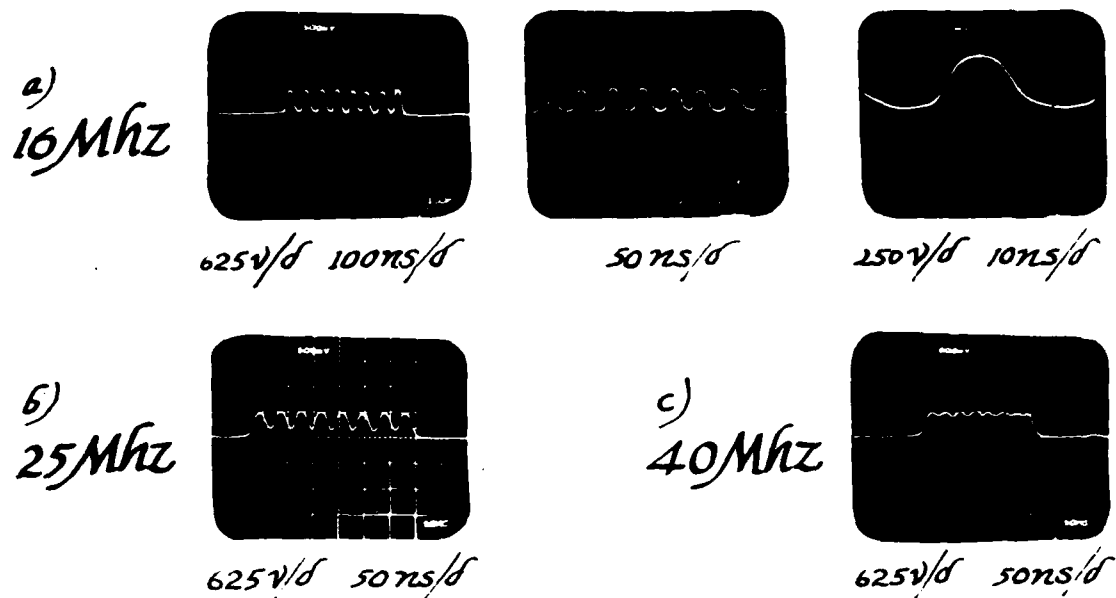


Fig. 6. Output pulse sequence at various repetition rates.

$C_1 = .00025 \mu\text{f}$, $C_2 = 3 \text{ parallel } 5 \text{ ns lengths } R_G 58$, $L_2 = 4 \text{ turns on } 375'' \text{ O.D. } .20'' \text{ I.D. } .5'' \text{ W Mn-Zn Ferrite}$

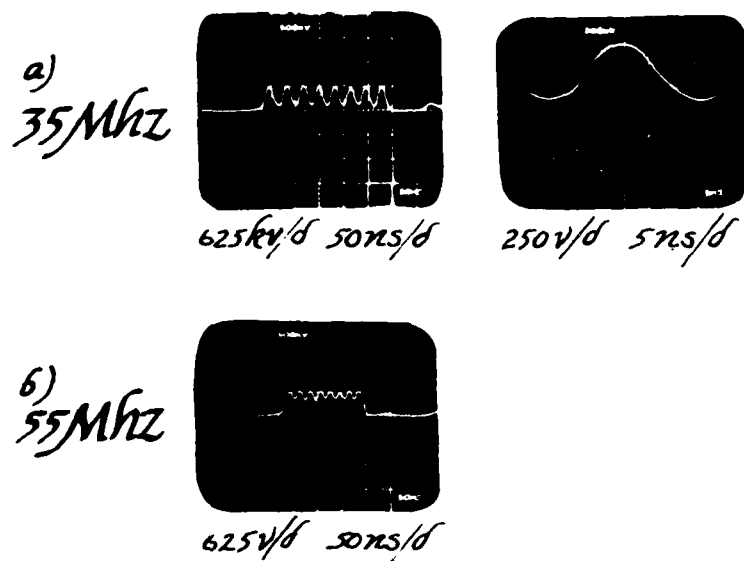


Fig. 7. Output pulse sequence at various repetition rates.

DISCLAIMER

This document was prepared as an account of work sponsored by an agency of the United States Government. Neither the United States Government nor the University of California nor any of their employees, makes any warranty, express or implied, or assumes any legal liability or responsibility for the accuracy, completeness, or usefulness of any information, apparatus, product, or process disclosed, or represents that its use would not infringe privately owned rights. Reference herein to any specific commercial products, process, or service by trade name, trademark, manufacturer, or otherwise, does not necessarily constitute or imply its endorsement, recommendation, or favoring by the United States Government or the University of California. The views and opinions of authors expressed herein do not necessarily state or reflect those of the United States Government thereof, and shall not be used for advertising or product endorsement purposes.

THE APPLICATION OF MAGNETIC PULSE COMPRESSION TO THE GRID SYSTEM OF THE ETA/ATA ACCELERATOR

D. L. Birx, E. G. Cook, L. L. Reginato, J. A. Schmidt, M. W. Smith

Lawrence Livermore National Laboratory
P. O. Box 808
Livermore, CA. 94550

Introduction

The ETA/ATA injector is essentially a 2.5 MeV triode with a hollow anode through which a 0 to 10 kA electron beam is injected into the downstream accelerator sections. A sketch of this device is presented in Figure 1. The 2.5 MeV anode potential is generated by ten series induction units each driven with a 250 kV, 50 ns pulse. At present, these pulses are generated by twenty water-filled Blumleins, switched into the structure almost simultaneously by twenty high-pressure gas-blown spark gaps. Replacement of these devices with magnetic switches is under consideration.

The electron beam is sourced by a cold plasma cathode and extracted by a screen grid. The cathode plasma is generated through the creation of 3000 simultaneous surface discharges arranged uniformly over the area of the ten inch diameter surface. A 100 kV pulse, 10 ns in duration and individually resistively coupled to each of the 3000 five-mil gaps, produces these discharges. This pulse must be timed approximately 60 ns prior to the application of the grid voltage.

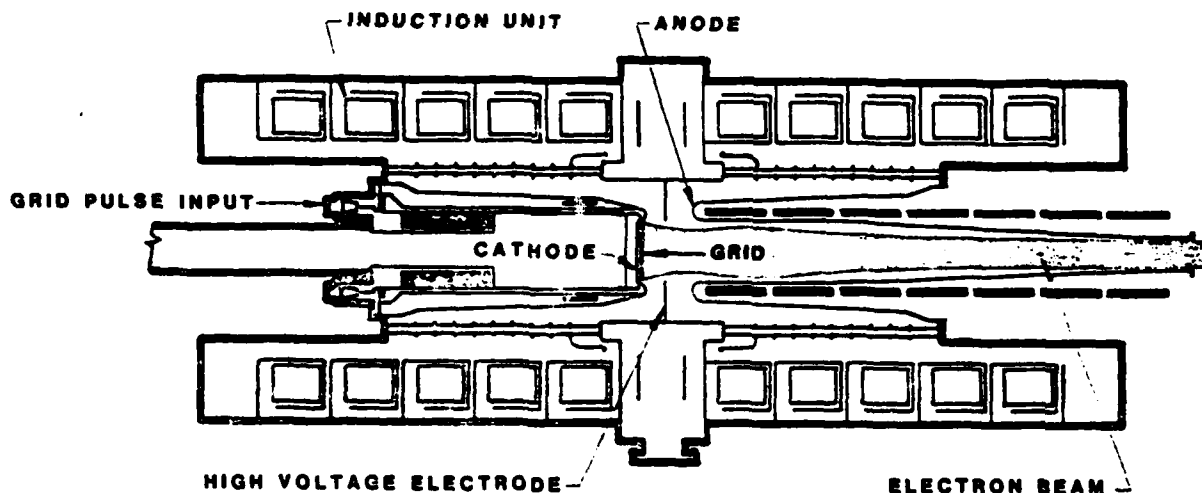
The grid-cathode gap is adjustable and is varied to provide an approximate 8Ω load impedance

to the grid drive pulse. The actual operating current is dictated by the experimentalists who are using whatever comes out of the end of the accelerator. Typically, the desired operating current will vary from 2 to 12 kA.

The grid driver must therefore generate a pulse into an 8Ω load which can be varied from 20 to 120 kV and can be accurately timed with respect to a point on the anode voltage waveform.

In order to keep low jitter in the injector accelerator cells, the pressurized gas system is normally adjusted to track large voltage variations. Since the grid adjustments do not necessarily follow those of the injector, operation of the two systems from a common gas supply became very limited and in many cases nearly impossible. A magnetic grid drive system was adopted in mid-1981 on the ETA to be totally independent of the injector and recently a similar system was built to replace the Blumlein spark-gap system of the ATA.

A block diagram of the cathode-grid electronics is presented in Figure 2. The remainder of this



2.5 MEV, 10KA ELECTRON INJECTOR
FIG. 1

*Lawrence Livermore National Laboratory is operated by the University of California for the Department of Energy under contract No. W-7405-Eng-48.

This work is performed by LLNL for the Department of Defense under DARPA (DOD) ARPA Order No. 3717, Amendment 41 monitored by NSWC under contract #N60921-81-LT-W0043, and DARPA (DOD) ARPA Order No. 4395 A#1.

This abstract is submitted to the Fifteenth Power Modulator Symposium, June 14-16, 1982, Baltimore, Maryland.

report will address the individual components illustrated there.

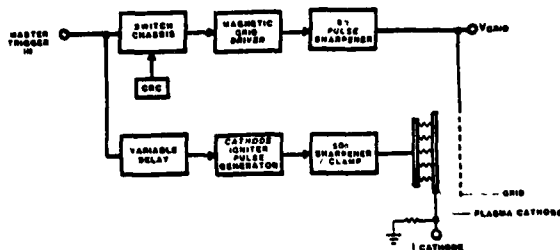
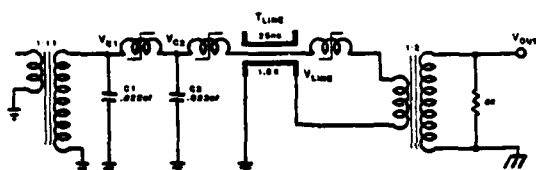


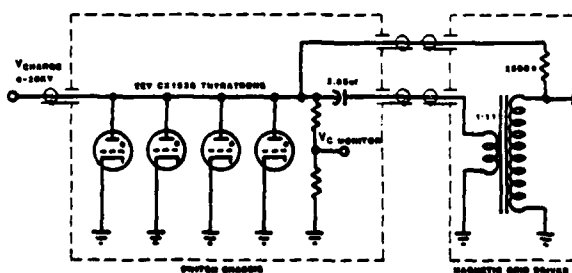
FIG. 3 BLOCK DIAGRAM OF CATHODE-GRID ELECTRONICS

Magnetic Grid Driver

The magnetic grid driver is a three-stage cascading magnetic switch. Each stage uses a 30 kg Metglas 2605 C0 core to provide a power gain of ≈ 4 in transferring the electrical energy between capacitors of equal value and then finally into an 8 Ω load. The final stage capacitor is actually a 1.5 μ F water-filled PFL. The circuit is depicted schematically in Figure 3. The output pulse energy is initially stored at ≈ 11 kV in a 2.65 μ F capacitor located in the "switch chassis" schematically illustrated in Figure 4. The bias resistor located in the magnetic switch provides rapid reset of the saturable magnetic cores between pulses and biases the cores so as to provide the maximum ΔB swing available.

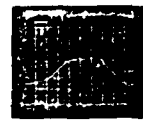


MAGNETIC GRID DRIVER
FIG. 3



SWITCH CHASSIS SCHEMATIC
FIG. 4

The data presented pictorially in Figure 5 shows an overlay of multiple two pulse burst. The output pulse of 110 kV into an 8 Ω dummy load possesses a 50 ns FWHM and 20 ns 10 to 90% risetime. The pulse shape is somewhat distorted by the resistive divider used to collect this data. A more detailed description of the magnetic grid driver follows below.

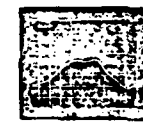
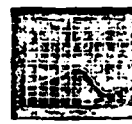
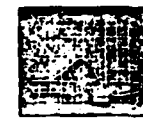


MAGNETIC GRID DRIVER
FIG. 5

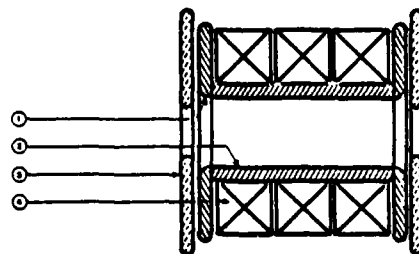
Operation of the Magnetic Grid Driver

A bank of four thyratrons discharges a 2.65 μ F capacitor into the single-turn primary winding. The Metglass input transformer charges the 0.022 μ F first-stage capacitor to approximately eleven times the primary voltage in 2.5 μ s. The saturation of the first stage inductor produces a 600 ns charge on the second stage.

The energy continues to cascade to higher and higher power levels finally applying a 50 ns FWHM pulse to the primary of a 2:1 step-up output transformer. This operation is pictured in Figure 6. The actual construction of the saturable inductors and both input and output pulsed transformers is illustrated in Figures 7 and 8.

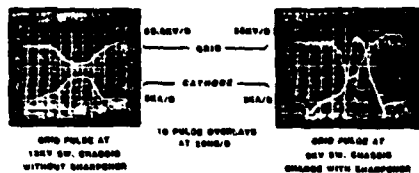


MAGNETIC SWITCH
FIG. 6



- ① 1/4" ALUMINUM GENERAL FRAME
- ② ALUMINUM CORE WINDINGS
- ③ 1/4" POLYETHYLENE INSULATION
- ④ 1/4" WIDE 2 1/2 IN. THICK METGLASS 2605 C0 CORES WITH 1/4" SPACER BETWEEN TURNS

METGLASS CORE DESIGN
FIG. 8



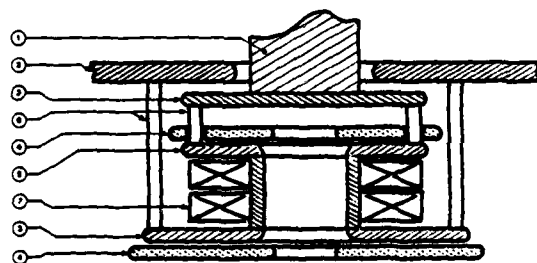
GRID DRIVER
FIG. 9

Grid Driver Installation

Before the grid driver could be installed on the machine it was necessary to further reduce the output pulse risetime. This was accomplished by placing a pulse sharpener in the transmission lines which connected the grid driver to the injector.

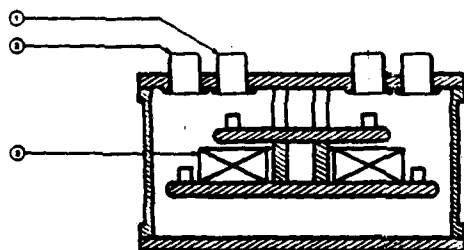
A pulse sharpener uses Zn-Ni ferrite cores to place an opening in the transmission line until the input to the sharpener is at full voltage. When the enclosed ferrite saturates, it removes the open and allows the pulse to proceed to the output. The risetime of the pulse out of the sharpener is only limited by the saturated inductance of the sharpener.

The effect of the sharpener is shown by the actual grid current voltage waveforms presented in Figure 9. This form of pulse sharpener is pictorially depicted in Figure 10.



- | | |
|--|---------------------------------|
| ① PRIMARY H.V. FEED-THRU | ③ ALUMINUM GROUND PLANE |
| ② 1/4\" ALUMINUM COORDINATOR | ④ 1/4\" POLYETHYLENE INSULATION |
| ⑤ ALUMINUM CORE CHANNEL | ⑥ 1/2\" DIA. BRASS SUPPORT RODS |
| ⑦ 1/2\" X 1/2\" IN. MYLAR WOUND WITH 1/4\" DIA. X 1/4\" WIDE MYLAR BETWEEN TURNS | |
| ⑧ TRANSFORMER CORE DESIGN - SINGLE TURN PRIMARY | |

FIG. 10



- | |
|---|
| ① 1 OF 5 H.V. INPUT FEED-THRU |
| ② 1 OF 5 H.V. OUTPUT FEED-THRU |
| ③ 1/2\" DIA. X 1/2\" IN. MYLAR WOUND WITH 1/4\" DIA. X 1/4\" WIDE MYLAR BETWEEN TURNS |

ON PULSE SHARPENER
FIG. 11

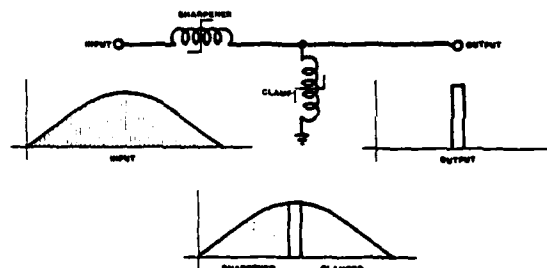
If the reader closely examines the cathode current waveforms depicted in Figure 9, a small pulse approximately 2 kA in amplitude and 10 ns in duration appears ≈ 60 ns before the main current pulse. This is the current from the cathode igniter pulse which also passes through the series resistors used to measure cathode current. This will be our next topic for discussion.

The Cathode Igniter Pulse

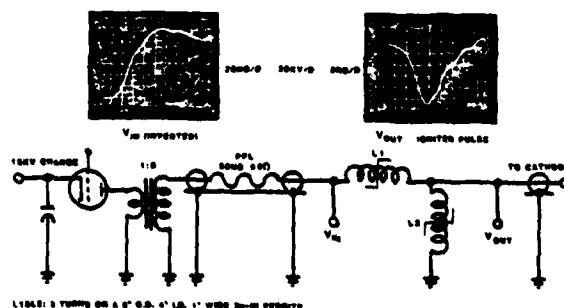
Research which led to the present plasma cathode design indicated that an ignition pulse which rose to at least 60 kV in a short a time as possible (≈ 10 ns) was mandatory to create a plasma sheath which was uniform to small fractions of a centimeter over the 500 cm² cathode surface. It was also observed that as this cathode plasma was further heated by continued application of igniter current that the plasma expansion velocity and temperature increased undesirably. In addition, as the pulse length approached several 100 ns the resistor network which coupled the pulse energy to the discharges would begin to undergo permanent changes in a direction which led to large increases in the entropy of system.

Experimentally, it was determined that a pulse 120 kV in amplitude with 10 ns FWHM lead to uniform emission, a tolerable 7cm/ μ s plasma sheath expansion velocity, and a $>10^6$ shot life.

A pulse generator was already available which produced a pulse 120 kV in amplitude, but with a 50 ns risetime and 200 ns FWHM. A pulse sharpener/clamp was constructed out of Zn-Ni ferrite cores supplied by Stackpole, Inc. This device represented in Figure 11 produced a satisfactory pulse and is now employed in ETA.



THEORY BEHIND IGNITER SHARPENER / CLAMP
FIG. 12



CATHODE IGNITER PULSE GENERATOR
FIG. 13

Appendix

The Use of Metglas in Fast (< 100 ns) Pulse Transformers

The use of Metglas in fast pulse transformers is of particular interest to the designers of induction linacs. An induction linac is simply a pulse transformer with an electron beam as a secondary. Both ETA and ATA are Zn-Ni ferrite core induction linacs. Ferrite was chosen because at the time it was the only material which exhibited satisfactorily low losses for 50 to 70 ns duration pulses. Metglas is now available and it may be time to once again examine the options. The higher ΔB_s of Metglas could reduce core volumes almost an order of magnitude if the present accelerator gradients were maintained.

It is worth taking a minute to examine upon what the core losses depend. The reader may have noticed that the magnetic grid driver uses a Metglas output transformer for a 50 ns FWHM pulse. It must therefore be assumed that Metglas can somehow be made to work in this application.

Calculation of Core Losses

There are three primary contributors to the core loss, the dc anisotropy energy, eddy current losses and spin relaxation viscous damping. The dc anisotropy energy can be determined by measuring

$$\int_{B_r}^{B_s} B \cdot dH$$

at low frequencies, but the eddy current and spin relaxation losses vary with frequency.

The losses in the metallic tape-wound cores is strongly influenced by the above mentioned frequency-dependent effects. Examination of these cores indicates that a saturation wave begins at the surface of the tapes and propagates toward the center. The propagation velocity is simply the domain wall velocity and is given by

$$v = \frac{2 B_s}{\beta} (H - H_0) \text{ [CGS]}.$$

where H_0 is the saturation field and β is given by

$$\beta = \beta_e + \beta_r$$

with β_e (β_r) being the eddy current (spin relaxation) viscous damping parameter. The saturation field of a tape of thickness d is approximately

$$H = H_{dc} + \frac{d}{4 B_s} \frac{\beta}{\tau_{sat}}$$

where

$$\beta_r = \left[\left(\alpha (1 + \alpha^2) B_s / \gamma \right) \frac{k}{A} \right]^{1/2} \text{ [CGS]}$$

and

$$\beta_e = \frac{(16 \cdot B_s)^2 d}{\pi \cdot \rho \cdot c^2} \text{ [CGS]}$$

here γ is the gyromagnetic ratio, k the anisotropy energy, the Gilbert damping parameter, and A the exchange stiffness constant.

For short pulses the dominant term is the eddy current loss and where $d(t)$ is the thickness of the saturated portion of the tape. It has always been felt that Metglas could not be used in these induction linac cores until a technique of producing 0.7 mil Metglas was developed. In actuality, it is possible to use 1 mil thick Metglas but only 70% of the total available area is useable. This would require the use of more Metglas than if 0.7 mil Metglas were in existence but still requires considerably less Metglas than ferrite.

REFERENCES

1. W. S. Melville, "The Use of Saturable Reactors as Discharge Devices for Pulse Generators," Proceedings Institute of Electrical Engineers, (London) Vol. 98, Part 3 (Radio and Communication), No. 53, 1951, p. 185.
2. R. A. Mathias and E. M. Williams, "Economic Design of Saturating Reactor Magnetic Pulsers," Transactions of the American Institute of Electrical Engineers, Vol. 74, Part 1 (1955).
3. R. O'Handley, L. I. Mendelson, R. Hasegawa, R. Ray, and S. Kaush, "Low-Field Magnetic Properties of FE₈₀B₂₀ Glass," Journal of Applied Physics, Vol. 47, No. 10 (October 1976).
4. D. L. Birx, E. J. Lauer, L. L. Reginato, D. Rogers, Jr., M. E. Smith, T. Zimmerman, "Experiments in Magnetic Switching," UCRL 85738, 1981 (EEE International Pulsed Power Conference, Albuquerque, New Mexico, June 1981).
5. D. L. Birx, "Basic Principles Governing the Design of Magnetic Switches," UCID 18831, Nov. 18, 1980.
6. E. M. Lassiter, P. R. Johannessen, and R. H. Soencer, "High Power Pulse Generation Using Semiconductors and Magnetic Cores," Proceedings Special Technical Conference on Nonlinear Magnetism and Magnetic Amplifiers, September 1959, p. 215.
7. D. L. Birx, et al., "Nonlinear Magnetism and the First 80 kV of the ETA, a 5 MeV, 10 kA Induction Linac" (UCRL in preparation), Lawrence Livermore National Laboratory, Livermore, CA, April 1982.
8. E. W. Manteuffel, and R. E. Cooper, "Direct Current Charged Magnetic Pulse Modulator," Proceedings Special Technical Conference on Nonlinear Magnetism and Magnetic Modulators, September 1959, p. 234.
9. D. L. Birx, et al., Fifteenth Power Modulator Symposium, Baltimore, Maryland, June 1982.

DISCLAIMER

This document was prepared as an account of work sponsored by an agency of the United States Government. Neither the United States Government nor the University of California nor any of their employees, makes any warranty, express or implied, or assumes any legal liability or responsibility for the accuracy, completeness, or usefulness of any information, apparatus, product, or process disclosed, or represents that its use would not infringe privately owned rights. Reference herein to any specific commercial products, process, or service by trade name, trademark, manufacturer, or otherwise, does not necessarily constitute or imply its endorsement, recommendation, or favoring by the United States Government or the University of California. The views and opinions of authors expressed herein do not necessarily state or reflect those of the United States Government thereof, and shall not be used for advertising or product endorsement purposes.

REGULATION AND DRIVE SYSTEM FOR HIGH REP-RATE MAGNETIC PULSE COMPRESSORS *

D. L. Birk, E. G. Cook, S. Hawkins, A. Meyers
L. L. Reginato, J. A. Schmidt, and M. W. Smith
Lawrence Livermore National Laboratory, University of California
P.O. Box 808/L-321
Livermore, California 94550

I. Summary

The essentially unlimited rep-rate capability of non-linear magnetic systems has imposed strict requirements on the drive system which initiates the pulse compression. An order of magnitude increase in the rep-rates achieved by the Advanced Test Accelerator (ATA) gas-blown system is not difficult to achieve in the magnetic compressor. The added requirement of having a high degree of regulation at the higher rep-rates places strict requirements on the triggerable switch for charging and dequeing. A novel feedback technique which applies the proper bias to a magnetic core by comparing a reference voltage to the charging voltage eases considerably the regulation required to achieve low jitter in magnetic compression. The performance of the high rep-rate charging and regulation systems will be described in the following pages.

The application of magnetic switching¹⁻⁵ to high repetition-rate pulsed power generation has not only greatly simplified the problem of operating high power systems at 10 kHz, but has generated a whole new spectrum of requirements for the input drive system.

Our interest lies primarily in creating short bursts of pulses rather than a continuous pulse train. The dc power supplies currently in use require at least one second to generate the energy required for each burst.

While it is possible to simply charge many capacitors in parallel and discharge them one at a time into the input of the magnetic switch, this technique becomes clumsy and bulky as the number of pulses in a burst increases. Therefore, it was desirable to develop a system which requires only one intermediate storage capacitor and recharge that capacitor in the time between pulses.

One method of accomplishing this is called "Command Resonant Charging." The concept is illustrated in Fig. 1 where switch S_1 is closed at the time T_1 and capacitor C_2 begins inductively charging from the energy stored capacitor C_1 . At the time T_{11} , switch S_{11} is closed to halt the charging process. Finally, after allowing enough time for switch S_1 to recover (open), switch S_{11} can be closed and the energy stored in C_2 is transferred to the load.

The act of closing switch S_{11} is called dequeing and is used to achieve a constant final voltage on C_2 even though the voltage on capacitor C_1 droops during the burst.

II. CRC Compensation

The major source of error associated with dequeing type regulation comes as a result of the interval between the time one measures the desired voltage on the intermediate storage capacitor and the firing of the dequeing tube. Attempts were made to minimize this interval, but because of turn-on times of thyratrons and pulse amplifiers as well as time lags in cables, time intervals much less than 1 μ s became impractical. Such a time lag could result in as much as a 7% voltage error with a 20 μ s charging time. This problem is illustrated in Fig. 2.

It is possible to compensate for this effect if one can predict the voltage on the capacitor in advance and start the dequeing process appropriately

ahead of time. To see how this could be done, let us examine the circuit depicted in Fig. 3.

Let

$V_c(t)$ = Voltage on Switch Chassis Capacitor

and

$V_m(t)$ = Voltage measured on divider.

A simple analysis gives

$$V_m(t_0) = V_c(t_0) + RC \dot{V}_c(t_0) + LC \ddot{V}_c(t_0)$$

While an expansion of $V_c(t)$ about the point $t = t_0$ yields

$$V_c(t_0 + t) = V_c(t_0) + \sum_n = 1 + \frac{\Delta t^n V_c^{(n)}(t_0)}{n} \\ \approx V_c(t_0) + \Delta t \dot{V}_c(t_0) + \frac{\Delta t^2}{2} \ddot{V}_c(t_0)$$

It becomes obvious that through the correct choice of values for R and L (i.e., $RC = \Delta t$ and $LC = \Delta t^2/2$). It is possible to make $V_m(t_0) = V_c(t_0 + \Delta t)$.

III. The ATA Master Trigger System

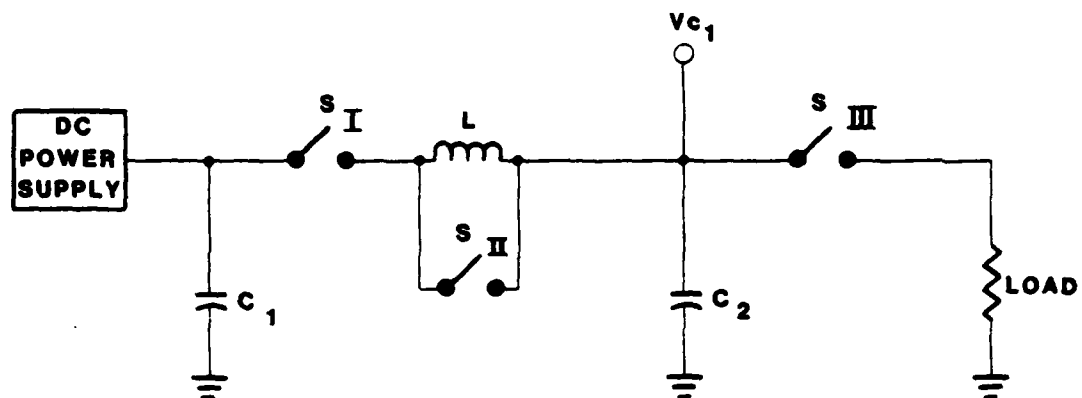
The early completion of the ATA master trigger pulser afforded an excellent opportunity to materialize ideas on an actual full-scale magnetic switch. This pulser was constructed to supply an ~ 100 -J pulse capable of providing a low-jitter trigger to four of the ATA spark gaps. A simplified schematic of what became of the final system is shown in Fig. 4.

The 0.5 μ f intermediate storage capacitor is charged via a single thyatron and 240 μ h inductor from a 150 μ f capacitor bank. Voltage on this capacitor is measured by a differential divider which subtracts off the voltage drop appearing on the output during charging. The capacitor is arranged in the circuit in this manner so that the charging current resets the magnetic switch.

The output of the differential divider is compared to a reference voltage and a single dequeing thyatron halts the charge at the desired voltage. A 2 K Ω bias resistor holds the magnetic material at $-B_{sat}$ until two thyratrons are fired providing a 1 μ s transfer of the energy in the intermediate storage through the 9:1 stepup transformer into the first stage capacitor of the magnetic switch. Two stages of compression yield a 150-kV pulse into the 12- Ω load.

IV. Control Circuitry

The dequeing circuit consists primarily of a TTL high-speed comparator and peripheral line driver. The



C_1 - Main Capacitor Bank

C_2 - Intermediate Storage Capacitor, $C_2 \ll C_1$

Fig. 1(a). Simplified schematic of Command Resonant Charged System.

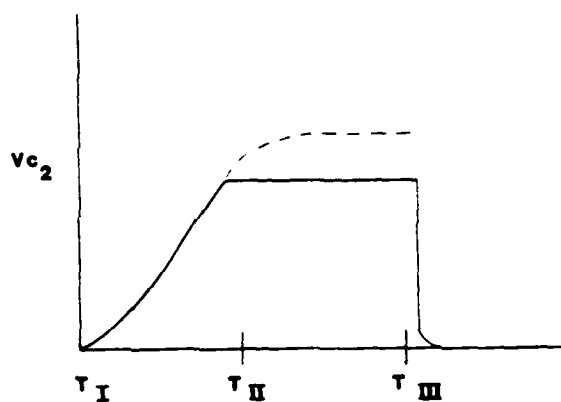


Fig. 1(b). Voltage waveform seen at C_2 .

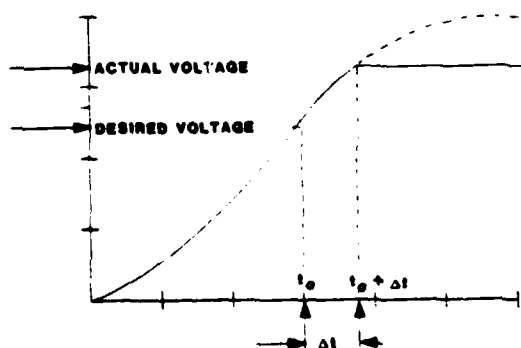


Fig. 2. Effect of time delay with dequiescing regulation.

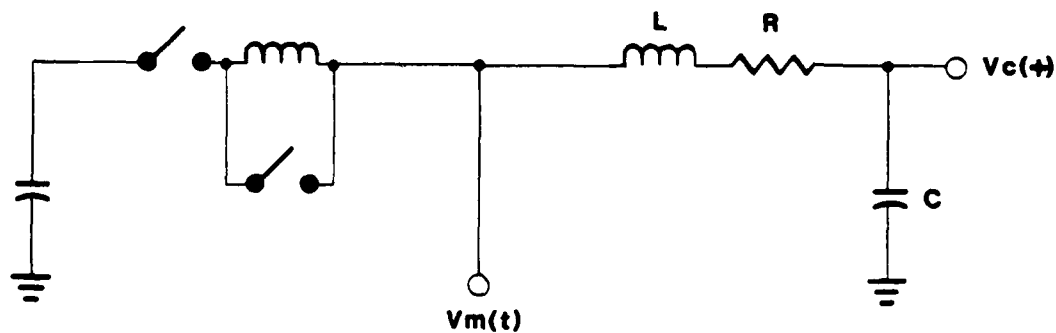


Fig. 3. Simplified schematic of CRC with phase lag introduced for passive compensation.

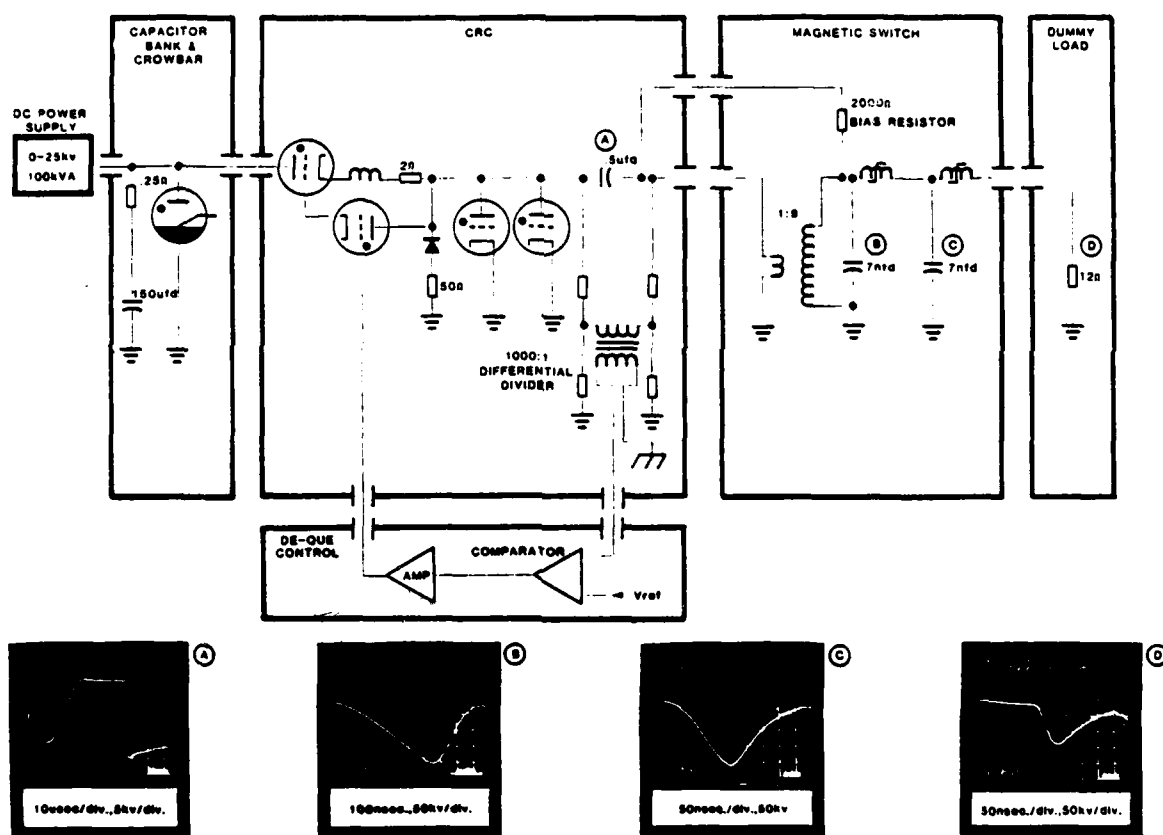


Fig. 4. 10 kHz ATA master trigger power conditioning.

output pulse drives a MOSFET amplifier. The output from this amplifier triggers the SCRs in a 3-kV, 50- Ω amplifier, which is actually an SCR-driven magnetic switch. The output from this amplifier triggers the CX1538 EEV thyatron. The complete system has demonstrated a jitter of less than 0.5 ns and is capable of running at up to 1 kHz average repetition rate.

A block diagram of this control system which is contained in a single 8-3/4-in.-high rack mount NIM bin is shown in Fig. 5.

The actual operation is presented by Fig. 6. Here it is possible to see the effect of deque regulation on a 50-pulse burst at 10 kHz. The variation of the output timing when there is no dequeing illustrates the most important reason for achieving good regulation on the input of a magnetic switch.

There has not been any mention above of how several magnetic systems can be synchronized together to control the output pulse timing to within fractions of a nanosecond. This is certainly a non-trivial matter; in fact, it was once assumed impossible. Thus, we address it here.

We will begin by stating that it is indeed possible. On the ETA accelerator the jitter between the timing of the anode voltage waveform, determined by the magnetic trigger system and the grid voltage waveform (determined by the magnetic grid driver) is typically 1 ns. This jitter is determined by the switch chassis thyatron jitter and changes in the saturation time of the inductors in the magnetic switch.

The thyatrons used are the EEV CX1538s. These tubes are built with a keep-alive electrode which provides a constant low-level ion density in the tube between pulses. The best measurement of jitter in the anode delay time we have made is an upper limit of 10.5 ns.

Variations in saturation times pose a much more serious problem. There are two effects which lead to these variations. The saturation time is derived by combining the material properties with Maxwell's equations.

$$\int_0^T V_L dt = NA \Delta B_s.$$

Therefore

$$\tau_{sat} = \frac{NA \Delta B_s}{\langle v \rangle}$$

where

$$\langle v \rangle \approx 0.5 V_0,$$

and if

$$\tau_{delay} \equiv \sum_{i=1}^n \tau_{sat}.$$

Then to number stages

$$\frac{\partial \tau_{delay}}{\partial V} = - \frac{\tau_{delay}}{V},$$

and

$$\frac{\partial \tau_{delay}}{\partial \Delta B_s} = \frac{\tau_{delay}}{\Delta B_s}.$$

Hence

$$\partial \tau_{delay} \equiv \text{Jitter} = - \frac{\partial V}{V} \cdot \tau_{delay} + \frac{\partial \Delta B_s}{\Delta B_s} \cdot \tau_{delay},$$

where

$$\Delta B_s = f(\text{temperature, reset bias}).$$

The changes in ΔB_s were easily handled by both accurately controlling the reset pulse timing and the temperature of the HV insulating oil in which these switches are immersed. The temperature control was achieved by circulating the HV oil through a heat exchanger.

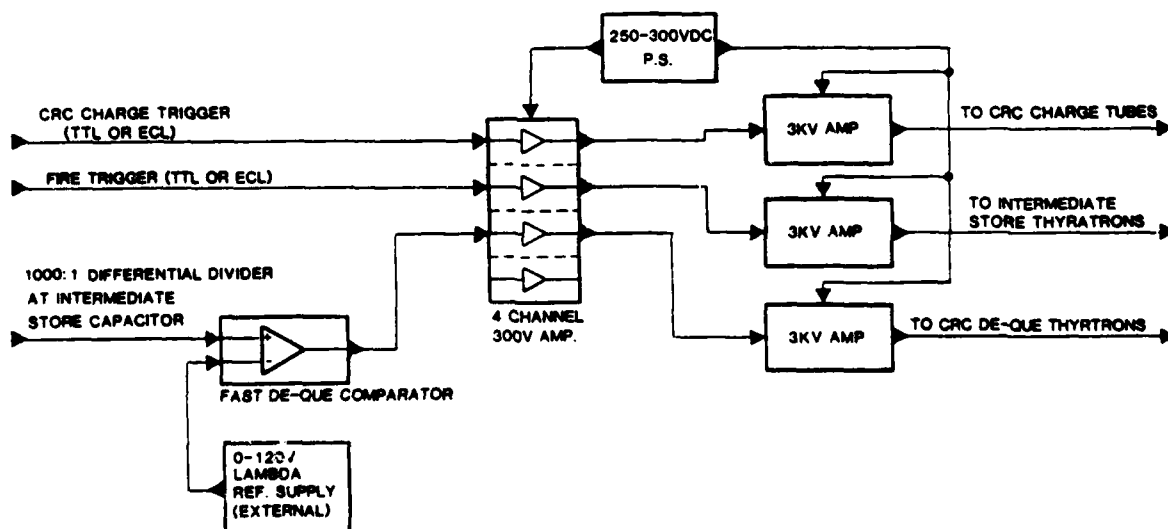
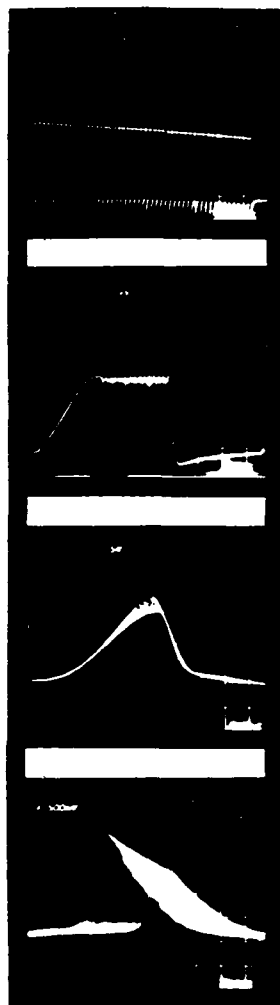


Fig. 5. 10 kHz controller (NIMS).

50 PULSE BURST WITHOUT DE-QUE REGULATION



INTERMEDIATE STORE
500nsec./div., 5kv/div.

INTERMEDIATE STORE
20nsec./div., 5kv/div.

MAGNETIC SWITCH
FIRST STAGE CAPACITOR
200nsec./div., 50kv/div.

OUTPUT PULSE
50nsec./div., 50kv/div. (12 OHM)

50 PULSE BURST WITH .1% DE-QUE REGULATION

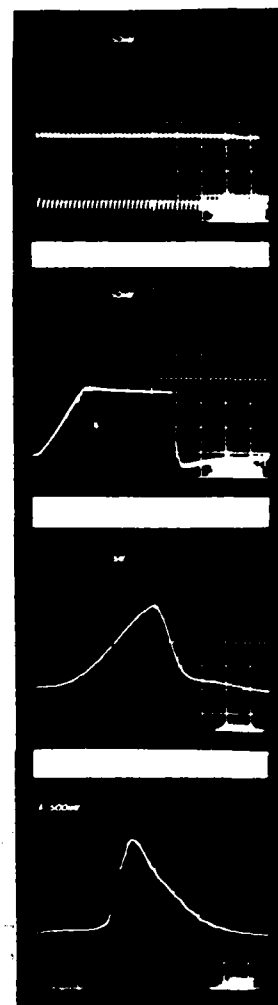


Fig. 6. Voltage regulation and jitter.

Returning to the problem of voltage variation, T_{delay} in our case is of order 1 μs and to obtain a 0.5 ns of output timing variation would require a voltage regulation of 0.05%. The actual voltage regulation measured was 0.05%, so in this case we will leave things as they are. However, an alternative for good regulation was developed. Measuring the voltage to 0.01% accuracy is fairly straightforward, and with this information the changes in timing of the output pulse can be simply calculated. In principle, it should be possible to delay the trigger to the switch chassis thyristors by varying amounts to compensate for this effect.

This is the operating principle of the "Voltage Variable Delays." These devices compare the voltage on the primary capacitor with a dc reference supply with better than 0.01% regulation. Any differences in voltages will induce a corresponding bias current in a saturable inductor located in the low-level trigger system. The changing bias current is adjusted to

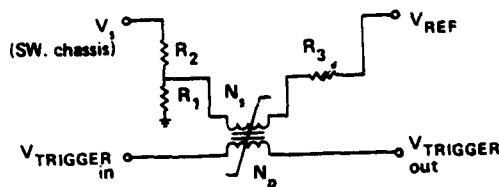
yield changes in saturation time which vary the thyristron trigger time to compensate for the predicted cumulative changes in saturation times of the magnetic switch. A demonstration of the usefulness of this device was provided by the ETA magnetic grid driver. We purposely spoiled the regulation on the CRC. The results are depicted in Fig. 7. The basic concept is further illustrated in Fig. 8.

V. Results

While magnetic switches do somewhat complicate the driving and control circuitry, we feel at least for our application that they are worth the extra nuisance.

Acknowledgments

The authors would like to thank W. S. Melville for inventing the magnetic switch.



$$I_{BIAS} = \frac{V_1 \cdot \frac{R_2}{R_1 + R_2} - V_{REF}}{\frac{R_1 \cdot R_2}{R_1 + R_2} \left(1 + \frac{R_3}{R_1} + \frac{R_3}{R_2} \right)}$$

$$\Delta I_{BIAS} = \delta V_1 \left(\frac{1}{R_1 \left(1 + \frac{R_3}{R_1} + \frac{R_3}{R_2} \right)} \right) = C_1 \delta V_1$$

$$\text{iff } \frac{\partial B}{\partial H} = \mu \text{ and } H = C_2 \cdot I_{BIAS}$$

$$\text{Since } \tau_{DELAY} = \frac{N_p A_p \Delta B_1}{V_{TRIGGER}} = C_3 \cdot \Delta B_1$$

$$\text{Then } \delta \tau_{DELAY} = C_1 \cdot C_2 \cdot C_3 \cdot \mu \delta V_1$$

Fig. 7. Principle of voltage variable delay.

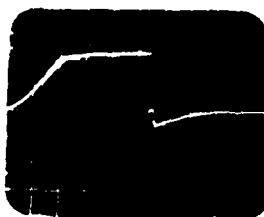
References

- 1W. S. Melville, "Use of Saturable Reactors as Discharge Devices for Pulse Generators," Proc. IEF, London, England, 1951, vol. 9A (3), p. 185.
- 2D. L. Bix, E. J. Lauer, L. L. Reginato, D. Rogers, Jr., M. W. Smith, and T. Zimmerman, Experiments in Magnetic Switching, Lawrence Livermore National Laboratory, Livermore, CA, UCRL-85738 (1981), also Proc. 3rd Inter. Conf. Pulsed Power, Albuquerque, NM, 1981.
- 3D. L. Bix, Basic Principles Governing the Design of Magnetic Switches, Lawrence Livermore National Laboratory, Livermore, CA, UCID-18831 (1980).
- 4F. J. Smith, Proc. 5th Symp. Hydrogen Thrusters and Modulators, 1958, p. 112.
- 5F. M. Lassiter, P. R. Johannessen, and R. H. Spencer, "High-Power Pulse Generation Using Semiconductors and Magnetic Cores," Proc. Special Technical Conf. on Non-Linear Magnetics and Magnetic Amplifiers, 1959, p. 215.

*Lawrence Livermore National Laboratory is operated by the University of California for the Department of Energy under Contract No. W-7405-ENG-48.

This work is performed by Lawrence Livermore National Laboratory for the Department of Defense under DAPRA (DOD) ARPA Order No. 4395 A#1, monitored by NSWC under document number N60921-82-WR-W0056.

switch chassis charge

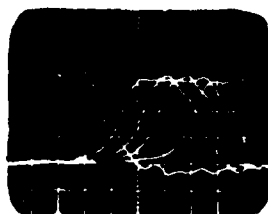


*5kv/d 100μs/d
5 Pulse burst @ 1kHz*

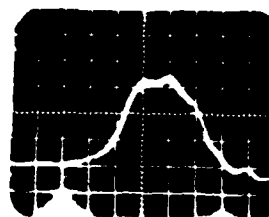
Output Pulses (ETA GRID DRIVER)

Measured by resistor divider

25kv/d 20ns/d



*Without voltage variable
delay*



*With voltage variable
delay*

Fig. 8. Voltage variable delay (3% input regulation).

METALLIC GLASSES FOR MAGNETIC SWITCHES

Carl H. Smith

Allied Corporation
Metglas Products
6 Eastmans Road
Parsippany, New Jersey 07054

Summary

Melt-spun ferromagnetic metallic glasses are available with high resistivity, high saturation induction and thin ribbon geometry. These properties make them of interest for magnetic compression of high power pulses. This paper presents background information on metallic glasses and their properties. Magnetic switching is discussed relative to these properties including some results of current research efforts utilizing metallic glass ribbon.

Introduction

Ferromagnetic metallic glasses, or amorphous metals, have received considerable attention recently as core materials for saturating inductors in magnetic switches.¹⁻⁵ The need for high-reliability, high-power, pulse sources for accelerators and lasers, often with capabilities of high repetition rates, has led several laboratories to refine and scale up in power level pulse compression techniques first invented for radar in the 1950's.⁶ Metallic glasses with attractive properties for saturable reactors - high saturation induction, high squareness ratio, and high resistivities - became commercially available in thin ribbon form at approximately the same time as this rebirth in interest in non-linear magnetics.

This paper presents a background on metallic glasses - what they are, how they are produced and their relevant magnetic and mechanical properties. A brief discussion on magnetic switching and its relation to the materials properties of glassy metals is included. Finally, some results of current research on magnetic switching for pulse power are presented.

Metallic Glasses

Glasses are solids in which the random order of a liquid has become frozen in place. They do not possess the usual long-range order found in crystalline solids. Duwez in 1960 found that such an amorphous structure could be produced in alloys of metals and semi-metals by extremely rapid quenching from the melt. The years since 1960 have seen tremendous world-wide activity in developing alloys, production technology, applications and scientific understanding of amorphous, rapidly-quenched alloys. Many articles review various aspects of this new class of metals.⁸⁻¹⁰ The existence of ferromagnetic metallic glasses has spurred much of this interest. Ferromagnetic exchange interactions require only short-range order.

Compositions

Most soft ferromagnetic metallic glasses of practical interest are eutectic (lowered melting point) or near-eutectic alloys of approximately 80 atomic percent of one or more transition metals Fe, Ni, Co and 20 atomic percent metalloids, or semi-metals B, Si, C and P. Various other elements such as Mo, Ge, Cr and Al are often added in smaller amounts. Alloys are chosen for desired magnetic properties, for glass forming ability and for stability against crystallization. Metallic glasses are, as are most products of physical metallurgy used in research and industry, not in an equilibrium state. At temperatures above approximately 60 percent of their melting points metallic glasses rapidly crystallize with an exotherm corresponding to their trapped latent heat of fusion. Alloys which are selected for commercial applications must have extrapolated lifetimes of hundreds or thousands of years at normal operating temperatures.¹¹

Production

Although amorphous alloys can also be produced by vapor deposition and by electroplating, current production of commercial quantities are achieved by forcing a thin stream of liquid metal into intimate contact with a moving, chilled metal substrate with high thermal conductivity.⁶ To achieve the required cooling rates of 10^5 to 10^6 K/sec, the ribbon produced must be thin - 100 micrometers or less depending upon the alloy and the apparatus. Widths greater than a few millimeters require the expedient of placing the nozzle of the crucible containing the molten alloy in very close proximity to the substrate. See Figure 1 for an example of planar flow casting. A continuous ribbon approximately 25 micrometers thick by 50 millimeters or more wide can be produced at 15 to 30 meters per second. Catching and winding the ribbon

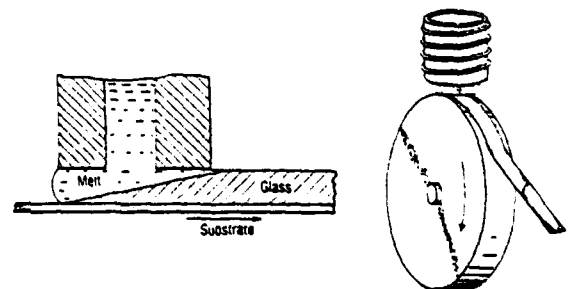


Figure 1. Production of metallic glass ribbon by planar flow casting.

and continuous metal feed to the nozzle are production problems which have been solved in a prototype METGLAS® ribbon production facility in Parsippany, NJ as shown in Figure 2. METGLAS ribbon is currently available with nominal 28 micrometer thickness, 25 and 50mm wide. Ribbon as wide as 170mm has been cast experimentally.

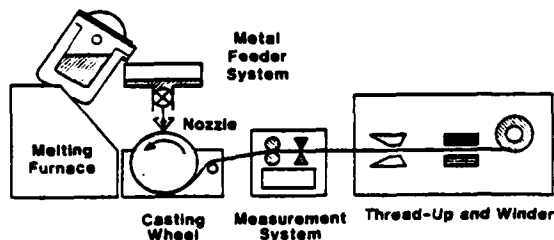


Figure 2. Production casting of metallic glass ribbon.

Properties

Ferromagnetic metallic glasses have a unique combination of mechanical strength and extremely soft magnetic properties. The strength is due both to their disordered structure and to the strong bonding between the metal and metalloid atoms. The soft magnetic properties are due to the lack of magneto-crystalline anisotropy and the lack of grain boundaries to impede domain wall movement. In addition, the atomic disorder results in resistivities which are two to three times those of crystalline metallic alloy tapes and, therefore, lower eddy current losses.

The properties of amorphous metals can be altered by annealing at temperatures below their crystallization temperatures. Annealing serves to relax the residual stresses from quenching, as well as the bending stresses introduced during core fabrication. These stresses can alter the magnetic properties due to the magnetostriction of the materials. In addition, the domain structure can be altered by annealing above or near the Curie temperature in the presence of a magnetic field. The easy direction of magnetization can be oriented parallel to the ribbon directions for maximum remanance and squareness or perpendicular to the ribbon direction to produce a more linear magnetic material with low remanance. Annealing alters the short range order, slightly increasing the saturation induction, but also somewhat increasing the brittleness of the material.

Table 1 summarizes some of the properties of three metallic glass alloys of interest for magnetic switches and modulators.

METGLAS 2605SC is an iron-based, high induction alloy made from relatively low cost raw materials. It was originally developed for distribution transformers.

METGLAS 2605CO has the maximum saturation induction obtained by substituting cobalt for some of the iron.

METGLAS 2826MB is an iron-nickel based alloy. The higher resistivity and extremely low coercive force make it potentially interesting for high frequency radar modulators.

Table 1. Properties of METGLAS Alloys.^{1,2}

	2605SC	2605CO	2826MB
<u>Physical Properties</u>			
Composition (atomic %)	Fe ₈₁ P _{13.5} S _{3.5} C ₂	Fe ₆₇ Co ₁₈ B ₁₄ Si ₁	Fe ₄₀ Ni ₃₂ Mo ₄ P ₁₃
Density (gm/cm ³)	7.3	7.56	8.02
Crystallization Temp (°C)	480	430	410
Resistivity (μΩ m)	1.25	1.30	1.60
Ultimate Tensile Strength (G Pa)	.7	1.5	2.4
<u>Magnetic Properties (as-cast)[†]</u>			
Saturation induction (T)	1.57	1.75	1.92
Induction at 80 A/m (T)	.80	.80	.70
Remanance from 80 A/m (T)	.67	.70	.60
Coercive force (A/m)	6.4	6.4	9.0
Curie temperature (°C)	370	415	353
Saturation magnetostriction (ppm)	30	35	12
<u>Magnetic Properties (field-annealed)</u>			
Saturation induction (T)	1.61	1.80	1.9
Induction at 80 A/m (T)	1.54	1.65	1.83
Remanance from 80 A/m (T)	1.47	1.60	1.60
Coercive force (A/m)	3.2	4.0	1.0

* METGLAS is Allied Corporation's registered trademark for amorphous alloys of metals.

[†] Some as-cast properties are influenced by diameter of toroid. Data taken on 42mm diameter toroids.

Magnetic Switching

Several papers mentioned previously discuss the basic concepts of magnetic switching. Recent comprehensive treatments are also available.¹³⁻¹⁵ Only the basic concepts will be discussed here to provide a framework for discussing the relevant properties of metallic glasses.

Basic Magnetic Switches

The non-linear permeability of a square-loop ferromagnetic material allows a saturable inductor to be used as a "closing" switch - that is a switch which delays the application of a voltage to a load as shown in Figure 3. Before the core becomes saturated, the high permeability of the core results in a high reactance and most of the voltage appears across the coil. As the core becomes saturated, the permeability of the core rapidly decreases to near unity and the reactance decreases to a low value thereby applying the full voltage across the load.

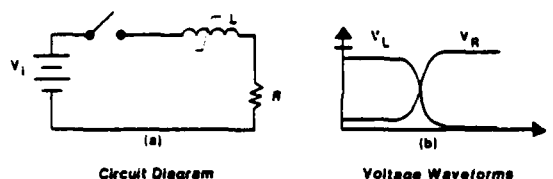


Figure 3. A magnetic switch.

When capacitors are added and several stages are present, we have the familiar Melville line in Figure 4 which compresses the pulse at constant voltage with gain in current.

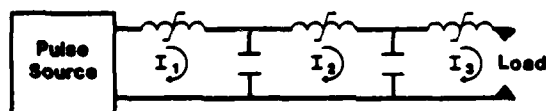
In either case, the hold-off time or time to saturate the core is simply:

$$t = \Delta B N A / V. \quad (1)$$

Where ΔB is the change in induction, N the number of turns, A the cross section area of the core and V the average voltage across the core. To make a compact unit, a large change in induction is desirable. Therefore, materials should have high saturation induction. The "let-through" or leakage current before saturation is the magnetizing or exciting current is related to the exciting field H_{ex} , the number of turns N and the magnetic pathlength l .

$$I_{ex} = H_{ex} l / N \quad (2)$$

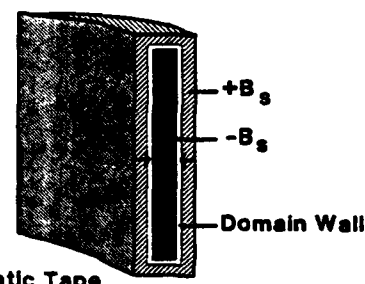
How thoroughly the switch turns on is related to the saturated reactance of the inductor which is both material and geometry dependent. What is desirable, then, is a square-loop material with high saturation induction, low losses and low saturated permeability. The first two properties imply a high unsaturated permeability.



Peak voltage in each stage constant
Current gain \approx Pulse Compression
Energy transfer efficiency ≈ 1

Figure 4. Series magnetic pulse compressor.

The behavior of a thin metallic, ferromagnetic ribbon in tape-wound cores under fast-pulse magnetization is described by saturation-wave theory proposed by Ganz.¹⁶ Each layer is divided into three regions shown in Figure 5 - a central region, uniformly magnetized in its original state, (shielded by eddy currents); an outer region, saturated in the direction of the applied field; and the domain wall, propagating inward as rapidly as allowed by eddy current shielding. Applying this theory to modulator cores, Nunnally has shown that parameters of interest, leakage current and eddy current losses, scale as the tape thickness squared divided by the resistivity, and the time between inner-wrap and outer-wrap saturation scales as the square root of the same factor, t/ρ .^{4,14} Therefore, thin materials with high resistivity are advantageous. Fabricating large cores from extremely thin materials without plastically deforming them and altering their magnetic properties is difficult. Therefore, high strength is a bonus.



Ferromagnetic Tape

Figure 5. Magnetization of a ferromagnetic ribbon in saturation wave theory.

Geometry

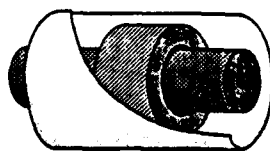
To allow a rapid switching and a fast pulse rise-time, there are several design considerations involving both material and geometry. The saturated inductance of the coil L_s is given by:

$$L_s = \mu_0 \mu_s AN^2 / l, \quad (3)$$

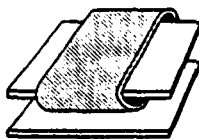
where μ_s is the saturated permeability of the material and l its magnetic pathlength. Therefore, in obtaining volt-second hold off, ΔBNA , in equation (1), it is better to increase A than to increase N and to choose materials with high B_s . Also increasing the magnetic pathlength decreases the difference between inner and outer pathlengths, therefore, decreasing the current rise-time at the sacrifice of increasing leakage current. Of course, stray inductances and inductances of all other circuit elements must be minimized.

Typical low inductance geometries are shown in Figure 6. Coaxial geometries with toroidal magnetic cores are often dictated in very high voltage systems. The capacitance of the coaxial conductors, sometimes with a water dielectric, may form part of the pulse forming line.

Stripline geometries with "racetrack" cores are used in laser modulators where rise-times on the order of 10nsec are often required. The saturated inductance is minimized by using the large l of a racetrack. The time between inner- and outer-wrap saturation is minimized by using magnetic material with low t/ρ as mentioned earlier and by using a relatively low core build so that the outer pathlength is almost the same as the inner pathlength.



Coaxial Conductors
Toroidal Core



Stripline Conductors
Racetrack Core

Figure 6. Low inductance geometries.

Reset

The flux excursion of the core, ΔB , depends upon what method is used to reset the core after saturation. If no reset is used, the core returns to its residual magnetization and ΔB is $B_s - B_r$. Therefore, a low value of remanence is desirable. With a cut core the demagnetizing field reduces the residual magnetization to nearly zero, and ΔB can be as large as B_s . If a pulsed reset is used and the core is saturated in the negative direction and allowed to return to minus remanence, the flux excursion will be $B_s + B_r$. In such a system high values of remanence are desirable. In a circuit without reset, ringing may serve to partially reset the core in a similar fashion. Finally, if a constant dc reset is applied to the core, the full flux swing of twice B_s is available.

Insulation

The method of reset and the necessity of insulation to substantially reduce inter-laminar eddy currents influences the fabrication of cores and whether or not they are annealed. The voltage induced between layers can be calculated for a tape of thickness t and width w by using Faraday's law of induction. A line integral is chosen encircling two adjacent layers and the voltage is assumed to be divided between the two interfaces.

$$V = w t dB/dt. \quad (4)$$

Since the inner and outer wraps do not saturate at the same time, dB/dt will exceed the change in induction divided by the average time to saturation. In a core with a large OD/ID ratio, the peak voltage between layers can easily be twice the average voltage.

Insulation can be applied either as a coating or as a separate inter-laminar layer with margins. Many of the coating methods developed for other ferromagnetic tapes can be used for amorphous metals. Coatings of MgO from magnesium methylete in methyl alcohol form an adherent film.¹⁸ Breakdown voltages of up to 40 volts for multiple coatings may be possible, but MgO is usually used for only a few volts per lamination which corresponds to saturating 50mm by 25 μ m tape with $B_s = 1.6T$ in 1 μ sec. However, care must be used in applying MgO since the methylete tends to hydrate before it is annealed, and most of the information developed on this technique utilized the much higher annealing temperatures of NiFe ribbons.¹⁹

Many other dip or spray coatings can be considered; however, chemical compatibility with the ribbon must be considered and water based processes will cause rust. The thermal coefficient of expansion also must be reasonably close to that of the metallic glass, $5-10 \times 10^{-6}/K$, to avoid stresses which will degrade the magnetic properties.

Vapor deposition of refractory oxides and condensation deposition of polymers such as Union Carbide Company's Parylene coatings have been suggested by several laboratories. However, the cost of the coating apparatus and in some cases the material make these techniques questionable for large switches. Also all coating techniques fail to insure adequate insulation at the edges - where the highest voltage stresses occur.

Interlaminar insulation by co-winding a thin polymer ribbon which is wider than the ferromagnetic ribbon has been successfully used with metallic glasses in large toroids.^{2,5} Mylar films are available in fractional mil thickness as are polyimide films. Polyimide films are much more expensive than Mylar, but can withstand the typical annealing temperatures for metallic glass ribbon of 350-400°C. Either film provides several hundred volts insulation even in fractional mil thickness. The typical breakdown voltage of one mil films is 5000 V/mil for Mylar and 7000 V/mil for polyimide.¹⁹

Fabrication

Most saturable switches use closed loop magnetic circuits. These are ideally suited to metallic glass ribbons which can be wound into toroids or racetracks. If the cores are to be annealed to maximize remanence, the insulation must withstand the annealing temperatures. Also any winding mandrel which is annealed with the core must have a coefficient of thermal expansion less than that of the metallic glass, $5-10 \times 10^{-6}/K$. Due to the extreme strength of metallic glasses aluminum mandrels have been known to buckle during annealing, due to their higher coefficient of thermal expansion. Even the accumulated winding stresses at 20-50 Newtons force can distort mandrels during winding.

Anneal cycles for large cores must be carefully designed to prevent overannealing due to accumulated time-at-temperature during slow heat-up and cool-down. Slowly heating to 50 to 100°C below the anneal temperature can insure more uniform high temperature exposure of all parts of the core. Smaller test cores can be used to test controlled-temperature cycles.

Encapsulating finished toroids after annealing, to protect them from mechanical damage or from rusting if used in a water dielectric, must be accomplished in such a manner to avoid stressing the ribbon. Impregnation is likely to put a face stress on the ribbon and, thereby, a compressive stress via the Poisson's ratio, due to changes in dimensions during curing. A coating of a viscous casting material, over a protective layer such as fiberglass tape provides protection without stressing the core. The exposed insulation margin may also prevent the encapsulant from penetrating between layers during such coating.

Cut cores of metallic glasses have been recently developed.²⁰ Care must be taken in both cutting and in choosing a method of binding. The ribbon, while hard and relatively difficult to cut, does not tend to smear over or the cut edge minimizing problems with shorted laminations at the cut.

Current Research

In the last two years, several papers have been presented with results on magnetic switching with metallic glasses. Several papers have been mentioned earlier, and additional results are discussed in other papers in this session.²¹ Most of these efforts have involved pulse sources for accelerators, lasers or radar. In most cases, magnetic switching is being

investigated due to its potential rep-rate or extended lifetime potentials.

A listing of some of the projects and the principal scientist are given in Table 2. (Completeness is not claimed.)

Table 2. Current Research in Metallic Glass Switching.

LLNL	D. Birx L. Reginato	Accelerators - Magnetic Trigger Systems and High Rep-rate Magnetic Switch ^{2,21}
LANL	W. Nunnally	Laser - Long Life Modulator ^{2,21}
Sandia	P. VanDevender M. Stockton E. Neau	Accelerator - Superpower Magnetic Switch for Long Lifetime ^{3,5}
JPL	T. Pacala J. Laudenslager	Laser - Pulse Forming Network ²²
Maxwell Labs	E. Chu	Laser - Modulator ²¹
ERADCOM	M. Weiner	Radar - Modulator with Saturating Transformer ²³

Prospects

The desire of many pulse-power engineers is to be able to use components produced in quantity for non pulse-power uses. The largest potential user for metallic glasses is the 60Hz distribution transformer market. Its demand for large quantities of core material and the low loss advantages of metallic glasses are expected to provide a large market for metallic glasses within this decade. The economies of larger scale production have already resulted in large reductions in price since kilogram size quantities were first available in 1979 at \$300/kg. These reductions are expected to bring the prices down to \$3-5/kg for transformer grade ribbon by 1986. See Figure 7. Of course, pulse-power designers always want something a little better - in the case of magnetic ribbon, always thinner. Ribbon with special properties will demand a premium, either due to production yield or due to additional qualification procedures.

Current production is nominal 29 μ m ribbon. Iron-based ribbon of 18 μ m has been produced on occasion. Whether 18 or even 12 μ m ribbon will be available commercially will depend upon future production experience and upon demand. By the end of the year, it is planned that 100mm wide ribbon will be available.

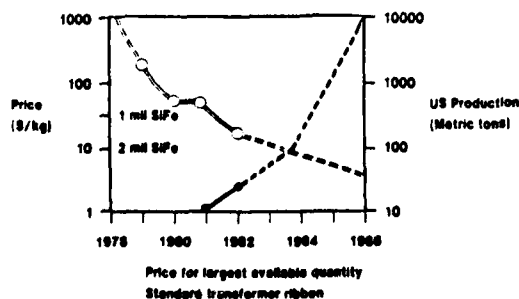


Figure 7. Price and production curves for metallic glass.

References

1. K. Aaland, "Elements of Magnetic Switching," Second Int'l Conference on Energy Storage, Compression and Switching, Venice, Italy, Dec., 1978.
2. D. L. Birx, E. J. Lauer, L. L. Reginato, D. of 3rd IEEE Int'l Pulsed Power Conference, Albuquerque, NM, June, 1981, p. 262.
3. J. P. VanDevender and R. A. Reber, "High Voltage, Magnetically Switched Pulse Power Systems," Proceedings of 3rd IEEE Int'l Pulsed Power Conference, Albuquerque, NM, June, 1981, p. 256.
4. W. C. Nunnally, "Stripline Magnetic Modulators for Lasers and Accelerators," Proceedings of 3rd IEEE Int'l Pulsed Power Conference, Albuquerque, NM, June, 1981, p. 210.
5. M. Stockton, E. L. Neau and J. P. VanDevender, "Pulsed Power Switching Using Saturable Core Inductors," J. Appl. Phys. 53, March, 1982, p. 2765.
6. W. S. Melville, "The Use of Saturable Reactors as Discharge Devices for Pulse Generators," Proceedings Inst. of Electrical Engineers, (London) Vol. 98, Part 3 (Radio and Communication), No. 53, 185, 1951.
7. W. Klement, R. H. Willens and P. Duwez, Nature 187, 1960, p. 869.
8. P. Chaudhari, B. C. Giessen and D. Turnbull, "Metallic Glasses," Scientific American 242, No. 4, April, 1980, p. 98.
9. L. A. Davis, N. J. DeCristofaro and C. H. Smith, "Technology of Metallic Glasses," Proceedings of the Conference on Metallic Glasses: Science and Technology, (C. Hargital, I. Bakonyi and T. Kemeny eds.) Central Research Inst. for Physics, Budapest, 1981, p. 1.
10. D. Raskin and L. A. Davis, "Metallic Glasses: A Magnetic Alternative," IEEE Spectrum 18, No. 11, November, 1981, p. 28.
11. A. Datta and R. J. Martis, "Accelerated Aging Behavior of an Iron Base Amorphous Alloy for 60Hz Applications," to be presented at 3rd InterMag-MMM Conference, Montreal, July, 1982.
12. Allied Corporation "METGLAS Electromagnetic Alloys," Catalog 15M-10/81, 1981.
13. D. L. Birx, "Basic Principles Governing the Design of Magnetic Switches," UCID 18831, Nov. 18, 1980.
14. W. C. Nunnally, "Magnetic Switches and Circuits," Los Alamos National Laboratory Report LA-8862-MS, May, 1981.
15. S. E. Ball and T. R. Burkes, "Saturable Inductors as High-Power Switches," Proceedings of 3rd IEEE Int'l Power Conference, Albuquerque, NM, June, 1981, p. 269.
16. A. G. Ganz, "Application of Thin Permalloy Tape in Wide-Band Telephone and Pulse Transformers," AIEE Trans. 65, April, 1946, p. 177.

17. S. D. Winter, R. W. Kuenning and G. G. Berg, "Pulse Properties of Large 50-50 NiFe Tape Cores," IEEE Transactions on Magnetics, MAG-6 No. 1, March, 1970, p. 41.
18. L. A. Suchoff, "Method of Forming an Adherent Film of Magnesium Oxide" US Patent 2,796,364, June 18, 1957.
19. W. J. Sarjeant, "Energy Storage Capacitors," Los Alamos Scientific Laboratory Report LA-UR-79-1044 March, 1979, p. 4.
20. Magnetics, a Division of Spang Industries, "Cut Cores with METGLAS Alloy Ribbon," Technical Bulletin MCC-100S1, 1982, Butler, PA.
21. IEEE Conference Record of 15th Power Modulator Symposium June 14-16, 1982, Baltimore, MD.
22. "New Switch Could Improve Excimer Laser Performance," Laser Focus, March, 1982.
23. M. Weiner at ARO Workshop on Amorphous Metals for Magnetic Switching, Ft. Monmouth, NJ, November 24, 1981.

DEVELOPMENT OF STRIPLINE MAGNETIC MODULATORS

W. C. Nunnally, J. Power, T. E. Springer,
A. Litton, P. N. Mace, and K. W. Hanks

Los Alamos National Laboratory
Los Alamos, NM 87545

Introduction

Stripline magnetic modulators are a subset of general magnetic modulator systems designed for high-power applications requiring a fast risetime into a low impedance load such as an electric discharge laser. This paper discusses the circuit and system requirements that lead to the use of the low inductance stripline geometry and discusses the experimental program to evaluate several core material, insulation, and fabrication process combinations. In addition, the partition of the observed energy loss into eddy current, other viscous, and hysteresis loss components is discussed.

Design Requirements for Stripline Magnetic Modulators

Magnetic modulators are used to time compress a low power, long duration pulse into a high-power, short-duration pulse. In a resonant transfer of energy, the total mesh inductance L_T is related to the energy to be transferred E_T in time T at voltage V_0 by

$$L_T = \left(\frac{V_0 T}{\pi} \right)^2 \frac{1}{E_T} \quad (1)$$

However, in an impedance transfer between transmission line sections to generate a transit time square pulse, only the risetime T_r is dependent on the total circuit inductance L_T and independent of the voltage or energy and is given by

$$T_r = 2.2 \frac{L_T}{(Z_T + Z_0)} \quad (2)$$

where Z_T and Z_0 are the input and the output transmission line impedances, respectively. Thus low total inductance is required to generate a small risetime in a low impedance load assuming the switching time is much less than the desired risetime. The total inductance is comprised mainly of the saturated switch inductance, which is given by

$$L_T = L_{sat} = \frac{\mu_0 \mu_{sat} N_T^2 A_T}{<L>} = \frac{\mu_0 \mu_{sat} N_T V_0 T_{sat}}{<L> \Delta B} \quad (3)$$

where μ_{sat} = saturated permeability,
 μ_0 = permeability of free space,
 N_T = number of conductor turns,
 A_T = the total core cross section,
 $<L>$ = the average core length,
 T_{sat} = saturation time, and
 ΔB = magnetic flux swing ($B_s + B_r$).

The shortest core or minimum value of $<L>$ for the inductance required in Eq. (3) occurs when $N_T = 1$. For low values of L_T at large voltages and saturation times on the order of 100 ns, $<L>$ can become large and physically can be satisfied in the two geometries shown in Fig. 1. Thus, the following considerations also influence the stripline geometry used.

1. system volume constraints
2. load geometry and coupling inductance constraints
3. capacitance, inductance, current density, or resistance reduction

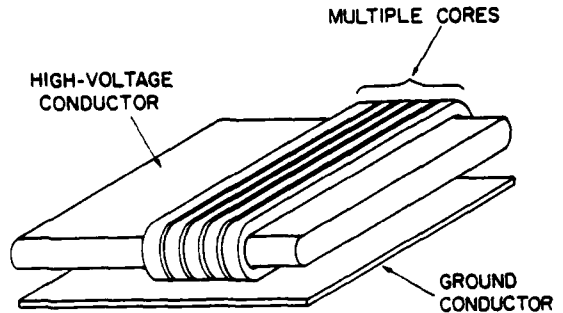


Fig. 1a. Low inductance stripline saturable inductor.

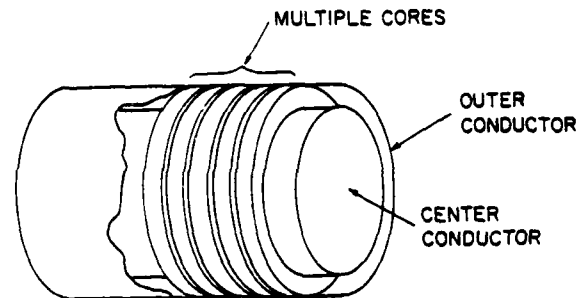


Fig. 1b. Low inductance coaxial saturable inductor.

Circuit Development for Fast Electric Discharge Lasers

The final stage circuit design for a magnetically switched laser driver is shown in Fig. 2a. Simulation of this circuit indicated an unacceptable energy loss to the inductance in parallel with the laser. Another solution to this problem is illustrated in Fig. 2b, where a transmission line with a two way transit time equal to the switch saturation time is placed between the output switch and the open laser load. Thus the energy leaking through the switch is stored in the transmission line, which also serves as a load to saturate the output switch. This arrangement is much more desirable if the laser breaks down instantaneously as the pulse doubles at the open circuit laser load. If the laser has a delay in breakdown or if a still lower impedance is required in the early phases of laser breakdown, the laser can be located at some point in between the output switch and the open circuit end of the transmission (Fig. 2c).

The development program addressed in this paper will evaluate the core material and fabrication/insulation techniques listed in Table I. The specific points of interest include evaluating the difference between annealed and unannealed core

TABLE I
PARAMETERS OF TEST CORE SETS

Core Set	Magnetic Material	Thickness (μm)	Width (cm)	<ε> (m)	Annealed	Insulation System
1	2605 SC	30	1.25	1.5	No	Kapton
2	50-50 NiFe	25	2.5	2.5	Yes	6 coats MgO
3	2605 Co	25	2.5	2.5	Yes	6 coats MgO
4	2605 Co	25	2.5	2.5	Yes	3 coats MgO 1/3 mil Kapton

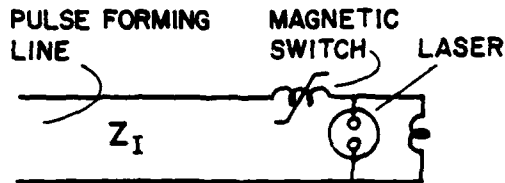


Fig. 2a. Bypass inductor.

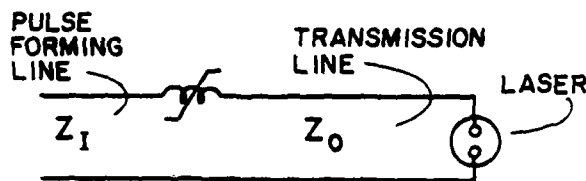


Fig. 2b. Transit time isolation.

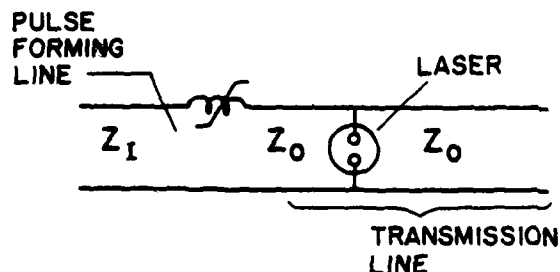


Fig. 2c. Intermediate location for breakdown delay or lower initial impedance.

systems with respect to losses and switching, evaluating the difference between film insulated and coating insulated materials and the accurate measurement of core loss to be partitioned into eddy current, other viscous and hysteresis categories for direction in material choice or future development.

Test System Description

An experimental facility consisting of a water-filled tank with plexiglas sides with the 1-m-wide, double-sided, 1-Q, stripline test circuit of Fig. 3

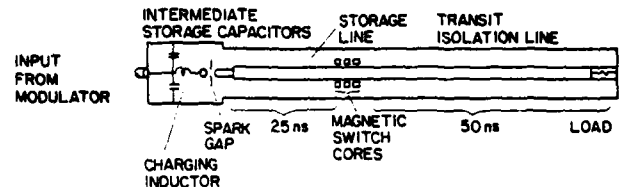


Fig. 3. Magnetic switch test circuit.

was constructed and instrumented to accurately measure core switching and energy losses as well as to develop a magnetically switched laser driver for the Applied Photochemistry Division at Los Alamos. The initial tests were conducted using a single pulse system and varying the switch saturation time by changing the series inductor of Fig. 3 and the initial voltage on the thyatron modulator-charged capacitor bank.

Experimental Procedure

The single-pulse energy loss was measured through the voltage and current waveforms and determined by

$$E_L = \int_0^{T_{sat}} V_s(t) I_s(t) dt \quad (4)$$

where

$V_s(t)$ = voltage across the magnetic switch
 $I_s(t)$ = current through the switch, and
 E_L = the total energy loss due to eddy currents, other viscous processes including spin relaxation damping, and hysteresis.

The voltage current and energy loss data were also calculated numerically in a circuit simulation coupled with a simulation of the magnetic field diffusion into the core laminations. An analytical representation for the local relationship of the magnetic flux density and the local permeability to the diffusing magnetic field were used to include the effect of material parameters. The material parameters include coercive force H_c , the material remanent and saturation magnetic flux densities B_r and B_s , and a viscous loss factor (VLF) defined by

$$VLF = \frac{E_A}{E_E} \quad (5)$$

where E_A is the remaining viscous energy loss and E_E the eddy current energy loss. The voltage drop due to stray (nonferromagnetic) inductance can be

subtracted from the experimental data or included in the calculated voltages, which are compared to the experimental values.

The computer simulation parameters were varied to obtain agreement with the observed waveforms. Variation of the hysteresis parameter (H_c) has a different effect on the simulated waveforms than does varying the effective material resistivity, and thus the hysteresis loss can be separated from the eddy current and similar viscous losses. The simulated eddy current loss is assumed to be accurate, and then the remaining energy loss is attributed to viscous factors.

Energy Loss Partition

Magnetic domain velocity measurements have shown that domain wall movement is resisted by a force proportional to the wall velocity or viscous damping. In addition, effects due to inclusions and irregularities in the material are taken into account by reducing the drive magnetic field H by an amount H_0 roughly equal to the coercive force. The viscous damping parameter, B , consisting of the eddy current contribution, B_E , and the relaxation component, B_R , is usually determined from the wall velocity, \dot{x} , given by²,

$$B = B_E + B_R = \frac{2B_s(H-H_0)}{\dot{x}} \quad (6)$$

The eddy current contribution is usually defined by

$$B_E = 1.2 \left(\frac{4B_s}{\pi c} \right)^2 \frac{d}{\pi \omega} \quad (7)$$

which decreases with material thickness d .

The relaxation contribution to B_R can be defined as

$$B_R = \frac{\alpha(1+\gamma^2)}{4\gamma} \left(\frac{K}{A} \right)^{1/2} B_s \quad (8)$$

where

- α = Gilbert damping constant,
- γ = gyromagnetic ratio,
- K = anisotropy energy,
- A = exchange stiffness constant, and
- B_s = saturation flux density.

If the parameters that determine B_E and B_R are relatively independent of frequency (slowly varying) in the range of interest, the contribution of B_E should diminish as the material thickness is reduced. In addition, the values for B_R in amorphous materials are extremely low; therefore, the spin relaxation damping should be small. In NiFe

materials, the spin relaxation damping is much less than eddy current effects until the thickness is reduced to 1/4 mil (.001 in.).³ The ratio of B_R to B_E can be equated to VLF, which can be determined from a computer fit of experimental waveforms assuming the calculated value of the eddy current energy loss is relatively correct. The relative importance of hysteresis loss can also be determined.

Preliminary Results

A 1- Ω stripline magnetic modulator output stage has been tested that delivers a minimum of 125 J at a peak power greater than 2.5 GW in a 50-ns pulse into a matched dummy load using core set No. 1. The effect of magnetic material losses produces a pulse base broadened to about 400 ns with a switched risetime of 40 ns when the magnetic switch is saturated in 100 ns. A much more plausible design is a system in which the output switch is saturated in more than 300 ns to reduce losses. Three core materials and two core insulation techniques have been evaluated at saturation times between 100 and 300 ns. A NiFe core exhibited such large losses that it has not been considered further. An annealed Metglas 2605 Co core with Kapton insulation remains to be evaluated.

Computer simulations of the magnetic switching or saturation process, (including the effect of material resistivity, material B-H characteristics, and the test circuit) have been used to partition the observed energy loss into eddy current loss, other viscous loss including spin relaxation damping, and hysteresis loss. The computer simulation results were matched to the experimental waveforms by adjusting the B-H curve width (H_c), the values for the effective material resistivity, and the values for the material saturation and remnant flux densities (B_s and B_r). The values of energy loss for the core sets evaluated are shown in Table II.

The NiFe core is not included because of high losses, and the Kapton insulated annealed core set No. 4 has not been delivered by the manufacturer. The ratio of B_R/B_E , determined from a computer simulation match to experimental data, can be used to calculate a Gilbert damping parameter, α using a calculated value of B_E and Eqs. (7) and (8). Values of α , usually determined with a ferromagnetic resonance technique, are on the order of 0.02 gm/cm²-s for metallic glasses. However the values determined from the simulation matches are much larger as shown in Table II. The value of α for core set No. 1 is on the same order of magnitude as those observed in wire saturation velocity measurements $0.1 < \alpha < 0.5$. The large ratio of B_R to B_E for core set No. 3 could indicate that the molybdate coat core insulation has failed and that most of the viscous loss is due to enhanced eddy currents. Evaluating core set No. 4 with Kapton insulation will help verify this observation.

TABLE II

PRELIMINARY CORE EVALUATION DATA

Core Set	B_E (gm/cm ² -s)	B_R/B_E	B_R (gm/cm ² -s)	α	T_{sat} (ns)	Energy Loss (kJ/m ³)			
						Eddy Current	Viscous	Hysteresis	Total
3	4.0	7	28	2.0	100	1.6	11.4	2	15
1	3.8	3	11.4	0.9	100	?	6	4	12
1	3.8	2	7.6	0.6	200	0.7	1.4	4	6

Another important observation from cores tested to date is that hysteresis energy loss is low compared to the viscous loss. In addition, because β_E is proportioned to the material thickness d , additional reduction of energy loss can be obtained by reducing the material thickness until $\beta_R \gg \beta_E$ or $\beta_R/\beta_E \gg 1$. Because β_E is proportional to the material thickness d . With the available material thicknesses, only changing material parameters can reduce the viscous losses appreciably.

Stripline magnetic modulators using long core lengths can be developed to drive low impedance loads (~ 2) with risetimes limited by magnetic saturation losses to about 50 ns when saturated in less than 300 ns. The observed core losses can be partitioned using computer simulation of the magnetic saturation processes. The partitioned loss information can then be used to determine the material thickness that minimizes the eddy current loss contribution to the total viscous loss. Further reducing the total energy loss further requires changing material parameters.

REFERENCES

1. C. Kittel and J. K. Galt, Solid State Physics, Academic Press, Inc. Publishers, New York, Vol. 3, p. 437 (1956).
2. R. C. O'Handley, J. Appl. Physics, Vol. 46, No: 11, p. 4996 (1975).
3. N. Menyuk, J. Appl. Physics, Vol. 26, No. 6, p. 692 (1955).

Metglas - trademark of Allied Chemical Corp.
 Kapton - trademark of E. I. DuPont Co.

MAGNETIC MODULATOR FOR LOW-IMPEDANCE DISCHARGE LASERS*

E. Y. Chu, G. Hofmann, H. Kent, T. Bernhardt

Maxwell Laboratories, Inc.
8835 Balboa Avenue
San Diego, California 92123

Summary

Recent applications of low-impedance discharge lasers in communication, isotope separation, etc., require a pulse power driver capable of operating reliably, as well as efficiently, for 10^9 to 10^{10} shots at repetition rates of 100 to 1000 Hz.

A promising approach for meeting these requirements is magnetic-pulse-compression technology. In this paper, we discuss the design of a 50 kV, 150 J/pulse, 0.5 ohm magnetic modulator for a mercury-bromide discharge laser. The modulator is basically a two-stage series-switching device whose output pulse shaping is obtained by using a 2-section type A or a 6-section line-simulating network. Switching inductor cores are constructed of Metglas® (Trademark Allied Corp.) ribbons with Mylar insulation.

Output pulses with risetimes of less than 40 ns (10-90%) and nominal pulse lengths of 120 ns are observed. Overall system efficiency is found to be approximately 75%.

Introduction

The idea of using saturating reactors as discharge devices for pulse generators was discussed by Melville¹ in 1951. Since then, applications have been largely limited to radar modulators. Recently, new system requirements not easily met by using conventional switching techniques (such as ignitrons, thyristors, and spark gaps), along with the availability of more suitable magnetic materials, have rekindled interest in magnetic-pulse-compression techniques. Birx², Nunally³, and VanDevender⁴ have discussed applications ranging from high rep-rate trigger systems to single-shot super-power generators.

The work we are reporting is motivated by the need for a pulse power driver with:

- Long life (10^{10} shots)
- High efficiency, (>70%)
- Moderate rep-rate (100 Hz)
- Low impedance (0.5 ohm)
- Fast risetime (<40 ns)
- High voltage (50-70 kV)

for a mercury-bromide laser which will ultimately be space-based. The driver presently in use employs an electrically triggered rail-switch for low inductance switching. To extend present rail-switch technology, though, to meet the rep-rate and life requirements of the space-based system constitutes a significant if not impractical switch-development effort. It is conceivable that thyristors may meet the life requirement of 10^{10} shots, but it is unlikely that a single thyristor would allow a sufficiently fast discharge for satisfactory long-life laser performance. However, the possibility of using parallel thyristors is currently being pursued at Mathematical Sciences Northwest.

*Work is supported by subcontract from Mathematical Sciences Northwest, Inc., NRCO Contract No. M00123-81-C-0939.

A more promising approach appears to be a magnetic pulse compression system. Since magnetic switching action does not require the formation of a conduction plasma, it does not have the life limitation normally associated with electrode erosion or cathode depletion, as in gaseous devices. The required starting switch in a magnetic-pulse compression system can be a single thyristor or a solid-state device, depending on trade-offs between cost and operating lifetimes.

To verify the compatibility of the magnetic switching modulator and the mercury-bromide laser, a system with the following performance parameters was constructed:

- Efficiency: $\approx 75\%$
- Impedance: 0.5 ohm
- Output pulse risetime (10-90%): 40 ns
- Nominal output pulse length: 120 ns
- Output pulse energy: 150-300 J
- Rep-rate: 0.1 Hz.

The Modulator

The modulator is a two-stage, series-switching, magnetic-pulse-compression device. Figures 1 and 2 show a block diagram and a simplified schematic diagram of the modulator. It consists of three sets of energy storage capacitors: the primary energy storage capacitor C_1 , the intermediate energy storage capacitor C_2 , and the pulse-forming network (PFN). The three sets of capacitors are chosen to have the same nominal capacitance to maximize energy transfer efficiency between stages.

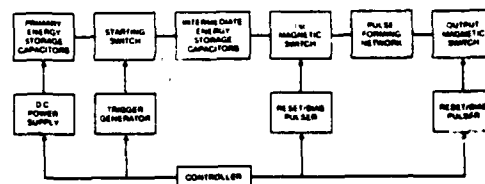


Figure 1. Block diagram of magnetic switching modulator

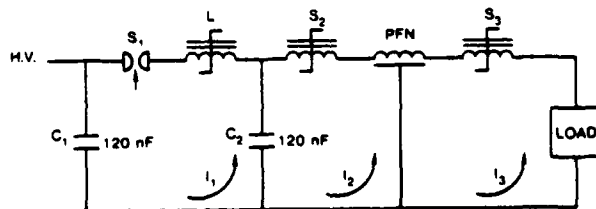


Figure 2. Simplified schematic diagram of magnetic switching modulator

The primary energy storage capacitor, consisting of ten 12 nF capacitors in parallel, is dc charged from the high voltage power supply. C_2 , consisting also of ten 12 nF capacitors in parallel, is resonantly charged by C_1 when the start switch S_1 receives a command pulse from the trigger generator. The magnetic switch S_2 is designed to remain unsaturated while C_2 is resonantly charged, and to saturate when C_2 reaches the desired voltage. The saturation of S_2 allows the energy stored in C_2 to discharge into the PFN. Similarly, the saturation of the output switch S_3 provides a rectangular pulse to the matched load.

L is a saturating reactor normally biased in the forward direction. It is saturated for energy transfer from C_1 to C_2 . Its function is to minimize the surging back of energy from C_2 to C_1 .

Control of the "volt-seconds" of S_2 and S_3 is achieved by bias current pulses through auxiliary windings. The exact bias is determined by the relative delay of the start of the reset/bias current pulse and the triggering of switch S_1 . The amount of bias required depends on the operating voltage of the modulator. The capability to vary the individual switch bias independently allows near-optimum operation of the modulator over a wide range of operating voltages (50 to 70 kV). This important and unique feature aids in the optimization of overall laser performance.

The geometry of the modulator is that of a tri-plate transmission line. The capacitors are arranged symmetrically on both sides of the high voltage bus plate. Current-return bus plates are arranged to minimize system inductance and to form a supporting structure as well as an EMI enclosure for the modulator. A cross section drawing of the modulator layout is shown in Figure 3, and a photograph in Figure 4.

Circuit Components

Capacitors C_1 , C_2

To achieve the high efficiency desired, it is important to minimize the dissipation in every component. To this end, capacitors C_1 and C_2 are of all polypropylene dielectric, extended foil construction. The individual capacitor has seven series sections to achieve the 70 kV voltage rating and each section has three parallel pads to achieve the desired capacitance. To minimize eddy-current losses in the capacitor windings, the number of turns per winding is minimized.

The equivalent series resistance (ESR) of each 12 nF capacitor is estimated to be less than 0.2 ohm, as determined by the differential measurement

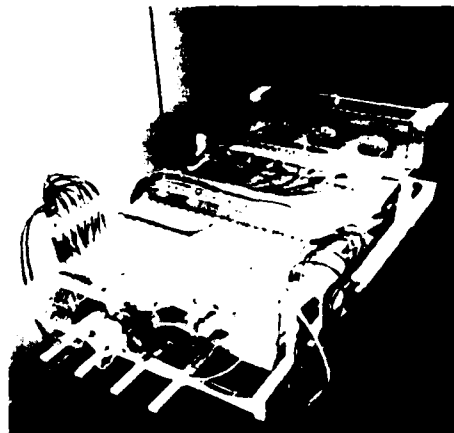


Figure 4. Photograph of magnetic modulator

technique. Based on these measurements, the energy dissipated in C_1 is expected to be less than 0.5%, and in C_2 less than 2% of the initial stored energy in C_1 .

Spark Gap S_1

A spark gap is chosen as the start switch for the present low rep-rate system as a matter of convenience. The spark gap is a conventional, three-electrode, 100 kV Maxwell switch (Model Number 40144). Triggering is achieved with a nominal 8.5 ns risetime, 50 kV trigger pulse. Jitter associated with the closure of S_1 is less than 2 ns.

For the 100 Hz, space-worthy system, the spark gap is expected to be replaced by one or more high voltage SCR stacks, voltage step-up transformers and additional pulse compression stages.

Magnetic Switches S_2 , S_3

The switching inductor cores are 1-meter-long "race-tracks," as shown in Figure 5. These cores are tape-wound cores constructed of 1650 layers of 1 mil (25.4 μ m) thick, 2 inch (5.1 cm) wide Metglas 2605 SC ribbons. Owing to the high voltage stress up to 300 V per turn during the saturation process between Metglas turns, 0.24 mil (6 μ m) thick Mylar is used, instead of conventional oxide, as insulation between the Metglas ribbons. The width of the mylar ribbon is 2.1 in.

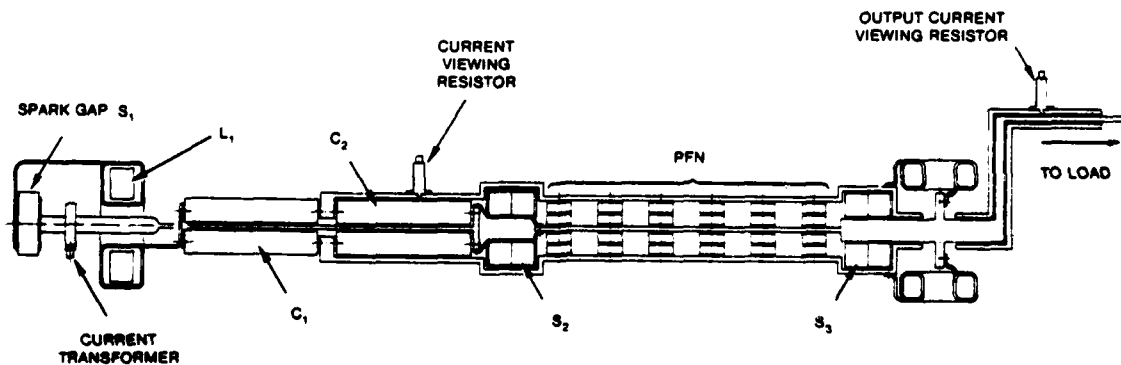


Figure 3. Physical layout of magnetic modulator



Figure 5. The 1-meter-long switch inductor core

(5.4 cm,) resulting in a 63 mil (1.6 mm) overhang on each side of the Metglas winding.

The Metglas and Mylar tapes are wound on a 1-meter-long aluminum mandrel which remains an integral part of the switching inductor core. Size, geometry of the cores, and the physical characteristics of the Metglas ribbons made winding of the cores nontrivial. Successful core winding was accomplished on a special winding machine, designed and built at Maxwell (patent pending) specifically for non-toroidal core manufacturing. The winding machine keeps the mandrel stationary in the vertical plane. A revolving platen winds the Metglas and the Mylar simultaneously onto the mandrel at constant speed, tape tension, and pressure.

Both S_2 and S_3 have magnetic cross-section areas of approximately 40 cm² and volumes of 0.01 m³. Switch S_2 has a five-turn winding, whereas S_3 has a one-turn winding. The reset/bias is provided by additional one-turn windings around the ends of the cores for both S_2 and S_3 .

The Pulse-Forming Networks

Two PFNs were designed and constructed:

- A two section type-A network
- A six-section line-simulating network.

Both are nominally 0.5 ohm and deliver 120 ns pulses into a matched load. The two networks are shown schematically in Figure 6. The line-simulating network has more sections and therefore, in principle, delivers flatter and faster-rising pulses. On the other hand, the variable inductor (see Figure 6a) in the two-section type-A network can be more easily adjusted to change the slope of the output pulse. Since the laser load is a non-linear, time-varying load, the type-A network may provide a better match for the load because of this adjustment feature.

The Reset Circuit

The basic reset circuit is shown in Figure 7. The 100 μ F capacitor is nominally charged to 300 V.

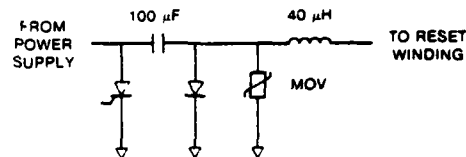
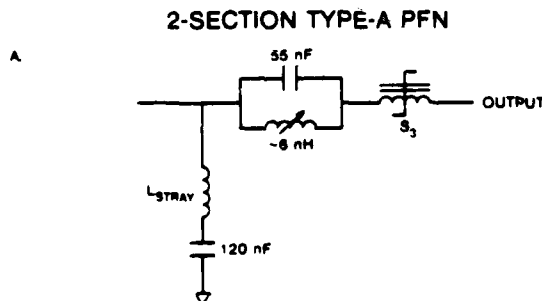


Figure 7. Basic reset circuit for resetting saturating inductor cores

Firing of the SCR results in a reset current pulse of approximately 350 A to the reset winding. The reset current risetime is approximately 100 μ s. Due to the presence of the diode, the current decay time is considerably longer. The spark gap is normally triggered during the decay of the reset current pulse.

Circuit Performance

The modulator has been operated with charging voltages ranging from 50 kV to 70 kV. System performance (efficiency and output pulse shape) is optimized by adjusting the current in the bias windings of each saturating inductor. Overall system efficiency (defined as the ratio of the output pulse energy to the energy stored initially in C_1) varies from 70% to 77% as the charging voltage varies from 50 kV to 70 kV.

Figure 8 shows a typical set of circuit current waveforms corresponding to a charging voltage of 60 kV. The peak dI/dt in the start switch S_1 is approximately 1.2×10^{10} A/s, whereas that in the output switch S_3 is 1.9×10^{10} A/s. Output waveforms into a matched resistive load are shown in Figures 9 and 10.

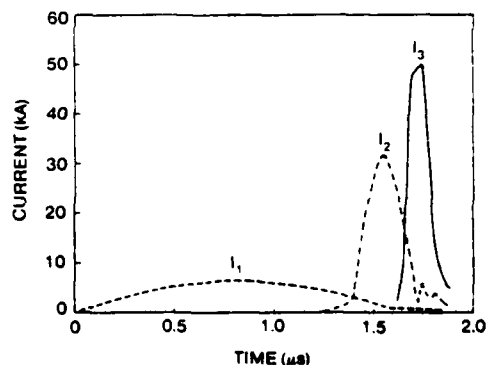


Figure 8. Magnetic modulator circuit currents at 60 kV charging voltage

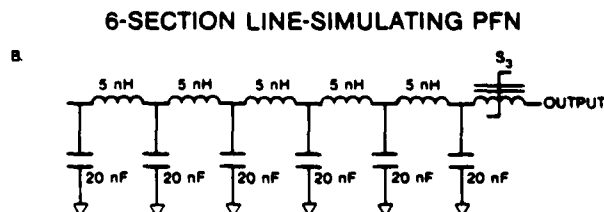


Figure 6. (A) Two-section type-A (B) Six-section line simulating PFN

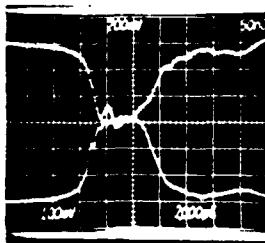


Figure 9. Output voltage and current waveforms with line-simulating PFN. Top trace, voltage 10 kV/div. Bottom trace, current 16 kA/div, time 50 ns/div



Figure 10. Output voltage and current waveforms with Type-A PFN. Top trace, voltage 10 kV/div. Bottom trace, current 19.2 kA/div, time 100 ns/div

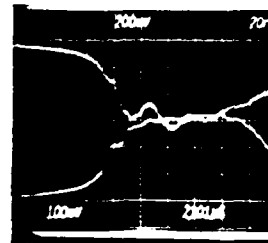


Figure 11. Output waveforms from five consecutive shots at 60 kV charging voltage. Top trace, voltage 10 kV/div. Bottom trace, current 16 kA/div. Time 20 ns/div for both.

By integrating the power going into and out of each component, one can determine energy dissipated in various parts of the system. Dissipation in S_2 and S_3 are observed to be approximately 2.3% and 9.6%, respectively. Also, due to the high charging and discharging currents, the dissipation in the PFN is about 5%. Approximately 8% of the initial stored energy is lost in C_1 , C_2 , S_1 , the buswork, and the reset circuit.

Figure 11 shows the overlay of the output voltage and current waveforms for five consecutive shots. Total jitter of the modulator output pulses is estimated from these waveforms to be less than 3 ns.

Discussion

As seen in Figure 9, 10, and 11, the prepulse associated with the output voltage pulse is typically 10% that of the charging voltage in amplitude, when the modulator is operated into a matched load. The prepulse occurs because the current required to saturate the output switch S_3 flows through the load in the circuit as in Figure 2. Since the prepulse is a slower-varying signal than the main pulse, the prepulse amplitude can be reduced by having a shunting inductor in parallel with the load.

The need for an alternate shunting path for the output switch saturation current becomes more severe when the magnetic modulator operates into a discharge laser, because the laser has a high initial impedance prior to the formation of a stable discharge. However, the performance of a simple shunting inductor as a low impedance prepulse current path is inadequate. This is because a low prepulse amplitude and a fast-rising output pulse would require an inductor value so low that the efficiency of the modulator becomes unacceptably low. To alleviate this problem, a transmission line with characteristics similar to the six-section line-simulating PFN can be inserted between the output switch and the laser discharge cavity (see Figure 12). The series transmission line acts as a large shunting capacitor holding the prepulse amplitude to an acceptable level during the discharge of C_2 into the PFN, including even the case when the modulator operates into an open circuit load.

Another solution to the prepulse problem is to connect a transmission line in parallel with the laser load, as shown in Figure 13. With its unattached end shorted, the transmission line will behave as a shunting inductor during the prepulse and a constant impedance during the main pulse. Using a 5 ohm, 60 ns shunting transmission line, this approach has resulted in prepulses with amplitudes less than 20% of the

charging voltage when the modulator operates into an open-circuit load and 10% of the charging voltage when operating into a matched load. Because of the relatively high shunting path impedance, the output switch impedance collapse time is long, resulting in a slow open circuit voltage risetime (about 80 ns). To improve the "turn-on" time of the output switch S_3 , a shunting capacitor of about 20 nF capacitance would be helpful.

Both the series transmission line and shunting transmission line schemes can be implemented simultaneously to yield a lower prepulse. In general, there is a trade-off between the prepulse amplitude and the system efficiency; and the design is often dictated by the maximum acceptable prepulse amplitudes.

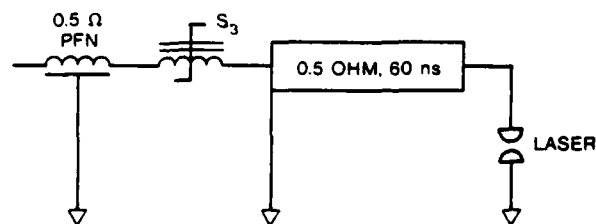


Figure 12. Series transmission line scheme to limit pre-pulse amplitude

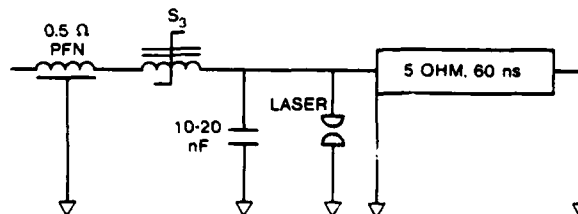


Figure 13. Shunting transmission line scheme to limit pre-pulse amplitude

Conclusion

A 0.5 ohm output impedance, two stage, magnetic modulator that meets all its design goals has been constructed. By varying the bias of each set of switching cores independently, the modulator can be operated efficiently over the 50 to 70 kV range of charging voltages. Although prepulse amplitudes can

be large when the modulator is operated into discharge laser loads, they can be reduced to acceptable levels by using either a matching, series transmission line between the modulator and the load on high-impedance shunting transmission line in parallel with the load.

In general, the satisfactory performance of the magnetic switches makes them desirable replacements for conventional switches (such as rail gaps, thyratrons) in fast pulsers. Their relative high efficiency and complete freedom from conventional plasma/electrode erosion and depletion effects make them prime candidates in long-life rep-rated systems.

Acknowledgements

This work is the result of a concentrated team effort. We gratefully acknowledge the assistance and support of Warren Butcher, William Caton, Elizabeth Lipka, Samuel Lloyd, Richard Robinson, and Roger Uhlenkamp. Discussions with Dan Birx, Thomas Burkes, William Nunally, and Vance Valencia were both stimulating and fruitful.

References

1. W. S. Melville, "The Use of Saturable Reactors as Discharge Devices for Pulse Generators," Proceedings, Institute of Electrical Engineers; London, England; Vol 98, pt 3, 185-207 (1951).
2. D. L. Birx, et. al., "Experiments in Magnetic Switching," Proceedings of the 3rd IEEE International Pulsed Power Conference, p. 262-268, (1981).
3. W. C. Nunally, "Scripline Magnetic Modulators for Lasers and Accelerators," Proceedings of the 3rd IEEE International Pulsed Power Conference, p. 210-213, (1981).
4. J. P. VanDevender and R. A. Reber, "High Voltage, Magnetically Switched Pulsed Power Systems," Proceedings of the 3rd IEEE International Pulsed Power Conference, p. 256-261, (1981).
5. Modulator presently in use at Mathematical Sciences Northwest.
6. W. C. Nunally, M. Kristiansen, and M. O. Hagler, "Differential Measurement of Fast Energy Discharge Capacitor, Inductance, and Resistance," IEEE Transactions on Instrumentation and Measurement, Vol. 24, No. 2, 112-114, (June 1972).

PULSE SHARPENING WITH A SERIES FERRITE MAGNETIC SWITCH IN LINE-TYPE AND BLUMLEIN MODULATORS*

Sol Schneider
Southeastern Center for Electrical Engineering Education (SCEE)**
St. Cloud, FL 32769

Summary

In fast risetime circuits, 10 ns or less, the current risetime of low pressure switches, such as thyratrons, is limited by the rate of fall of anode potential. This can cause high resistive switch losses during commutation. A series magnetic switch introduced in the circuit initially acts as a high impedance limiting the current flow and then dependent upon the saturation magnetization, mean cross-sectional area, and the applied voltage switches at a predetermined time to a low impedance. This enables the voltage across the thyatron to fall to a low value before substantial current flows and permits faster current risetimes. In addition, since the commutation dissipation is substantially reduced, the anode-grid gas density, which controls the rate of ion generation, is maintained. Experiments have demonstrated the inclusion of a ferrite magnetic switch in a line-type thyatron modulator can materially assist in achieving a fast current risetime. Risetimes of < 3 ns have been achieved using commercial triode and tetrode thyratrons and readily available ferrite material. The technique was also applied to a Blumlein pulser. In addition to a magnetic assist in series with the thyatron, it was necessary to use a magnetic sharpening switch in series with the load to achieve fast risetimes and good pulse shapes. At 20 kV output, a risetime of 4 ns and a falltime of 5 ns were achieved with essentially a flat top.

Introduction

Many applications for millimeter wave, laser, and accelerator systems require fast current risetime, high repetition rates, high voltage pulses. Available switches for use in capacitor energy storage applications do not have the combination of characteristics required for these pulsers. The most versatile and reliable switch for these applications is the triggered hydrogen or deuterium filled thyatron. The thyatron, however, is limited in its ability to meet the current risetime, high repetition rate, and voltage hold-off capability simultaneously. Improvements in the thyatron are under development which will aid, but are unlikely to fully achieve these objectives. An approach to achieve the objectives is to use a hybrid system consisting of the thyatron and magnetic switches.

Background

A short discussion of the commutation process in a hydrogen thyatron is necessary to appreciate why a magnetic assist to delay onset of the main current pulse will provide fast risetimes. This discussion is based on the study^{1,2} performed by S. T. Martin and S. Goldberg, EG&G, under a United States Army Signal Corps contract. The hydrogen thyatron is a positive grid device. The triggering is initiated by the application of a positive grid pulse with high voltage hold-off obtained by operating on the "left side," or low

pressure regime, of the paschen curve. After breakdown of the grid-cathode region and the grid current reaches a critical value, the anode-grid region starts to conduct and commutation starts. The anode voltage falls rapidly and the cathode current rises at a rate determined by the rate of fall of anode potential and the circuit inductance. At low di/dt , experimental observations made on a 4C35 hydrogen thyatron with a reservoir show that the anode potential falls exponentially over most of its range, is relatively independent of anode voltage over a wide range of values, and is strongly affected by the switch pressure. The instantaneous anode potential over several time constants can be described by:

$$e_b = e_{py} - A e^{-t/T_a} \quad (1)$$

where

- e_b = instantaneous anode potential,
- e_{py} = peak forward voltage,
- T_a = anode fall time constant, and
- A = constant

For the 4C35 as e_{py} varied from 2 to 10 kV, the time constant was relatively insensitive to voltage and dropped from 5.1 ns to 3.4 ns. The pressure sensitivity was large with the anode fall time constant varying from 28 ns at 26.7 pascals to 2 ns at 93.3 pascals hydrogen (1 torr = 133 pascals).

Fast risetime characteristics can be obtained by using high pressure, however, at the expense of recovery time. On the 4C35 operated at 100 A and 1000 V the recovery time constant was close to 10 μ s at 35.5 pascals and increased to 63 μ s at 102.6 pascals. For high repetitive rate operation, this becomes a severe limitation. Therefore, it is necessary to compromise on pressure and seek circuit techniques to achieve fast risetimes and high repetitive rates.

The measurements described above refer to gas pressure. Since it is actually the gas density which controls the rate of ion generation, the temperature of the grid-anode region will affect anode fall time. Thus, techniques that reduce anode dissipation will lead to faster anode fall times and rates of rise of current since the gas density is maintained.

Twenty-five years ago³, at ERADCOM we studied a circuit technique to reduce anode dissipation in thyratrons. The commutation dissipation was experimentally determined to be the major source of anode dissipation and is described by expression:

$$P_c = e_{py} i_b P_{rr} \frac{T_a^2}{2(T_a + T_c)} \quad (2)$$

where P_c = anode dissipation, i_b = peak current, P_{rr} = pulse repetition rate, and T_c = circuit risetime. This implies that maintaining a high pressure to minimize T_a was important. Since maintaining a high pressure was often not consistent with obtaining high hold-off voltages and fast recovery characteristics for some operating conditions, another approach

*Support was provided by the Naval Surface Weapons Center, Dahlgren, VA. Facilities for this work was provided by the US Army Electronics Technology and Devices Laboratory, Fort Monmouth, NJ.
†Consultant, Little Silver, NJ

for minimizing anode heating would be to increase T_c . This is not consistent with rise time requirements for narrow pulses. An alternate approach is to delay the initial rise of current, minimizing i_b , until the fall of anode voltage had taken place. The technique investigated was the use of a magnetic assist or saturable reactor in series with the hydrogen thyatron.

The characteristics of a magnetic assist are a function of the hysteresis loop for the material used. Figure 1 depicts a major loop for a ferromagnetic material. The flux density in gauss, is plotted as a function of the magnetic field, H in oersteds. When a magnetic field is applied in the forward direction, B increases in a somewhat linear fashion and then saturates. During the rising portion of the curve, the permeability, μ is given by the derivative of B with respect to H . During this interval the element appears inductive where the inductance is proportional to the permeability, and opposes a change in current. In the saturated region the derivative of B with respect to H approaches zero and, correspondingly, the inductive effect of the material vanishes. The same analysis holds when the applied magnetic field is reduced and then reversed in direction.

Probably the most straight forward and simplest design is to surround a current carrying conductor with a ferromagnetic material. A straight wire assist was used for this study. An assist of this design is simple to construct and is amenable to stacking since cylindrical sections can be added in series. The design tends to reduce stray capacitance and minimizes lead inductance. For this design, delay is given by:

$$t_d = \frac{A \Delta B}{10^2 e_{py}} \text{ } \mu\text{s}, \quad (3)$$

when t_d = delay, A = mean cross-sectional area in cm^2 , ΔB = total change in flux in gauss, and e_{py} = anode forward voltage. The magnitudes of the setting and resetting magnetic fields determine the total change in flux density, ΔB . The magnetic field, H , is given by:

$$H = \frac{4\pi i_b}{10L} \text{ oersteds}, \quad (4)$$

where i_b = conduction current in amperes and L = mean magnetic length in cm. Figure 2 depicts the current and voltage waveforms of a line type modulator operating with and without a magnetic assist. Figure 2(a) shows normal operation and depicts the anode voltage and current. Figure 2(b) depicts the influence of the magnetic assist in series with the load. Anode voltage on the thyatron decays during the period, t_d . A large voltage is developed across the magnetic assist and decays after the period, t_d , when the magnetic assist switches. The current rises to a low value during the interval, t_d , and then rises to full magnitude. Figure 3 shows the effect of a magnetic assist on power dissipation on a 5948 thyatron operating at 15 kV epy. The results are given for three different lengths of Supermalloy. Supermalloy has a ΔB of 12 to 15 kilogauss and a saturation field of 0.02 oersted. In these studies several nickel-iron alloys were used, including Supermalloy, Square Permalloy, and Deltamax. These materials have a large flux swing from 12000 gauss for Permalloy to 28,000 gauss for Deltamax and provide large delays. The materials were rejected in favor of microwave ferrimagnetic materials to provide faster switching times. One material selected was the Transtech type TT 1-3000 magnesium manganese ferrite with zinc substitution. It has a good square loop characteristic and is recommended for operation at K-band frequencies. A supply of this material was available in the form of long cylindrical beads. The beads are 500 mils long with an outer diameter of 200 mils and an inner diameter of 100 mils. A second material available was Ferroxcube

Ferrite Shielding Beads and Chokes. Type 5639031/48 was available in dimensions very close to the TT 1-3000. The beads are 472 mils long with an outer diameter of 220 mils and have double holes, each 35 mils in diameter. The Ferroxcube is a manganese zinc ferrite.

The delay per ferrite cylinder or bead assuming a square wave was calculated using the relationship in Equation (3). At 20 kV, the delay per bead for each material is:

- a. MgMnZn Ferrite - 0.97 ns/bead
- b. MnZn Ferrite - 1.4 ns/bead

The MgMnZn ferrites were used in single fold strings of 8 providing a delay of 7.7 ns/string. The MnZn ferrites were used in strings of 5 with the lead returning thru the second hold and provided a delay of 6.9 ns/string.

Conventionally the magnetic assist is placed in series with the anode of the thyatron and the high voltage side of the pulse forming line. This requires high voltage insulation of the assist from ground for the entire interpulse interval (milliseconds), exposes the assist to the hot anode, and requires differential voltage measurements to observe the assist behavior. For this series of experiments the assist was placed in series with the load. The effect reduces the high voltage insulation requirement for the pulse duration (nanoseconds), limits the heat exposure to the temperature of the load, and by interchanging the load and the assist permits direct measurement of the assist behavior. Both materials have good square loop properties and the saturation magnetization is in the order of 3000 gauss for the type TT 1-3000 and 3300 gauss for the type 5639031/48 material.

In the second phase of this program, this technique was applied to a Blumlein circuit which reduces the voltage requirements for a line-type modulator by a factor of 2. A consequence of this type of circuit is that the switch operates at one-half of the impedance of a conventional line-type modulator. The current risetime, assuming a lossless switch, and non-inductive load, will increase unless the inductance of the circuit can also be reduced by a factor of two. The output of the Blumlein circuit is two pulses forming lines in series discharging into the load. Since the initial risetime of the current pulse is poorer than a conventional line-type modulator, the output pulse requires sharpening to achieve the required risetime. The addition of a magnetic switch in series with the load compensates for the inherently poorer risetime characteristics of the Blumlein circuit. The switch operates in the same manner as the assist in series with the thyatron. It delays the onset of the main current pulse until the peak voltage is across the magnetic switch at which time it switches. The current risetime is then primarily determined by the switching speed and saturated inductance of the magnetic switch and the inductance of the load.

Line-Type Modulator Experiments

In the first phase of this study, the magnetic assist was applied to a hydrogen thyatron line-type modulator (Fig. 4). Direct current resistive charging was used since a small low average current power supply was conveniently available. To obtain fast risetimes, coaxial pulse forming lines were used. The networks consisted of 1 to 3 each RG 214 coaxial cables in parallel to provide network impedances of 50, 25, and 16.6 ohms. Pulse lengths from 25 to 150 ns were used. The results presented will be at the narrow pulse widths since longer pulse widths did not provide sufficient additional data of interest. The loads consisted of Allen-Bradley 2 watt carbon resistors in parallel and had nominal impedances of 45, 27.5 and 15 ohms.

respectively. The negative mismatch was used to provide inverse current after the pulse in addition to the recharge current to reset the magnetic switch. A Cober pulse generator was used in some parts of the investigation when it was established that a stiff grid drive was necessary. The Cober is a hard tube generator with a risetime of a few nanoseconds, 200 ohms impedance, and variable output up to 2000 V. A "top hat" cylindrical return was mounted on the tube to minimize circuit inductance. All measurements were made at repetition rates varying from 10 to 500 Hertz dependent upon the limitations of the power supply. A voltage probe³ with high frequency response was used for all measurements across the load and ferrite string. The probe was used in conjunction with either a Tektronix 7834 or 7904 scope with a 50 Ω input 7819 preamplifier.

Thyratron types used during these experiments were the ITT 8613 triode, the ITT F199 tetrode, and the EEV 1164 tetrode. Except for the 1164, the tubes were all rated for at least 20 kV operation. The use of a ferrite assist improved the risetime to under 5 ns for all the tube types and with a stiff drive reduced the risetime to between 2 and 3 ns. Discussion will be limited to a few cases for the 8613 triode and the F199 tetrode.

The triode is the more difficult switch to achieve a fast rise time because it has no preionizing electrode to ignite a diffuse discharge near the cathode to aid in cathode utilization. In the case of the 8613 it was necessary to age the cathode with a 1 μ s pulse width. It was also necessary to use a fast risetime stiff grid drive of 1000 volts and a raised heater voltage between 5 and 10% to get adequate electron emission to perform definitive tests.

Normal operation of the thyratron is shown on Fig. 5. The sweep speed is 10 ns/half-cm (reduced scale). The trace starting one centimeter higher is the fall of anode potential and takes about ns to fall to a few hundred volts. The load voltage or current takes about as long to peak. During this period about half the energy being switched is dissipated in the anode. This results in anode heating which reduces the anode-grid gas density and slows the rate of ion generation.

Figure 6 shows the result of adding a magnetic switch in series with the load and thyratron. A delay of 15.5 ns was introduced. The two load voltages or current waveforms are shown. The shape of the pulse has changed from essentially a cosine (Fig. 6a) to a square pulse (Fig. 6b). There are instabilities on the top of the square pulse which are attributed in part to noise in the detection system and in part to emission instabilities in the thyratron. This indicates the need for a tetrode structure with a larger current and/or more delay introduced to allow the discharge to utilize more of the cathode. The improvement in risetime is over a factor of five. These measurements were taken at a peak load current and voltages of 630 A and 9.5 kV respectively. The operating voltage was 20 kV with a negative mismatch of 5%.

Tetrode thyratrons performed considerably better and provided clean pulse waveforms. Figure 7 shows the load voltage obtained with an EEV 1164 with the same magnetic assist used for the thyratron. The anode voltage is 13 kV, the maximum voltage the switch can handle. A very stiff control grid drive pulse was also necessary on the this switch for fast rise times.

Line Type Modulator Efficiency

In addition to pulse shape it is necessary to measure the efficiency of the system and to determine dissipation in the various elements. The three major

elements for dissipation measurements are the thyratron, the magnetic switch and the load. A series of measurements were taken using a 20.5 ns 50 Ω coaxial line as the pulse forming line and a 47 Ω resistive load. Three cases are presented for operation at 22 kV peak voltage and 225 A peak current. The ITT F199 tetrode thyratron was used. In this case a nominal control grid drive was satisfactory. Reservoir heater voltage was set at 6.7 volts ac to achieve a fast anode voltage fall time. The ferrites used were the MgMnZn ferrite. The three cases shown are for no assist, an assist with a 15.5 ns delay, and an assist with a 23 ns delay. The voltage waveforms across the thyratron, the ferrite, and the load are shown on Figures 8, 9 and 10. The case with the 15.5 ns delay gives the best load current waveform. From this data the dissipation as a function of time were plotted for the thyratron, the ferrite, and the load and are shown on Figures 11, 12 and 13. Table I summarizes the results and shows the percentage dissipation in each of the elements. As expected from the voltage wave shapes the case with the 15.5 ns delay gave the most efficient energy transfer, 85%. Considering the narrow pulse width of the line, 20.5 ns, the result is exceptionally good. An excessive amount of delay, 23.2 ns, increases the ferrite dissipation by a factor of 2.5 and adds additional inductance which deteriorates the wave shape. Switch dissipation becomes negligible in this case.

Table I. Dissipation

Element	No Ferrites	Ferrites	
		15.5 ns delay	23 ns delay
Thyratron	35.8%	5.4%	0.4%
Ferrite	--	8.9%	23.1%
Load	66.9%	85.0%	77.9%
Total	102.7%	99.3%	101.4%

Blumlein Modulator Experiments

In a conventional line type modulator, assuming the pulse forming line and the load are matched, it is necessary to charge the pulse forming line to twice the pulse voltage delivered to the load. For very high pulse voltages on the load, greater than 100 kV, reliable high repetition rate reliable switches capable of over 200 kV operation are not presently available. Two basic circuit approaches are available to overcome this problem. The first approach is to use a step-up pulse transformer between the load and the pulser. This is commonly used. If, however, fast risetimes, less than 0.1 μ s, are required the inductance of the pulse transformer is a severe limitation. The second approach, which does not require a transformer, consists of charging pulse forming networks in parallel and discharging them in series. The two most common circuits are the Marx and Blumlein configurations. The Marx is used extensively for very high voltage essentially single-shot applications using spark-gaps as the switches. For high repetition rate operation the Blumlein circuit is usually preferred and was specifically studied.

The Blumlein circuit is the two network case of a Darlington circuit. A schematic of the circuit is shown in Figure 14. The circuit works in the following manner. Pulse forming networks #1 and #2 are charged to the desired level by a common power supply through a charging resistor. (A charging resistor consumes half of the charging power. This technique was used for convenience in this experiment. In practice, the charging circuit would be designed for resonant

charging increasing the efficiency from 50% to over 95% and decreasing the power supply voltage by a factor of 2. If operation below resonant frequency is desired, a charging diode is placed in series with the charging inductor to maintain the voltage on the network.) The thyatron is then fired discharging PFL #1. This is equivalent to reversing the potential of this line, thus putting it in series with the PFL #2. The two networks then discharge in series thru the load. If the load has an impedance equal to the series rearrangement of the network, pulse voltage equal to the original dc charging voltage appears across the load. The reversing process results in a fixed time delay equal to half the pulse width between the firing of the switch and the application of pulse voltage to the load. Although the switch only holds-off half the voltage it must pass double the peak current required in a conventional line-type modulator. The Blumlein circuit usually delivers a poorer pulse shape to the load because of the increased loop inductance and the poorer current risetime in the initial discharge.

Since earlier experiments had indicated that a tetrode mode of operation was desirable, most of the experiments were performed with a modified EG&G HY-8 tetrode thyatron, a 20 kV switch. Separate flying leads for the filament and reservoir heaters were provided to permit variation of cathode temperature and reservoir pressure. Initial experiments with excellent results were obtained at normal settings. Since very stiff triggers are used in these experiments to obtain dense plasma in the cathode-grid region, the tube had considerable clean-up which was compensated by adjusting the heaters. The auxiliary grid driver was an EG&G TM-30. The control grid driver was a Cober hard-tube pulser.

The pulse forming lines were made from a single length of RG-214U cable. A two inch section of outer braid was removed to form the two separate pulse forming lines. Resistors were placed around the stripped section to form the load of 83 Ω . The load was deliberately negatively mismatched to provide reset current. A photo (Fig. 15) shows the experimental set-up. On the bench is an HY-8 thyatron with the high voltage end of one Blumlein attached to the anode return and the braid attached to a ferrite assist attached to the cathode flange. On the right three Blumleins with loads are shown. Only one is in use and has a ferrite sharpening switch in series. A Sarjeant type voltage probe is across the load.

The magnetic assist for the thyatron and the sharpening switch were made from the same material and had the same geometrical design previously discussed. The reason is simply that both applications are quite similar with respect to voltage, current, and delay requirements.

The series of figures shown are results obtained from 14 kV to 20 kV with filaments voltage at the normal operational levels of 6.3 Vac. Figure 16a shows the output of the Blumlein (14 kV) with no ferrite assist or ferrite sharpening switch. It is essentially sinusoidal in shape. In Fig. 16b a ferroxcube assist with a 9.9 ns delay was placed in series with the HY-8. The Blumlein output pulse became more rectangular, but still provided an unsatisfactory pulse. A MgMn:Zn sharpening switch with a delay of an 11 ns delay was placed in series with the load. Figure 16c shows the result, an excellent pulse output for a Blumlein circuit.

The next set of scope pictures is almost an idealized result. Figure 17a shows the Blumlein output voltage at 20 kV and 2 ns/minor division sweep speed. Figure 17b shows the pulse with the vertical scale expanded 2.5X. The risetime of the pulse is about 4 ns and the falltime is about 6 ns. The top is not perfectly flat. The first ns is about 10% low.

The loss can probably be attributed to the initial discharge thru the thyatron and may be the result of not optimizing the magnetic assist.

Conclusions

The investigation demonstrated the value of a ferrite magnetic assist in series with a thyatron in achieving a fast risetime. The behavior of the switch system is explainable and predictable. Rise-times < 3 nanoseconds have been achieved with both triodes and tetrodes where no attempt has been made to minimize the inductance or design the switch for high pressure operation. The design of the magnetic assist was based on readily available materials and shapes with no attempt to optimize the magnetic assist material or design.

EG&G has successfully applied the technique to the development of low voltage (6 kV) tetrode thyatrons⁶ for millimeter wave applications. Using the same material and the same cylindrical ferrite design in a linear format, EG&G achieved 1 ns risetime with < 50 μ s recovery. The ferrite assist, as predicted, permitted operation at lower hydrogen pressure to achieve the high repetition rate.

Thereafter, effort was concentrated on the use of magnetic material in a Blumlein pulser. The Blumlein pulser is inherently slower than a conventional line-type pulser. In addition to a magnetic assist in series with the thyatron, it was necessary to use a magnetic sharpening switch in series with the load to achieve fast risetimes and good pulse shapes. At 20 kV, a risetime of 4 ns and a falltime of 5 ns were achieved with essentially a flat top pulse.

Acknowledgements

The author appreciates the support provided by L. Luessen, Naval Surface Weapons Laboratory and S. Levy, US Army Electronics Technology and Devices Laboratory. Bob Burtis and Bill Beattie provided invaluable assistance in performing parts of these experiments.

References

1. S. T. Martin and S. Goldberg, "Research Study on Hydrogen Thyatrons," Final Report, Contract No. DA 36-039 SC-15372, June 1953.
2. S. Goldberg and J. Rothstein, "Hydrogen Thyatrons," *Advances in Electronics and Electron Physics*, Vol. XIV, pps. 207-264, Academic Press, 1961.
3. J. Creedon and S. Schneider, "A Magnetic Assist for High Power Thyatrons," *Proceedings of the Sixth Symposium in Hydrogen Thyatrons and Modulators*, May 1958.
4. C. Eichenauer, "A Magnetic Assist to Hydrogen Thyatron Switch Tubes," *Fourth Hydrogen Thyatron Symposium*, May 1955.
5. W. J. Sarjeant and A. J. Alcock, "High Voltage Probe System with Subnanosecond Rise Time," *RSI*, Vol. 47, No. 10, pps. 1283-1287, Oct 1976.
6. S. Friedman, "Nanosecond Pulser Thyatrons," Second Interim Report No. DELET-TR-80-0282-5, prepared for US Army Electronics Technology and Devices Laboratory, Jan 1982.

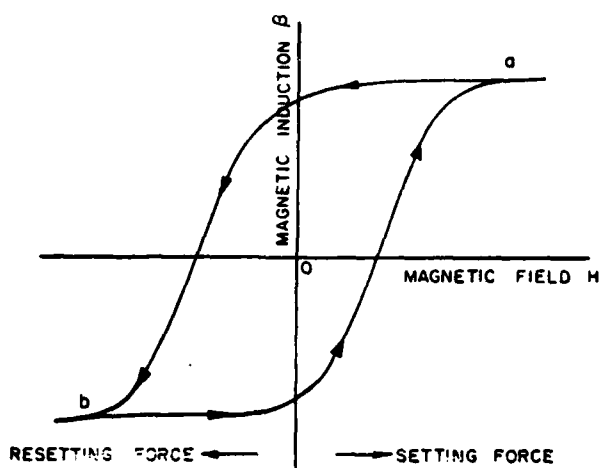


Figure 1. Major Hysteresis Loop for a Ferrimagnetic Material.

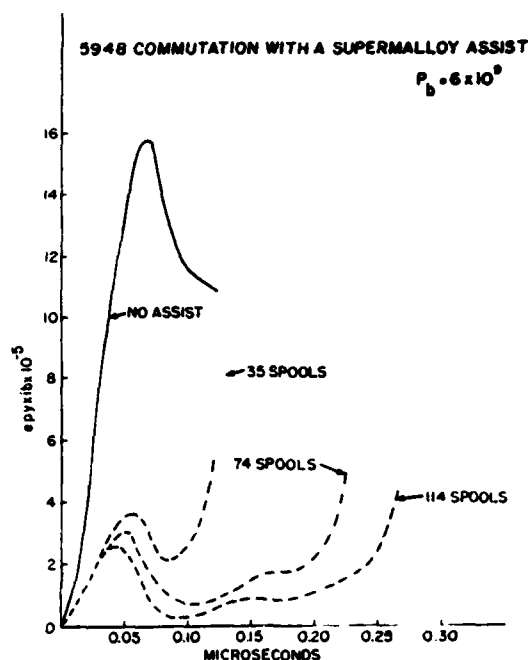


Figure 3. Instantaneous Power Dissipation in a 5948 Thyatron w/o and with a Series Supermalloy Assist. Results are shown for three different delays.

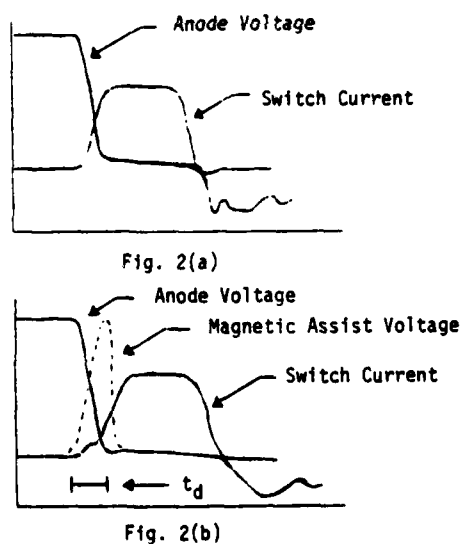


Figure 2. Voltage and Current Waveforms of Switch in a Line-Type Modulator. Fig. 2(a) No Magnetic Assist; Fig. 2(b) With a Series Magnetic Assist.

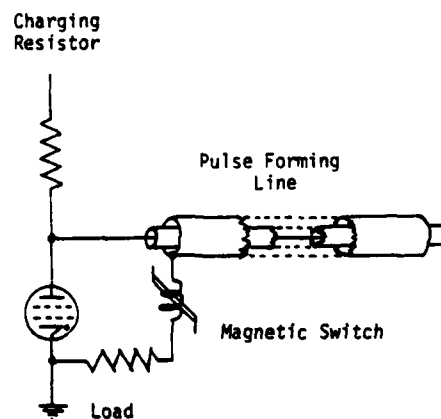
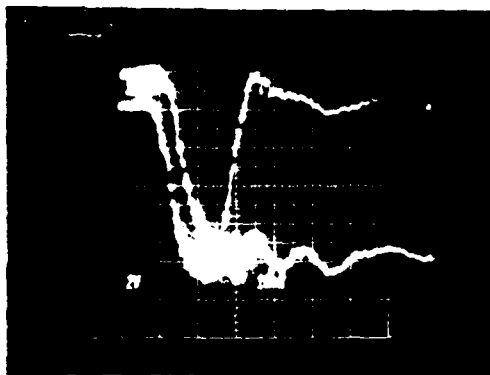


Figure 4. Line-Type Modulator with a Magnetic Switch in Series with Thyatron, Load, and Pulse Forming Line.



Upper starting trace - anode potential
Lower starting trace - load voltage

Figure 5. Current pulse and anode fall of IT&T 8613 w/o magnetic assist. Sweep speed is 10 ns/half-cm.

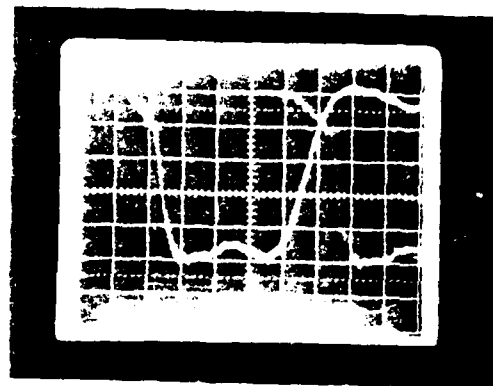


Figure 7. Load voltage using an EEV 1164 tetrode thyatron with MgMnZn ferrite assist. Sweep speed is 5 ns/cm.

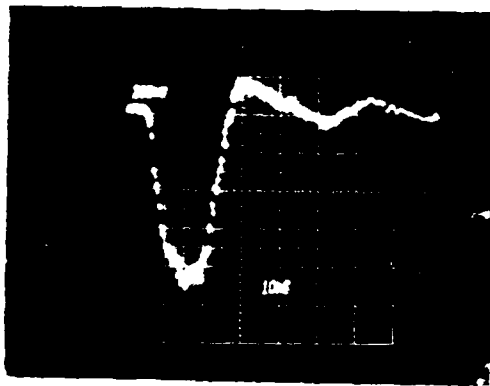


Fig. 6a. Load voltage w/o assist

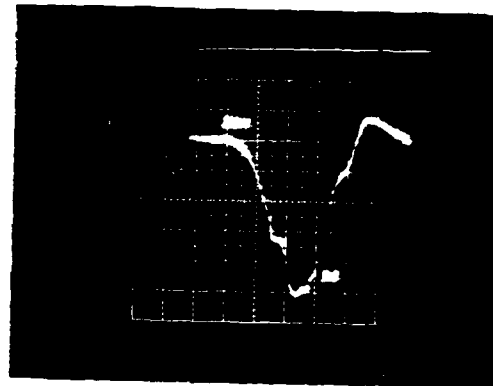


Fig. 8a. Anode voltage

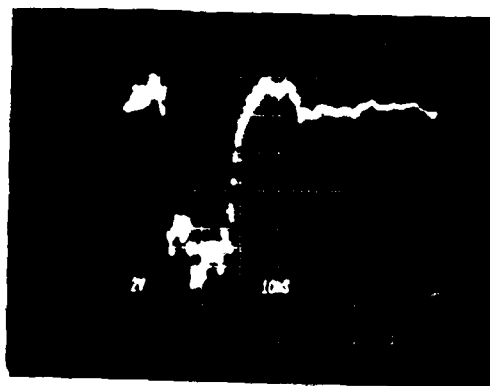


Fig 6b. Load voltage with MgMnZn magnetic assist.

Figure 6. Load pulse using an IT&T 8613 triode with and w/o magnetic assist. Sweep speed is 10 ns/half-cm.

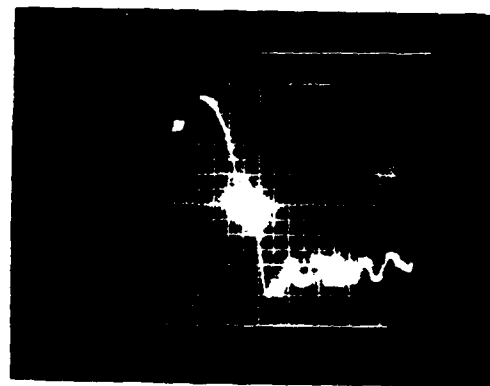


Fig. 8b. Load voltage

Figure 8. Voltage waveforms at 22 kV using an F199 thyatron w/o magnetic assist. Sweep speed is 5 ns/half-cm.

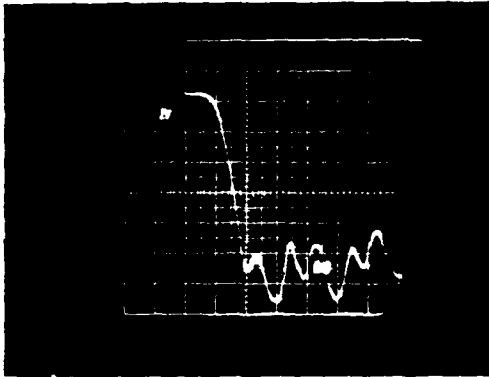


Fig. 9a. Anode voltage

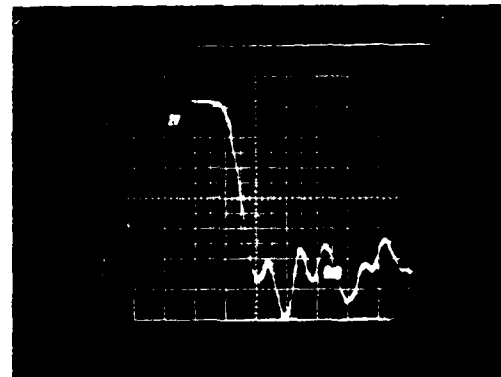


Fig. 10a. Anode voltage

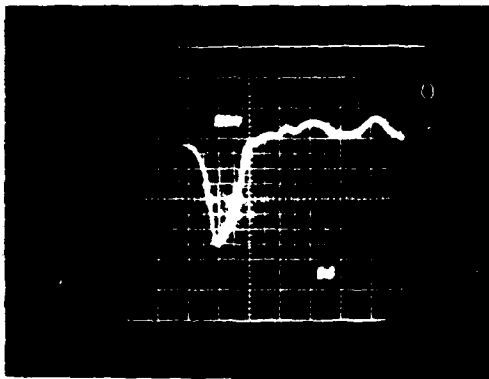


Fig. 9b. Ferrite voltage

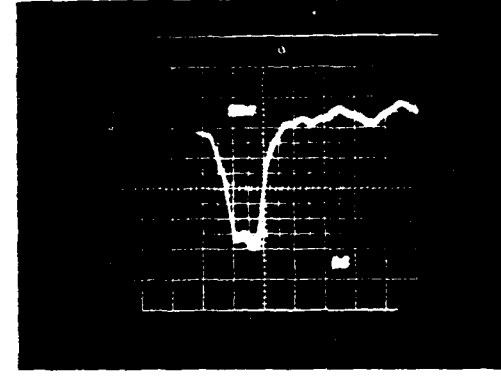


Fig. 10b. Ferrite voltage

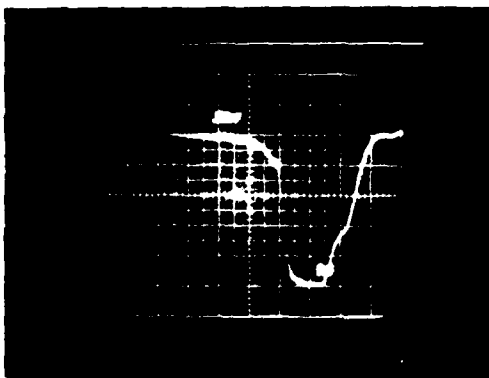


Fig. 9c. Load voltage

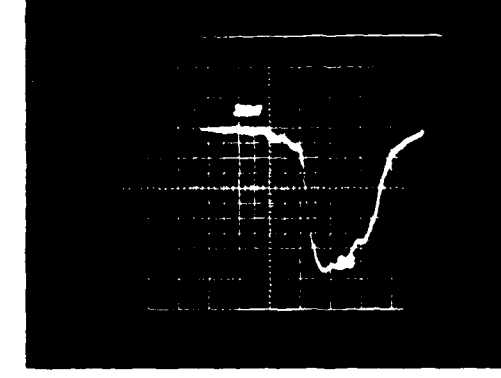


Fig. 10c. Load voltage

Figure 9. Voltage waveforms at 22 kV using an F199 tetrode thyatron with a MgMnZn ferrite assist providing a delay of 15.5 ns. Sweep speed is 5 ns/half-cm.

Figure 10. Voltage waveforms at 22 kV using an F199 tetrode thyatron with a MgMnZn ferrite assist providing a delay of 23 ns. Sweep speed is 5 ns/half-cm.

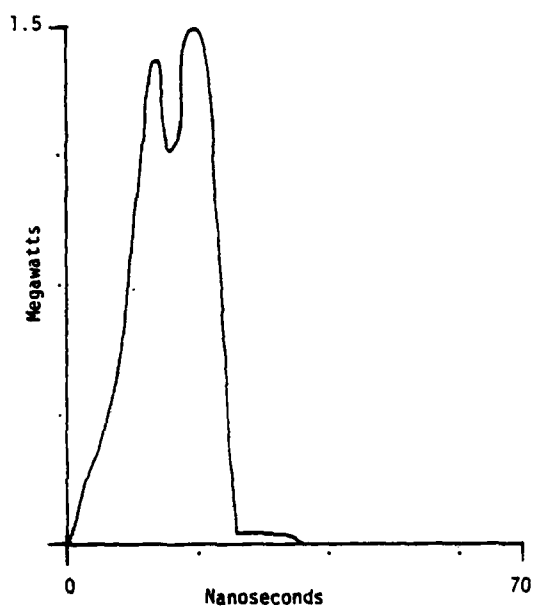


Fig. 11a. Power Dissipation in Switch

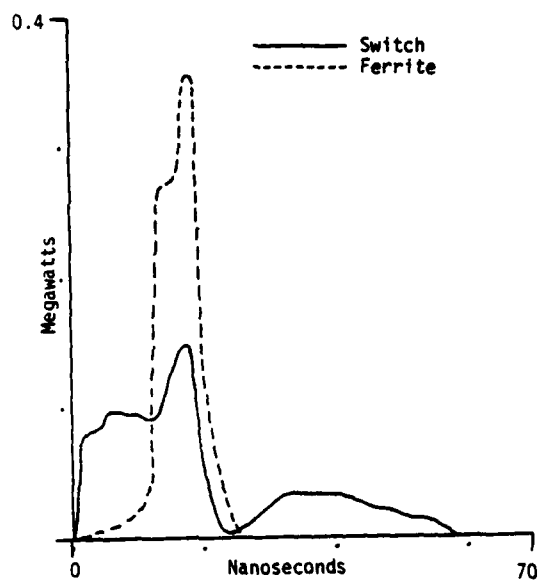


Fig. 12a. Power Dissipation in Switch and Ferrite Assist.

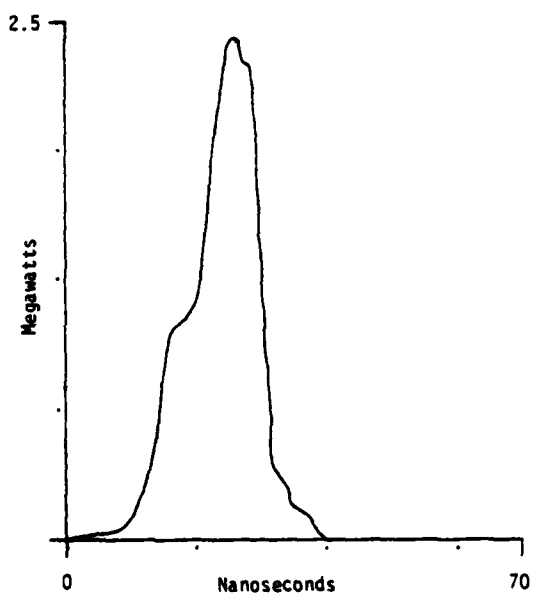


Fig. 11b. Power Dissipation in Load

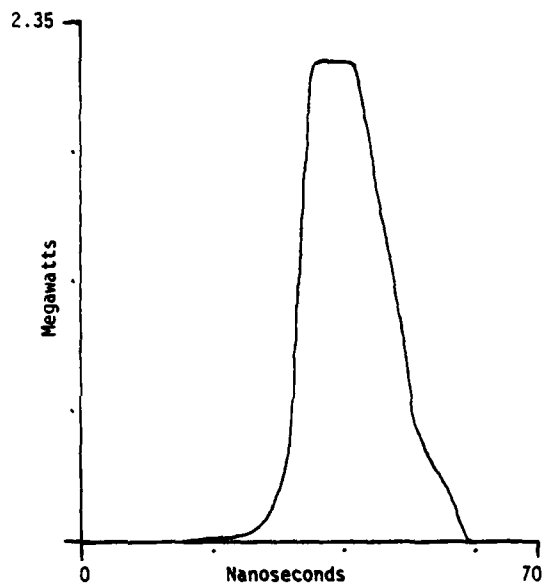


Fig. 12b. Power Dissipation in Load.

Figure 11. Instantaneous power dissipation during the pulse without an assist. Results corresponds to Figure 8 data.

Figure 12. Instantaneous power dissipation during the pulse with a 15.5 ns magnetic assist delay. Results correspond to Figure 9 data.

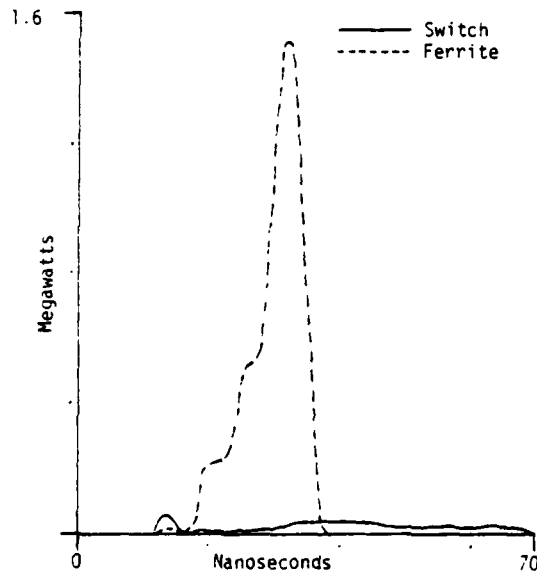


Fig. 13a. Power Dissipation in Switch and Ferrite Assist.

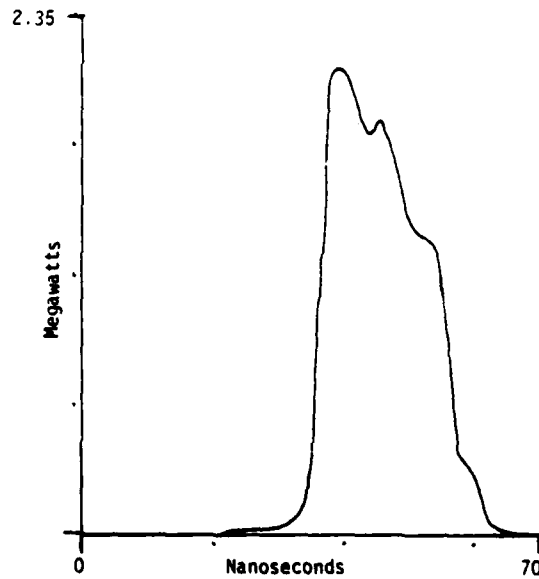


Fig. 13b. Power Dissipation in Load

Figure 13. Instantaneous power dissipation during the pulse with a 23 ns magnetic assist delay. Results correspond to Figure 10 data.

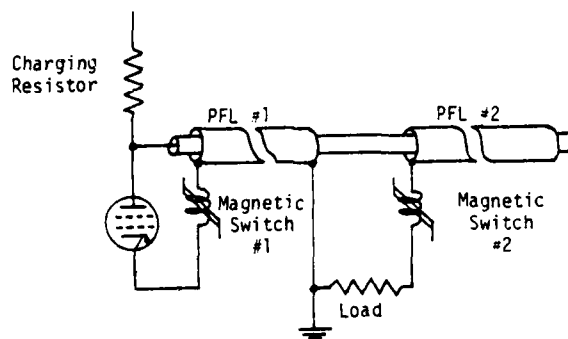


Figure 14. Blumlein Modulator Using a Tetrode Thyatron in Series with a Magnetic Switch and a Pulse Sharpening Magnetic Switch in Series with the Load.

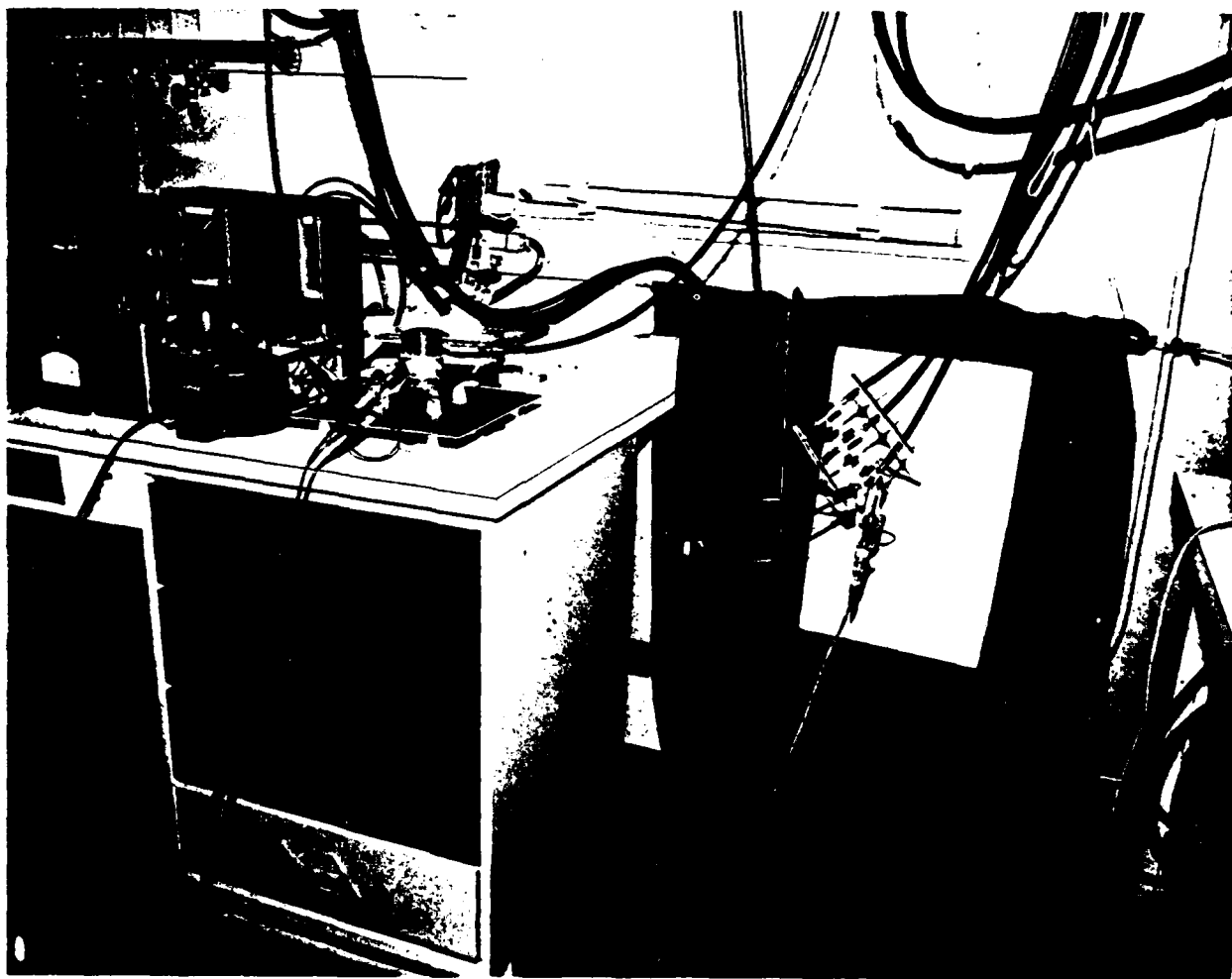


Figure 15. Experimental set-up of Blumlein pulser.

TESTS OF A LOW-PRESSURE SWITCH PROTECTED BY A SATURATING INDUCTOR*

E. J. Lauer and D. L. Bix

University of California
Lawrence Livermore National Laboratory
Livermore, California 94550

Summary

Low-pressure switches and magnetic switches have been tested as possible replacements for the high-pressure switches currently used on Experimental Test Accelerator (ETA) and Advanced Test Accelerator (ATA). When the low-pressure switch is used with a low-impedance transmission line, runaway electrons form a pinched-electron beam which damages the anode. We have tested the use of the low-pressure switch as the first switch in the pulsed-power chain; i.e., the switch would be used to connect a charged capacitor across the primary winding of a step-up transformer. An inductor with a saturating core is connected in series so that, initially, there is a large inductive voltage drop. As a result, there is a small voltage across the switch. By the time the inductor core saturates, the switch has developed sufficient ionization so that the switch voltage remains small, even with peak current, and an electron beam is not produced. A 15 μ F capacitor was used with charge voltages up to 50 kV. The time-to-current maximum was 5 to 8 μ s. The current terminated at about 50 μ s, and the voltage could be reapplied at about 100 μ s.

Introduction

The Livermore low-pressure switch tests were started with the idea of developing a faster repetition-rate replacement for the high-pressure Blumlein switches currently used on ETA and ATA.⁽¹⁾ Measurements, together with theoretical and numerical modeling, resulted in a rather complete understanding of the essential mechanisms involved.^(2,3,4) From the practical point of view, the tests met some but not all of the requirements for an acceptable line switch. Briefly, the current increases exponentially with time (until the voltage collapses), with the exponential rate constant proportional to gas density. Hence, increasing the gas density results in a smaller current rise time. However, there is a maximum Pd (gas pressure times gap distance) above which the switch prefires; i.e., self-breaks before the trigger pulse occurs.

Originally, the Blumlein and the switch were charged in about 20 μ s, and the limiting Pd was about 0.05 Torr cm of N₂ or argon (N₂ had a smaller rate-of-rise at its prefire limited maximum pressure). With a line having a characteristic impedance of $Z_0 = 5.4 \Omega$, an initial charge voltage of $V_0 = 50$ kV, $d = 1$ cm, and the maximum pressure of N₂ or heavier gas, the rise time was ≤ 20 ns. With higher voltages, d had to be increased and, holding Pd approximately constant, P had to be decreased. The rise time was then too slow. A magnetic modulator was installed and used to charge the line and switch in about 0.15 μ s. This shorter charge time had the result that the prefire limited Pd increased about

three-fold. After these changes were made and with $V_0 = 250$ kV, $d = 4$ cm, and the maximum pressure of N₂, the current rise time was 20 ns. The jitter was excellent (≤ 1 ns). The trouble was that the runaway electrons in the low-pressure switch formed a pinched electron beam at about the time that the voltage fell to $V_0/2$ and the current rose to $V_0/2Z_0$. The electron beam damages the anode (vaporizes local regions). The voltage holding recovery time is not reproducible from pulse to pulse, probably because of the anode damage.

In the tests reported here, the role of the low-pressure switch has been changed from that of the final line output switch to that of the first switch in the pulsed power chain; i.e. the switch is used to suddenly connect a charged capacitor across the primary winding of a step-up transformer. An inductor with a saturating core is connected in series with the switch and capacitor so that, initially, there is a large LI voltage drop across the inductor and only a relatively small voltage across the switch. By the time the inductor core saturates and the inductance drops, the switch has developed sufficient ionization, so the switch voltage remains small even with the peak current. Therefore, an energetic electron beam is not produced, there is no anode damage, and the voltage-holding recovery time is reproducible. Numerical calculations predict that the energy delivered to the anode in the case of an unprotected line switch is typically 0.3 of the stored energy, whereas in a typical case of a transformer-capacitor resonant charge circuit, only 10^{-3} of the stored energy is deposited on the anode.⁽⁵⁾

In the present tests, the low-pressure Blumlein switch has been adapted to the resonant charge mode to find the maximum rate of energy transfer that does not cause anode damage and spoil the voltage-holding recovery time.

Apparatus

The circuit used for these tests is shown in Figure 1. The water dielectric was removed from the Blumlein and replaced with SF₆ gas to minimize the capacitance that is not in series with the saturating inductor. R is a damping resistor in place of the transformer load. R was approximately adjusted for critical damping of the LC circuit with L in its saturated state. An ETA switch chassis and step-up transformer is used to apply a test voltage pulse to the LPS at an adjustable delay time. The switch voltage was measured two ways: one method was with the combination R-C divider shown and labeled (VS), the other method (not shown) was using a fast response time capacitive divider (CD) mounted in the outer Blumlein wall. The switch current was measured with the wall resistor (a stainless steel foil resistor in series with the outer Blumlein wall).

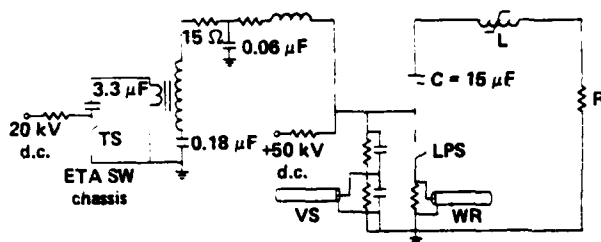


Figure 1. Circuit: L is 3 or 5 turns around a metglas core with a 24-in. o.d., a 10-in. i.d., and a 4 x 1-in. length.

The low-pressure switch cathode is shown in Figure 2. It has a diameter of 10 in. and has 12 trigger electrodes located on a 6-in.-diam circle. Flowing gas enters the gap through an annular crack around each trigger electrode.



Figure 2. A 10-in.-diam cathode with 12 trigger-channels located on a 6-in.-diam circle.

The sequence of events in a test is:

1. A master pulser opens the solenoid valve. The gas flow becomes constant after about 1 ms.
2. At 8 ms, the LPS is triggered by applying 25 kV to the 50-Ω, 60-ns trigger cables.
3. At an adjustable delay time, the ETA switch-chassis thyratrons are triggered to apply the test pulse to the LPS.

Results

Figure 3 shows a set of measurements with 5 series turns in inductor L. The capacitor is 15 μF, and the charge voltage is the maximum, tried (50 kV). The energy stored and transferred, $CV^2/2$, is 18.75 kJ. This is enough to drive the complete ETA accelerator (the gun and 10 accelerating cavities). The quarter-cycle time for the current to rise to its maximum is about 8 μs. The peak current is about 40 kA. The delay time until the core saturates is about 2 μs. The current seems to turn off at about 55 μs (on the 120 A/d sensitivity a "ground loop" current is observed flowing through the wall resistor). The switch recovers its voltage-holding ability reproducibly at about 75 μs. There is no damage to the anode. Using the fast time response ion gauge technique,⁽³⁾ the gas pressure at the trigger electrode location is 0.04 Torr. At the time of the experiment (8 ms), the pressure in the 520-l expansion chamber is 4×10^{-5} Torr. The expansion volume probably could be decreased fifty-fold without causing Pd breakdown in the insulator region.

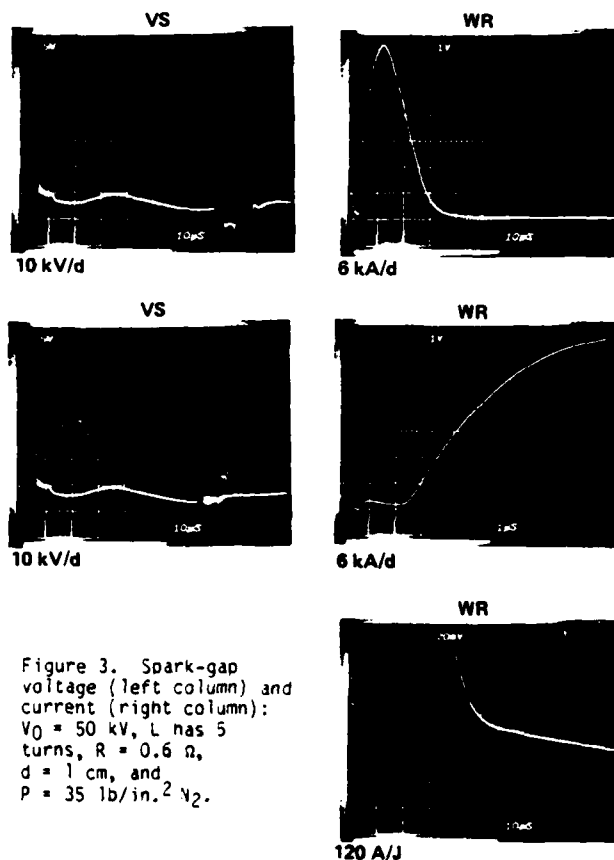


Figure 3. Spark-gap voltage (left column) and current (right column): $V_0 = 50$ kV, L has 5 turns, $R = 0.6$ Ω, $d = 1$ cm, and $P = 35$ lb/in.² N_2 .

Figure 4 shows a similar set of measurements with three turns in L. The charge voltage is again 50 kV. Now, the current quarter-cycle time to maximum is 5 μs, and the peak current is about 100 kA. There is some doubt about this current reading, because the foil wall resistor was damaged by sparking and had to be replaced just after this case. The current turns off at 50 μs. Voltage holding recovery occurs at 110 μs. The gas conditions are the same as those for Figure 3.

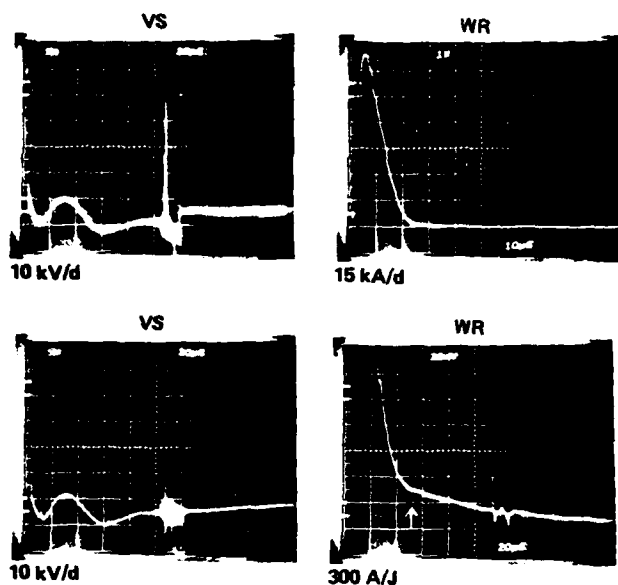


Figure 4. Spark-gap voltage (left column) and current (right column): $V_0 = 50$ kV, L has 3 turns, $R = 0.41 \Omega$, $d = 1$ cm, and $P = 35$ lb/in.² N_2 .

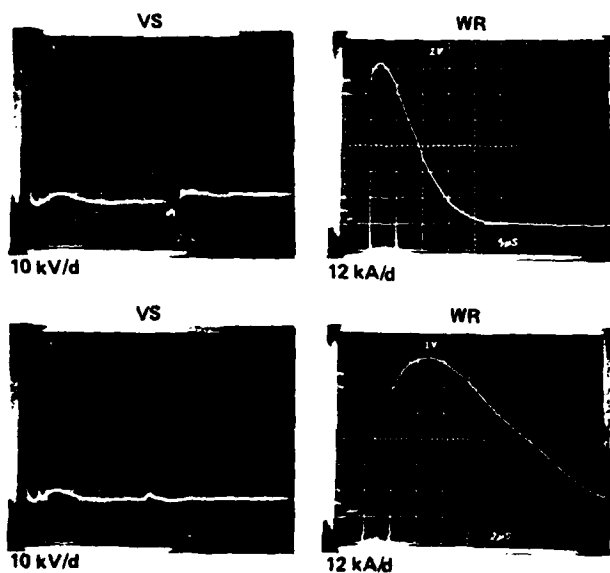
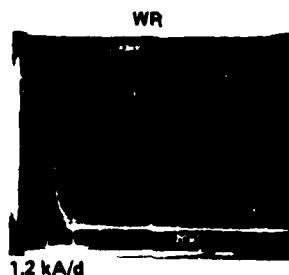


Figure 5. Spark-gap voltage (left column) and current (right column): $V_0 = 42$ kV, L has 3 turns, $R = 0.44 \Omega$, $d = 1$ cm, and $P = 35$ lb/in.² N_2 .



The measurements of Figure 5 are also with three turns in L , but R is increased slightly. The charge voltage is 42 kV. For $V_0 > 45$ kV, the recovery time changed discontinuously from about 110 μ s to ∞ . Also, visually, the discharge appeared pinched. Upon inspection, there was no evident damage to the anode. With three turns and 42 kV, the core saturates after about 1 μ s. The current turns off at about 35 μ s.

Figure 6 shows that the recovery time is independent of charge voltage, unless anode damage occurs.

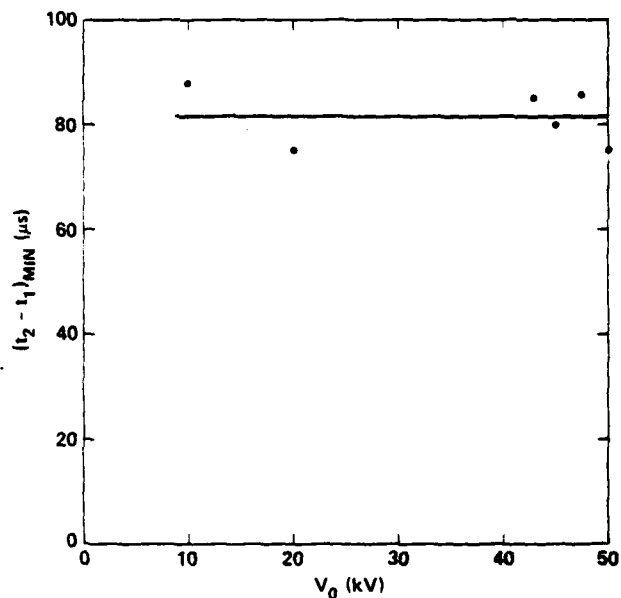


Figure 6. Voltage holding recovery time vs initial gap voltage: L has 5 turns, $R = 0.6 \Omega$, $d = 1$ cm, and $P = 35$ lb/in.² N_2 .

Figure 7 shows recovery time vs valve-orifice pressure for two gap distances. Channel pressure varies as the 1/2 power of gas flow rate and the flow rate varies linearly with orifice pressure. If the recovery time was controlled by the mean time for gas ions to diffuse through the gas to the electrodes, then the recovery time would scale as

$$\tau_c \left(\frac{d}{\lambda} \right)^2 = \frac{1}{P} (Pd)^2 = Pd^2$$

where τ_c is the mean time between scattering collisions of ions with gas molecules, and λ is the corresponding mean free path. Figures 6 and 7 indicate that ion diffusion is involved, although there may be some pinching and anode heating for $d = 2$ cm.

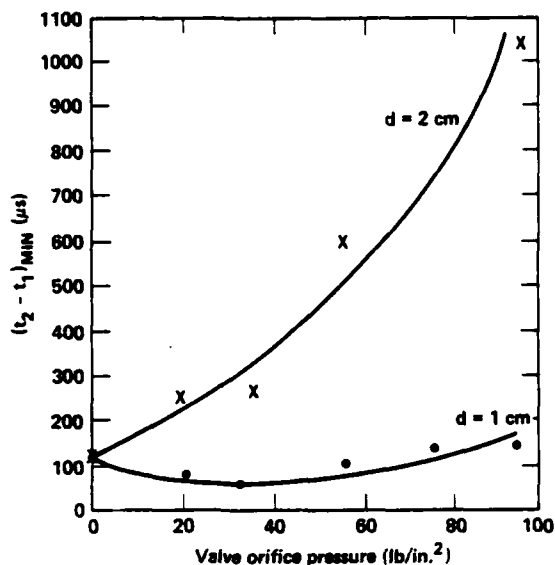


Figure 7. Voltage holding recovery time vs valve pressure: $V_0 = 41$ kV, N_2 gas, and 5 turns around metglas.

Figure 8 shows the voltage collapse and the current build up near time zero. The voltage is measured using the fast-time resolution capacitive divider. The time integral of the IV product (heat delivered to the anode) is approximately

$$(300 \text{ A}) \times (17 \times 10^3 \text{ V}) \times (10^{-7} \text{ s}) = 0.5 \text{ J.}$$

The stored energy $CV^2/2$ was $9 \times 10^3 \text{ J}$.

There was a fractional variation of the charge voltage, V_0 , from pulse to pulse of about 5×10^{-3} . This caused a similar variation of the saturation time of L. This will be corrected in future tests by regulating the charge voltage.

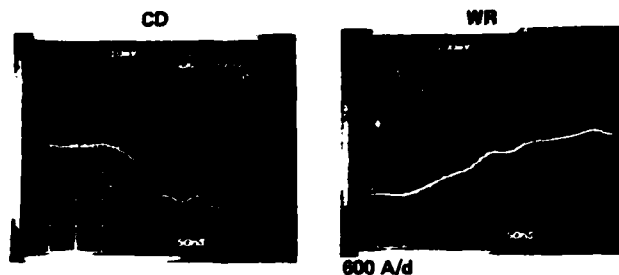


Figure 8. Spark gap voltage vs time (left trace) and current vs time (right trace): $V_0 = 35$ kV, L has 5 turns, $d = 1$ cm, and $P = 35$ lb/in.² N_2 .

References

- (1) E. J. Lauer, Status of Low-Pressure Switch Research and Development, Lawrence Livermore National Laboratory, Livermore, CA, UCID 17998 (December 1978).
- (2) E. J. Lauer, S. S. Yu and D. M. Cox, Onset of Self-Breakdown in a Low Pressure Spark Gap, *Phys. Rev. A23*, 2250 (1981), also Lawrence Livermore National Laboratory, Livermore, CA, UCRL 84216 (1981).
- (3) E. J. Lauer, D. L. Birx, J. A. Masamitsu, R. E. Melendez, I. D. Smith and S. S. Yu, Low Pressure Switch Progress Report, Lawrence Livermore National Laboratory, Livermore, CA, UCID 18848 (November 1980).
- (4) E. J. Lauer and D. L. Birx, Low Pressure Spark Gap, presented at the Third IEEE International Pulsed Power Conference, Albuquerque, New Mexico, 1-3 June 1981, Lawrence Livermore National Laboratory, Livermore, CA, UCRL 85739 (1981).
- (5) Ian Smith, Pulsed Sciences, Inc., private communication (July 9, 1981).

AN IMPROVED 50 KV PULSER DESIGN*

J. A. Oicles, E. S. Fulkerson
Lawrence Livermore National Laboratory
P.O. Box 5508
Livermore, CA 94550

Summary

A compact 50 kilovolt pulser has been developed as a gas switch trigger. This unit combines a grounded grid thyatron with a ferrite loaded step-up transformer to provide the required output voltage. A magnetic switch at the output brings the risetime down to the ten nanosecond range. Unit operation is specified into a 25 ohm resistive load. Integral with the pulser package is the necessary low level support electronics to power the thyatron and to provide trigger and diagnostic functions. Package volume is less than .02 m³.

Introduction

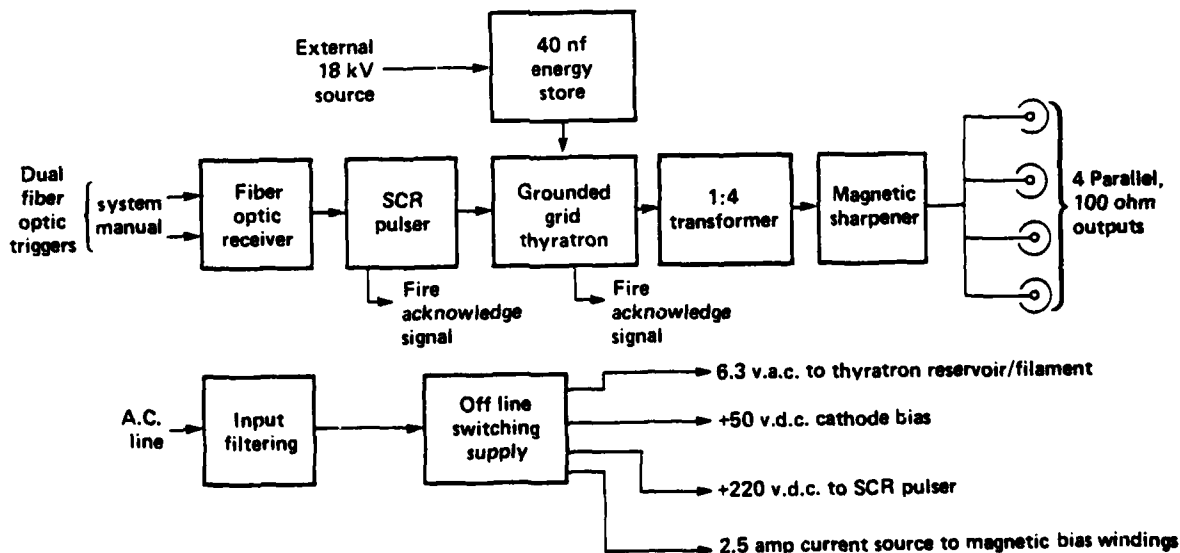
Plasma shutters employing electrically exploded foils will prevent repulse damage to large optics in the Nova laser system. These shutters are presently in an advanced state of development. Switchout of the 3 KJ electrical energy store to the foil is by a four section rail gap gas switch. Triggering the switch is a compact 50 kilovolt thyatron based pulser which has been reported on previously¹. The following provides an update on this technology at the final design point in the project.

Figure 1 provides an overview of the pulser design. The unit accepts dual fiber optic triggers; one the main system trigger and the other a local, manual trigger for test and maintenance purposes.

These triggers are electrically ORed to provide a 50 volt, minimum input to a pulse generator based on small silicon controlled rectifiers. Several changes have recently been made to this circuit resulting in improved noise immunity and lower cost which will be discussed in a future paper. The SCR pulser fires a grounded grid thyatron, which dumps a 40 nf capacitor bank into a fast step-up transformer. New to the design is a simple magnetic switch which compresses the output risetime from the previously attained 22 nanoseconds to the nine nanosecond regime. The resultant output waveform is depicted in Figure 2. Included in the package is a compact regulated power supply to support the unit from the a.c. line, except for the 18 KV high voltage input which is externally supplied from the same source that charges the main plasma shutter energy store.

Output Transformer

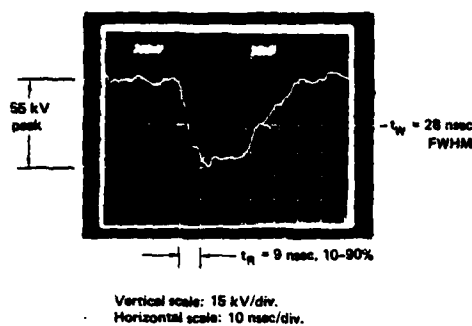
We initially used a manganese-zinc ferrite, Ferroxcube 3C8, in the output transformer because of its availability and high saturation flux density. With this ferrite, we obtained a 22 nanosecond output risetime as previously reported. Investigation showed little risetime degradation through the transformer; the output speed was essentially determined by the turn-on time of the tube. Lacking a simple method of measuring thyatron current in this compact device, we hypothesized that this current was very high due to transformer losses, thereby increasing



UNIT BLOCK DIAGRAM

Figure 1

*This work was performed under the auspices of the U.S. Department of Energy by Lawrence Livermore National Laboratory under Contract No. W-7405-ENG-48.



OUTPUT WAVEFORM

Figure 2

anode fall time. Discussions with A. Faltens at Lawrence Berkeley Laboratory and L. Reginato at LLNL indicated that a high permeability nickel-zinc ferrite would result in lower losses in this application.

We obtained ferrite from two vendors. The first, which has been tested at this writing, is Ceramic Magnetics CMD5005 material. The second, which has just started test, is TDK PE11B. Also considered, but not purchased, was Stackpole C/7D. The materials are compared in Table 1.

We were somewhat surprised to note that performance with the new ferrite was only marginally better with the 3C8; less than 10 percent improvement in output amplitude was obtained, and a risetime improvement only noticable with a 50 ohm load in place of the required 25 ohm load.

Using a special 1.2 ohm resistive dummy load in place of the transformer, our risetime problems were then traced to the thyatron, as discussed below. Our final design does employ the Ni-Zn material, however, despite the lack of significant performance improvement. The high resistivity of the material allows it to be used uninsulated in the transformer, providing greater design freedom, fewer parts (a molded silicon insulator was envisioned for the Mn-Zn ferrites), and hence greater reliability. Another problem encountered with this ferrite was a lack of pulse-to-pulse amplitude repeatability. This was traced to the ferrite coming back to a random point on the BH curve. A reset bias current is therefore provided to place the cores in a predetermined state before each shot. Less than five watts of power are

required using a d.c. current source from the switching power supply. This same current provides the necessary reset to the magnetic output switch.

Thyatron Limitations

The switching device used is an EG&G HY-1102. It is a hybrid thyatron/spark gap with interesting characteristics for single shot and low repetition rate applications. Despite the existence of a metallic vapor arc internally when switching, the device has a lifetime of approximately 10^8 shots in this lightly loaded (10 kA) application.

We selected the tube at the recommendation of G. Krausse of Los Alamos National Laboratory, who is using a similar tube, the HY-1313, in a spark chamber application. He is achieving current risetimes of less than 20 nanoseconds to 30 kA with these devices, over a factor of three faster than the LLNL unit. Subsequent discussions revealed several differences to what initially appeared to be a very similar operating situation:

- 1) The HY-1313 is a special version of the HY-13, a tetrode version of the HY-1102. We have tested the HY-13 and found it comparable to the HY-1102 in di/dt performance. The HY-1313 has a more open grid structure designed to improve risetime, which also appears to degrade holdoff capability. For the plasma shutter application, reliable holdoff is critical.
- 2) Krausse also obtained an additional 20 percent improvement in risetime by pulsing the auxiliary (simmer) grid positive rather than taking the cathode negative as is normally done to trigger the tube.
- 3) Los Alamos triggers the tube with a very energetic source; two kilovolts with a three ohm source impedance. According to Krausse, this yields a 15 percent risetime improvement over a 50 ohm drive system.
- 4) Current rate of rise is load dependent; higher current loads are driven with faster current risetimes. We have also investigated use of the HY-1102 as a Pockels cell driver at the one kiloamp level and risetime under these conditions is only 15 nanoseconds.

Despite the poor risetime, we were reluctant to depart from the simple approach using the HY-1102 with a small SCR trigger. This implementation has been reliable with acceptably low prefire rate and 200 picoseconds peak-to-peak jitter.

TABLE 1

FERRITE COMPARISON

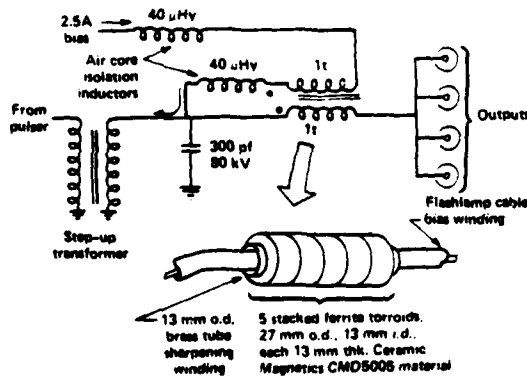
PARAMETER	UNITS	CMD5005	PE11B	C/7D	3C8
Initial Permeability	-----	1200 min	400 min	850 typ	2700 min
Max Flux Density (at 10 Oersteds)	Gauss	3000 min	3000 min	3200 min	4400 min
Coercive Force	Oersted	.23 max	.5 max	.25 typ	.20 TYP
Bulk Resistivity	ohm-cm	10^8 min	10^5 min	10^5	100 approx.

Magnetic Sharpening

A fast risetime in this application is desirable for two reasons. First, in order to maintain the reliability of the 10 unit Nova plasma shutter system, involving ten units, each with redundant triggers, timing of eight different shutter fire events with respect to the input trigger is measured and analyzed with the computer system. Timing discrepancies in excess of five to ten nanoseconds will not degrade system performance but will be an indication that maintenance is required. This threshold discrepancy is short in comparison with a 22 nanosecond trigger. The second factor to consider is the improved performance of the rail gap switches with fast triggers. Multichanneling is enhanced, with resultant lower inductance, lower time jitter and longer life. The rail gap designer has specified a trigger risetime of 10 nanoseconds or less to optimize this effect.

Our improving understanding of the magnetics and of the switch led us to explore a simple magnetic sharpening switch for the unit. Sharpening was added at the secondary side, since the 1.2 ohm impedance at the primary severely restricts the geometry one can use without significantly increasing primary loop inductance. The same Ni-Zn ferrite in the output transformer has good characteristics as a switch, so some smaller cores of CMO5005 material were obtained and tested. The concept was proven in surprisingly short order. Compression to the eight to ten nanosecond regime were attained, along with a ten percent increase in output voltage. The implementation is shown schematically in Figure 3. The series sharpener isolates the main switch from the 25 ohm resistive load, allowing the thyatron to turn on in less than 10 nanoseconds. An initial, high voltage pulse is impressed on the 300 pf capacitor which forms an interim energy store. Saturation of the switch after approximately eight nanoseconds switches out the pulse, with the charged capacitor providing a low impedance source for the leading edge.

Two air core isolation chokes are used to allow the low voltage 2.5 ampere bias source to simultaneously reset both the sharpener and the output transformer as shown in the figure. The effect of bias changes is minimal provided that at least 1.75 amperes is maintained, so this source is unregulated.



MAGNETIC SWITCH SCHEMATIC

Figure 3

Support Electronics

A switching regulator was the logical choice for the low voltage power conditioning in the unit. Both compactness and high efficiency inherent in that approach are important properties since the trigger units are redundant and mount in the compact SF₆ filled pulser housing. The supply design is straightforward, operating directly off the a.c. line and switching at 25 kHz. 6.3 volts at approximately nine amperes are provided for the thyatron filament and reservoir. Remote sensing capability is provided to ensure accurate regulation at the tube. No attempt was made to separately supply filament and reservoir so that optimal operating voltages could be provided for each. It is likely that some performance increase could have been obtained by separately fine tuning filament and reservoir, but this was unnecessary with the addition of magnetic sharpening.

A 220 volt supply is also included for the SCR pulser and optical receiver. A resistive divider from this supply also provides +50 volts of cathode bias. It is interesting to note that the grounded grid thyatron will operate quite well with zero bias between grid and cathode. Occasional prefires do occur under these conditions, however. The filament supply floats on this bias voltage. A high voltage three terminal regulator, the Texas Instruments TL783, provides the 220 volt regulation. A low voltage, unregulated supply provides approximately 2.5 amperes of bias current for the magnetics, with the current limited by the d.c. resistance of the isolation chokes in the high voltage section.

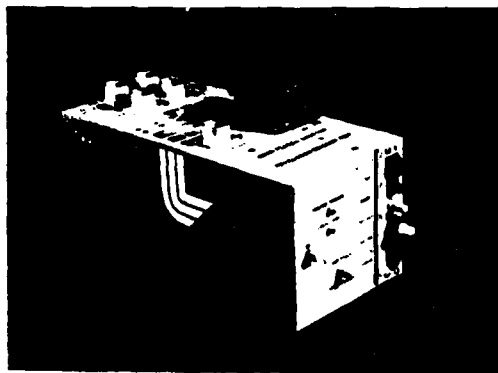
All these supplies must tolerate the noise pulse generated when the trigger unit fires. Various forms of passive isolation filtering, combined with careful packaging attention, ensure that circuit damage does not occur in this severe environment. Two stages of a.c. line filtering are also included to prevent noise conduction to the low level electronics outside the pulser housing.

Packaging

A large effort has gone into the packaging of this unit. A small package was desired, consistent with the limited space in the pulser housing. High voltage is involved, and a solid dielectric system was selected for compactness and simplicity. A separate low level electronics compartment was created to shield the power supply, and the SCR pulser is provided with a separate enclosure within that compartment for double shielding.

The transformer and magnetic switch are insulated using a system of solid dielectrics. Although yielding the desired compactness and simplicity, this approach requires careful attention to detail so that reliability is not sacrificed. Our confidence in the dielectric integrity is reinforced by the excellent performance of two prototypes and several brass-boards, none of which were as conservatively designed or meticulously implemented as the production version. Finally, the solid dielectric system is used only on the pulse side of the unit at low repetition rate; no d.c. high voltage is impressed on the potted unit.

Dow Corning DC-3110 is the encapsulant used. Additional dielectric integrity for the secondary is provided by an acrylic tube and plate system for the transformer secondary, with a compressed silicone gasket between them. The use of compressed elastomer



PROTOTYPE PULSER PACKAGE

Figure 4

gaskets to yield near bulk dielectric strength along material interfaces was extensively investigated² and this technique is used throughout the plasma shutter.

Figure 4 shows the most recent prototype, which is configured similarly to the final unit now in detail design. The prime difference in production chassis will be an increase in height of approximately four cm to accommodate the magnetic switch and to allow additional low level circuit board area. Production dimensions will be 19 cm wide x 23 cm high x 38 cm long. Figure 5 gives two cross sections of this layout.

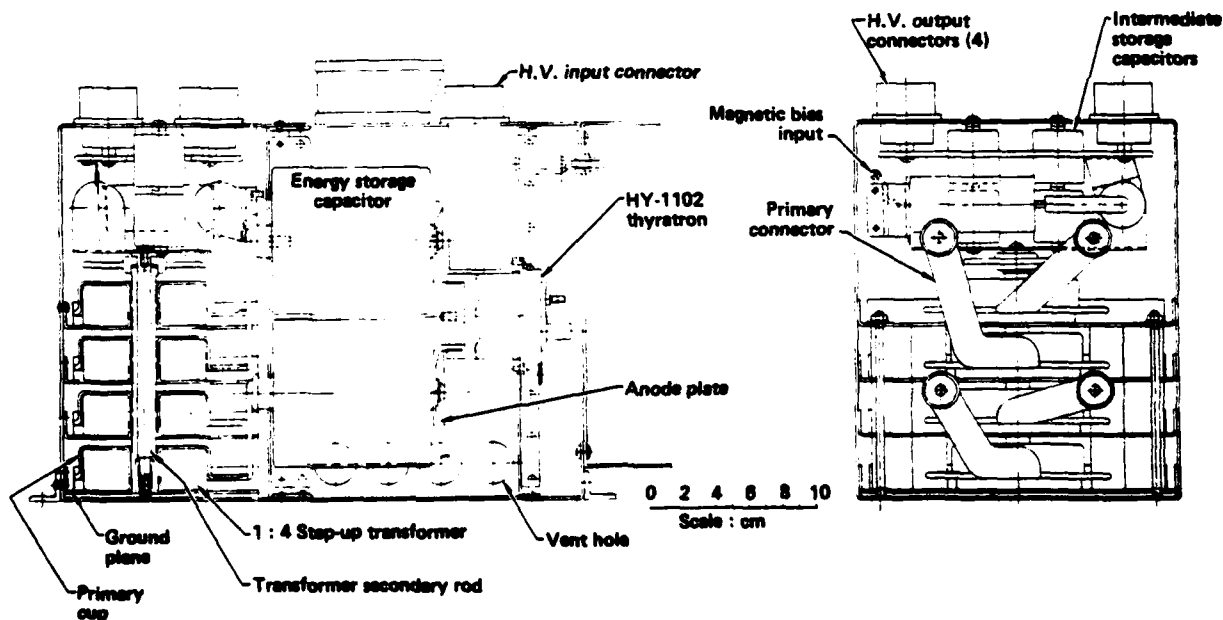
Conclusions

By combining a grounded grid thyatron, a fast ferrite loaded step-up transformer, and output magnetic sharpening, a high performance pulse generator has been developed suitable for triggering large gas switches. It is apparent that this technology could also be applied elsewhere, with higher repetition rates, opposite polarity output, or use with pulse forming networks in place of the simple capacitive energy store possible. Such a compact device has required great attention to detail, particularly in terms of solid dielectric integrity, and extensive testing will be carried out on production prototypes as they become available.

1. J. A. Oicles, E. S. Fulkerson, "A Reliable Trigger Unit for Rail Gap Switches" 9th Symposium on Engineering Problems of Fusion Research, Chicago, Illinois, 1981; UCRL Preprint No. UCRL-86028.
2. R. Anderson, "Final Report - Plasma Shutter Pulser Study Contract PSA111601" American Control Engineering Inc., San Diego, CA, July 1981.

DISCLAIMER

This document was prepared as an account of work sponsored by an agency of the United States Government. Neither the United States Government nor the University of California nor any of their employees, makes any warranty, express or implied, or assumes any legal liability or responsibility for the accuracy, completeness, or usefulness of any information, apparatus, product, or process disclosed, or represents that its use would not infringe privately owned rights. Reference herein to any specific commercial products, process, or service by trade name, trademark, manufacturer, or otherwise, does not necessarily constitute or imply its endorsement, recommendation, or favoring by the United States Government or the University of California. The views and opinions of authors expressed herein do not necessarily state or reflect those of the United States Government thereof, and shall not be used for advertising or product endorsement purposes.



FINAL PACKAGE PARTIAL LAYOUT

Figure 5

HIGH VOLTAGE HIGH POWER PULSE TRANSFORMER

Robert L. Haumesser
Clarence Controls, Inc., Buffalo, NY

Dr. David L. Lockwood
Clarence Controls, Inc., Buffalo, NY

Dr. A. S. Gilmour, Jr.
State University of New York at Buffalo (SUNYAB)

Dr. J. O'Connell
ERADCOM, Ft. Monmouth, NJ

Introduction

This paper is a report on the design, development, testing, and present status of the re-build program of a high power, high voltage pulse transformer.

The unit was originally designed under the auspices of Mr. J. O'Laughlin, AFWL, and was constructed by the Raytheon Corporation. It is not the intention of this paper to discuss in detail the multiple aspects of the transformer design; however, a few general comments on the design of such a unit may be in order.

Design

The design goals of the transformer were as follows:

Output voltage	163 kV
Output current	32 kA Peak
Input voltage	19.2 kV
Pulse width (90%)	10 μ sec.
Pulse rise time (10-90%)	2.0 μ sec. max.
Pulse droop (10 μ sec.)	1% max.
Pulse rep rate	125 pps
Burst mode	100 sec. on; 10 min. off
Volume	0.53 cu. met. max.
Weight	500 kg. max.

The completed unit is an iron core transformer, using copper sheet conductors. Layer-to-layer and winding-to-winding insulation is provided by multiple wrappings of 5 mil mylar, separated by kraft paper. The entire assembly is immersed in a liquid dielectric (ethylene glycol).

Figures 1 and 2 show the completed unit. The large unit to the right in these figures is a transformer built to essentially the same specifications, but designed conservatively with no low-weight goals. That unit weighs approximately 10,000 lbs.

Figure 3 is a view of the core-coil assembly before immersion in the dielectric tank. The unit uses a cut core (C-core). These are two coils in parallel, one around each core leg. The parallel high voltage terminations can be seen at the left of the structure. The feed-throughs on the top cover are utilized for a distributed primary input, in order to maintain a low inductance feed path.

Considering the enormous peak power levels involved in such a device, it might be thought that thermal consideration would present a predominant design limitation. However, because of the low duty cycle (0.125% on during burst), and the long period between bursts, it is possible to design the units under adiabatic conditions (total lost energy absorbed in the temperature rise of the core and coils during the burst) and still obtain reasonably sized conductors.

A more difficult problem is to obtain a design exhibiting a low enough leakage inductance to achieve the required pulse rise time. The leakage inductance design goal for this transformer was 0.1 microhenry maximum. The leakage inductance of a layer-wound coil may be estimated from the expression

$$L = 3.19E-8 N^2 l/n^2 h \left[\frac{\epsilon_{Cu}}{3} + \epsilon_{Sp} \right]$$

where L = leakage inductance, henrys

N = number of turns

l = mean length per turn, inches

n = number of interleaves

h = height of conductor layer, inches

ϵ_{Cu} = total thickness of conductor, inches

ϵ_{Sp} = total thickness of insulation between windings, inches

Leakage inductance can be reduced by minimizing the number of turns, the mean length per turn, and the conductor and insulation thickness, or by maximizing the number of interleavings and the conductor height. However, these parameters are inter-dependent, sometimes in an indirect fashion. For example, increasing the number of interleavings reduces leakage inductance, but it also increases the total inter-winding insulation thickness and the mean length per turn, both of which increase the leakage inductance. Because of their effect on the core window area and form factor, the total transformer size and weight are also strongly dependent on the values of these parameters. Their selection and evaluation form a large part of the design process.

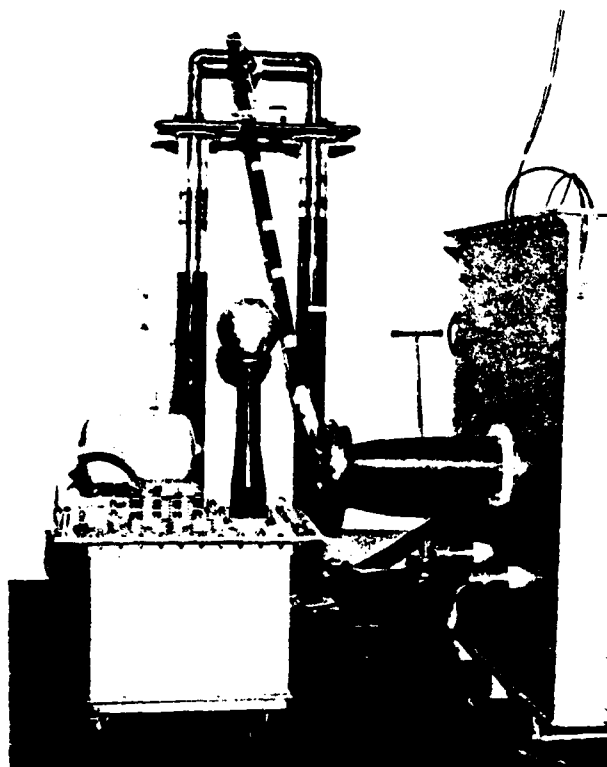


Figure 1. 5 GW Pulse Transformer

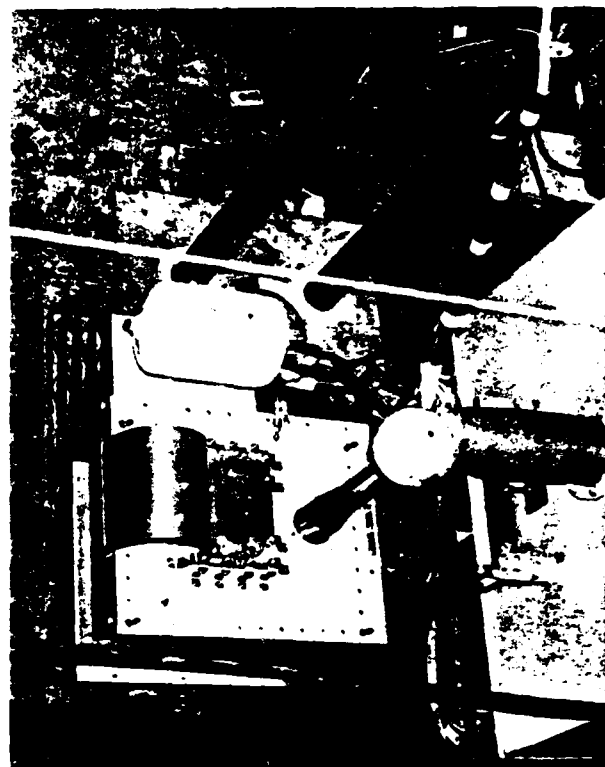


Figure 2. 5 GW Pulse Transformer
Top View

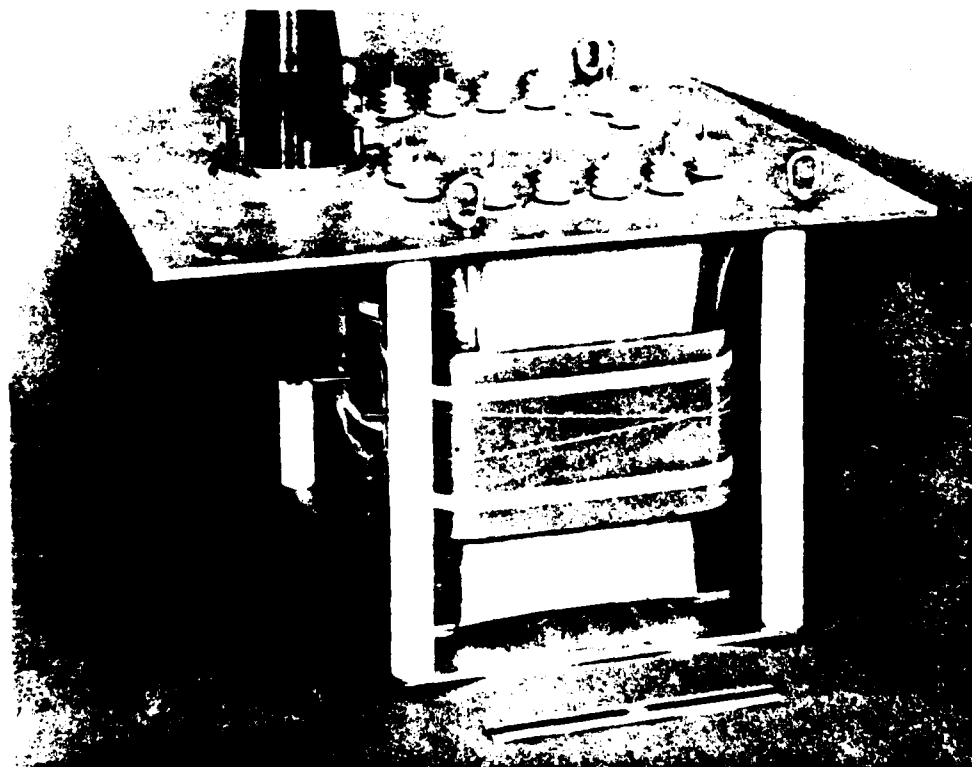


Figure 3. 5 GW Pulse Transformer, Core-Coil Assembly

Testing

Following completion of the build and checkout of the transformer, it was shipped to U.S. Army ERADCOM, Ft. Monmouth, New Jersey, for testing.

High voltage/high power test of the iron core transformer utilized a brassboard line type modulator. Initially, only 3 one megawatt average power modules of the multimewatt device were used. The test plan was to first evaluate high voltage performance before proceeding to high average power levels. To that end, charging chokes totaling 9.5 henries were used to obtain a resonant frequency of 6.8 Hz. Relevant pulser characteristics are given below.

PULSER CHARACTERISTICS (3 MODULES)

Peak Voltage	40 kV
Energy	24 kJ
Peak Current	120 kA
Pulse Width	11 μ sec
Rise Time	1 μ sec
Pulse Rep Rate	6.8 Hz
Impedance	0.167 ohm

The secondary of the pulse transformer was connected to a low inductance copper sulfate load with a nominal impedance of 12 ohms. The transformer was provided with a separate bias reactor during the bulk of the testing to be described to provide 50 Amps dc of core reset.

The voltage was increased slowly until 8.1 kV was measured at the primary of the pulse transformer. Figure 4 shows the load current and voltage obtained at this point. The measured secondary voltage was 70 kV giving a calculated step-up ratio of 8.7. The load current was 6 kA. The rise time from the 10% to the 90% point was 2.2 μ sec. and the fall time over the same interval was 4.5 μ sec.

The first indication voltage breakdown inside the pulse transformer occurred when the secondary voltage reached 106 kV at a load current of 9.5 kA (Figure 5). The power was shut off after a breakdown was heard in the transformer. No external signs of arcing were visible and the test continued. On the next run, where the voltage was increased in a stepwise fashion, two breakdowns were heard at a secondary voltage of 117 kV and a load current of 10.2 kA. After the two failures, the pulse transformer continued to run below secondary voltages of less than 100 kV. The last attempt to increase the voltage reached a secondary voltage of 122 kV and a load current of 9.8 kA before a series of breakdowns occurred. The slightly lower value of load current here is due to higher impedance of the liquid load. After this failure, glycol was seeping out of the seal on the transformer case and testing was terminated and sent to Clarence Controls, Inc. for failure analysis.

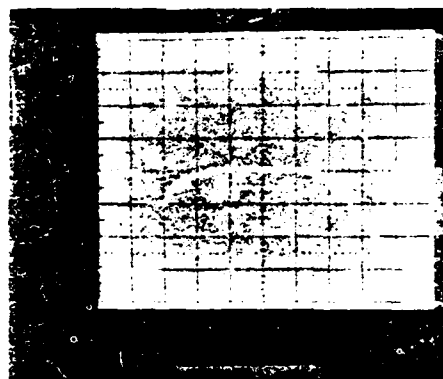


Figure 4

UPPER TRACE: Load Voltage, 20kV/cm
LOWER TRACE: Load Current, 2KA/cm

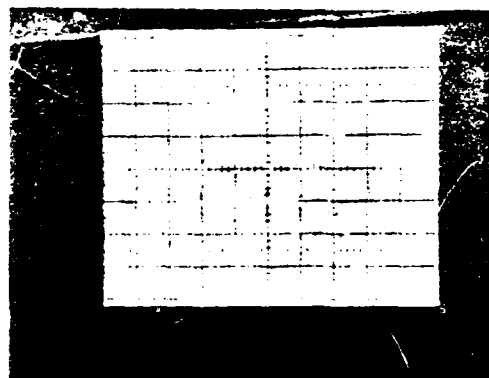


Figure 5

UPPER TRACE: Load Voltage 50kV/cm
LOWER TRACE: Load Current 5kA/cm

Failure Analysis

Upon receipt at Clarence Controls, Inc., the transformer had been mostly drained of dielectric. A few inches of a dark brown, oily substance remained in the bottom of the tank. This was presumed to be ethylene glycol, but no effort at analysis was made, due to the extreme degree of contamination.

The core-coil assembly is mounted to a plate, which in turn is suspended from the top cover by four support rods, bolted at the mounting plate and welded to the top cover. One of these rod-to-cover welds had broken and subsequent inspection showed cracks in the three remaining welds.

The disassembly sequence is shown in figures 6 through 11.

In figure 6, the high voltage bushing has been removed and the cover, along with the core-coil assembly, has been removed from the core. The assembly is inverted as shown.

Figure 7 is similar to figure 6, but showing the side on which the failure occurred.

In these two figures (6 and 7), the paralleled coil output terminations may be seen. The two separate coils had been over-wrapped with 20 layers of 5 mil mylar.

Figure 8 is a view of the damaged coil after the first 10 layers of outer wrap had been removed. Note the evidence of arcing in the remaining outer wrap insulation and in the mylar sleeve around the primary ground terminal below the outer wrap.

Figure 9 is a view of the same area with all the outer wrap insulation removed along with the primary ground mylar sleeve insulation. The coil insulation seen here is the outermost wrap of the individual damaged coil.

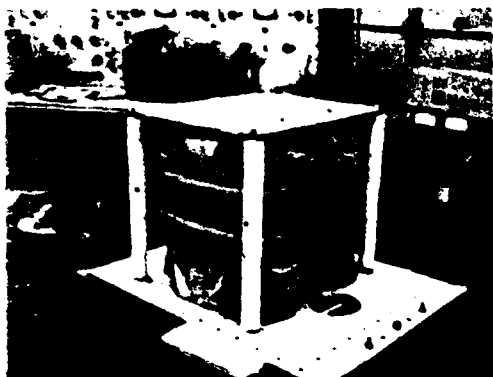


Figure 6

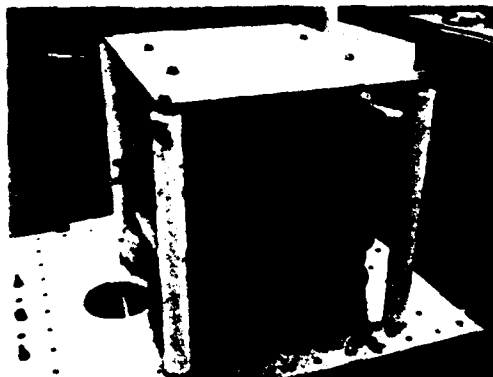


Figure 7



Figure 8



Figure 9

In figure 10, the core-coil assembly has been removed from the cover and re-inverted to its normal position.

Finally, figure 11 is a view of the damaged coil after removal from the core structure. Results of the failure were evident throughout the seven layer thickness of the outer secondary winding, but appeared to be most predominant at the outermost (highest voltage) copper layer.

It, therefore, appears that the breakdown occurred from the outermost secondary copper layer to the center grounded strap of the outer primary winding. A similar voltage gradient condition exists adjacent to the grounded straps of the outer primary winding at each end of the coil, except that at the termination end, 5 x 12 inch 5 mil thick mylar pad was inserted between each layer of insulation between the outer secondary and the outer primary. This type of barrier should be provided adjacent to all coil termination straps.

A detailed analysis of the localized field distributions, as conducted by Dr. A. S. Gilmour, Jr., of the State University of New York at Buffalo, follows.

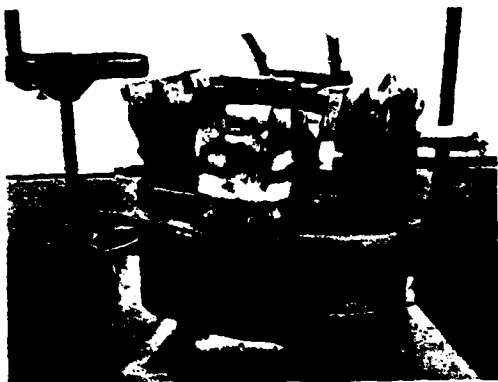


Figure 10

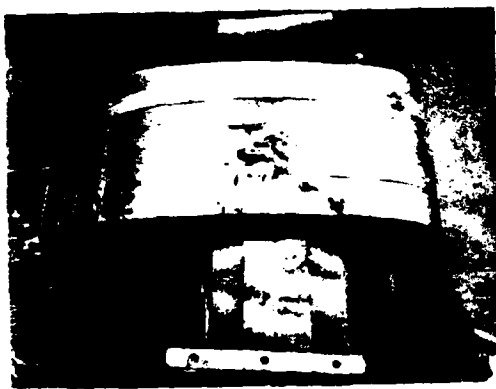


Figure 11

A cross sectional view of the subject transformer is shown in Figure 12. The primary design voltage was 20 kV and the secondary design voltage was 163 kV. The pulse width was 10 μ sec. This section contains an analysis of the potential distributions and electric fields in and near the windings. Particular emphasis is given to the high-field region identified in figure 12. This is the region at the edge of the outer foil of the secondary winding on the transformer where failure occurred. The failure mode was severe arcing in two locations at the edge of the foil. A separate report contains analytical derivations of typical field and potential distributions found in transformers and capacitors. The primary result of these derivations is a calculation of the field enhancement factor at the edge of a foil in a transformer or capacitor.

Winding Configuration

Each of the two coils of the transformer consisted of several windings. As is shown in figure 13, two primary windings were interleaved between three secondary windings. This configuration resulted in a calculated leakage inductance of less than 0.1 μ H for the entire transformer.

The conductors used for the windings were copper foil. For secondary windings #1 and #2 the foil was 5 inches wide and 0.008 inch thick. For secondary winding #3 the foil was 4 inches wide and 0.008 inch thick. For the primary windings, the foils were 5 inches wide and 0.032 inch thick. (Each 0.032 inch thick conductor consisted of 2 each 0.016 inch conductors). The numbers of turns on the windings were:

Secondary #1	7
Secondary #2	12
Secondary #3	6
Primary #1	3
Primary #2	3

Terminals on top of
tank (not shown)

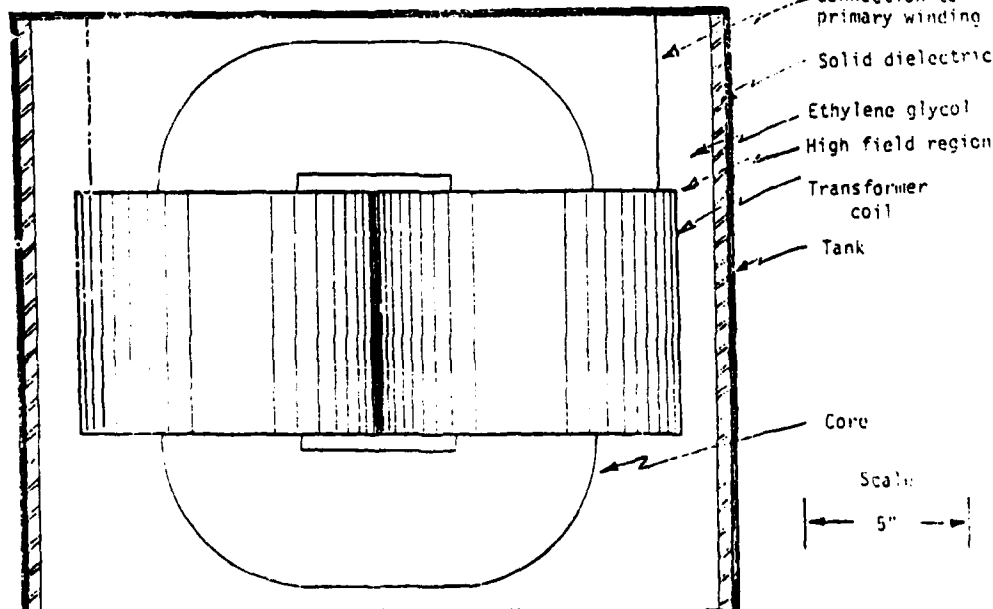


Figure 12. Cross Sectional View of Transformer

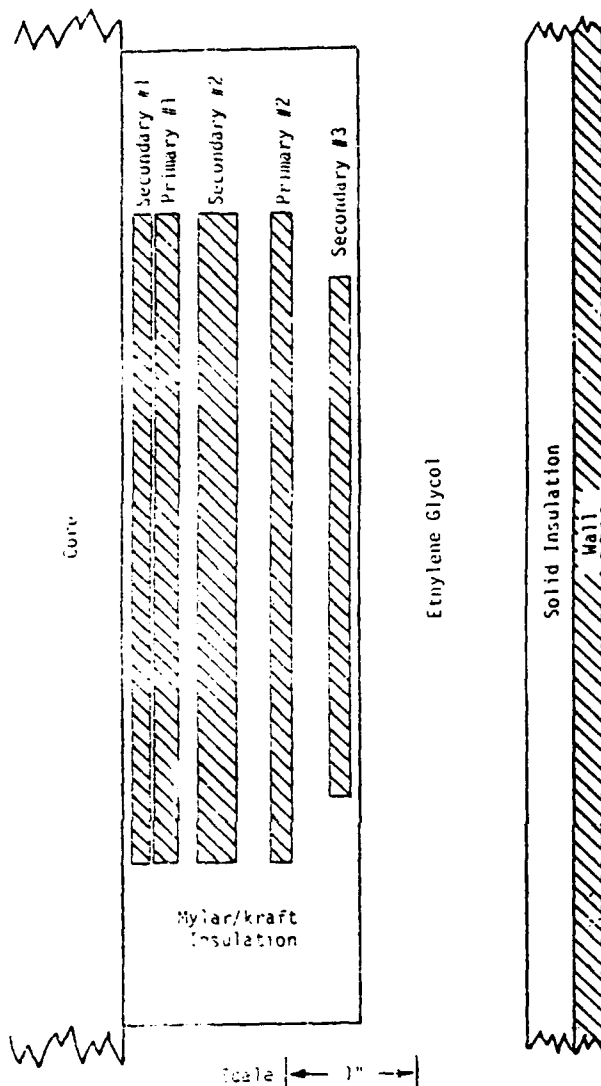


Figure 13. Winding and insulation configuration in 5 GW pulse transformer

The windings were separated and surrounded by sheets of 0.005 inch mylar separated by 0.001 inch kraft paper. The entire transformer was immersed in ethylene glycol. Thus, the dielectric constant of the insulation system ranged from 2.5 for mylar to 40 for ethylene glycol.

Potential Distribution

The potential distribution throughout the windings is plotted vs distance from the core in figure 14. Winding locations are indicated by the finely cross hatched areas. The uppermost solid line is the potential distribution near the center of each winding. The dashed lines show the potential distribution at the edges of the windings.

Thus, for example, secondary winding #1 was

connected so that the high-voltage side was adjacent to the core. Then, the potential of the winding decreased as distance from the core increased. The low voltage side was approximately 0.25 inch from the core.

The potential at the center of the insulating layer between secondary winding #1 and the core is shown to drop linearly from the voltage level at the inner surface of the winding to zero at the core. At the edge of secondary winding #2, toward the core, the potential distribution in the insulation is shown to be concave downward. Thus, the electric field at the inner surface of the inner conductor of secondary winding #1 is higher near the edge of the winding than at the center of the winding.

As distance from the core and from secondary #1 increases, the potential increases through primary #1 and then through secondary #2. From the high side of secondary #2, the potential drops to zero through primary #2 and then increases to the maximum value of 163 kV at the outer side of the 3rd secondary winding. The potential then drops rapidly through the layer of mylar/kraft insulation surrounding secondary #3. Because of the high dielectric constant of the ethylene glycol, the potential drop across this fluid is small. Finally, there is a substantial potential drop across the relatively low dielectric constant insulating liner of the transformer tank.

Insulation failure occurred in the high field region (encircled region #3 in figure 14) at the edge of the outermost layer of secondary #3. There, as is shown by the dashed line, the gradient in potential was extremely high.

Electric Field Calculations

Two techniques were used for determining electric field distributions in the high field regions of the transformer windings. The three high field regions designated by circles 1, 2 and 3 in figure 14 were considered. Analytical techniques were used for regions 1 and 2. For region 3, potential contours were determined by a finite difference technique. The fields in region 3 are calculated to be far larger than in regions 1 and 2 and are considered first.

Shown in figure 15 are the details of the winding and insulation configuration near region 3. The surfaces defining the potential distribution are the secondary winding with voltages from 120 to 163 kV, and the wall of the transformer tank and the low-side connection to the primary winding, all at zero potential.

Shown in figure 16 are the equipotential contours near the edge of the outer turn of the secondary winding. The edge of the winding is shown with square corners because the copper foil used to fabricate the winding was sheared and the edges were not rounded prior to use in the transformer. As was indicated in figure 14, the effect of the ethylene glycol was to force an extremely sharp potential gradient in the mylar/kraft insulation layer surrounding the secondary winding.

The field level between the 130 kV and 150 kV contours in figure 16 is on the order of 1000 V/mil. The direction of this field is predominantly perpendicular to the surface of the winding. If the insulation was not defective, it should be able to withstand this field level.

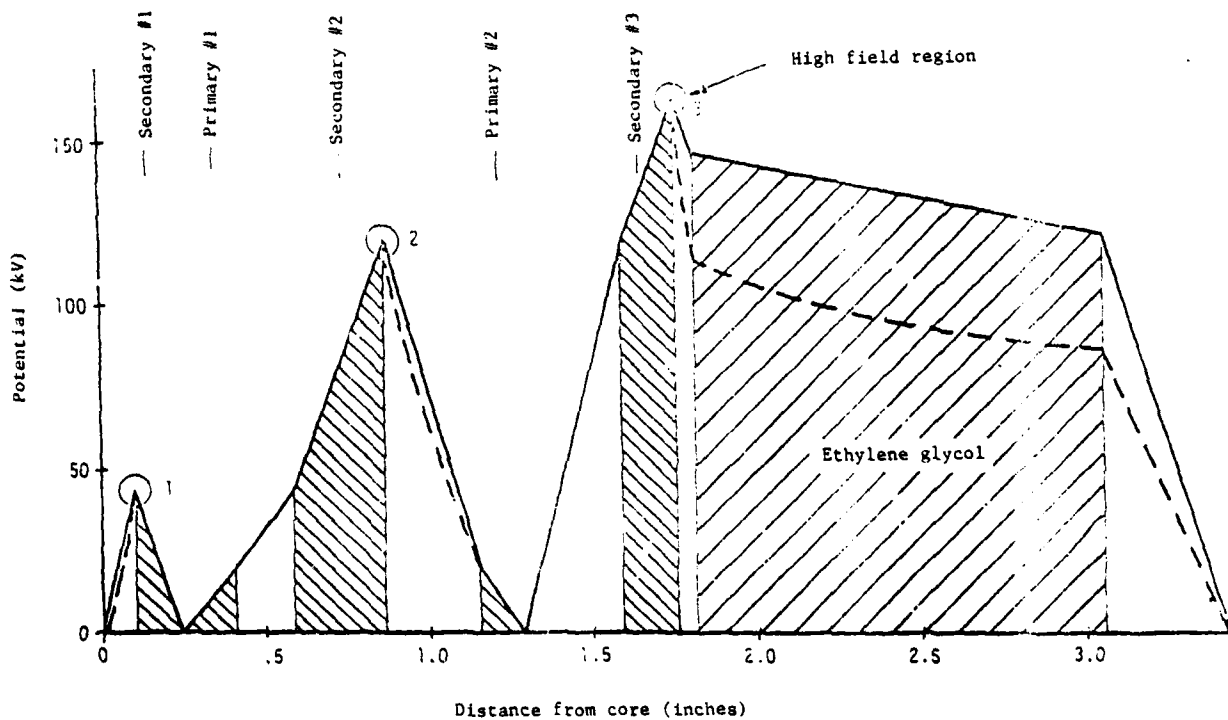


Figure 14. Potential as a function of position
 — at center of winding
 - - - at edge of winding

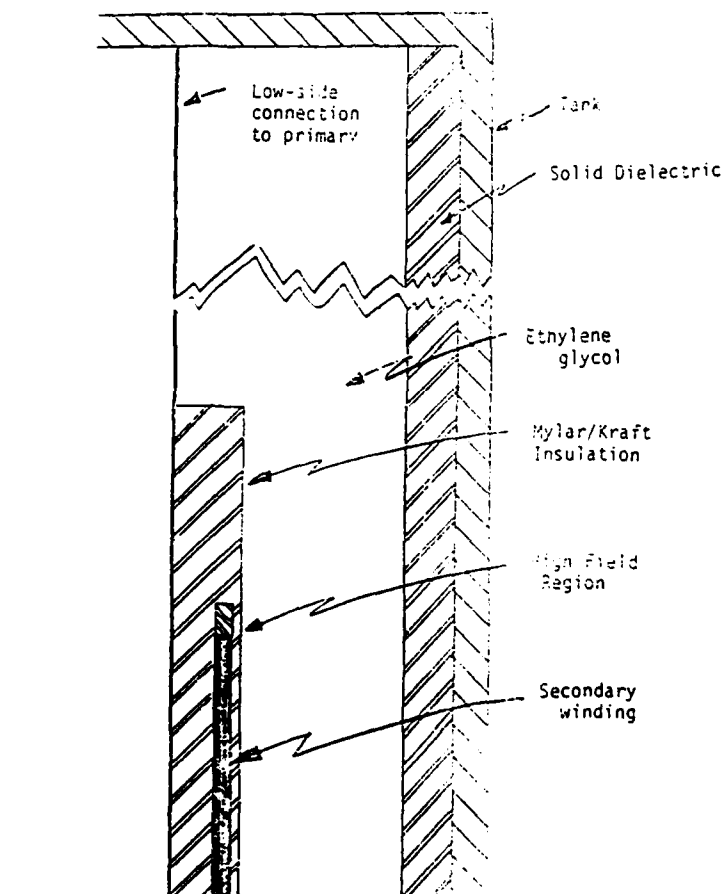


Figure 15. Expanded Cross Sectional View of High Field Region

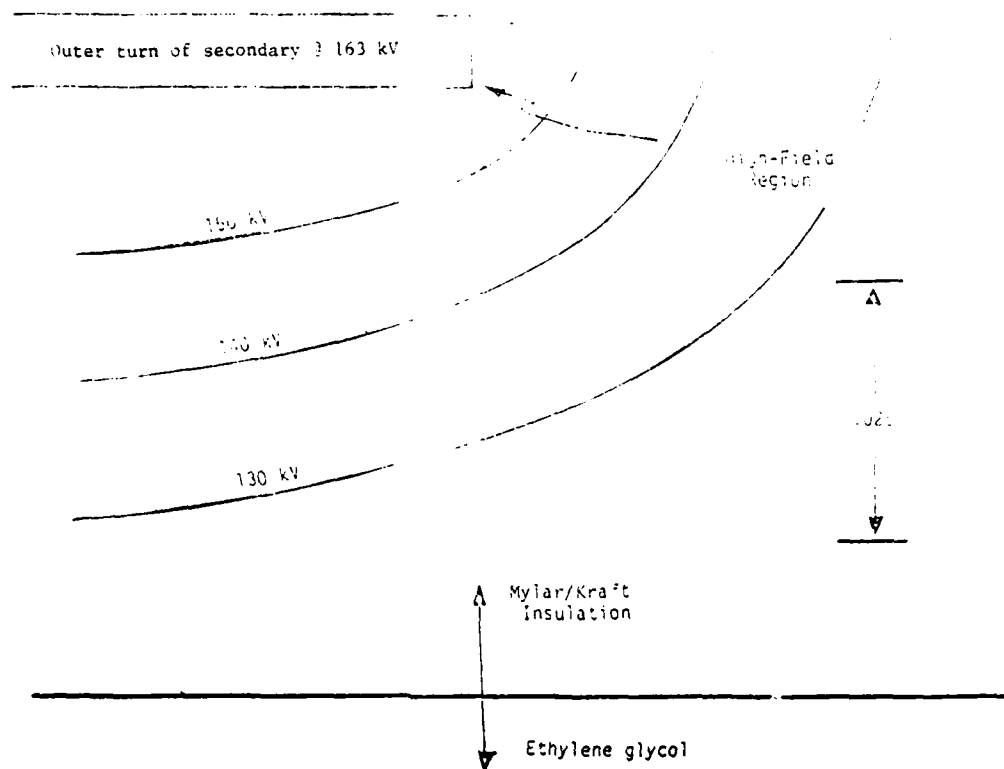


Figure 16. Equipotential Contours in High Field Region

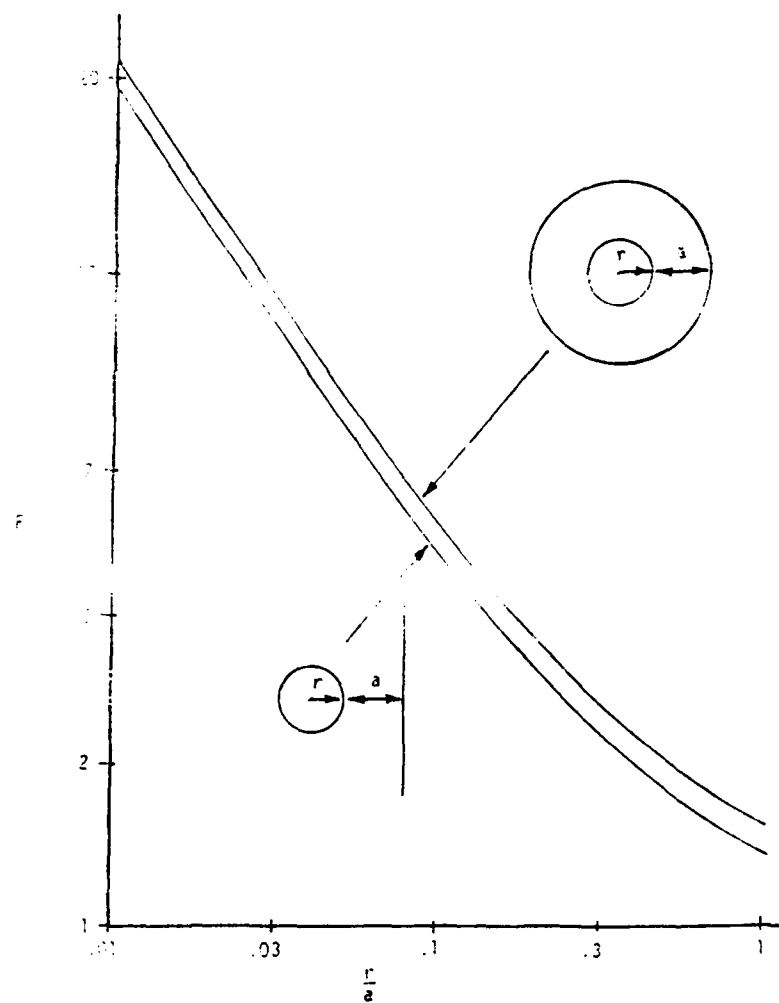


Figure 17. Field enhancement factor, F , for concentric cylinder and for cylinder - plane electrode configurations.

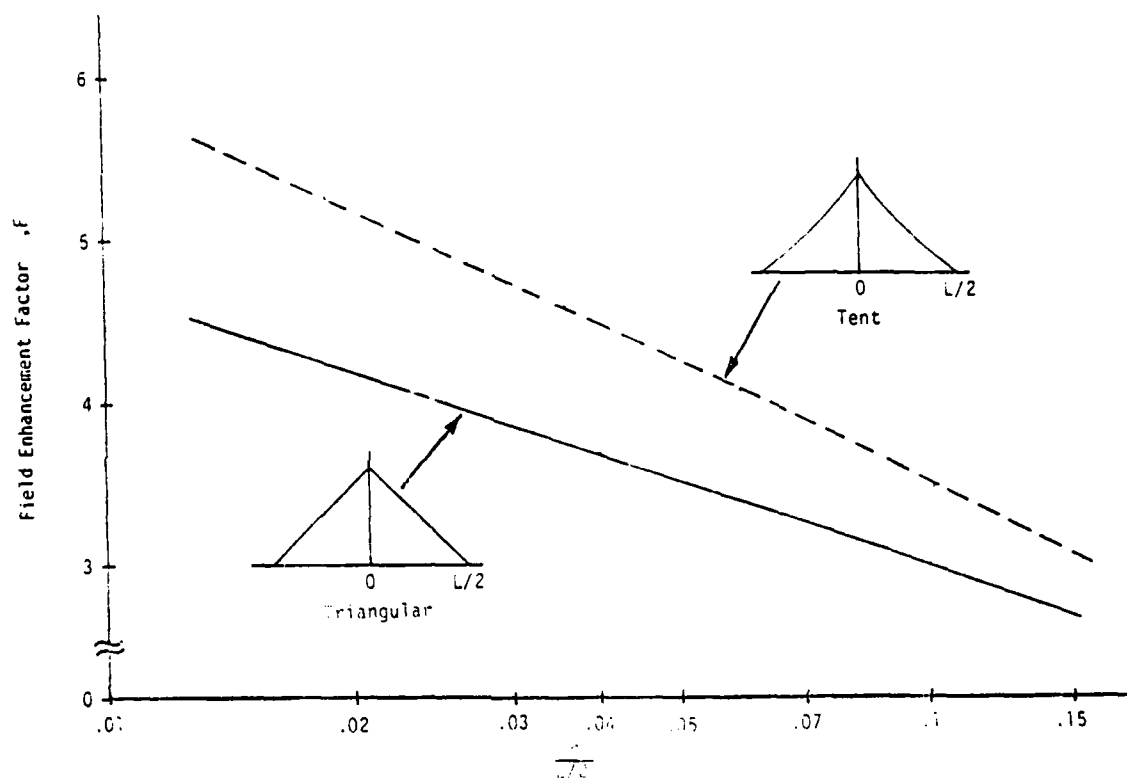


Figure 18. Field enhancement factor as a function electrode edge radius normalized with respect to electrode separation.

Between the 130 kV and 150 kV contours near the edge of the winding, the direction of the field is predominantly parallel to the surfaces of the layers of insulation. A level of 1000 V/mil along the surface of an insulating layer is extremely high and would very likely cause failure of the insulation.

Near the edge of the outer turn of the secondary winding, the field is far above 1000 V/mil. In particular, the field at the corner of the conductor is extremely high. This field may be estimated with the aid of equations that have been derived for electrode and potential configurations similar to that near the corner of the winding. For example, for concentric cylinders and for a cylinder parallel to a plane plate, the electric field is as shown in figure 17. The field at the corner of the outer winding is comparable to the field at the surface of the cylindrical conductor of radius, r , in figure 17. The 150 kV potential profile has a curvature between that of the outer cylindrical electrode and that of the plane in figure 17. Thus, we would expect the field enhancement factor, F , for the corner of the electrode in figure 16 to fall between the two curves in figure 17.

The radius of curvature of the corner of the sheared edge of the outer turn of the secondary is not known, however, it is certainly far less than 0.001 inch. The spacing between the 150 kV profile and the corner of the electrode (which corresponds to a , in figure 17) is about 0.007 inch. As a result r/a is much less than 0.1 and so the field enhancement factor, F , is on the order of 7 to 10. Multiplying $\Delta V/a$ at the corner of the electrode (163 kV-150 kV or 13 kV divided by 0.007 inch) by F , the field at the corner is found to be well in excess of 10,000 V/mil! To make matters even worse, a significant component of this field is parallel to the surface of the insulation layers. This field is far too high to be supported by the insulation and failure is to be expected.

The field in regions 1 and 2 of figure 14 may be estimated with the aid of the profiles shown in figure 18. One is triangular and the other is basically tent shaped. For this analysis, the radius of curvature of the edge of the high voltage electrode is assumed to be one half of the thickness of the electrode. As a result, the field enhancement factors that are calculated are less than are present for sheared electrodes such as those in the subject transformer.

One side of each the potential profiles in regions 1 and 2 of figure 14 is like the triangular profile of figure 18 and the other side is like the tent shaped profile. As a result, the field enhancement factors for regions 1 and 2 would be expected to fall between the two lines given in figure 18. Since the normalized radius for regions 1 and 2 is in the range of .01 to .03, the field enhancement factors for electrodes with rounded edges would be approximately 5. For sharper cornered electrodes this factor would probably be in excess of 10. Thus, the maximum field in regions 1 and 2 of figure 14 would be in the range of 2000 to 3000 V/mil parallel to the surface of the layers of insulation. This is well in excess of the field level that can be expected to be supported in these regions and so failure can be expected to occur eventually even though it did not occur during the very brief testing performed on the subject transformer.

Failure Analysis Summary

In summary, the configurations of the windings and the insulation system in the subject 5 GW pulse transformer have been described. The potential profiles within the windings have been determined and three regions in which extremely high field levels existed have been identified. The electric fields in these regions have been calculated. The highest field level is in the region where failure of the transformer occurred and is estimated to have been well in excess of 10,000 V/mil. The field level in the other two regions is estimated to have been in the 2000 to 3000 V/mil level in a direction parallel to the surface of the insulation. This high field level would probably have resulted in eventual failure of the transformer, had it not already failed because of breakdown in region 3.

One of the reasons for the extremely high field levels at the edges of the windings is that the copper foil used for winding fabrication was sheared and the edges were apparently not subsequently treated to remove the sharp corners resulting from shearing. Even if the edges of the foils had been rounded, field levels would have been very high and failure may have resulted. Improved winding and insulation configurations would be necessary to prevent failure.

Dr. Gilmour's analysis provides valuable insight into the problems of very high localized potential gradients and possible failure modes. However, the existence of high local potential gradients based on static voltage conditions does not necessarily result in a catastrophic failure. Such a failure will occur only if a sufficiently conductive path to a potential sink (ground) is present for the energy involved. Such a path was present in the subject transformer to the outer primary ground strap. The introduction of dielectric barrier into this path will prevent repetition of the breakdown in the rebuilt transformer. Because of the high surface potential gradients, there will be surface charge flow, leading to a potential field redistribution. These capacitance-like effects will result in dielectric losses, but they should not be significant, particularly for short term considerations.

Transformer Rebuild

The subject transformer was rebuilt by Clarence Controls, Inc. The cores and case assembly were cleaned and re-used. The coils were re-wound, using all new materials. Changes and/or precautions taken in the re-winding procedure included:

1. Foil edges were hand finished to eliminate burrs and produce a smooth rounded edge, insofar as possible.
2. Primary and secondary grounds were brought out separately, to simplify instrumentation and testing.
3. Additional insulating pads were inserted adjacent to all coil termination straps.

At the time the abstract for this paper was written, it was expected that the rebuild and testing of the transformer would have been completed by the time of this presentation, and the results could have been reported. For various reasons, the program is about six to eight weeks behind schedule, and the rebuilding is just being completed. It is expected that testing of the rebuilt transformer will be completed at ERADCOM, Ft. Monmouth by the end of July 1982. Results of these tests will be published as soon as they are available.

ANALYSIS OF A HIGH POWER, PREIONIZED GAS SWITCH WITH LOW INDUCTANCE AND LONG LIFE*

by

A. Ramrus and N.R. Pereira

Maxwell Laboratories, Inc.
8835 Balboa Avenue
San Diego, California 92123
(714) 279-5100

ABSTRACT

Pulse power requirements for laser isotope separation (LIS) call for an output switch capable of switching 60 kV into a 0.5 ohm load with an inductance of 10 nH and life exceeding 10^8 shots. With the exception of life, these requirements can in principle be attained with advanced multichannel spark gaps. The limitation on life occurs because electrode erosion of the channels pits the electrodes. Channeling can be avoided with preionization as done in lasers. We have analyzed the feasibility of using preionization to inhibit the formation of channels in a repeated gas switch. One technique includes the use of X-rays from a thermionic diode. This X-ray generator can provide preionization electron densities in the range of 10^7 to 10^8 cm⁻³ as required to promote uniform discharge at atmospheric pressures. Detailed design of a system capable of meeting the LIS requirements is presented.

*This work was funded by Los Alamos National Laboratory, Order Number 9-L62-7440U-2.

INTRODUCTION

Pulsers for laser isotope separation take the general form of a pulse-charged transmission line which is repetitively discharged into a laser load. A critical component in the pulser is the output switch that repetitively discharges the pulseline into the laser, then recovers during the interpulse period. In one design, the output switch is located between the charged pulseline and the laser load, as shown in a simplified view in Figure 1. The pulsepower requirements for this output switch call for a 60 kV, 75 kA, low inductance switch capable of operating at a 1250 Hz pulse repetition rate. The specifications are shown in Table 1. Once perfected, these rep-rate pulsers may be installed in plants which must operate for weeks without significant down time or maintenance. Therefore, an important requirement for the switches is their lifetime, which should exceed 10^9 discharges in order to attain weeks of continuous operation.

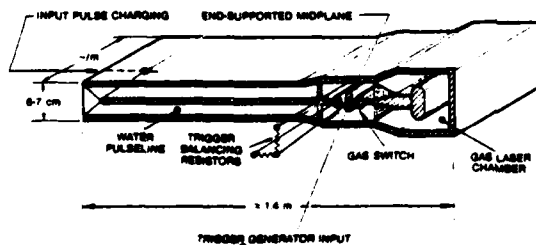


Figure 1. Simplified cross-section of pulseline, output switch and laser.

TABLE 1
SWITCH PARAMETERS FOR LASER ISOTOPE SEPARATION PULSERS

Parameter	Specification
Voltage	60 kV
Rep-rate	To 1250 Hz
Pulse width	60 nsec
Coulombs per pulse	5 mC
Energy loss	<10 percent of switched energy
Jitter	2.5 ns
Current	75 kA
Voltage reversal	100 percent
Inductance	<10 nH
Life	> 10^8 closures

Were it not for the lifetime requirement, gas-plasma rail switches developed over the last five years would meet the requirements with only modest improvement. These conventional rail switches operate by generating channels which emanate from a field-enhanced trigger electrode. Plasma channels cause erosion of the electrodes at a rate which appears to exclude this type of rail switch from the long lived applications of interest to the isotope separation plant designer.

One approach to the elimination or reduction of erosion is to prevent plasma channeling in rail switches. To accomplish this, we adapted the technology developed for preionized discharge lasers. Preionized discharge lasers operate by initially conditioning an appropriate gas mixture with ionization and excitation by fast electrons, UV light or X-rays. Subsequently, a fast risetime uniform field of 1-10 kV/cm is applied which causes the gas to undergo a steady uniform discharge for periods up to about 100 ns.

During this discharge, energy is being pumped into the laser medium which serves as the load. For efficient laser pumping, the effective resistance of the laser load should match the pulser impedance. In cases of interest to a laser isotope separation program, the load resistance is in the range of 0.5 ohm. In practice, the resistance is variable and depends on the configuration of the laser, the character of the applied waveform and the laser gas.

We have explored methods by which configurations similar to those used in lasers can be used in low inductance switches. For lasers, an important objective is to maintain the matching resistance for the entire pulse duration. In contrast, for switching purposes, the objective is to have the minimum possible resistance in order to minimize loss, while maintaining uniformity in the discharge for low erosion.

Figure 2 shows a range of current densities with the laser discharge and spark gap regimes cross-hatched. A laser discharge has a relatively high resistance, indicated by the conductivity (on the vertical scale) as function of current density (solid line), while arcs have a low resistance. Electrode melting is the main life-limiting factor for spark gap switches, and this prohibits operation of our switch in the melting regime (cross-hatched) beyond about 200 kA/cm² for our parameters. The resultant operating regime falls in between the laser discharge and the electrode melting limits, as indicated by the bar in Figure 2. The current density can be controlled by selecting the proper electrode geometry.

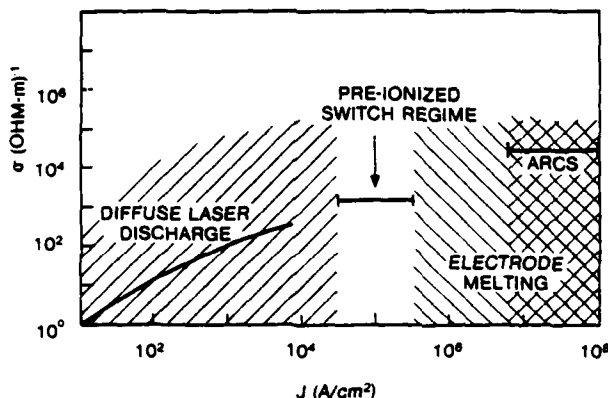


Figure 2. Current density regimes for diffuse laser discharge, electrode melting, and arcs. The conductivity in these regimes is suggested by the solid line.

This paper summarizes the results of Maxwell's feasibility study of a switch design capable of meeting the above specifications. To meet this objective, a three electrode X-ray preionized switch was conceptually designed. Switch resistance, inductance and the X-ray power requirements were estimated. Particular attention was focused on the resistance because this could only be estimated after simplifying assumptions were made on the switch plasma parameters. This leads us to conclude that experiments are essential to demonstrate whether a preionized, uniform discharge switch has a sufficiently low resistance to be useful in low loss applications.

BACKGROUND

Pulse Power

The conceptual design of the uniform discharge switch results from developments in pulse power and in laser technology. In pulse power, two operational switch designs were considered: (1) rail switches which operate reliably in the 50 kV to 100 kV range with an inductance of 10 nH to 20 nH over a 50 cm width¹ and (2) gas-blown single-channel switches, for rep-rate operation in the voltage range of 50 kV to over 100 kV^{2,3}.

Triggering of the uniform discharge is similar to that of multichannel rail switches in that both have midplanes which are overvolted in order to initiate the conducting plasma. However, the rail switch has a sharpened midplane and does not use preionization, other than that which occurs from corona along the

midplane. In contrast, the trigger electrode in the uniform discharge switch is a robust midplane about 1 cm thick. Figure 3 shows the cross-section of a standard Maxwell rail switch now under extensive use in high current, low inductance applications throughout the world. The overall width (measured along the rail and perpendicular to current flow) is about 20". When designed for 50 kV, this switch has 10 nH of equivalent series inductance; for 100 kV, it has 20 nH.

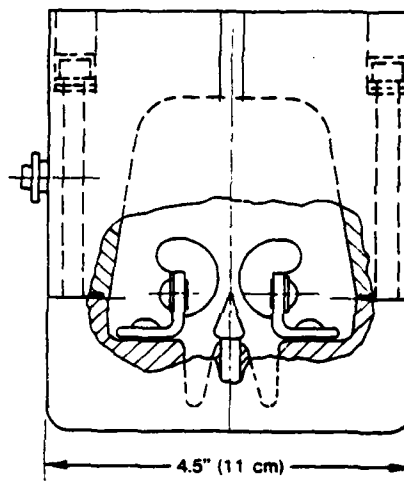


Figure 3. Cross-section of 50 kV rail switch with 10nH effective inductance. Rail length is 14" and switch length is 19.5".

Spark gaps which operate at rep-rates up to 1 kHz have also been developed at several laboratories. The flow designs of gas purged switches and that considered for uniform discharge switches are similar. The objective of the flow design is to purge the arc products from the interelectrode spacing and to bring these products into a zero field region as rapidly as possible so that re-strike does not occur when the switch is re-charged.

Lasers

To attain uniform discharges at atmospheric pressure in lasers, the gas can be first preionized; then an electric field is applied across the laser chamber. A simple physical model to estimate the preionization requirements was proposed by Palmer⁴ and extended by Levatter and Lin⁵ and others.

This model applies to the breakdown of moderately overvolted gaps in which a single electron starts an avalanche. The secondary electrons rapidly drift away from their place of birth, antiparallel to the field direction, and then diffuse laterally. The result is a streamer, a cone-shaped region with positive, stationary ions, and a head of negative electrons. The electric field from these separated charges soon exceeds the breakdown field. The self-field acts on other electrons in the neighborhood of the streamer, which then form their own streamers. The process is assisted by photoionization. Soon the gap is bridged by interlocking sparks, and a single arc-channel forms.

Individual spark breakdown is prevented by providing sufficient electrons distributed throughout the gas so that the streamer heads overlap before their self-field is sufficient to cause further avalanching. For this the initial electron density should exceed the value:

$$n_e > 1/r_c^3$$

where r_c is the streamer head radius when the streamer self-field starts to exceed the external field. This radius r_c is typically about 0.01 cm, roughly corresponding to n_e of 10^6 cm^{-3} .

A useful gas switch should have a non-conducting state, wherein the voltage across the electrodes is insufficient to break down the gas. With a short trigger pulse the gas should go over into a highly conducting stage, which can be maintained by a relatively low voltage drop. Following are general comments on the losses which occur in plasmas with residual electric field.

A stable homogeneous high-current discharge has a thin sheath near the negative electrode. Beyond the sheath the electric field is constant. It should be emphasized that this field, also called the sustaining field of the discharge, is always less than the breakdown field for the gas before the discharge has occurred; if the gas remains relatively cold during the discharge the sustaining field will be comparable to the breakdown field. In contrast, if the gas is vibrationally and/or electronically excited to a substantial degree (in addition to being weakly ionized) the sustaining field may be substantially lower than the initial breakdown field. For switching purposes, reducing the sustaining field is mandatory to reduce losses.

The sustaining field must decrease over a 1-10 ns time scale. This means that in this short time the gas composition must be altered, to contain many excited states and other easily ionizable molecules. For this we need a large power density which is equivalent to a large current density. Because of this consideration, there is an upper limit to the discharge area that can be used for a switch with a given resistive loss. The lower limit of this discharge area is the allowable current density which may be attained without melting electrode material.

In conclusion, to create uniform discharges suitable for switching, we must promptly deposit sufficient energy density in the gas. In addition, we must minimize the total energy deposition in order to benefit the switch efficiency. A possible configuration for the discharge plasma is a thin ribbon 0.1 cm thick, 1 cm long and 75 cm wide. Then, the desired heating will occur due to the high power dissipation in this limited volume.

We evaluated the use of air as a switching medium suitable for preionized switching. Low switch resistance can occur only if we rapidly ionize the air to create the low resistance plasma. To accomplish this the energy must be deposited in electron ionization rather than in molecular vibration or rotation. Therefore, a monatomic gas such as argon may be preferable if an electronegative component, such as O_2 , were added. Interestingly, we have considerable experience with gas mixtures consisting of an inert and electronegative gas. Maxwell's product line of multichannel rail switches employs Argon - SF_6 . We probably cannot select SF_6 for this particular switch, because the environment in which the switch will be employed cannot tolerate

contamination by gases which are strong infrared absorbers. However, there are other electronegative gases potentially suitable for switching.

Discharge Resistance

We now consider the resistance of the plasma generated between an arbitrary pair of switch electrodes spaced at about 1 cm, in a uniform-field configuration at one atmosphere pressure.

The discharge resistance depends on the kinetics of the various species present in the switch plasma. Factors, that cannot be completely specified at this time, such as applied waveshape, gas species, and pressure, also have a significant influence on the discharge resistance. Table 2 shows discharge resistivity and resistance for several assumed ionization fractions. These calculations show desirably low final values of resistance. To attain any given ionization fraction, it is necessary to deposit at least the ionization energy into the gas. For example, this ionization energy falls into the range of 10 to 30 eV and for an ionization density of $2.5 \times 10^{21} \text{ m}^{-3}$ (i.e. 0.1% at atmospheric pressure) 4-12 kJ/m³ is required. For the discharge volume of 10 cm^3 (10^{-5} m^3) we would need 40 to 120 mJ. This energy is readily available during the early stages of switch closure and would be deposited within the first nanoseconds provided the prompt energy goes into ionization rather than into molecular vibration. To compensate for these losses, up to a factor of three higher energy density may be required, but that is still acceptably small.

TABLE 2
PLASMA RESISTANCE IN A RIBBON-SHAPED DISCHARGE
WITH CROSS-SECTIONAL AREA OF 10 cm^2
AND LENGTH OF 1 cm

Assumptions	Ionization %	Resistivity, r ohm-cm	Resistance, R m-ohm
A	1.0	0.04	5
B	0.1	1.0	130
B	1.0	0.1	13

A - Strong ionization; electron temperature $T_e = 1 \text{ eV}$; $r_1 = 6.53 \times 10^4 T_e^{3/2} \text{ ohm-cm}^{6,7}$

B - Weak ionization; momentum transfer cross-section, $= 7 \times 10^{-16} \text{ cm}^2$; $T_e = 1 \text{ eV}$, $r_2 = m_e f_c / (n_e e^2)$ where the electron collision frequency $f_c = m_0 q_c v_{th}$, $v_{th}^2 = kT_e / m_e$.

In practice, a monatomic gas such as argon, with small quantities of an electro-negative gas such as H_2 , or O_2 may be more suitable. For higher pressure, the required energy is proportionally higher but still within acceptable limits.

The NRL CHMAIR air chemistry code⁸ can analyze the switch behavior as a function of time by following the kinetics of the air during preionization.⁹ Using this code, the ionization growth from X-rays, and the discharge characteristics of the switch in a given circuit were studied. In contrast, the previous calculations ignored the complicated interactions between the various processes. The CHMAIR calculation of resistance is shown in Figure 4.

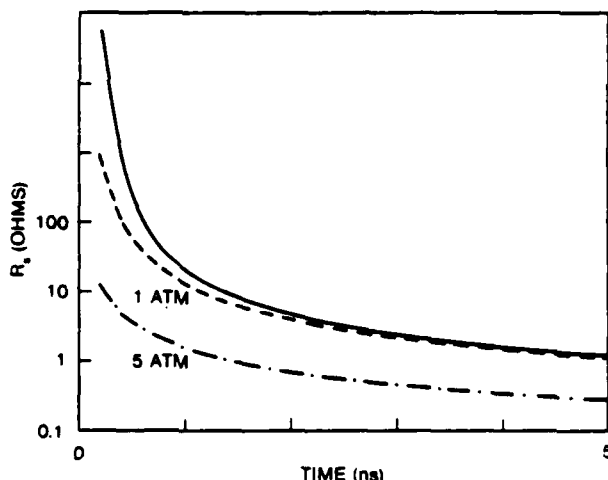


Figure 4. Switch resistance R_s versus time for electrode area 1 cm^2 (solid) and 100 cm^2 (dashed), at 1 atmosphere, and for 5 atmosphere and 100 cm^2 (dot dashed).

The switch is part of a series circuit with resistance $R_L = 1 \text{ ohm}$, and assumed inductance of 10 nH . The voltage is 60 kV over an assumed 1 cm switch gap, with electrode area varying between 100 cm^2 and 1 cm^2 . This 60 kV/cm field was selected as a reasonable simulation of the breakdown conditions in a pulse charged air switch at one atmosphere pressure. The resistance falls precipitously in the first ns to about 10 ohm , and decreases more slowly over the next 5 ns to about 2 ohm , with an apparent limiting value of 1 ohm . Other calculations have shown this resistance is insensitive to electrode area. This calculation suggests that air is not suitable to meet the objective of low loss. The relatively large amount of energy which goes into the vibrational modes explains the relatively high resistance obtained with CHMAIR.

Erosion

Electrode erosion is the primary life-limiting mechanism in gaseous discharge switches. The main causes of erosion are electrode melting, ejection of material evaporation, and, in some cases, sublimation. This problem is most severe when channeling occurs because the current densities are high, and tend to melt the electrodes at the channel contact points. There is recent evidence that erosion rates are further increased when the gas flows through the spark gap at high speeds. In static cases, erosion rates of $0.01\text{--}0.1 \text{ mg/C}$ have been measured.¹¹ At high flow speeds, erosion rates may increase to 0.5 mg/C to 1 mg/C .

The main effect of erosion is to alter the electrode gap spacing and shape which affects switch performance. The tolerable amount of erosion depends on the gap spacing; small gaps at high pressure can tolerate less change than can large gaps. Consider Figure 5, where we assume that a section of electrode material whose height equals the gap spacing, d , is uniformly eroded. The lost volume is $W b d$ from two electrode surfaces. In that case, the total eroded mass is:

$$M_e = p (W \times b \times d)$$

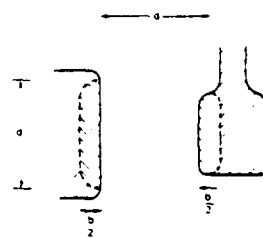
where p is electrode density, W is rail width, and b is eroded depth, assumed equal from each of two electrodes.

For N discharges of Q coulombs each, the erosion rate is:

$$R_e = b W d p / Q N$$

In our case, $W = 75 \text{ cm}$, $Q = 5 \text{ mC}$ per pulse, the density p is 15 g/cm^3 and d is 0.5 cm . Consider the allowable electrode change of 10% of d . Then, b is 0.05 cm . The allowable rate R_e for 10^8 shots is:

$$R_e = 0.06 \text{ mg/C}$$



EROSION RATE R_e FOR N DISCHARGES

$$R_e = \frac{b W d p}{N Q}$$

Figure 5. Geometry for erosion calculation.

This rate may be attainable in single shot switches without gas flow. For flow speeds of about 60 m/s , we would expect much larger erosion rates if channeling occurred. We conclude that the reduction in erosion rate to be obtained by the uniform discharge switch is required for the specified life. From a uniform discharge switch we expect extremely low erosion rates because the electrode temperatures are low compared to those in the arc contact points between arc and electrode.

Electrode Melting

In an arc discharge electrode melting dominates over other erosion mechanisms. The energy input to the electrode occurs at the surface. In the first few nanoseconds the current rises linearly with time, and the corresponding energy has some time to be conducted away. Therefore the effective energy input is not singular at the electrode surface, but is spread out over a small layer.

The typical thickness d of a thermal conduction layer is^{12,13}

$$d^2 = (D/C_p) t_p$$

where D is the heat conductivity, C_p the heat capacity, and t_p the pulse time. Typical values are $D = 4 \text{ (Jcm}^{-1} \text{ s}^{-1} \text{ K}^{-1})$ and $C_p = 3.5 \text{ (Jcm}^{-3} \text{ K}^{-1})$ (for copper), so that, approximately d^2 in $\text{cm}^2 = t$ in seconds.

To find the temperature rise T_d we assume that the heat spreads evenly over a layer width d . Then

$$T_d^2 = (J^2 V_d^2 t_p) / (DC_v)$$

where J is the current density and V_d the effective voltage that accelerates the ions or electrons which subsequently collide with the electrodes and transfer their energy. For V_d we take an estimated value of 200 V, corresponding to a typical sheath voltage. We ignore any voltage drop due to the plasma/electrode interface, (from oxide layers or otherwise) and we also ignore any Joule heating.

Figure 6 shows the temperature rise in copper electrodes as function of current density and pulse time. For our nominal 100 ns pulse and an allowable temperature increase $T_d = 100$ degrees K, the current density is limited to 2×10^5 A/cm². However, we plan to work at about 10 kA/cm², and the temperature rise should not exceed 15 degrees per pulse.

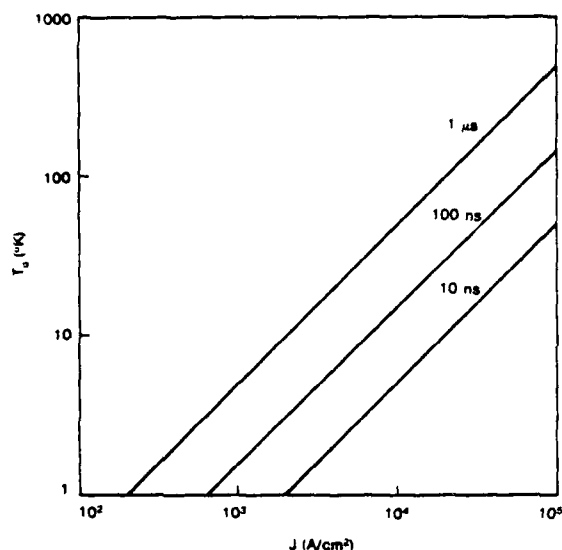


Figure 6. The temperature rise T_d in the electrode thermal diffusion layer for different pulse time t_p as a function of current density J .

The temperature rise depends weakly on the electrode material through the $-1/2$ power of (DC_v) . Table 3 gives these quantities for various elements that are commonly used as electrodes. The factor (DC_v) is also entered. Copper is clearly the best material because of its low temperature rise, but it melts more easily than the other materials. It may be best to use a tungsten/copper mixture, or perhaps tungsten-plated copper.

For rep-rate, average power dissipated in the electrodes must be carried away. The electrodes in our switch are immersed in flowing gas; separate electrode cooling should not be necessary.

SWITCH DESIGN

Following is a discussion of the switch hardware as shown in Figure 7.

TABLE 3
THERMAL CONDUCTIVITY AND HEAT CAPACITY
FOR VARIOUS METALS

	$C_v (\text{J cm}^{-3} \text{ } ^\circ\text{K}^{-1})$	$D (\text{J cm}^{-1} \text{ s}^{-1} \text{ } ^\circ\text{K}^{-1})$	DC_v
Copper	3.5	3.9	3.7
Molybdenum	2.8	1.5	2.0
Tantalum	2.5	0.5	1.1
Tungsten	2.8	2.0	2.4

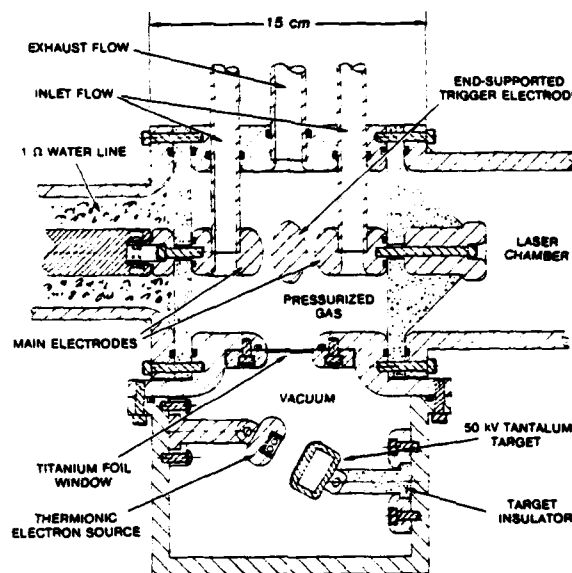


Figure 7. Conceptual design of a preionized 60 kV rep-rate switch.

Pulseline Design

The cross-sectional dimensions of the 0.5 ohm pulseline are based on an assumed pulseline width of 0.75 m. A practical match to the laser leads to a stack of two 1 ohm pulselines connected in parallel to drive the 0.5 ohm laser load. For compactness, we use water for the striplines dielectric. The overall pulseline size would then be about one meter on each side including allowances for insulation at the edges of the charged conductor.

The impedance is estimated from the formula

$$Z = 377 \text{ ohm} \times h / (k 0.5 \text{ W})$$

where Z is pulseline impedance, k is relative dielectric constant, h and w are plate spacing and width, respectively. Substituting $k = 80$ for water, and $Z = 1 \text{ ohm}$, 0.75 m width yields a plate separation of 1.8 cm. In this way, the 1 ohm impedance is obtained in a line whose electrostatic field is about 33 kV/cm, substantially below the 70-100 kV/cm breakdown field of a rep-rated water system. A part of this line is shown in the drawing.

High-Voltage Insulation

The switch electrode connected to the pulseline must be insulated for the full 60 kV charge voltage. Consider the overall gap spacing, which is the sum of the distances between the trigger electrode and the two main electrodes. The insulation (breakdown) strength is assumed to be comparable to that of air, about 25-30 kV per cm-atmosphere. To prevent breakdown we would use a design stress about 75% of that value, or 20 kV/cm-atmosphere. The operating pressure is specified by an engineering compromise between the desirability of operating at maximum pressure with minimum gap in order to reduce losses, while maintaining a sufficiently large gap to be relatively insensitive to erosion effects. For this design, we select an overall gap spacing of 1 cm. For a midplane which is balanced at $V_0/2$, or 30 kV, this is 0.5 cm of insulation gas between the trigger and each of the main electrodes. To support 60 kV, this gap has the operating field 60 kV/cm, and requires a pressure of at least three absolute atmospheres for a gas whose dielectric strength equals that of air.

Triggering

The trigger electrode is shown at mid-potential in this design. Offsetting the midplane at other than mid-potential may be desirable for optimum performance. The trigger applied to the midplane would have the risetime of about 15 kV/ns. In 4 to 5 ns, the midplane voltage attains over 60 kV. This voltage adds to the midplane potential so that a midplane charged to +30 kV would acquire either -30 kV or +90 kV, depending on the trigger polarity.

In the mechanical design, the trigger extends to each end of the 0.75 m switch and is supported at its ends. Also, it receives its trigger pulse at the ends, very much as Maxwell now triggers its standard rail switches. The mechanical design of the attachment is straightforward because the ends of the switch have adequate space for mechanical support and electrical insulation. For clarity, the ends of the trigger electrode are not shown in the drawing.

Inductance

Switch inductance was estimated by separately considering the electrode hardware and the plasma ribbon-shaped discharge. The total electrode inductance, for the paralleled top and bottom sections shown in Figure 7, was 4 nH. To this the plasma inductance was estimated at 1 nH, for the total of 5 nH. This value is acceptably low for the required output risetimes. Ignoring switch resistance, the output e-fold risetime of a 5 nH switch into the total impedance of 1 ohm (0.5 ohm for the pulseline, in series with 0.5 ohm for the laser load) is 5 ns.

Praionizers

The praionizer consists of a thermionic cathode which emits electrons into a tantalum X-ray bremsstrahlung source. The tantalum target electrode contains a water channel for cooling.

There are attractive alternative X-ray sources. For example, the thermionic electron source can emit electrons into a double window consisting of a tantalum and an aluminum (or titanium) foil that forms a cooling channel. The forward bremsstrahlung is sufficiently intense to provide the required praionization. This design is more compact, and requires less power, although more complex.

Razor cathodes are often used as electron sources, although here they may not be suitable as field emission sources because of the nonuniformity in emission. Recent work¹⁰ with carbon felt is promising because felt cathodes emit electrons uniformly. In that case, the field emission source would eliminate the power requirements for the heater in the thermionic cathode. At this writing, carbon felt cathode life is limited to the 10^6 shot range due to degradation of emission from the felt.

GAS DYNAMICS

Flow Velocity

The required flow speed is obtained by dividing the required flow distance of gas by the period between the successive pulseline chargings. To move the gas from the discharge location at the electrode midpoint to a field free region requires about 3-4 cm of motion. This must be done every 0.5 ms in a system operating at 1250 Hz (0.8 ms interpulse period, 0.5 ms between charges). Therefore, the flow speed is about 60 m/s, or Mach 0.2.

Flow Direction

The switch gas enters the insulating tubes, goes through the switch electrodes, moves across the electrodes, and exits at the central outlet port at the top center of the switch. In this way, fresh gas enters the switch through the tubes where they bridge the high-voltage insulation.

Flow Power

The flow power must be supplied by a compressor or blower installed in the flow circuit between the inlet and the outlet ports. To estimate compressor power, consider a switch operating at 3 abs. atm. of a diatomic gas ($k = C_p/C_v = 1.4$) flowing at 60 m/s. The flow area obtained from the cross-section of 75 cm x 1 cm is $75 \times 10^{-4} \text{ m}^2$. Compressor power is approximately proportional to pressure drop across the switch. A drop of 5-10 psig is anticipated corresponding to the ideal power requirement of 20 to 38 hp. A practical compressor is about 65% efficient. Therefore, actual compressor power falls in the range of 31 to 58 hp (23 to 43 kW). The anticipated rating is 30 hp corresponding to 22 kW. This is 14% of the 160 kW average power delivered to the load.

X-RAY PREIONIZER ELECTRICAL DESIGN

Pulse Power Requirements

To specify the pulse power required for the thermionic X-ray diode, consider the rate of electron production within the interelectrode spacing. We expect the primary loss of electrons in electronegative gases to be caused by electron attachment. Therefore, the rate equation governing the electron density n_e is

$$dn_e/dt = S - n_e/t_a$$

where t_a is the attachment time for the electronegative component in the gas. In the case of air, this attachment would occur to the oxygen molecules. The attachment time is given by

$$t_a = [k_a n_a]^{-1}$$

where t_a is the (electron energy dependent) attachment coefficient, and n_a is the number density of attaching molecules (e.g. oxygen). For air at atmospheric

pressure $n_a = 5 \times 10^{18} \text{ cm}^{-3}$ and k_a , the attachment coefficient, is about

$$k_a = 10^{-11} \text{ cm}^3/\text{s}$$

Therefore, the attachment time is 20 ns. Although this number was calculated for one abs. atm. of air, the result is insensitive to pressure.

We now estimate the source strength which is required to generate an equilibrium electron density of 10^8 cm^{-3} . At equilibrium $dn_e/dt = 0$ and $n_e = St_a$. Hence, the electron production rate is

$$S = n_e/t_a = (10^8 \text{ cm}^{-3})/20 \text{ nsec} = 5 \times 10^{15} (\text{cm}^{-3} \text{ s}^{-1}).$$

To obtain the X-ray generator power requirements, consider the X-ray flux passing from a line source through a cylinder 10 cm in radius, where this radius is the distance from the line source of X-rays to a parallel line which is at the midpoint of the rail switch. The rate of X-ray energy deposition per unit mass in the gas is

$$dD/dt = IVf_a m / 2\pi r L$$

where I and V are the current and voltage respectively, applied to the line source of the X-ray generator, f is the X-ray production efficiency, L is the spark gap length and a_m the mass absorption coefficient of X-rays in the gas. (For this estimate, we neglect the attenuation of 20 keV photons through a foil, such as several mils of titanium, which separates the X-ray generator from the spark gap.) This energy density, divided by the energy required to create an ion-electron pair W , must equal the required electron production rate

$$S = 5 \times 10^{15} \text{ cm}^{-3} \text{ s}^{-1}$$

Therefore,

$$S = d_0 IV f_a m / 2\pi r L W$$

where d_0 is the density of the gas. The X-ray generator current per unit length is given by

$$I/L = \frac{2\pi r W S}{d_0 V f_a m}$$

For example, consider a 50 kV X-ray source with an efficiency of 0.5 percent and a linear absorption coefficient of $5 \times 10^{-6} \text{ cm}^{-1}$,

$$I/L = 14 \text{ A/cm}$$

For a 75 cm line source, this corresponds to 1000 A. We assume a pulse width of 40 ns. Consider a 50 kV X-ray source operating at 1.2 kHz. The average power (exclusive of thermal losses) is nominally

$$P = IVt(\text{prf}) = 2.4 \text{ kW}$$

This represents a relatively small power loss (2%) compared to the 160 kW overall power of the module.

Other designs which include a thermionic diode are more efficient. The design which includes direct emission of the thermionic electrons into a tantalum foil separating the diode from the switch would reduce by the factor three the distance of the X-ray source from the switch. This would result in a nominal reduction of a factor of 9 in X-ray source power. However, the foil would require cooling, and this introduces some additional complexity in the design.

Magnetic Modulator

The pulse power requirements for the X-ray pre-ionizer electron source are as follows:

$$V = 50 \text{ kV}$$

$$I = 14 \text{ A/linear cm of source length}$$

$$t_e = 40 \text{ ns}$$

$$f = 1250 \text{ Hz}$$

For a 0.75 m source, the total peak current required is 1 kA. The short pulse length, relatively high peak power (70 MW) and high pulse rate places rather severe burdens on the pulse power.

A magnetic modulator shown in Figure 8 is efficient and cost-effective. This is a type "A" pulse-forming network (PFN), whose energy is switched into the e-beam load with a magnetic switching transformer. The PFN is resonantly charged via thyatron V_1 and transformer T_1 . Transformer T_1 is a 1:4 step-up transformer which provides 100 kV charge voltage to C_N . The intermediate energy store C_1 is dc resonantly charged from a nominal 17 kV power supply for a multiple laser system; it is expected that a single power supply provides power for many X-ray preionizer pulse power systems.

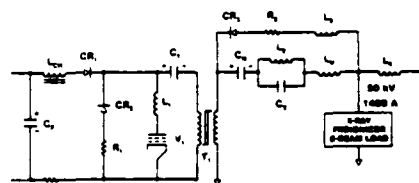


Figure 8. X-Ray preionizer pulse power magnetic modulator

The type A PFN was selected as the best compromise after consideration of pulse shape, series inductance and overall circuit efficiency. To obtain the necessary output pulse length, the effective pulse width of the PFN has been chosen as 90 ns to yield a 50 ns flat-top (portion above 50 kV). The 50 kV/1 kA load presents a 50 ohm load; hence, it can be shown that for a matched system, the network elements will have the following values:

$$C_N = 0.387 \quad t_e/Z_N = 0.7 \text{ nF}$$

$$C_2 = 0.256 \quad t_e/Z_N = 0.5 \text{ nF}$$

$$L_2 = 0.0606 \quad t_e/Z_N = 270 \text{ nH}$$

$$L_1 = 0.190 \quad t_e/Z_N = 860 \text{ nH}$$

The energy stored in C_N is transferred to the load by the magnetic switching transformer T_1 whose saturated (secondary winding) inductance is small compared to the required series inductance of L_N .

Modest switching losses in the transformer are present. The eddy currents losses, when added to those from the core and leakage current, yield an estimated total switching loss of 2 J per pulse or 2.5 kW. The energy which must be transferred from C_1 to C_N is the 2 J plus $50 \text{ kV} \times 1000 \text{ A} \times 90 \text{ ns} = 5 \text{ J}$, for the total of 7 J.

Standard thyatrons are suitable for this circuit. Thyatron losses are estimated at 1 J per

pulse. This, added to the losses above, results in the loss energy of 3 J per pulse. The total power for a modulator operating at 1250 Hz is therefore 13 kW.

U.V. Preionization of Electrical Discharges

An alternative preionizer source is UV light. This can come from many sources, both external to the discharge or internal in the form of sparking arrays or corona discharges¹⁴. The UV is typically absorbed over short distances of about 1 cm, depending on gas, wavelength, etc., which can lead to pronounced non-uniformities in the discharge. This is bad for laser discharges, but acceptable for switches when the switch dimensions are comparable to the light penetration length.

Two options are available for generating the required amounts of U.V. In one, we use spark discharges, although this technique may result in similar life limiting process as do spark gaps. Another technique calls for use of Xenon flashlamps along the meter width of the switch.

Radioactive Preionization

A moderate amount of radioactive ionization can also provide sufficient electrons^{15,16}. Each disintegration with energy E (in eV) produces $N = E/30$ eV electrons. Typical alpha-disintegrations have an energy $E = 4-8$ MeV or $N = 2 \times 10^5$ electrons, while beta - energies are of order $E = 20 - 400$ keV, for $N = 2 \times 10^3$ electrons. These electrons are generated fairly uniformly along the particle track, which has a typical range $R = 3$ cm and $R = 5$ cm (for atmospheric air and the cited parameters). This corresponds to about 7×10^4 electrons/cm and 400 electrons/cm.

CONCLUSIONS

Preionization

The feasibility of reliably attaining the preionization level of 10^7 to 10^8 cm⁻³ is within the present state of art. At this point we lean towards the thermionic or field emission bremsstrahlung X-ray source but the near future may see UV or microwave sources equally practical. In certain applications, radioactive sources are suitable.

Uniform Discharge

On the basis of laser developments to date, uniform discharges are attainable in pulse power systems using the prescribed preionization. The suitability of this discharge for switching is the main issue to be addressed in future experimental work.

Of particular concern is the switch resistance which may be too high for switching applications if the energy deposition during the early time of the discharge is insufficient or does not contribute to ionization. Consequently, the details of electrode design may be critical to control the discharge volume and therefore, the deposited energy density. These considerations favor a monatomic gas mixed with an electronegative component, in a mildly field enhanced switch geometry in order to obtain a ribbon-shaped discharge about 0.1 cm thick.

Erosion

To minimize erosion by electrode melting, current density should not exceed 100 kA/cm², and this would be accomplished if the uniform discharge switch operated as intended. The exact boundaries of allowable current density must be determined experimentally.

Mechanical Design

We have concluded the mechanical design requirements to attain long life, low inductance, and easy maintenance can be met. The design is based on the relatively high gas breakdown strength of about 80-90 kV/cm at 3 abs. atm. and the design stress of 60 kV/cm. These values correspond approximately to those of air.

ACKNOWLEDGMENTS

The authors wish to thank Professor S.C. Lin of U.C.S.D. for his assistance throughout this program, and V. Valencia of Maxwell for the analysis of the preionizer modulator requirements.

REFERENCES

- 1 Engineering Bulletin of August 1979, "Rail-Gap Switch, Catalog 40100."
- 2 A. Ramrus, "Development of a 100 kV Multi-megawatt Gas Switch," Proc. Thirteenth Pulse Power Modulator Symposium, June 1978.
- 3 A. Ramrus and J. Shannon, "Testing of a 100 kV 100 Hz Rep-Rate Gas Switch," IEEE Trans. Plasma Science, Vol. PS-8, No. 3, September 1980.
- 4 A.J. Palmer, Appl. Phys. Lett. **25**, 128 (1974).
- 5 J. Levatter and S.C. Lin, "Necessary Conditions for the Homogeneous Formation of Pulsed Avalanche Discharges at High Gas Pressures," J. Appl. Phys. **51**(1) January 1980.
- 6 Physics of Fully Ionized Gases, p. 137, 138, L. Spitzer.
- 7 H.M.S. Massey and J. Burhop, "Electronic and Ionic Impact Phenomena", 2nd Ed., Vol II, Oxford, 1969.
- 8 R.F. Fernsler, A.W. Ali, et al, NRL Memorandum Report 4110, (1979). We are grateful for permission to use this code.
- 9 R.F. Fernsler, NRL, private communication.
- 10 J.I. Levatter, "Cathode Preionizer Life Tests and Application to a Discharge Excited Laser", LASL Final Report on Contract 4-X11-8668W-1.
- 11 J.E. Gruber and R. Suess, "Investigation of the Erosion Phenomenon in High-Current, High-Pressure Gas Discharges," Institut fuer Plasma Physik, Garching bei Muenchen, December 1969.
- 12 G.S. Belkin and V. Ja. Kiselev, "Electrode Erosion in Pulsed High-Current Discharges," Sov. Phys. Tech. Phys., **11**, 280 (1966).
- 13 V.E. Il'in and S.V. Lebedev, "Destruction of Electrodes by Electric Discharges of High Current Density," Sov. Phys. Tech. Phys., **7**, 717 (1963).
- 14 H. Seguin and J. Tulip, Appl. Phys. Lett., **21**, 414 (1972).
- 15 I. Bigio, IEEE J.Q.E., **14**, 75 (1978).
- 16 I. Bigio, J. Physique, **C7**, **40**, 365 (1979).

HIGH POWER SPARK GAP TEST RESULT*

Rudolf Limpacher
Avco Everett Research Laboratory
Everett, MA 02149

Rich Schneider
Physics International Company
San Leandro, CA 94577

Abstract

A vortex flow spark gap was tested at repetition rates up to 40 pps with voltages up to 130 kV and average power transfer of 0.51 MW. An underdamped discharge circuit was used with a period of 19 μ sec to demonstrate switch recovery with a charge transfer of over one coulomb per pulse. No command charge system was required with the L-C charging circuit. The switch recovered with ring-up times of 16.9 msec and 12.8 msec. No hold-off degradation was observed over burst times consisting of 1000 shots.

The switch was typically operated at 56 psig with \approx 60 scfm of air flow, but reliable operation was found with a gas flow of as low as \approx 15 scfm. The switch demonstration was limited to a repetition rate dictated by the power supply capability. The maximum duration of the burst was governed by heating of the load resistor.

Introduction

Spark-gap switches are used in many pulsed power systems where the operating requirements exceed the Hydrogen Thyratron limits in voltage, current, or rise-time. A particular case of this is in high energy Marx generators employed in large pulsed power systems. These generators have been in use for many years as single-shot systems, but, to date, none has been built that could be repetitively pulsed. The program described here undertook to develop and test a spa-k-gap that would be a satisfactory switch for such a system.

Using a typical Marx-generator from an existing pulser as a model, we constructed a test-bed that would duplicate the duty conditions required of the switch. This test-bed is a single-stage Marx that stores 0.25 coulombs at 125 kV and discharges into an underdamped L-C-R circuit such that the total charge-transfer through the switch is 0.75 coulomb per shot. This and the peak current (> 160 kA) represent quite well the performance requirements in the model Marx.

The baseline switch design was patterned after a lower voltage switch that had been developed at PI and successfully employed in applications up to \approx 50 kW average power at frequencies to > 1800 Hz.

The goal for this new switch was to increase the power handling ability to \approx 375 kW with higher voltage stand-off but at the more modest rep-rate of 25 Hz. Additionally, it was hoped that we could identify the problem areas that would need to be addressed to extend performance to 1,500 kW at 100 Hz for the same voltage and coulomb requirements. The experiments were to be done in two parts; 1 - with autocharging, to determine when it would be necessary to implement command-charging, for switch recovery, and 2 - with command-charge, to extend the rep-rate to the goal.

In fact, switch recovery was good enough that the limit of the modulator's ability to recharge the test-bed was reached while still operating in the autocharging mode and the command-charge feature was never implemented. This represented an achieved switch performance

of 40 Hz and > 500 kW average power with dielectric strength recovery ≤ 12.8 ms.

Test Facility and Circuit

The test-bed was integrated with a modulator and trigger-generator that existed at AERL to form the complete test facility. A six-ampere power supply and a 100-ampere power supply are available, and the six-ampere supply was employed since the rep-rate was not expected to exceed 25 Hz. The test circuit is shown schematically in Figure 1. The 2 k Ω large copper sulfate resistor, located between the D.C. power supply and a 6.4 μ F filter capacitor, served as a short-circuit current limiting resistor. The filter and choke combination yields peak ring-up currents of 20-30 A. An air driven vacuum switch assembly served as the means to obtain the first full test bed capacitor charge by sequentially turning on the primary power followed by the switch closure. The next components in line are the 18 henry air inductor followed by the high power blocking diode. Not shown on the diagram is a voltage probe and an air actuated shorting switch. The shorting switch allowed the discharge of both the filter and test bed capacitor as part of the automatic shut down procedure. A coaxial high voltage cable transmitted the power to the electrostatically shielded pulsed power room which contained both the test bed and trigger generator. The available trigger generator, rated for 30 pps with an output of 30 kV, was modified during the test period to extend its performance range to 40 pps. The trigger signal was stepped up with a 6:1 (turns ratio) transformer which was integrated into the test bed. The trigger signal polarity was selected to be negative to facilitate break down of the positively charged switch. In series with the trigger was a Trigger Isolation Gap (TIG).

The original test bed circuit was selected to store 15 kJ at 125 kV. The combination of the load resistor and inductor were selected to yield a peak discharge current of \approx 150 kA and a total switch charge transfer of \approx 0.75 coulombs. Unfortunately, the original capacitors did not survive the initial check out period. This forced us to utilize two available capacitor stacks with a net capacitance of 2.1 μ F. This reconfiguration increased the circuit inductance such that the discharge period was longer, reducing the peak current, however, the total charge transfer was increased to \approx 1 coulomb. A small change to the load resistor was also made. These circuit modifications increased the "on" time of the switch rendering switch recovery even more difficult. The ring up period is given by;

$$\tau_C = \pi \sqrt{L_S C_{eff}} = 16.9 \text{ ms}$$

where

$$C_{eff} = \frac{C_b C_F}{C_b + C_F}$$

and

*The work reported was performed under DAAK40-79-C-0197 with Defense Advanced Research Project Agency.

$L_s = 18$ henries is the charging inductor

$C_b = 2.15$ μF is the test bed capacitor, and

$C_f = 6.4$ μF is the filter capacitor.

The use of a finite value filter capacitor has the effect of reducing the ring up period and reducing the voltage ring up ratio. This requires a power supply voltage setting of ≈ 80 kV, significantly higher than 50% of the test bed voltage; however, well within the capabilities of the available facility.

Air was the only dielectric gas tested. A compressor with a dryer in series charged up a large gas storage bank to 2000 psig. A dome regulator allowed the presetting of the output pressure. Two lines with two separate remote controlled and sequenced valves controlled and supplied the flow. The gas was typically turned on ~ 10 seconds prior to the power supply turn on. The dome regulator pressure setting in conjunction with the sonic input orifices determined the switch mass flow for each side of the switch separately. A strain gauge pressure transducer was installed upstream of both orifices. With this arrangement the gas flow injection into each half of the switch could be selected separately. Once the mass flow was selected the switch pressure was determined by the area of a second set of sonic orifices, located at the end of the exhaust gas lines. From a practical point we selected the area ratio of the two sonic orifice sets. This yielded a given flush factor and the dome regulator settings controlled the switch pressure. A pressure transducer monitored the steady state switch pressure, while another sampled the plenum pressure. A small amount of nitrogen flow was used for the TIG.

A picture showing the test bed prior to installation is seen in Figure 2, while Figure 3 shows the switch with the inner envelope removed.

Instrumentation and Control

The experiment was automatically sequenced. The number of pulses and repetition rate were preprogrammed to an electronic generator, and additional timers were used to sequence the remaining events such as the turn on of the power supply, gas flow, recorders, vacuum switch actuation, data acquisition, and the electronic pulse generator. These timers also controlled the shutdown, initiated either by the completion of the preselected burst count or through the detection of a fault. Other set points, such as a minimum and maximum dome regulator pressure, maximum power supply voltage and current, minimum trigger generator voltage, etc. had to be preselected and served as trip points to protect the facility and test bed during the critical time of the automatic sequence.

As instrumentation, we used a voltage divider to yield the capacitor charge voltage. This divider was located downstream of the blocking diode. The charging current was monitored by two separate current transformers. They were located on the high voltage side and return of the charging system. In addition the integration of the charge current served as an independent check of the switch voltage. Charge current was recorded simultaneously on the optical strip chart recorder, on an oscilloscope, and on a channel of a Digitizer. We used two monitors for the discharge currents, a current transformer as well as a Rogowski loop. Both signals were recorded on an oscilloscope and Digitizer. Two additional current transformers were used to monitor the primary as well as secondary currents of the trigger transformer. With an additional voltage monitor on the secondary side of the transformer the trigger system and the TIG breakdown was monitored.

We utilized four channels of strain gauge pressure transducers. We typically recorded the pressure upstream

of an input orifice and output orifice, the pressure between the inner and outer envelope as well as the switch pressure. All these transducers were connected by a three foot long 1/4 Tygon line to obtain electrostatic insulation. No attempts were made at this time to get msec type pressure resolution.

Two dual channel oscilloscopes, two dual channel high-speed digitizers with 200 MHz throughput and two strip chart recorders were used to record a number of important functions. A 24-channel strip chart recorder recorded the output of strain gauges and timing signals. This recorder was typically used with a paper speed of 10 inches/sec (maximum 80). A 12-channel optical recorder was used for signals requiring kilohertz type response and could be operated at the maximum paper speed of 160 in/sec and did allow the direct recording of the switch test bed charging cycle. In combination with passive pulse stretching circuits a recording of trigger and discharge signals was obtained. This type of diagnostics did not only yield timing information of submillisecond resolution, but also gave some quantitative information of average signal level and duration.

Gas Flow System

For this experiment we used an available gas flow system with a maximum mass flow capability of 2 lbs/sec of air. This mixing and gas flow system can be used with practically any kind of noncorrosive gas mixture; however, only air was used for these experiments.

The air supply system consists of a 10 cfm air compressor and air dryer. Dry air is stored in cylinders at 2000 psig and provided the storage for extended run durations. The output can be regulated between 0-250 psig. Two one inch lines served as supply lines from the dome regulator output to the test bed.

Experimental Result

We started the experimental effort by determining the spark gap self breakdown curve over the voltage range from 48 to 100 kV. For this purpose we use the complete test bed, pressurized the TIG such that it would not self-trigger, selected a static spark gap pressure and slowly charged the capacitors. This procedure yielded the following straight line fit with 95% of all data points following within $\pm 3\%$:

$$V_{SB} = 48 \text{ kV} + 2.67 \frac{\text{kV}}{\text{PSI}} P \quad (1)$$

where P is the switch pressure in psig. It further was shown that by recharging the capacitors within ≈ 1 minute without flushing the gap breakdown did generally occur at 10-20% low voltage. This indicated that flushing of the hot gas and removing of other by-product is desirable.

The operating switch pressure was selected empirically to yield good switch performance. We found that a pressure of 56 ± 4 psig gave a high reliability of repetitively pulsed operation with minimal gas flow requirement. Runs up to 68 psig were undertaken with no noticeable changes. By using 56 psig in Equation 1 we conclude that for most of the 130 kV runs, the switch operated at 66% of static breakdown. This is close to the theoretical optimum of a mid-plane gap. As one side of the gap breaks down the second half is overvolted by 1.32. Operating closer to the self-breakdown voltage will increase the prefire probability, while operating at a higher pressure may cause difficulties in breaking down the second half of the switch or cause significant jitter.

For the majority of runs an output orifice of 0.201" diameter was used. This orifice was calibrated and yielded a discharge coefficient of 0.75. This yields a mass flow of 3.9×10^{-2} lb/sec (17 gr/sec) of

air per switch side.

A convention adopted for the evaluation of a gap recovery is the number of times the volume between the electrodes has to be flushed in a time period given by previous shot and the time full voltage is reapplied to the gap. Using the volume defined by the electric field of $E > 0.8 E_{max}$ a volume per side of $\approx 30 \text{ cm}^3$ is obtained. It follows that the volume exchange with the 0.201 orifice was 1.6 times during the 16.7 msec recharging time. Of interest is to note that experimentally the pretrigger rate appeared to be less at 40 pps than at lower repetition rate. This is not unexpected since with a fixed recharge time the switch did not have to hold off full voltage as long at the higher repetition rate. It remains to be shown if this trend would continue to the maximum (60 pps for this charging inductor) repetition rate, or if other effects would start to dominate.

We proceeded to set up a run condition by typically dialing in eight shots. This number was convenient since our digitizer had a maximum storage of eight shots. Once the diagnostic and switch performance was satisfactory we increased the burst durations to several seconds, typically without degradation of performance. At 20 pps we made several 500 pulse bursts and one 1,000 shot burst with full charge and a voltage of 130 kV. One 500 shot burst had no pretrigger pulse. The 1,000 pulse burst had 12 pretriggered pulses randomly distributed throughout the run. All breakdowns occurred at or nearly at full charge and full recovery took place for the next recharging. The heating of the load resistor did limit us to 1,000 full charge shots. From the available diagnostics it was not clear what caused the pretrigger problem, however, some data indicated that most likely the TIG was the culprit since the pretrigger statistics could be altered by the TIG gas flow rate and pressure.

As we increased the repetition rate beyond the 25 pps, the run duration was limited to a few seconds by the power supply. We obtained one second, full charge (130 kV), bursts at 40 pps without pretriggers, with no change in the waveform or indications of switch or test bed problems. To increase the 40 pps data base we selected to reduce the test bed capacitor to 50% (1.1 μF) this not only allowed us to operate the power supply for longer durations but also tested the switch with a 12 msec recovery time. With this set up we made several one second bursts and one 1400 shot burst without major problems.

Finally we reduced the output orifices, reducing the flush factor from the original value 1.6 to 1.24, 0.91, 0.65, 0.51, and 0.31 respectively. With the 0.51 flush the incidence of pretriggers began to be noticeable, while with a flush of 0.31 5% of the shots pretriggered. The number of shots taken at these conditions was not sufficient to derive self-fire statistics; however, from this flow reduction test it can be concluded that this type of switch can be operated with a reasonable reliability with a flush factor of 0.5 to 1.0 for full recovery without flow modification. Further reduction may be possible with flow improvement.

Figure 4 b,c show the discharge current superpositions for a burst of 40 pulses and repetition rate of 40 pps at a charge voltage of $\approx 130 \text{ kV}$. The superposition of the recharging current is shown in Figure 4 a. Figure 5 shows the first eight traces of a 500 pulse burst at 20 pps, as recorded by the two digitizers. The top trace is the trigger signal, while the lower trace gives the discharge current. A typical optical recorder trace is given in Figure 6.

During the test series we accumulated a total of 5419 shots on the spark gap and transferred a total of ≈ 5056 coulombs. The erosion of the electrode material turned out to be less than anticipated, and consequently, was not accurately determined. The measured change in gap was less than 0.001-0.002 inches and the change in

mass of each electrode was less than 0.5 grams. Both of these figures are consistent with an erosion rate of $< 10^{-4} \text{ gr/coul}$; however, the accuracy of the measurements are about the same magnitude as the change. From the electrode discoloration it appears that most arcs struck predominantly around the inner and outer edges. This implies that more rounding is needed to relieve the enhancement and insure more uniform erosion.

Summary

Initial Marx switch tests were performed on a particular switch with a power transfer of ≈ 0.5 megawatt, voltage of 130 kV, repetition rate of 40 pps, ring up period of 16.7 msec and charge transfer of approximately one coulomb per shot. These tests demonstrated successful spark gap switch performance up to the various limits of the selected facility. These tests were performed with a straight L-C charging without the use of a command charge system. With the use of air the switch recovered fully during the 16.9 msec charging time with a minimum flush factor of ≈ 0.5 . Half power test with ring up time of 12 msec indicate that the repetition rate of this type of switch may be at least extended to the 80-100 pps repetition rate range. An upper limit of $1.0 \times 10^{-4} \text{ gr/coulombs}$ electrode erosion was observed. Full energy runs with 1000 shots suggest that with some switch modifications this type of switch may be used reliably for long duration applications.

Acknowledgment

The authors would like to acknowledge the formidable laboratory assistance of S.M. Freshman, Dave Drury, C.J. Thieme, and H. Kishi whose effort and expertise were substantially responsible for the success of these tests.

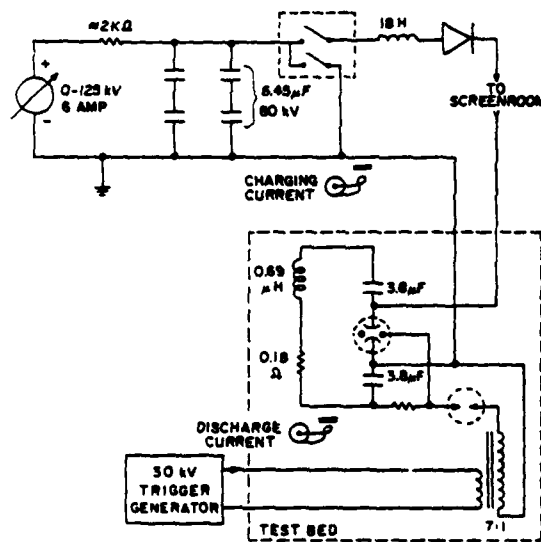


Figure 1 Simplified electrical schematics of the initial Marx switch test facility. The two 3.8 μF capacitors were replaced during the tests by a 2.1 μF capacitor stack.

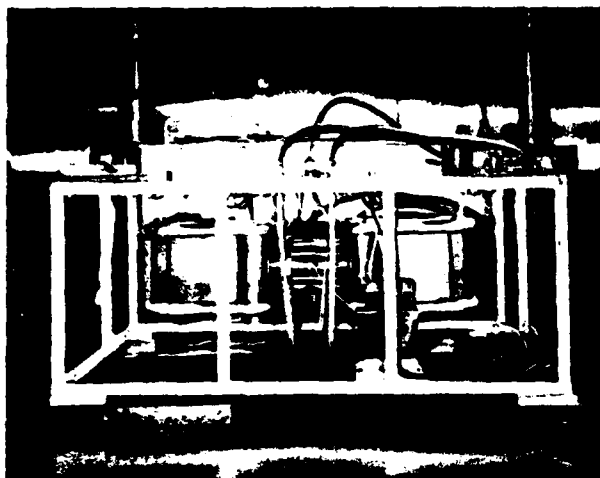


Figure 2 Test bed removed from oil tank. The load resistor is hidden behind the capacitor and spark gap assembly.

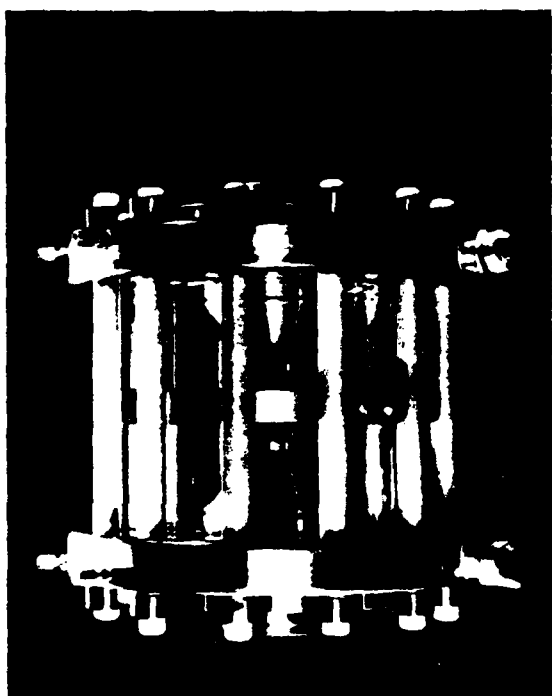


Figure 3 Photograph of spark gap with the inner envelope removed.

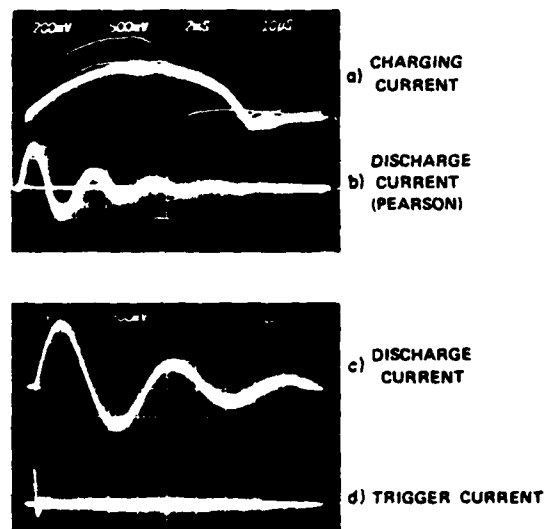


Figure 4 Oscilloscope traces for a typical 40 pps, 130 kV, 18.2 kJ, 1.6 flush, and 40 pulse burst.

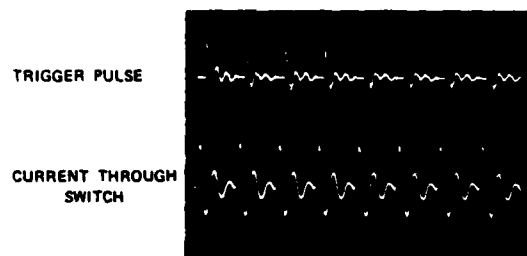


Figure 5 Trigger signal and switch current of the first eight pulses as recorded by one digitizer. The recording is of a 20 pps, 130 kV, 18.2 kJ, and 500 pulse burst.

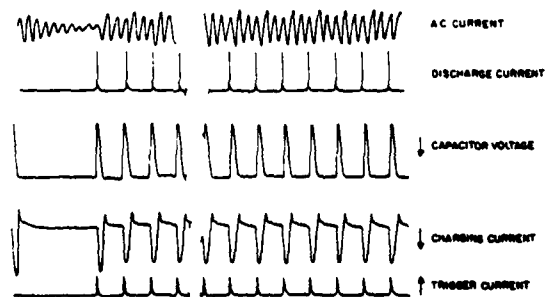


Figure 6 Beginning and end of a 20 pps, 130 kV, 18.7 kJ, and 500 pulse burst optical recorder trace. The trigger timing is synchronized to the zero crossing of the primary power shown on the top trace. The recording starts with closure of the vacuum switch. The first triggered pulse occurred about 160 msec later.

R. G. Adams, J. R. Woodworth, C. A. Frost
Sandia National Laboratories
Albuquerque, New Mexico 87185

Summary

We have been exploring the use of high-beam-quality UV lasers to trigger megavolt gas switches essential in many large pulsed-power systems. Using less than 0.1 joule from a KrF oscillator-amplifier laser system (unstable resonator with ~ 100 microradian divergence) to trigger a 2.8 MV gas switch insulated with SF₆, we have achieved triggering with a 1- σ jitter of 0.5 nsec for voltages varying from 70% to 90% of the self-breakdown voltage of the switch. The triggering delay between the laser pulse and the switch closure is relatively insensitive to switch voltage variations, changing by as little as 1.5 nsec for a 10% change in voltage. Parametric studies of laser triggering with lenses of different focal lengths and at various input laser energies have been discussed.

Abstract

We are investigating the use of UV lasers to trigger multi-megavolt gas switches found in many large pulsed-power systems. Using 77 mJ from a low-divergence (100- μ rad) KrF laser system to trigger a 2.8-MV switch, we have demonstrated a 1- σ jitter of 0.5 ns for a series of applied voltages ranging from 65% to 90% of the self-break voltage. (Jitter is defined as deviation of the data points from a best fit line through the data.) In this sequence of measurements, the triggering delay was relatively insensitive to voltage variations, changing by only ~ 2 ns for a 10% change in voltage. The low-divergence KrF beam is focused through a hole in one switch electrode, forming a breakdown arc in the high-pressure SF₆ between the electrodes. Breakdown arcs have been demonstrated which stretch all the way across the 11-cm electrode gap in the 2.8-MV switch. The sudden appearance of this conductive breakdown arc triggers the switch. Techniques, applications and results will be discussed.

Introduction

Today various areas of pulsed-power research demand low jitter triggering of high voltage, high current gas switches. This requirement is especially vital for Inertial Confinement Fusion (ICF) work being conducted with the Particle Beam Fusion Accelerators (PBFA) at Sandia National Laboratories. For example, PBFA-I is a light-ion-beam fusion driver constructed to deliver in 40 nsec a particle beam having a total energy of 10⁶ joules to an ICF target.¹ Timing of this particle beam is controlled by up to thirty-six gas switches, each of which must hold off a pulsed voltage of about 2.8 megavolts, then be triggered with temporal jitter of a few nanoseconds and conduct a current of about 10⁵ amperes repeatedly without damage. Other triggering applications involve 6 MV switching for PBFA-II (now under construction).

Extensive experimental research and some theoretical treatment involving laser-triggering of gas switches using visible and infrared lasers has already been performed; an excellent review of this work is

given by Guenther and Bettis.² These visible/IR experiments typically focus the laser beam to produce a point plasma on one switch electrode, thereby triggering the switch. Generally, this technique attains excellent results for moderate voltage switches having short gap spacings (≤ 1 cm); however, for large gaps (~ 10 cm) operating at voltages above one megavolt, the triggering behavior is somewhat degraded. Subnanosecond jitter typically is obtained only at voltages well above 90% of self-breakdown voltage (SBV) or with extremely high laser power, and also most results are obtained only in gas mixtures consisting mainly of argon at very high pressures.²

Accordingly, we have directed our efforts towards a different mechanism to trigger the switch. Instead of generating a point plasma at one electrode, we utilize a volume interaction between the UV-laser radiation and the insulating gas in the switch to produce an ionized channel between the switch electrodes. Bradley and Davies³ investigated such volume interactions of UV laser radiation with dielectric gases in a switch in 1971, but since the only UV lasers available then had poor beam quality and low output energies, the technique was not pursued further. Recently, Rapoport et al.⁴ determined that SF₆ gas breaks down in a KrF laser field (248 nm) at an order of magnitude lower intensity than does room air and utilized this technique to trigger an 80 kV spark gap insulated with SF₆. This result is significant because most high voltage switches use pure SF₆ (a common, high-dielectric-strength gas) to minimize electrode spacing and required gas pressure. Previously, we used a KrF laser for UV laser triggering of both a 0.5 MV pulse-charged switch⁵ and a multi-megavolt switch.⁶ This paper reports a further extension of that work to the full scale testing of a 2.8 MV SBV gas switch similar to those in use on PBFA-I.

Apparatus

The gas switch used in these experiments had 10 cm diameter hemispherical stainless steel electrodes which were spaced 11 cm apart. The laser beam entered the switch through a 6 mm diameter hole in the (grounded) anode and was focused to a point approximately centered between the electrodes. The laser energy that passed through the arc struck the cathode and formed a point plasma on the cathode surface, which may have assisted the triggering process. The switch was insulated with 3100 torr of SF₆. The voltage source for the switch was a 35-stage Marx generator used in the circuit shown in Figure 1. This circuit provided a pulse with a (1 - cos ωt) waveform rising to about a 3 MV peak voltage in 650 nsec. The switch was triggered on the rising portion of this waveform. The switch voltage was monitored by integrating the signal from a current viewing resistor (CVR) located in series with the peaking capacitor. Switch closure was monitored with a B probe located adjacent to the switch. This probe provided a signal proportional to the derivative of the current through the switch.

The laser used in these experiments was a KrF oscillator-amplifier system that provided a 6 mm x 20 mm rectangular beam with an output energy of 0.13 J per pulse and a 20 nsec pulse length (FWHM). The laser divergence half angle, measured by scanning a pinhole across the focused beam, was 100 microradians. This

* This work performed at Sandia National Laboratories supported by the U.S. Department of Energy under contract number DE-AC04-76DP00789.

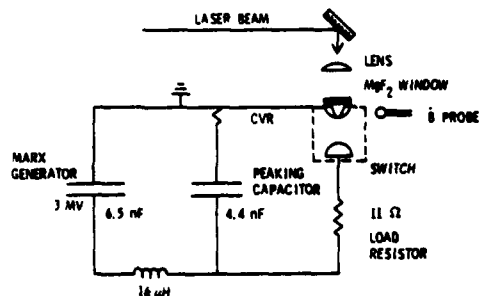


Figure 1. Schematic of the basic components for the 2.8-MV switch experiments.

system, which has been previously described,⁵ consisted of a KrF oscillator in a stable cavity configuration with the output spatially filtered to obtain a low-divergence beam. This low-divergence beam was injected into the amplifier which employed a positive-branch confocal unstable resonator with a magnification of ten. Optically, our oscillator-amplifier setup was similar to that described by Goldhar et al.⁷ except that we had no provision for spectral line narrowing. It was necessary to reduce the timing jitter between the oscillator and amplifier to less than ± 2 nsec in order to obtain a repeatable low-divergence output from the amplifier.

Three dielectric-coated UV mirrors were used to steer the laser beam to the top of the oil-filled tank containing the switch and Marx generator. The time history of the laser pulse was monitored with an ITT F4018 UV photodiode (response time < 1 nsec). Laser energy was measured with a 2.5 cm diameter Scientech calorimeter, which was positioned immediately before the lens that focused the laser beam into the switch. A final diagnostic to check beam quality was a glass cylinder having a UV entrance window and filled with 1600 Torr of SF_6 . The laser beam could be diverted and focused into this cylinder to form a visible breakdown arc in the SF_6 . Pictures were taken of successive arcs in this cylinder to determine shot-to-shot repeatability of the arc; typically, the lengths of breakdown arcs were repeatable to $\pm 10\%$. For some experiments, the laser beam was uniformly attenuated by partially transmitting dielectric-coated mirrors.

To determine switch closure relative to the arrival of the laser pulse in the switch, the signals from the UV photodiode and the β monitor were monitored on a dual-beam oscilloscope (Tektronix 7844) and a CAMAC-micro-computer. The computer system employed level crossing discrimination using LeCroy model 2228A time-to-digital converters (TDC) to measure the interval between the time the photodiode signal and the β signal crossed predetermined threshold voltages (see Figure 2). The switch voltage was digitized with a LeCroy model 2259A peak sensing analog-to-digital converter and recorded. The micro-computer provided no pulse shape information but defined the delay interval to an accuracy of ± 100 psec. The oscilloscope traces provided overall pulse shape information and a cross check of the delay interval to an accuracy of ~ 1 nsec. Since the absolute value of the delay interval was a parameter of interest in these experiments, cable lengths and optical paths for the UV photodiode and switch current signals were determined to an accuracy corresponding to ± 1 nsec.

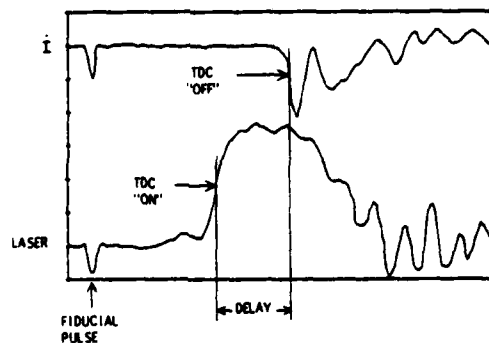


Figure 2. Oscilloscope traces showing time dependence of the laser pulse (lower trace) and time derivative of switch current (upper trace). Approximate times at which the time-to-digital converters turned "on" and "off" and the subsequent value of "delay" are shown for this shot. After switch closure, the trace showing the laser pulse becomes dominated by electrical noise. Time scale is 10 ns per division.

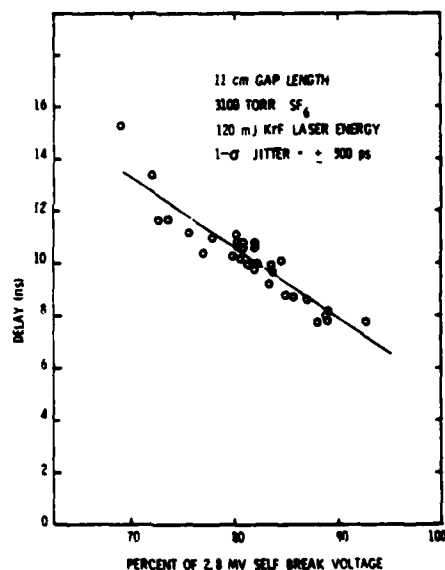


Figure 3. Graph of time delay to switch closure versus voltage for a 2.8 MV KrF laser-triggered switch. Laser energy was focused by a 100 cm focal-length lens to produce an arc centered in the 11 cm gap. The 1- σ jitter, defined as deviation from a least-squares fit to the straight line through the data, is 500 psec.

Results

The results of two different experiments are reported in this section. In order to determine optimal focus, laser-triggering performance was examined with 120 mJ of laser energy focused into the switch through different lenses with focal lengths

Table I. - KrF Laser Triggering Results for 120 mJ Input Laser Energy

Focal Length of Lens (cm)	Laser Arc Length (cm)	1- σ Jitter (ns)	ΔT Delay 80-90% of SBV (ns)	T Delay at 80% of SBV (ns)
200	11	0.77	1.4	10
100	6	0.50	2.8	11
50	3	0.76	2.8	13
20	1	3.2	13	31

ranging from 20 cm to 200 cm. The lens was placed as shown in Figure 1 and located so that the breakdown arc in the SF₆ was roughly centered in the 11 cm electrode gap. Plano-convex Suprasil-quartz lenses were used with the flat side toward the focus to minimize third-order image aberrations. Figure 2 shows a typical oscilloscope trace of the laser pulse from the UV photodiode and the derivative of the switch current as seen by the B monitor. The laser pulse shape and the I signal rise time were both repeatable to better than 10%, although the I leading pulse amplitude did scale with switch voltage. Figure 3 shows typical triggering delays plotted versus percent of the 2.8 MV self-breakdown voltage of the switch taken with a 100 cm focal-length lens. A straight line fit to the data is also shown. Jitter, defined as deviation of the data from the straight line has a one standard deviation (1- σ) value of 500 psec for the data shown. The switching delay is relatively insensitive to voltage, with delay changing by only 2.8 ns between 80 and 90% of the self-breakdown voltage (ΔT Delay in Table I). A summary of the data obtained with the different lenses is shown in Table I. For lenses with focal lengths of 50 cm or longer, subnanosecond jitter was obtained in the 2.8-MV switch.

Table I also lists the visible arc length observed in the SF₆-filled glass cylinder for each lens. It is interesting to note that with the 50 cm focal-length lens, subnanosecond jitter was obtained even though the visible arc extended only about one-third of the distance between the two electrodes. The value of the switching delay at 80% of SBV (T Delay in Table

I) shows a clear trend with delay increasing as the breakdown arc becomes shorter. It should be noted that there is still some arbitrariness in the absolute value given for T Delay. The laser pulse itself had a risetime of approximately 5 ns. The risetime of the current in the switch was greater than 8 ns. Therefore, the voltage level selected as the "beginning" of the laser and switch current pulses had a strong effect on the value of "delay" that was observed; this result is inherent in the use of level crossing discriminators. For the data presented in Table I, the "delay" clock started about 2 ns after the beginning of the laser pulse and stopped about 4 ns into the switch current pulse. For the data presented next, slightly different voltage levels were chosen, resulting in differing absolute values of delay.

Switching performance was also examined as a function of laser pulse energy using a 50 cm focal-length lens. Figure 4 shows the time delay as a function of percent of self-breakdown voltage for five different input laser energies. Also shown in Figure 4 for each laser energy is a least-squares-fit to a straight line, which reveals that the delay can be well represented between ~ 65-90% of self-break voltage by a linear function. Further details of this linear time delay behavior are listed in Table II. It is apparent that delay decreases with increasing laser energies. Perhaps more important for practical switches is that the slope of the delay versus percent of SBV line decreases with increasing laser energy. From Table II for the highest tested laser energy of 127 mJ, the delay varies by only ~ 1.5 nsec for a variation of switch charge

Table II. - Behavior of 11 cm Gap PBFA I Switch Triggered with a Low Divergence KrF Laser Focused with a 50 cm Focal Length Lens

Switch Input Laser Energy (mJ)	Laser Arc Length (cm)	T Delay at 80% of SBV (ns)	ΔT Delay 80-90% of SBV (ns)	1- σ Jitter (ns)
127	3.1	17	1.5	0.66
110	2.5	*	2.4	0.53
77	1.7	19	2.5	0.51
60	1.6	*	2.6	0.35
40	1.3	21	3.3	0.71
30	1.1	26	5.7	1.56
27	1.0	28	7.0	1.32

* Different triggering levels were used on these two scans, producing displaced delay values.

voltage of about 280 kV (10% of the SBV). Further, the 1- σ jitter of the fitted line generally increases with decreasing laser energy. It is noteworthy that subnanosecond switching jitter is obtained for laser energies as low as 40 mJ. Finally, inspection of Figure 4 also reveals that the extent of the linear dependence region increases with increasing laser energy. Therefore, for laser energies above 40 mJ, predictable switch performance can be obtained below 80% of the self-break voltage where the prefire probability is low.

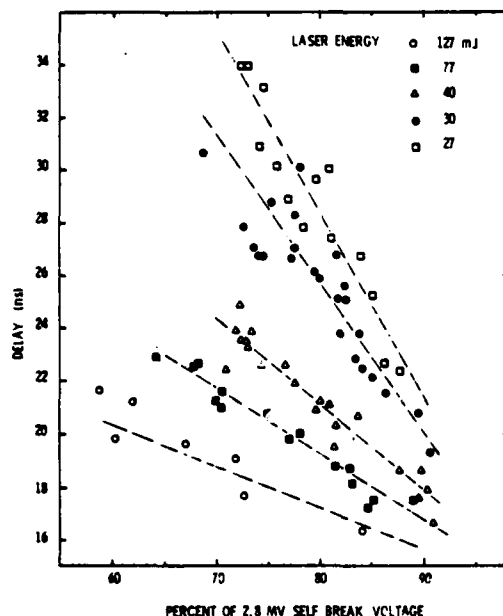


Figure 4. Graph of time delay to switch closure versus voltage for a 2.8 MV KrF-laser-triggered switch. Energies varying from 127 to 27 mJ were focused by a 50 cm focal-length lens to produce an arc centered in the 11 cm gap. Least-squares-fit lines to the data are shown for each laser energy.

Switching delay as a function of percent of SBV over an extended range for a laser input energy of 127 mJ is illustrated in Figure 5. Here the linear region extends from ~55 to 90% of SBV, and delays shorter than 40 nsec occur for charging voltages down to about 45% SBV. Even in the low 45-55% SBV region, jitter is only a few nanoseconds. For voltages less than 45% SBV, the delay increases very rapidly. All of the time delay data versus percentage of SBV exhibit the same general shape, but the onset of the rapid increase in delay occurs at higher voltages as laser energy is lowered.

The delay time at 80% of SBV as a function of laser energy is shown in Figure 6. For this switch, an energy threshold at ~40 mJ is exhibited, as delay very rapidly increases for input laser energy less than this value. The time delay to switch closure at 80% of SBV at this threshold energy level is about 22 ns, which very closely corresponds to the laser pulse width. This sudden increase in delay times when the delay becomes longer than the "effective laser pulse length" has been previously observed in visible² and infrared laser triggered switching investigations.

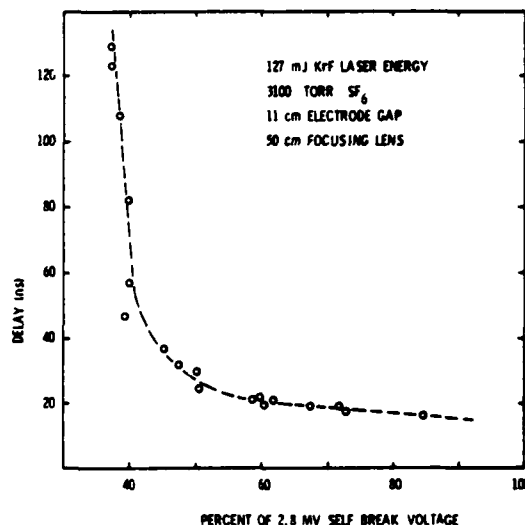


Figure 5. Graph of delay versus voltage for a 2.8 MV, KrF laser-triggered switch with 127 mJ of laser energy focused by a 50 cm focal-length lens. The "low jitter" triggering region extends below 60% of the self break voltage of the switch.

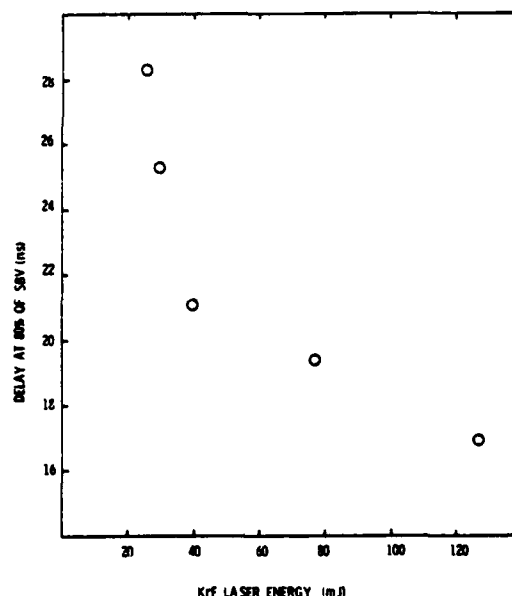


Figure 6. Graph of switching delay at 80% of the self-breakdown voltage of the switch versus laser energy focused by a 50 cm focal-length lens. Delay increases sharply after the delay becomes longer than the ~20 nsec long laser pulse.

Switch jitter and the slope of the linear-fit line of the switching delay as functions of laser energy are shown in Figure 7. The jitter increases rapidly for energies less than 40 mJ (i.e. switching delays longer

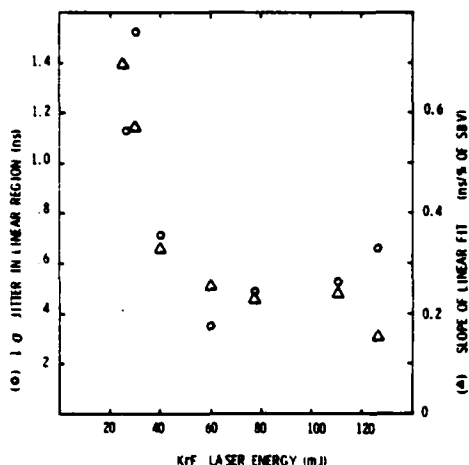


Figure 7. Graph of the 1- σ jitter and the slope of the linear-fit line of delay versus voltage as a function of laser energy. Both jitter and slope rise sharply for laser energies below 40 mJ.

than the laser pulse width.) Similarly, the slopes of the linear-fit delay lines increase to undesirably large values for laser energies below the threshold value. In fact, all the data shown in Figures 6 and 7 exhibit remarkably similar shapes, rising rapidly for energies below threshold and remaining relatively insensitive to energies above threshold. One explanation which was advanced by Guenther and Bettis² is that for switching delays less than the laser pulse width, the laser radiation functions as a continuous ionization source which smooths out variations in the avalanche buildup of the breakdown arc in the switch. Low switching jitter results if the laser pulse is repeatable. However, once the switching delay exceeds the laser pulse width, the statistical fluctuations in avalanche buildup produce much larger switching jitter.

Finally, gas breakdown with no applied voltage was briefly examined experimentally. The minimum laser energy capable of producing a visible arc in the SF₆-filled glass pipe at the focus of a 50-cm-focal-length lens was found to be 5 mJ. The 100 μ rad beam divergence implies a threshold breakdown intensity of about

$2.6 \times 10^9 \text{ W/cm}^2$ in 3100 Torr of SF₆ for a 20 nsec KrF laser pulse. This intensity agrees well with earlier breakdown thresholds measurements³ and within a factor of 2 with other investigations⁴ which defined breakdown differently.

Conclusions

We have demonstrated that UV-laser triggering can produce subnanosecond jitter in a 2.8-MV, SF₆-insulated gas switch with < 50 mJ of laser energy. This subnanosecond jitter has been obtained at voltages between 75% and 90% of the self-breakdown voltage, where prefires are unlikely. The switching delay is short (10-25 ns) and is relatively insensitive to voltage with delay changing by as little as 1.5 ns between 80 and 90% of the self-breakdown voltage of the switch. In one case, low-jitter triggering (a few ns jitter) has been demonstrated at only 50% of the self breakdown voltage of the switch. Thus, UV-laser-triggered switches appear to exceed all of the triggering requirements for large multiple-switch, pulsed-power generators such as PBFA-I. The use of UV lasers provides dramatic improvement in command-trigger performance and yields results unobtainable with other methods.

Acknowledgements

Many people have contributed to this project. We would like to thank Mr. W. B. S. Moore for the design and operation of the 2.8 MV switch test facility, Drs. T. A. Green, W. C. Sweatt and R. A. Gerber for helpful discussions, and R. A. Klein, M. M. Dillon and S. R. Babcock for their invaluable technical assistance.

References

1. T. H. Martin, G. W. Barr, J. P. VanDevender, R. H. White and D. L. Johnson, Proceedings of the IEEE 14th Pulse Power Modulator Symposium, June, 1980, p. 300.
2. J. R. Bettis and A. H. Guenther, IEEE J. Quantum Elect. QE-6 (8), 483 (1970).
3. L. P. Bradley and T. J. Davies, IEEE J. Quantum Elect. 1971, QE-7, (p. 464).
4. W. R. Rapoport, J. Goldhar, and J. R. Murray, IEEE Trans. on Plasma Sci., PS-8 (3), 167 (1980).
5. "UV Laser Triggering of High Voltage Gas Switches," J. R. Woodworth, C. A. Frost and T. A. Green, To be published in the Journal of Applied Physics, July 1982.
6. "UV-Laser Triggering of 2.8-Megavolt Gas Switches," J. R. Woodworth, R. G. Adams, and C. A. Frost, To be published in IEEE Transactions on Plasma Science, December, 1982.
7. J. Goldhar, W. R. Rapoport and J. R. Murray, IEEE J. Quantum Elect. QE-16, (2), 235 (1980).

ELECTRODE EROSION IN HIGH POWER SPARK GAPS*

A.L. Donaldson, R. Ness, M.O. Hagler, and M. Kristiansen
Plasma and Switching Laboratory
Department of Electrical Engineering
P.O. Box 4439
Texas Tech University
Lubbock, Texas 79409

Summary

The erosion rate for hemispherical electrodes 2.5 cm in diameter made of graphite, copper-graphite, copper-tungsten, brass, and stainless steel has been examined in a spark gap filled with air or nitrogen at 1 atmosphere. The electrodes were subjected to 50,000 unipolar pulses (25 μ s, 4-25 kA, 5-30 kV, .1-.6 coul/shot) at repetition rates ranging from 0.5 to 5 Hz. A conditioning process, indicated by a shifting and narrowing of the self-breakdown voltage distribution, and several spectacular surface patterns (craters, nipples and dendrites) up to .6 cm were observed. Anode erosion rates varied from a slight gain for several materials in nitrogen to $5 \text{ ucm}^3/\text{coul}$ for graphite in air. Cathode erosion rates of .4 $\text{u cm}^3/\text{coul}$ for copper-tungsten in nitrogen to $25 \text{ u cm}^3/\text{coul}$ for graphite in air were also measured.

Introduction

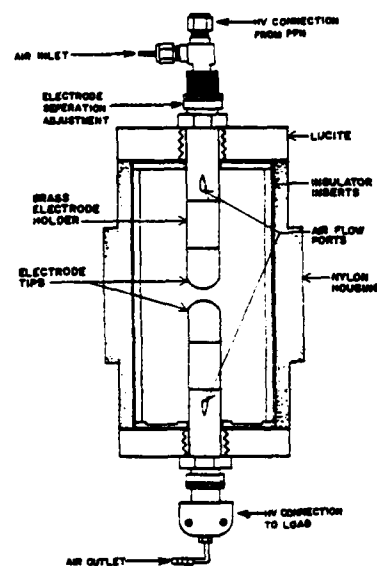
High energy spark gaps capable of lasting for 10^8 shots are seen as one of the critical components in pulsed power systems used for nuclear isotope separation, electromagnetic pulse simulation and thermonuclear fusion reactors. The performance of a pressurized spark gap as a high energy rep-rated switching device is characterized by the following parameters: hold-off voltage, recovery time, delay time, and jitter.¹ The switch lifetime is determined by the degradation of these parameters resulting from electrode erosion, gas decomposition and disassociation and insulator damage occurring as energy is dissipated in the switch.²

The purpose of this study was to measure the erosion rate of different electrode materials as a function of current in order to generate a data base from which theoretical models describing the complex erosion process could be developed and verified. In addition, the self-breakdown voltage distributions and the electrode and insulator surfaces were examined in an effort to further define the erosion characteristics and to reduce the material parameter space used in future studies.

Experimental Apparatus

Spark Gap

The spark gap shown in Fig. 1 was designed to facilitate frequent electrode and insulator replacement and to allow for accurate control over electrode alignment and gap spacing. The electrodes are composed of three parts: the brass support (which also serves as a channel for air flow), the brass adapter and the electrode tip. The hemispherically shaped electrode tips are 2.5 cm in diameter and are made from the various materials studied. The Lucite inserts provide protection for the main gap housing and also provide a surface which gives a permanent history of the discharge debris which is deposited on the walls.



MARK II SPARK GAP

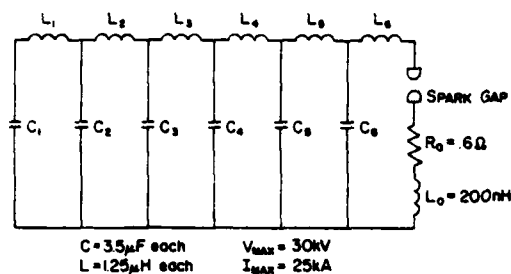
Fig. 1. Spark gap for erosion studies.

Test Circuit and Conditions

Numerous experiments have measured erosion rates for high current (10-800 kA) oscillatory discharges, and a few exist for high current (> 10 kA) unipolar discharges in brass and copper.³⁻⁹ Because of the nature of many switching applications, a test circuit capable of delivering a unipolar pulse was chosen for this study. The circuit, shown in Fig. 2, consists of a six section type E pulse forming network (PFN) which is resistively charged to the self-breakdown voltage of the spark gap by a 30 kV, 1 Amp constant voltage power supply.¹⁰ When the gap breaks down, the PFN is discharged into a matched .6 Ω high power load. The wave form of the discharge current is shown in Fig. 3. The test conditions are summarized below:

Voltage:	< 30 kV
Current:	< 25 kA
Total Capacitance:	21 μ F
Charge/shot:	< .6 coul
Energy/shot:	< 9 kJ
Pulse width:	\approx 25 μ s
Rep-rate:	.5-5 Hz
Gas:	Air or N ₂
Pressure:	1 Atm (absolute)
Flow rate:	\approx 1 Gap volume every 5 sec.
Gap spacing:	\leq .8 cm

* This work was supported by the
Air Force Office of Scientific Research



PFN Equivalent Circuit

Fig. 2. Test circuit for erosion studies.



Fig. 3. Discharge current waveform (time base is 10μs/div).

Materials Tested

The electrode materials tested were: brass (SAE 660), stainless steel (304), copper-tungsten (K-33),¹¹ graphite (ACF-10Q), and copper-graphite (DFP-1C).¹² This combination allowed for: 1) a comparison with existing data given for brass and stainless steel,¹³ 2) utilization of materials thought to give good spark gap performance,¹⁴ and 3) the testing of one new material, namely copper-graphite. The major properties of the materials tested are given in Table I.

Table I. Properties of Electrode Materials Tested

Material	Composition	Tmp	ρ	λ	c
B	Cu 83%, Pb 7%, Sn 7%, Zn 3%	980	8.7	.29	.09
SS	Fe 69%, Cr 19%, Ni 9%, Mn 2%	1430	8.0	.04	.14
CT	W 67%, Cu 33%	W-3400 Cu-1080	13.5	NA	NA
G	C 100%	4200	1.83	.21	.20
CG	C 84%, Cu 16%	Cu-1080	2.97	.42	.21

Tmp: Melting temperature, °C (graphite sublimates); ρ: Density, g/cm³; λ: Thermal conductivity, cal/cm-sec-°C; c: Specific heat, cal/gm-°C; B: Brass, SS: Stainless-steel, CT: Copper-tungsten, G: Graphite, CG: Copper-graphite.

Experimental Results

Erosion Characteristics

The change in mass of the spark gap electrodes after 50,000 shots was measured with an analytical balance with a precision of ± 5 mg. The individual test conditions and resulting erosion rates are given in Table II. Although many authors report erosion rates in μgm/coul, the actual factor determining $\mu\text{cm}^3/\text{coul}$ lifetime is the volume eroded, hence the units $\mu\text{cm}^3/\text{coul}$. The results for brass are discussed later because of the failure of the electrodes due to gross material extraction.

Table II. Electrode Erosion Rates

Electrode	Gas	V	Q	CE	AE
SS	Air	10.3	.21	1.8	1.2
SS	Air	10.6	.22	1.5	1.0
SS ¹	Air	18.0	.37	1.6	1.5
SS ^{2,3}	N ₂	7.8	.16	0.7	+0.0
CT	Air	9.5	.20	1.2	0.4
CT	Air	11.5	.24	1.2	0.3
CT	Air	18.0	.37	1.2	0.5
CT ³	N ₂	14.8	.31	0.4	0.4
CG	Air	8.3	.17	8.5	0.4
CG	Air	16.2	.34	8.6	+0.0
CG ³	Air	11.4	.24	7.2	0.0
CG ³	N ₂	14.8	.31	13.5	0.8
G	Air	9.2	.19	24.1	3.5
G	Air	10.6	.22	24.6	3.6
G	Air	16.0	.33	23.5	5.0
G ³	N ₂	12.9	.27	15.7	0.0

V: Average Voltage, kV; Q: Charge/shot, coulombs; CE: Cathode erosion, $\mu\text{cm}^3/\text{coul}$; AE: Anode erosion, $\mu\text{cm}^3/\text{coul}$; 1: 32,000 shots, 2: 22,000 shots, 3: Experiment performed at approximately 85% of maximum power; + indicates a gain in mass was measured.

Material: A ranking of the erosion rate for each material from smallest to largest is:

Cathode: Copper-tungsten, stainless steel, copper-graphite, graphite

Anode: Copper-graphite, copper-tungsten, stainless steel, graphite

As expected, the copper-tungsten composite gave the lowest erosion rate. Somewhat surprising, however, was the excellent performance of the stainless steel and the poor performances of the graphite materials as cathodes. From the results given for stainless steel in a pulsed discharge it is seen that the high erosion rate reported by Grueber and Sues for an oscillatory discharge was primarily due to its poor performance as an anode material.¹⁵ The studies for graphite were done at a much slower repetition rate (0.03 Hz) and thus, gave significantly lower erosion rates.¹⁶

Polarity: Unlike previous experiments where oscillatory current conditions masked any polarity effect, a distinct difference in the cathode and anode erosion rate and most likely the erosion mechanisms themselves was observed for a unipolar pulse. The ratio of cathode to anode erosion varied from 1.5 for stainless steel to 16 for copper-graphite. Carder reported ratios of 2.5 to 5 for brass under similar conditions.¹⁷

Cathode erosion rates are plotted in Fig. 4 and show a linear dependence upon the quantity $Q = \int i dt$ over the entire range of currents. This indicates that the main source of energy producing molten material and subsequent vaporization and droplet ejection is the arc and not localized i^2R losses in the electrode material.

Anode erosion rates are widely scattered with some anodes experiencing a gain in mass due to material transfer from the cathode to the anode. For graphite

and copper-tungsten, an anode erosion rate approximately proportional to $Q^{1.5}$ was observed.¹⁸

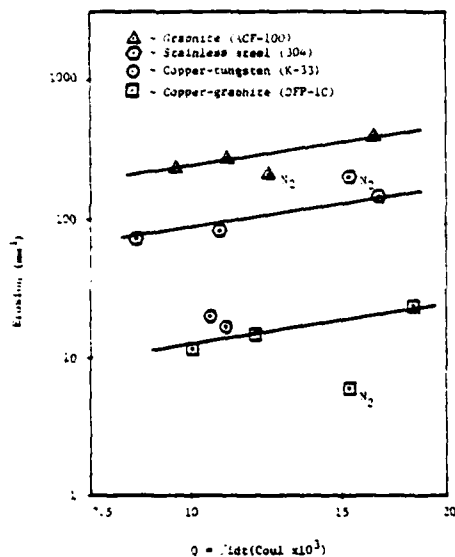


Fig. 4. Cathode erosion rates for different electrode materials.

Gas: The erosion rate for copper-graphite increased slightly in N_2 , whereas the rates for all the other materials were smaller by a factor of 2-3. However, because of other factors effecting spark gap performance, namely the voltage distribution and the coating of the insulator surfaces, the use of pure N_2 is not recommended.

Surface Conditions

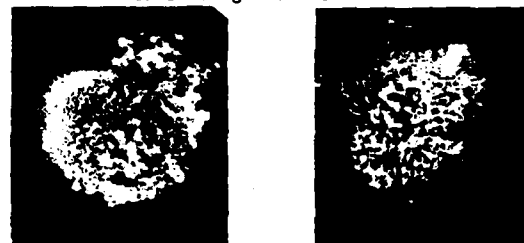
The surface of the electrode tips and the insulator inserts were examined after 50,000 shots. The analysis techniques utilized were Auger electron spectroscopy (AES), scanning electron spectroscopy (SEM), and optical photography and microscopy. Some of the more general results are presented here with a more thorough discussion to be given in another paper.

Brass: The surfaces of the brass electrodes are shown in Fig. 5. Large scale melting is evident with dendrites or metallic protusions up to .6 cm in height existing on the surface. The self-breakdown voltage for these electrodes dropped from 20 kV to 30 kV in approximately 2000 shots as a result of the macroscopic field enhancement. In addition, the voltage distribution was characterized by a series of "jumps" due to large particles being blown off the ends of the protusions. Originally it was thought that the material being "pulled out" of the bulk electrode was lead but AES analysis indicated the surface is composed primarily of copper and oxygen with a noticeable absence of zinc. From these results and those found by Marchesi and Maschio it is quite obvious that brass is limited in its use at higher levels of charge transfer.¹⁹

Cathode: The cathodes for the remaining materials are shown in Fig. 6. Considerable erosion has taken place, especially on the graphite materials, and the stainless steel and copper-tungsten cathodes show evidence of severe melting. All the cathodes showed a distinct tendency to form a large scale crater whose diameter increases with increasing gap spacing and current. The idea of using a cathode cup in spark gaps is not new, but it is interesting that the electrode erosion results in this shape.^{20,21}

Anode: The anodes corresponding to the cathodes

shown in Fig. 6 are shown in Fig. 7. The graphite and copper-graphite anode erosion occurs primarily in a band .8 cm wide located .3 cm from the center of the electrode. This pattern is consistent with the results of Johnson and Pfender which showed that an annular-shaped attachment region of high current density can exist at the anode.²² The copper-tungsten and stainless steel anodes indicate that melting and vaporization has taken place over the entire surface. Like the cathode, the diameter of the anode erosion region increases with increasing current.



a) Anode

b) Cathode

Fig. 5. Surface of brass electrodes after 50,000 shots.



a) Copper-graphite



b) Graphite



c) Copper-tungsten



d) Stainless steel

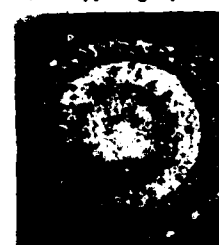
Fig. 6. Surface of cathodes after 50,000 shots.



a) Copper-graphite



b) Graphite



c) Copper-tungsten



d) Stainless steel

Fig. 7. Surface of anodes after 50,000 shots.

Insulator: The insulator surfaces are covered by a coating of recondensed electrode material. The one notable exception was for graphite electrodes in air in which no coating was found on the insulator surface. A dramatic difference is seen in Fig. 8 for the case of graphite run in nitrogen. The entire surface of the insulator is covered with a thick coating of fluffy black material which is thought to consist of monatomic layers of amorphous carbon.²³

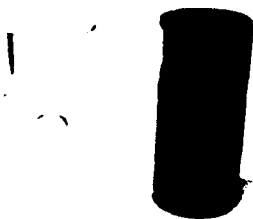


Fig. 8 Lucite insulator inserts for graphite electrodes in air and nitrogen.

All the insulators were covered with solid particles 10-100 μ m in size scattered within a 5 cm band centered on a plane passing through the center of the gap and parallel to the electrode surfaces. This indicates that a considerable portion of the solid or molten material is ejected parallel to the electrode surfaces. Although the mechanism for this ejection is not fully understood, similar results have been reported in vacuum arcs.²⁴ A typical particle which was found on the insulator surface is shown in Fig. 9.



Fig. 9 A stainless steel particle 50 μ m in diameter on the surface of the lucite insulator insert.

Self-breakdown Voltage Distribution

The self-breakdown voltage of the spark gap was recorded continuously for the first 2000 shots and thereafter was sampled at intervals of 10,000 shots. A sample of approximately 400 shots was taken and used to calculate the mean (\bar{V}) and the standard deviation (σ_V) of the self-breakdown voltage.

Material: The standard deviations for different electrode materials are shown in Fig. 10 and 11. In an air atmosphere the graphite electrodes have the smallest σ_V , and therefore, the most narrow distribution of breakdown voltages. This combination is followed by copper-graphite, stainless steel, and copper-tungsten, respectively. Examination of the electrode surfaces with SEM indicated a direct relationship between the width of the distribution and the field enhancement due to the different microscopic surface conditions for each material.

Shot Number: In both air and nitrogen the mean decreases 5-20% during the first 15,000 shots and then

increases at different rates, depending on the electrode material. This increase in \bar{V} is a result of the electrode erosion producing an increase in the gap length. Also, in Fig. 10, it is seen that except for the case of stainless steel σ_V remains fairly constant after 20,000 shots. This suggests a conditioning process during the first 10-20,000 shots where the tip of the electrode is worn away and the electrode surface conditions required to initiate a discharge become more uniform. It is thought that the conditioning process for stainless steel occurs on a larger time scale, and thus, was not fully completed after 50,000 shots.

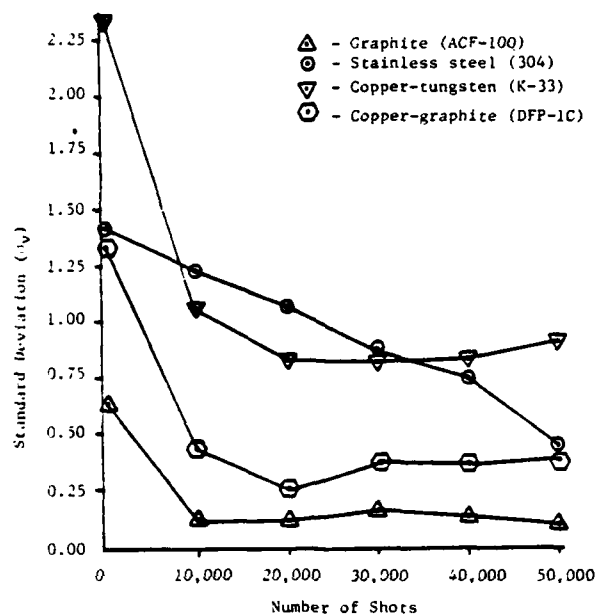


Fig. 10 The standard deviation of the self-breakdown voltage vs. shot number for different electrode materials in air.

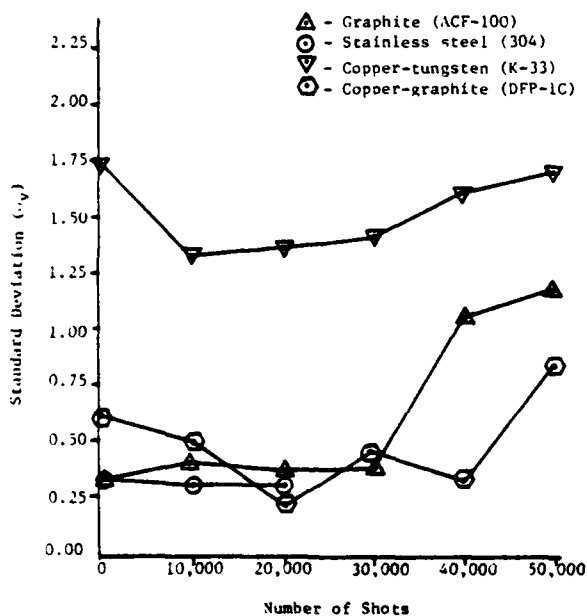


Fig. 11 The standard deviation of the self-breakdown voltage vs. shot number for different electrode materials in nitrogen.

Gas: Data from the same experiments in a nitrogen atmosphere, shown in Fig. 11, indicate that the best electrode materials for a narrow distribution are the graphite composites. The large changes in σ_v for both graphite and copper-graphite are due to low voltage dropouts where the breakdown was often as low as 50% of the mean. These dropouts occur primarily in nitrogen with increasing frequency after 20-30,000 shots. The graphite electrodes were examined after the experiment and a macroscopic growth was found on the anode which may have caused the dropouts. These results, as well as those obtained by Affinito et.al. indicate that the combination of graphite and nitrogen should be avoided.²⁵

Conclusion

The erosion rates and self-breakdown voltage distributions were determined for several materials utilized in high energy spark gaps. The results from these preliminary studies have led to the following conclusions:

- 1) The electrode erosion rates and mechanisms are highly polarity dependent, and thus, results for oscillatory and unipolar discharges can be considerably different.
- 2) A large amount of the erosion occurs in the form of solid and molten material which is removed parallel to the electrode surface.
- 3) Cathode erosion rates are proportional to the total amount of charge transferred.
- 4) Stainless steel may be an economical replacement for copper-tungsten composites as a cathode material.
- 5) Graphite composites can give narrow self-breakdown voltage distributions but have very high cathode erosion rates.
- 6) The stability of the self-breakdown voltage is dependent upon electrode micro-surface structure which is a distinct property of the electrode material.
- 7) Certain electrode-gas combinations lead to "dropouts" or voltage breakdown as low as 50% of the mean. One of the worst of these combinations was graphite and pure nitrogen.

Acknowledgements

The authors wish to express their sincere appreciation to the following people for their various contributions to this work and its presentation: Dr. Allen Bowling, Sam Prine, Dr. Lynn Hatfield, George Jackson, Ken Rathbun, Brian Maas, Amer Shauket, Bob Conover, Pat Darden, Don Johnson, Marie Byrd, Sharon Lipscomb, and the photography crew at Texas Tech University Engineering Services.

References

- 1) Lloyd B. Gordon, dissertation (Texas Tech Univ., 1982) (unpublished).
- 2) L.B. Gordon, M. Kristiansen, M.O. Hagler, H.C. Kirbie, R.M. Ness, and L.L. Hatfield, "Material Studies in a High Energy Spark Gap," submitted to the IEEE Transactions on Plasma Science.
- 3) J.E. Gruber and R. Suess, "Investigations of the Erosion Phenomenon in High Current, High Pressure Gas Discharges," Max Planck Inst. fur Plasmaphysik Garching, bei Munchen IPP 4/72 (Dec, 1969)
- 4) R.A. Burden and T.E. James, "Statistical Performance Data for a High Current 60 kV Spark Gap Switch," Proc. 7th Symp. Fusion Technology, Grenoble, France (Oct, 1972) 24-27.
- 5) G.S. Belkin and V. Ya. Kiselev, "Electrode Erosion in Pulsed High-Current Discharges," Soviet Phys.-Tech. Phys. 11, (1966) 280.
- 6) G. Marchesi and A. Maschio, "Influence of Electrode Materials on Arc Voltage Waveforms in Pressurized Field Distortion Spark Gaps," 5th Int. Conf. on Gas Discharges, (Sept, 1978).
- 7) Y. Suzuki, Y. Kawakita, M. Kume, and M. Kawai, "A 150-kV, 100-kA Spark Gap Switch for Marx Generators," Proc. 3rd IEEE Int. Pulsed Power Conf., Albuquerque, New Mexico, USA (1981) 444.
- 8) B. Carder, "Gas Spark Gap Electrode Heating and Erosion," Physics International Report PIIR-13-74, (Dec, 1974).
- 9) R. Basharov, E.N. Gavrilovskaya, O.A. Malkin, and E.S. Trekhov, "Erosion of Cathode Material in a Pulsed Discharge between Parallel Electrodes," Soviet Phys.-Tech. Phys. 12, (1968) 1383.
- 10) G.N. Glasoe and J.V. Lebacqz, Pulse Generators, Dover Publishing Co., New York, (1965) 175.
- 11) Manufactured by Schwarzkopf Development Corp. Holliston, Ma.
- 12) Manufactured by Poco Graphite, Inc., Decatur, Tx.
- 13) J.E. Gruber and R. Suess
- 14) G. Marchesi and A. Maschio
- 15) J.E. Gruber and R. Suess
- 16) D. Affinito, E. Bar-Avraham, and A. Fisher, "Design and Structure of an Extended Life High Current Sparkgap," IEEE Trans. on Plasma Science, PS-7, (Sept, 1979) 162.
- 17) B. Carder
- 18) H.W. Turner, and C. Turner, "Choosing Contact Materials," Electronics and Power 14, (1968) 437.
- 19) G. Marchesi and A. Maschio
- 20) F.S. Goucher, J.R. Haynes, W.A. Depp, and E.J. Ryder, "Spark Switches for Radar," Bell Sys. Tech. Journal, 25, (1946) 563.
- 21) Rodney Petre, thesis (Texas Tech Univ., 1980) (unpublished).
- 22) D. Johnson and E. Pfender, "Modeling and Measurement of the Initial Anode Heat Fluxes in Pulsed High-Current Arcs," IEEE Trans. on Plasma Science PS-7, (1979) 44.
- 23) Lloyd B. Gordon, dissertation
- 24) J.E. Daalder, "Cathode Spots and Vacuum Arcs," Physica, 104C, (1981) 91.
- 25) D. Affinito, E. Bar-Avraham, and A. Fisher

AD-A119 664

PALISADES INST FOR RESEARCH SERVICES INC NEW YORK
IEEE CONFERENCE RECORD OF 1982 FIFTEENTH POWER MODULATOR SYMPOS--ETC(U)
1982
82-CH-1785-5

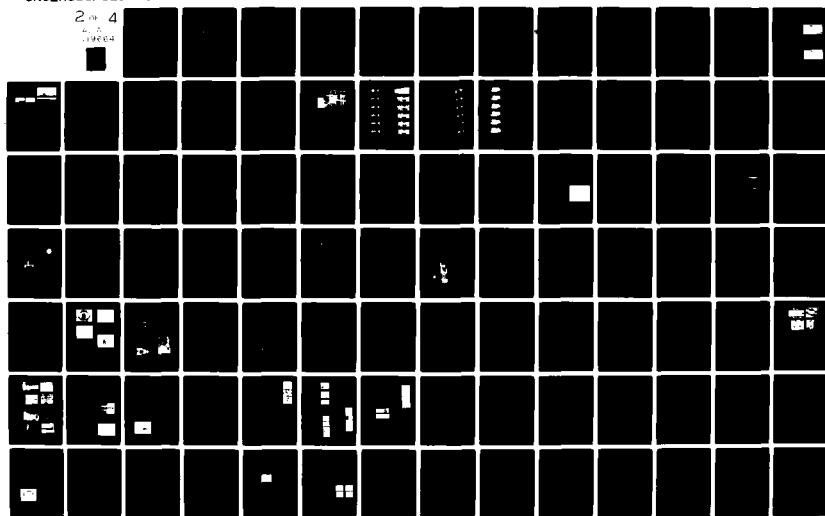
F/G 9/5

UNCLASSIFIED

NL

2 of 4

4-1-1984



SPARK EROSION CHARACTERISTICS OF GRAPHITE AND CO GAS

K. J. Bickford, K. W. Hanks, and W. L. Willis
University of California, Los Alamos National Laboratory
P. O. Box 1663, Los Alamos, New Mexico 87545

Summary

The spark erosion characteristic of high-purity graphite and CO for 1-kHz gas blown rail-gap applications has been experimentally evaluated. The test configuration simulates a single channel, 1650-A arc discharge per linear inch of electrode length, with a 44-kV self-breakdown voltage and a transverse gas flow of 98 m/s. The dielectric gas was seeded with a small quantity of azulene vapor and a downstream uv preionization spark was used to assist the self-breakdown of the test electrodes. The erosion characteristics of other, more conventional electrode materials and dielectric gases were also examined and the results are presented graphically. Commercially pure tungsten in air was determined to exhibit the least erosion rate (2.1×10^{-6} cc/C) for this duty, as compared to graphite and CO (75×10^{-6} cc/C).

Introduction

Gas blown rail-type spark gaps are reasonable candidates for solution of the fast, high power switching problems inherent in pulsed gas-discharge lasers. The low inductance geometry and the reduced, distributed electrode erosion of multichannel operation are key factors in meeting high di/dt switching requirements and solving electrode wear limitations at repetition rates approaching 1 kHz. The erosion wear characteristic of an electrode material is obviously a result of many complicated and undefined interactions between the electrode material, the dielectric gas and flow parameters, peak current, voltage, coulomb transfer and repetition rate. An optimum material or class of materials needs to be identified for use in gas blown, high repetition rate rail-gap applications. The most practical approach to this purpose is empirical experimentation with candidate electrode materials and conventional dielectric gases operating at appropriate stress levels.

Experimental Hardware and Operating Parameters

General

An electrode holder/gas-flow configuration was fabricated as shown schematically in Fig. 1. The electrode spacing (0.635 cm), the active electrode length (2.54 cm), the gas flow velocity (98 m/s), and the rep-

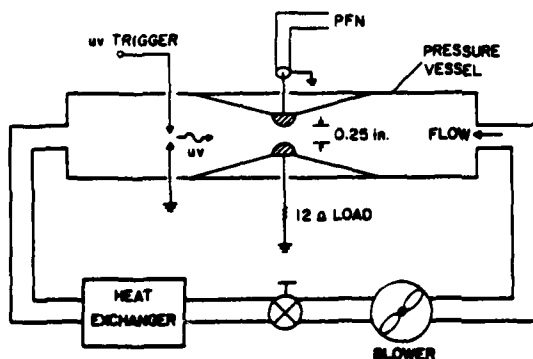


FIGURE 1. ELECTRODE AND GAS-FLOW SCHEMATIC

etition rate (1 kHz) were held constant. A 12-Ω cable PFN was resonantly charged (Fig. 2) and discharged through the test electrodes into a low-inductance 12-Ω ohmic load. Self-breakdown was assisted by a low intensity uv preionization spark located 4.4 cm downstream. Gas input temperature of the closed-cycle system was held near room temperature (70-79°F) by a water-cooled heat exchanger. Gas outlet temperature was monitored at the downstream throat of the electrodes by a thermometer; heat generation due to the uv preionization spark was negligible. Electrode weight was measured with a 5-decimal gram balance at various operating intervals and the electrode volume lost was calculated from these weight measurements. Azulene vapor was injected into the dielectric gas from a heated (160°F) flow-cell. The azulene partial pressure was small and appeared to have no effect on the erosion performance of the electrode materials.

Operating parameters of the electrical driver circuit and flow system are listed in Table I.

Graphite and CO/Azulene

A high purity graphite material was machined into two identical electrodes, each with a 0.635-cm radius along the length, and an overall length of 3.8 cm. The ends were machined to a radius of 0.635 cm; the active length of the electrode was 2.54 cm. Full power operation of the test circuit generated a linear current density along the electrode length of 650 A/cm, with a peak single-channel current of 1650 A and 44 kV self-breakdown. The PFN voltage risetime was adequately slow (550 ns) that multichanneling of the arc discharge did not occur, so the erosion rates of the electrodes can be scaled to full-size rails operating in multichannel mode with one discharge per inch of rail length. Azulene vapor was injected into the CO dielectric gas and the system was operated for 5.46 million shots (1310 Coulombs). Current and voltage waveforms are shown in Fig. 3. Results of the erosion wear are plotted in Fig. 4.

The seeded azulene vapor creates single-photon electron ionization from the uv preionization spark, reducing temporal jitter in the self-breakdown of the main electrodes by eliminating the statistical electron formation time (1,2,3). In addition, because a copious amount of azulene vapor actually reduces the self-breakdown potential, the excess electron density effectively increases the E/P ratio in the dielectric gas by increasing E, similar to inserting a small conducting body between the electrodes or reducing the electrode spacing. With CO gas and experimental configuration used, only a very small effect of the azulene seed in the CO gas could be detected. A more energetic uv preionization source might produce better jitter reduction and enhanced control over the self-breakdown voltage; closer spacing between the uv spark and the main electrodes may also be appropriate. The main electrode self-breakdown time preferred to lock onto the initialization of the uv spark, not onto the peak uv fluence. The ohmic transition phase of the uv spark occurs during initialization and maximum energy is dissipated in the spark during this interval, producing more energetic radiation. This may enhance the photoionization processes or create secondaries emitted from the electrode surfaces. The azulene vapor appeared to "burn out" of the CO gas faster than it could be replaced by the hot flow cell. The uv preionization spark lost

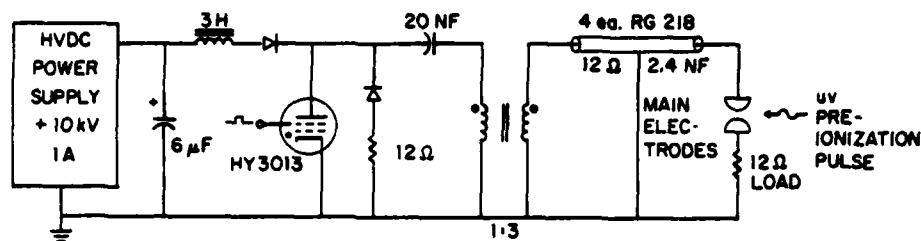


FIGURE 2. 1 kHz, 3.5 kW HIGH VOLTAGE PULSE-CHARGE DRIVER FOR PRIMARY DISCHARGE.

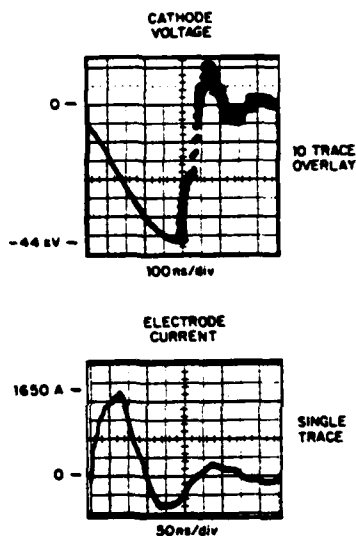


Figure 3. CATHODE (PFN) VOLTAGE AND MAIN DISCHARGE CURRENT WAVEFORMS.

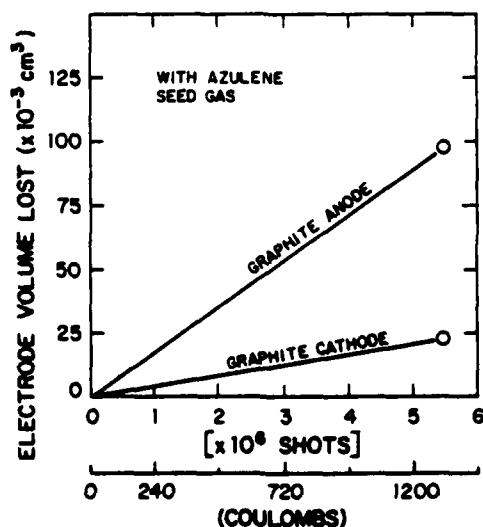


FIGURE 4. 1 kHz ELECTRODE EROSION OF HIGH PURITY GRAPHITE IN CO₂. ELECTRODE RADIUS/SPACING RATIO = 1.0.

effectiveness after several minutes of operation at 1 kHz. Probable cause of seed gas burn-out is the large amount of uv radiation from the main discharge.

Examination of the eroded surfaces of the graphite showed evidence of microscopic pitting probably caused by sublimation or burning. The erosion was probably not caused by localized chipping from mechanical or thermal shock; no evidence of graphite particulate contamination of the gas flow system was observed. The anode evidenced 20-30% more erosion than the cathode, indicating that electron bombardment accounts for significantly more energy deposition than does the cathode-fall effect (4). This was a universal observation for all electrode materials tested, not just for graphite. Because of the extreme erosion rate of graphite at this particular duty, no experimentation with the anisotropic properties of graphite were performed, nor were any attempts made to reduce oxidation erosion by spiking the CO with CO₂. In addition, self-preionization effects due to corona were observed during single-shot trials, which caused prefires at all repetition rates up to 1 kHz. The coronas phenomenon

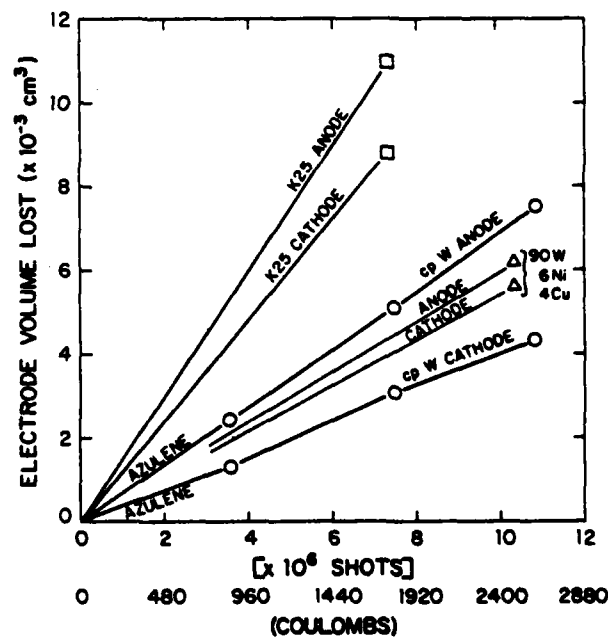


FIGURE 5. 1 kHz ELECTRODE EROSION CHARACTERISTICS OF COMMERCIAL PURE TUNGSTEN, K25 COMPOSITE, AND A 90% TUNGSTEN MATERIAL, IN CO₂. ELECTRODE RADIUS/SPACING RATIO = 1.0.

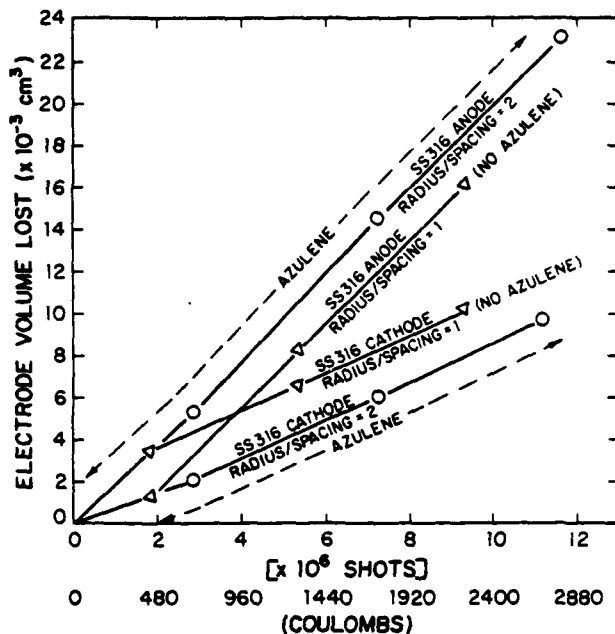


FIGURE 6. 1 kHz EROSION CHARACTERISTICS OF 316 STAINLESS STEEL IN CO_2 , FOR TWO DIFFERENT ELECTRODE RADIUS/SPACING RATIOS.

was manifest as low intensity, light blue, self-initiated impulse streamers occurring at random at the ends of the electrode gap. Increasing the system pressure was ineffective in preventing their inception except at extreme pressures where the gap would not break at all.

Other Electrode Materials and Gases

CO_2 and dry air were used as dielectric gases with commercially pure tungsten (cpw), 90W 6Ni 7Cu, K25 composite (75W 25Cu by Plansee), 70/30 brass, and 316 stainless steel. The results of these tests are shown in Figs. 5-8. Operating parameters were maintained as in the previous experiment. Electrode shapes and dimensions were identical to those used in the graphite/ CO test, except for a single SS 316 run where the electrode radius was doubled, creating a radius/spacing

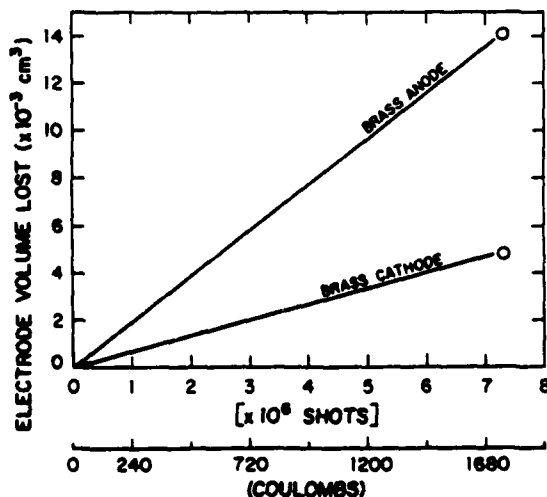


FIGURE 7. 1 kHz ELECTRODE EROSION OF BRASS (70/30) IN CO_2 . ELECTRODE RADIUS/SPACING RATIO = 1.0.

ratio = 2. This had no effect on the erosion rate.

The essential metallurgical property affecting erosion at this duty appears to be high temperature strength, hence the best performance by refractories.

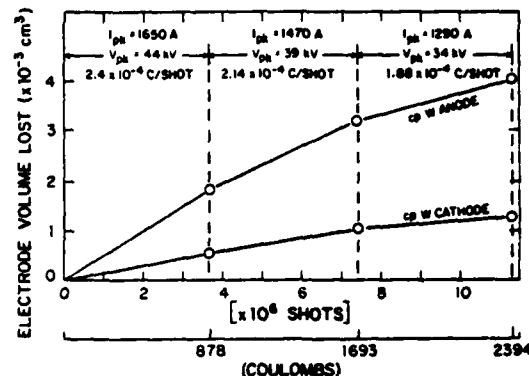


FIGURE 8. 1 kHz ELECTRODE EROSION OF COMMERCIAL PURE TUNGSTEN IN AIR FOR DIFFERENT I_{pk} , V_{pk} , AND COULOMB TRANSFER PER SHOT. ELECTRODE RADIUS/SPACING RATIO = 1.0.

TABLE I

Full power operating parameters at 1 kHz.

$V_{br} = 44 \text{ kV}$	$I_{pk} = 1650 \text{ A}$	$C/\text{shot} = 0.24 \text{ mC}$	
	<u>CO</u>	<u>CO₂</u>	<u>Air</u>
Gas Pressure	12.4 PSIG	18 PSIG	18 PSIG
SCFM Flow	63	127	131
ΔT rise	25°F	15°F	13°F
Efficiency	78%	67%	77%

Efficiency was determined by ΔT rise of the gas flowing through the electrode gap, using $\text{eff.} = (1 - \text{energy diss.}/\text{energy switched}) \times 100\%$. Energy dissipated was calculated from the relation,

$$ED = \frac{K (\text{SCFM}) (\Delta^\circ\text{F})}{\text{pps}}$$

where,

$$K(\text{air and CO}) = 0.34, \text{ and } K(\text{CO}_2) = 0.43.$$

Oxygen in the presence of tungsten appears to retard the erosion process, perhaps by the formation of protective oxides (5). The 90W material in CO_2 was subjectively judged to be the best combination of those tested: erosion rates of the cathode and anode were nearly equal and only slightly higher than cpw/air. The machinability of the 90W 6Ni 4Cu material is substantially better than cpw. Air with 90W needs to be tested.

CO_2 gas did not exhibit as good a self-breakdown characteristic as air; the extreme temporal jitter with CO_2 and 550-ns charge time was virtually eliminated by adjusting the uv preionization spark initiation to the peak of the PFN charge voltage. This was accomplished both with and without azulene.

Azulene vapor seed in CO_2 produced reasonable results in that the self-break voltage could be shifted about the peak of the PFN voltage approximately $\pm 10\%$

by adjusting the timing of the uv spark. The magnitude of this effect is very dependent on the partial pressure of azulene vapor, and as with CO/azulene, the effectiveness was eliminated by burn-out after several minutes of full power operation at 1 kHz.

References

1. L. L. Alaton, editor, High Voltage Technology, (Oxford University Press, London, 1968).
2. E. Nasser, Fundamentals of Gaseous Ionization and Plasma Electronics, (Wiley-Interscience, New York, 1971).
3. J. M. Meek and J. D. Craggs, editors, Electrical Breakdown of Gases, (Wiley-Interscience, New York, 1978).
4. J. D. Cobine, Gaseous Conductors, (Dover Publications, Inc., New York, 1958).
5. Glasoe and Lebacqz, Pulse Generators, MIT Radiation Laboratory Series, Vol. 5 (McGraw-Hill, New York, 1948).

LONG-LIFE TRIGGERED SPARK GAP
FOR A
CO₂ TEA LASER POWER CONDITIONER*

J. N. Elkins
United Technologies Research Center
Silver Lane, MS 81
East Hartford, CT 06108

S. Friedman
EG&G
35 Congress Street
Salem, MA 01970

M. Weiner
US Army Electronics Technology and Device Laboratory
Fort Monmouth, NJ 07703

Summary

Long-life, compact power conditioners are currently being developed for pulsed CO₂ laser applications. Prior experience had indicated that the weakest link in the power conditioner lifetime was frequently the spark gap switch which typically failed after much less than 1 million shots. In this work the lifetime issue has been addressed in an experimental program which defined the switch performance requirements and then investigated the effect on life of the electrode material, gas-fill composition, pressure, and electrode geometry. The performance goal was 10 million shots.

Sixteen spark gaps, having various combinations of these parameters to be optimized, were operated at an accelerated rate on a simulated laser load to end of life. The parameters which consistently resulted in a life of greater than 10 million shots include: an N₂, O₂, Xe gas mixture at high pressure, a recessed trigger support, and a long electrode-to-electrode insulator wall. The walls are ceramic, the outside diameter is 1.0 inch, and the length is 1.5 inch.

A total of six triggered spark gaps having these parameters were tested, gas fill analyzed, and autopsied. Five of the six exceeded the lifetime goal of 10 million pulses and one lasted 19 million. The gaps were tested in a Marx circuit switching 1 kA. Load current was periodically changed to a 2 kA damped ringing pulse to simulate laser faults. Static tests, conducted every one-million pulses, included measurement of static breakdown voltage and the minimum trigger voltage. The occurrence of pre-fires and no-fires was monitored continuously by diagnostic circuitry and recorded.

Introduction

A long-life triggered spark gap for use as the switching element in compact power conditioners for pulsed CO₂ laser applications has been developed. This spark gap has a demonstrated operating life of over 10 million pulses and meets all the electrical, geometrical, and environmental (MIL-STD-883C) requirements for use in a pulsed CO₂ laser power conditioner having the electrical specifications listed in Table 1.

Table 1. Spark Gap Electrical Requirements

Load	CO ₂ Laser (Simulated)
Nominal Load Discharge Voltage	25 kV
Energy to Discharge	3 Joules
Normal Discharge Current-Peak	1 kA
Fault Discharge Current-Peak	2 kA
Pulse Width (50%)	200 nsec
Pulse Risettime (10% to 90%)	100 nsec
Pulse Faltime (90% to 10%)	100 nsec
Pulse Rate	1 Hz
Misfire Rate	<1%

Sixteen gaps were tested, with two different electrode materials (Elkonite* and molybdenum) and three different gas mixtures (N₂+O₂+Xe, Xe+O₂, and pure Xe). The combination of electrode materials and gas mixture found to give the required 10 million pulse life was Elkonite/N₂ (69%)+O₂ (1%)+Xe(30%).

Test Circuitry

A schematic of the spark gap test circuit is shown in Fig. 1. The 0.017 μ F energy storage capacitors were charged in parallel through the 56 kilohm resistors, and discharged in series through the spark gap under test and a simulated CO₂ laser load consisting of a triggered spark gap in series with a resistor whose value which approximates the laser dynamic impedance at peak current. The triggered load gap was either an EG&G GP-20 or GP-46B gap, triggered by capacitive coupling between the trigger electrode and the high-voltage side of the spark gaps. This load scheme was found to be more stable than over-voltage spark gaps. A typical current waveform is shown in Fig. 2a.

To simulate a 1% laser fault rate, the 16.5 ohm resistor (Fig. 1) was replaced by 8 ohms for 5000 shots at the end of each 0.5 million life test cycle. This produced the current pulse shown in Fig. 2b. Currents were measured using a current transformer.

To accelerate testing, three identical circuits were operated simultaneously, as shown in Fig. 3, each at a 5 Hz pulse rate. The energy storage capacitors were charged from a command charge power supply, with the charging and trigger signals provided by a custom designed control circuit. Each spark gap was triggered using a standard EG&G TM-11A trigger module.

*This work was supported by Contract DAAK20-80-C-0290 monitored by the Electronics Technology & Devices Laboratory, US Army Electronics Research and Development Command (ERADCOM), Fort Monmouth, New Jersey.

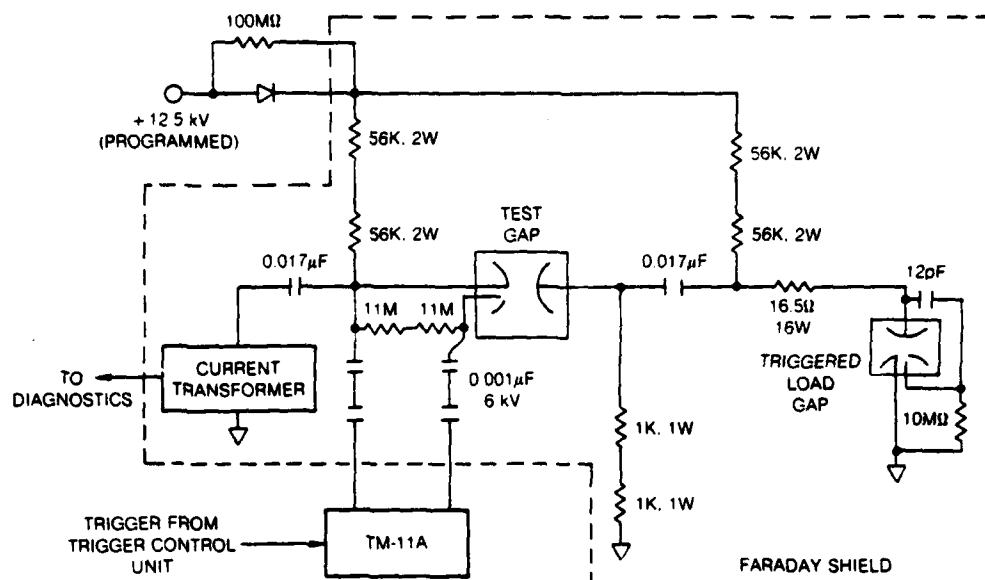


Figure 1. Spark Gap Test Circuit

The time sequence of circuit events is as follows:

Time (msec)	Event
0	Trigger main power supply
0-120	Voltage on test gaps rises to 12.5 kV
120-175	Voltage on test gaps swells at 12.5 kV
175	Signal to main power supply stops
180	Test gap #1 triggered
180.1	Test gap #2 triggered
180.2	Test gap #3 triggered
200	Trigger main power supply, beginning cycle again

By triggering the three gaps 100 μs apart, instead of simultaneously, any pre-fires caused by crosstalk could be readily distinguished from normal firing. Typical spark gap voltage waveforms are shown in Fig. 4.

Diagnostics

The diagnostic circuitry monitored the current through each of the gaps under test and detected when a gap fired without being triggered (pre-fire) or did not fire when triggered (no-fire). A block diagram of the diagnostic circuitry is shown in Fig. 5. When the trigger signal from the control electronics was applied to the gap under test, a one-shot was triggered simultaneously, closing Gate A for 20 μs. When the spark gap subsequently fired, a 10 μs one-shot was triggered, and the differentiated pulse sent to Gate A. If the positive spike (corresponding to the differentiated trailing edge of the 10 μs pulse) reached Gate A within 20 μs after the gap was triggered, Gate A was still closed; therefore, no signal was sent to the strip-chart recorder. Thus, if the gap fires within 10 μs of being triggered, no pre-fire signal was generated. If the gap fired at any other time, then Gate A was open, and the differentiated trailing edge of the 10 μs pulse triggered the 100 ms one-shot, sending a pre-fire signal to the strip-chart recorder. A prefire signal could also be generated if the gap had a delay time greater than 10 μs, but no such cases were observed.

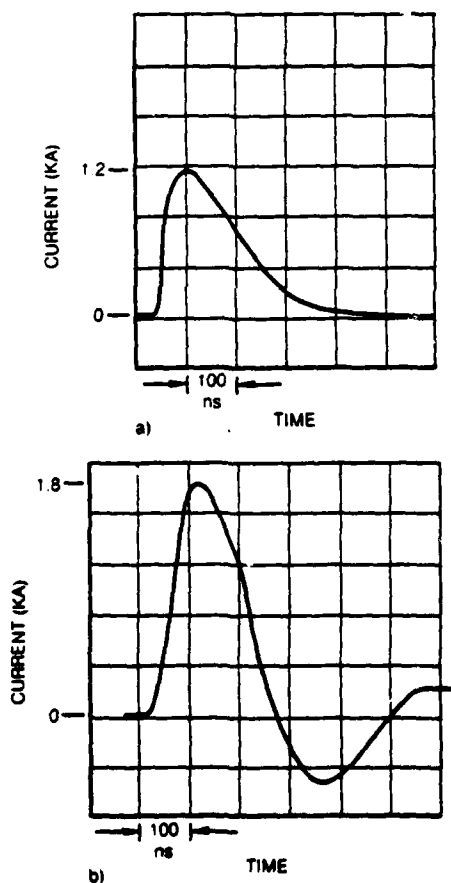


Figure 2. Spark Gap Current Waveform

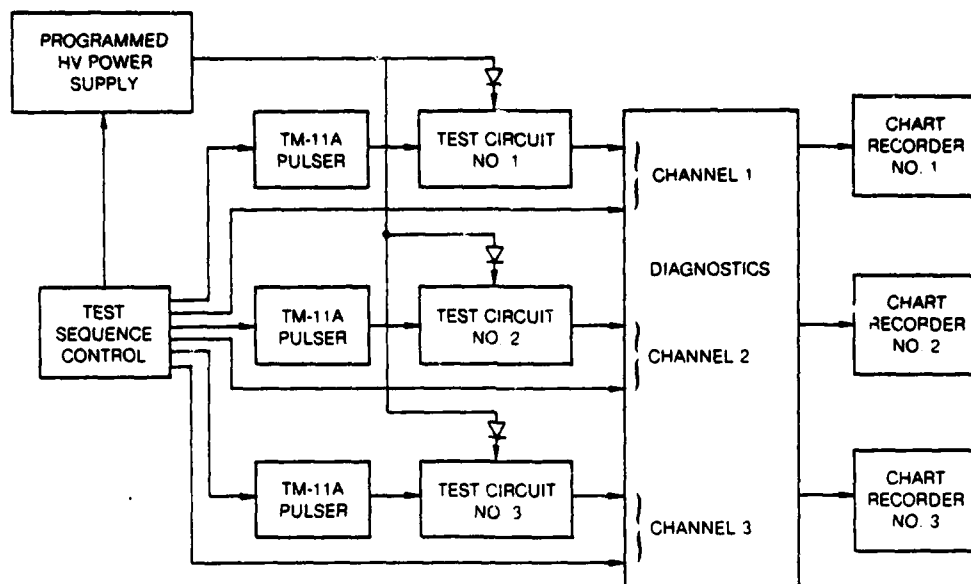


Figure 3. Spark Gap Test Scand

If the no-fire detector, the roles of the 20 μ s and 10 μ s one-shots were reversed. The 10 μ s pulse was synchronized with the gap trigger, while the 20 μ s one-shot only fired, thereby closing Gate B, when the gap fired. Thus, if the gap failed to fire within 10 μ s of being triggered, then Gate B was open when the differentiated trailing edge of the 10 μ s pulse arrived, and a no-fire signal was sent to the strip-chart recorder. The circuit was configured so that a no-fire signal sent to the strip-chart recorder had approximately twice the amplitude of a pre-fire signal. The chart, therefore, indicated both the number and nature of any misfires that had occurred.

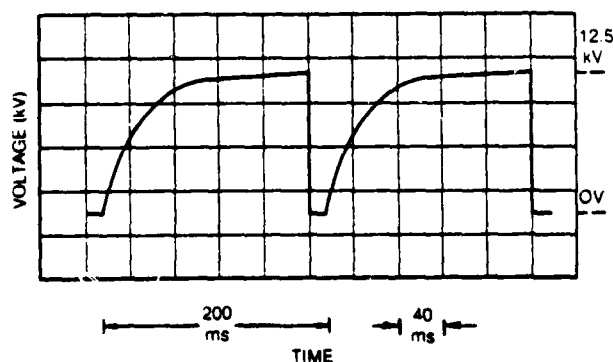


Figure 4. Spark Gap Charging Voltage

Testing Procedure

The spark gaps were life tested at a 5 Hz pulse rate. Numerous static tests were performed and the gaps were operated for a period at the specified 1 Hz rate every one-million pulses. In addition, testing under simulated laser fault conditions (Fig. 2b) was conducted every half-million shots in order to distribute any fault effects more realistically. Fault, static, and 1 Hz tests were performed as follows:

1. Normal testing was stopped and the gap operated at 5 Hz under fault conditions for approximately 5000 pulses;
2. The specified holdoff voltage of 15 kV dc was imposed across the gap for one minute. If no breakdowns occurred, the gap was deemed highly reliable for the much shorter holdoff time required in actual operation. A resistor was used to limit the gap current in case of breakdown;
3. Self-breakdown voltage was measured, using the same setup;
4. The gap was put back in the life-test setup, and minimum trigger voltage measured under actual operating conditions by gradually reducing the TM-11A output until triggering became erratic.
5. The gap was operated at 1 Hz for 5 minutes (300 pulses) while monitoring the charging voltage waveform with an oscilloscope.

At the completion of the life testing, the gas constituents of each gap was analyzed and then the gap was subsequently autopsied.

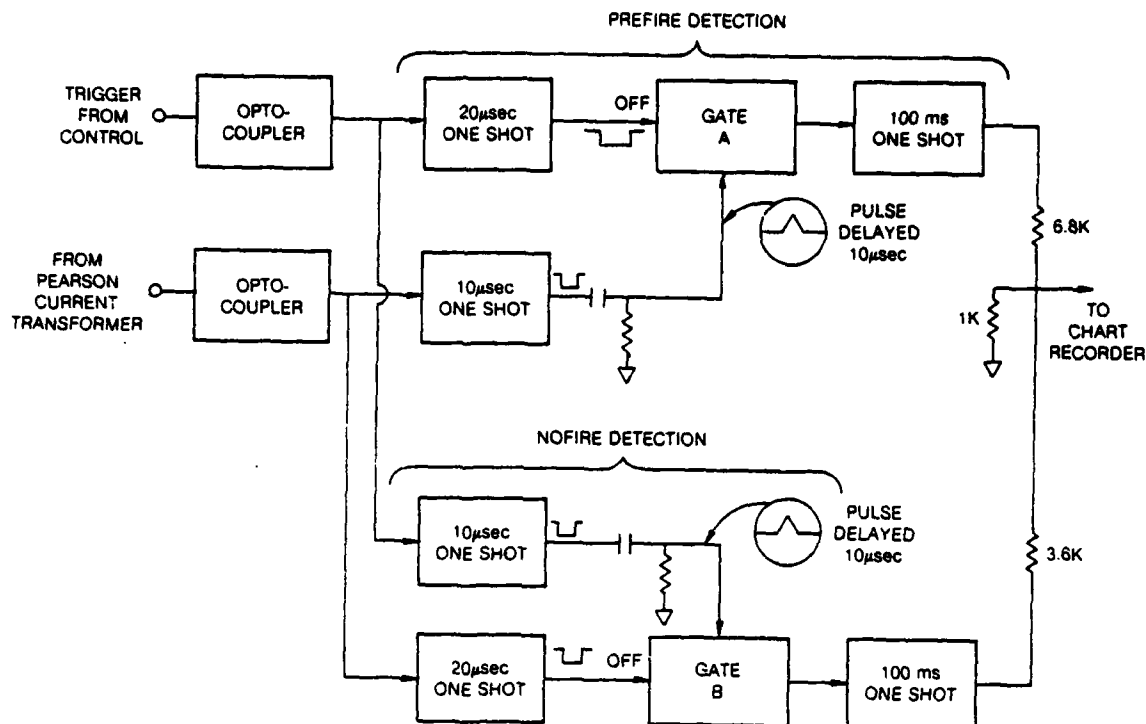


Figure 5. Diagnostics

Spark Gap Design

The long-life gap, designated GP-4610 is shown in Fig. 6. The cross section of a standard GP-46B spark gap is shown in Fig. 7a. The cross section of the long-life gap is shown in Fig. 7b.

Two aspects of the design were specifically changed to promote long life. First, the inter-electrode spacing was made relatively small. Second, the ceramic spacer between the trigger probe tip and adjacent electrode was recessed. The changes are readily apparent by comparing Fig. 7a and Fig. 7b.

The small inter-electrode spacing helps increase life by decreasing the rate at which SBV declines with gas cleanup. From Paschen's Law $SBV \propto \text{constant} \times p d$. Where p is the pressure and d the inter-electrode spacing. Thus, the rate of change of SBV with p is lower for smaller d . Small inter-electrode spacing also increases the gap electric field, which theoretically decreases the resistive phase time constant, thereby reducing dissipation. According to a semi-empirical formula developed by Martin³, the resistive phase time constant T is proportional to $\sqrt{p/E}$, where E is the gap electric field. If we take E to be inversely proportional to d , and $p d$ to be a constant fixed by the desired gap voltage, then T varies as $d^{3/2}$. The extender (Fig. 7b) reduced d by a factor of about 4, thus theoretically reducing T by a factor of 3. The reason for using an extender (Fig. 7b), to decrease d , instead of simply shortening the entire gap, was to avoid increasing the chance of gap failure via external flashover or internal breakdown along the insulator.

Recessing the ceramic spacer between the trigger probe tip and the adjacent electrode prevents trigger shorting caused by coating of this ceramic spacer with

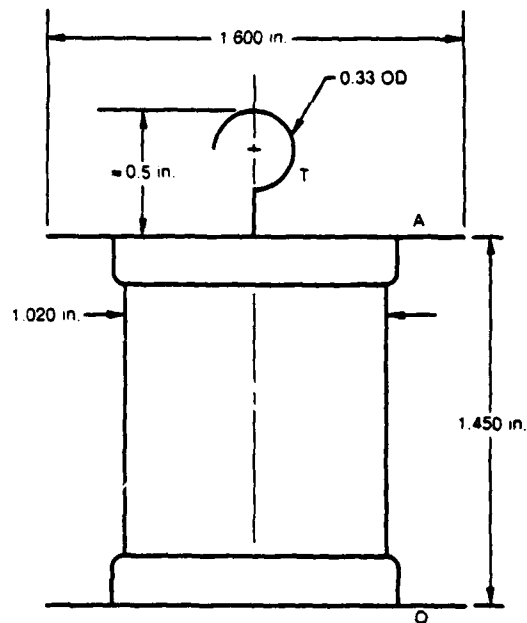


Figure 6. EG&G GP4610 Triggered Spark Gap

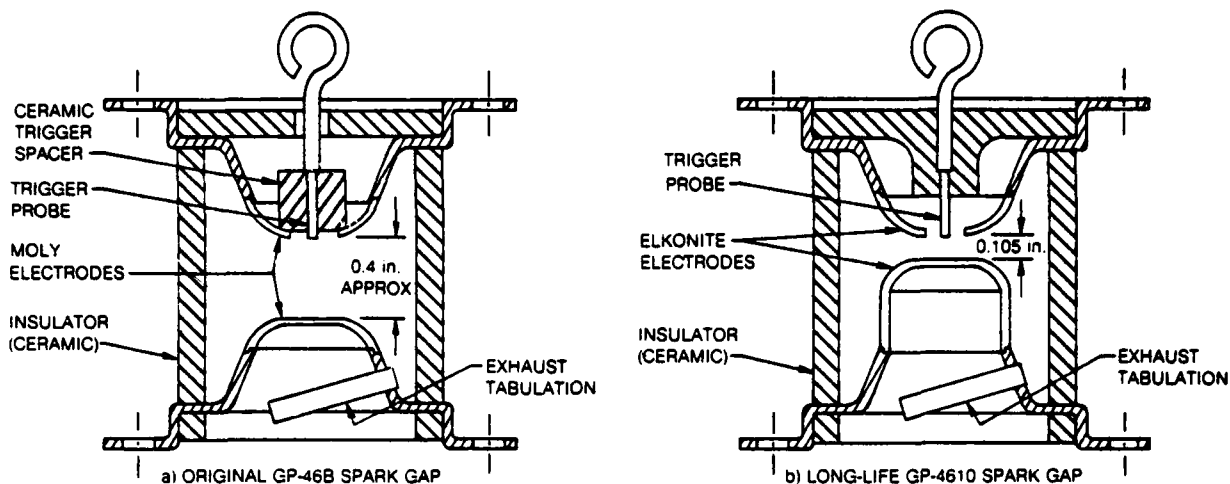


Figure 7. Spark Gap Designs

sputtered debris. Normally, the main discharge keeps this ceramic clean but experience has shown that at the relatively low current level involved in this application the discharge would not have sufficient power to clean effectively.

All the gaps tested were of the design shown in Fig. 7b. Parts were carefully selected to maintain a ± 0.005 inch tolerance on the inter-electrode spacing.

Test Results

A total of sixteen GP-4610 gaps were constructed, utilizing Elkonite (copper infiltrated tungsten) and molybdenum electrode materials and three types of gas mixtures (N_2+O_2+Xe , $Xe+O_2$, and pure Xe). Table 2 lists the data for all the gaps in order of decreasing life. It can be seen that the combination of parameters giving best life was Elkonite electrodes, N_2+O_2+Xe gas mixtures and an initial SBV of 30 kV.

The dominant failure mechanism was abrupt loss of holdoff due to internal breakdown along the insulating wall, caused by deposition of sputtered electrode material. This condition was evidenced by a rapid increase in the pre-fire rate, and in some cases, onset of continuous conduction.

Those gaps which had extremely short life ($<10^6$ pulses) were found upon autopsy to have heavy wall deposits, along which substantial tracking had occurred. The tracking always emanated from near the base of one of the electrodes, suggesting that braze material was involved. The correlation of extremely short life with pure Xe may, therefore, indicate some unfavorable interaction with the braze material. It was thought that adding a small amount of O_2 would oxidize the wall deposits, rendering them nonconductive. However, $Xe+O_2$ gaps failed to fire at voltages much below SBV, as described further below.

Table 2. Life Test Results

GAP#	ELECTRODE MATERIAL	GAS FILL	INITIAL SBV(KV)	LIFE (SHOTS)	AVG. PERCENT MISFIRE		FAILURE MODE
					PREFIRE	NO-FIRE	
1	Elkonite	N_2+O_2+Xe	30	19.2×10^6	<.001	.05	Loss of Holdoff
2	"	"	"	15.8×10^6	<.01	<.001	"
3	"	"	"	$>11.4 \times 10^6$	<.001	"	Still operating when test ended
4	"	"	"	$>11.4 \times 10^6$	"	"	"
5	"	"	"	10.3×10^6	"	"	"
6	Moly	"	"	9.5×10^6	.2	.2	Loss of Holdoff
7	Elkonite	"	27	7.4×10^6	.01	<.001	"
8	Moly	"	30	1.1×10^6			"
9	"	"	25	0.8×10^6			"
10	"	"	30	0.5×10^6			"
11	Moly	Xe	25	$\sim 10^4$			"
12	Elkonite	"	"	$\sim 10^4$			"
13	"	"	20	$\sim 10^4$			"
14	Moly	N_2+O_2+Xe	30	--			Min. operating voltage too high
15	Elkonite	$Xe+O_2$	"	--			"
16	"	"	"	--			"

Visual observations of the other long-lived gaps during operation revealed a gradual build up of wall deposits, which upon autopsy, were found to be fairly uniform, indicating that nothing beyond simple sputtering of electrode material had taken place.

None of the autopsies, including those of the short-lived gaps, revealed significant electrode damage beyond a rounding of the trigger probe tip and the inside edge of the adjacent electrode. This caused the minimum trigger voltages to rise with life as illustrated in Fig. 8.

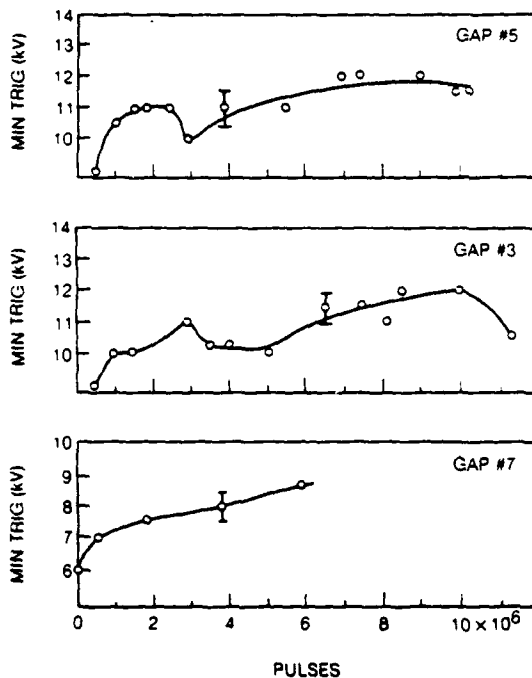


Figure 8. Representative Minimum Trigger Voltage vs Life Data

Representative curves of SBV versus life are shown in Fig. 9. The sharp initial decline in SBV seen for gap was characteristic of gaps tested early in the program and prompted the increase of the initial SBV of later gaps to 30 kV. As a consequence, these gaps had frequent no-fires for the first few hours of operation, but subsequently SBV declined until the end of life, which was always relatively abrupt. The transition from normal operation to total failure usually occurred over a period of just a few hours.

Three of the gaps tested failed due to an increase in minimum operating voltages with life. These gaps were Elkonite/Xe+O₂ gaps, and a molybdenum/N₂+O₂+Xe gap. Apparently initial conditioning of the electrodes during pumping and filling had raised the minimum operating voltage too far, particularly in the case of the Xe-O₂ gas mixture. Avoiding the Xe-O₂ gas mix, and slightly reducing the initial SBV, should eliminate this problem in the future.

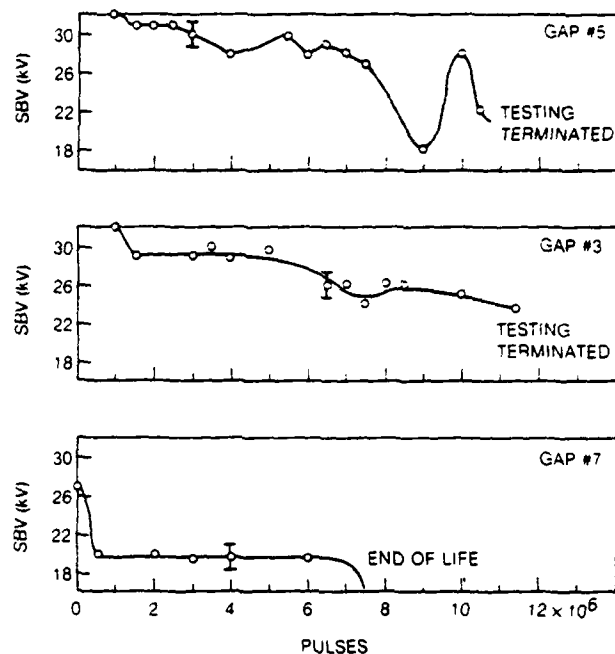


Figure 9. Representative SBV vs Life Data

It should be noted that all gaps must undergo an initial conditioning before reaching their rated SBV. This conditioning is done by firing them anywhere from a few times to a few hundred times as required.

Conclusions

Lifetime in excess of 10⁷ pulses have been demonstrated with triggered spark gaps having Elkonite electrodes, N₂+O₂+Xe gas fill, 30 kV SBV, small inter-electrode spacing, and a recessed ceramic insulator between the trigger electrode tip and adjacent electrode. Of the six such gaps tested, only one lasted less than 10 pulses. Misfire rates (pre-fires plus no-fires) were 1.0 percent or less for all six gaps.

Acknowledgements

The design for the GP-4610 spark gap was proposed by David Turnquist now at Impulse Electronics. The spark gap diagnostics were designed and constructed by Richard Dolbear of EG&G. Gas fill analysis was performed at UTRC by Eugene Brull.

References

1. Martin, J. C., AWE, Aldermaston, England, SSWA/JCM/1065/25, 1965 (unpublished).
2. Craggs, J. D., "Spark Channels" in Craggs, J. D., and J. M. Meek, *Electrical Breakdown of Gases*, John Wiley, New York, 1978, pp. 801ff.
3. Rourke, R. C., Maxwell Laboratories Inc., San Diego, California, MLT5-69, 1969 (unpublished).

RECOVERY OF ELECTRIC STRENGTH IN PRESSURIZED SPARK GAPS

S. L. Moran, L. F. Rinehart, and R. N. DeWitt

Naval Surface Weapons Center
Dahlgren, Virginia 22448

Summary

The recovery of electric strength of various gases in a small pressurized spark gap is measured using a two-pulse method. The first pulse is used to overvolt and break down the gap. The second pulse is used, after a variable time delay, to determine the electric strength of the ionized gas. Varying the time delay to the second pulse provides a plot of electric strength versus time-after-breakdown.

The time delay between the first and second pulses can be varied from less than 100 ns to greater than 100 ms. Breakdown and recovery voltages can be measured in gases at pressures from atmospheric up to 7 MPa (1000 psig).

The spark gap used in these experiments is an untriggered pressurized gas spark gap composed of 1.9-cm diameter flat electrodes with rounded edges. Gap spacing is 0.127 mm (5 mils), and the energy discharged is 0.4 J at voltages up to 20 kV.

Recovery curves at various pressures have been obtained for nitrogen, hydrogen, helium, air, oxygen and argon using brass electrodes with essentially no gas flow during the recovery period. Statistical analysis shows a Gaussian distribution of the data for both the first- and second pulse breakdowns.

A theoretical explanation of the data is being developed which explains recovery in terms of the ratio of neutral particles to charged particles in the gap volume. A time dependent recombination coefficient is used to obtain this ratio as a function of time-after-breakdown.

Introduction

Many applications of spark gap switches require high repetition rates. Since repetition rates are often limited by the recovery time of the spark gap, a better understanding is needed of the dominant factors involved with the electric recovery of the gas. Investigations are being made to determine the electric strength (voltage recovery) of the gas as a function of time-after-breakdown for small spark gaps. Considerable experimental recovery work has been performed with spark gaps operating at or below atmospheric pressure, and at power line frequencies.¹ Our efforts are directed towards high pressure spark gaps which are highly overvolted by impulses. To obtain this information, two high voltage pulses, with a variable time delay between them, are applied to the gap. The first pulse is used to overvolt and break down the gap, while the second pulse is introduced during the recovery period following the initial breakdown. The voltage rise of the second pulse is limited by the electric strength recovery that has occurred since the first pulse breakdown. By varying the time delay between the first and second pulses, a plot of voltage holdoff versus time is obtained.

This paper describes an experimental apparatus which is superior to one previously constructed and described in reference 2. A description of the setup and procedure is given along with electric strength recovery data at various pressures for six gases; nitrogen, hydrogen, helium, air, oxygen and argon. A brief description is given of the theoretical approach used to explain the data in terms of the ratio of neutral to charged particles in the gap.

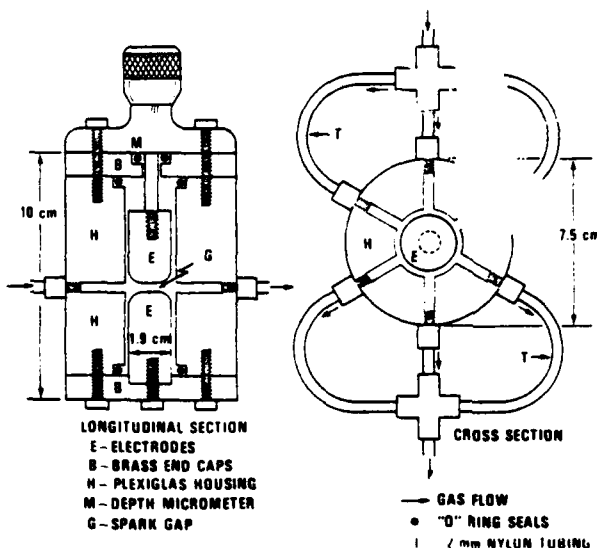


Figure 1. Spark gap

Description of Experiment

Spark Gap and Gas System

The spark gap and housing are shown in Figure 1. The spark gap area is between the ends of two removable solid cylindrical electrodes which are 1.9 cm in diameter. The outer one-third of the diameter is rounded to reduce field enhancement. The flat surface of the spark gap is 0.635 cm in diameter. The gap is surrounded by a Plexiglas housing which contains three inlet and three outlet holes 2 mm in diameter which direct the gas flow more evenly across the electrode surfaces. Total gas volume inside the gap is approximately 1 cm³. The gap is sealed with o-rings and can withstand pressures up to 7 MPa (1000 psig). The gap spacing is adjusted by a micrometer attached to one electrode and can be adjusted under pressure to 0.01-mm (0.5-mil) accuracy.

The gas flow system is shown in Figure 2. Pressure is regulated from the gas bottle and is measured by a single gauge accurate to 7 kPa (1 psi) over the range from atmospheric to 7 MPa. The gas tubing is split three ways at the spark gap and is recombined before connecting to a set of metering valves. The gas pressure is dropped to atmospheric across the metering valves before passing through one of four possible flow

meters used to measure flow rates from 0.1 to 1000 cm³/s. All gases used in these experiments are ultra-high purity.

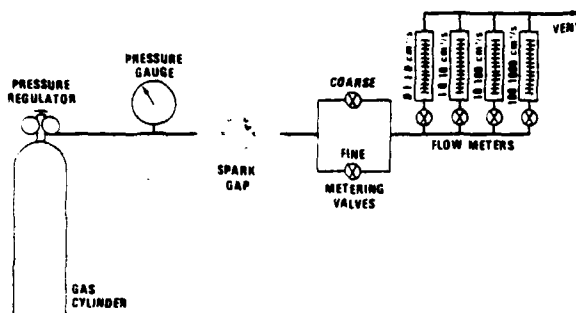


Figure 2. Gas pressure and flow instrumentation

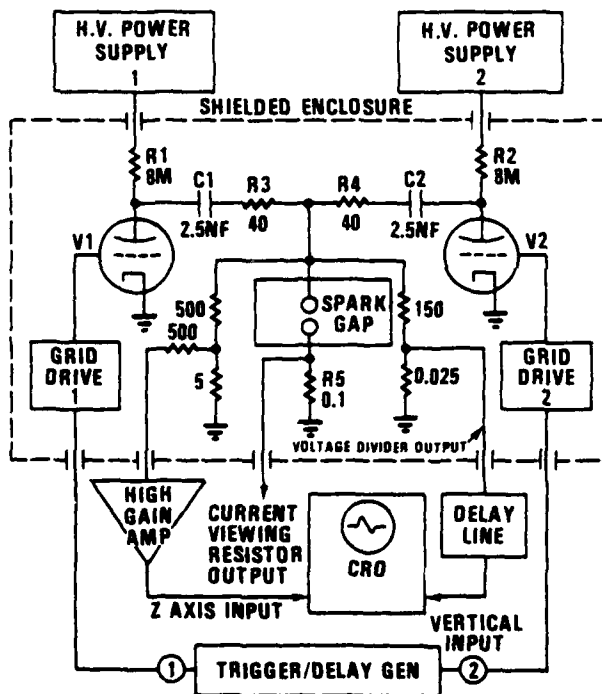


Figure 3. Two-pulse circuit

Two-Pulse Circuit

A diagram of the two-pulse circuit is shown in Figure 3. The trigger/delay generator, shown at the bottom of the diagram, has two outputs which control the time delay between the first and second pulses (100 ns to 250 ns) as well as the repetition rate of the pulse pairs (0.5 to 5 pulse pairs per second). The outputs of the trigger/delay generator are used to trigger two 8613 hydrogen thyratrons, V_1 and V_2 . C_1 and C_2 are charged through R_1 and R_2 by two high voltage power supplies. Operating limits of the thyratrons require the voltage to be between 4 and 20 kV. To generate the first pulse, which is used to break down the gap, V_1 is triggered and discharges

C_1 through R_3 , the spark gap, and R_5 . After the desired time delay, the second pulse, which is used to measure the voltage holdoff of the ionized gap, is generated by triggering V_2 which discharges C_2 through R_4 , the spark gap, and R_5 . R_3 and R_4 are Carborundum resistors used to limit the current to 500 A to protect the thyratrons; R_5 is a current-viewing resistor. Voltage is measured with a resistive voltage divider across the spark gap. The voltage waveform across the gap is shown in Figure 4.

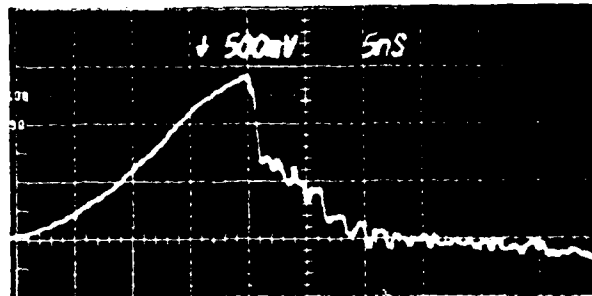


Figure 4. Voltage waveform across spark gap

The voltage rises to the striking potential of the gap in 20 ns and then falls abruptly to an intermediate level from which it tapers off more slowly. This intermediate level is the point where a rising $L di/dt$ voltage waveform intercepts the trailing edge of the pulse. L is the inductance of the spark gap and current-viewing resistor, about 100 nH, and di/dt is about 10^{10} A/s. Oscillations following the breakdown are associated with the inductance and stray capacitance of the spark gap. Figure 5 shows the current through the gap (voltage across R_5), which is limited to 500 A at 20 kV and discharges the 2.5-nF capacitor in 500 ns (5T). The energy discharged through the gap depends only on the energy stored in the capacitors and not on the breakdown voltage of the spark gap.

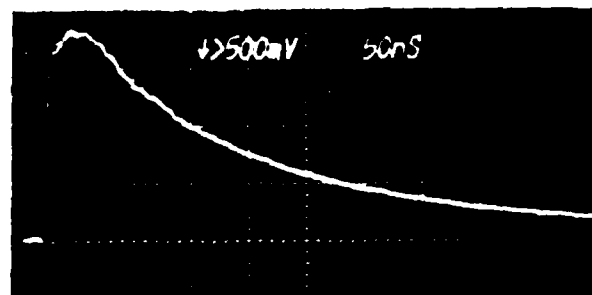


Figure 5. Current waveform through spark gap

First- and second pulse amplitudes are obtained from oscilloscope photographs. However, it is difficult to obtain photographs of two 20-ns pulses separated by many milliseconds due to the high-intensity blooming of the baseline. The problem becomes worse with multiple trace photographs, but can be overcome using the configuration shown in the lower part of Figure 3. A second voltage divider is placed across the spark gap and connected to a high-gain amplifier.

The output from this amplifier is used to control the intensity (Z axis) input of a Tektronix 7104 oscilloscope, thereby making the intensity of the trace proportional to amplitude. The propagation time through the high-gain amplifier and oscilloscope Z-axis circuit is 150 ns. It is, therefore, necessary to pass the voltage waveform signal through a 150-ns delay line (33 m of RG-58 cable). This technique allows the baseline of the oscilloscope trace to be dimmed or blanked completely while maintaining bright pulse spikes, as shown in Figure 6.



Figure 6. Single-shot photographs of 20-ns pulses 1 ms apart

Experimental Procedure

Prior to collecting recovery data, the spark gap electrodes are polished down to a clean surface and conditioned with at least 100,000 shots in the gas to be tested. After repeated conditioning and polishing, the flat electrode surfaces become slightly domed. This causes the effects of conditioning to be more pronounced near the center of the electrode tip. The maximum deviation from a flat surface was .013 cm for these experiments. Gap spacing is measured at the desired gas pressure by closing the micrometer until an ohmmeter indicates the gap is shorted and then opening the micrometer to the desired spacing.

The gas flow is adjusted so that the total volume of the spark gap is exchanged between pulse pairs but remains essentially motionless between the first and second pulses. This changes the gas between pulse pairs to prevent any long-term buildup of impurities, but does not allow the gas to change significantly during the recovery period. Since high gas pressures create high gas densities in the spark gap and since the flow rate is measured at atmospheric pressure, the gas flow must be increased as pressure is increased to assure that the gap volume is exchanged between pulse pairs.

Since gas temperature may affect gap recovery, thermocouples were placed inside the gap volume and the gas tubing to measure the temperature of the gas at various pressures and flow rates. Results show that the gas temperature is about 36° C and does not vary more than 3° over the range of pressures and flow rates used for this data.

Because the spark gap fires during the voltage rise, the statistically varying time-to-breakdown causes statistically varying breakdown voltages. Therefore, recovery data must be averaged. Data are obtained photographically using multiple image photographs similar to the one shown in Figure 7.

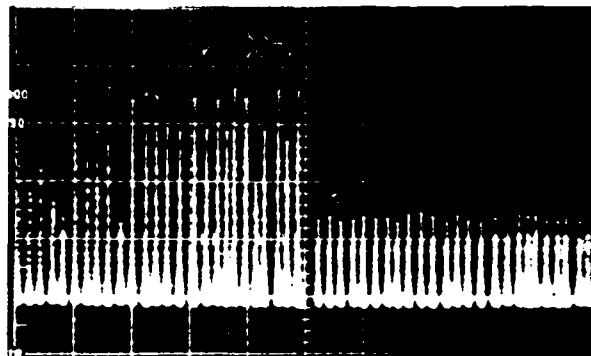


Figure 7. Multiple image photograph of breakdown amplitudes with a delay time of 1 ms

The horizontal sweep rate of the oscilloscope is adjusted so that the chosen time delay between the first and second pulses is one-half the oscilloscope screen width. The camera shutter is open while the pulse pairs are firing about once per second. The trace is manually advanced slightly for each pulse pair until the beginning of the trace has moved halfway across the screen. This creates a multiple image photograph of about 30 pulse pairs, each with the same time delay. The first pulses are on the left half of the picture, and the second pulses are on the right half. The mean and the standard deviation of the voltages are then calculated to provide one data point for the recovery graphs.

Experimental Results

As can be seen in Figure 7, there is significant variation in the breakdown voltages of both the first and second pulses due to the statistically varying time-to-breakdown. The amplitudes show that for a given time delay there is no correlation between a particular first-pulse breakdown voltage and the corresponding second-pulse breakdown voltage. Measuring hundreds of amplitudes shows that the statistical variation of first-pulse amplitudes forms a Gaussian distribution about the mean. An example of this distribution is the cumulative probability versus breakdown-voltage graph shown in Figure 8. Observation of smaller populations of second-pulse amplitudes indicate that their distribution is also Gaussian.

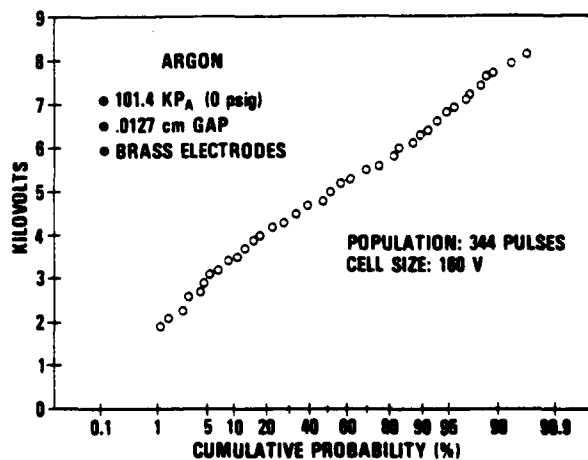


Figure 8. Cumulative probability versus first-pulse breakdown voltage

An example of a recovery curve (nitrogen at 1400 kPa) is shown in Figure 9. Each pair of means and standard deviations (σ) is obtained from one photograph containing about 30 pulse pairs. The 100% line represents the mean of all first-pulse data points in the 13 photographs used to generate this curve.

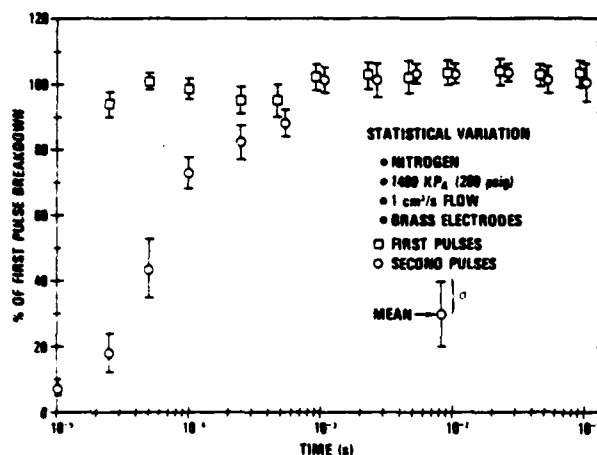


Figure 9. Recovery curve for nitrogen at 1480 kPa with 0.013 cm gap

Figures 10 through 15 show the percent-electric-strength versus time-after-breakdown curves for six gases at various pressures. Brass electrodes are used with a gap spacing of 0.013 cm. The data points for these graphs are the means of the second-pulse amplitudes. The standard deviations and the first-pulse means are not shown.

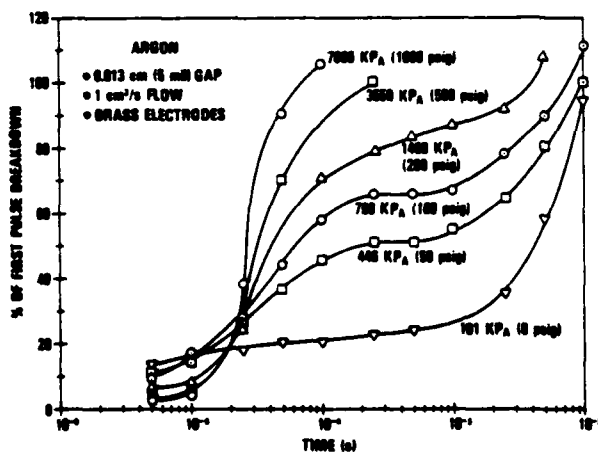


Figure 10. Percent recovery versus time for argon at various pressures

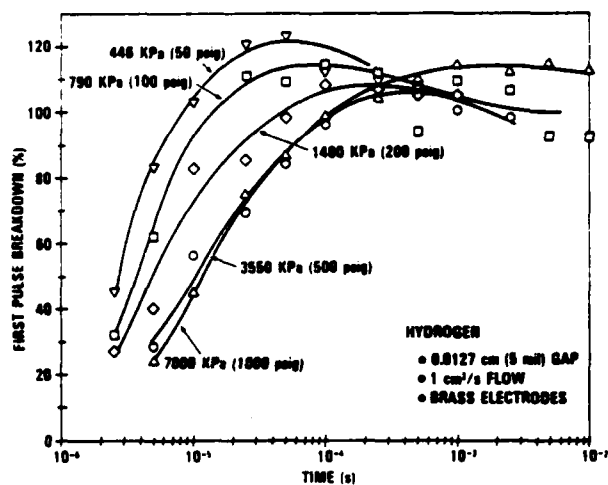


Figure 11. Percent recovery versus time for hydrogen at various pressures

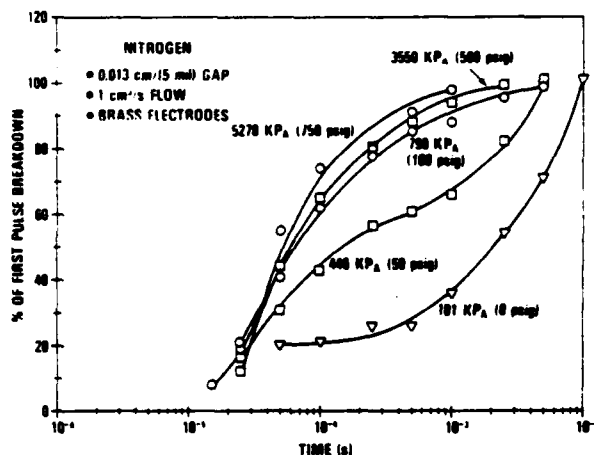


Figure 12. Percent recovery versus time for nitrogen at various pressures

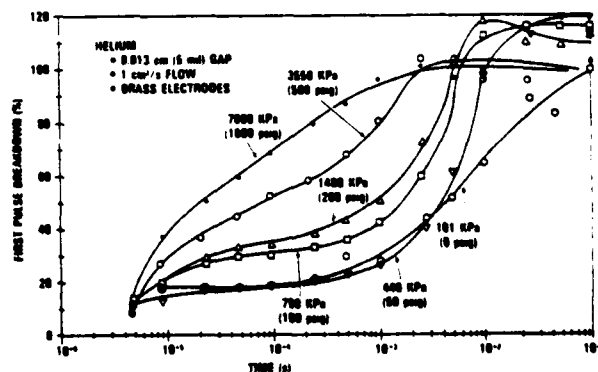


Figure 13. Percent recovery versus time for helium at various pressures

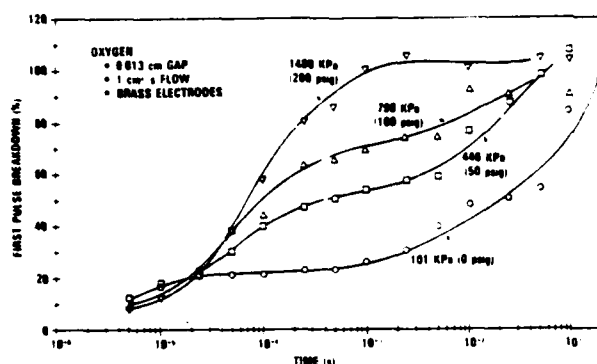


Figure 14. Percent recovery versus time for oxygen at various pressures

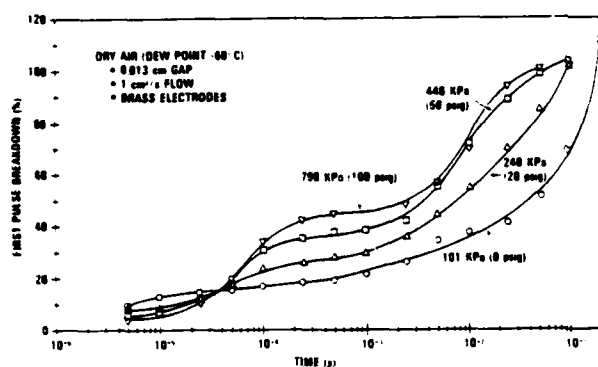


Figure 15. Percent recovery versus time for dry air at various pressures

The graph for argon shows that complete recovery varies from about 10 msec at one atmosphere to 100 usec at 7 MPa. The recovery curves for hydrogen are more erratic and show that increasing pressure does not necessarily decrease recovery time. Complete recovery for hydrogen occurs between 10 and 100 usec for pressures above 50 psi. Recovery results at atmospheric pressure are erratic and are still under investigation. Hydrogen tended to overshoot or exceed 100% by as much as 20%, as did helium.

Recovery curves for hydrogen and argon were also obtained on an earlier two-pulse system with approximately a 0.5- μ s rise time⁵. Even though the spark gap geometry was different and the energy discharged was in the millijoule range, the recovery curves were similar in shape, and recovery times were generally within a factor of two.

The recovery curves for nitrogen, oxygen and dry air are limited to lower pressures due to the high electric strength of these gases and the voltage limitations of the experimental apparatus. Gas flow rate was varied by an order of magnitude in A , N_2 and H_2 without greatly affecting the recovery times.

Model

After the first-pulse breakdown, a column of plasma exists in the gap which leads to a lower electric strength when voltage is applied by the second pulse. During the delay between pulses, the neutral particle density in the plasma column is increasing since recombination processes are occurring among the charged particles. A percentage recovery, R , can be defined as the relative density of neutral particles to the total number of particles. When all recombination processes have ended, R will equal one and the gas will have recovered. At any time, the total particle density N is the sum of the neutral particle density n_n and the charged particle pair density n , that is

$$N = n_n + n$$

The rate of recombination is governed by the decrease in charged particle density according to the general equation

$$\frac{dn}{dt} = D\nabla^2 n - \alpha n^2 - \gamma n$$

where the terms on the right-hand side describe diffusion, recombination and attachment, respectively. The coefficients of these terms are temperature dependent. When the diffusion term can be ignored and the gas is non-attaching, γ is equal to zero and the general character of the recovery curves will be described by the simple equation

$$\frac{dn}{dt} = -\alpha n^2$$

If α is not a function of time, the solution is

$$n = \frac{n(0)}{1 + \alpha n(0)t}$$

A normalized charge particle density n' can be introduced by

$$n' = \frac{n}{n(0)}$$

while the percent recovery is

$$R = \frac{n_n}{N} = \frac{1 - \frac{n}{n(0)}}{1 + \frac{n}{n(0)}}$$

The total particle density N is directly proportional to pressure; therefore R is pressure dependent. The equation for R gives the characteristic S-shape, shifting to the left with pressure, that usually appears in the recovery data plots.

It is well known that for short time scales, the recombination coefficient is time dependent.^{1,4} The process of spark breakdown will result in initial columns of ionized gas, and the charged particle reduction rate is described by the general equation above where $n = n(t)$. Numerical solution of the equation gives the normalized charged particle density $n(t)/n(0)$, while the condition $N = n_n(t) + n(t)$ gives the neutral particle density. Finally, the ratio $r = n_n(t)/n(t)$ allows $R = r/(1+r)$ to be evaluated. Introducing this time dependence for the recombination coefficient causes the shape of the recovery curves to vary with pressure, providing a qualitative fit to the experimental curves.

The actual gas parameters, coefficients and initial conditions are being implemented to obtain a quantitative fit.

Conclusions

For a given time delay, there is no statistical correlation between a particular first-pulse breakdown voltage and the corresponding second-pulse breakdown voltage. The statistical variation of voltage amplitudes for both the first and second pulses forms a Gaussian distribution about the mean. The standard deviation of the first-pulse data tends to decrease as the spark gap pressure is increased from atmospheric (17 - 22%) up to 7 MPa (2 - 10%). The standard deviation of the second-pulse data shows a tendency to increase as pressure is increased and is generally between one-fourth and twice the first-pulse standard deviation.

With the possible exception of hydrogen, increasing pressure significantly decreases recovery time. For most gases, the shape of the recovery curves tends to vary from concave up at low pressures to concave down at higher pressures. An explanation of the recovery data, based on a model with a time-dependent recombination coefficient appears to provide the proper recovery curve shapes. Quantitative evaluation of these curves is under way.

Acknowledgment

The authors are indebted to L.C. Johnson for her valuable assistance with this work.

This work is supported by the Navy's Pulsed Power Technology Program and the NSWC Independent Research Program.

References

1. G.A. Farrall and J.D. Cobine, "Recovery Strength Measurements in Arcs from Atmospheric Pressure to Vacuum," IEEE Transactions on Power Apparatus and Systems (August 1967).
2. S.L. Moran and L.F. Rinehart, "Voltage Recovery Time of Small Spark Gaps," Third IEEE International Pulsed Power Conference (June 1981).
3. A. von Engel, Ionized Gases (London: Oxford University Press, 1965).
4. L.B. Loeb, Basic Processes of Gaseous Electronics (Berkeley and Los Angeles: University of California Press, 1961).

Flow Visualization in a Gas Blown Spark Gap

R. J. Pederson
H. J. Carper

Mechanical Engineering Department
Texas Tech University
Lubbock, Texas 79409

Summary

This paper presents results obtained during the initial phase of a study of effects of fluid mechanics and heat transfer on the performance of gas blown spark gaps. Air was blown between hemispherical electrodes with arc pulse rates of up to 300 pps. A Mach-Zehnder interferometer system was used to visualize the gas density variations during the flushing process. High-speed photographs show the flow patterns as the heated gas resulting from arc discharges convects out of the gap. These interferograms also show the effects of boundary layers near the electrodes, as well as the path of a typical prefire arc passing through the heated gas from the previous arc discharge. From this initial investigation, it is apparent that the interferometer represents a useful tool to obtain qualitative information about flow patterns in gas blown spark gaps. Work is continuing to develop this tool to obtain quantitative data for the post-arc gas density distribution as a function of time.

Introduction

It is well known that there is an important influence of the interelectrode fluid mechanics and related heat transfer processes on the performance of gas blown spark gap switches. In fact, for heavy-duty, rep-rated operation of these types of switches, the fluid mechanics often becomes the controlling factor in governing maximum rep rate. In general, the qualitative nature of switch behavior is such that if it is desired to increase rep rate, the gas blowing rate must also be increased in order to flush the postarc hot gas from the gap more rapidly. However, the physics of the flushing process is complex and poorly understood, and quantitative relationships between gap recovery time and the fluid mechanics and heat transfer are needed.

One problem involves relating gap breakdown voltage to the nonuniform gas density distribution which exists in the gap after an arc discharge and which changes with time as the hot gas is purged from the gap. The related problem is to determine, for a given arc discharge, this postarc gas density distribution history as a function of fluid mechanics, heat transfer, and electrical variables. Important variables influencing the gas density distribution history are the characteristics of the arc, properties of the electrode materials, electrode geometry, type of gas, and the mass flowrate through the interelectrode region.

In an effort to address the problem of experimentally determining the gas density distribution history following an arc discharge, the work reported here was undertaken. The short time scale on which the energy released by the arc and the subsequent flushing process occurs, the physically small space involved, and the high voltage potential between the electrodes render the use of probes to measure local density difficult if not impossible. Thus, the

approach taken in this study was to use an optical method and high-speed photographic techniques in an initial attempt to visualize the flow in a gap, and to determine if effects on the gas density distribution history of several of the aforementioned variables could be seen. The electrode geometry chosen for this study is somewhat simplified, and the gas velocities and rep rates are admittedly low compared to those contemplated in practical gas blown spark gap designs. However, it was felt that many of the questions associated with the experimental methods could be answered using these simplified conditions.

Experimental Setup

A photograph of the experimental setup is presented in Figure 1. An electrode configuration consisting of two 1-inch diameter brass electrodes with spherical ends was used for all experiments. The electrodes were mounted between parallel insulating plates with no side enclosures. Thus, the electrodes were open to the laboratory air environment. Flushing of the interelectrode gap was accomplished by a jet of air issuing from a 2-inch diameter PVC pipe connected to a variable flowrate blower. The exit of the pipe was placed about two inches from the electrodes with the axis of the jet perpendicular to the axis of the electrodes. The gap was thus exposed to an essentially uniform free-stream blowing velocity with a direction normal to the path of the arc discharge. Arcs were generated by a relaxation oscillator arrangement with a 0-20 kV, 10 kW power supply. The values of the charging and load resistors were 100 k Ω and 25 Ω , respectively.

The electrode assembly was placed in the test section of a Mach-Zehnder interferometer with 6-inch diameter optical elements and a 15 mW helium-neon laser light source. The orientation of the blowing jet was such that a side view of the flushing process could be observed. Two different high-speed, 16-mm motion picture cameras were used to obtain the sample interferograms presented. With a 110-volt power supply, one camera provides full-frame pictures at up to about 4,800 pictures per second, and the other provides half-frame pictures at about twice the rate of the full-frame camera. A telephoto lens was employed with each camera.

Discussion of Results

The results of the present study are presented in Figures 2-5. Each figure presents a series of interferograms printed from 16-mm, high-speed, black and white reversal film (Kodak TRI-X Reversal film No. 7278). Since the prints were made from positives, they appear as negatives; that is, what would normally appear white to the eye appears black on the prints. This is particularly evident for the arcs shown in the figures.

All figures show a sequence of six photographs obtained at a camera speed of approximately 4700

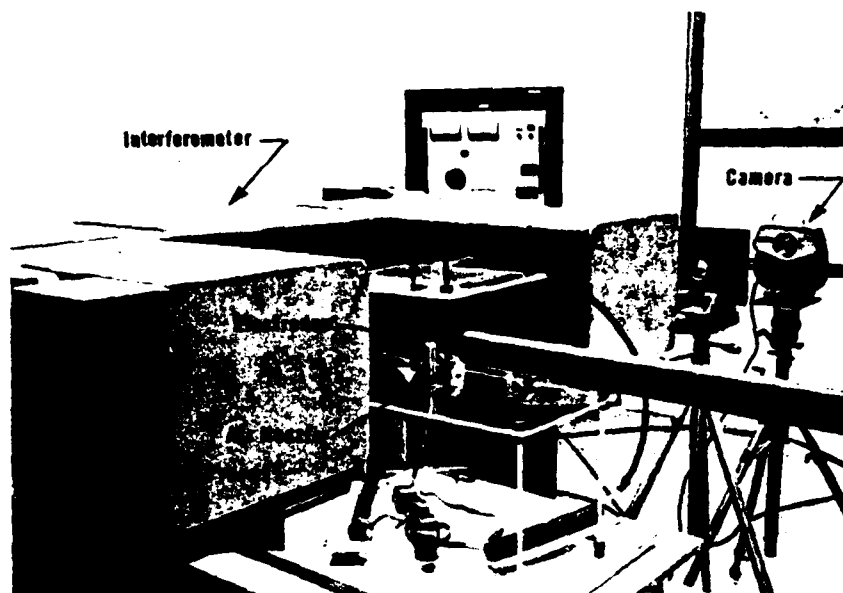


Figure 1. Experimental Setup

frames per second. The exposure time for each picture is about 80 μ s. In all pictures, the tips of the hemispherical electrodes appear to the upper and lower left. For reference purposes, the black line drawn on each picture indicates the vertical axis of the electrodes. Lighting conditions, the position of the electrodes within the frame, and the field of view vary somewhat between figures due to the exploratory nature of the investigation.

The flow of air is from left to right in all photographs. As discussed earlier, the flow approaches the electrodes as a uniform stream discharging from a 2-inch diameter pipe about two inches from the electrodes. The electrodes and air stream are located in a large room, and because of this, the pressure is essentially constant throughout the interelectrode region.

The infinite fringe method of utilizing the interferometer is illustrated in all figures. With this method, the undisturbed flow field appears as a region of uniform intensity on the photographs. The presence of a density variation within the test section results in a variation of the index of refraction in that region and a local change of velocity for the light passing through. This light is recombined with the light passing through the reference section at the second splitter plate, and a series of interference fringes are formed. Photographs of these fringe patterns convey information about the integral of the density variation along the optical axis of the test section. For this particular application, the density disturbance is three-dimensional in nature, and these single-view photographs cannot be directly interpreted to yield local density within the disturbed regions. They can, however, be used to infer the general extent of the affected region and its motion. It is these general characteristics that are being described at this time. Work is presently underway to improve the quantitative capabilities of the interferometer as applied to this situation.

Figure 2 presents photos of the density variation of the gas in the interelectrode region following an arc discharge. The blowing velocity was 5 ft/s, and the capacitance of the discharge capacitor was 0.01 μ F. The gap spacing was 0.15 in. and the breakdown voltage was approximately 12.5 kV. The resulting arc current waveform was underdamped, had a maximum current of approximately 200 A, and decreased to zero in about 10 μ s. An arc discharging at the minimum electrode separation point is seen in Figure 2(a) along with fringes generated during the time of exposure. Also shown in the far right of the picture is a region of lower gas density due to a previous arc. This region appears somewhat faded due to a decrease in the background lighting toward the right of the photos. The sequence of photos 2(b) through 2(f) shows a general flattening of the affected region as it moves out of the gap. Also evident is a general elongation of the affected region, with the upstream edge moving to the right much slower than the downstream edge. It should be mentioned here that the apparent velocity of the affected region is due to a combination of heat transfer and fluid motion. The general tendency is for the fringe pattern to maintain its shape as it progresses out of the gap, at least for a distance of one to two gap spacings. This would seem to indicate a laminar flow pattern in this region. Beyond this distance the flow separates from the electrodes, and the upper and lower portions of the heated region are caught in a relatively low velocity recirculation region behind both the upper and lower electrodes. This gives rise to the long "tails" evident in the heated gas from the previous arc.

Figure 3 presents results for the same conditions as those for Figure 2, except that the capacitance of the discharge capacitor was increased to 0.32 μ F. The breakdown voltage was also essentially the same (~ 12.5 kV). This resulted in an overdamped arc current waveform peaking at approximately 450 A and decreasing to zero in about 20 μ s. A different

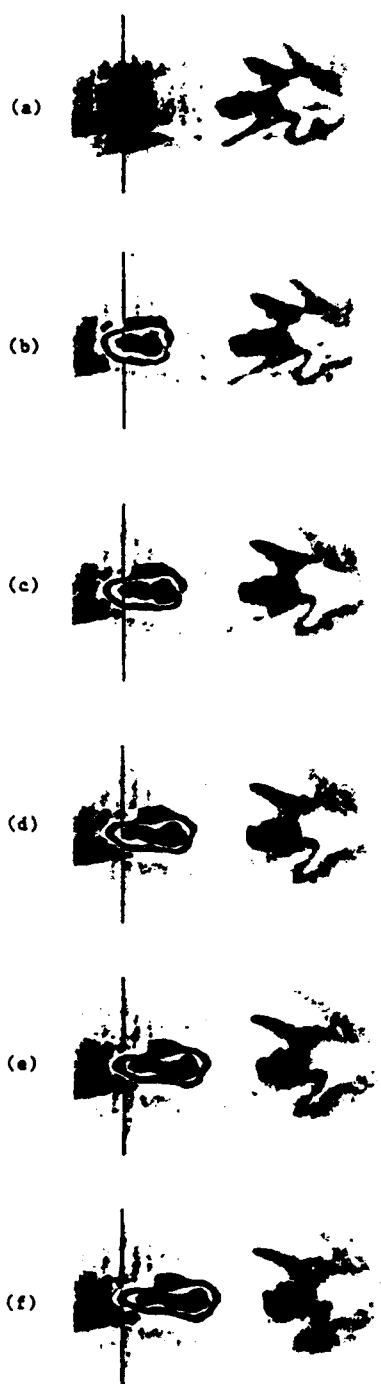


Figure 2. Interferograms for Low Jet Velocity (~ 5 ft/s) and Small Capacitor (~ 0.01 μ F).



Figure 3. Interferograms for Low Jet Velocity (~ 5 ft/s) and Large Capacitor (~ 0.32 μ F).

camera setup was used for these photos resulting in a slightly larger magnification and a somewhat different region of the flow field covered in the photos. The photos in Figure 3 are somewhat out of focus and this results in a slight optical distortion of the electrode shape. A much slower arc repetition rate was used in Figure 3. Because of this, heated gas from the previous arc does not appear in this sequence.

A comparison of Figures 2 and 3 shows the effect of the energy of the arc discharge on the density distribution within the electrode region during single-shot operation. Apparent in the figures is the difference in the size of the region affected by the discharge. For the smaller discharge, the heated region is primarily confined to the central region between the electrodes with only a small portion in contact with the upper electrode. As expected, the higher energy discharge results in a much larger affected area with a much larger contact area between the affected region and the electrodes. This larger contact area emphasizes the importance of the electrodes in the overall problem of cooling the interelectrode region.

Figure 4 presents a sequence of photos illustrating the phenomena to be avoided in repeated operation of a spark gap, that is, restrike. The overall conditions for these photos are the same as in Figure 2. In fact, these photos came from the same roll of film. Again, an arc discharging at the minimum electrode spacing is seen in the left portion of Figure 4(a) along with a region of lower density from a previous arc in the right portion. Figures 3(b) and 3(c) show the heated region moving downstream, and in Figure 3(d) a restrike is seen to occur through the heated region as opposed to occurring at the minimum electrode separation distance. Figures 3(c) and 3(f) show the heated region from the initial arc and the restrike continuing to be moved from the interelectrode space.

Comparing Figures 2 and 4, one can see that the general shape of the region heated by the initial arc is essentially the same in both cases. However, comparing photos (c) and (d) of each sequence, it appears that an additional half-fringe is present in Figure 4. This would seem to indicate that the heated region in Figure 4 is slightly hotter, and this may account for the restrike observed in this sequence.

Figure 5 shows the result of increasing the approach velocity to approximately 22 ft/s. The small capacitor was again used, but the gap spacing was reduced to 0.1 in., resulting in a lower breakdown voltage (~ 10 kV) and consequently lower energy release in the arc. Figure 5(a) shows the affected area immediately after the arc discharge and Figures 5(b) through 5(f) show the movement of the heated gas out of the interelectrode region. The rate at which the heated region moves out of the gap is noticeably higher for this case. For the situations shown in Figures 2, 3 and 4, the upstream edge of the heated region moves to the right at approximately 6 ft/s, while the downstream edge moves at about 16 ft/s. With the higher jet velocity, Figure 5, the upstream edge exits the gap region at about 19 ft/s while the downstream edge moves at about 28 ft/s. These velocities give indications of the movement of the central portion of the heated region. However, as is evident in Figure 5, the region near the electrodes stays relatively hot even after the core region is cooled. This is a result of the much

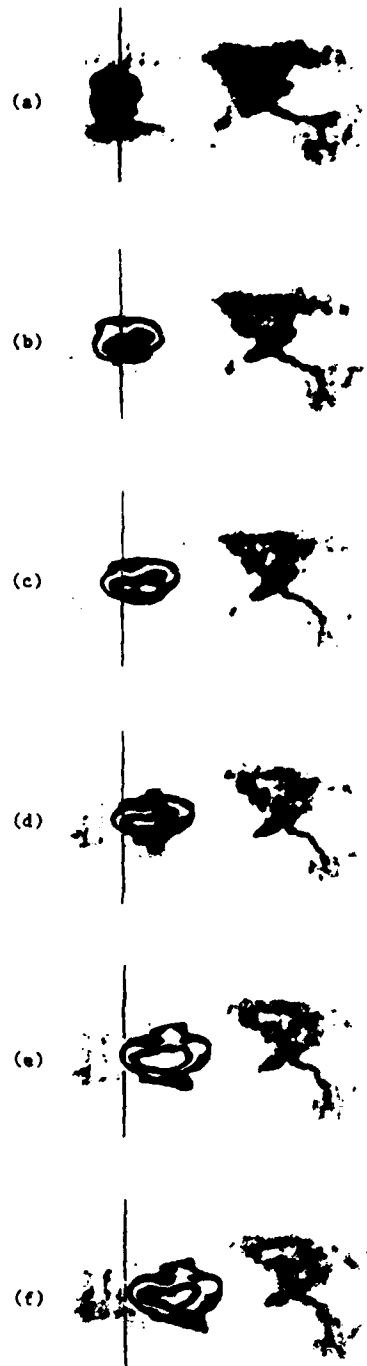


Figure 4. Interferograms Showing Restrike for Low Jet Velocity (~ 5 ft/s) and Small Capacitor (~ 0.01 μ F).

lower velocities in the boundary layer near each electrode. Work is currently being done to investigate the possibility of visualizing restrikes for these higher velocities.

Conclusions

The interferometer was used to visualize the density distribution in a gas blown spark gap of simple geometry. The interferograms obtained clearly show the effects of the heating of the gas by the arc and the flushing of this heated region by the purging gas. The effects of the magnitude of the blowing velocity, of the characteristics of the arc, and of the hydrodynamic boundary layers on the electrodes can be seen. Similar qualitative results could be readily obtained for more practical gap designs provided that light can be passed through the gap region. Work is continuing on this technique to provide quantitative as well as additional qualitative information for the study of the fluid mechanics and heat transfer aspects of gas blown spark gaps.

Acknowledgment

The authors wish to acknowledge the partial support of this work by the Air Force Office of Scientific Research.

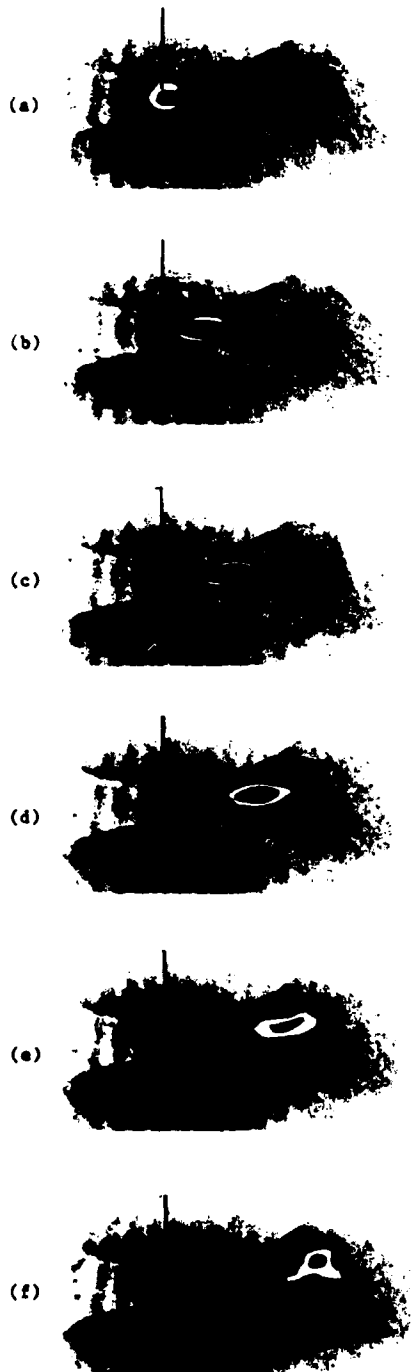


Figure 5. Interferograms for High Jet Velocity (~ 22 ft/s) and Small Capacitor (~ 0.01 μ F).

SPARK-GAP SWITCHES ILLUMINATED BY KrF LASER THROUGH UV OPTICAL FIBERS

Kouichi Kunitomo, Yasuaki Itoh, Minoru Obara, and Tomoo Fujioka

Department of Electrical Engineering
Faculty of Science and Technology, Keio University
3-14-1, Hiyoshi, Kohoku-ku, Yokohama-shi, 223, Japan

Summary

KrF (248 nm) laser triggered spark gaps with UV optical fibers to transmit the laser beams have been developed. When it was illuminated by a unfocused KrF laser beam through an optical fiber, it could operate at V/V_B of 90% with less than 5 nsec jitter for switching an SF₆-gas-insulated spark gap (V_B : triggered voltage, V_B : self-breakdown voltage). This technique is found promising for nanosecond synchronization of a system consisting of many pulse power modules.

Introduction

Laser triggered spark gap (LTSG) [1] has been studied as the highly reliable switch in pulse power technology, because it can operate in short switching time with low jitter and hardly operates erroneously by electrical noise. In the early works, only high-power lasers in excess of tens of megawatt were used to produce metal plasma on the electrode surface. Therefore, the used lasers were limited to high-power lasers in the infrared and visible spectral regions. However, it is recently reported that a gas-insulated spark-gap can operate with subnanosecond jitter when triggered with UV lasers of as low as several millijoule energy [2][3]. UV raregas halide excimer lasers are used in some experiments since insulating gases such as SF₆ can be ionized easily by two or three photon absorption processes in the UV spectral region. Conventional LTSGs have structural limitations on the extension of the applications, because the laser beam propagates through the air and they must use many optical components. Therefore, it would be satisfactory for the use as a switch in a single module. This scheme is potentially capable of triggering multimodules of pulse power machines in low jitter timing. If many optical components are replaced with UV optical fibers for simplicity, UV-LTSGs are usable for multimodule system at least in terms of laser engineering. For the first time we would like to report the fundamental work on the SF₆-gas-insulated spark gap switches illuminated by KrF laser (248nm) through UV optical fibers. The LTSG with optical fibers can eliminate the alignment of the laser beam into spark gaps and the environmental problem, and can be easily coupled to many switches without beam splitters. This type of spark gap switch was found to be promising for triggering multimodules of pulse power machines in low jitter timing.

Experiment

The experimental arrangement is schematically shown in Fig. 1. The electrical circuit is a capacitor-transfer-type circuit from C₁ to C₂. The C₁ is an 80-nF capacitor, and the C₂ is a 30-nF capacitor consisting of eleven 2.7-nF BaTiO₃-series ceramic capacitors. The charging time is about 180 nsec. As a dummy load we used a 2.5-Ω copper sulfate

resistor. The LTSG works as an output switch. The electrodes of the spark gap are a pair of half-sphere (25-mm diameter) brass electrodes. The gap spacing is 2 mm. The optical fiber is coupled to the center of the electrode (anode), the end of which is placed 1 mm behind the electrode surface. The optical fiber is a commercially available step-index-type, whose core is made of fused quartz ($n_1=1.45$) of 1-mm diameter and its clad is silicon ($n_2=1.02$) of 1.25-mm diameter. The KrF laser oscillator was driven by Blumlein pulse forming lines. A typical laser pulse is 18 nsec FWHM with an energy of 40 mJ and a beam cross-section of 2-cm height x 0.3-cm width. This laser output was focused onto the one end of the optical fiber by a CaF₂ lens ($f=6.0$ cm). We adjusted the intensity on the end of the fiber by changing the distance between the end surface and the focal point.

Prior to the experiment, KrF laser transmission characteristics through the optical fiber was measured. The detailed results will be published elsewhere. The loss of the optical fiber was dependent on the focused laser power and was measured to be 2 dB/m when the end of the fiber was illuminated by an intensity of 100 MW/cm². The 2-m long optical fiber was used experimentally. The voltage waveform on the dummy load was monitored by a voltage monitor. The laser pulse waveform was detected by a biplanar phototube. Both signals were displayed on a Tektronix 7844 dual-beam oscilloscope. The time jitter and delay were measured by averaging every 10 shots.

Results and Discussion

In Fig. 2, the time history of a typical charging voltage on the C₂ capacitor is shown by the upper trace (a), while the trigger laser pulse and the voltage waveform on the 2.5-Ω dummy load are also shown by the lower trace (b). In Fig. 2(a), delay time is hereafter defined as the time delay between the rise of the laser pulse and the rise of the voltage on the resistive load.

Shown in Fig. 3 is the dependence of the delay time on the value of V/V_B at which the laser trigger is done. Here, the illuminated intensity at the exit end of the optical fiber is 2 MW/cm². As can be seen in Fig. 3, the laser trigger is effective at the value of $V/V_B = 70\%$, and the time jitter of less than 5 nsec is obtained at $V/V_B = 90\%$. Under this condition the time delay is 20 nsec and the velocity of the streamer formation is estimated to be 10^7 cm/sec.

Figure 4 shows the delay time dependence on the illuminated intensity at $V/V_B = 90\%$. It is seen that the delay time is strongly dependent on the illuminated intensity. This would be attributable to the initial electron number density produced by the laser photons.

In conclusion, we have developed for the first time the LTSG with UV optical fibers. It operated in 5-nsec time jitter when triggered with a KrF laser pulse at 90% of the self-breakdown voltage for an SF₆-gas-insulated spark gap. The illuminated KrF laser (248 nm)

energy was less than $10 \mu\text{J}/\text{shot}$.

In the future, both the use of the lens in a spark gap and development of optical fibers through which more intense UV can be transmitted will be able to lead this type of spark gap to more reliable switching elements.

This work was supported by a Grant-in-Aid for Scientific Research from The Ministry of Education, Science and Culture.

References

- [1] A. H. Guenther and J. R. Bettis, J. Phys. D. (Applied Phys.) 11, 1577 (1978).
- [2] W. R. Rapoport, J. Goldhar and J. R. Murray, "UV-laser triggered SF_6 spark gap for low jitter timing," UCRL-82697 (1980).
- [3] J. R. Woodworth, C. A. Frost and T.A. Green, 3rd IEEE International Pulsed Power Conference, June 1-3, 1981, Alb. NM. Digest of Technical Papers p.154.

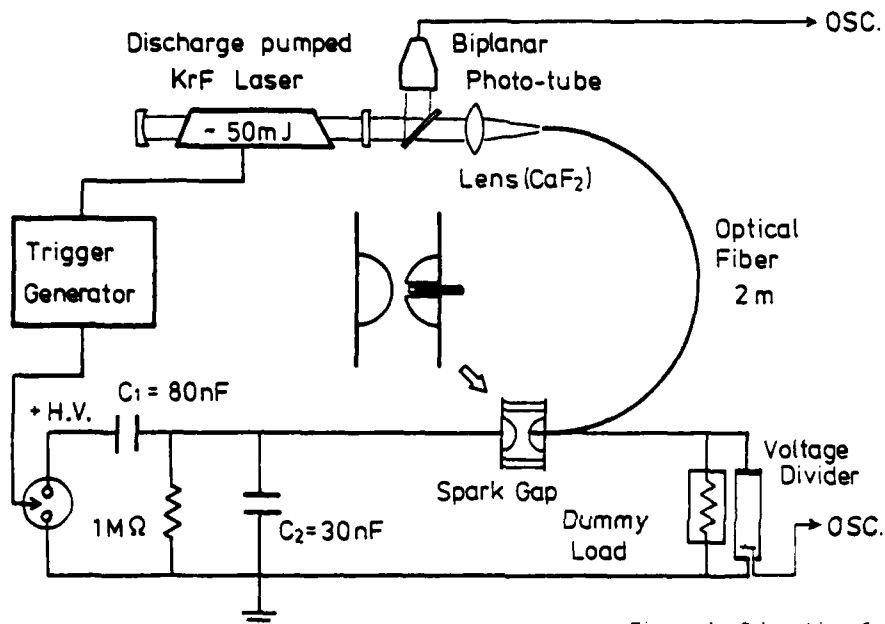


Figure 1 Schematic of the experimental setup.

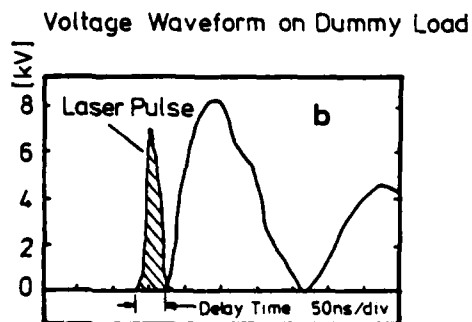
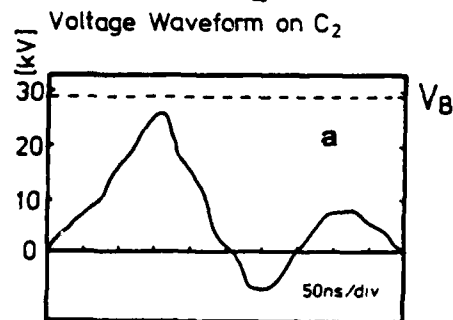


Figure 2 Time histories of (a) a typical charging voltage on the C_2 capacitor without self-breakdown, and (b) the trigger laser pulse and the voltage on the resistive load.

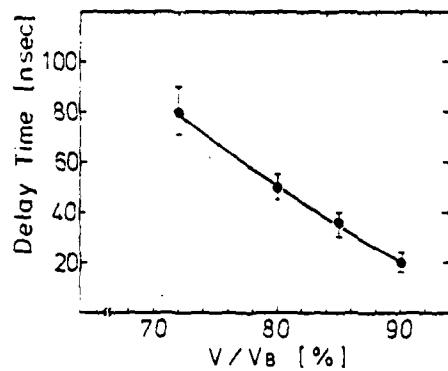


Figure 3 Dependence of the delay time on the value of V/V_B at which the laser trigger is done.

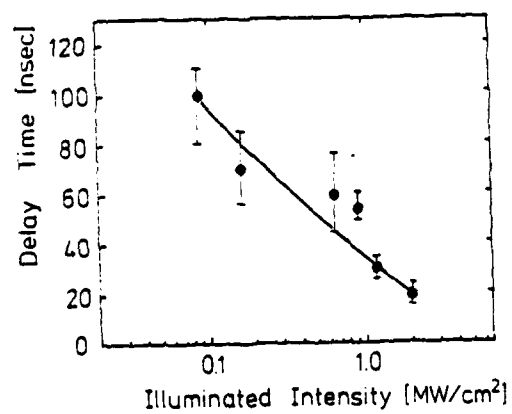


Figure 4 Dependence of the delay time on the illuminated intensity at $V/V_B=90\%$.

UV RADIATION TRIGGERED RAIL-GAP SWITCHES

R.S. Taylor and K.E. Leopold
National Research Council of Canada
Division of Physics
Ottawa, K1A 0R6, Canada

Summary

UV radiation from either an excimer laser or a corona discharge has been used to initiate sub-nanosecond jitter, multichannel breakdown in a gas insulated rail-gap consisting of two uniform field electrodes.

Introduction

Numerous low inductance devices are capable of switching high voltages from low impedance pulse forming lines (PFL) to low impedance loads. These include: the dc-triggered surface spark-gap,¹ which is still under development and may prove useful as a low repetition rate, high charge transfer switch; magnetic switches,² which on the basis of preliminary results, appear promising for specific high repetition rate applications although to assess their full capability, more information is needed on switch dissipation, switching speed and the general scalability of these devices; and rail-gap switches, which over the years have provided a versatile and scalable approach to switching high voltages.³⁻⁸ Recently such switches have received considerable attention due to their important role in the development of high output energy, long optical pulse duration excimer lasers.^{9,10} In the past, rail-gap switches have been triggered using three-electrode, field distortion techniques³⁻⁶ and have been successfully employed in low repetition rate, high charge transfer switch applications.³ More recently coherent uv radiation^{6,7} from an excimer laser and incoherent uv radiation from a corona discharge⁸ have been used as trigger sources.

The first laser-triggered rail-gap experiments demonstrated that only a few millijoules of unfocused KrF laser radiation was required to produce multichannel breakdown in an edge-plane rail-gap.⁷ The technique was extended to uniform field electrode gaps⁶ by using Ar gas together with a few ppm of gas additive (fluorobenzene), selected to produce efficient two-photon ionization at the KrF laser wavelength (248 nm). Although this approach was very successful at producing multichanneling, the use of an Ar-additive gas mix resulted in a low switch voltage hold-off and substantial switch dissipation.

This paper describes recent important developments in laser triggering of uniform field electrode rail-gaps which permit subnanosecond jitter, multichannel switch breakdown with good voltage hold-off and switch dissipation. This paper also describes the use of a simple corona trigger source, which when appropriately designed to incorporate some of the important features of laser triggering, results in similar low jitter, multichannel switch performance.

Experimental

The rail-gap test facility is shown in Fig. 1. It consisted of a three-element distilled water dielectric pulse forming line (PFL) which was pulse charged in a few us from a Marx bank primary energy source. The two way energy transit time of the line was ~50 ns and a line impedance of 1 Ω was employed. The PFL was connected to a gas insulated rail-gap switch. A short section of transmission line connected the switch to a matched CuSO_4 resistive dummy load. A secondary line was employed in order to simulate a test facility that had previously been used with a realistic (initially high impedance) excimer laser load.⁶ The extension of the line after the switch was necessary to improve the switch performance to a level obtained with resistive dummy loads. The voltages on the PFL and resistive load were measured using a fast risetime (1 ns) high voltage probe- CuSO_4 resistive divider combination. A pair of low inductance current viewing resistors were incorporated into one of the ground returns of the dummy load to measure the current.

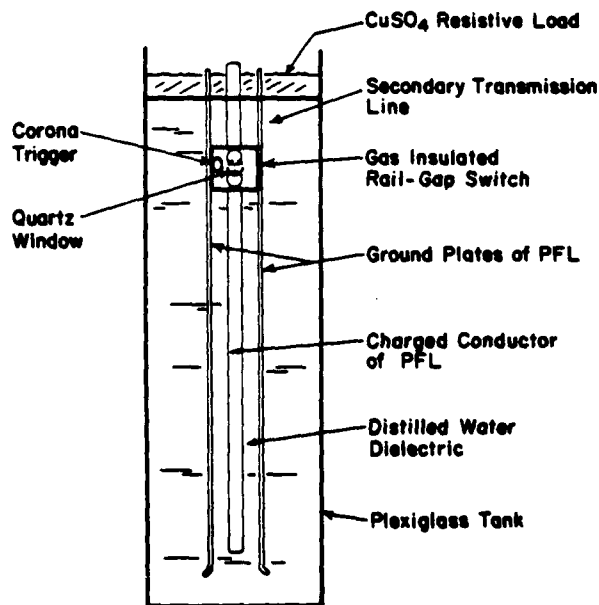


Fig. 1 Schematic of the uv-radiation triggered rail-gap test facility.

The rail-gap switch (Fig. 2) consisted of two 3 cm diameter, 50 cm active length brass electrodes which were mounted in a perspex housing at a gap separation of either 0.7 or 1.4 cm. Calculated values of the electrode field enhancement factors¹¹ are sufficiently low (1.0-1.3) for the electrodes to be considered essentially uniform field. Experiments using different electrode profiles indicated that improved switch performance resulted when the field enhancement factor of the positive polarity electrode ($f \sim 1.3$) was somewhat greater than that of the negative electrode ($f \sim 1.1$). The switch gas mix and pressure were chosen so that breakdown only occurred in the presence of the laser trigger pulse. This mode of operation ensured a low probability of switch prefire and permitted maximum energy transfer from the primary energy storage source to the PFL. The degree of switch overpressure was typically 10-30% with a somewhat narrower range for optimized multichannel breakdown. The gas mix was chosen on the following basis. Excellent multichannel switching was possible with pure Ar; however, a 50% N_2 , 50% Ar gas mix increased the breakdown voltage of the switch without substantially reducing the multichanneling. Approximately 1% SF_6 was added to this mix in order to stabilize the breakdown threshold on a shot to shot basis. For static gas fills of the switch, the performance deteriorated as a function of the number of shots. This was attributed to a depletion

of gas impurities which could undergo photoionization at the laser wavelength. A few parts per million of a gas additive (e.g. fluorobenzene) was therefore added to the gas mix to ensure a sufficient quantity of easily ionized molecules for the duration of each experiment.

The laser trigger source consisted of a 10 ns duration (FWHM) uv pulse produced by a KrF (248 nm) excimer laser. The laser utilized unstable resonator optics to permit the propagation of the laser beam ($1 \times 0.5 \text{ cm}^2$) for many metres without significantly altering the beam profile. Calibrated uv attenuators and apertures were used to vary the KrF energy and spatial distribution at the entrance to the switch.

Fig. 3 shows the time dependence of the voltage on the PFL. At a time (T) corresponding to the crest of the charging cycle the laser beam was directed through a quartz window and down the rail-gap axis to initiate multichannel breakdown.

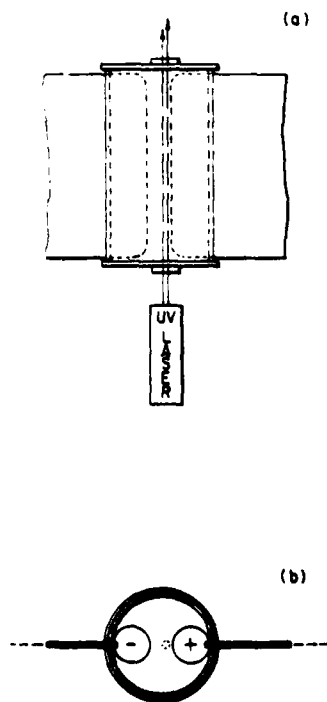


Fig. 2 Laser-triggered rail-gap switch.

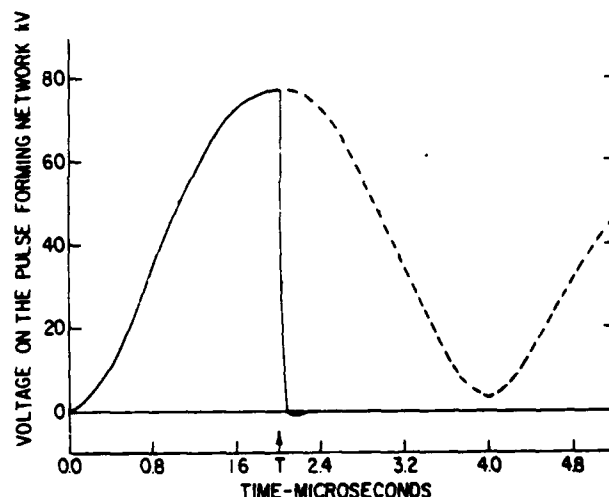


Fig. 3 Typical charging voltage on the PFL.

Results and Discussion

Laser Triggering Experiments

Fig. 4 shows the dependence of the number of visible channels in the switch as a function of the KrF energy. For KrF energies $\leq 1 \text{ mJ}$ the number of channels increases with laser energy, however for energies $\geq 1 \text{ mJ}$ the switch performance is essentially independent of the laser energy. These data indicate that reliable triggering, which is insensitive to large variations in laser energy, should be possible using even the smallest commercially available excimer lasers.

Alternatively this data also implies that an average sized (100-200 mJ) commercial KrF laser should be capable of simultaneously triggering ~10 such rail-gaps.

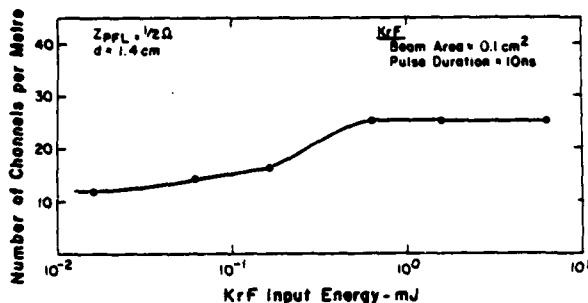


Fig. 4 Switch performance as a function of the laser energy into the switch.

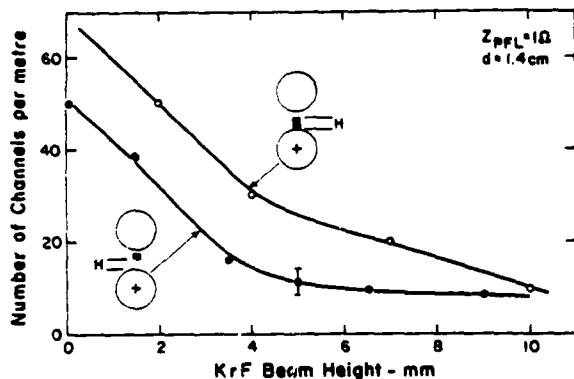


Fig. 5 Switch performance as a function of the spatial distribution of the KrF laser.

Fig. 5 illustrates one of the most important and interesting features of this triggering technique. One observes optimum multichanneling when the laser beam irradiates a narrow region ($2 \times 2 \text{ mm}^2$) close to but not necessarily touching the positive polarity electrode. When the laser beam is moved away from the positive electrode or if the aperture height is increased to permit greater irradiation of the interelectrode gap, the switch performance drops significantly. This rather dramatic observation requires further study since it may provide some fundamental information on the development of multiple arc discharges.

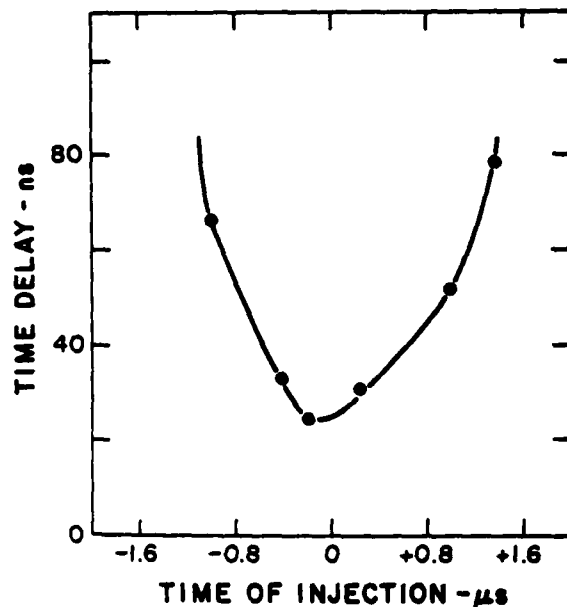


Fig. 6 Time delay as a function of the laser pulse injection time.

Fig. 6 shows the dependence of the time delay measured from the peak of the laser pulse to the start of switch breakdown (10% risetime of the current pulse in the dummy load) as a function of the time of injection of the laser pulse about the time (T) (defined in Fig. 3). The measured standard deviation jitter in the time delay (at time (T)) is only ~250 ps. Furthermore, the small variations in the time delay for rather large changes in the injection time ensure that even poor synchronization ($\pm 50 \text{ ns}$) of the laser pulse to the peak of the PFL voltage waveform can result in nanosecond jitter between the laser pulse and switch breakdown.

Table I outlines some typical performance characteristics of the laser triggered rail-gap. Two gap separations (0.7 cm and 1.4 cm) were tested over a voltage range of 30-100 kV.

Table I

Typical Performance Characteristics of the Laser Triggered Uniform Field Electrode Rail-Gap

Breakdown ^a E/P	40 kV/cm-atm
Channels/metre	50-70
dI/dt Load	$\sim 3 \times 10^{12} \text{ A/s}$
Time Delay Jitter	~250 ps
Switch Losses	~15%
% Switch Prefire	< 1%

^aObtained for a 1% SF_6 , 50% N_2 , 49% Ar gas mix.

As expected the voltage hold-off for a fixed gas pressure (1.5 atm) and standard gas mix scales linearly with the electrode separation. Experiments with the 0.7 cm gap demonstrated that the voltage hold-off also scales linearly with gas pressure in the 1.5 to 3 atm range tested.

The switch speed as measured by $(dI/dt)_L$ is presently limited by the rather high self-inductance of the rail-gap (~10 nH) and improvements in this value are anticipated with a more compact switch design. A rough estimate of the switch dissipation was obtained by comparing the stored energy on the PFL ($1/2 CV^2$) with the integrated current and voltage waveforms on the resistive dummy load. This loss amounts to ~15%.

Corona Triggering Experiments

The above results suggest that laser triggering should provide a powerful and elegant means of simultaneously triggering more than one rail-gap; however, to trigger a single rail-gap switch, it would be advantageous to avoid the complexity of requiring even a small laser. Therefore, a simple and inexpensive trigger source was sought which would be the incoherent uv radiation analogue to laser triggering. In particular the source should produce a short duration (< 10 ns) pulse of very uniform uv radiation that can be formed into a narrow beam to irradiate a positive polarity electrode. A trigger source based upon a corona discharge was designed to satisfy these requirements. Although corona triggering⁸ has recently been used to trigger a rail-gap with a jitter < 20 ns the corona triggered rail-gap

described in this paper is unique in the following ways:

- the switch electrodes are of uniform field geometry.
- the uv radiation is confined to a region near the positive polarity electrode.
- nanosecond or better jitter and high voltage hold-off switch operation is demonstrated.

Schematic diagrams of the corona trigger assembly are shown in Fig. 7. The corona discharge source was formed as a capacitive element from two ~55 cm long copper strips, which were offset from one another along their width and which sandwiched a thin (0.37 mm) sheet of mylar. A 500 pf capacitor was dc charged to 10 kV then rapidly discharged through a spark-gap to produce a fast burst (5ns FWHM) of uv radiation, originating from a glow discharge at the copper-mylar interface. The total energy stored in the 500 pf capacitor was ~25 mJ. A ~1 cm diameter glass tube with a 1 mm slot (Fig. 7 (c)) served to produce a narrow beam of uv radiation. It was determined that the beam width at the positive polarity electrode was ~3 mm.

The experiments were performed with an electrode gap separation of 1.4 cm and with a 1.5 atm pressure standard gas mix. The voltage hold-off capability of the switch was ~75 kV. Since the corona trigger assembly did not prevent the use of laser triggering it was possible to obtain a direct comparison of the two techniques on consecutive shots.

When the corona trigger assembly was first inserted into the switch but not fired it was noted that the laser triggered switch performance was poorer than that obtained without the presence of the assembly. This behaviour was believed to be the result of uncontrolled corona emission at the glass tube and/or at the copper-mylar interface which occurred during the charging cycle. Such uncontrolled emission of uv radiation

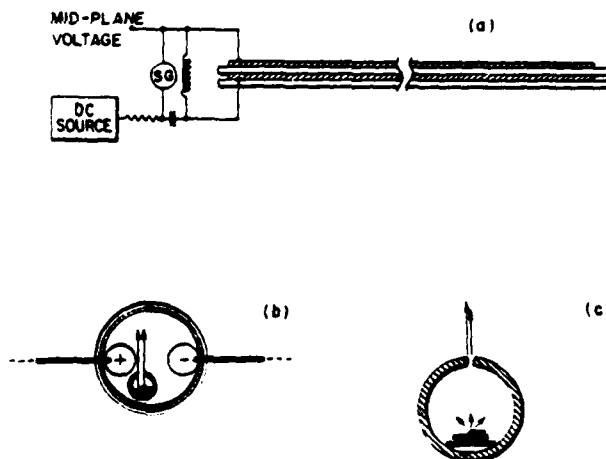


Fig. 7 Corona trigger assembly.

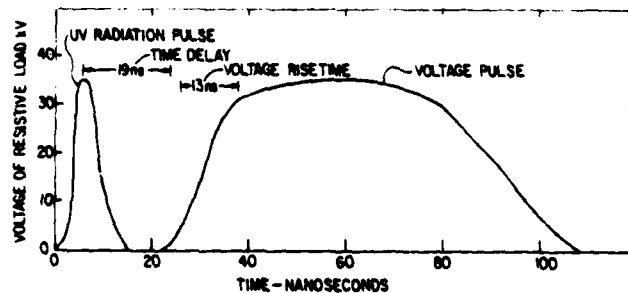


Fig. 8 Corona trigger pulse together with the voltage across a matched 1 Ω resistive dummy load for a 50 ns long PFL charged to 75 kV.

was counterproductive to good multichannel performance. The placement of the corona-trigger ensemble as far as possible away from the stressed electrode and at the same time allowing the copper electrodes to float at the mid-plane potential (Fig. 7) during the PFL charging cycle improved the laser triggering performance to a level obtained without the insertion of the corona trigger ensemble. As might be expected such steps also resulted in a significant improvement in the corona triggering performance and when the corona discharge was initiated at the crest of the charging cycle the following observations were made:

- Multichannel ($\sim 25/\text{mm}$) switch breakdown occurred only when the corona discharge fired.
- Time delays and jitters as well as the voltage (Fig. 8) and current waveforms measured on the resistive load were similar to that obtained with laser triggering.

However the number of channels as well as the operating gas pressure range were lower than that observed with laser triggering. Provided one can make an analogy between laser and corona triggering then the data shown in Fig. 4 implies that the reduced performance is probably the result of insufficient uv illumination. Supporting evidence for this conclusion was obtained from an experiment in which the glass tube slot width (Fig. 7) was reduced from 1.0 to 0.5 mm. According to the data shown in Fig. 5 a narrower uv beam should improve the switch performance; however, the number of channels actually decreased consistent with the insufficient uv radiation hypothesis. Since the present corona trigger design is far from being optimized it should be a relatively straightforward matter to increase the intensity of the source and improve the switch multichanneling.

Conclusions

The technique of laser triggering has been used to initiate multichannel, sub-nanosecond jitter breakdown in a rail-gap consisting of two uniform field electrodes. Similar switch performance was demonstrated using a simple and inexpensive triggering mechanism based upon incoherent uv radiation generated in a corona discharge. The key experimental considerations which when taken together, permitted such successful triggering were:

- the use of an overpressured mode of switch operation, which prevented breakdown in the absence of a trigger pulse.
- the use of a short duration pulse of spatially uniform uv radiation timed to occur at or near the crest of the PFL voltage.
- the use of a 1% SF_6 , 50% N_2 , 49% Ar gas mix, which promoted multichannel operation.
- the control of the uv illumination to a region near the positive polarity electrode.

The low values for the switch jitter and the relative ease in producing multiple laser beams makes laser triggering an attractive technique for simultaneously triggering many rail-gaps. On the other hand, the simplicity of a corona triggering approach makes it useful for triggering individual rail-gaps. Both approaches incorporate uniform field electrodes, a feature which should be conducive to long switch lifetime. Furthermore since both trigger mechanisms are capable of high repetition rates, the uv radiation triggered rail-gap switch is a possible candidate for high average power switching applications.

References

1. H.M. von Bergmann, J. Phys. E, Sci. Instrum., Vol. 15, pp. 243-247, 1982.
2. D.L. Birx, E.J. Lauer, L.L. Reginato, D. Rogers Jr., M.W. Smith, T. Zimmerman, 3rd IEEE International Pulsed Power Conference, Albuquerque, N.M., pp. 262-268, 1981.
3. Maxwell Scientific Laboratories, San Diego, Ca., private communication.
4. G.R. Neil and R.S. Post, Rev. Sci. Instrum., Vol. 49, pp. 401-403, 1978.
5. H. Meuth, S.O. Knox, E. Sevillano and F.L. Ribe, 3rd IEEE International Pulsed Power Conference, Albuquerque, N.M., pp. 35-38, 1981.
6. R.S. Taylor, A.J. Alcock and K.E. Leopold, 3rd IEEE International Pulsed Power Conference, Albuquerque, N.M., pp. 157-160, 1981.
7. R.S. Taylor, A.J. Alcock and K.E. Leopold, 14th Pulse Power Modulator Symposium, June 3-5, Orlando, Fla., pp. 32-37, 1980.
8. D.B. Cohn, W.H. Long, Jr., E.A. Stappaerts, M.J. Plummer and J.B. West, Rev. Sci. Instrum., Vol. 53, pp. 253-255, 1982.
9. S. Watanabe, A.J. Alcock, K.E. Leopold and R.S. Taylor, Appl. Phys. Lett., Vol. 38, pp. 3-6, 1981.
10. J.I. Levatter, K.L. Robertson and S.C. Lin, Appl. Phys. Lett., Vol. 39, pp. 297-299, 1981.
11. H. Watson, IEEE Transactions on Plasma Science, Vol. PS-8, pp. 154-159, 1980.

FUNDAMENTAL PROCESSES IN HYDROGEN THYRATRONS

Shekhar Guha, Joseph Kunc, Howard Cole, and M.A. Gundersen

Departments of Electrical Engineering and Physics
SSC 420
University of Southern California
Los Angeles, CA 90007

Abstract

The results of a study of electron excitation processes in hydrogen thyratrons are reported. Using spectroscopic methods with extremely good spatial and temporal resolution the electron energy and density in the device during its normal operation are measured. These data are applied to study the molecular excitation processes in the device. A theory of thyatron operation based on these fundamental mechanisms is being developed to describe the steady-state phase.

Electron densities above 10^{13} cm^{-3} were measured from Stark broadening of hydrogen Balmer emission. Current density and arcing as a function of electron density were observed. Average electron energies in the grid-anode and grid-cathode regions during the steady-state conduction phase were observed to be uniform. Evidence is presented suggesting lower values for average electron energies than previously reported, and mechanisms for this are discussed. Data is presented pertaining to the relative roles of single and multi-step excitation processes.

Introduction

To develop a switch with more desirable characteristics, including higher repetition rate, pulsed current, rate of rise of current and stand-off voltage, a deeper understanding of the nature of the fundamental processes taking place in the discharge medium is needed. Although the physics of the thyatron has been studied,⁽¹⁻³⁾ important processes taking place in the discharge medium, such as those involving the excited atomic and molecular species, details of energy transfer processes involving excited species, the electron energy distribution function, and the roles of excited molecular and atomic species in the formation of atomic and molecular ions are generally not understood.

The hydrogen thyatron is characterized by several features. The pressure of the gas in a hydrogen thyatron is usually maintained around 500 microns ($\sim 2 \times 10^{-6} \text{ cm}^{-3}$). The grid anode spacing is usually small so that

the tube operates essentially on the low p-d or left-hand side of the hydrogen Paschen curve. The small grid-anode spacing is thus used to achieve higher stand off voltage, and this also reduces the recovery time.

This paper reports a spectroscopic study of emission from commercially available glass enclosed hydrogen thyratrons, and includes observation of the formation of various excited atomic and molecular species. Electron densities during conduction were measured from Stark-broadened Balmer linewidths.⁽⁴⁻⁶⁾ Average electron energy have been measured and studied.^(7,8) Temporally resolved studies of the breakdown of the different regions of the thyatron tube (the grid-cathode region and the grid-anode region) as a function of applied voltage.⁽⁷⁾

Experiment

Fluorescence data were obtained from hydrogen thyratrons (ITT 5C22 and ITT Kuthe 5949) at variable repetition rates. Fluorescence was collected by a lens ($f=7.5 \text{ cm}$), and focused on to the slit of a 3/4 meter spectrometer (Spex 1400) by a second lens ($f=15 \text{ cm}$). The experimental arrangement of spectroscopic studies is similar to that described in reference 6. The light intensity is measured by a photomultiplier (RCA C31034) which is thermoelectrically cooled to -30°C to reduce dark noise to a few pico-amperes. The photomultiplier output was fed into a fast transient digitizer (Tektronix 7912AD) for time resolved detection or into a electrometer (Keithley 610 BR) when measuring time averaged intensities. A movable aperture placed in front of the tube was used to select the spatial region from which light is collected. The current in the tubes was varied from about 10 amperes to greater than 500 amperes and was monitored using a wide band pulse current transformer (Pearson Electronics). Other data were obtained using standard methods as indicated.

Discussion

In order to investigate the possibility that an atomic or molecular species plays a role in recovery the

time delay between the application of a voltage pulse to the grid of the tube and breakdown in grid cathode space was measured as a function of time between pulses. This was done both in the presence and in the absence of an applied anode voltage. It was observed that for a given anode voltage, the anode region breakdown is delayed relative to the breakdown of the grid region. The time delay is seen to decrease with increasing repetition rate. At a given repetition rate, the delay also decreases with increasing grid voltage. The normal operation of the 5949 tube was limited to a pulse repetition rate of about 100 Hz with the anode voltage at its highest allowed value (20 kV). In the absence of the anode voltage, (for observation in the grid cathode region) the frequency could be increased to 5 kHz, above which the behavior of the tube becomes erratic. By comparing these data with hydrogen Balmer emission intensity, it was observed that the ratios of the intensities of the various Balmer lines remain constant throughout the conduction period, suggesting a near-equilibrium condition exists for the electron energy distribution function during the steady state phase.

In hydrogen the region of negative glow is a pale bluish color whereas the positive column is pink. Under normal operation only the region very near the thyratron cathode has the characteristic blue color of the negative glow. In the remaining part of the tube, both in the anode-grid and in the grid-baffle-grid region, the discharge is pink in color, indicating that the positive column, e.g. the region of electrical neutrality, extends on both sides of the grid. This observation suggests that the cathode double sheath is ordinarily not in the vicinity of the grid. A double sheath in the anode region was not observed under normal operation. The measurement of the ratio of the intensities of three Balmer lines from the different regions of the tube during the conduction period also supports this conclusion. The spectral broadening of the Balmer line at 4861 Å at three different currents was also measured. The instrumental and Balmer line profiles were assumed to be Lorentzian in shape and the actual value of the Balmer linewidth was obtained by subtracting the instrumental linewidth from the measured width of the line.

Bekefi⁽⁴⁾ has plotted the variation of the electron densities in a plasma as a function of the Stark broadened Balmer linewidths, from which we obtain the electron densities in our thyratrons at different currents. The electron density thus obtained ranges in value from $3 \times 10^{13} \text{ cm}^{-3}$ to $2 \times 10^{14} \text{ cm}^{-3}$.

At high repetition rates the behavior of the tube becomes erratic, and the tube starts arcing, characterized by a sharp increase of the current at localized spots inside the tube. The color of the discharge during the arc was the same as that of the positive column of the glow discharge. The transient nature of the arc prevented the measurement of the electron density during the arc by measurement of Stark broadened linewidth, but it may be anticipated that it is considerably higher.⁽⁵⁾ A molecular emission spectrum obtained during the discharge, showing the formation of excited metastable C^3_u state is shown in figure 2 of reference 6.

In reference 1 the decay of the plasma by ambipolar diffusion to the walls and electrodes and subsequent recombination has been considered, and time constants for these processes estimated. The repetition rate limitations at high current suggest that other mechanisms also contribute to the decay of conductivity. From time resolved Balmer emission⁽⁷⁾ it may be noted that the upper Balmer state takes several hundreds of nanoseconds to decay, although the radiative lifetime is much less. The observation of the atomic and molecular spectra suggest that the creation of the excited species during conduction is important, and that the role of the long lived excited neutrals in increasing the decay time of the plasma is therefore worth investigating. The excited molecular states are the chief source of negative ion production,^(7,8) and the negative ions affect the plasma conductivity as well as provide a source of free electrons on decaying.

Processes Affecting the Electron Energy Distribution Function

The degree of ionization is relatively large, and for electron average energies of order 1 eV, the e-e collision frequency will be larger than

all other elastic and inelastic collisional frequencies.⁽⁸⁾ The amount of energy transferred during e-e collisions (energy loss factor) is on average much larger than for electron-heavy particle collisions. This suggests that the electron distribution function will be near Maxwellian if the influence of inelastic collisions and the plasma field is small.

The inelastic electron-neutral (e-n) processes that have considerable cross sections in the energy range mentioned above are rotational and vibrational excitation of the hydrogen molecule by electron impact. The rotational excitation energy thresholds are the order 0.01 eV and the appropriate threshold for vibrational excitation is 0.52 eV. The threshold energies for other inelastic processes are much larger. The appropriate cross sections for these inelastic processes are of the order of 10^{-16} cm² and thus remarkably lower than those for elastic e-e and e-n collisions at the impact energy of the order of 1 eV. However, rotational and vibrational excitation of molecular hydrogen can produce a large departure of the electron distribution tail from its Maxwellian form in weakly-ionized plasmas ($X < 10^{-4}$), but does not cause significant deformation of the lower energy range form of the distribution function.⁽³⁾ For the plasma considered here ($X \sim 10^{-2}$), e-e collisions will largely neutralize the influence of inelastic collisions, causing a tendency of the electron distribution to be Maxwellian over most of the energy range. In addition, the electron thermalization time is more than two orders of magnitude lower than the time of the entire discharge.

An additional factor that can cause a significant deviation of the electron distribution function from a Maxwellian form is a strong plasma field. The measurements cited above suggest that the electric field during the steady-state stage of the discharge is of the order of 10 V cm⁻¹ whereas the electron temperature is of the order of 1 eV. Assuming these values, the critical plasma field is about one order of magnitude smaller.⁽⁸⁾ This indicates that the plasma field is not strong and that the influence of collisions on the plasma behavior should be more important than the electric field. Summarizing the above discussion, inelastic

collisions such as rotational and vibrational molecular hydrogen excitation should not produce a significant departure of the electron distribution function from a Maxwellian form. Thus, the assumption of Maxwell distribution function for estimation of electron temperature and drift velocity from plasma transport equations seems to be appropriate. However, it should be remembered that this assumption should be used very carefully for the estimation of rates with large threshold energies (for example, electronic excitation or ionization).

It is noteworthy that the two inelastic processes (rotational and vibrational excitation) the vibrational excitation seems to be more important than the rotational excitations, despite the fact that the latter has a much lower threshold than the former, and both have comparable values of maximum cross sections. This results from the fact that for temperatures of the neutral normal hydrogen being equal to about 800°K the population of the first five rotational levels are of the same order, and the cross sections for processes of the first and second kind differ little in absolute value. This is very different in the case of vibrational excitation, because the population of the first vibrationally excited level is about two orders of magnitude lower than the population of the ground state and the appropriate first and second kind process rates differ significantly from each other. The maxima of the 0-1 energies of about 3.5 eV which also supports neglecting the influence of the inelastic collisions in the estimation of the electron temperature and drift velocity in our range of electron energy. However, the average contribution of the inelastic processes is taken into account by using the "effective" energy loss factor instead of the elastic collision loss factor.

Summary and Conclusion

The atomic and molecular emission from the different regions in glass enclosed hydrogen thyratron tubes have been studied spectroscopically. The formation of excited atomic and molecular species have been observed and various mechanisms which contribute to long lived ionization processes have been discussed. The average electron

energy during the conduction phase is estimated to be about 0.5 eV, and the average electron density to be ~ 10 cm/sec. The temporal behavior of the Balmer emission intensities show that even several hundred of nanoseconds after the end of the current pulse, the Balmer transitions are taking place. Because of the lifetime of the Balmer emission is only ~ 20 nsec, this demonstrates that excited atomic levels are being formed after the conduction phase. The mechanism for the formation of these excited states is possibly through the long lived excited metastable molecular states.

The purpose of this work is to provide deeper insight into thyatron operation and behavior, through an investigation of basic physics. This work is continuing, and a more clear as well as thorough-going review will be published as the research is developed further.

The research to date strongly suggests that a much clearer "picture" will be obtained. In addition, preliminary studies of other gases in thyatrons have been conducted and will be available.

References

1. S. Goldberg and J. Rothstein, "Hydrogen thyatrons," *Adv. Electronics & Electron Phys.* **14**, 207-264 (1961).
2. S. Goldberg, Hydrogen Thyatrons, vols. I (1953), II (1956), and III (1957) with D.F. Riley.
3. D. Turnquist et al., "New Hydrogen Thyatrons for Advanced High Power Switching," *IEEE Trans. Plasma Sci* **PS-8**, 185 (1980).
4. G. Bekefi, C. Deutsch, and B. Yaakobi, "Spectroscopic Diagnostics of Laser Plasmas," in Principles of Laser Plasmas, ed. G. Bekefi (Wiley, 1976), p. 549-669.
5. S.K. Dhali, P.F. Williams, R.J. Crumley, and M.A. Gundersen, "Electron Densities in Laser-triggered Hydrogen Sparks," *IEEE Trans. Plasma Sci* **PS-8**, 164 (1980).
6. M. Gundersen and S. Guha, "Formation of Metastable Species in Hydrogen Thyatrons," *J. Appl. Phys.* **53**, 1190 (1982).
7. S. Guha, H. Cole, and M.A. Gundersen, to appear in *IEEE Trans. Plasma Sci.*
8. J. Kunc and M. Gundersen, to appear in *IEEE Trans. Plasma Sci.*

A HIGH POWER, TRIPLE GRID THYRATRON AND ITS TEST CIRCUIT

H. Menown & B. Newton
English Electric Valve Co. Ltd.,
Chelmsford, Essex, U.K.

R. F. Lambiase *
AGS, Brookhaven National Laboratory,
Long Island, New York, USA

Abstract

As part of the polarised proton experiment on the AGS at Brookhaven National Laboratory, a requirement has arisen for a special thyatron device to switch the pulsed quadrupole magnets.

The magnet drive-current waveform consists of a series of triangular pulses of alternate polarity, with amplitude increasing from 400A in the first pulse, to 2.7kA in the last pulse. Pulse rise-time is $2\mu\text{s}$ with a linear fall to a base line of about 3ms. Over 3.5 Coulombs are switched in the largest pulse. The pulse series is repeated every 2.5 seconds leading to an average switch current approaching 4A.

EEV has designed a special thyatron to switch this circuit, and built a suitable test station.

Introduction

One of the projects in progress at the Brookhaven National Laboratory on Long Island, New York, uses the Alternating Gradient Synchrotron to accelerate polarised protons to an energy of about 26 GeV. This work is being carried out in conjunction with Associated Universities, Inc.

To maintain a high percentage of polarisation during the acceleration cycle it is necessary to pass as quickly as possible through the intrinsic resonances caused by the horizontal components of the alternating gradient fields of the AGS. Twelve pulsed quadrupoles will be used to jump these intrinsic resonances (1)

The eight pulses required to energise these quadrupoles are of triangular form and alternating polarity with amplitudes rising from 400A to 2.7kA. A burst of pulses is generated once every 2.5 seconds. Figure 1 shows this pulse sequence. The circuit devised at Brookhaven National Laboratory for producing the alternating polarity pulses is shown in Figure 2. It consists of two similar sub-circuits feeding current into the

quadrupole.

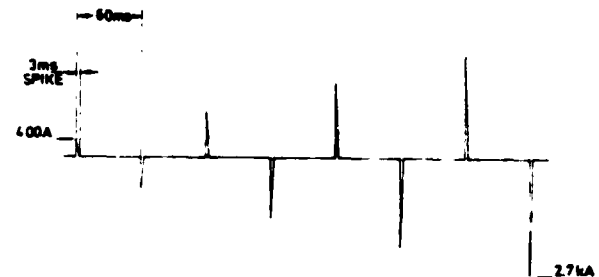


Fig. 1. Current Pulse Burst for Quadrupole.

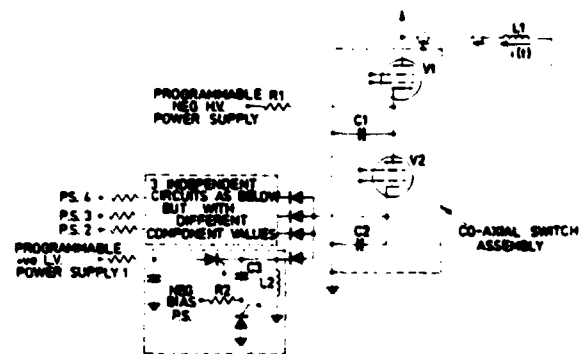
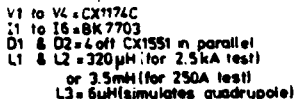


Fig. 2. Mirror Image Supply for Supplying Opposite Polarity Pulses.

Circuit Analysis and Experimental Procedure

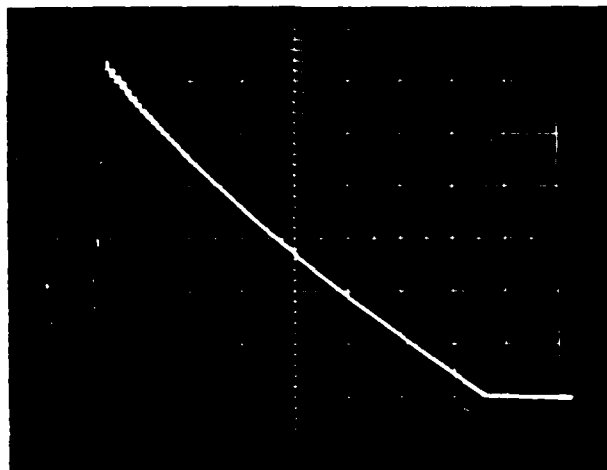
For test purposes EEV has built a simplified version of this circuit which produces six pulses of equal amplitude, three positive interlaced with three negative, into a 6uH inductor which simulates the quadrupole (Figure 3).



Each positive 2.5kA pulse is generated as follows:-

- so that the overall current waveform in L3 is triangular with an amplitude of 2.5kA.

Figure 4 shows an oscillogram of the pulse this circuit produces. Both thyratrons in each half of these circuits conduct throughout the duration of the pulse they switch so that at the maximum level the charge conducted per pulse is approximately 4.0 Coulombs. The average current at the burst rate of 3 pulses every 2.5secs is thus 4.8A, somewhat higher than the 3.9A average current expected in service in the Brookhaven modulators.



To produce the fast current rise into the 6uH inductor load a voltage of 17kV is required on each 0.25uF capacitor before the first thyatron switch is triggered. At the moment of switching this voltage rises across the load in less than 100nsec and it is also applied across the adjacent thyatron in the opposite sub-circuit as a positive voltage step between anode and cathode. To meet these rigorous requirements a triple grid tube has been developed at EEV (CX1174C). The screen grid is not connected internally

to the cathode but brought out to a separate connection so providing the design engineer a whole range of modes of use in a variety of pulse circuits. In pulse modulator service with pulse widths of no more than 10 μ sec it is possible to connect the screen direct to the cathode. With longer pulses this is not recommended.

Ideally the screen should be connected to the cathode using a high value resistor (typically 1k Ω) which limits the current flow to a few milliamps. It is necessary to bypass this resistor with a low inductance capacitor which acts as a short circuit to the fast transients. In practice a low inductance resistor of about 3 ohms has been used. This limits the screen current to acceptable levels and still allows sufficient isolation by the screen grid.

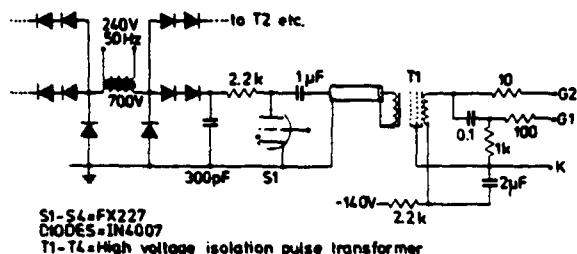


Fig. 5. CX1174C Trigger Circuit

The trigger circuitry for each CX1174C is shown in Figure 5. A high voltage isolation pulse transformer is necessary because none of the thyatron cathodes is connected to ground. The design of the transformer for V3 needed most care because it is subjected to the 17kV fast transient whenever V2 fires. This causes a pulse of capacitive current between the primary and secondary electrostatic screens and the connections to the latter must ensure that this current flow does not couple to the ferrite core and thereby cause sufficient output on the secondary winding to trigger V3. To keep leakage reactances small, the numbers of turns on the windings were held to a minimum consistent with effective triggering. The final design has 14 turns on both primary and secondary and has a ferrite core with no intentional air-gap. This core saturates about 1.5 μ sec after the start of the pulse and is reset in the interpulse period by the current flowing in the primary during recharge of the 1 μ F energy storage capacitor.

The two triggering grids of the CX1174C are driven simultaneously via the circuitry shown. This results in an anode delay time which is typically 0.12 μ sec at 15kV anode voltage and which only increases by about 0.02 μ sec as the anode voltage is reduced to 750V. Jitter is less than 5nsec and drift is typically 10nsec.

Tests on the new tubes show that they are capable of switching the 2.5kA, 3.6msec triangular pulses. Using one half of the test circuit two thyratrons have run for 200,000 pulses.

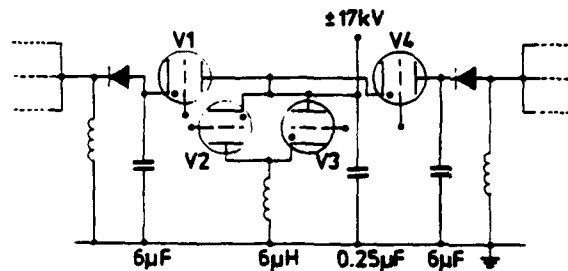


Fig. 6. Alternative Test Circuit.

To meet other requirements, figure 6 shows an alternative circuit which now has only one 0.25 μ F capacitor. This forms part of both the positive and negative fast front generators and has to be charged to positive and negative potentials alternately. Similarly, instead of two separate high voltage power supplies only one is needed but it must be capable of delivering positive or negative outputs on demand. The two thyratrons V2 and V3 are now connected in inverse parallel and the effect of triggering either of them is simply to collapse the voltage across all the other thyratrons.

At EEV the time between successive pulses in the burst is set at 50msec because this is an odd number of half-cycles of the power supply frequency of 50Hz. This allows the trigger generators and all capacitor charging power supplies to be phase locked to the power source whose half cycle time of 10msec is also used in the system clock pulse interval. This considerably simplifies the overall system design. The proposed alternating polarity supply for the 0.25 μ F capacitor is shown in figure 7. It uses a pair

of diode-pump circuits whose output diodes are triggered CX1551 thyratrons. In these tubes the grid 1 is connected to a positive dc pre-ionising supply and the grid 2 is negatively biased to keep the tube in a non-conducting state. At the correct time in the system cycle the required tube is made conductive by an optically coupled system which connects the grid 2 to the grid 1 pre-ionising supply.

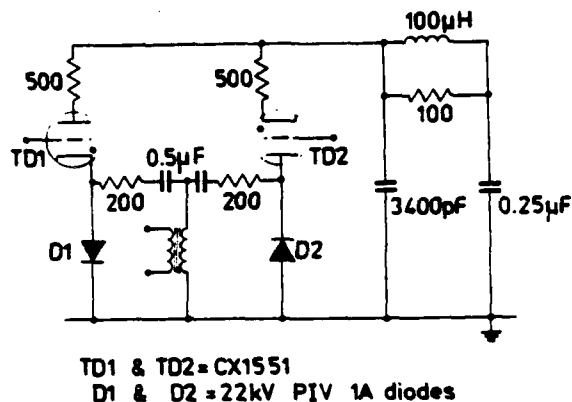


Fig. 7. Alternating Polarity Power Supply.

Conclusion

We have developed the CX1174C triple-grid thyatron for operation in circumstances in which a conventional double grid thyatron has proved to be unsuitable. The circuit which necessitated the development of this new thyatron and which has been used to test it simulates a circuit to be used at Brookhaven National Laboratory to produce polarised proton beams.

References

1. Acceleration of Polarised Protons in the Brookhaven AGS. IEEE Transactions on Nuclear Science, Vol. NS-28 No. 3, June 1981 pp 2031-2033.

Acknowledgements

The Authors wish to thank the Directors of the English Electric Valve Co Ltd for permission to publish this paper.

* Work performed under the auspices of the U.S. Department of Energy.

INSTANT-START CATHODES FOR HIGH AVERAGE POWER
HYDROGEN THYRATRONS

S. Friedman

EG&G Inc., Salem, MA 01970

R. Petr

Math Sciences Northwest, Inc., Bellevue, WA 98004

J. McGowan and J. O'Connell

ERADCOM, Ft. Monmouth, NJ 07703

Abstract

A dispenser-type cathode has been used in a high average power hydrogen thyatron. The tube successfully cold-starts and runs at an average power of 600 KW in 1-second bursts. It has also cold-started and run CW at an average power of 50 KW.

The maximum average power attainable with this tube has not yet been determined, but is expected to be around 1 MW in 120-second bursts.

The cathode consists of a large number of vertical plates of barium aluminate impregnated tungsten, and is 4.5 inches in diameter had has a total emitting area of 600 cm².

Auxiliary cathode heater power was required only for initial activation. As the thyatron was aged, the cathode heater voltage was reduced gradually to zero. Thereafter, the tube could be restarted with no cathode heater power, even after being off for 48 hours. (The hydrogen reservoir is of the standard titanium hydride type, and requires auxiliary heater power for operation.)

In addition to their instant-start capability, dispenser cathodes can sustain several times the current density of oxide-coated cathodes without arcing. When arcing finally occurs, it does not destroy the dispenser material. It is therefore possible to construct compact, ultra-low inductance, high current cathodes that can sustain severe overloads for extended periods. Such cathodes are presently being developed for 2-, 3-, and 4.5-inch diameter thyatrions.

Introduction

Most hydrogen thyatrions utilize thermionic oxide-coated cathodes. These cathodes need to be operated at temperatures above 800°C, and they arc at current densities exceeding 10 to 30 amperes/cm². The resulting auxiliary heater power and surface area requirements become onerous when high peak currents are desired. For example, the EG&G megawatt average power HY-7 thyatron (40 KA peak current) requires over 1 KW of cathode heater power. The cathode takes up almost one-third of the tube volume, and is responsible for much of its inductance (Figure 1). In addition, the cathode warmup time is almost 20 minutes.

Clearly significant incentives exist for developing a compact cathode that can operate without auxiliary heater power. We have been investigating the use of dispenser-type cathodes for this purpose. Such cathodes have been used in thyatrions by British and Russian workers, and emission current densities of 30 amperes/cm² have been obtained from these cathodes in high-voltage electron guns at Avco-Everett. (1,2,3) However, in all these applications the cathodes were externally heated to thermionic temperatures.

Dispenser cathodes are made from a porous tungsten matrix filled with barium aluminate, and sometimes calcium oxide as well. Emission results from the chemical formation of free barium at elevated temperatures (800 to 1200°C). The barium migrates to the

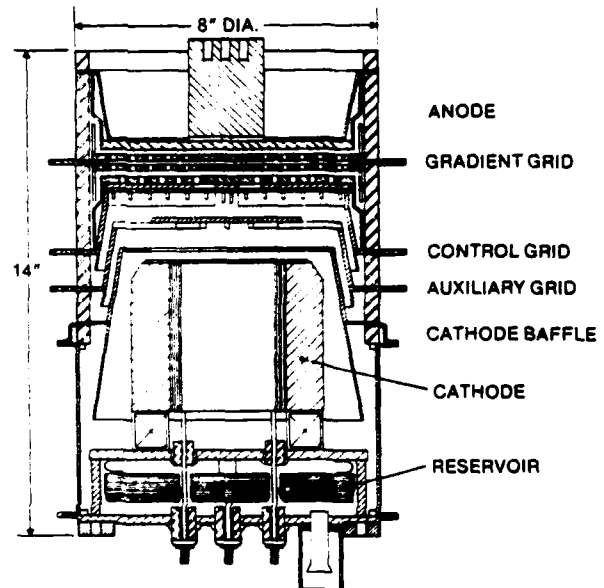


Figure 1. HY-7 Megawatt-Average-Power Thyatron.

surface and forms a monolayer which substantially lowers the surface resistance of the cathode. (4) This monolayer enables the initiation of a thyatron discharge even after the cathode returns to room temperature. Furthermore, the low surface resistance (around 0.1 ohm-cm²) permits substantial current densities to be sustained without arcing, thus allowing high peak currents from relatively compact cathodes. We typically obtain up to 80 to 100 amperes/cm² at room temperature, and over 200 amperes/cm² at a few hundred degrees Centigrade without arcing. By contrast, oxide-coated cathodes have a surface resistance of 2 to 10 ohm-cm² at room temperature, and arc on almost every shot.

An additional advantage of dispenser cathodes is that, unlike oxide-coated cathodes, they are not degraded or significantly damaged by accidental arcing.

In 1979, EG&G developed 2-inch diameter dispenser cathode thyatrions which started repeatedly at room temperature, and could be run continuously with no cathode heater power other than that supplied by the discharge itself (Figure 2). These tubes operated at 20 KV, 500 A peak current and 10 KW DC average power. Their operating characteristics (including anode delay, jitter, and life) were comparable to those of conventional 2-inch diameter thyatrions. The dispenser

cathode tubes relied on power from the discharge to keep the bulk cathode temperature high enough to maintain activation (that is, the generation of free barium); hence the term "plasma-heated thyatron."⁽⁵⁾

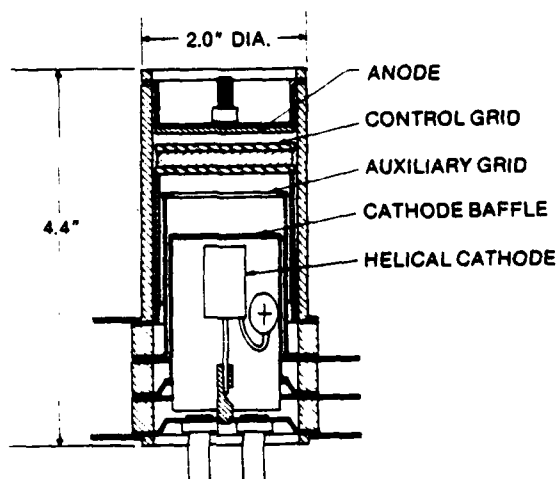


Figure 2. 10 KW Average Power Dispenser Cathode Thyatron. The cathode was a helical coil of dispenser material.

Subsequent experiments showed that cold-start capability and significant life could be achieved without having to maintain high bulk cathode temperatures. For example, the "arch-cathode" tube of Figure 3 repeatedly cold-started and operated for several hundred hours even though temperature measurements (made by measuring the volume resistance of the cathode) showed that the bulk cathode temperature during CW operation never exceeded 400°C. Excellent performance was also obtained well below activation temperatures with a 3-inch diameter thyatron using the "plate-cathode" shown in Figure 4; the operating characteristics of this tube are compared with those of its oxide-cathode counterpart in Table 1.

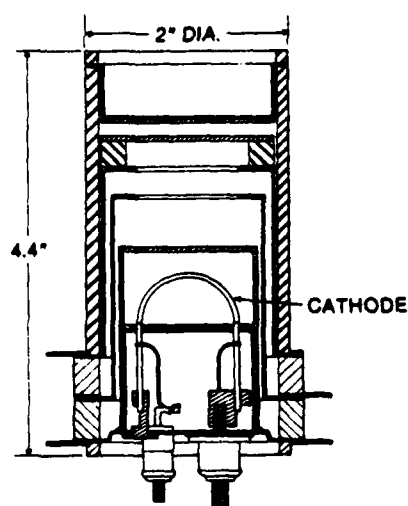


Figure 3. "Arch-Cathode" Thyatron.

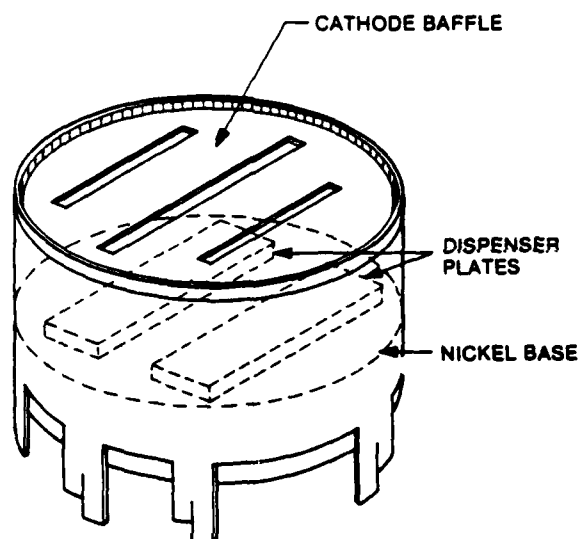


Figure 4. "Plate-Cathode" for 3-Inch Diameter Thyatrons. The plates are 1 inch x 0.5 inch x 0.1 inch, and are copper brazed to a nickel base. The cathode baffle acts as a heat shield, and blocks evaporating nickel and barium.

Table 1. Comparison of 3-Inch Diameter Dispenser and Oxide-Coated Cathode Thyatrons.

Characteristics	Oxide Cathode	Dispenser Cathode
Cathode Heater Power	100 W	Zero
Hydrogen Pressure	450 μ	450 μ
Anode Voltage	25-30 KV	30 KV
Peak Current	1.5-2 KA	1.5 KA
DC Average Current	1.5-2 ADC	2 ADC
Keep-Alive Current	50-200 mA	50 mA
Jitter	2 ns	2 ns
Anode Delay Time	50-100 ns	40 ns

The ability of dispenser cathodes to operate for long periods at relatively low bulk temperatures (surface temperatures may still be high, as discussed below) is significant because it greatly reduces the constraints on cathode design and thyatron operation that high temperature operation would otherwise have imposed.

Meanwhile, scaling of the peak current arc limit with cathode area was confirmed by testing a tube having an 80-cm² dispenser cathode. This cathode consisted of a large number of arch-shaped pieces (Figure 2), and had an order of magnitude larger area than any previous dispenser cathode. Data obtained with this tube established 80 to 100 amperes/cm² as a good working value for the low temperature arc limit current density, independent of cathode size, geometry, and peak current.

With the above results in hand, a cold-start version of the 8-inch diameter HY-7 megawatt average power thyatron was constructed. This tube, designated HY-7312, is described in detail in the next section. Test results follow.

Next, the physical mechanism responsible for the high emission current densities obtained with dispenser cathodes in thyatrons is discussed. Implications of this mechanism for thyatron operation will also be discussed.

We then conclude with a description of our plans for future devices in which dispenser-type cathodes can be used to advantage.

Dispenser Cathode Megawatt Average Power Thyatron

The dispenser cathode megawatt average power thyatron is designed to operate at 40 KV peak anode voltage, 40 KA peak current, 120 Hz pulse repetition rate, and 10 μ s pulse width in 2-minute bursts. The envelope is a compact, lightweight version of the HY-7; its dimensions are compared with the HY-7 in Figure 5.

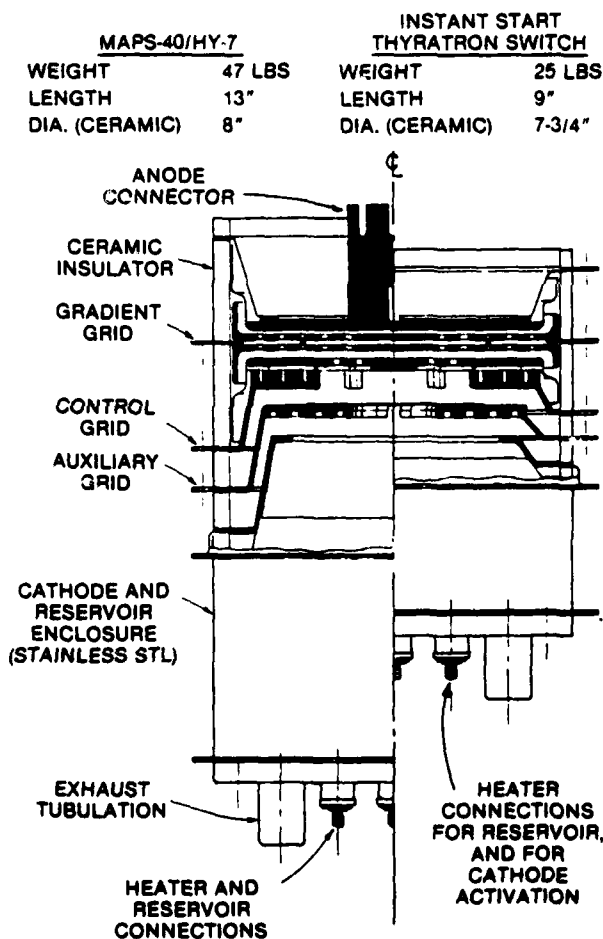


Figure 5. Comparison of HY-7 and HY-7312 Thyatrons.

The HY-7312 cathode (Figure 6) consists of a large number of vertical plates copper brazed to a 4.5-inch diameter nickel base. The plates are made from a pressed and sintered mixture of tungsten powder, barium aluminate, and nickel. Such a mixture is commonly used in cathodes for EG&G flashtubes. Barium is released by the reaction

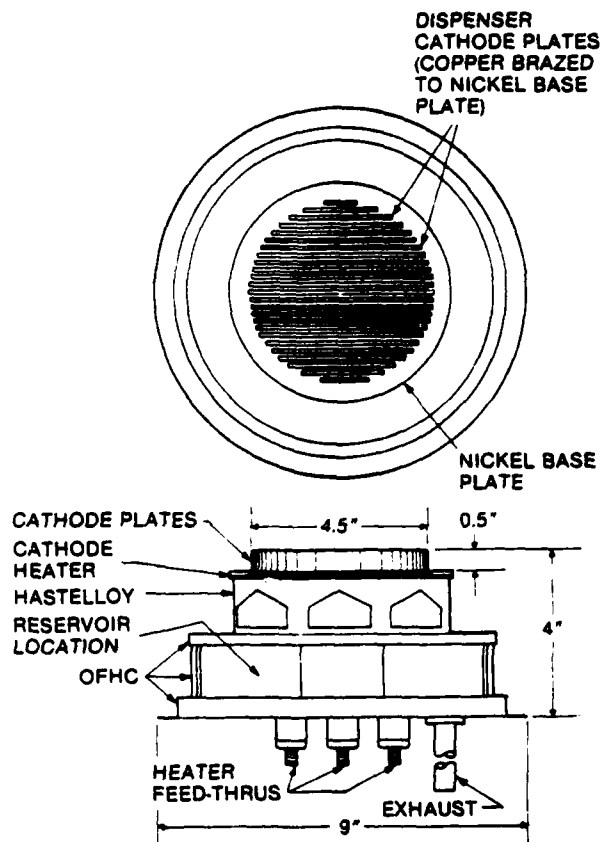


Figure 6. HY-7312 Megawatt-Average-Power Dispenser Cathode.

Nickel constitutes about 1% of the mix by weight, and serves as the binder in the sintering process, thus permitting sintering to be carried out well below the sintering point of tungsten, where the barium aluminate would boil off.

The cathode plates are 0.5 inch high x 0.1 inch thick, giving a total emitting area of 600 cm². A peak current of 40 KA therefore corresponds to a conservative 67 amperes/cm².

Heat for the cathode is supplied primarily by the passage of RMS electron current, I_p , through specific resistance, R_0 . The power contributed is $I_p^2 R_0/a$, where "a" is the cathode surface area. Using HY-7 ratings (Table 2), $I_p^2 = (40 \text{ KA})^2 \times 125 \text{ Hz} \times 10^{-5} \text{ sec}$. R_0 is less than the room temperature value 0.1 ohm-cm². Using these values gives an upper value of 330 watts.

Some additional power is supplied by plasma ions accelerated through the cathode sheath. From Langmuir⁽⁶⁾, the average space-charge limited ion current is approximately 1/60 the average electron current (1/60 being the square root of the electron/deuterium mass ratio). Since the average electron current is 40

amperes, the ion current is 0.67 ampere. Multiplying by a typical thyatron cathode sheath drop of 20 volts gives only 13 watts. This is probably an underestimate, because the grid-cathode voltage drop in dispenser cathode thyatrons is larger than in conventional thyatrons by 50 to 100 volts. However, even if all the additional voltage is attributed to the sheath, the ion bombardment power is still on the order of only 100 watts.

The power contributed by volume resistive heating of the cathode is negligible due to the large cross-sectional area and short length of the cathode.

Thus, the total discharge power going to heat the HY-7312 cathode is at most about 400 watts, as compared to the more than 1 KW of auxiliary heater power used in the oxide cathode HY-7. Since the HY-7 cathode operates near 800°C, the HY-7312 cathode must be substantially cooler and, therefore, far below activation temperatures. Despite this, startup and operation of the HY-7312 with no auxiliary cathode heater power has been achieved as expected, as described in the next section.

Operating Characteristics of the HY-7312 Dispenser Cathode, Megawatt Average Power Thyatron

The HY-7312 has been operated CW at EG&G, and in burst mode at ERADCOM, under the conditions listed in Table 2. Thus far, the average power attainable has been limited by the test apparatus, and not by the HY-7312. This average power has been 50 KW CW, and up to 600 KW in 1-second bursts.

Table 2. Operating Characteristics of HY-7312 Dispenser Cathode Megawatt-Average-Power Thyatron.

Characteristics	HY-7	HY-7312 (to date)*	
	Max. Ratings	CW	Burst
Cathode Heater Power	1 KW	Zero	Zero
Hydrogen Pressure	300u	300u	300u
Anode Voltage	40 KV	40 KV	30 KV (40 KV)
Peak Current	50 KA	2.4 KA	30 KA (20 KA)
DC Average Current	50 ADC	2.5 ADC	18 ADC (30 ADC)
Pulse Repetition Rate	125 Hz	415 Hz	30 Hz (75 Hz)
Pulsewidth	10 us	2.5 us	20 us
DC Average Power	1 MW	50 KW	270 KW (600 KW)
Jitter	<10 ns	2 ns	Not measured
Anode Delay	<200 ns	50 ns	Not measured
Anode Delay Drift	<100 ns	100 ns	Not measured
Keep-Alive Current	40-500 mA DC	50 mA DC	50 mA DC
Burst Time	120 sec	-	1 sec
Off Time	300 sec	-	5 sec (10 sec)

* These are simultaneous values, and are test-kit limited. They are not maximum tube ratings. Values are given for operation in 1-ohm (2-ohm) kits.

Initial aging of the HY-7312 was done CW at EG&G, with the cathode heater on. The tube attained its rated maximum anode voltage of 40 KV after approximately 8 hours of 415 Hz operation in a 30-ohm test kit, after which the cathode heater voltage was reduced gradually to zero over a period of a few more hours. The control grid was monitored continuously for signs of arcing, as evidenced by erratic fluctuations or

sudden drops in the control grid voltage. When these were observed, the anode voltage was reduced for a few minutes, until it could be raised again without causing arcing. As the tube aged, the grid-cathode drop decreased from over 1500 volts to around 800 volts.

In all other respects, aging of the HY-7312 proceeded in essentially the same manner as a standard oxide-cathode HY-7.

Once aged, the HY-7312 was successfully slapped-on over 50 times at the 40 KV-50 KW DC level, with no cathode heater power. The slap-on tests were conducted over a period of days, with off-times ranging from a few seconds to 12 hours.

After 24 hours of CW operation at 50 KW DC average power, the HY-7312 was installed in a 1-ohm kit at ERADCOM for testing at the megawatt average power level. There, the tube has been successfully slapped-on, with no cathode heater power, after being off for as long as 48 hours. The limits of tube performance, expected to be comparable to those of the HY-7 (Table 2), have yet to be attained; test-kit modifications to achieve this are in progress.

Discussion

The physical mechanism of cathode emission and its implications for thyatron life and reliability are now discussed.

The most noteworthy aspects of dispenser cathode operation in thyatrons are that 1) the cathodes emit without arcing even when they are at bulk temperatures well below that required for activation, and 2) the emission current densities in thyatrons are several times those observed in vacuum (80 to 100 amperes/cm² as compared to 10 amperes/cm² in vacuum).

Conventionally, the liberation of free barium and its migration to the surface is sustained by keeping the cathode at temperatures around 1000°C or higher. We have shown that the bulk temperature of cathodes in our recent cold-start tubes cannot be more than a few hundred degrees Centigrade. Therefore, electron emission is undoubtedly being sustained by the action of the discharge at the cathode surface. This action probably involves intense local heating, plus Schottky emission via the high electric fields in the plasma sheath.^(7,8)

Cathode sheath electric fields can reach hundreds of KV/cm, easily producing an order of magnitude increase in emission over the zero-field saturation level. This is demonstrated in detail in the Appendix.

As for the effect of local heating, it is significant that surface analysis (via electron dispersive spectroscopy-EDS) of un-activated cathode plates revealed spots of free barium precisely opposite those places where the plates had been tack-welded to their nickel base in preparation for brazing. This demonstrates clearly that brief, highly localized bursts of heat, such as occur under discharge conditions, can indeed activate the cathode.

The cathode emission mechanism described above has certain implications for thyatron cold startup capability and life.

First, the cathode must be activated before the thyatron is turned on for the first time. Otherwise, it will either fail to commutate, or will arc, usually to the cathode baffle or supporting structure. This behavior has occurred in isolated cases, but, in general, the same procedure used to activate oxide-coated cathodes has provided reliable initial startup.

Second, the extent of cathode activation via local discharge heating must be sufficient to allow the tube to be cold-started after it has been off for some indefinite period. Here our results have been erratic. The 2-inch diameter tubes with relatively small, thermally well isolated cathodes (Figures 2 and 3), cold-started reliably throughout life. Thus

far, the HY-7312 has only been operated at anywhere near its rated average power for a few hours, so it is too early to assess its reliability. Our experience thus far with experimental tubes (mostly 3- and 4-1/2-inch diameters) has been that, although they can run CW with no auxiliary cathode heater power for hundreds of hours, they become progressively harder to cold-start after only a few tens of hours, and begin requiring short periods of auxiliary cathode heater power to reestablish commutation. (The possibility that excessive gas cleanup was causing this problem was investigated, but pressure measurements showed this not to be the case.)

Clearly, further improvement is needed in either the thermal design of the cathodes, the initial activation procedure, the cathode material itself, or all three.

While the larger dispenser cathodes can certainly be designed to run hotter, it would be more advantageous if the necessity for this could be avoided by use of better activation procedures and cathode materials.

Under our present activation schedule, the cathodes are held at around 1000°C for about 1 hour. The activation thus achieved is probably marginal; 1200°C for several hours would be more in keeping with standard practice for dispenser cathodes.

Regarding the cathode material, it is known that the type used in the 3-inch diameter tubes and in the HY-7312 has drawbacks. It was used primarily because of its ready availability, low cost, and the ease with which it could be brazed to supporting structures. However, the absence of calcium oxide in the formulation significantly reduces its emission capability⁽⁹⁾, and the nickel, while it facilitates sintering and brazing, tends to seep into and block the pores through which free barium migrates. SEM studies have shown that this "nickel poisoning" was a substantial factor in the failure of at least one thyatron to date. The cathodes used in the 2-inch diameter tubes were made from pure pressed tungsten, impregnated with a mixture of barium and calcium aluminate after sintering. Cathodes of this type are known to provide higher emission, and to be less susceptible to poisoning.

Future Application of Dispenser Cathode Thyatrons

Dispenser cathode thyatrons are expected to find significant applications in areas where reduced weight and volume are desired, since cathode heater supplies and isolation transformers will not be needed. The larger the thyatron, the greater the advantage. EG&G is therefore continuing to develop dispenser cathode models of the HY-7 megawatt-average-power thyatron, including a double-ended version for use where high inverse voltages are present and reverse conduction is desired. By making the anode from dispenser material, emission from the anode might be sufficient to establish reverse conduction in a nondestructive glow mode.

The elimination of auxiliary heater power would also be a boon in applications involving large numbers of intermediate-size thyatrons, such as accelerators and large laser systems. Therefore, we are also developing dispenser cathode thyatrons in the HY-5 size (4.5 inches diameter, 5 KA peak current), and the 1802 size (3 inches diameter, 1.5 KA peak current).

The high current densities obtainable from dispenser cathodes make them potentially important in fast pulse, low-inductance, high-peak current applications. EG&G is presently developing a number of multi-stage thyatrons for applications requiring pulse lengths on the order of 100 nsec, switch inductances of 50 nH, and peak currents in excess of 10 KA. Oxide-coated cathodes are poorly suited for this regime because the large surface area required necessitates tall, multi-vaned structures. These structures not only have high

inductance, but suffer from short life due to the poor accessibility of much of their surface to the discharge. When pulse lengths are short, the discharge simply does not have time to penetrate far into the structure, resulting in over-utilization of the vane tips and rapid destruction of the emissive coating there. By contrast, dispenser material can emit 5 to 10 times as much current per unit area when hot, thus enabling us to construct shorter cathodes having lower inductance and more uniform utilization. The high current density capability of dispenser cathodes will make them extremely useful in these applications regardless of whether or not practical cold-start operation is realized.

Acknowledgments

Many people have contributed significantly to the dispenser cathode work at EG&G.

Overall technical direction was provided initially by David Turnquist, and subsequently by Robert Caristi.

Frank Feith of the Flashtube Department provided us with cathode material, processing, and invaluable technical guidance.

The surface analysis work was supervised by John Roy and Mark Anderson, and much of the technical background information on dispenser cathodes was researched by John Bell. Most of the experimental thyatrons, including the HY-7312, were constructed by Alan Hardiman.

This work is being supported by ERADCOM, LANL, and NSWC (Dahlgren Laboratory).

Appendix on Schottky Emission

In thyatrons, much of the voltage drop in the grid-cathode region occurs across a cathode sheath roughly a Debye length thick. This results in a very high electric field at the cathode surface. Under these conditions, the cathode emission current density, J , is enhanced over its "zero-field" value, J_0 , in accordance with the Schottky formula,

$$J \approx J_0 \exp(0.44 \sqrt{E/T})$$

where, E is the electric field in volts/meter; T is the cathode surface temperature in °K.⁽¹⁰⁾

The value of E depends on the sheath voltage drop, V , and the Debye length, d , according to

$$E \approx V/d$$

where

$$d^2 = \epsilon_0 k T_p / n e^2$$

with T_p and n being the plasma temperature and density, respectively. In thyatrons, $k T_p / e$ is typically 3 electron volts, and n can be as high as 10^{20} m^{-3} , particularly near the cathode where vaporized material (in this case, barium) contributes to the plasma density. For dispenser cathodes, measurements point to V being on the order of 100 volts, giving $E \approx 7.8 \times 10^7$ volts/meter; therefore, $J/J_0 \approx 20$ for $T \approx 1300^\circ\text{K}$.

Detailed experimental verification of the validity of Schottky theory for dispenser cathodes in gas discharges is provided in Speros et al.⁽⁷⁾

References

- (1) B. Baker and R. Wheldon, Electronic Eng., p. 24, January 1964.
- (2) G. Pivoravov and L. Maizel, Radiotekhnika i elektronika 3, No. 8, p. 1073, 1958.

- (3) H. Friedman and J. Eninger, 3rd IEEE Int. Pulsed Power Conf., p. 27.6, Albuquerque, New Mexico, 1981.
- (4) J. Cronin, IEEE Proc. 128, Pt. 1, No. 1, p. 19, 1981.
- (5) D. Fleischer, D. Turnquist, S. Goldberg and N. Reinhardt, IEEE Trans. on Electron Devices ED-26, 10, p. 1444, 1979.
- (6) I. Langmuir, Phys. Rev. 33, 6, p. 954, 1929.
- (7) D. Speros and P. Bucilli, Journ. App. Phys. 41, 4, p. 1512, 1976.
- (8) A. Pengelly and D. Wright, Brit. Journ. App. Phys. 5 11, p. 391, 1954.
- (9) A. Venema, Phillips Tech. Rev. 19, 6, p. 177, 1957.
- (10) J. Cobine, Gaseous Conductors, Dover, Inc., N.Y. p. 118, 1958.

THYRATRON SWITCH GENERATION OF MULTI-KILOVOLT
PULSES IN THE NANOSECONDS REGION FOR LINAC ELECTRON
GUN DRIVE

H. D. Kitchin, Cardon Instrument Co., Earls Colne,
Colchester, Essex, U.K.

J. M. Salome, CEC, JRC, Central Bureau for Nuclear
Measurements, Geel, Belgium

Abstract

The Geel Electron Linear Accelerator (GELINA) provides very intense short bursts of electrons which are used to produce neutrons for time of flight experiments. The injector is of the triode gun type requiring a grid pulse of several kV to achieve the necessary electron beam current. The application of a hydrogen thyatron tube for the generation of drive pulses having durations of less than 4 nanoseconds at voltages of several kilovolts has been examined from theoretical and practical points of view.

The relationship between the risetime of the fundamental thyatron switching function and the pulse generated using the classical charge line technique is examined theoretically, and the results applied to establishing the thyatron capability needed.

Thyatron switching characteristics for a number of tubes, derived from the EEV Co. CX1157, have been evaluated over a range of triggering conditions and the requirements for optimum operation established. It has been found that switching transitions having risetimes down to 3 nsec can be obtained and that the generation of pulses having a 3ns half amplitude width is feasible at several kV peak amplitude for the intended application by using advanced circuit techniques.

Some of the experimental results obtained with special tubes operating under various conditions are presented.

1. Introduction

The CBNM Electron Linear Accelerator produces most of the time intense neutron bursts for neutron time-of-flight experiments (1). After acceleration to about 120 MeV (150 MeV at zero current), the electron beam is slowed down in a heavy metal target producing bremsstrahlung which then generates neutrons via (γ, n) reactions (2). The energy resolution of the neutron data is strongly dependent on the parameters of the electron bursts which have to be very intense and short (3). Several modifications have been

made particularly at the injection side to improve the peak current and shorten the burst width. At present, the triode gun is driven by a pulse amplifier using UHF tubes to provide pulses down to 4ns width at 5kV peak drive. It is of coaxial construction and is operated with cathode drive via a 50 Ω coaxial line. Special features of the gun are a very low inductance and capacitance enabling better matching of the line than was possible with earlier guns of conventional construction.

At the output of the anode, electron beam pulses of 4 to 5ns long and more than 20A are obtained and injected into a pre-bunching cavity and then into the first section of the accelerator. This paper describes some of the recent theoretical and practical work concerned with the operation of the gun and the use of hydrogen thyatrons for the generation of drive pulses below 4ns FWHM* at repetition rates of up to 1kHz.

2. The Electron Gun

The main elements of the gun construction are shown in fig. 1, where it is to be noted that almost the whole of the electrically functional assembly is configured in coaxial form and proportioned for 50 Ohms operation. To a first approximation the equivalent circuit is that shown in fig. 2, where the gun impedance, Z_k is shunted by a fixed load resistor, R_L , chosen to match the 50 Ohm line which connects the gun to the pulse source. The gun capacitance, C , is 5pF and forms with the source and termination a basic RC time constant of 125psec, having a theoretical risetime of under 300psec. This fundamental theoretical performance capability is, however, influenced by some practical features which could degrade the risetime performance, but it has been estimated that these should not prevent the attainment of risetimes and pulse widths down to 1nsec. In consequence, it was considered worthwhile to conduct an investigation into techniques for producing shorter pulses than those currently being

used around 4 to 5nsec.

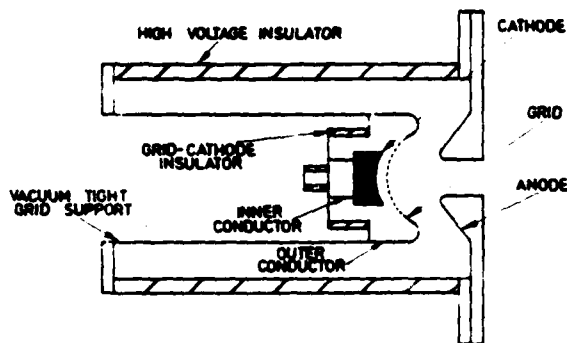


Fig. 1. Co-axial Short Pulse Electron Gun

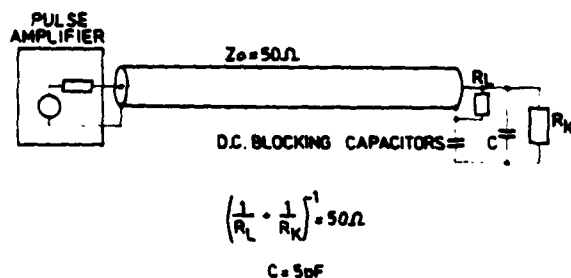


Fig. 2. Basic Circuit of Gun Assembly

3. Thyatron Pulse Generators

Well known amongst the techniques for high voltage pulse generation is the use of a hydrogen thyatron, although its application to the generation of pulses appreciably shorter than 5nsec frequently involves the tube working in a 'spark gap' mode which can appreciably reduce tube life. Nevertheless, the advantages offered by this type of tube encouraged a programme of work to establish how far it might go towards attaining the target of generating a 3nsec pulse at 5kV in a 50 Ohm circuit, whilst maintaining normal thyatron operation. Because the grid electrode in a thyatron can only perform a trigger function the thyatron must be used as a switching element. It is, therefore, necessary to depart from the pulse amplifier configuration of the existing drive equipment and embody the thyatron into a system where the pulse width is determined by external elements. The classical 'charge line' technique for short pulses is to use the thyatron in conjunction with a charged coaxial line

as illustrated in fig. 3. Between pulses the capacitance of the line is charged from a high voltage source, via a resistor. When the line capacitance is charged to a potential of twice the required peak pulse amplitude the thyatron is triggered on its grid. In the ideal case with a lossless line and an ideal switch a rectangular pulse of duration equal to twice the delay time of the line is produced in a matched load. In practice the switch exhibits a finite time of transition from non-conduction to full conduction, characterised by the 10-90% rise-time. Also, the line will not be ideal and the pulse produced will exhibit finite rise and fall times and may be of lower amplitude than ideal. Parasitic capacitive and inductive elements may also give rise to ringing and overshoot phenomena. For short pulses the line imperfection can be relatively insignificant and careful attention to construction can minimise ringing and overshoot, leaving the major factor determining pulse performance as the thyatron switch risetime.

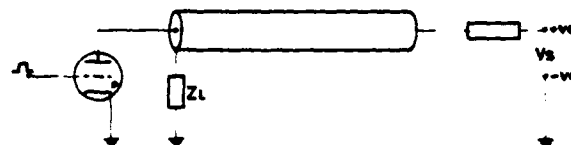


Fig. 3. Line Generator Circuit with Grounded Switch Cathode.

4. Pulse Width Amplitude and Risetime Relationships

The general effect of reducing the charge line delay time so as to achieve a reduction in pulse width is illustrated in fig. 4. which shows the basic charge line circuit at the top with the pulse in the load formed by the summation of the forward and reflected waves in the line circuit. In this simple case a linear ramp transition has been assumed, and it is evident that when the line delay is reduced below a certain point any reduction in pulse width will be associated with a reduction in pulse amplitude. Superficially, it may be imagined that pulses of appreciably less width than the risetime could be produced if the sacrifice in pulse amplitude could be accepted, and this indeed might be the case if an ideal ramp transition could be produced. However, such a transition cannot even be approached in the time region under consideration because of its bandwidth requirements, and it is of consider-

able interest to establish the nature of the relationship between pulse width, amplitude and switch risetime which applies in a practical case.

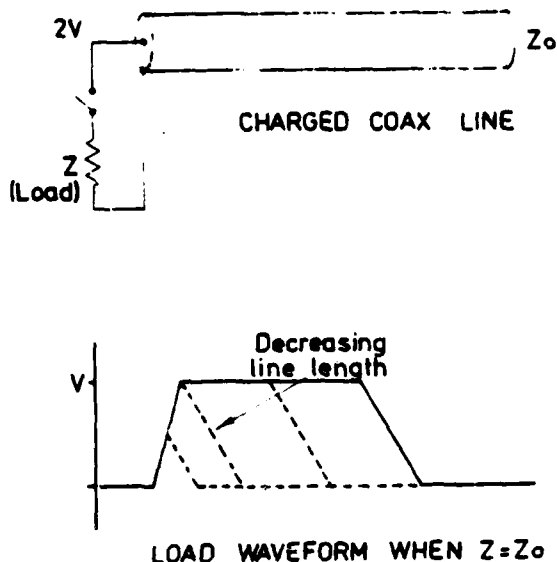


Fig. 4. Effect of Shortening Line with Finite Risetime Switch.

To investigate this aspect of pulse generation theoretically it is necessary to define the law obeyed by the transition. It has been shown (4, 5, 6, 7) that a good approximation, which has some fundamental theoretical physical basis, postulates thyatron conduction as obeying an exponential law. Of the various ways in which this can be expressed a suitable choice is one which represents the thyatron by a series combination of a constant inductance, and some valve parameter which is an exponential function of time. It has been found with small ceramic tubes of cylindrical construction as used in the tests to be described that the inductance is not a major factor in a 50 Ohm system having a low inductance coaxial tube housing. In this case the thyatron can be adequately represented by an exponentially changing resistance function for the transition period of switching action. If it is assumed that the charge line reflects the transition at the open circuit and with only a change of sign then the pulse produced in the load can be obtained by linear summation of the propagated and reflected transitions. On this basis, a detailed analysis has been carried out for the exponential transition

to establish the relationships between pulse width, amplitude and risetime. As expected the pulse amplitude falls progressively to zero as the charge line delay time is reduced to zero, but the pulse width does not decrease indefinitely, instead tending to a finite limit. This limiting pulse width is 80.1% of the risetime of the transition. An interesting consequence of this is that the effectiveness of the system, when expressed as the ratio of pulse amplitude to pulse width, exhibits a broad maximum around a value of two-way line delay very nearly equal to the thyatron switch risetime. At this point the pulse amplitude is some 80% of its maximum possible value of half the line charging voltage and the pulse width is 15% greater than the risetime. From these calculations it is possible to predict the voltage and risetime capabilities which the thyatron must fulfil to meet a given width and amplitude of pulse. Fig. 5 shows such a curve for the case of a 5kV, 3ns width pulse requirement. The two-way delay time of the charge line is also implicit in the calculations for the curve of fig. 5 and the actual values are marked on the curve at selected points. The limiting case for zero risetime shows that a 10kV thyatron capability and a 3ns charge line delay time is required, as expected for such an ideal case. The limit at the other extreme shows that the maximum allowable risetime is 3.8nsec, at which point an infinite voltage capability is needed owing to the pulse amplitude having dropped to zero. This curve clearly shows the extent to which pulse performance depends upon risetime when pulse widths of the order of the risetime are required, and emphasises the need to control risetime very closely if pulse performance is to be maintained in this region. For example, to meet a specified 5kV, 3nsec pulse, a variation of -10% to +10% on a nominal 3nsec thyatron risetime will require the thyatron voltage capability to increase from about 13 kV to 19 kV.

5. Thyatron Switching Characteristics

It is evident from the results presented in Section 4 that the limit to the minimum pulse width attainable using only linear elements in the tube circuit will be set by the switching characteristics of the thyatron. Accordingly, a number of different thyatron tubes were examined, including both standard production and experimental types. These were supplied by the English Electric Valve Co. Ltd., and the general appearance of a typical tube is shown in fig. 6. The tubes were of ceramic construction incorporating two grids and with separate connections for the tube heater and

gas reservoir.

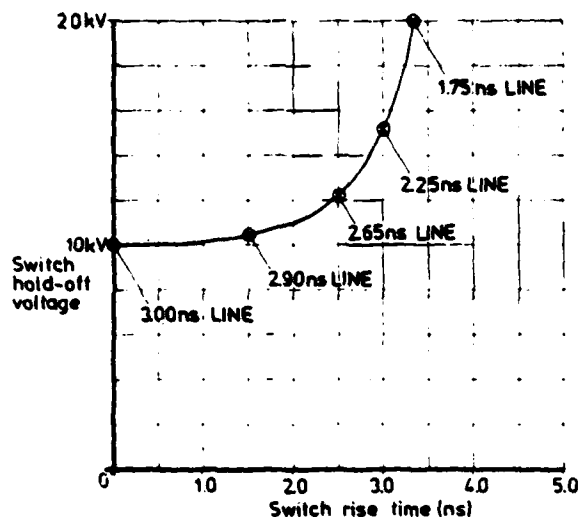


Fig. 5. Conditions for a 3ns FWHH Pulse of 5kV amplitude into a matched load.

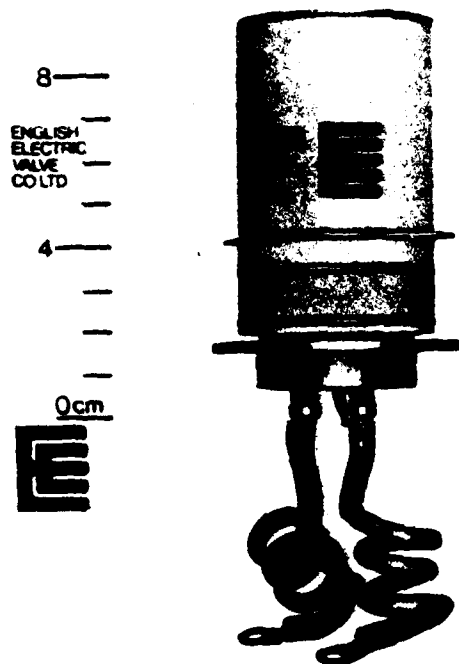


Fig. 6. Experimental Ceramic Thyatron.

The tests were carried out using an experimental apparatus of the charged line type having parasitic elements minimised as far as possible, and into which thyratrons could be placed to investigate individual

performance. Figure 7 shows the general construction, and figure 8 the circuit block diagram. Pulse drive was used to Grid No. 1, as it has been established that this is more favourable to the attainment of the shortest risetime.

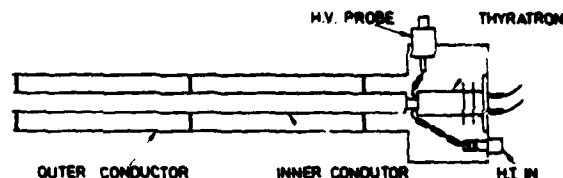


Fig. 7. Construction of Test Apparatus.

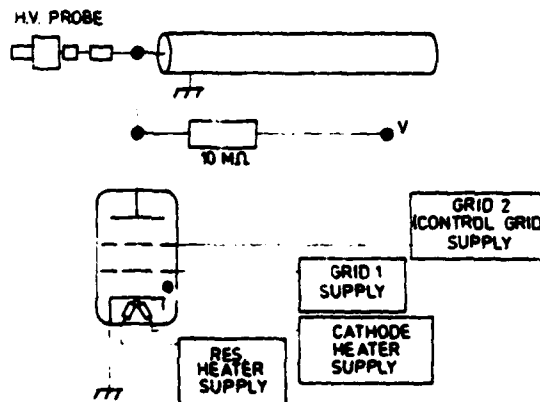


Fig. 8. Test Apparatus Circuit.

It is to be noted that some aspects of thyatron behaviour can be masked by inadequate resolution in the test apparatus and measuring instrument used, and care was taken to avoid this situation as far as possible.

Part of the test programme was aimed at studying the influence on anode transition risetime of the following factors:

- Gas pressure.
- Drive amplitude to Grid No. 1.
- Drive amplitude to Grid No. 2.
- Risetime of drive to Grid No. 2.
- Delay between Grid No. 1 and Grid No. 2 pulses.
- Peak anode voltage.
- Peak anode current.

The following dependencies have been observed between electrode operating conditions and anode switching transition speed for the range of tubes tested:-

- (i) Heater Voltage: The main effect of variation in heater voltage is to affect tube operating temperature, and in consequence gas pressure. In this respect it has a similar effect to variation in reservoir voltage. However, it should be emphasised that the cathode operating temperature has a considerable influence upon tube life and departures from manufacturer's recommended ratings should not be contemplated without consultation.
 - (ii) Reservoir Voltage: This is by far the most important tube operating parameter affecting speed of the anode transition, owing to its direct effect on gas pressure. Generally, speed improves as reservoir voltage is increased, but often with a gradually diminishing effect. The extent of this depends very much on the choice of reservoir design parameters by the manufacturer. It is to be emphasised that operation with reservoir voltages outside the maker's published limits can greatly endanger tube life and could result in catastrophic failure.
 - (iii) Grid No. 1 Drive Pulse: The rise-time of this pulse is relatively uncritical although it should be small compared with the pulse length. A few tens of nanoseconds is easily obtained with present day techniques and has been found to be satisfactory. The pulse width is not critical but must be adequate to allow the maximum grid current to be achieved prior to the Grid No. 2 trigger pulse being applied. A few hundred nanoseconds is suitable. The amplitude of grid current is important, being dependent on the peak anode current and the tube construction. For the fastest type of tube tested a grid current of 10-20 Amps is usually satisfactory for anode currents of up to 200 Amps.
- Sufficient grid current is essential to avoid inflections in the anode transition, as the presence of these can seriously degrade risetime performance. The drive voltage required by the valve is only a few hundred volts at most, but considerably more source voltage than this can be advantageous in reducing the time taken to reach maximum current.
- (iv) Grid No. 2 Drive Pulse: Tests revealed that reducing the risetime of the drive pulse below about 15nsec or so had no measurable effect on the anode transition risetime. Anode delay time may be affected but some of this is attributable to the shift in timing reference point on the leading edge of the drive pulse. A similar conclusion was reached regarding amplitude of the current and voltage of the drive pulse and no effect on the anode transition risetime was discernible over a 10:1 range of drive amplitudes. However, jitter does increase as the drive amplitude is reduced or drive risetime is increased, and where low jitter is important adequate drive pulse amplitude and fast risetime are essential. The drive circuit impedance should be low and the circuit design should be such as to preserve the maximum speed of the input pulse. The duration of the drive pulse has not been found to be critical; a convenient width lies in the region of 50-150nsec. The pulse must be delayed to follow the Grid No. 1 drive pulse, ensuring that the Grid No. 1 discharge is established before the Grid No. 2 trigger pulse occurs. As bias is required for Grid No. 2 the circuit must include provision for this.
 - (v) Anode Voltage: The anode voltage which the valve will 'hold-off' (i.e. without self triggering before the Grid No. 2 pulse occurs) is dependent upon the gas pressure and falls as the pressure is increased. This

is one of the main factors affecting the extent to which the pressure can be raised to reduce anode risetime. Tube operating conditions are inevitably a compromise between risetime and anode voltage 'hold-off'. Measurements have shown that the anode risetime reduces as the voltage is reduced when the circuit and charge line and all other factors are kept constant, but this decrease is not proportional to voltage and so the best power-speed capability is obtained at the highest voltage for which the tube is designed.

- (vi) Anode Current: The anode risetime is influenced by the magnitude of the peak anode current, and at a constant voltage it increases as anode current is increased. The risetime increases much more slowly than the increase in anode current so that the best tube power-speed capability occurs at the highest current. However, for fast pulse working the limit to anode current may be set by the onset of inflections and irregularities in the anode transition waveform.

6. Pulse Generation Tests

To examine how the results of the theoretical pulse width risetime and voltage relationships described in section 4 relate to practical performance, tests were carried out using a type of tube found to have the fastest anode transition in a circuit of the charged line type operating at the 50 Ohm impedance level. Capacitor divider monitoring probes were incorporated; one at the anode of the thyatron to monitor the anode voltage transition and another across the load. A typical result illustrating waveforms at the anode and across the load is shown in fig. 9 for a charge line having a two way delay of 3nsec. The anode transition risetime is 3.0ns and the pulse width is 3.85ns. The anode supply was 10kV which produced a 3.3kV peak pulse amplitude. Similar results over a range of risetimes were obtained and are plotted as the curves marked 'A' in fig. 10. Also shown in fig. 10 are curves for the theoretical relationships referred to in section 4 which are marked 'B'. The practical results exhibit a lower amplitude and somewhat greater pulse width than the

theoretical prediction.

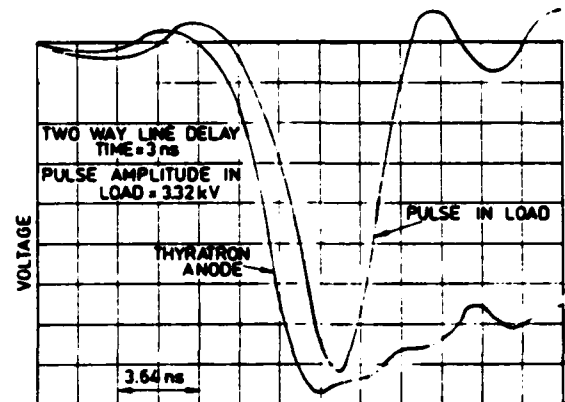


Fig. 9. Voltage Waveforms at Thyatron Anode and in Load for Experimental Pulse Generator.

One possible explanation is that the shape of the anode voltage transition departs from the assumed law, and indeed, examination of the waveform shows this to be so. This aspect of the transition was examined in more detail by plotting the anode transition on a logarithmic amplitude scale, as a tube obeying the assumed law should give a straight line. Using the anode transition of fig. 9 taken between the peak to peak limits, the logarithmic plot is shown in fig. 11 as a solid line. Whilst the law is obeyed quite well over the central region extending to nearly 2 decades there is an increasing departure at each end.

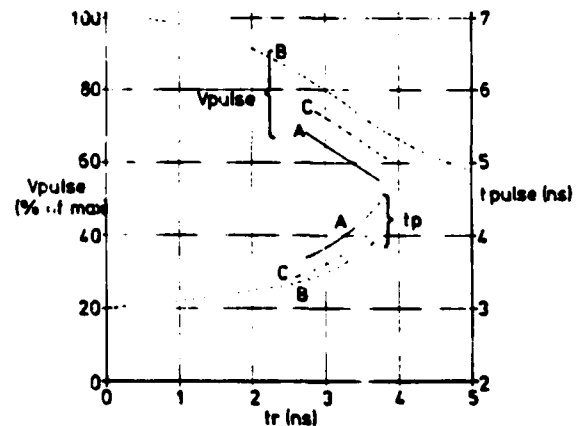


Fig. 10. Curves A & C; experimentally

observed dependency of pulse amplitude and pulse width on thyatron rise-time using the apparatus shown in Fig. 7. Curve B; theoretically predicted relationship; two way line delay time 3.0ns.

At the end nearest the time origin some of this departure is attributable to the noticeable ripple before the transition, whilst at the other end it is attributable to a more abrupt finish to the transition.

A better fit between the measured and ideal transitions is achieved if the amplitude of the latter is made greater than the actual peak to peak value of the measured transition. In the present case an amplitude corresponding to a supply voltage of 10.91kV has been found to be a good choice for the idealised transition, and the revised plot of the measured transition is shown by the ringed points in figure 11 when interpreted in this way. The points now lie on, or close to, the straight line representing an ideal exponential transition over the major part of the range, only deviating significantly at the extreme points.

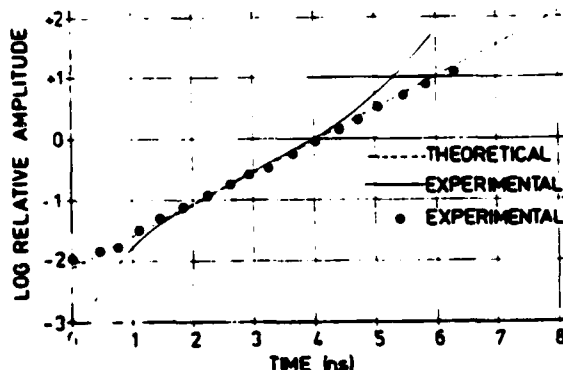


Fig. 11. Anode transition of Fig. 9 plotted logarithmically to show extent of agreement between experiment and theory - see text for details.

Replotting the results of curve 'A' of Fig. 10 after making allowance for this revision results in curve 'C' which shows appreciably closer correspondence with the theoretical predictions, especially regarding pulse width. The remaining discrepancy may well be accounted for by the cumulative effects of risetime contributions from the apparatus, the residual discrepancy between

the theoretical and measured transitions and stray capacitance and inductive effects. The attainment of transitions having 3nsec risetimes from a thyatron operating at 10kV or more offers the possibility of generating pulses down to 3nsec width at the 5kV amplitude required by the electron gun if the voltage efficiency could be improved. A well known technique which doubles the pulse amplitude is the Blumlein circuit where two identical lines are charged in parallel and effectively discharged in series, so providing an output voltage equal to the charging voltage in the ideal case. The line impedance required becomes half of the load impedance, so that the discharge tube has to be capable of passing greater current than in the basic single line circuit. Hydrogen thyatrons of the type tested will handle the increased current without serious degradation of the risetime at voltages up to at least 10kV, provided the points noted in section 5 are taken into account, so that the adoption of this technique should yield a significant gain in capability. Another technique, especially applicable to lower repetition rate requirements is the technique of 'command' pulse charging (7). This enables the statistical nature of gas discharge breakdown to be exploited by restricting the application of voltage to a short period just prior to the instant of thyatron triggering, and it seems likely that by applying this technique to the Blumlein circuit the best of the experimental valves tested could yield a 5kV, 3ns pulse suitable for the electron gun application.

References

1. A. Bensussan, J. M. Salome, GELINA: A Modern Accelerator for High Resolution Neutron Time of Flight Experiments, NIM 155 (1978) 11-23.
2. J. M. Salome, R. Cools, Neutron Producing Targets at GELINA, NIM 179 (1981) 13-19.
3. J. M. Salome, K. H. Bockhoff, Performance Improvements of the Geel Linac Neutron Source, Proceedings Int. Conf. on Nuclear Cross Sections for Technology, Knoxville, TN, Oct. 22-26, 1979, 534-536.
4. A. E. Harrison, 'Ionisation Time of Thyatrons': Trans. AIEE. Vol. 59. p.747, 1940.
5. C. J. Mullins, 'Initiation of Discharge in Arcs of the Thyatron type': Phys.

Rev. Vol. 70, Sept. 1946.

6. J. B. Woodford & E. M. Williams, 'The Initial Conduction Interval in High Speed Thyratrons': J. App. Phys., Vol. 23, No. 7 July 1952.
7. D. Turnquist, R. Caristi, S. Friedman, S. Merz & R. Plante, 'New Hydrogen Thyratrons for Advanced High Power Switching': 2nd IEEE International Pulsed Power Conference, Lubbock, USA, 1979.

* Full Width Half Height.

Acknowledgements

Acknowledgement is made that the work on which this paper is based was supported by the Commission of the European Communities. The assistance of the English Electric Valve Co. Ltd., in providing tubes and helpful discussion is also acknowledged.

HIGH DI/DT OPERATION OF MULTI-GAP THYRATRONS

BY

WM. H. WRIGHT, JR.

US Army Electronics Technology & Devices Laboratory, ERADCOM
Fort Monmouth, NJ 07003 Phone (201) 544-5404

INTRODUCTION:

For the past several years, NSWC and ET&D Lab, ERADCOM, have been working together to advance the technology base in high power switching and power conditioning and to develop a thyatron for the extremely demanding ETA/ATA application, whose requirements are: peak hold-off voltage, 250 kV, pulse charged in a few microseconds; peak current, 40 kA; pulse width, 60 nanoseconds, rising in 10 nanoseconds; repetition frequency, greater than 1 kHz. The present ETA/ATA switch is a gas-blown spark gap with satisfactory hold-off and risetime, but limited in repetition frequency and life. The thyatron, with its diffuse discharge as opposed to the filamentary discharge of the spark gap, has inherently faster recovery for higher repetition frequency operation and is erosionless, for a much longer operational life. The thyatron operates at low gas pressure, at a few hundred microns, on the left side of the Paschen minimum, gets its voltage holdoff by reducing electrode spacing, and is normally limited by field emission effects to 40 to 50 kV per gap. For operation at voltages higher than this, multiple gaps must be used with some mechanism for dividing the total voltage among the gaps.

THYRATRON DESIGN, HY-5525:

When a switch is closed between an energy store and a load, the rate of rise of current can be limited by circuit inductance, switch closure time, or both. In nearly all previous applications, circuit inductance limited the rise and switch closure could be considered fast, so that during the time the switch impedance (mainly resistive) was falling there was little current through the switch and dissipation stayed low. For fast circuits, switch closure time becomes the limitation on current rate of rise and the switch has to pass large currents while the voltage across it is still high. For this application with peak voltage of 250 kV and peak current of 40 kA, if the current rises to half peak value while the voltage drops to half peak value, a reasonable approximation for a switch-limited circuit, the peak dissipation within the switch reaches 2.5×10^9 watts. To keep average power dissipation within the tube low enough to

avoid thermal damage, the time during which this dissipation is present, the switch closure time or anode fall time, must be kept very short, on the order of a few nanoseconds. The major factor controlling anode fall time is gas pressure within the switch, with higher pressures giving faster fall times. For high-voltage, low-inductance (HVLI) thyratrons, a pressure of 500 microns (u) is a good goal. High pressures, however, are inimical to good voltage hold-off because on the left side of the Paschen curve, where thyratrons operate, increasing pd (pressure-distance product) produces a lower breakdown voltage. Reducing electrode spacing to compensate for higher pressure helps, but field-emission problems, aggravated by reduced spacing, will limit hold-off.

The design of the HY-5525 is shown in the cutaway of Figure 1, and the tube itself in Figure 2. The tube envelope is 4.5 inches in diameter and the tube stands 6.3 inches high from the cathode flange to the anode flange. It has five gaps and the overall length of the high voltage sections is short enough to provide a low total inductance. The tube is designed for use with a 12-inch diameter current return. The inductance of the tube/return combination is about 40 nH. The tube should have been capable of generating a 10 kA, 60 ns current pulse with a risetime of 10 to 15 ns at a pulse repetition frequency of 1 kHz in a burst mode. The gap spacing (Figure 1) varied from .121 inch at the control grid to .115 inch at the anode to improve the voltage distribution across the tube (C_{gap}/C_{stray} is about 12 for a 12 inch return and about 15 for a 14 inch return), but even the .115-inch gap is well above the spacing (.090 inch) where experimental results show that field emission may become a concern. The upper insulator is 1.515 inches long. This is more than adequate according to the results of ceramic tests. A ratio of baffle thickness to internal grid height is such that reasonably good stage isolation without triggering problems was expected.

TEST FACILITY, DESIGN AND PERFORMANCE:

The philosophy followed in the design and fabrication of the test facility for the HVLI thyatron was to produce all conditions of the eventual application simultaneously. Our experience with non-simultaneous, or simulated, testing has been that it often produces unrealistic, and dangerously optimistic, data.

To generate the required fast pulses, while avoiding the mechanical difficulties of a Blumlein circuit, a water-filled coaxial pulse forming line (PFL) was designed for 250 kV peak charging voltage, 60 ns pulse width, 3 ohm characteristic impedance, and 10 nF distributed energy storage capacitance. A water-immersed 3 ohm load in series with the center conductor matched the PFL and maintained the desired 6 ohm system impedance. The thyatron mounted below the PFL in an oil tank with a heavy acrylic plate separating the oil from the water. A large diameter current path was maintained throughout for low inductance and good risetime: 7.7 inch dia center conductor in the PFL; 6 inch dia load resistor; 5 1/4 inch dia conductor through the acrylic plate to the thyatron. The connection from the thyatron to the feedthrough was made with beryllium-copper finger stock operated at 2.5 kA/linear inch around the diameter, which is a conservative current density. The current return from the thyatron cathode to the PFL was a 12 inch dia cylinder, the same diameter as the outer cylinder of the PFL, and a distributed, low inductance .07 ohm current viewing resistor (CVR) was in series with the current return to monitor the current waveform. The low inductance configuration was maintained by joining the current return to the PFL with 24 bolts around a 14 inch bolt circle. An insulated joint between the PFL and the grounded gantry prevented grounding problems on the diagnostics. Figure 3 is a schematic cutaway of the PFL, load, thyatron, CVR, and current return. Figure 4 shows the PFL supported in its gantry; the structure was about 9 feet tall. Figure 5 shows the current return, the CVR, the finger stock connector, and the HY-5525 in its socket.

The water in the PFL was circulated continuously through a high-purity mixed-bed deionizer, and a layer of transformer oil floating on the water helped prevent atmospheric gases, particularly CO₂, from lowering the resistivity. The 1/e decay time was approximately 40 us; when the thyatron was triggered within a few us after charging the PFL, the energy loss through the water resistance was negligible.

The PFL was pulse-charged with a (1 - cosine) waveform through a 1:4.5 stepup transformer from a .2 uF intermediate storage capacitor switched by a 7890 thyatron. This capacitor was resonantly charged from a power supply, filter bank, choke, and charging diode circuit. A 225 kV, 1 amp average current diode stack between the transformer and the PFL prevented the PFL charge from ringing back into the transformer. The charging circuit was operated up to 140 kV, delivering 98 joules per pulse, in a burst mode up

to 1 kHz for burst lengths of a few hundred pulses with a pulse-to-pulse droop of only .15%.

The PFL was characterized and diagnostics developed by operating in a charge-discharge mode with a well-behaved single-gap thyatron, an HY-53, operating at 25 kV and high enough gas pressure to be near self-break voltage, so as to ensure fast anode fall and current rise times, about 17 ns, as shown in Figure 6. The gas pressure was lowered slightly until the anode fall time increased, and a corresponding increase in current rise time was noted, indicating that the current rise was controlled by the tube characteristics rather than by the circuit. A multigap thyatron was expected to be slower than a single gap tube, and the circuit being faster than the single gap tube gave reasonable assurance that the evaluation of the multigap tube was not circuit limited.

EXPERIMENTAL RESULTS:

Prior to evaluation at ERADCOM, the HY-5525 was run at EG&G to the limits of their 80 kV, 30 ohm, 2.6 kA modulator, pulse charged in 8 us, with a discharge rise time of 150 ns. These results are shown in Figure 7 and indicate good gap hold-off and gap addition. The asterisks on the lowest stage curve are ERADCOM data and reproduce the EG&G data up to 7 kA.

Figure 8 shows operation of all five gaps of the HY-5525 at 400 microns, 32 kV, with a 20 ns fall time. Figure 9 is representative of an envelop of no-fire, fire, and pre-fire traces for the lower two gaps of the HY-5525 in the ERADCOM modulator at 700 microns pressure, with a smooth, well-controlled change from fire to pre-fire above 12.7 kV and 2 kA. As the gas pressure was reduced and more gaps added, the hold-off voltage increased and with it the peak current. After a brief period of operation at 7 kA the tube performance became erratic, jumping suddenly from fire to pre-fire, sometimes even from no-fire to pre-fire, with no operating range. The hold-off decreased dramatically, even at very low gas pressures. Reducing cathode heater voltage, cooling the cathode and thereby the lowest grid increased lowest stage hold-off, giving an indication of grid emission.

The capacitive division of the pulsed anode among the five gaps was checked and found reasonable. In an attempt to overcome the grid emission problem on the lowest grid, the tube was run with two gaps and the voltage division distorted by an unequal voltage divider. The highest total hold-off was found with only 2% of the voltage across the lowest gap.

The lowest gap was operated for many hours in a resonantly charged, 10 us, 3 ohm modulator at 10 Hz to determine what effect pulse heating of the interior surfaces, particularly the control grid, would have on the low hold-off/grid emission problem. By carefully operating the tube near, but below, the prefire voltage level, the lowest gap was conditioned up to 22 kV at 350 microns, at which it had held off only 3 kV before aging. The

improvement, however, was tenuous; a brief burst of pre-fire pulses would drive the hold-off down to 7 to 8 kV and would require many hours of aging to bring it back to 20 kV.

After aging in the 10 us modulator, the gaps were checked for d.c. hold-off with the cathode hot, with and without gas in the tube. Without gas, all gaps were quite similar, between 27 and 36 kV, and independent of polarity. With 450 microns of gas, the hold-off ranged from 2 to 25 kV, very low in gap 4, and quite polarity sensitive.

The tube was returned to the EG&G 80 kV, 30 ohm test kit and reconditioned to nearly its original operating characteristics except for gap four, which never regained hold-off. The envelope was then broken open to examine the internal structure.

AUTOPSY RESULTS:

The uppermost cathode vane had been stripped clean of its oxide coating, leaving shiny nickel, and the outer edges of the next few lower vanes showed some signs of use. Other than this, the cathode looked brand-new. Its surface layer was white and soft, indicative of good cathode material, rather than hard and grayish, which occasionally happens with chemical reconversion to carbonates or with other cathode failure. There were no signs of arcing anywhere within the cathode region.

A failure mode which had been postulated prior to the autopsy, i.e., migration of cathode material into the high voltage structure, was not borne out by inspection. If there were any emissive material on electrode surfaces, it was not evident.

There were no gross mechanical defects such as melted or warped electrodes, and the concentricity of electrodes in the ceramic cylinders, while not perfect, was no worse than in tubes which have operated well.

There were no effects to cause field-enhancement between the electrodes, such as whiskers of metal or rough surfaces caused by arcing. There was evidence of minor arcing between electrodes, but no more than is commonly seen after normal conditioning.

There was evidence of serious arcing between the edges of the box-grid sections and the ceramic walls, presumably from the edge of the grid to the deposits of metal on the ceramics. These deposits, copper and molybdenum, depending on their uniformity, could provide field-grading to resist breakdown or field-enhancement to encourage it. There were also whitish deposits, probably alumina, on the electrode surfaces near the arc spots. These arc marks were most severe in the anode region. Arcing in the same region has also been noted during the conditioning of HY-7 thyratrons.

There was nothing observed in the autopsy to explain either the extreme difference in degradation and reconditioning between the fourth and the other gaps or the polarity sensitivity of the fourth gap.

CONCLUSIONS:

The most logical hypothesis for degradation of holdoff is damage resulting from current starvation. The current requirements of the circuit, which demands full design cathode current capability in the nanosecond time frame, cannot be met by the present cathode structure, and results in arcing from the side of the box-grid structure to the deposits on the wall. The arcing is a runaway situation, in that the deposits cause arcing which in turn deposits more metal on the ceramics.

For high di/dt operation, the thyatron cathode must be designed not only for adequate area for current handling capability, but the vane structure must be sufficiently open to allow the discharge to utilize this area fully. The cathode in the tube evaluated here, even though it had more than enough area for the current demanded, probably caused the failure of the upper stages of the tube by not emitting electrons quickly enough.

It has become more evident that a thyatron must be conditioned, or "aged", in an operating environment similar to that in which it will be run, particularly with respect to modulator impedance and peak current level. Though not proven conclusively here, conditioning under realistic di/dt may also be important.

If a thyatron is to be operated with pulse charging of the anode voltage, the capacitive voltage division is inescapable and the grid-cathode space must not fire too easily, else a self-triggering mode is invited, which even external capacitive loading and negative grid bias will not cure.

REFERENCES:

- 1: Cathode Phenomena and Life in Hydrogen Thyratrons, Seymour Goldberg, Proceedings of the Seventh Symposium on Hydrogen Thyratrons and Modulators, 1962

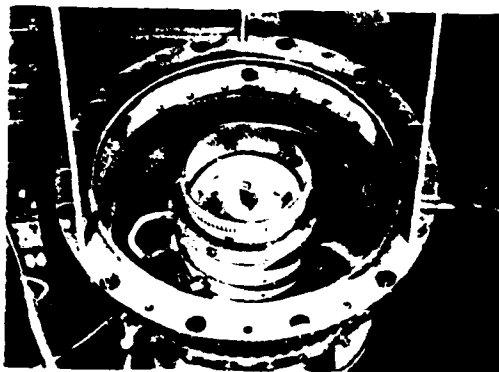


FIGURE 5
THYRATRON SOCKET AND CURRENT RETURN N

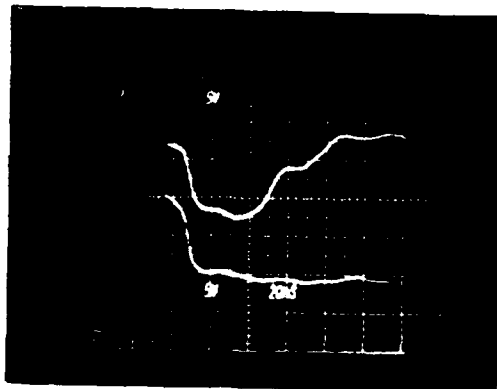


FIGURE 6
PFL RESPONSE WITH SINGLE GAP TUBE
UPPER: CATHODE RETURN CURRENT UNCALIBRATED
LOWER: ANODE VOLTAGE, 5 kV/MINOR DIV.
HORIZONTAL: 20 ns/MINOR DIV.

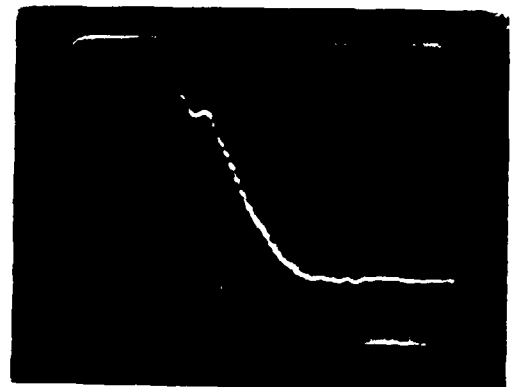
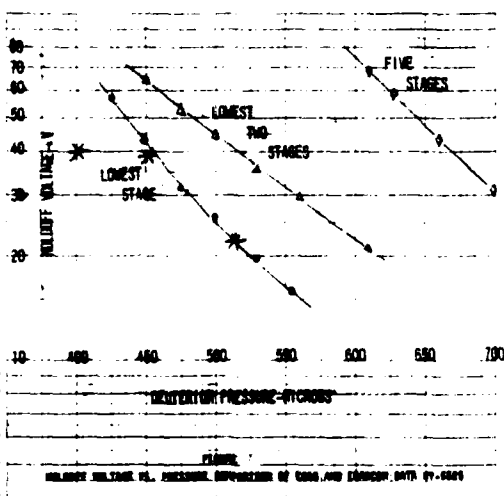


FIGURE 8
ANODE FALL WAVEFORM OF HY-5525,
ALL FIVE GAPS ACTIVE,
32 kV PEAK ANODE VOLTAGE
400 μ GAS PRESSURE
FALL TIME = 20 ns

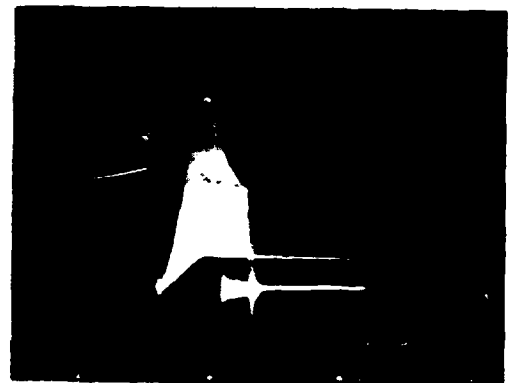


FIGURE 9
FIRE/PREFIRE ENVELOPE TWO GAPS OF HY-5525
VERTICAL: 2.44 kV/MINOR DIV.
HORIZONTAL: 1 μ s/MINOR DIV.

**EXPERIMENTAL HIGH VOLTAGE, LOW
INDUCTANCE HYDROGEN THYRATRON —
HY-5525**

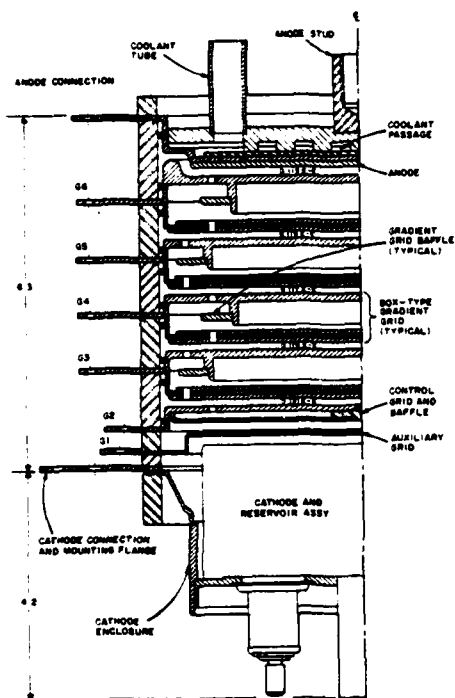


FIGURE 1
CUTAWAY OF HY-5525



FIGURE 2
HY-5525

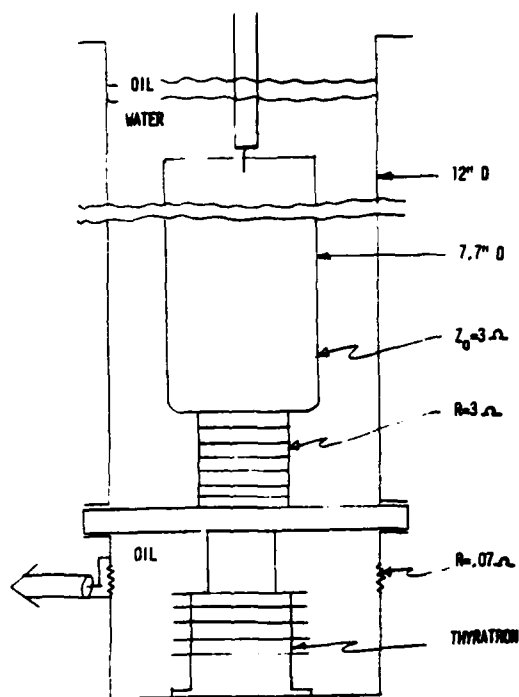


FIGURE 3
CUTAWAY VIEW OF PFL, LOAD, THYRATRON & CVR

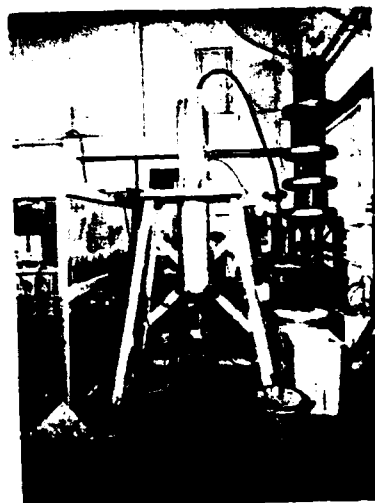


FIGURE 4
PFL AND SOCKET IN SUPPORT GANTRY

MULTIPLE PULSE ELECTRON-BEAM CONTROLLED SWITCH

V.E. Scherrer, R.J. Comisso+,
R.F. Fernsler+, and I.M. Vitkovitsky

Naval Research Laboratory
Washington, DC 20375

Summary

The electron-beam (e-beam) controlled switch is a promising opening switch candidate¹ for inductive storage pulsed power applications where repetitively pulsed (> 1 kHz) output power of $\sim 10^{10}$ W is required. Several authors¹⁻¹¹ have reported theoretical analysis and experimental results for e-beam controlled switches. The development of this switch requires a number of experiments to be performed to determine the gas conductivity, rate of change of conductivity, switch efficiency, and the effects of energy deposition in the gas on the switch recovery. Such experiments, which would establish the feasibility of the e-beam switch for high power applications, are being carried out with simple gas mixtures over a range of ambient gas pressures and electron beam current densities. Comparisons are made between experiment and theory^{1,2} to understand the basic mechanisms involved in switch operation. Single pulse experiments are also used to provide a data base for establishing the repetitive capability of the switch. A typical design goal involves charging of a storage inductor over a period of several microseconds, voltage and current levels at the load of 200-500 kV and 10-100 kA, with a pulse-to-pulse separation of ~ 100 μ sec. Initial experiments characterizing the performance of a second pulse have been carried out.

E-Beam Switch Concept

The principles of an e-beam controlled switch for repetitive operation are discussed in Ref.(1). An inductive storage system using an e-beam controlled switch to generate a pulsed high power output is shown schematically in Fig. (1). When the e-beam is turned on, the switch resistance drops to a low value, resulting in energy transfer from the source W_0 to the inductor L . When the e-beam is turned off (and SW-2 is closed) the switch resistance becomes large and switch current is

shunted to the load R_L . After the pulse, SW-2 opens and the process is repeated for a second pulse by making the e-beam switch conduct again. The switch SW-2 is generally not required except for specific applications. The most significant problem associated with the use of such a switch is the energy loss by joule heating in the switch. To minimize this heating, the switch resistance must be as low as possible while the switch is conducting. Such heating can also lead to late time breakdown making repetitive pulse operation impossible. On the other hand, this switch promises to provide a repetitive opening capability with a very fast fall time of the switch current. Potentially, the opening time of the switch can be substantially faster than that achieved with fuse arrays.

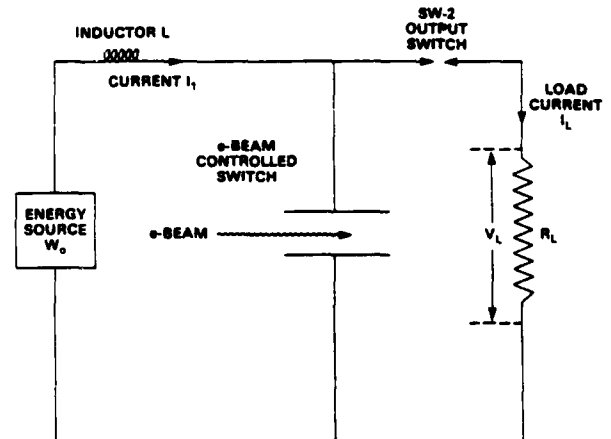


Figure 1. Schematic of an inductively driven pulser using an e-beam controlled switch.

A measure of the switch performance that determines how practical such a switch can be is the current gain, ϵ . It is defined as the ratio $(\bar{i}_n - \bar{i}_e)/\bar{i}_e$, where \bar{i}_n is the total current flowing in the switch, \bar{i}_e is the injected e-beam current, and the bar indicates peak values. A current gain

of at least 10 is considered necessary for a practical system.¹

Theoretical predictions¹ indicate that the resistivity ρ , switch current fall time, τ_p , and current gain ϵ depend on the ambient gas pressure. Limiting values of pressure depend upon the properties of the thin window between the evacuated ($\sim 10^{-5}$ Torr) e-beam diode and the high pressure ($\sim 10^3$ Torr) switch, electron energy requirements, and the strength of the switch chamber. A switch pressure of 10 atm appears feasible.

The upper limit of current density that can be switched in the repetitive pulse mode depends on energy deposition in the switch by joule heating. Excessive energy deposition is manifested in delayed breakdowns¹² which would preclude multiple pulse operation, as discussed later in detail.

Description of the Experiment

The experiment, shown schematically in Fig. (3), contains three principal parts: a high voltage pulser, consisting of a low voltage (< 10 kV) source and a pulse-forming network; an e-beam diode; and a gas cell test chamber. In the pulser,¹³ a 20 kA current

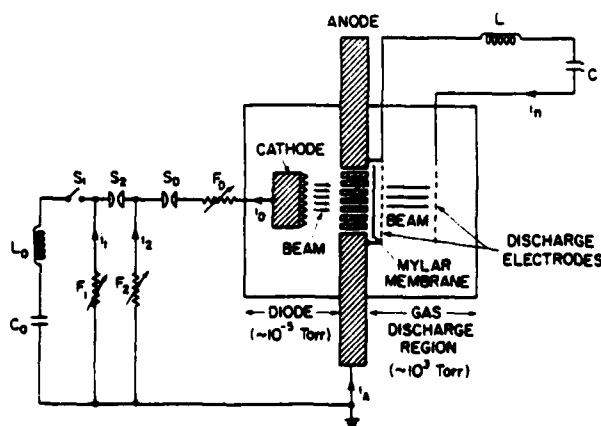


Figure 2 Schematic of the experiment

source charges an inductive store, with exploding wire fuses F_1 and F_2 serving as opening switches

that produce a 200 ns (FWHM), 200 kV pulse across the diode. The fuse F_0 is chosen to open after 200 ns, limiting plasma generation in the diode. Two pulse-forming networks can be coupled to the diode for double-pulse studies of the e-beam switch.¹³ The test chamber is isolated from the diode by a 0.005-cm mylar window and is normally filled with a mixture of two gases at a pressure of 1-3 atm. The resistance of the cell during discharge is determined by measuring the current through and voltage across it. The circuit voltage is sustained by the capacitor C. The circuit is described by:

$$V_0 = R(i_n - i_e) + L \frac{di_n}{dt} + \frac{1}{C} \int i_n dt, \quad (1)$$

where R is the switch resistance, V_0 is the initial voltage on capacitor C, and L is the circuit inductance. We can neglect the last term in Eq.(1) ($< 5\%$ correction). At the time of peak i_n (i.e. when $di_n/dt = 0$) the switch resistance is

$$R_0 = \frac{V_0}{i_n - i_e}. \quad (2)$$

The resistivity at peak net current, ρ_0 , is related to R_0 through the switch geometry. The fall time of the current through the switch is estimated from

$$\tau_F^* = \frac{L}{|V_2|} \bar{i}_n, \quad (3)$$

where V_2 is the transient voltage peak associated with the rise and fall of switch current and is indicated in Fig. (3).

The diagnostics used in the experiment include calibrated Rogowski loops and voltage dividers for measuring the diode voltage and current, V_D and i_D respectively; and the voltage across and net current through the discharge, V_d and i_n respectively. Blue cellophane and film techniques were used to verify the time integrated beam uniformity.

Single-Pulse Experimental Data

For the switch concept that we have described, the following parameters are important: current gain, resistivity, switch current fall time and recovery characteristics. Also of importance is the effect of energy deposition on these parameters. Switch performance is expected to improve as the pressure is increased. Therefore, the experiments were focused on the accumulation of data to determine how ρ , τ_p^* , and ϵ vary with gas composition and pressure. These measurements are also necessary to understand the basic physical processes involved in the switch and to provide input for theoretical analysis and scaling. We report primarily results for O_2 - N_2 mixtures because the atomic and molecular data are better established than for other gas mixtures.

An example of results for one discharge of the switch using a 20% O_2 -80% N_2 mixture at 1 atm pressure, is shown in Fig. (3). The incident e-beam current density, j_e , was 24 A/cm^2 . The top two traces show diode voltage, V_D , and current i_D , while the inferred e-beam current into the switch, i_e , is in the bottom section of the figure. The difference in decay time between i_D and i_e is due to plasma formation in the diode and the energy dependent transmission of electrons through the mylar window. Plasma current through the switch, $i_p = i_n - i_e$, and voltage across it, V_d , are shown in the center two traces. ρ is plotted as a function of time in the bottom section. The fast fall, low minimum resistivity ($\sim 30 \text{ }\Omega\text{-cm}$) followed by a fast rise, result in good switching performance.

The quantities ρ_0 , τ_p^* and ϵ are plotted as a function of percent O_2 in N_2 in Fig. (4) for j_e in the range 2.5 - 6.7 A/cm^2 . Shown also for reference are the beam rise and fall times, τ_R^B and τ_F^B . The gas pressure was 1 atm. The results indicate that O_2 concentrations of 10-20% yield resistivities of 200 - $300 \text{ }\Omega\text{-cm}$, a current gain over 10, and τ_p^* about equal to that of the e-beam. E/P , where E is the applied electric field and P is ambient gas pressure, was 10.5 V/cm-Torr in this case. No late-time electrical breakdown was observed.

The scaling of ρ_0 and ϵ with electron beam current density is illustrated in Fig (5). A ρ_0 as small as $20 \text{ }\Omega\text{-cm}$ is observed, but at the sacrifice

of current gain. These plots are the result of varying j_e over a wide range, using the same 20% O_2 - 80% N_2 mixture discussed earlier. The data in Fig. (5), demonstrate that j_e must be below 10 A/cm^2 to approach $\epsilon = 10$ for this gas mixture at $P = 1 \text{ atm}$.

Fig. (6) illustrates the effect on the net current in the discharge when the pressure is increased from 1 atm to 3 atm for a 20% O_2 concentration in N_2 , and $E/P = 10.5 \text{ V/cm-Torr}$.

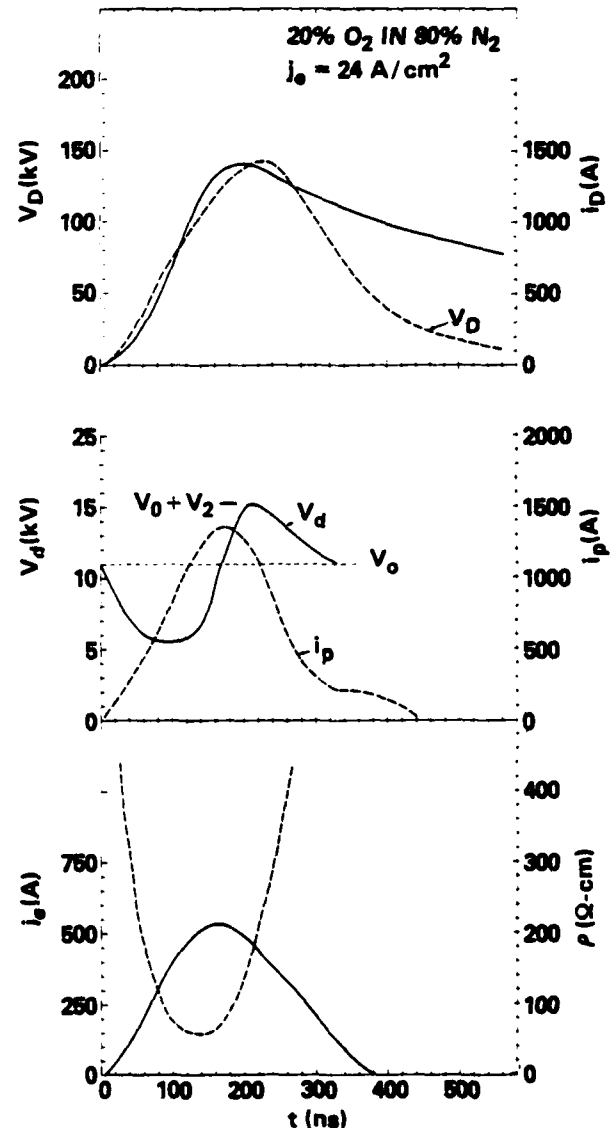


Figure 3. An example of measurements made on a single shot.

The input e-beam current was the same in both cases.

An illustration of how ρ_0 changes with pressure is shown in Fig. (7) where ρ_0 is plotted against P with constant $E/P = 10.5$ V/cm-Torr and $j_e = 5.0 \pm 0.3$ A/cm². The data show that for O₂ concentrations up to 20%, ρ_0 changes little with pressure. This is most likely because the duration

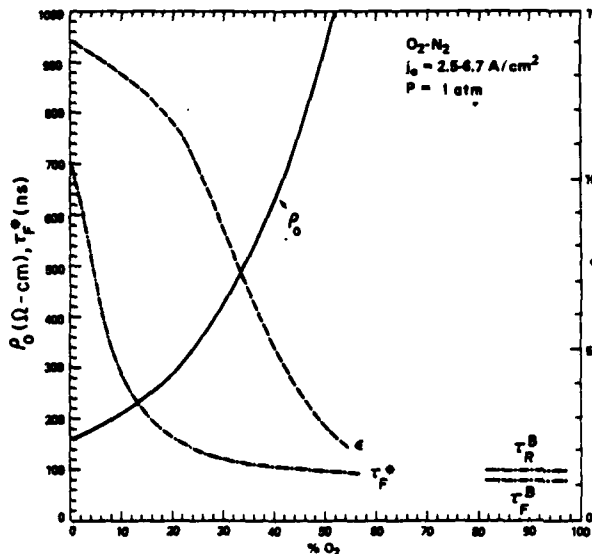


Figure 4. Dependence of ρ_0 , τ_p^* , and ϵ for various percentages of O₂-N₂.

of the e-beam pulse is too short for the discharge to reach equilibrium at the lower percentages of the attaching gas, as explained in what follows.

ρ_0 changes substantially with P for higher concentrations. In Fig. (8) τ_p^* is plotted versus P for O₂ concentrations of 10, 20, and 50% in N₂. E/P was 10.5 V/cm-Torr; j_e was 5.0 ± 0.3 A/cm².

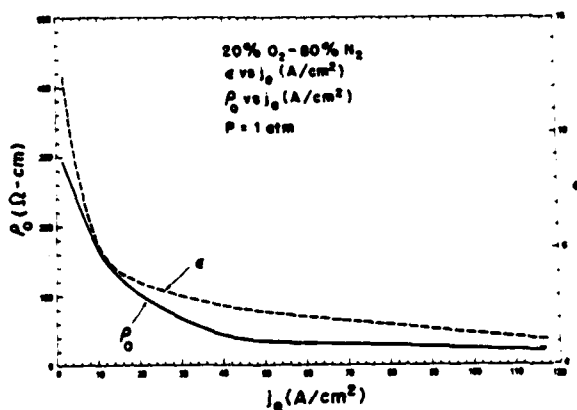


Figure 5. Illustration of change in resistivity, ρ_0 , and current gain, ϵ , as a function of beam current density, j_e .

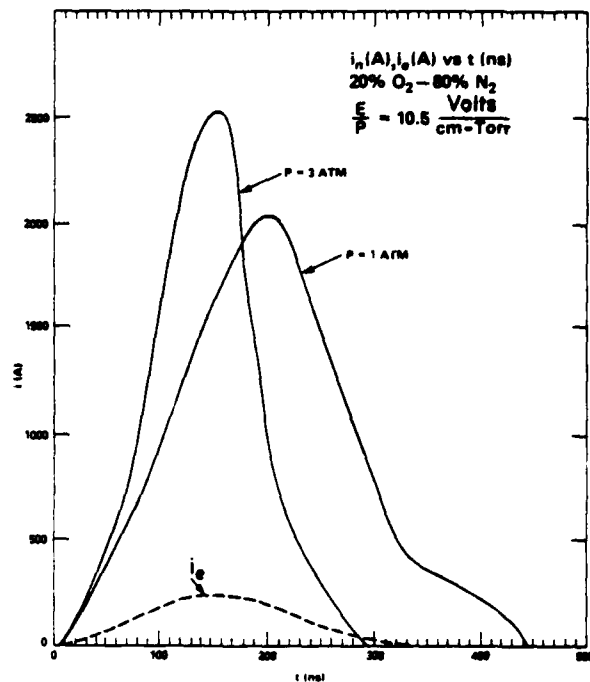


Figure 6. Effect of ambient gas pressure on switch current time history.

We illustrate the dependence of current gain on pressure with the data presented in Fig. (9) for 5% O₂ in N₂. E/P was 10.5 V/cm-Torr and j_e was 5.0 ± 0.3 A/cm² as before. ϵ increases from 7.6 to 11.8 when pressure is increased from 1 to 3 atm.

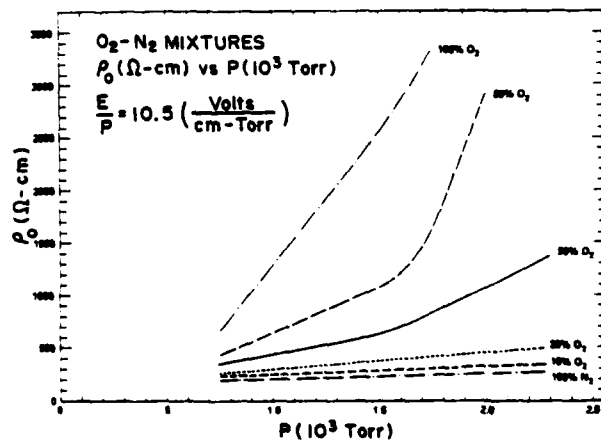


Figure 7. Effect of ambient switch pressure on ρ_0 .

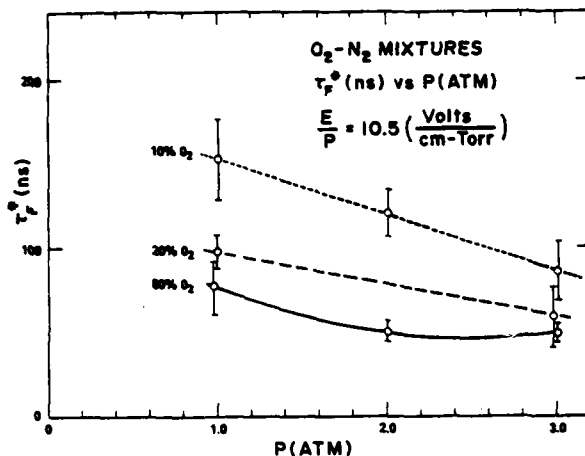


Figure 8. Effect of ambient switch pressure on τ_p^* .

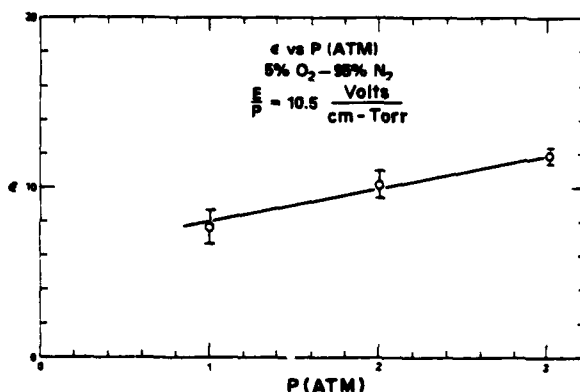


Figure 9. Effect of ambient switch pressure on current gain.

As Figs. (4)-(9) indicate, trade-offs exist between obtaining low resistivity ρ_o , short fall times, τ_p^* , and high current gains, ϵ . These trade-offs can be understood by expressing the continuity equation for the discharge plasma electron density, n_p , as

$$\frac{\partial n_p}{\partial t} = S j_e P - n_p \tau_f^{-1} \quad (4)$$

where the beam ionization parameter S depends on the α -beam energy and gas composition and where

τ_f^{-1} characterizes the discharge plasma electron loss rate. The switch resistivity is given by

$$\rho = (en_p \mu)^{-1} \quad (5)$$

where μ is the electron mobility. Minimum resistivity, ρ_{\min} , is attained when the left-hand side of Eq. (4) goes to zero. This yields upon substitution in Eq. (5)

$$\rho_{\min} \tau_f = (e S j_e \mu)^{-1} = \frac{f(E/P)}{j_e} \quad (6)$$

where the product (μj_e) is a function of gas composition and the field parameter E/P . Expressing the switch plasma current density as

$$j_p = E/\rho_{\min} \quad (7)$$

leads to

$$\epsilon_{\min} = \frac{P}{j_e} f(E/P) \quad (8)$$

and

$$\frac{\epsilon}{\tau_f} = P \frac{E/P}{f(E/P)} \quad (9)$$

where switch current gain $\epsilon = j_p/j_e$. Breakdown limitations constrain the field parameter to $E/P \leq 10$ V/cm-Torr.

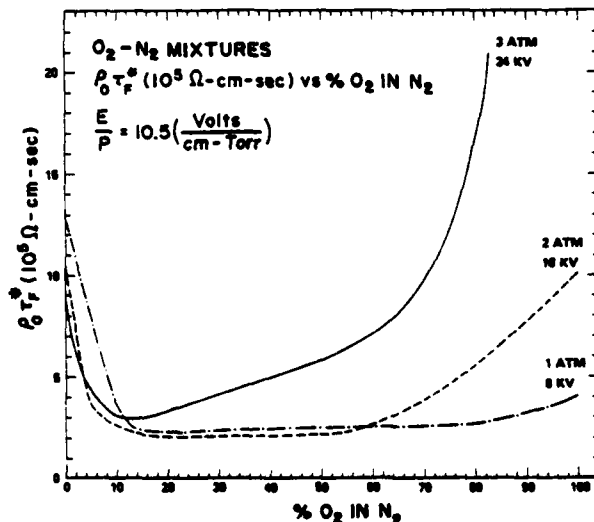


Figure 10. Effect of varying percent O_2 in N_2 and gas pressure on the product $(\rho_o \tau_p^*)$.

Eqs. (6), (8), and (9) describe the qualitative behavior of e-beam controlled switches. These scaling relationships are valid, however, only if the e-beam pulse persists for a time longer than τ_p and shuts off in a time shorter than τ_p . The impact of this restriction can be seen by contrasting Eq. (6) with Fig. (10), in which the product $\rho_0 \tau_p^*$ is plotted for three different gas pressures as a function of O_2 concentration. Since electron mobility in N_2 and O_2 is similar, Eq. (6) predicts that $\rho_{\min} \tau_p$ is nearly constant independent of gas pressure, P , or O_2 concentration. At low concentrations of the attaching gas O_2 , τ_p becomes long compared with the beam duration, and hence ρ_0 never reaches ρ_{\min} . Similarly, at high concentrations and/or high pressures, τ_p becomes smaller than the beam fall time; as a result the estimated switch fall time, τ_p^* , approaches the beam fall time rather than τ_p . This effect is also seen in the data in Fig. (4), where τ_p^* approaches τ_p^B at high O_2 concentrations.

Late-Time Breakdown

One possible failure mode for the e-beam switch when operated repetitively is breakdown involving a self-sustaining arc from which the switch could not recover. We observe that in some cases breakdowns do occur late in time, well after the e-beam has been turned off. This phenomena is described with the aid of Figs. (11) and (12).

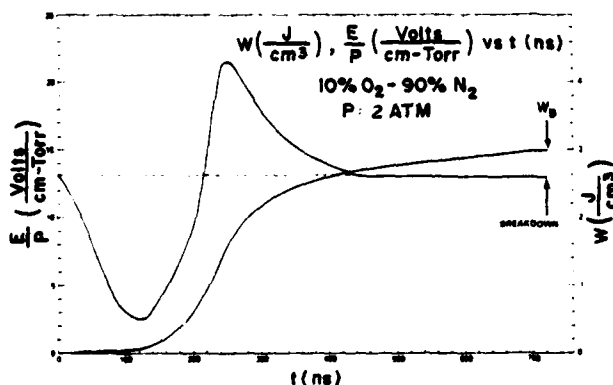


Figure 11. Plot of E/P and energy absorbed by the switch gas, as a function of time.

In one curve of Fig. (11) the parameter E/P is plotted versus time, beginning with the ambient $E/P = 13$ V/cm-Torr. E/P decreases, during the rise of current in the switch, to a minimum of 2.5 V/cm-Torr. It then reverses, crosses the ambient line and peaks at 21.5 V/cm-Torr, before declining to the ambient of 13 V/cm-Torr at 440 ns. At a much later time, 720 ns, the switch breaks down discharging the system. The second curve is a plot of resistive energy deposited in the switch per unit volume, W . At the time of breakdown, W attains a value of W_B . The occurrence of breakdown at late times, i.e., long after E/P peaks, suggests that breakdown is influenced more by deposited energy than transient E/P .

This effect is seen in Fig. 12 in which a plot of W_B as a function of P for $E/P = 11$ V/cm-Torr is shown for air and for a mixture of 10% O_2 in N_2 .

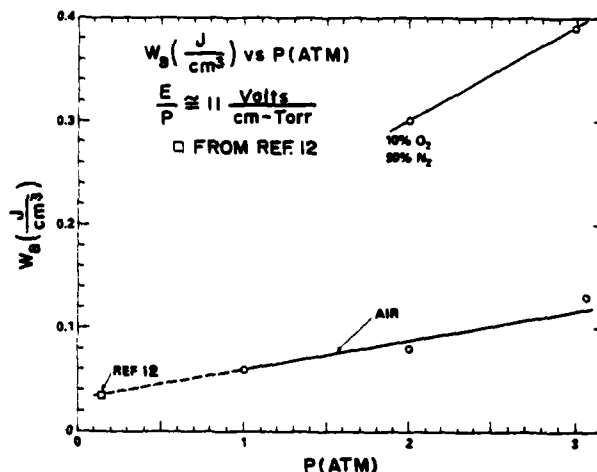


Figure 12. Breakdown energy per unit volume for 10% O_2 in N_2 and air.

Shown also on the curve is one point from Ref. 12 obtained in an experiment where $P = 0.13$ atm. This point lies on a straight line extension of our data. The exact mechanisms responsible for late time breakdown will require further study.

Double-Pulse Experiments

Some of the problems associated with repetitive

operation were investigated in a double-pulse experiment. The principal objective was to confirm that switch characteristics are the same for the two pulses. The circuit of Fig. (2) was used with two pulse forming networks.¹³ The second pulse was coupled through a solid dielectric explosive switch. Two pulses, separated by 300 μ -sec, were applied to the e-beam diode to produce two distinct successive ionizations of the switch gas. The switch was filled with 50% CO₂-50% Ar with P = 1 atm and E/P = 10.5 V/cm-Torr. The current and voltage diagnostics described previously were used to observe switch performance. The switch was observed to turn on and off with approximately the same characteristics for both pulses. These observations indicate that the switch can be turned on and off at least twice. We expect similar results for pulse trains, but emphasize the importance of energy deposition limits on late time breakdown.

Conclusions

We have presented a concept for a repetitive e-beam switch and supported it by experimental data. The data indicate that an optimum balance between several contradictory requirements may be realized by proper choice of gas mixture and operating pressure. We expect to continue this research effort by: 1) studying the effects of increasing pressure on critical parameters, 2) studying the effect of energy deposition on pulse-train switch operation, 3) seeking optimum gas mixtures, and 4) obtaining a switch conduction time of 1 μ sec.

We wish to acknowledge the expert support of H. Hall, L. Miles and J.M. Cameron in obtaining the data. This work was supported by the Naval Surface Weapons Center, Dahlgren, Va. and Office of Naval Research, Arlington, Va.

+JAYCOR Inc., Alexandria, VA. 22304

References

1. R.F. Farnsler, D. Conte and I.M. Vitkovitsky,

IEEE Trans. Plasma Sci. PS-8, 176 (1980).

2. R.J. Comisso, R.F. Farnsler, V.E. Scherrer, and I.M. Vitkovitsky, accepted for publication, IEEE Trans. Plasma Sci., Special Issue on Plasma Switches (1982).

3. P. Bletzinger, Proc. of Workshop on Repetitive Opening Switches, Tamarron, Colorado, Texas, Tech. Univ. Report (April 1981), pp. 128.

4. V.E. Scherrer, R.J. Comisso, R.F. Farnsler, L. Miles and I.M. Vitkovitsky, Third International Symposium on Gaseous Dielectrics, Knoxville, Tenn. Mar. 7-11, 1982.

5. R.O. Hunter, Proc. IEEE First Int. Pulsed Power Conf., Lubbock, TX (1976), ICS:1-6.

6. J.P. O'Loughlin, Proc. IEEE First Int. Pulsed Power Conf., Lubbock, TX (1976), IIIC5:1-6.

7. B.M. Kovalchuk and G.A. Mesyats, Sov. Tech. Phys. Lett., 2, 252 (1976).

8. K. McDonald, et. al., IEEE Trans. Plasma Sci., PS-8, 181 (1980).

9. Lawrence E. Kline, Proc. of Workshop on Repetitive Opening Switches, Tamarron, Colorado, Texas Tech University Rept. (April 1981), pg 121.

10. R.F. Farnsler, A.W. Ali, J.R. Greig, and I.M. Vitkovitsky, Naval Research Lab Memo Report 4110, (1979).

11. J.W. Dzimianski and L.E. Kline, Westinghouse Electric Corp. Report DYD-555-85-AA, (1979).

12. S.A. Genkin, Yu. D. Kosolev, V.G. Rabothin, and A.P. Khuziv. Sov. J. Plasma Physics 7(3), 327, 1981.

13. B. Fell, R.J. Comisso, V.E. Scherrer, and I.M. Vitkovitsky, J. Appl. Phys. 53, 2818 (1982).

A PRELIMINARY STUDY OF THE BREAKDOWN MECHANISM OF SURFACE DISCHARGE SWITCHES

S. T. Pai and J. P. Marton
Opto-Electronics Ltd.
Oakville, Ont. Canada L6L 5K9

SUMMARY

The breakdown mechanism of multichannel surface discharge switches were studied experimentally and theoretically. Experiments have been carried out using N_2 and other gases at pressures ranging from one to five atmospheres. Several different dielectric materials were used as substrates, having plain and cylindrical surface geometries. The observed results were interpreted by a physical model which was developed for this purpose. In the model, the major physical processes, i.e. electron production, electron loss and diffusion, were treated in the presence of the dielectric surface. In addition, electron losses due to electron traps on the dielectric surface has also been taken into consideration. The model yields an analytical expression for the breakdown voltage of a given surface spark gap. For the cases studied, the model predictions fit the observed results reasonably well. Based on the information obtained from this study, several prototypes of pulse charged multichannel surface switches were constructed. Because of their multichannel character, the inductance of these switches is considerably lower than that of single channel switches. The holdoff voltage of the prototypes ranged up to 200 kV under 500 ns risetime pulsed voltage conditions. The lifetime was found to be in excess of 10 million shots at 6 mC per shot, which represents a total charge transfer of over 60 thousand Coulombs.

1. Introduction

As demands for switches which are capable of switching large currents with fast risetime have been steadily growing, workers in the field of high power pulse technology have been looking at multichannel switches as one of the possible devices that can meet this demand.

Multichannel railgap switches have been well studied and widely used in high power pulse field in recent years.¹⁻⁵ Their performance, however, have indicated that such switches usually require high voltage fast trigger pulses to initiate multichannel breakdown. These switches also have difficulty achieving subnanosecond current jitter. On the other hand, recent work has demonstrated that subnanosecond jitter is readily achievable by Multichannel Surface Discharge Switches without fast risetime high voltage trigger pulses.⁶⁻⁷

The use of Multichannel Surface Discharge Switches in the high power pulse field was first reported in 1977. Since then a fair amount of research and development work has been carried out by many institutions and industries.⁸⁻¹¹ A common shortcoming associated with such switches in the past has been substrate and electrode erosion, which limited the useful life to 10^3 - 10^4 shots at high power. Various

attempts have been made by investigators to deal with this problem. One of the common approaches has been to select the best dielectric material by trial and error, which on the one hand caused multichanneling and on the other withstood the very high plasma channel temperatures without significant deterioration. Although some improvements have been achieved by this approach, long life of surface switches could still not be made reliably.

It has been suggested that further improvements in the lifetime of these switches may be made by separating the substrate from the electrodes sufficiently far enough to reduce the plasma erosion of the surface significantly. The problem found with this approach was that it effected the multichannel performance of the switch in unpredictable ways. The unpredictability stemmed from the lack of knowledge about the effect of surfaces on plasma channel discharges. Prior to the work carried out in our laboratory, there could be no information found about the role a dielectric surface played in a discharge, as to how the substrate effected the breakdown voltage, or how it helped channel formation in a high electric field. The present work is part of a continuing effort in our laboratory to gain basic understanding of the relationship between the dielectric surface and the performance of a Multichannel Surface Discharge Switch. The final goal of this work is to design a variety of practical, long lifetime fast switches with optimum performance and characteristics.

2. The Effect of A Surface on Breakdown Voltages

The influence of the dielectric surface on the performance of surface discharge switches were experimentally tested on the basis of the physical model proposed recently.¹² According to the model, the basic effect of a dielectric surface is to enhance the charge density in the gap. The effect may be described in terms of two competing factors. One is the volumetric effect and the other is the diffusion effect. The mathematical expression describing the charge density in terms of these effects is in the form of

$$n = \frac{G}{R^2} J_0 \left(\frac{2.405r}{R} \right) \exp\left(-\frac{t-t_0}{\tau}\right) + n_0 \quad (1)$$

In the expression, n is the charge density in the gas between the electrodes, R is the distance between the surface and electrodes, G and n_0 are constants and may be determined experimentally, J_0 is the zero order Bessel function, r is the spatial coordinate, t is the time after the field is switched on, t_0 is the time at which the surface charge density on the dielectric reaches its saturated value n_0 , τ is a time constant and

is defined by

$$\frac{1}{\tau} = f_c - \left(\frac{2.405}{R}\right)^2 D. \quad (2)$$

In (2) f_c is the net rate of electron production and D is the electron diffusion coefficient. Both are assumed to be constant.

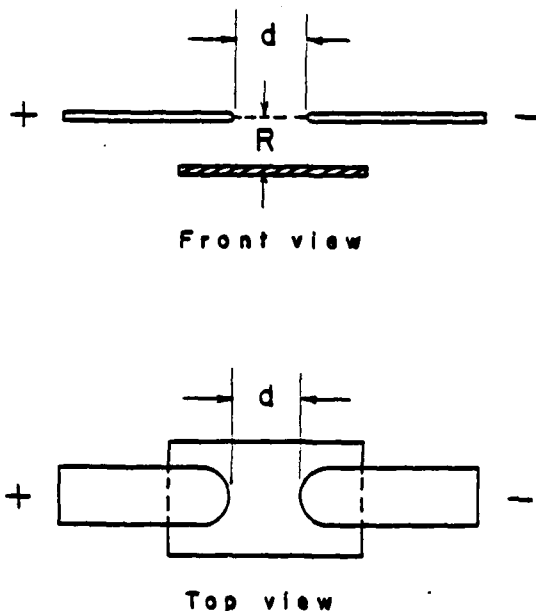


Figure 1 Schematic diagram of typical experimental setup showing the electrodes and the substrate.

For an experimental setup similar to that shown in Figure 1, expression (1), predicts that, as the distance R between the surface and the electrodes increases, the effective volume R^2 appearing in the denominator of the first term also increases hence the charge density decreases. At the same time, as R increases the exponential term increases, which increases the charge density as a result of the increased electron diffusion length. The net result is shown in Figure 2. From the figure we can see that at $R=R_m$ the charge density is maximum.

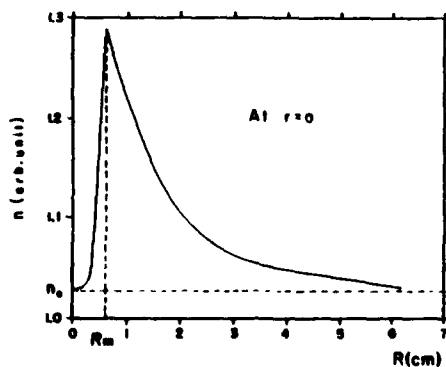


Figure 2 Charge density as a function of substrate distance.

The second expression obtained from the model gives the breakdown voltage of a given surface spark gap in terms of the distance R and other variables. Its analytical form is

$$V_B = a \left[\frac{G}{R^2} J_0 \left(\frac{2.405r}{R} \right) \exp\left(-\frac{t-t_0}{\tau} + n_0 \right) \right]^{-1} \quad (3)$$

where a is a constant to be determined experimentally. Equation (3) is plotted in Figure 3. The solid curve is calculated from Equation (3) while the open circles are the experimental results. The experiments were carried out under atmospheric pressure of dry air using a set-up shown in Figure 1. The substrate was quartz. The voltage was increased slowly until breakdown occurred. The breakdown voltages were measured at various values of R while all other conditions were kept constant.

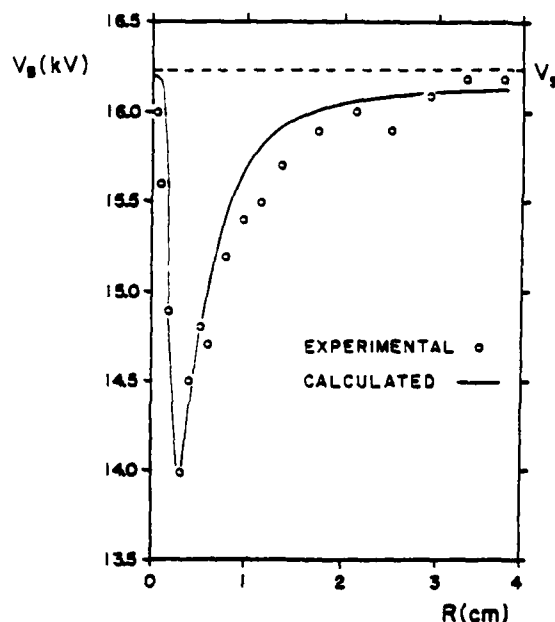


Figure 3 Breakdown voltage as a function of substrate distance for quartz substrate.

From this result, we can see that as the value of R increases from zero, the breakdown voltage decreases, reaches minimum at $R=R_m$, then it increases. At large or very small values of R , the breakdown voltage approaches the static breakdown voltage V_s . It is quite clear that the general effect of the dielectric surface on the spark gap is to lower its breakdown voltage. The extent of the lowering depends on the electrode-substrate distance, reaching its peak value at $R=R_m$.

3. Multichanneling

Investigation of multichannel behaviour of the surface discharge switch were carried out under pulse charged conditions. The schematic diagram of the experimental set-up is shown in Figure 4. In the experiments, voltage pulses were formed by discharging the storage capacitor C through the pulse

forming network. The rate of rise of the impulsing voltages at the surface discharge switch ranged from 0.1 kV/ns to 0.3 kV/ns with a maximum peak value of 68 kV. The switch was filled with gases of N_2 , SF_6 and air at pressures ranging from 0 to 30 PSIG.

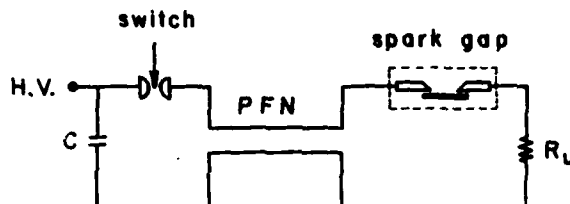


Figure 4 Schematic diagram of the pulse charged switch experiment.

Under pulse charged condition it was found that the total number of plasma channels in a given surface discharge switch could be approximately expressed by

$$N = \frac{A}{a} \left\{ \tan^{-1} \left[\frac{S_r \Delta t}{a} \right] + \frac{2d^2 S_r}{\mu V_s} \frac{1}{2} + \tan \left(\frac{a}{A} - \frac{\pi}{2} \right) \right\} + \frac{\pi}{2} \quad (4)$$

In the expression, A and a are parameters which may be determined experimentally, S_r is the rate of voltage rise and is assumed to be a constant for a given voltage pulse, Δt is defined as

$$\Delta t = B(t_i - t_r) \quad (5)$$

here t_i and t_r are risetimes of the current and voltage pulses respectively and B is a proportionality constant. μ is the electron mobility.

An inspection of (4), shows that the number of channels is closely related to the static breakdown voltage V_s . As V_s decreases, the number of channels increases. From the foregoing, we saw that the general effect of a dielectric surface in a gas spark gap is to lower the static breakdown voltage, therefore it follows that the effect of the dielectric surface is also to increase the number of channels. Now, as V_s is closely related to R , in order to achieve the optimum number of channels in a surface discharge switch, a proper electrode-substrate separation is crucial.

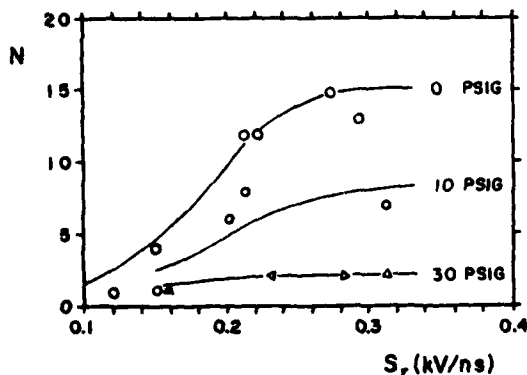


Figure 5 The number of channels as a function of voltage risetime.

The number of channels as a function of the voltage pulse risetime is plotted in Figure 5, and the same number of channels as a function of the static breakdown is plotted in Figure 6. The values of A , a and t were determined experimentally. In Figure 5, the solid curves are calculated from Equation (4) and the symbols are the experimental results.

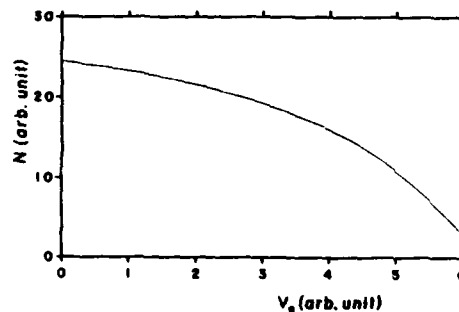


Figure 6 The number of channels as a function of the static breakdown.

4. Surface Deterioration

Surface deterioration tests were carried out with impulsing voltage pulses. The experimental set-up is similar to that shown in Figure 4. Dielectric materials of pc board, ceramics, quartz, teflon and cermet were tested respectively under identical conditions of 10,000 shots, 10 oscillations per shot, 200 Joules per oscillation and with $R=0$, i.e. the substrates were in contact with the electrodes. The total charge switched during these experiments for each substrate was $2 \times 10^7 J$. The electrodes used were brass with an edge radius of 3 mm and the conditions of the tests were $P=15$ PSIG of N_2 , $V_0=62$ kV, $R_L=1\Omega$, $d=1.25$ cm. Optical microscopy and electron optical analysis have been made on all substrates studied. Some typical results are shown in the following figures.

In Figure 7, a PC board substrate is shown after 10,000 shots with its own clad Cu electrodes. The low magnification picture is optical and the other three are SEM pictures. There are light and dark areas visible on the substrate along the length of the switch which is typical of all substrates used. The dark area corresponds to heavy discontinuous material deposition which was x-ray analysed in the SEM. The analysis showed the elements Cu, Si, Ca and Al. The darker areas appear to be eroded more than the light ones. The effect is shown in the two low mag. SEM pictures, where the glass fiber fabric is shown exposed for the dark area and less exposed for the light area. The former picture also shows the heavily damaged anode. The damage appears

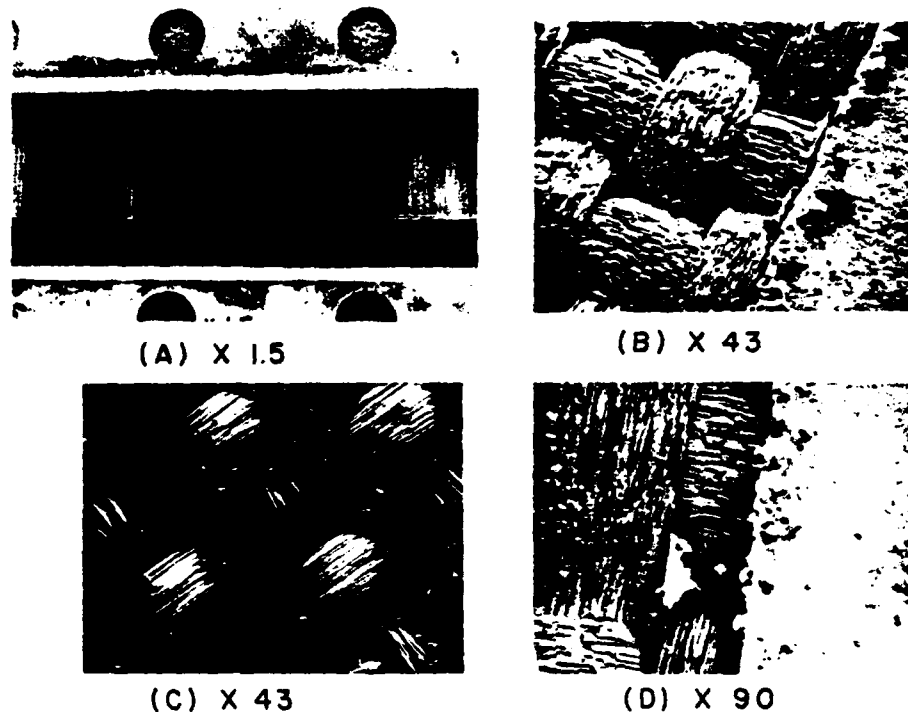


Figure 7 A printed circuit board substrate after 10,000 shots.
(A) Optical picture, (B) (C) (D) SEM pictures

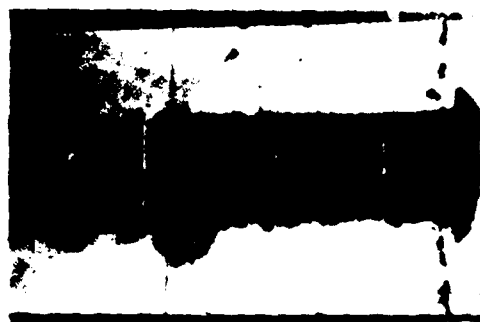
to be caused by melting. The erosion of the glass fibers is also visible in the higher mag. SEM picture. Here the upper strands appear to be broken. The missing parts have likely been either melted and evaporated or have been sputtered by the hot plasma column.

In Figure 8 a ceramic substrate is shown after 10,000 shots in a similar fashion as that of the PC board. Here the electrodes were brass and are not part of the picture. The white vertical lines in the optical picture are breaks which were caused by demounting the substrate from its holder. The cathode and anode positions are marked. Here again light and dark areas are seen. The dark areas were analysed to contain Cu, Zn, Al and Si. The light areas contained Al and Si only. The light areas also appear to contain partially melted substrate material. This is seen in the x80 picture. A closer inspection of this also reveals cooling cracks in the molten region. The x800 image shows part of the molten zone. The fingerlike objects were analysed to contain Al and Si only. The small spheres in the x43 picture, located outside the plasma track were analysed to be Cu and Zn. They form a discontinuous layer from electrode to electrode. It has also been observed during life testing that the light and dark areas shift with time, i.e. the line containing electrode metal deposit at one time may be eroded down to the substrate some few minutes later. During the same time some light areas may change to dark.

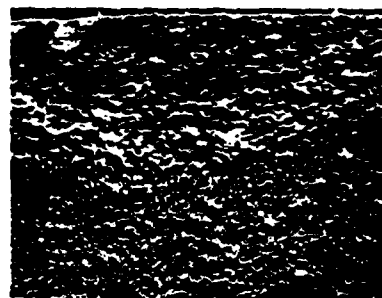
In Figure 9 a cermet layer of approximately 50 micrometers thick is covering an alumina substrate. The composition of the layer is SnO_2 and borosilicate glass. The damage after 10,000 shots is quite similar to that seen in Figure 8 for bare ceramic. Here again the breaks have been caused by demounting. In the x16 image, erosion of the sintered oxide layer down to the bare substrate is visible. The x80 picture shows metal particle deposition on the right hand side (dark area) and its absence in the left hand side. The SEM analysis this time showed the elements of Cu, Zn, Sn, Al and Si as expected. The x90 picture shows two merged eroded channels terminating at the anode (bottom). The heavy roughness outside the channel region was determined to be electrode material.

Quartz and teflon showed quite similar features to the others shown here, except that on quartz the electrode metal deposition was more pronounced than of the teflon. This is not surprising, as a quartz surface has a high affinity to metal vapors while that of teflon is nearly zero. Also, teflon eroded much more than quartz.

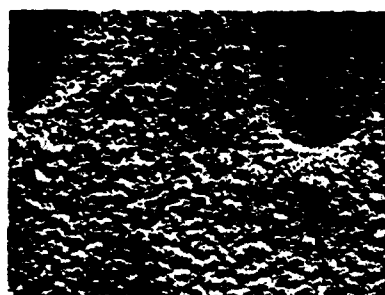
The general observation from experiments is that during channeling, there are two simultaneous processes taking place. One is the deposition of electrode metal on the substrate, which forms a dark coating on the substrate and the second is the removal of the substrate surface which cleans the metal deposit from it. Performance of the switch can thus deteriorate in two ways. One is when the rate of electrode material deposition is greater



(A) X 1.5



(B) X 80



(C) X 43

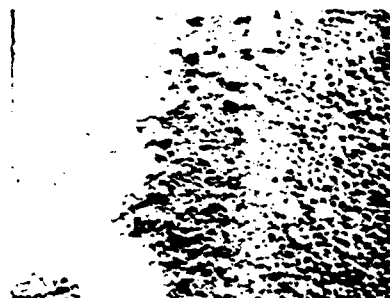


(D) X 800

Figure 8 Ceramic substrate after 10,000 shots showing molten regions and electrode metal deposits on the surface (A) optical picture (B) (C) (D) SEM pictures.



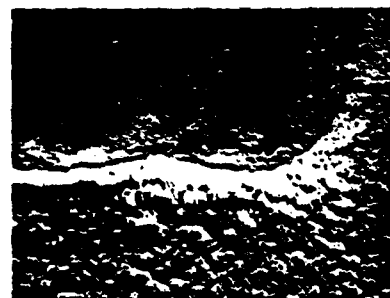
(A) X 1.5



(B) X 80



(C) X 16



(D) X 90

Figure 9 Cermet substrate (50μ thick on ceramic) after 10,000 shots showing features similar to those of Figure 8. (A) Optical picture (B) (C) (D) SEM pictures.

than the substrate surface erosion which leads to short circuit (short circuit resistance of several megohms). The other is the excessive depth of erosion of the substrate, which in itself would not be detrimental, but because it is not generally uniform along the length of the MSG, it leads to nonuniform channeling.

Another observation is that when substrates are in contact with the electrodes, there is an excessive amount of material loss from the surface of the substrate, but when they are removed to a distance of a few millimeters, the erosion decreases to acceptable values. Results on teflon are shown in Figure 10.

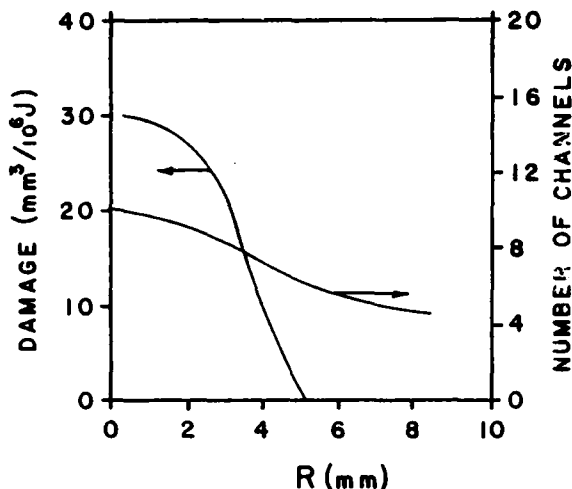


Figure 10 Number of channels and substrate damage as a function of substrate-electrode distance for teflon substrate.

Table 1 is a summary of typical test results on substrates which were in contact with the electrodes. Before-test and after-test values of V_h and N are presented together with the total volume of material loss. The loss rate of the brass electrode is also included. Note that teflon suffered the greatest material loss, but suffered the least deterioration in V_h and is a close second to quartz in N . Teflon appears to be a good candidate for a commercial switch with long life.

Table 1
Lifetesting results for various substrates and brass electrodes after 10,000 shots, 2×10^7 Joules.

SUBSTRATE	V_h (KV)		N		Material Removed mm/MJ
	Initial	Final	Initial	Final	
PC Board	68.0	62.0	15	4	22.0
Bare Ceramic	65.1	61.0	10	6	5.0
Pyromet	76.8	69.1	8	5	7.0
Quartz	61.4	58.2	10	9	4.0
Teflon	56.0	56.0	12	8	0.3
Brass Anode	-	-	-	-	0.1

5. Options and Limitations for Switch Design

In view of the information presented above, it appears that there is always some conflict between competing characteristics of the switch and that this competition may profoundly influence performance. For example, if one chooses to keep the surface close to the substrate, e.g. at $R=R_m$ to obtain the maximum number of channels, the holdoff voltage becomes minimum, and the surface damage will be severe. On the other hand, increasing R beyond R_m will decrease the number of channels, but will increase the holdoff voltage and decrease the surface damage. Therefore the design of a practical switch involves several compromises amongst conflicting factors. Such designing is now possible using the formula derived from the present model.

Using the present model, we have designed and constructed several versions of Multichannel Surface Discharge Switches. Each of them has some special features in order to meet specific applications. One of the versions is shown in Figure 11. This

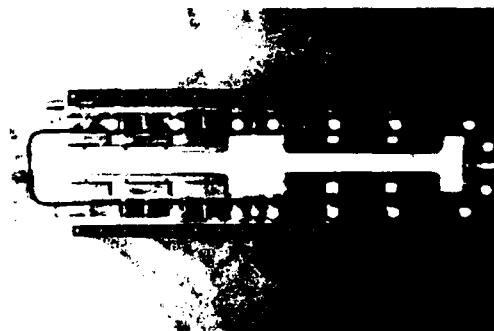


Figure 11 Photograph of a Multichannel Surface Discharge Spark Gap. The electrodes are 40 cm long.

particular switch is designed primarily for high voltage pulse charged applications e.g. large scale excimer lasers. The switch consists of 2 pairs of 20 cm long electrodes, and the average number of channels under normal operating conditions at 75 kV is about 30. This is shown in Figure 12. The maximum



Figure 12 Open shutter photograph of a single shot multichanneling along one pair of the 20 cm long electrodes.

holdoff voltage of the switch is 140 kV when it is filled with pure SF_6 gas. It also can be operated with N_2 , air and other gases or their mixtures. Some typical data in this regard is shown in Figure 13. The inductance

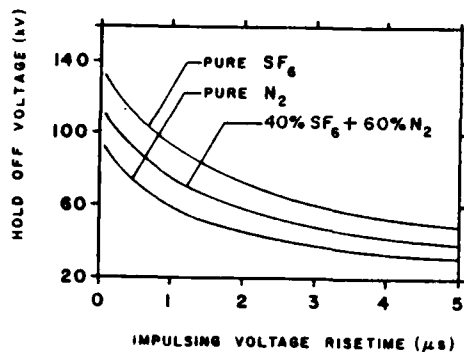


Figure 13 Holdoff voltage as a function of gas composition and voltage risetime for the 40 cm switch with $d=2.5$ cm and $P=14$ PSIG

of the switch is less than 20 nH and its lifetime is 10 million shots at 6 mc/shot. The current jitter is less than $1/2$ ns. The switch can be triggered reliably without the use of a high voltage fast trigger pulse generator, which is essential for other types of multichannel switches. Figure 14 shows the switch closing event when simply triggered at different points

on a slowly rising impulsing voltage pulse.

In conclusion, we should like to point out that there are several design factors which may critically effect the performance of a surface discharge switch. Primarily they are: the physical properties of the substrate and the electrodes, the dimensions and the geometry of these and the physical layout of the switch. Fortunately, the present model provides quantitative guidelines for the design of switches with respect to these factors and enable us to construct switches for specialized applications with predictable and reliable performance.

References

- (1) G.R. Neil and R.S. Post, Rev. Sci. Instrum 49, 401, (1978).
- (2) Maxwell Laboratories, Inc., USA, Engineering Bulletin, Aug. 1979. Catalog #40100 Railgap Switch.
- (3) R.S. Taylor et al, Proc. 14th Pulse Power Modulator Symposium, June 3-5, 1980.
- (4) Aviation Week and Space Technology, 114, #21, 70 (1981).
- (5) R.S. Taylor et al, Proc. 3rd Inter. Pulsed Power Conf., June 1-3, 1981.
- (6) H.M. von Bergmann, J. Phys. E. 15, 243, (1982).
- (7) J.P. Marton, NRC Switch Project, Phase II Final Report, 1982.
- (8) P.N. Dashuk et al, Proc. All-Union Conf. Eng. Problems of Fusion Reactors Leningrad USSR, July 28-30, 1977.
- (9) W.J. Sarjeant et al, Proc. 13th Pulse Power Modulator Symp., June 20-22, 1978.
- (10) W.J. Sarjeant, IEEE, Trans. Plasma Science PS-8, #3 216, (1980).
- (11) M. Meada et al, Jap. J. Appl. Phys. 20, 129, (1981).
- (12) S.T. Pai and J.P. Marton, Filamentary Breakdown of Gases in the Presence of Dielectric Surface, submitted to J. Appl. Phys for publication, 1982.

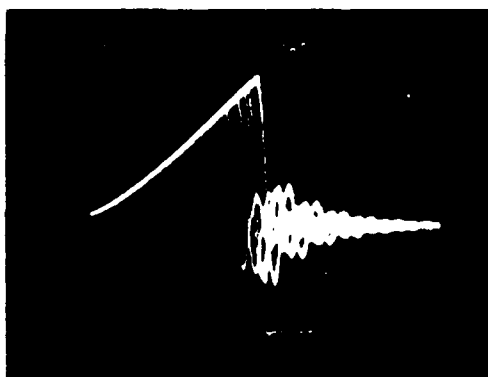


Figure 14 Slow pulse charged switch triggered at various points near the top of the voltage pulse.

TESTS OF A DIELECTRIC-VACUUM SURFACE FLASHOVER SWITCH*

Ian Smith (Pulse Sciences Inc.),
Gene Lauer (Lawrence Livermore National Laboratory),
and Morton Levine (Lawrence Berkeley Laboratory)

Summary

Dielectric-vacuum surface flashover switches were developed and tested as a means to switch a coaxial water Blumlein. The Blumlein was charged to as much as 150 kV (250 kV in self-break tests) and the switch was required to trigger with nanosecond jitter and carry up to 30 kA for 50 ns with a 20 ns rise. Recovery time was of interest as an indicator of very high repetition rate capability.

Plastic and alumina surface switches were tested with charge times ranging from 0.2 to 20 μ s and with a variety of field distortion trigger configurations. Plastic switches achieved RMS jitters from less than 1 ns to a few ns and alumina switches from a few ns to tens of ns. Alumina recovered much faster (in 100-200 μ s) than plastic (1-2ms) and showed less surface wear. Switch closures were almost always single channel and risetimes were from 15-30 ns 10-90%.

The results show that a vacuum-dielectric surface flashover switch has potential as a fast-rise low jitter switch in the 1-10 kHz range, although further tests in true multipulse operation (rather than single pulse and recovery tests) are needed to demonstrate this.

Introduction

The flashover of a vacuum-dielectric surface was of interest as a mechanism for high repetition rate (>1kHz) low jitter (≤ 1 ns) high di/dt (>kA/ns) switching because it was felt that the flashover might be followed by rapid recovery of insulation strength as in the case of a pure vacuum discharge. Switches using pure vacuum have not so far achieved the necessary low jitter or rapid rise of current. However, the presence of the dielectric surface should supply a rapid triggering and breakdown mechanism and thus make ~ 1 ns jitter possible. Many experimenters have found that the flashover of a vacuum-dielectric surface produces a nanosecond-like transition to very low impedance with negligible pre-breakdown current. One desirable consequence of this is that very little energy is deposited in the discharge or on the dielectric.

Vacuum surface flashover occurs at a critical field that is fairly reproducible, independent of electrode spacing, and only weakly dependent on the voltage duration in the range 10 nsec to 10 μ sec. These properties make it suitable for use in a three-electrode field-distortion switch. An important aid to breakdown under trigger should be available because the breakdown field is a strong function of the angle between the electric field and the surface, Fig. 1. It can be arranged that the trigger pulse both increase the field and re-orient it from the direction in which the surface is strong to the direction in which it is weak.

* Work supported by Lawrence Livermore National Laboratory.

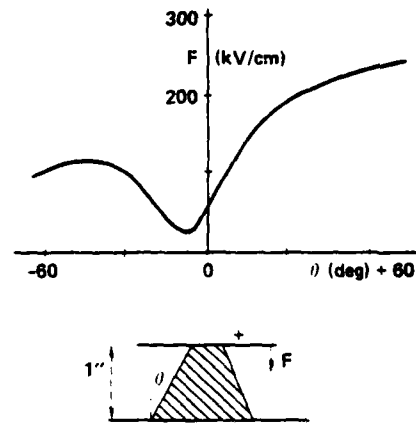


Figure 1. Effect of angle on 30 ns flashover of epoxy cone.
(From Ref. 1)

A conical switch surface was chosen, since this could withstand the charge voltage over the shortest distance. It was decided to test both an inside and an outside surface, since in the coaxial geometry the magnetic forces would push the discharge away from the surface in the first case and onto it in the second; in practice no difference in results could be ascribed to this. Most of the tests were made with the trigger electrode in the vacuum, though some used a trigger entirely embedded in the plastic. It was desired to test with trigger electrode locations near the anode and the cathode. Tests began with plastic surfaces, which could be readily formed and reshaped. After experience was gained with these, alumina was tested. Some experiments were done with a liquid film on alumina.

Apparatus

The tests were done on the LLNL Switch Test Stand developed in the ETA-ATA program. This includes a vertical water Blumlein, the high voltage electrode of which ends at a large Lexan interface designed to hold off the 250 kV as it passes down into a large vacuum tank, Fig. 2, which is pumped by a 6 in. diffusion

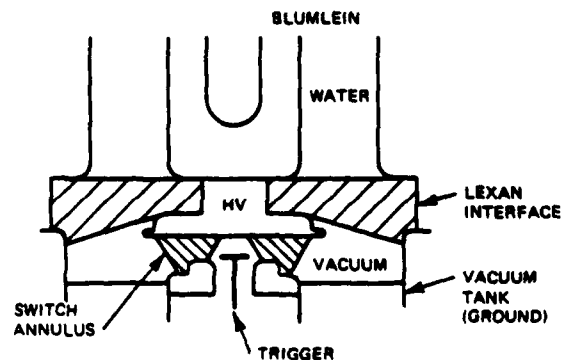


Figure 2. Schematic of Blumlein, vacuum tank and annular switch.

pump. The switch surfaces were mounted below the Lexan interface with a low inductance path to the grounded tank. The trigger pulse entered the vacuum tank from below.

The most tests were done with annular switch bodies like that shown in Fig. 2. The discharge surface was usually the inside surface, but the trigger electrodes could also be placed on the outside surface. The trigger electrode consisted of two diametrically opposite steel blades about 1/4 in. wide with sharp ends placed about 1/8 in. from the surface, at 1/4 in. from the ground end.

At first the Blumlein was charged by a resonant air-core transformer that created an initial negative voltage rising in 8 μ s followed by a larger positive peak at a total time of 20 μ s. Later an iron-core transformer was used to provide a positive voltage rising in 2 μ s. A magnetic compression stage between the transformer and the Blumlein was used to reduce the charge time to about 0.2 μ s.

The drive to the transformer was provided by a capacitor switched in by a thyatron. The trigger pulse was provided after a pre-set delay by a thyatron-driven, stacked-cable generator employing ferrite stage isolation. To test switch recovery, a second charge pulse could be provided by a second capacitor thyatron combination, but there was no provision for a second trigger pulse.

Switch voltage was measured with a capacitive probe in the water, and switch current by a stainless steel viewing resistor in the ground return. Both diagnostics had nanosecond resolution.

Plastic Switch Tests

Lucite and Delrin surfaces were tested in the annular configuration of Fig. 2. The switches were triggered near the first negative peak of the resonant transformer waveform. This polarity makes the cone angles positive in the convention of Reference 1, and gives the highest breakdown fields. The trigger electrode was held at ground during charge, reasoning that its positive edge would not emit electrons or spoil the field angle. A negative trigger pulse was expected to cause electrons to be sprayed on the cone surface, as well as enhancing the field and reversing the angle.

The 1 1/4 in. high internal surface self-broke at just over 150 kV on average. It could be triggered with a few ns rms jitter down to about 40 kV, using a trigger pulse of about 100 kV. Breakdown times were typically 30-60 ns. Typical results for Delrin are shown in Fig. 3. Jitter is slightly greater at 40 kV and 125 kV. Results for Lucite were similar.

The risetime is closely exponential with a time constant of 12-15 ns. This implies an inductance of about 70 nH. From this one would estimate a channel diameter of about 1 mm. When triggering was on an external surface observation through a viewport usually showed a single bright channel of about this size, lying straight along the surface. On a fresh surface the channel was not straight but took an erratic bent path, and longer risetimes were seen.

Though the breakdown was not always at the same trigger electrode, it only formed at one electrode on each shot. This would be expected considering the jitter is a few ns and the first channel to form would rapidly remove voltage from the other.

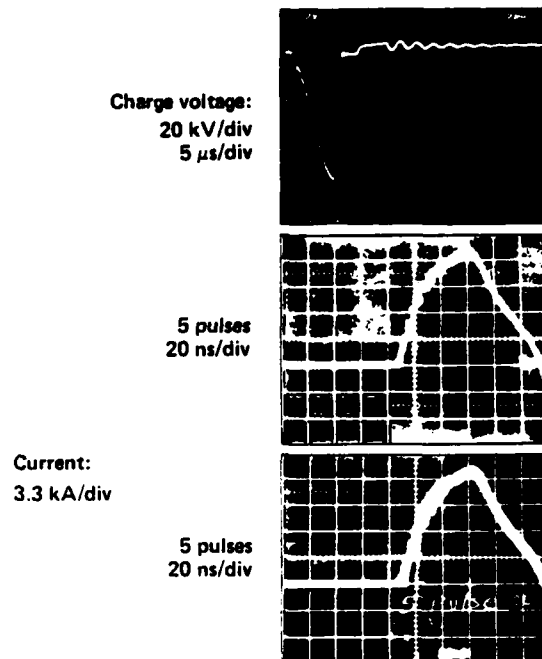


Figure 3. Trigger test of delrin flashover switch.

The use of a trigger electrode embedded in the dielectric was tested using the outside surface of an epoxy cone, Fig. 4. There it was reasoned that a trigger electrode initially grounded should be placed near the cathode, since it would then repel electrons from the surface, discouraging breakdown. When driven by a positive trigger pulse, the trigger electrode would draw electrons to the surface, initiating a breakdown avalanche. Therefore the switch was triggered on the positive second swing of the resonant charge. However, the switch triggered very poorly; possibly electrons drawn onto the surface cancelled the trigger field in a stable fashion.

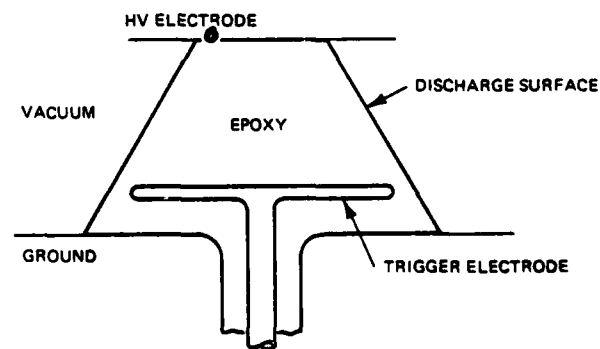


Figure 4. Epoxy switch with embedded trigger electrode.

It was found that a negative trigger pulse applied to the epoxy switch with embedded trigger during the first or subsequent negative swing of the charge voltage produced sub-nanosecond jitter over a voltage range of about 3:1. Fig. 5 illustrates that multiple pulses cannot be distinguished in 5 or 10 shot overlays on 10 ns/div.

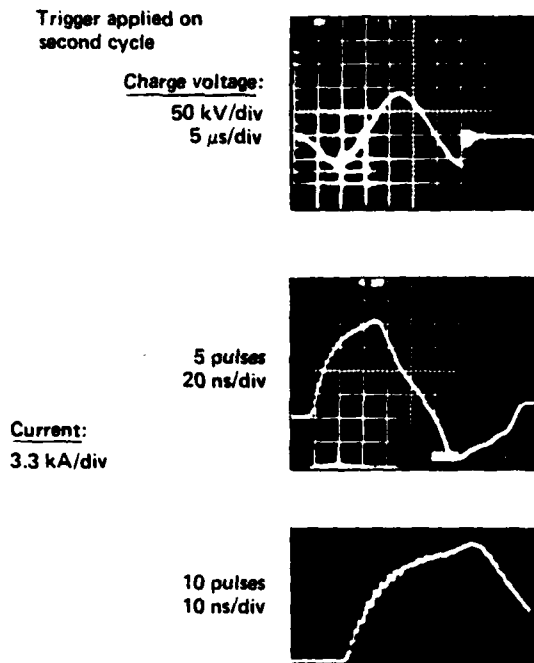


Figure 5. Low jitter of epoxy flashover switch.

The plastic switches recovered their voltage holding capability in 1-2 ms. This is illustrated for the Delrin switches in Fig. 6. The lower trace on each oscillogram is the first charge pulse, in which breakdown is triggered at 80 kV. The scope trace is swept upwards at 500 μ s/div. and a second charge pulse is applied at various times after the first. Premature breakdown occurs unless the delay is more than about 800 μ s. Recovery to near the initial 150 kV hold off requires about 2 ms.

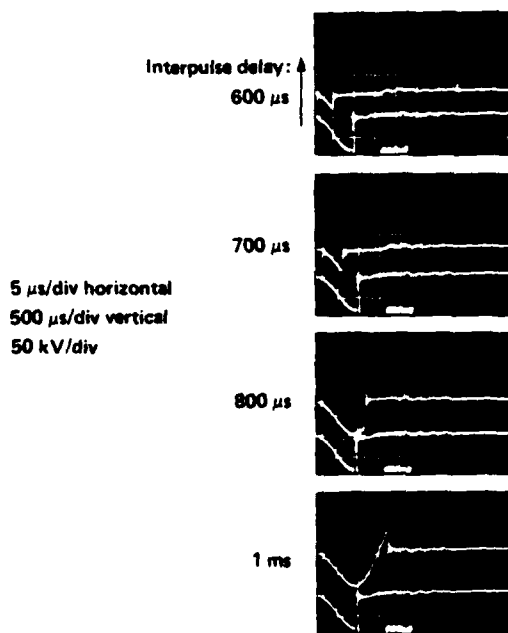


Figure 6. Recovery of delrin flashover switch at 80 kV.

When the annular switches were triggered on the inner surface, the recovery time was controlled by the size of the aperture around the trigger electrode, if this aperture was less than about an inch in diameter. This was attributed to a low pumping rate which allowed the pressure to remain high following the discharge. Measurements with a fast ion gauge, and also with the pump shut off, showed that a few $\times 10^{-2}$ litre-torr of non-condensable gas was released by the plastic surface on each pulse.

Repeated firing tended to remove material, making grooves in the plastic. Long life would not be expected in repetitive operation.

Alumina Switch Tests

The first tests with alumina were made with the same annular shape used for Lucite and Delrin and shown in Fig. 2. The Blumlein was charged negative in about 8 μ s with the resonant transformer and triggering was from the anode ground.

The recovery of voltage holding was much more rapid for alumina than for plastics. Fig. 7 shows that recovery to 80 kV requires just over 100 μ s. Breakdown voltage is very close to that of a cold switch after 200 μ s. It was noted that only about 10^{-3} litre-torr of gas was released on each pulse, much less than from the plastic.

Vacuum Trigger Electrode, Unbiased 80 kV

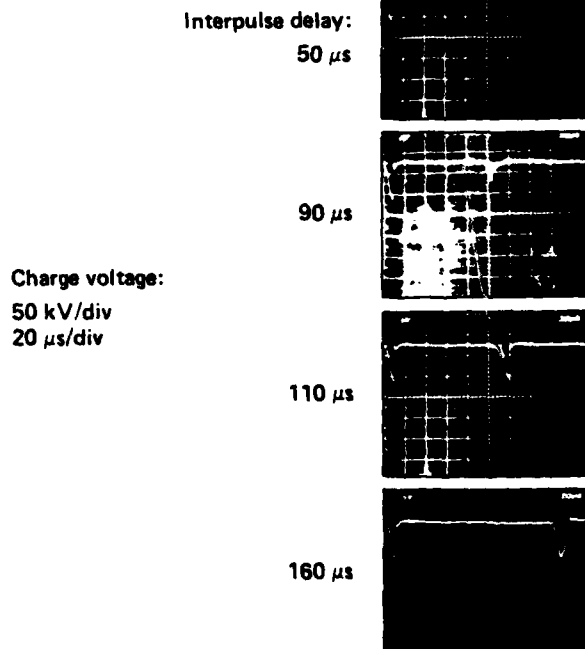


Figure 7. Recovery of alumina annulus flashover switch.

Risetimes were similar to those obtained with plastic switches, suggesting that a single multimetre-like channel was being formed. This was confirmed by direct observation when the switch was triggered on the outside conical surface.

Jitter of the alumina switch was tens of nanoseconds, with breakdown times well over 100 ns. In an effort to reduce jitter, resistor chains were added to bias the trigger electrode during charge at a potential corresponding to its physical position, and a pulse sharpening spark gap was placed in the trigger circuit; these changes had no effect.

A new alumina switch was then designed for use with the iron core transformer and magnetic modulator. Since this gave a 200 ns charge time, the cone height was reduced to 1 in. The Blumlein charge voltage waveform was now unipolar and positive, so the cone angle was reversed from that of previous surfaces. The cone formed the outside surface of a solid alumina disc. Because the ground was now the cathode, the trigger electrode was biased off ground during charge by resistor chains; if grounded it would have emitted electrons prematurely.

When pulse charged to 250 kV, this switch self-broke quite reproducibly just after the peak voltage. Trigger tests were made between about 80 kV and 160 kV. Because of fluctuations in the charging voltage, it was difficult to control the timing of the trigger with respect to the output of the magnetic modulator, and this made it hard to measure jitter accurately; it was approximately 2 ns rms. Fig. 8 shows the collapse of charge voltage on successive overlaid shots; the magnetic modulator fluctuation shows up as a voltage variation at the time of triggering. A similar jitter was obtained, at voltages up to 100 kV, when the switch was charged in 2 μ s, by bypassing magnetic modulator stages.

Blumlein charge:
Voltage overlays
50 kV/div

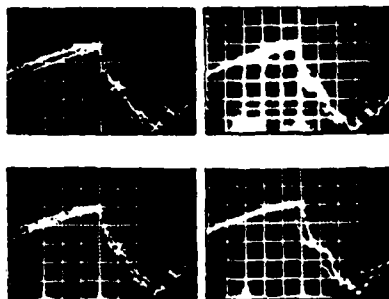


Figure 8. Triggering test of fast-charged alumina switch at 150 kV.

The e-fold risetime of the switch current was in the range 7-10 ns, Fig. 9, considerably less than the risetimes of the switches tested earlier. This cannot be entirely explained by the smaller height of the switch, and suggests that the channel is larger, perhaps even approaching 1 cm in width. To the eye, the discharge appeared more diffuse, but still had a bright millimetre-like core. The risetimes were similar for fast-charged self-breakdowns and triggered pulses with 200 ns and 2 μ s charge times.

Recovery times for this switch were similar to those of the annular alumina switch given earlier. However, recovery was less reproducible, and occasional prefires would occur even after 200 μ s delay. This may have been due to the air spark gap used as a trigger isolation and pulse sharpening gap;

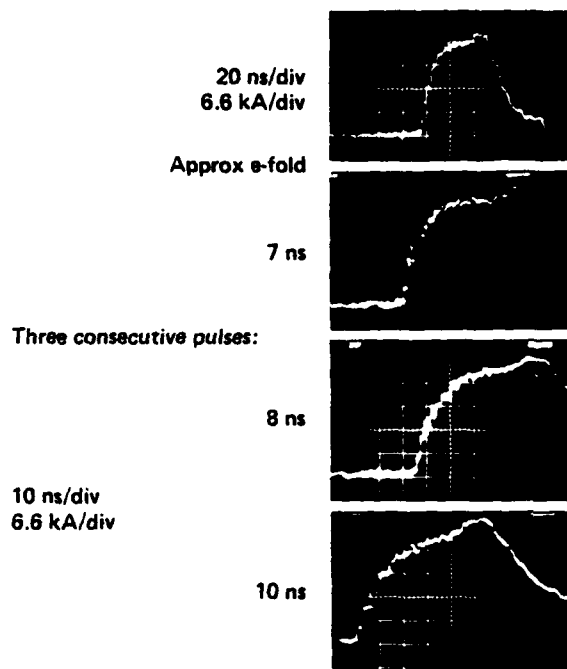


Figure 9. Current pulse shape for fast-charged alumina switch, triggered at 150 kV.

since this cannot recover in 200 μ s the trigger bias will be incorrect on the second pulse.

Tests were typically made at 10 pulses per minute. The discharge regions of the alumina switches were darkened, but not worn away. Thus a long lived switch is possible.

A liquid surface could also be considered where long life is required. A test was made of the annular switch shown in Fig. 2 in which a coat of Dow Corning 704 diffusion pump oil was applied to the alumina. The switch triggered with low jitter (a few nanoseconds) whereas the bare alumina in this configuration had shown tens of nanoseconds jitter. The recovery was not tested. The quantity of gas released on each pulse was small, similar to that from alumina rather than plastic.

References

1. I. D. Smith Impulse Flashover of Insulators in a Poor Vacuum, First International Conference on Breakdown in Vacuum, Boston MA, 1964.

OPTICALLY ACTIVATED SWITCH FOR NANOSECOND PULSERS

By

M. Weiner, J. Carter, R. Youmans, US Army Electronics
Technology and Devices Laboratory, ERADCOM, Fort Monmouth,
NJ 07703, Phone (201) 544-5404

T. Burke, Rutgers College of Engineering, P.O. Box 909,
Piscataway, NJ 08854, Phone (201) 932-3871

SUMMARY

Optically activated semiconductor switches have received growing attention in recent years because of their ability to rapidly switch at the kilovolt level. Pulsers designed based on this physical mechanism appear capable of producing extremely narrow pulsewidths (less than 2 nanosecond) at very high pulse repetition frequencies (greater than 100 kHz). These pulsers will be extremely useful in future high resolution mm wave systems, in which the pulsers modulate grid-
ded tubes such as extended interaction amplifiers and traveling wave tubes.

In this paper an investigation of the switching characteristics of intrinsic silicon, using both Nd:YAG and GaAs lasers, is reported. The semiconductor samples were mounted in 50 ohm transmission lines and terminated with 50 ohm loads. Measurements of the increased conductivity (which is a measure of the switching efficiency), risetime, and recovery time were obtained for various optical inputs and bias levels on the sample. Pulse bias permitted the use of higher voltages (up to 3 kV). Measurement results are explained in terms of the carrier transport model. Overall, the results demonstrate that optically activated semiconductors are well suited for high speed modulator applications.

Introduction

A promising approach for producing nanosecond pulsers makes use of the phenomenon observed when a semiconductor is illuminated with laser light¹⁾⁻⁽³⁾. The light energy produces secondary hole and electron carries in the semiconductor, which causes the resistivity to drop from its initially high state to a much lower value. In a typical device configuration (Figure 1) the center conductor of a transmission line (either coax or stripline) is interrupted and a section of semiconductor material is connected in series. One surface of the semiconductor is

metallized except for a small gap which is exposed to the laser light. When the gap is illuminated, carriers are created, causing the device to switch.

In this paper the suitability of such switches for high speed pulsers, applicable to millimeter wave transmitters, is addressed. We seek compact pulsers able to provide peak voltages of 1-3 kV, peak currents greater than 50A, pulsewidths of less than 2 ns, and pulse repetition frequencies greater than 100 kHz. In order to help define the pulser limitations of the optical switch, several measurements were conducted. These included measurement of risetime, recovery time, and gap resistance, obtained as functions of bias voltage and optical energy.

Fabrication of Targets

The optical switch consists of a rectangular prism of high resistivity single-crystal silicon in which aluminum electrodes have been evaporated on one side leaving an exposed rectangular gap across the polished surface. The following is a description of the material, dimensions, and fabrication procedure.

The silicon used for the switch is nearly intrinsic, with a resistivity of $10^4 \Omega\text{-cm}$, obtained in boule form from Wacker. The silicon was cut into wafers 0.5 mm thick and polished on both sides. The silicon wafers were cleaned in an ultrasonic cleaner with organic solvents and etched with mineral acids before the aluminum was deposited.

Two different techniques were used to form the aluminum electrodes: evaporation and photolithography. In the first, aluminum was evaporated over the silicon wafer masked with 1 mm wide metal bars, leaving uncoated stripes. In the photolith process, aluminum was evaporated over the entire wafer surface. Negative photoresist was applied, then exposed through a rubylith mask. The

aluminum was etched from the exposed areas with a phosphoric acid solution. After electrode formation, the aluminum was annealed at 400°C for 30 minutes, and the wafer cut into 1 cm long devices. Approximately 1 micron of aluminum was evaporated in both cases.

Final dimensions of the semiconductor target were 10 mm X 1 mm X 0.5 mm with a single face (10 mm X 1 mm) metallized. The gap in the metallization was 1 mm X 1 mm. The gap dimensions were chosen to obtain the necessary hold-off voltage (1-3 kV) and off-state resistance ($\approx 500 \text{ k}\Omega$). Clear epoxy was placed over the gap to improve voltage hold-off. In order to provide electrical connections, gold ribbon was bonded to the aluminum using a thermo-compression type bonder. Gold wire leads (7 mil diameter) were then bonded to the gold ribbon. The finished device was mounted in a General Radio insertion unit (type GR 874X) using indium solder.

Description of Lasers

Two types of lasers were employed. The optical parameters of each are briefly described. The first was a Nd:YAG type with a pulse energy of 17 mJ, a pulsewidth of 24 ns, and a risetime of 20 ns. Beam diameter was approximately 6mm. A Pockels cell Q-switch concentrated the output within the 24 ns pulsewidth. Operation of the Nd:YAG laser was limited to single shot. The second laser was a GaAs type made by Optel (model SLS 5010) with a total pulse energy of 0.3 uJ, a pulsewidth of 5.5 ns, a risetime of 3.5 ns, and a beam divergence of $10^\circ \times 30^\circ$. The maximum pulse repetition frequency was 5 KHz. Energy output for both lasers was measured with a TRG thermopile, model 101. The optical pulse shape was observed with a high speed EGG photodiode, model FND-100. Neutral density filters calibrated for both wavelengths were used to control the output energy.

Test Circuit

The test circuit, in simplified form, is shown in Figure 2. The test sample, mounted in the coaxial line, is pulse biased to the desired voltage. Pulse bias instead of dc bias was employed in order to avoid thermal runaway problems which are present at the higher dc voltages. Energy storage was in the form of either a 50 Ω coaxial line (100 ns long) or a capacitor (0.6 uF). For measurements involving longer recovery times ($> 100 \text{ ns}$), the capacitor was chosen to insure full voltage during recovery. For risetime, gap resistance, and shorter recovery time measurements, the coaxial line storage was chosen. The bias pulse width for the coaxial line and the capacitor were 30 us and 300 us, respectively.

Timing of the laser pulse was adjusted so that the laser was switched on only after the semiconductor and storage element were charged up to the full voltage by the pulse bias. In the

case of the Nd:YAG laser the timing was complicated by the necessity for first turning on the flash lamp. After initiation of the flash lamp a delay of $\approx 100 \text{ us}$ was provided, allowing sufficient pumping time for the Nd:YAG. The bias pulse was then initiated followed shortly afterwards by the activation of the Q-switch. The switched voltage pulse was lowered with wide band attenuators and then terminated into 50 Ω . The waveform was observed with a Tektronix 7834.

Experimental Results

Gap Resistance

Figure (3) shows a typical variation of the on-state gap resistance as a function of the Nd:YAG optical energy incident on the gap. The off-state resistance is $\approx 500 \text{ k}\Omega$. The optical energy represents that part of the energy falling on the exposed gap, and excludes the remainder of the beam which is incident on the metallized surface or elsewhere. Reflection from the surface (which is substantial and may be as high as 30%) is not taken into account.

Note the decrease in gap resistance, caused by the production of more carriers, as the optical energy is increased. Beyond 50 uJ, however, the resistance appears to be constant at about 2-3 Ω . An important point to be made here is that for a 1 mm X 1 mm gap (which can support a voltage of several kilovolts), optical energies of 50 uJ or more are required for efficient switching (90% or greater). Measurement of the gap resistance as a function of voltage (200-3000 Volts) showed relatively small variations.

In fact the required optical energy for the laser is twice the previous estimate if one considers that the only energy which counts is that which is in the risetime portion of the optical pulse. Assuming a half-sinusoidal wave shape, then the required energy from the Nd:YAG laser is approximately 100 uJ.

Figure 4 shows the gap resistance for the GaAs laser. Of course, the gap resistance is larger because of the smaller output from the GaAs laser. Extrapolation to energy levels needed for efficient switching (90%) is difficult to estimate. It appears, however, that slightly less excitation energy, using the GaAs laser, is needed for efficient switching. Pulse repetition frequency was operated up to 2000 Hz (burst mode) with no changes in the output.

Recovery Time

Figure (5) shows the recovery time (Nd:YAG laser excitation) as a function of the optical energy for several pulse bias values. The recovery time here is defined as the time interval between the termination of the laser pulse and the point at which the semiconductor returns to its high resistivity state. As mentioned previously the time constant for the capacitive energy

storage is chosen sufficiently large to insure no loss in semiconductor voltage during the recovery time. It is seen that the recovery is a strong function of the energy, ranging from tens of microseconds when the energy is 25 μJ , down to ≈ 1 μs when the energy is 0.5 μJ . As noted in Figure (5) a substantial increase in the recovery time occurs at the higher energies when the voltage is increased from 400 to 600 volts.

Figure (6) shows the recovery time as a function of the pulse energy for GaAs excitation. As may be seen the recovery time was in the 13-17 ns range. There was minor variation with bias voltage.

The recovery times shown in Figures 5 and 6 are considerably shorter than previously reported values for silicon, which gives a typical value of 20 μs . The reason for this may be the existence of impurities in the material, which serves as additional recombination sites and effectively reduces the recovery time. At the higher optical energies these sites become filled so the recovery time is still long. In the case of the GaAs excitation the extremely short recovery time observed may be connected with surface recombination sites. In the case of GaAs the absorption is concentrated near the surface, so that surface recombination takes on more importance.

Risetime

Risetime of the output pulse was essentially limited by the risetime of the laser. In the case of the Nd:YAG this meant a risetime of about 20 ns, and in the case of the GaAs, a risetime of 3-4 ns. The fact that the risetime limitation is determined by that of the laser is not surprising. By illuminating the entire gap region carriers are created throughout the entire drift region, the electric field collapses at the same time throughout the region, and transit time limitations no longer apply. In fact, if the energy in the risetime portion of the optical pulse exceeds the minimum amount needed for efficient switching, one should expect a risetime from the semiconductor to be somewhat less than the optical risetime. This was not observed (Nd:YAG excitation), possibly as a result of the slow rate of rise in the early stages of the optical risetime.

The total illumination of the target neutralizes the transit time limitation, but it does not influence the other nemesis of high speed switching, capacitance effects. Fortunately, in this case, these effects are minor because of the small capacitance of the 1 mm wide gap. Finally, since laser risetime is the major factor in determining the semiconductor switching time, one understands the interest in using mode locked lasers (which have picosecond pulsewidths) for producing pulses with risetimes measured in picoseconds.

Conclusions

Silicon targets, illuminated by Nd:YAG and GaAs lasers, were investigated for their switching behavior. Measurements of gap resistance, recovery, and risetime were obtained to help determine pulser limitations. With Nd:YAG excitation it was found that approximately 100 μJ (contained in the risetime portion of the pulse) are required for high efficiency ($\geq 90\%$) and low gap resistance ($\leq 5 \Omega$). In the case of the GaAs laser the required energy level appears somewhat more promising (based on extrapolation of low energy measurements). Any final conclusions, however, must await planned measurements using higher energy laser diodes.

For compact, high PRF pulsers the GaAs lasers are considerably more attractive, compared to the Nd:YAG type. As was noted, however, the GaAs laser does not produce as much pulse energy, resulting in a drastic loss of efficiency. One possible approach is to reduce the required laser energy by operating the semiconductor in an avalanche mode. In this mode the laser is used to "tickle" the semiconductor into an avalanche mode and relatively little excitation energy is required. Unfortunately the avalanche process is difficult to initiate without resorting to low temperatures. An alternative is the brute force approach in which laser diode arrays (with the number of diodes exceeding 25) are employed to obtain high energy output.

Recovery times were much lower than anticipated. For the Nd:YAG they were a few microseconds (0.5-500 μJ excitation), and for the GaAs they were tens of nanoseconds (10^{-3} - 10^{-2} μJ). Bulk impurities and surface recombination are believed responsible for the fast recovery. In any event, the additional recombinations sites (done unintentionally in this case) are a definite aid in reducing the recovery time, and thus improving PRF capability.

Risetime was limited for the most part by the risetime of the laser: ≈ 20 ns for the Nd:YAG laser and 3-4 ns for the GaAs. The risetime of the GaAs is limited by the driver. Development of drivers with sub-nanosecond risetimes for higher energy laser diode arrays is planned.

References

1. G. Mourou, M. Knox, "High Power Switching with Picosecond Precision", Appl. Phys. Lett., Volume 35 (7), pp. 492-495, Oct, 1979.
2. J. A. Buck, K. K. Li, J. R. Whinnery, "Optoelectronic Switching in a Stub Transmission Line", J. Appl. Phys., Volume 51 (1), pp. 769-771, Jan, 1980.
3. D. H. Auston, "Picosecond Optoelectronic Switching and Gating in Silicon", Appl. Phys. Lett., Vol 26 (3), pp. 101-103, Feb, 1975.

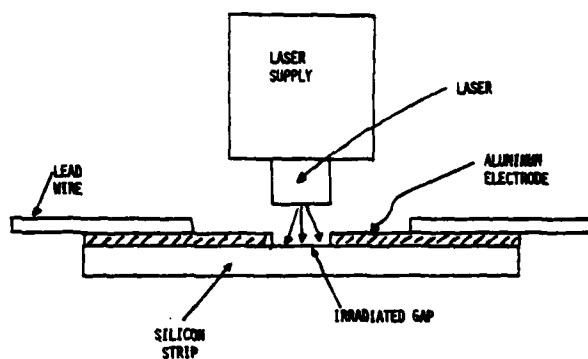


Figure 1. Optically Activated Switch.

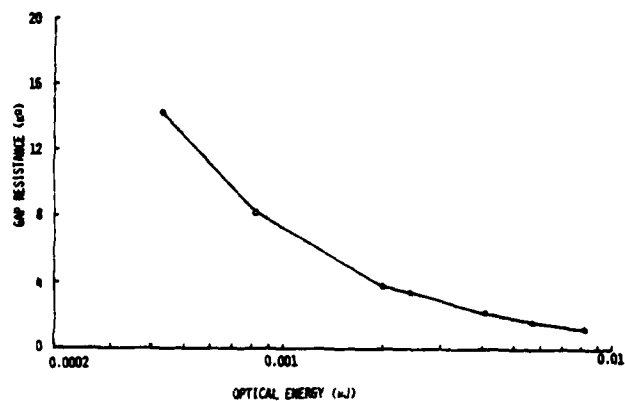


Figure 4. Variation of Gap Resistance with Optical Energy. GaAs Excitation. Bias Voltage: 400V

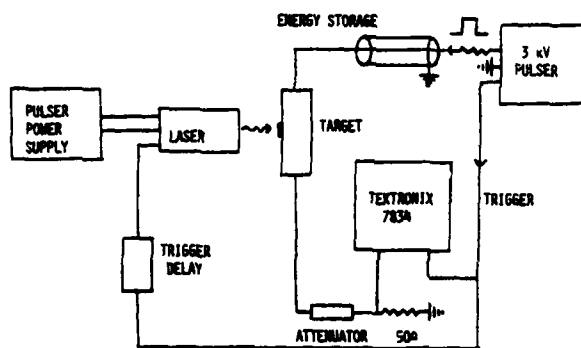


Figure 2. Block Diagram of Test Circuit

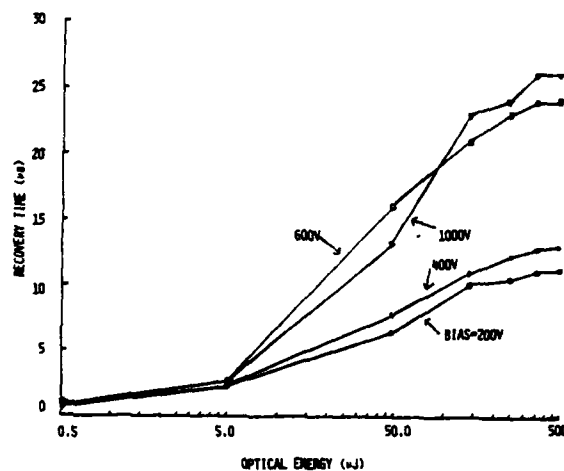


Figure 5. Variation of Recovery Time with Optical Energy. Nd:YAG Excitation.

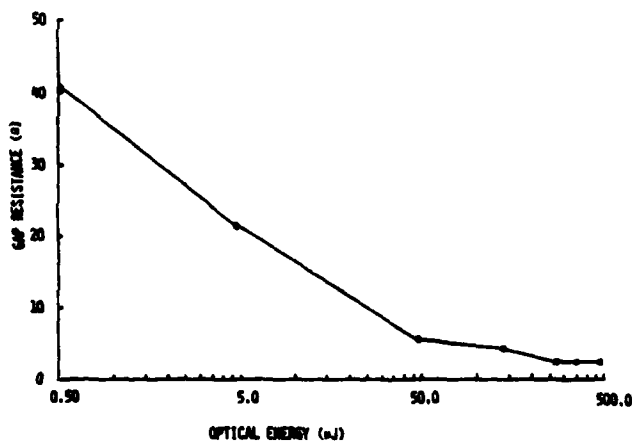


Figure 3. Variation of Gap Resistance with Optical Energy. Nd:YAG Excitation. Bias Voltage: 400V

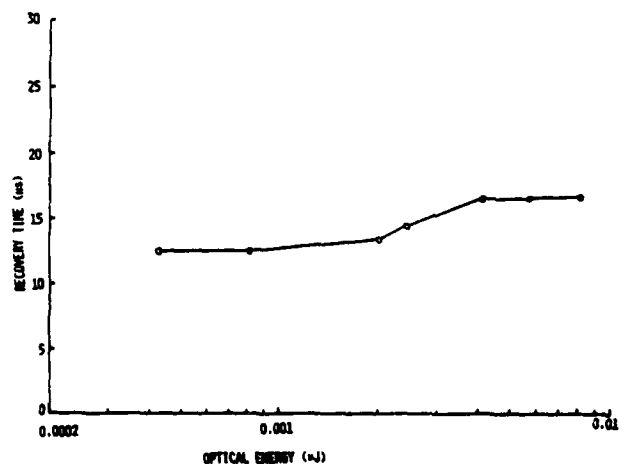


Figure 6. Variation of Recovery Time with Optical Energy. GaAs Excitation. Bias Voltage: 400V.

AREA EFFECTS IN THE BREAKDOWN OF WATER

SUBJECTED TO LONG-TERM ($\sim 100 \mu s$) STRESS*

M. T. Buttram
Sandia National Laboratories
Albuquerque, New Mexico 87185

Abstract

The breakdown of water subjected to long term ($\sim 100 \mu s$) stress has been studied for water capacitor areas of 80 and 400 cm^2 at a 1 cm spacing. A hysteresis-like behavior was observed. A sample with a minimum initial dielectric strength, E , was found to continue to break down to 60% of E after an initial spark. The maximum initial breakdown field was found to scale as $A^{-0.25}$ where A is the plate area.

Introduction

The goal of the work reported in this paper is to measure the effect of capacitor plate area on the electrical breakdown strength of very pure, chilled water. Water is the most common dielectric used in the current generation of high power, high-energy pulsed power systems. Unfortunately water capacitors normally are unable to hold a charge for more than a few microseconds. This severely constrains the design of water dielectric pulsed power systems. As an example, if a 100 kJ system must be charged in one microsecond, the average power of the charging system must be 10^{11} watts. At present this limits the options for the charging system to Marx generators, which implies spark gap switching and potential reliability problems. If the charging time could be extended by two to three orders of magnitude other options, such as direct charging from a fast discharge mechanical store through a slow pulse transformer, might become attractive. The problem with water as a dielectric is its low resistivity, typically $2.5 M\Omega\text{-cm}$ in conventional pulsed power systems. Voltage applied to a water capacitor decays through the internal resistance of the capacitor with an exponential time constant $\tau = \epsilon\epsilon_0$ where ϵ and ϵ_0 are respectively the water resistivity and permittivity ($90\epsilon_0$). For $2.5 M\Omega\text{-cm}$ water τ is $18 \mu s$ and every microsecond 10% of the energy in the capacitor is lost.

To improve this situation ϵ must be substantially increased. At room temperature large volumes of water can be maintained near $18 M\Omega\text{-cm}$ if proper care is taken. To achieve higher resistivity the temperature must be lowered, with ϵ reaching a maximum near $80 M\Omega\text{-cm}$ for $0^\circ C$. The dielectric constant increases slightly as well to 90 giving $\tau = 640 \mu s$ as a practical limit.¹ (Ice has a substantially higher resistivity but its frequency response is poor and it is unsuitable for pulsed power applications.)

For submicrosecond charging times the scaling law of J. C. Martin² describes the breakdown strength, E (MV/cm), of water,

$$E = K \frac{1}{t^{1/3}} \frac{1}{A^{0.25}} \quad (1)$$

K is 0.3 or 0.6 depending upon whether the field E is measured at the positive or negative electrode, t is the effective time that the field is applied to the

capacitor which is the time that E exceeds 63% of its maximum value, and A is the capacitor plate area in cm^2 . Fortunately this $t^{-1/3}$ dependence of E disappears between one and ten microseconds giving way to a much flatter time variation. Equation 1 predicts a breakdown field of 31 kV/cm for an 81 cm^2 sample at $t = 250 \mu s$. Instead the strength is measured to be 150 kV/cm for this relatively small capacitor area. The dependence of E upon capacitor plate area for long pulses is presently unknown. Measurement of this area effect for long pulses is the goal of the experiment reported in this paper. In addition, some of the problems involved in handling larger volumes of ultra-pure, chilled water in a pulsed power environment will be explored. Both types of data will be valuable for designing future high energy pulsed power devices.

The experiment has two major parts, a) a pulsed power system capable of charging the test water capacitor to 350 kV maximum and holding that voltage for a controlled duration up to $100 \mu s$ and b) a water purification system capable of maintaining the water in the test capacitor as near to $80 M\Omega\text{-cm}$ and $0^\circ C$ as is practical. The pulsed power system consists of a 10 kJ, 1 MV Marx generator connected to the water capacitor through a damping resistor. A triggered crowbar limits the pulse duration. Water purification requires a high flow (30 gal/min) ion exchange bed and a vacuum deserator to remove residual CO_2 from solution. To achieve $0^\circ C$, a 30000 BTU/hr chiller was required, together with some care in thermally insulating the tankage. Data will be taken with a sequence of capacitor areas of 80 cm^2 , 400 cm^2 , 2000 cm^2 , and 10,000 cm^2 . Thus far results are available for the smaller areas only.

Description of the Experiment

a) Pulsed Power System

The pulsed power system charges the water capacitor whose dielectric strength is being measured. The interpretation of the results is simplified by applying a square pulse. This was achieved with the circuit of Figure 1. A Marx generator which for the present purpose may be modeled as a capacitor C_M and inductor L_M in parallel with resistor R_M , charges the test capacitor C_T . Because of the series resistance R_p , the discharge consists of a transfer of charge between C_M and C_T until both come to a common voltage V_p . Thereafter the common voltage decays as the capacitors slowly discharge through R_M , the internal resistance of the Marx generator, and R_T , the internal resistance of the water capacitor. After the initial discharge, the charge originally stored in C_M is shared between C_M and C_T . The final voltage is $V_p = V_0 C_M / (C_M + C_T)$ where V_0 is the initial voltage on C_M . Sometimes V_p is too large even at the smallest practical V_0 ($\sim 500 kV$). In those instances an additional (oil) capacitor C_s is placed across C_T to reduce V_p as required.

The experiment uses an existing 16-stage Marx generator modified for long pulse service. C_M is 22 nF. The maximum value of V_0 is 1000 kV. The electric field in parallel plate capacitor C_T with area A (square centimeters) and spacing d (centimeters) is

*This work is sponsored by the Naval Surface Weapons Center, Dahlgren Labs., Dahlgren, VA. under work order N6092182-MN-D0055.

$$E_F = \frac{V_0}{d + \frac{\epsilon A}{C_M}} \quad \frac{V_0}{d + 3.3 \times 10^{-4} A} \quad (2)$$

There is a maximum spacing d beyond which a given value of E_F cannot be reached. As an example, if $E_F = 175$ kV/cm is an upper limit on the field likely to be required based on the data of Reference 1, then for $V_0 = 1000$ kV, d cannot exceed 2.4 cm. Thus the typical plate spacing in the water capacitor must be of the order of 2 cm. At 2 cm C_M is 36 nF, and the energy stored in C_M at peak charge is 2.6 kJ. The initial energy stored in the Marx generator is 11 kJ.

The waveform on the water capacitor as calculated for the circuit of Figure 1 is given in Figure 2. It rises in 2 to 3 microseconds and droops 12 percent in 100 μ s. At that point the Marx generator is generally crowbarred. An experimental waveform is shown in the lower trace of Figure 3. Peak voltage in this case is 320 kV, corresponding to an open circuit Marx voltage of 800 kV. The upper trace shows timing marks in coincidence with the Marx generator trigger and the crowbar. The measured pulse drop is 15 percent compared to the 12 percent expected.

This waveform is from a run of 1200 shots at a rate of 1 pulse per 5 sec. This particular run was terminated by a failure of the resistive voltage monitor. Developing a monitor capable of handling the stress of this long pulse for long runs has proven difficult. A capacitive divider is now in use. Another problem is pretriggering of the crowbar switch. Electrical noise from the firing of the Marx generator occasionally pretriggers the crowbar trigger system. A bias control which turns off the crowbar trigger when the Marx is fired has been developed but is not completely effective in preventing crowbar prefires.

To allow processing of large statistical samples of water breakdown data including a measurement of the time to breakdown, it was necessary to develop an automatic data acquisition system. To distinguish crowbar prefires from water breakdowns current shunts were installed in the crowbar circuit and on the ground return from the water capacitor. The presence or absence of a crowbar current and the sign of the capacitor current each produce an unambiguous signature distinguishing crowbar from water breakdown. This gives a twofold redundancy to the measurement.

b) Water System

The water system consists of four major components, i) a mixed resin bed deionizer, ii) a vacuum deaerator, iii) a 30,000 Btu/hr chiller, and iv) two 420-gal thermally insulated tanks. The deionizer ("polisar") assembly is diagrammed in Figure 4. Water from the experimental tank is passed through two to four parallel 15 gal/min mixed bed resin deionizers. After deionization the water is sterilized (99.9% bacteria kill) and filtered (0.2 micron) and returned to the capacitor tank.

Water leaving the deionizer is nearly free of ions except for dissolved CO_2 (carbonic acid) which the resin beds remove relatively inefficiently. CO_2 and other dissolved gases are removed by spraying the water into a vacuum vessel (deaerator) maintained by a modest roughing pump which must be isolated from the water by a cold trap placed between the deaerator and pump.

Keeping the purified water near 0°C requires an estimated 20,000 Btu/hr of chiller capacity to be provided by the system shown in Figure 5. The chiller is rated at 30,000 Btu/hr at 0°C (water temperature). Refrigerant is fed to an evaporator located along one wall of the water compartment. Water is pumped downward through the evaporator coils and removed from the tank at the top on the opposite side. The goal of using this arrangement is to establish an upward flow pattern through the test capacitor. The water is then pumped to the deionizer system.

Tankage was prepared by partitioning an existing stainless steel tank attached to the Marx generator into two 420-gallon compartments. The tanks are lined with PVC plastic to minimize leaching of ions from the walls which would be a severe problem even though they are stainless steel. One compartment holds the test capacitor, the second serves as a holding tank for the clean, cold water. There is only one evaporator, the one in the capacitor tank. No provision was made to chill water in the holding tank. However, the walls of both tanks are lined with 3" of foam insulation which maintains the water temperature for a reasonable time.

In operation the chiller has proved capable of freezing water in the evaporator assembly unless the temperature is monitored and the chiller is turned off when the temperature drops too low. The deaerator assembly only needs to be run occasionally and is valved out of the system during data runs. The deionizer must be run continuously to maintain water quality. Water resistivity is measured with a parallel plate water resistor located just beyond the recirculation pump (see Fig. 4). The water temperature at this point is 5 to 6°C warmer than in the tank. Since the water resistivity follows the curve of Reference 1, tank resistivity can be estimated using the tank water temperature. It is near $80 \text{ M } \Omega\text{-cm}$.

Results

Data have been taken with test capacitor diameters of 10 and 22.5 cm (80 and 400 cm^2 areas). The edge radius in each case was 1.27 cm. The plates were made of 304 stainless steel. Some initial data with the smaller capacitor were taken at a 4 cm spacing where the field enhancement factor (FEF) at the edges of the capacitor is large. Breakdowns tended to concentrate near the outer edge in this case. Most of the 80 cm^2 data were taken with the 1 cm gap shown in the field plot of Fig 6. The field enhancement factor in this configuration is 2%. For the 400 cm^2 sample shown in Fig 7, a 1 cm spacing also corresponds to a 2% FEF. The allowable upper limit of the field enhancement for this experiment was arbitrarily set at 10%. Typical water conditions were temperature less than 2°C and resistivity greater than $70 \text{ M}\Omega\text{-cm}$.

The first data taken were approximately 650 pulses on the 80 cm^2 capacitor near 100 kV/cm with a 4 cm spacing. During this period diagnostics were being developed. Generally the water broke down although there was one sequence of 170 pulses with out any breakdowns.

Next the capacitor spacing was reset to 1 cm to limit the field enhancement at the edges. A 75 nF capacitor, C_2 , was added in parallel with the Marx generator to lower the output voltage. Forty-eight pulses were taken at 97 kV/cm. The water capacitor sparked on the first eight pulses. On the remaining 40 pulses the capacitor did not break down.

Next a series of 250 shots at fields from 94 to 145 kV/cm resulted in no water breakdowns. At 163 kV/cm the first 9 pulses did not spark the capacitor. Twenty-nine subsequent pulses all led to breakdowns. After this run the sample was left unpulsed in the water for 6 days. At the end of that time the sample would not break down until a 182 kV/cm field was applied.

Subsequently the breakdown of the 80 cm² sample was found to follow a "hysteresis-like" loop. Fig 8 is an attempt to illustrate what happens. Beginning at 109 kV/cm 10 pulse samples were taken with no breakdowns to 182 kV/cm. No breakdowns in 10 pulses limits the breakdown probability to less than 30%. At 182 kV/cm 92 shots were taken. On the first pulses no breakdowns occurred. Thereafter the capacitor broke down on every pulse. After waiting several minutes for any residual debris to flush from the gap a series of 20 shots at 182 kV/cm again resulted in 100% breakdown probability. Thereafter the field was reduced in runs of 20 pulses, all of which resulted in 100% breakdown probability until 109 kV/cm was reached. At 109 kV/cm the capacitor broke down on the first pulses, then breakdown stopped. Subsequently no more breakdowns occurred at this field. The field was then raised in 9 kV/cm steps with 100 shots at each step. Again no breakdowns occurred until 182 kV/cm. At 182 kV/cm seventy-six pulses without breakdown were followed by 24 in all of which the water sparked. The field was lowered to 127 kV/cm then to 109 kV/cm but this time breakdown did not stop after 100 pulses at each field. The experiment was terminated at this point due to arcing of the transfer resistor R₀.

Once breakdown had occurred the sample continued to break with virtually 100% probability until the field was reduced to at least 60 to 70% of the initial breakdown field. Peak discharge current through the sample in the initial breakdown was only 160 to 180 amps in a 10 μ s exponentially decaying waveform. Nevertheless sufficient "damage" resulted to "decondition" the electrodes so that subsequent breakdowns occurred at much lower fields. Because of the location of the sample inside the water tank it is impossible to say that there are no small bubbles on the electrode surfaces to act as spark initiation sites. However, it was observed that few bubbles were produced, as few bubbles were rising to the surface following a spark. Bubble production may have been reduced by degasation of the water.

Qualitatively equivalent results were obtained with the 400 cm² sample at a 1 cm spacing. Initial breakdown occurred at 120 kV/cm and once breakdown had occurred the capacitor arced on every pulse. Breakdown ceased at 70 kV/cm. Again the "hysteresis range," defined as the field at which breakdown ceased divided by the field at which it began, was 60%, precisely as observed in the 80 cm² sample. These data are summarized in Table I. The most obvious difference between the results at 80 and 400 cm² plate areas was the reduction in the fields at which breakdown began from 180 kV/cm for the smaller capacitor to 120 kV/cm for the larger one. If one ascribes this to an area effect such that the breakdown field is inversely proportional to plate area to some power, that power is 0.25. Obviously these data are preliminary and the value of this power may well change as more data are accumulated.

TABLE I

Capacitor Plate Area	Minimum Breakdown Field	Maximum Holdoff Field	Hysteresis Range
80 cm ²	110 $\frac{\text{kV}}{\text{cm}}$	180 $\frac{\text{kV}}{\text{cm}}$	60%
400	70	120	60%

Conclusions

Water breakdown has a "hysteresis-like" behavior in that a field that will not break down a properly conditioned capacitor will cause breakdown with 100% probability once the capacitor has been sparked. No amount of flushing of water through the capacitor (for example one hour corresponding to five volume changes) will prevent breakdowns. This implies that the capacitor plates rather than the fluid retain a "memory" of previous sparks. Long term exposure (6 days) to the ultra-pure water may return the capacitor plates to a conditioned (non-breaking) state. This could result from chemical destruction of spark inception sites by the water. This hysteresis was observed with capacitor plate areas of 80 and 400 cm² for which the fields at which breakdown began and quit are given in Table I. If the reduction in maximum holdoff field and minimum breakdown field in the larger sample is attributed to an area effect such that the field is inversely proportional to area to a power, that power is 0.25 from these two data points. The preliminary nature of these data needs to be emphasized.

Figure Captions

1. Electrical Schematic of the Pulse Power System
2. Computed Voltage Waveform on the 10⁴ cm² Water Capacitor
3. Experimental Voltage Waveform on a Dummy Capacitor; Peak Voltage is 320 KV.
4. Schematic of the Water Processing System
5. Schematic of the Chiller and Water Tank Assembly
6. Field plot of the 80 cm² capacitor at a 1 cm spacing
7. Field plot of the 400 cm² capacitor at a 2 cm spacing
8. "Hysteresis" loop breakdown for the 80 cm² sample. The arrows indicate the order in which the data were taken.

References

1. D. B. Fenneman and R. T. Gripshover, "Electrical Performance of Water Under Long Duration Stress," Proceedings of the 1980 14th Pulsed Power Modulator Symposium, Orlando, FL, 1980.
2. J. C. Martin, "Nanosecond Pulse Techniques," AMRE Report SSWA/JCM/49, 1970 (unpublished).

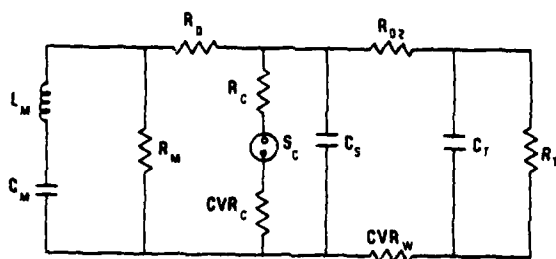


Figure 1

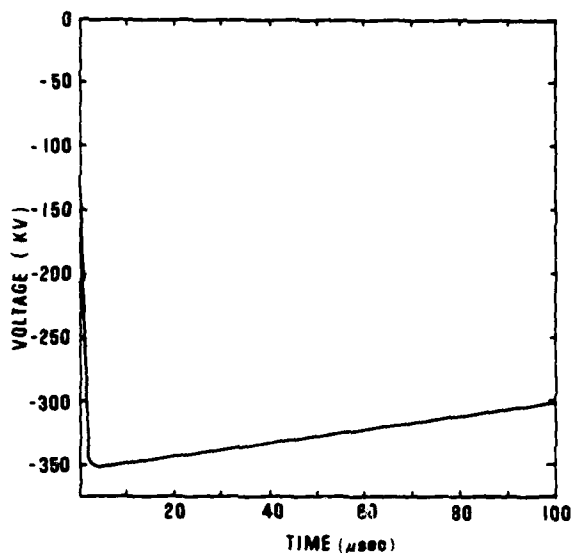


Figure 2

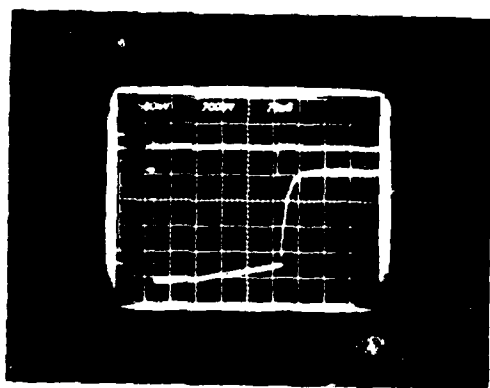
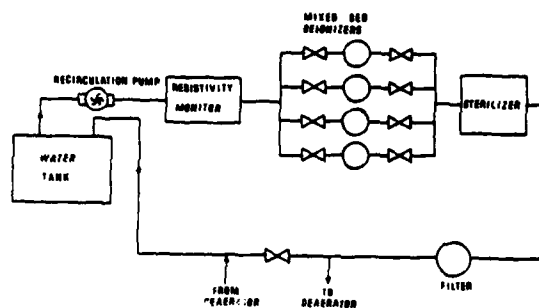


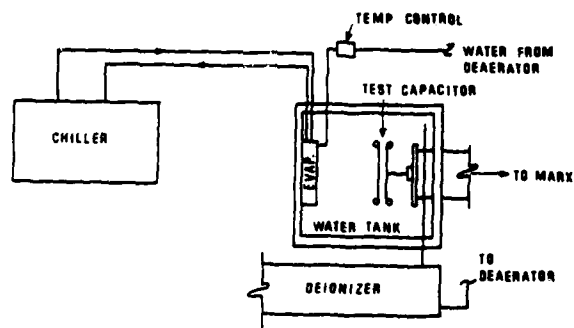
Fig. 3

Experimental Voltage waveform on a Dummy Capacitor, peak voltage is 320 kv.



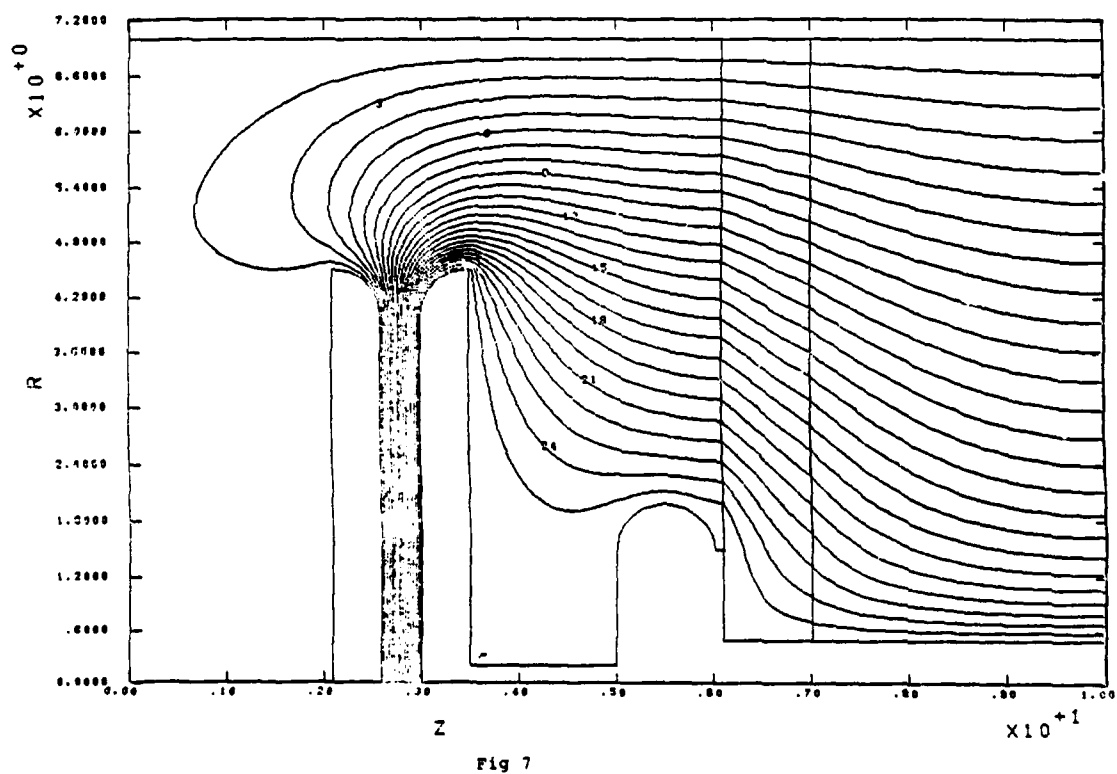
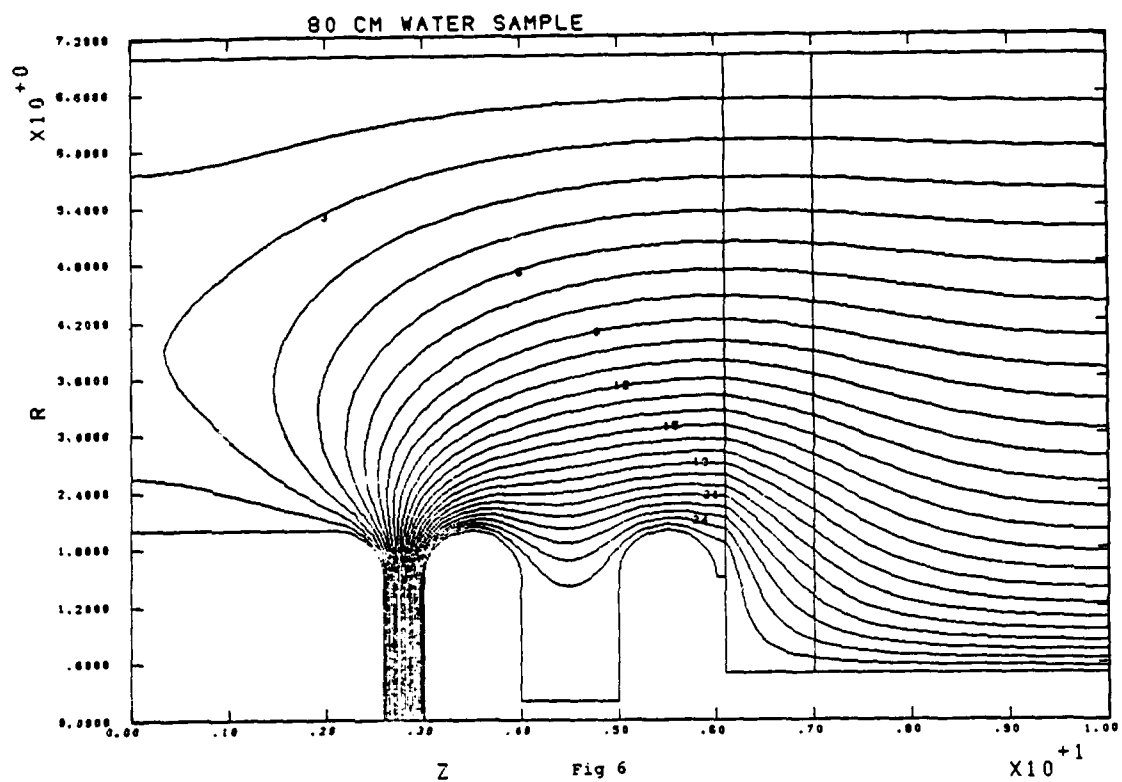
WATER PURIFICATION SYSTEM

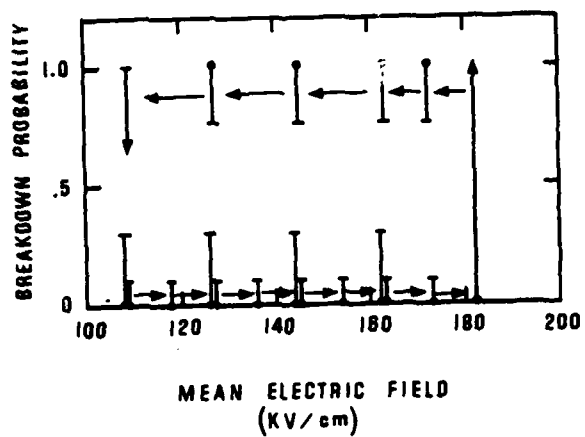
Figure 4



REFRIGERATION CIRCUIT

Figure 5





WATER/GLYCOL MIXTURES AS DIELECTRIC FOR PULSE FORMING LINES IN PULSE POWER MODULATORS

R. J. Gripshover and D. B. Fenneman

Naval Surface Weapons Center
Dahlgren, Virginia 22448

Summary

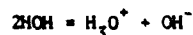
Experiments are described which indicate good potential for the use of cooled ethylene glycol/water mixtures as dielectric in the pulse forming lines of high power modulators. Purification of these mixtures by conventional deionizing techniques is found to produce resistivities more than 60 times greater than the theoretical maximum of pure water. The long-term electrical strength is found to exceed the strength of pure water. The variation of resistivity, dielectric constant, Debye relaxation time and electrical strength with temperature and mixture ratio is presented.

The ability of these cooled mixtures to hold charge for long times can simplify the design and reduce the cost of modulator charge circuitry. How the other electrical properties of these mixtures impact the design of large-scale modulators is analyzed.

Introduction

At the last symposium¹, we reported finding that with conventional purification techniques, the conductivity of water cooled to near 0° C could be reduced to the point that water could be charged to fields in excess of 10 MV/m for time periods extending to 100 microseconds with only about 10% ohmic heating loss. Because long-term charging of liquid pulse forming lines (PFL's) reduces demands on charging circuitry, this suggested that the first intermediate energy store (e.g., a capacitor bank or Marx bank) might not be required. Unfortunately, even 100-microsecond charging times are still about a factor of ten too fast to consider PFL charging by rotating machinery. Further cooling of water freezes it and results in loss of dielectric constant, so this performance is an absolute limit for that liquid.

The conductivity of pure liquids is due to a dissociation reaction, e.g., in water:



which produces the charge carriers. The charge carrier density from this reaction is exponentially dependent on temperature and is reduced about a decade for every 30° C of cooling. The use of freezing point depressant polar liquids in water immediately suggests itself as a means of achieving lower conductivity polar liquids. The maximum freezing point depression is 50° C for the 60/40-by-weight mixture of ethylene glycol/water². This promises that PFL charging times in excess of a millisecond could be achieved.

The purposes of this paper are to: (a) present data to show that the cooled glycol/water mixtures do display the expected exponential increase in resistivity as a function of temperature, (b) present expected values of the electrical properties of interest to the designer of pulsed power machines, and (c) indicate the way these electrical properties

impact on the design in the light of other design limitations and goals.

In the next section the electrical properties of glycol/water mixtures are presented. In the last section, the way the electrical properties impact the design of devices in the light of other external constraints is presented.

Electrical Properties of Glycol/Water Mixtures

The properties of major interest to the designer of pulse power machines are the intrinsic time constant, τ (a quantity closely related to the conductivity), the (complex) dielectric constant ϵ_r , and the electrical strength E_{max} . This section presents the results of measurements of these quantities and their variation with temperature and mixture ratio. The liquid conditioning apparatus is diagrammed in Figure 1. The main loop is continually run to insure temperature stability and to maintain the highest possible deionization. The deaeration loop is run for the day preceding testing, but not during testing, as it hampers the cooling process. A more complete discussion of the apparatus and methods is found in reference 3.

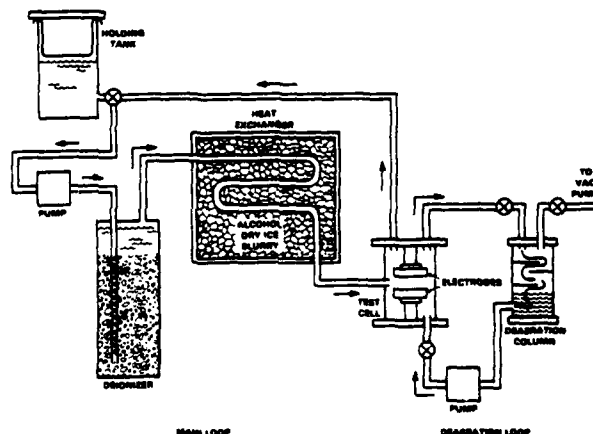


Figure 1. Liquid Conditioning System.

Intrinsic Time Constant

The intrinsic time constant of a liquid is defined by

$$\tau = \epsilon_0 \epsilon_r \rho = \epsilon_0 \epsilon_r / \sigma \quad (1)$$

where ρ is the resistivity, σ is the conductivity, ϵ_r is the relative dielectric constant, and $\epsilon_0 = 8.85 \times 10^{-12}$ F/m in SI units. It is more convenient to discuss the conductive properties of the liquid in terms of the intrinsic time constant rather than the resistivity, as it is measurable directly and relates

directly to the ohmic heating loss in the liquid. Figure 2 displays the character of the intrinsic time constant, and how it is measured. It can be shown that the energy lost to ohmic heating in charging a liquid over a time period t_c divided by the energy stored at the end of the charging period is

$$\frac{W_{\text{ohmic}}}{W_{\text{stored}}} = \alpha \frac{t_c}{\tau} \quad (2)$$

where α is a dimensionless constant which depends only on the charging waveshape and which has values ranging from 0.5 to 1.0 for commonly employed charging waveforms.

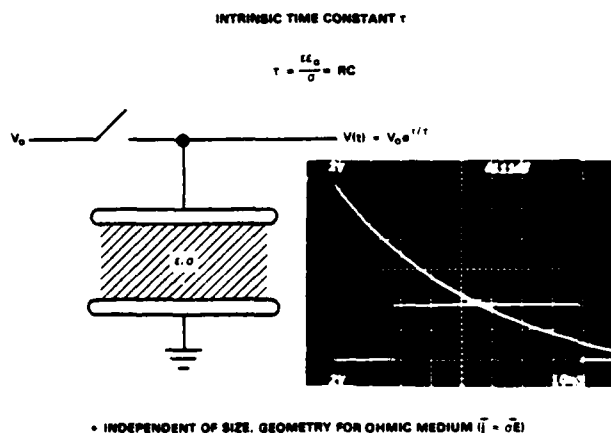


Figure 2. Measurement of Time Constant.

Voltage V_0 is impressed on electrodes immersed in the liquid. When the voltage source is removed by opening the switch, the voltage decays exponentially as shown. The intrinsic time constant is the time for the voltage to fall from 10 volts to 3.68 volts ($=10/e$). This time is shown as the duration of the 4 volt square wave. This time is also displayed in tenths of microseconds in the upper right. Oscilloscope time scale is 10 milliseconds/division. The liquid is 60% by weight glycol at -36°C .

Figure 3 shows the results of measuring this quantity for various weight fractions, w , of water/glycol mixtures as a function of temperature. The results indicate that these cooled liquids can support fields with low loss for periods extending into the millisecond time frame. This confirms the expected dramatic reduction of the charge carrier density with temperature. These very optimistic results are tempered somewhat due to the discovery of a new decay mechanism operative at high voltages-charge injection. This somewhat complicated phenomena is briefly discussed under High Voltage Measurements.

Dielectric Constant

In the least complex formulation of the Debye theory of dielectrics^{4,5}, the dielectric constant is considered a complex number which depends on the frequency content of the applied electric field, the temperature, and, in the case of mixtures of polar liquids, on the weight fractions of its components:

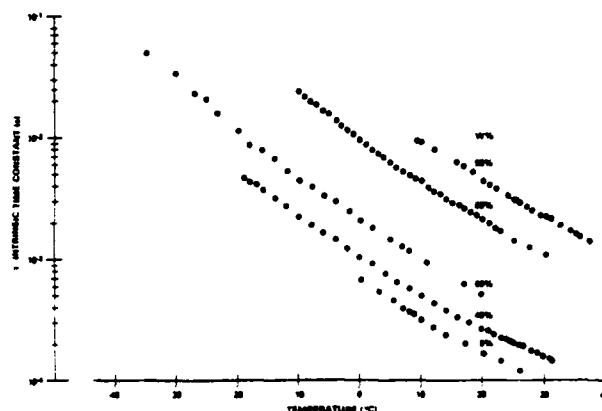


Figure 3. The Intrinsic Time Constant of Glycol/Water Mixtures.

$$\epsilon_r(\omega, T, w) = \epsilon_\infty(\omega) + \frac{\epsilon_s(T, w) - \epsilon_\infty(\omega)}{1 + j\omega\tau_D(T, w)} \quad (3)$$

where $\epsilon_s(T, w)$ is the static dielectric constant of the liquid, $\epsilon_\infty(\omega)$ is the dielectric constant at infinite frequency, which we take to be the square of the index of refraction:

$$\epsilon_\infty(\omega) = n_D^2(\omega). \quad (4)$$

$\epsilon_\infty(\omega)$ has negligible temperature dependence. $\tau_D(T, w)$ is the Debye relaxation time and represents the characteristic exponential time for a randomly oriented dipole to line up with a suddenly applied electric field. The simple theory assumes that this characteristic time is the same as the time for an aligned dipole to change to random alignment upon the sudden removal of the aligning field. This can be expected to show temperature dependence.

The Debye parameters $\epsilon_s(T, w)$ and $\tau_D(T, w)$ were determined by measuring the complex impedance of a small coaxial probe immersed in the liquid using a Hewlett-Packard 4815A RF vector impedance meter. The impedance of the probe is

$$Z = Z_r + jZ_i = j(\omega L - 1/\omega C_0 \epsilon_r(\omega, T, w)) \quad (5)$$

where L is the inductance of the probe and C_0 is its empty capacitance. Any real losses in the probe due to skin effect or radiative resistance have been neglected. Substituting the Debye expression (3) and separating real and imaginary parts results in

$$\omega C_0 \epsilon_s = \frac{1 + (\omega\tau_D)^2}{1 + \frac{\epsilon_\infty}{\epsilon_s}(\omega\tau_D)^2} \cdot \frac{\omega L - Z_i}{|Z - j\omega L|^2} \quad (6)$$

$$\omega\tau_D = \frac{1 + \frac{\epsilon_\infty}{\epsilon_s}(\omega\tau_D)^2}{1 - \frac{\epsilon_\infty}{\epsilon_s}} \cdot \frac{Z_r}{\omega L - Z_i} \quad (7)$$

These equations can then be solved recursively for the quantities $\epsilon_s(T, w)$ and $\tau_D(T, w)$. Measurements of the complex impedance were made over the frequency range 0.5 - 108 MHz. Figures 4 and 5 show the results of

the measurements. The values of $\epsilon_s(T, \omega)$ agree well with measurements by Akerlof⁶ for $T > 20^\circ \text{C}$. The Debye model was found to represent the frequency behavior over this broad frequency range very well (within $\sim 2\%$). The Debye relaxation time, while displaying exponential increase with decreasing temperature, does stay below a nanosecond, indicating that the fluids are effective for the few nanoseconds of rise time required for some applications.

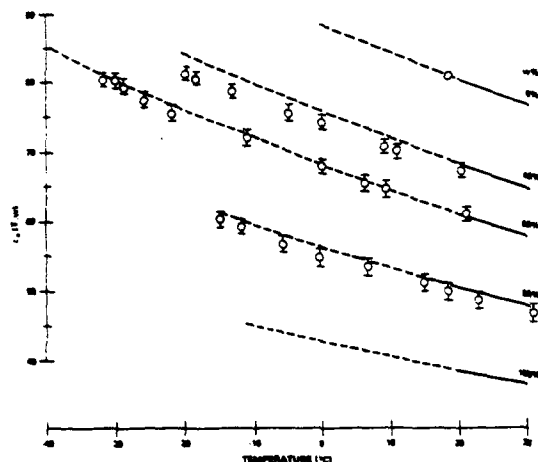


Figure 4. The Static Dielectric Constant of Glycol/Water Mixtures.

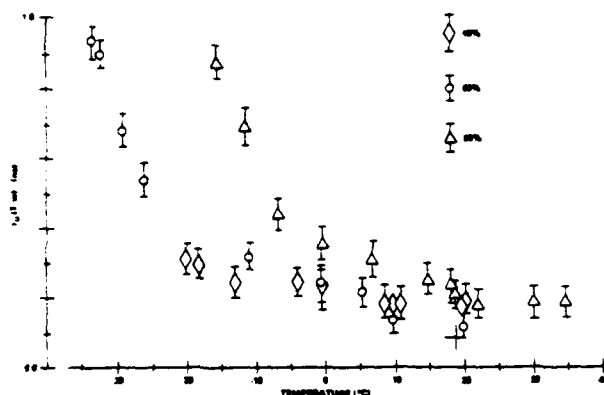


Figure 5. The Debye Relaxation Time of Glycol/Water Mixtures.

High Voltage Measurements

The glycol/water mixtures were tested in the high voltage circuit shown in Figure 6. This is the same circuit described in reference 1 and used for the long-term water testing. Probe P2 is a capacitive probe which has a droop time in excess of 0.1 second. In high voltage testing with these very long stress times, a new decay mechanism becomes apparent. Figure 7 displays the decay waveforms for glycol/water mixtures at low and high temperatures for low and high voltage. At high temperature it is seen that the voltage across the plates bleeds faster than would be indicated by the intrinsic time constant. At low temperatures the decay is more complex, showing a change in the sign of the

derivative of voltage with time. This anomalous behavior is now fairly well understood to be due to charge injection. It is explained in detail in reference 7. Briefly: Charge injection decay occurs when, under the action of high fields, part of the surface charge detaches and enters the bulk liquid. Under the action of the field, the charge is then transported to the opposite electrode. The characteristic time for this decay is the transport time for the detached charge to travel between the plates:

$$\tau_{tr} = \frac{\ell}{\mu E} = \frac{\ell^2}{\mu V} \quad (8)$$

where ℓ is the plate separation, and μ is the mobility of the injected charge. The charge injection decay mechanism will dominate the decay when $\tau_{tr} \ll \tau$. Note that this decay mechanism depends on the plate geometry and voltage, whereas intrinsic decay is solely a property of the liquid. Since large liquid-filled PFL's can be expected to have electrode spacings in excess of 50 mm, charge injection is probably not of crucial importance in single-pulse devices. In repetitive systems, more research is required to understand its importance.

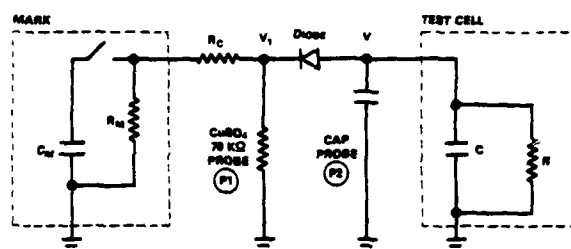


Figure 6. High Voltage Test Circuit.

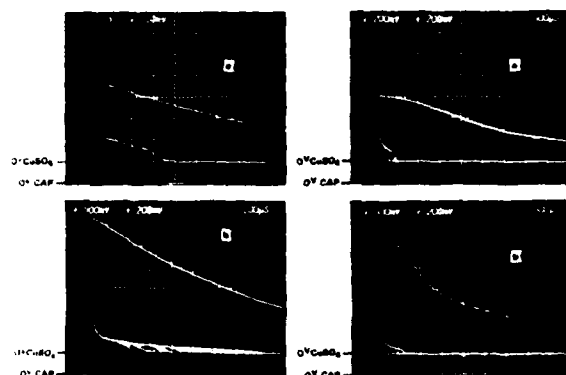


Figure 7. Decay of High Voltage in Glycol/Water Mixtures.

In the above figure, the left column shows decay at room temperature at low (a) and high (b) voltages. The right column shows decay at low temperature (-10°C). In all cases the voltage decay is faster than indicated by the value of τ . The anomalous decay apparent for the low temperature case is due to charge injection. Capacitor (P2) probe constant = 68 kV/V. The liquid is 80% glycol.

Electrical Breakdown

When the voltage on the test plates is increased beyond a certain value, electrical breakdown in the

liquid results. At these very long stress times, the field at breakdown and the time at which breakdown occurs no longer have a clear functional interdependence such as the familiar $E_{\max} t_{\text{eff}}^{1/2} = \text{constant}$ for short ($\sim 1 \mu\text{sec}$) pulses. For the long-pulse testing, E_{\max} was determined in the following way. In reference 1, it was found that onset of breakdown for pure water for the same electrode area was about 13 MV/m. The technique used to determine E_{\max} for the glycol/water mixtures was to apply the stress of 13 MV/m at which pure water would begin to break down (breakdown probability - 0.1). If the mixture survived ten tests at this level, the stress was increased 0.5 MV/m and ten more tests made. The maximum stress was increased in this manner until a breakdown was experienced. E_{\max} was then defined as the maximum stress applied to the plates which did not result in breakdown for ten successive tests. The results of this testing technique are summarized in Table 1. Because of the variation in temperature and mixture ratio, and due to the phenomenon of charge injection, the effective time of stress application varied over a considerable range. Thus, each value of E_{\max} has an effective stress time associated with it. Following historical practice⁸, the effective stress time, t_{eff} , is defined as the time for which the applied stress exceeds 63% of its maximum value. In Table 1, t_{eff} and three figures of merit - E_{\max} , W_{\max} , and A - are listed for the various mixtures tested, where

$$W_{\max} = \frac{1}{2} \epsilon_0 \epsilon_r E_{\max}^2 \quad (9)$$

$$A = W_{\max} \cdot t_{\text{eff}} \quad (10)$$

Because of the limited data base for these tests, the absolute values for the various figures of merit must be considered fairly (say 20%) uncertain. Nevertheless, we conclude that all the glycol/water mixtures have electrical strength figures of merit as good and quite possibly better than pure water.

Table 1. Electrical Strength of Glycol/Water Mixtures.

W	T (°C)	ϵ_r	r (mil)	t_{eff} (mil)	E_{\max} (MV/m)	W_{\max} (kJ/m ²)	A (J-s/m ²)
0	0	80	.87	.35	13.	69.	16.
40	25	67	.30	.10	16.	76.	8.
	-11	79	2.70	.40	16.	90.	36.
60	30	60	.30	.10	16.	65.	20.
	-21	77	16.00	.97	14.	67.	66.
80	25	40	1.40	.45	21.	90.	43.
	-10	60	23.00	1.00	17.	77.	77.
90	25	40	2.5	.30*	27.	120.	26.

*LIMITED BY EXTERNAL IMPEDANCE

Design Considerations

The two principal thrusts of this work are: (a) relatively long charge times are possible using water and water mixtures; and (b) system impedance can be varied over a wide range without making changes in its geometry. We will now discuss some of its implications of these facts for the pulsed power system designer. For the sake of brevity, we will consider coaxial PFL's discharging into matched loads. However, most of the conclusions still apply either directly or in a modified form for PFL's of other geometries. We will also address the question of impedance mismatch toward the end of this discussion.

The long charge times are irrelevant if the repetition rate is high (e.g., for a repetition rate of

10 kHz the system must be recharged and be ready to fire again in less than 100 μsec). For long charge times the intrinsic power gain is greater, thus requiring less peak power from the prime power source - an obvious advantage. The longer charge times also permit the use of rotating machines such as homopolar generators, alternators, and rotary flux compressors. Typically, these rotating machines can supply millisecond pulses (the active rotary flux compressor is usable to $\sim 100 \mu\text{sec}$ at reduced efficiency). Rotating machines are inherently repetitive devices and potentially offer many advantages in size, weight, and reliability.

By varying the dielectric constant of the liquid dielectric, the characteristic impedance and the pulse length of the pulsed power machine can be varied (however, not independently). If the characteristics of the load are not fixed, the pulsed power system designer has many options in designing his system. Even when the load impedance is fixed, there are many trade-offs which must be made that affect efficiency, voltage reversal in the load and PFL, size, cost, etc. We will now describe some of these trade-offs.

Consider a coaxial PFL of length ℓ , inner radius a , and outer radius b discharging into a matched load as shown in Figure 8. The characteristic impedance is:

$$Z_c = \frac{1}{2\pi} \sqrt{\frac{\mu}{\epsilon}} \ln \frac{b}{a} = \frac{60}{\sqrt{\epsilon_r}} \ln \frac{b}{a} \quad (11)$$

where $\epsilon = \epsilon_0 \epsilon_r$, $\mu = \mu_0$ and $(\mu_0/\epsilon_0)^{1/2} = 377 \text{ ohms}$.

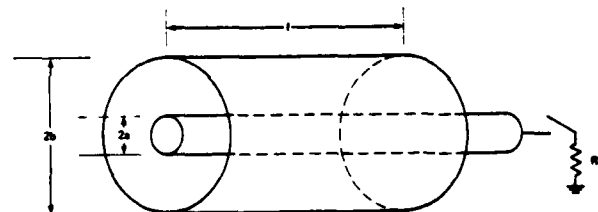


Figure 8. Coaxial PFL.

The highest electric field in an idealized coaxial structure occurs at the surface of the inner conductor. If V_{\max} is the breakdown voltage of the PFL, the maximum electric field is given by

$$E_{\max} = \frac{V_{\max}}{a \ln b/a} \quad (12)$$

It can be shown that the maximum voltage on the PFL for a given E_{\max} and outer radius (b) occurs when the ratio of the outer to inner radius is $b/a = e = 2.72$. With this ratio, the maximum voltage is:

$$V_{\max} = \frac{b}{e} E_{\max} \quad (13)$$

Note that the maximum voltage per unit outer radius depends only on E_{\max} . The impedance at this ratio will be dependent on the dielectric constant of the material as is shown in Tables 2 and 3.

Maximum power output for a given E_{\max} and b is obtained when $b/a = \sqrt{e} = 1.65$. With this ratio⁹

$$P_{\max} = \frac{\sqrt{\epsilon_r} E_{\max}^2 b^2}{(4) \cdot 2.60e} = \frac{\sqrt{\epsilon_r} E_{\max}^2 b^2}{1305} \quad (14)$$

where P_m is the maximum output power of a given PFL. Note that P_m depends on the square of E_{max} and b and on the square root of the relative dielectric constant of the dielectric.

In many applications, the principal factor in the cost of a PFL is the total surface area (TSA) of the inner and outer conductor [TSA = $2\pi\ell(b+a)$]. A minimum total surface area is obtained for a given P_m , E_{max} , ϵ_r , and b when the ratio $b/a = 2.09$. With this ratio,

$$P_m = \frac{\sqrt{\epsilon_r} E_{max}^2 b^2}{1423} \quad (15)$$

Again P_m depends on the square of E_{max} and b and on the square root of ϵ_r . For a given ϵ_r , E_{max} , and b the maximum power output is lower, but only by about 8%.

On the other hand, if the load impedance (and therefore Z_c for a matched load) is specified, the minimum TSA is obtained when the ratio $b/a = 9.19$. Then the maximum power is given by:

$$P_m = \frac{E_{max}^2 b^2}{Z_c (68.63)} \quad (16)$$

This requires that the dielectric constant satisfies

$$\sqrt{\epsilon_r} = \frac{60}{Z_c} \ln \frac{b}{a} = \frac{133}{Z_c} \quad (17)$$

Tables 2 and 3 will help clarify these results. In these tables, basic designs are presented for PFL's which will supply a megajoule pulse with a pulse length of 1 μ sec ($= 10^{12}$ watts for 1 μ sec). For these designs, the breakdown strength of the dielectric is assumed to be 100 kV/cm. Table 2 is for water with $\epsilon_r = 80$; Table 3 is for air with $\epsilon_r = 1$.

In these tables, the major design parameters are given as a function of the ratio of b/a . The ratios for maximum power per unit b , maximum power per unit surface area (for a given ϵ_r), and the maximum voltage per unit b are listed along with ratios which give representative impedances on either side of these values. Note that the impedance values for reasonable b/a ratios for the water line are in the 1 - 10 ohm range, while the impedance values for reasonable values of b/a for the air line are in the 10 - 100 ohm range. The only change is the dielectric constant of the liquid dielectric. For low impedance loads a high dielectric constant is desirable; for higher impedance loads (> 50 Ω) a lower dielectric constant is imperative.

The length of the PFL is

$$\ell = \frac{v t_p}{2} = \frac{t_p}{2\sqrt{\mu_0 \epsilon}} = \frac{t_p}{2(377)\epsilon_0 \sqrt{\epsilon_r}} \quad (18)$$

where t_p is the output pulse length and v is the propagation velocity. Hence, as soon as the pulse length and ϵ_r are specified, the PFL length is determined. The line length is inversely proportional to the square root of ϵ_r ; for long pulses practicality dictates that ϵ_r be large, which implies that the line will be a low impedance line. A water line of 16.8 meters length is practical for 1 μ sec pulses; however, a 150-meter air line is of questionable practicality.

In analyzing Tables 2 and 3, keep in mind that all of the lines listed will deliver an output pulse of

1 terawatt for 1 μ sec, into a matched load. Some of these designs are clearly impractical (e.g., the 50-ohm water line with outer radius $b = 329$ meters!). The intent of these tables is to indicate the range of applicability. We will now point out the highlights of these tables.

The charge voltage (V_c) for a given impedance and P_m is constant (since $V_c^2 = 4 P_m Z_c$), and increases with the square root of the characteristic impedance ($V_c = \sqrt{Z_c}$). If the charge voltage is divided by the outer radius, it reaches a maximum for $b/a = e$, as indicated above.

The inner radius monotonically decreases with increasing Z_c ($a = \ell/\sqrt{Z_c}$ for a given P_m , E_{max} , and ϵ_r). The outer radius b has a minimum for a b/a ratio of 1.65 (maximum power per unit b). To obtain the maximum power for a given outer radius, this b/a ratio must be used. The tables show how b becomes impractically large for high impedance water lines and low impedance air lines.

The total surface area varies nearly the same as b , except that it minimizes for a b/a ratio of 2.09, as indicated above. The total surface areas listed for the water lines with impedances between 1 and 10 ohms are practical.

The dielectric volume monotonically increases with impedance. This is expected since at very low impedance the inner radius approaches the outer radius and the field distribution between electrodes becomes uniform with little field enhancement at the inner conductor. Hence all of the dielectric can be stressed to near the breakdown field. Since the dielectric is expected to be the least costly item in a large system, it is not important to minimize its volume.

If the load is not matched to the PFL, reflections will occur at the PFL/load interface. This results in lower peak power in the load. The reflected power will return to the load at a later time (unless difficult precautions are taken) and is, at best, wasted. At worst, it is very detrimental to the load. It can cause voltage reversals in the PFL and load which are frequently very undesirable.

These undesirable aspects of mismatching the load and PFL sometimes can (or must) be accepted. We will therefore now briefly discuss the energy transfer into a mismatched load. We will define the efficiency as the energy dissipated in the load in the desired pulse time (the electrical length of the PFL) divided by the total energy stored in the PFL. If x is defined as the ratio of the load impedance R to the characteristic impedance Z_c of the PFL ($x = R/Z_c$), then it can be shown that the efficiency is given by

$$\eta = \frac{4x}{(1+x)^2} \quad (19)$$

Note that for $x = 1$, the efficiency is 1 as it should be. The function $4x/(1+x)^2$ is relatively slowly varying. For example, if $x = 2$ (or 4), the efficiency is 89%; if $x = 5$ (or 1/5) the efficiency is 56%.

This paper has shown that any dielectric constant between - 35 and 90 is available to the pulsed power system designer. Other water mixtures should extend this range to - 10 to 90. Values above 90 seem improbable for conventional liquids. Note that the above equations for maximum power are all proportional to the square of the electrical strength. Significant improvements would be attained with even modest increase of this important parameter.

Table 2. Design Parameters for One Megajoule, One Microsecond PFL.

WATER: $\epsilon_r = 80$, $E_{\max} = 10$ MV/m, Length = 16.8 m.

				Max Power b	Max Power TSA	Max Voltage b	
b/a	1.015	1.16	1.65	2.09	2.72	4.44	1726
Z_c (Ω)	0.1	1.0	3.4	5.0	6.7	10.0	50.0
Charge Voltage V_c (kV)	632.5	2000	3688	4472	5177	6325	14,142
$\frac{V_c}{b}$ ($\frac{kV}{m}$)	147	1282	3048	3549	3672	3364	43
a (m)	4.24	1.34	0.73	0.60	0.52	0.42	0.19
b (m)	4.30	1.56	1.21	1.26	1.41	1.88	329
TSA (m^2)	900	305	204	196	203	243	34,672
Dielectric Volume (m^3)	29	33	49	65	90	177	5,697,835

Table 3. Design Parameters for One Megajoule, One Microsecond PFL.

AIR: $\epsilon_r = 1$, $E_{\max} = 10$ MV/m, Length = 150 m.

				Max Power b	Max Power TSA		Max Voltage b	
b/a	1.002	1.017	1.18	1.65	2.09	2.30	2.72	5.29
Z_c (Ω)	0.1	1.0	10.0	30.0	44.2	50.0	60.0	100.0
Charge Voltage V_c (kV)	632.5	2000	6325	10,954	13,297	14,142	15,492	20,000
$\frac{V_c}{b}$ ($\frac{kV}{m}$)	17	164	1409	3034	3527	3626	3680	3150
a (m)	37.9	12.0	3.80	2.19	1.80	1.70	1.55	1.20
b (m)	38.0	12.2	4.49	3.61	3.77	3.90	4.21	6.35
TSA (m^2)	71,493	22,779	7792	5463	5250	5275	5425	7117
Dielectric Volume (m^3)	2261	2296	2680	3881	5178	5822	7219	18,341

Acknowledgements

The authors are indebted to K. Chilton, L.W. Hardesty, L.C. Johnson, and V. Gehman for valuable assistance with this work. We also would like to acknowledge valuable discussions with Dr. Ed Ball.

This work is supported by the Navy's Pulsed Power Technology Program and the NSWC Independent Research Program.

Footnote

* This power is one-fourth the power that would be transmitted into a matched load by a cable. When a PFL is switched into a matched load, the voltage across the load is one-half the PFL charge voltage (V_C). Since the voltage is half, the power across the load is one-fourth the power that would be present if the load were continually connected to a cable delivering its maximum power.

References

1. D.B. Fenneman and R.J. Gripshover, in Conference Record XIVth Pulsed Power Modulator Symposium, IEEE 80 CH 1573-5 ED (1980).
2. R.C. Weast, Handbook of Chemistry and Physics, 52nd ed., (Cleveland: Chemical Rubber Co., (1972), p. D-120.
3. D.B. Fenneman, "Pulsed High Voltage Dielectric Properties of Ethylene Glycol/Water Mixtures," submitted to Journal of Applied Physics.
4. H. Frohlich, Theory of Dielectrics (London: Oxford University Press, 1968).
5. C.P. Smyth, Dielectric Behavior and Structure (New York: McGraw-Hill, 1955).
6. G. Akerlof, Journal of American Chem. Society (1932), 54, 4125.
7. M. Zahn, D.B. Fenneman, S. Voldman, T. Takada, "Charge Injection and Transport in High Voltage Water/Glycol Capacitors," submitted to Journal of Applied Physics.
8. D.B. Fenneman and R.J. Gripshover, in IEEE Trans. on Plasma Science, PS-8 (1980), p. 209.
9. D.B. Fenneman, in Proceedings of Symposium on High Energy Density Capacitors and Dielectric Material, ed. C.W. Reed (Washington, DC: National Academy Press, 1981).
10. P. Lorrain and D. Corson, Electromagnetic Fields and Waves, 2nd ed. (San Francisco: Freeman and Co., 1970), Sec. 13.2. (See, also, problems at end of Chapter 13.)

HIGH REPETITION RATE, LONG LIFE CAPACITORS DEVELOPED FOR LASER ISOTOPE SEPARATION MODULATORS

V. Valencia, D.K. Haskell, R.A. Cooper

Maxwell Laboratories, Inc.
8835 Balboa Avenue
San Diego, California 92123
(714) 279-5100

Abstract

An atomic vapor laser isotope separation (LIS) research program was undertaken by Jersey Nuclear-AVCO Isotopes, Inc. (JNAI) to design a commercial uranium enrichment plant. Jersey Nuclear-AVCO Isotopes, Inc. was a joint venture by Exxon Nuclear Company and AVCO-Everett Research Laboratory, Inc. Exxon concluded its research and development activities in nuclear enrichment and reprocessing because of uncertainties in the outlook for private participation in these operations." This laser isotope separation process involves vaporizing uranium with e-beams and selectively ionizing U^{235} with flash lamp pumped dye laser beams, as shown in Figure 1. A commercial enrichment plant would require several hundred laser systems. Each system would run at 500 Hz to 1200 Hz, 24 hours-a-day continuously. This established the requirement of very reliable, high repetition rate capacitors for the flash lamp modulators with desired lifetimes exceeding 50,000 hours.

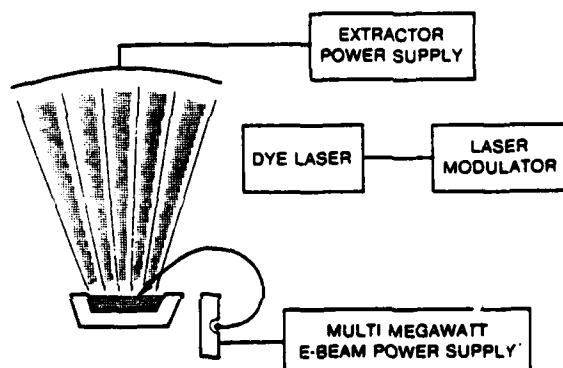


Figure 1. LIS process

This paper discusses the specifications for the required energy storage pulse capacitor, and Maxwell Laboratories' design which met the customer requirements. The performance data will be reviewed along with the construction. None of the supplied capacitors failed, even after obtaining greater than 10^{10} charge/discharge cycles. One unit, after nearly 3×10^9 charge/discharge cycles, was disassembled and examined. The data indicated that Maxwell's capacitor is an excellent candidate for reliable, long life, high pulse rate applications. Ongoing improvements in technology, dielectric films and oils will mean even superior capacitors can be designed for applications satisfying these types of requirements.

Laser Requirements and Objectives

As noted above, the JNAI LIS process required a number of flash lamp pumped dye lasers which must exhibit commercial reliability and life. Early in the

program, it became quite clear that within the laser pulse power system, a number of components were critical in meeting overall system reliability and life goals. Among these critical components were the laser pump energy pulse capacitors- C_p as shown in the simplified schematic of the laser modulator in Figure 2. Circuit operation, although simple in principle, placed severe requirements on each and every component, particularly the pulse capacitors.

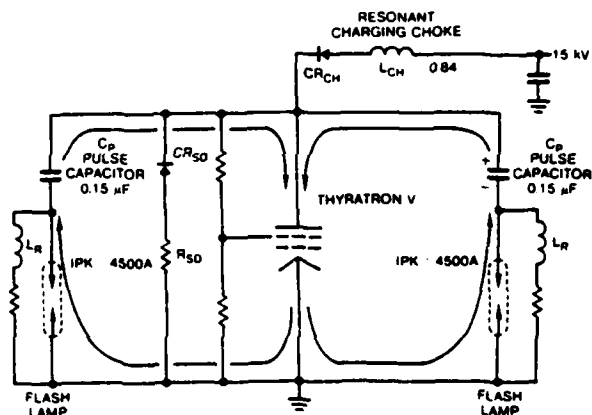


Figure 2. Simplified laser modulator schematic

As shown in Figure 2, the capacitors C_p are resonantly charged to a nominal 60 Joules in 1.5 ms. On command, thyatron V_I switches the stored energy of the pulse capacitors into the highly nonlinear flash lamp loads. Because of certain thyatron requirements, the inductors L_R must be adjusted to make the discharge circuit slightly oscillatory; hence, a 10-20% voltage reversal is experienced by the capacitors on each pulse. Residual post-pulse energy (due to the voltage reversal) is dissipated in the power resistor R_{SP} .

The capacitor operating requirements are shown in Table 1. The combination of these performance specifications together with the desired lifetime make the capacitors unique.

TABLE 1
LIS LASER MODULATOR PULSE CAPACITOR REQUIREMENTS

	CAPACITANCE	0.15 μ F	
	OPERATING VOLTAGE	30 kV	
	PULSE RATE	550 Hz	
VOLTAGE REVERSAL	8 kV	SELF INDUCTANCE (ESL)	50 nH
PEAK DISCHARGE CURRENT	4.5 kA	SELF RESISTANCE (ESR)	100 m Ω
CURRENT RISE TIME	0.6 μ s	OPERATING AMBIENT	40°C
CURRENT PULSE WIDTH (FWHM)	1.0 μ s	OPERATING ENVIRONMENT	OIL
LIFETIME: 50,000 HRS			

Vendors

Early capacitor candidates (non-Maxwell) were based on "single shot" technology and, as a result, exhibited lifetimes of from several minutes to several tens of hours. Once the pulse capacitor was recognized as a critical component, three capacitor manufacturers, including Maxwell Laboratories, were asked to satisfy the requirements. Only Maxwell Laboratories was successful in meeting all the performance specifications and up to the conclusion of the program had provided capacitors which accumulated over 21,000 hours of operation at pulse repetition frequencies exceeding 550 Hz without a single failure.

The other two vendors essentially gave up after a half dozen failures. Late in the capacitor development program, a fourth supplier's capacitor satisfied the operating requirements and exhibited individual capacitor operating times comparable to the Maxwell capacitors; however, the total capacitor operating hours of the fourth supplier were less than half those experienced by the Maxwell capacitors. There were no failures in the fourth vendor's units.

Vendor A provided the original capacitors, followed later by two additional designs. Maxwell Laboratories supplied the first acceptable test units and later the capacitors were used in the prototype system for a total of 14 capacitors. Vendor B was added because of the problems encountered with Vendor A's capacitors. They delivered two units. Vendor C was asked to supply capacitors for test and evaluation as a result of the continuing problems with Vendor A's and B's pulse capacitors. Three units were tested to develop a reliable second source for pulse capacitors.

Capacitor Design and Construction

The severity of this requirement presented Maxwell with a unique design and manufacturing challenge. The criterion of the capacitor's performance was a high average power density with high reliability over a considerably long life. These requirements posed a set of problems different than those usually associated with conventional single shot pulse discharge capacitors. The successful design of such a capacitor would depend upon the proper selection of materials, their quality, and the manufacturing processes used to produce the final unit.

The critical design consideration was thermal stability. In a capacitor operated at this pulse repetition rate, the major portion of the power loss is resistive- the capacitor's equivalent series resistance (ESR). Components of the ESR are contact resistance, skin effect in the electrodes, and dielectric losses. These losses are increasing functions of frequency. For this reason a dielectric system using predominantly polypropylene film with paper to aid in impregnation, and the impregnant PXE was chosen. Of all the available dielectrics, it was evident that polypropylene film exhibited significant superiority for this application. The main reasons being:

- Intrinsically high dielectric strength- >10,000 volts per mil
- Unique combination of temperature coefficients of dielectric constant and dissipation factor that result in self-stabilization at about 80°C

- The property of the film to absorb the impregnant and wet thoroughly greatly reduces the occurrence of partial discharges during operation
- The extremely low dissipation factor (.00017) that remains stable over a wide frequency range and improves with temperatures up to 80°C. This fact permits greater power transfer without thermal runaway.

The extremely low dissipation factor and the high dielectric strength of the polypropylene film were the dominant factors in determining the dielectric system used.

The impregnant was chosen in much the same manner. PXE has a broad range of attributes that make it superior for this type of capacitor. It has a consistently high dielectric strength compared to other impregnants. It exhibits low loss over a wide frequency range, necessary for thermal stability. This material has a low viscosity and low surface tension which allows the material to easily and completely wet the film surfaces. It has the ability to inhibit partial discharges as well as to scavenge the by-products generated by the partial discharges. Environmentally, it is nontoxic, and biodegradable.

The dielectric system of the Maxwell capacitor, because of its low losses, is not the dominant portion of the ESR. Therefore, it is not a significant factor in calculating temperature rise.

The heating in the capacitor is predominantly due to the power loss caused by the magnitude of the discharge current and the resistive losses in the foil, solder and electrodes. From the average and peak currents, the rms current is calculated:

$$\begin{aligned} I_{(\text{peak})} &= 4500 \text{ Amps} \\ I_{(\text{avg.})} &= 2.5 \text{ Amps} \\ I_{(\text{rms})} &= \sqrt{4500 \times 2.5} = 106 \text{ Amps} \end{aligned}$$

With the capacitor's effective resistance being a maximum 50 m Ω at the operating frequency, the capacitor losses can be calculated.

$$I_{(\text{rms})}^2 \times \text{ESR} = (106)^2 \times .05\Omega = 562 \text{ watts.}$$

To be able to dissipate this heat and keep the dielectric hot spot at or below 80°C required sufficient surface area. The Maxwell capacitor size was 7.25" x 14" x 15.5" and had 861 square inches to radiate the heat. Assuming the capacitor was 50 m Ω this translated to a surface heat flux of .65 watts per square inch. Figure 3 shows data of heat dissipating surface temperature versus surface heat flux for various temperatures of cooling oil. In a 40°C oil bath, the surface temperature rise, assuming .65 watts/per square inch, is approximately 16°C.

Using this data, the average surface temperature should be approximately 56°C. In a properly designed capacitor, there is a thermal gradient from the hot spot to the case of about 20°C. Therefore, the hot spot is approximately 76°C, which is within the temperature range where polypropylene exhibits its lowest losses. In actual operation, surface temperatures were monitored and the results were as predicted.

Another important design consideration was that of inductance. The equivalent series inductance (ESL) effectively limits the maximum rate at which the

capacitor can deliver current. To achieve a low inductance design, several manufacturing methods were employed. Each capacitor winding was comprised of multiple series sections and used extended foils as termination. Keeping the width to length ratio of the capacitor windings as high as possible and paralleling the inductances of the pads resulted in a net decrease in inductance of the capacitor stack. By the arrangement of conductors and terminals, the internal inductance can also be reduced. By using a low profile insulator, the inductance was reduced by providing the creepage distance in the radial direction which also allowed a reduction in conductor length.

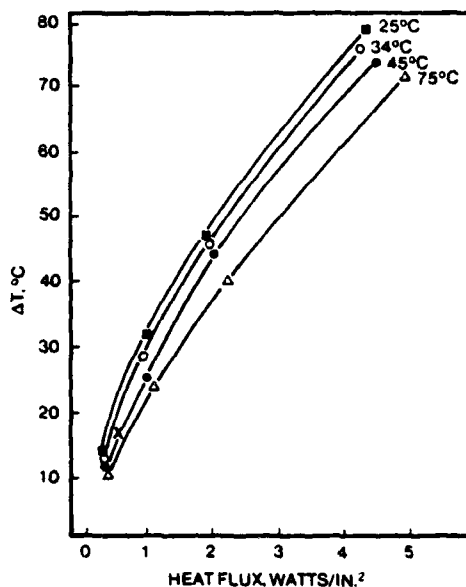


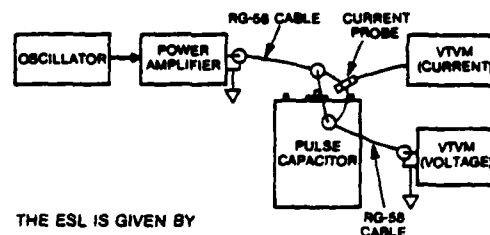
Figure 3. Dissipating surface temperature rise versus heat flux for various temperatures of cooling oil

ESL and ESR Measurements

In order to make valid comparisons between different capacitor designs, two techniques for accurate measurement of equivalent series resistance (ESR) and equivalent series inductance (ESL) were investigated. The first method involves charging the capacitor to several hundred volts and then viewing the current waveform while discharging it into a short; the actual procedure used is a differential technique which eliminates the switch and other hardware losses and inductances. The second method uses an rf oscillator to drive the capacitor at its self-resonant frequency; at resonance the voltage and current are in phase, so ESR and ESL may both be easily determined. This latter technique, as shown in Figure 4, became the preferred method.

The results of these measurements are found in Table 2. The Maxwell capacitor, Cat. No. 33580, was measured using both techniques since it was considered the best design. This allowed the comparison of it with the other designs regardless of the procedure utilized. Note that the Maxwell capacitor exhibited the lowest values of both ESL and ESR. Based on these values, Vendor A's units were deemed unacceptable.

Vendor B's capacitor compared favorably but it didn't perform successfully under full power test conditions.



THE ESL IS GIVEN BY

$$ESL = \frac{1}{(2\pi f_o)^2 C}$$

f_o = RESONANT FREQUENCY
 C = MEASURED CAPACITANCE

THE ESR IS GIVEN BY

$$ESR = \frac{V_o}{I_o}$$

V_o = VOLTAGE AT f_o
 I_o = CURRENT AT f_o

Figure 4. Circuit for determining ESL and ESR

TABLE 2
PULSE CAPACITOR COMPARISON

CAPACITOR TYPE	ESL (nH)	ESR (mΩ)
MAXWELL #33580	42 ¹⁾ 47 ²⁾	26 ¹⁾ 66 ²⁾
VENDOR A TYPE 1	106 ²⁾	190 ²⁾
VENDOR A TYPE 2	59 ²⁾	140 ²⁾
VENDOR A TYPE 3	75 ¹⁾	87 ¹⁾
VENDOR B	49 ²⁾	80 ²⁾
VENDOR C	47 ¹⁾	35 ¹⁾

1) SELF-RESONANT OR STANDING WAVE METHOD

2) DIFFERENTIAL DISCHARGE METHOD

Performance Data

Repetition Rate

The modulators were generally operated at approximately 550 Hz, while the test stand modulator was operated at times up to 600 Hz. As the project neared conclusion, the frequency was increased to 1000 Hz for about 80 hours with bursts to around 1250 Hz.

Operation and Theoretical Life

Fourteen Maxwell capacitors were tested for a total of 21,000 hours or approximately 4.2×10^{10} combined charge/discharge cycles. All individual capacitors were operated for over 10^9 to 10^{10} cycles without failures. Vendor A's capacitor experienced failure after 104 to 400 hours ($<10^9$) and Vendor B's two units failed at eight minutes and after 1836 hours (3.7×10^9). Vendor C had three units tested without failure; they also reached 10^9 to 10^{10} cycles. The

continuous power at 550 Hz and 28 kV (nominal) was 32.3 kW and at 1000 Hz it was 58.8 kW.

The theoretical design life of the Maxwell capacitor is $>4 \times 10^{10}$. This is based on accelerated life test data at higher voltage stresses on similar dielectric systems. The combination of the much lower voltage stresses in this design and the properties of the PXE oil could extend the life to greater than 10¹¹ cycles or 50,000 hours at 550 Hz. This is supported by two findings— one, the lack of a permanent capacitance change with time and the near new internal appearance of a capacitor after more than 1500 hours of operation.

Capacitance Change

It was found that the capacitance decreased during the first thirty minutes of full power operation. This phenomena is felt to be a thermal capacitance change; permanent capacitance decrease occurred in Vendor A's and B's capacitors in addition to the "warm up" change. Because Vendor A's and B's units were operated in the same modulator, their "warm up" change was lumped together. Table 3 gives these typical values. Note that the permanent and warm up changes of Vendors A and B are significantly greater than the Maxwell unit. The Maxwell capacitor had no apparent permanent capacitance change VS -2.7% and -4.1% while having half the warm up change -1.86% VS -3.93%.

TABLE 3
THERMAL INDUCED CAPACITANCE CHANGES

CAPACITOR	HOURS OF OPERATION	MEASURED CAPACITANCE	PERMANENT CHANGE	WARM-UP CHANGE
VENDOR A TYPE 2	0	0.146 μ F	-2.7%	-3.93%
	361	0.142 μ F		
VENDOR B	0	0.146 μ F	-4.1%	
	361	0.140 μ F		
MAXWELL	0	0.159 μ F	-0%	-1.89%
	1149	-0.159 μ F		

Capacitor Examination

After 1504 hours of operation or nearly 3×10^9 charge/discharge cycles, an unfailed capacitor was returned to Maxwell Laboratories for examination. Two years following manufacture, this capacitor, Cat. No. 33580, serial no. 87401, was measured for capacitance and dielectric loss (dissipation factor). The capacitance was unchanged while the dissipation factor improved from .1% (.001) originally to a reading below the scale on the bridge.

A sample of the insulating oil was removed and its volume resistivity was measured. The oil was still well above the minimum acceptable value. There was no evidence of gas in the capacitor. When the fill plug was loosened, the oil was still under a positive pressure.

The cover-insulator assembly was removed by milling the weld and the capacitor winding assembly was withdrawn from the case. The major insulation (between case and windings) was examined for any carbonation caused by localized heating of electrode interfaces. None was found. The solder was bright with no evidence of oxidation. To check the solder bonding between the extended foil and connecting tabs, the two were pulled apart. This required a screwdriver for prying, pliers and a considerable amount of force to separate. The foil actually tore

away from the windings and remained attached to the swage (solder).

These two things, solder appearance and bonding, are very important aspects to observe when analyzing capacitor construction. Solder oxidation not only degrades the dielectric system as a whole, but leads to poor contact between foil and collecting tab. This can cause high contact resistance with arcing between the foil and the solder swage which in turn generates gas, etc. leading to an "avalanche effect." In this case, the Maxwell unit had the appearance of a new, unused capacitor.

The capacitor windings were then examined for thoroughness of impregnation, margin control (wander) and any signs of corona damage. All sections were well-impregnated, regardless of their position in the stack. A random check of margins in several different windings showed them to be uniform, which in turn assures an even voltage division. There was no evidence of corona in any of the windings. The foil edges were looked at under magnification for signs of browning or tracking and none were found.

Overall, the capacitor was in excellent condition. The assembly was done well, all windings were aligned with no squaring off of the corners, the swaging was good and there was no damage to the dielectric system. After dissecting this capacitor, there is no reason to believe that it would not have lasted beyond its designed life.

Advances in Technology

Dielectric Films

Successful high repetition rate capacitors require low dielectric loss films. Polypropylene is recognized as the best film to date. In recent years, there have been improvements in the basic film. Standard polypropylene film usually requires a paper wick, in between the layers of film, to promote complete impregnation. However, there is now available hazy or roughened films where the surface of at least one side allows the complete impregnation of an all-film winding. This further reduces dielectric losses and heating in a capacitor while increasing energy density.

Manufacturing techniques have produced a more reliable polypropylene film with a higher dielectric strength and less defects. This has put more importance on the quality and type of dielectric fluid used.

Dielectric Oils

Manufacturers are constantly seeking insulating oils with high dielectric constants and low dielectric losses. The ideal impregnant for high repetition rate must possess a more complete set of properties. These properties are:

- High dielectric strength
- Low dielectric loss
- The ability to wet and possibly swell dielectric films
- Ease of handling (low susceptibility to contaminants)
- The ability to maintain low levels of partial discharges (corona) even at high voltage stresses while having the ability to absorb any resulting by-products (primarily gas) produced by these discharges

AD-A119 664

PALISADES INST FOR RESEARCH SERVICES INC NEW YORK
IEEE CONFERENCE RECORD OF 1982 FIFTEENTH POWER MODULATOR SYMPOS--ETC(U)
1982

F/G 9/5

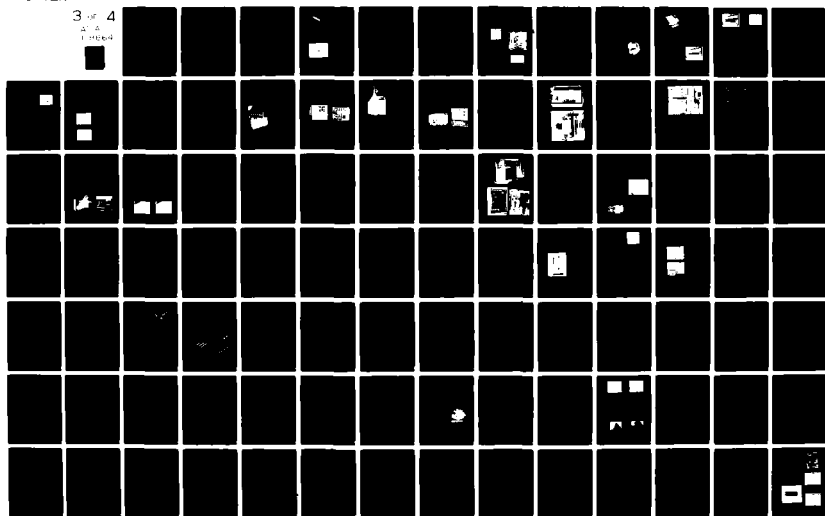
UNCLASSIFIED

82-CH-1785-5

NL

3 of 4

A 1
1 1984



The oil must be able to maintain or improve these properties under conditions of rising temperature and also have long life stability.

When the basic principles defining the chemistry required to produce these properties are established, then new insulating oils can be more easily found or created.

Today there are several oils producing promising results which indicate an improvement over the PXE used in this original Maxwell capacitor design, as well as improved PXE.

Conclusion

The requirement for a very reliable, high repetition rate capacitor used in flash lamp modulators has been met. The Maxwell capacitor delivered to Jersey Nuclear-AVCO Isotopes, Inc. demonstrated that the capacitor required for 50,000 hours of continuous operation at over 500 Hz is now available.

Acknowledgements

The authors wish to express their thanks to Jon Jasper of Exxon and Paul Hoffman of Capacitor Engineering Services for their contributions in the development of this capacitor.

MINIATURIZED PULSE FORMING LINES

BY

John Carter

US Army Electronic Technology and Devices Laboratory (ERADCOM)
Fort Monmouth, New Jersey

Introduction

There are a number of laser and microwave transmitter requirements where fast pulse rise time and minimum size and weight are of equal importance. The combined requirements of fast rise time and minimum size and weight make it desirable to eliminate the pulse transformer from the line type modulator transmitter design, since the leakage inductance of the transformer increases rise time and the transformer is an extra component increasing size and weight. The elimination of the pulse transformer in the line type modulator imposes an extra burden on the pulse forming device. The pulse forming device must be charged to twice the voltage required by the load (laser or microwave tube) and must also do the job of impedance matching between the pulse forming network and the load. One approach to the problem is to use a coaxial cable as the pulse forming device. The coaxial cable has fast rise time; however there are two disadvantages to this approach. The time delay per unit length is small, making the coaxial cable, PFL, too bulky for a number of transmitter applications. A second problem is the limited impedance range that can be achieved with the coaxial transmission line design. This is true with a straight center conductor coaxial transmission line because the inductance is fixed once the diameter of the center conductor is determined. In order to increase the range over which the inductance can be varied the straight center conductor is replaced with a continuous wound coil of wire in the form of a helix. The center conductor is wound in a tight helix hence the magnetic flux between the inner and outer conductor may be neglected. The inductance may be further increased by winding the helical inner conductor upon a ferromagnetic core. In order to demonstrate the feasibility of this approach, a number of experimental pulse forming lines were designed, fabricated, and tested.

Experimental Design

The design equation for a helical coaxial pulse forming line of the type shown in figure 1

are given in equations 1 to 4.(Fig. 2)

The final helical line design parameters for a 200 ohm PFL are given in Figure 3. The center conductor is a grooved bakelite rod. The insulated 22hf wire is wound using the groove in the bakelite rod to anchor the wire. The number of turns per cm. is 8.62 for a total of 88 for the 10.2 cm. length of the PFL. The space between the inner and center conductor of the coaxial line is filled with Stycast having a dielectric constant of 12. The outer conductor is a brass tube with an inner diameter of 1.27 cm.

Some comments are in order regarding the use of equations 1 through 4. The major problem area is the use of equation 2 for the capacitance. The equation assumes a solid center conductor which is not true for the helix coaxial center conductor. Experimental data indicates that the effective capacitance is about one half the value calculated by equation 2.

Experimental Results

A photograph of the prototype helical pulse forming line is shown in figure 4.

The test circuit used to evaluate the helical PFL is shown in figure 5. An 1154 thyatron is used as a switch to discharge the helical PFL which is charged through a 500 K resistor by a d.c. power supply. The voltage and current of the non inductive load resistor is observed using voltage and current probes with less than 1 ns rise time.

The inductance and capacitance of the pulse forming line were measured on an impedance bridge at a frequency of 1 megahertz. The inductance was 3.15 microhenrys and the capacitance was 61 picofarads. These values give us a calculated impedance of 227 ohms and a pulse width of 28 nanoseconds.

A typical output pulse is shown in figure 6. The measured dependence of load voltage on load resistance for a constant charging voltage of 2 kV is shown in figure 7. Taking the voltage drop of

the thyatron into consideration it is seen that the measured impedance is very close to the design value of 200 ohms.

Conclusion

The experimental results agree closely with the design equations. The helical pulse forming line results in a significant reduction in the length of the transmission line required to achieve a given pulse width. For example, the approximately 30 nanosecond pulse width measured for the prototype line would require at least 30 feet or 914 cm. of RG-213 cable. Thus a reduction in length of 90 times has been achieved. It should also be noted that co-ax cable at impedance levels higher than 75 ohms is not readily available.

The technique described above has been used to achieve practical PFL designs over the impedance range of 20 to 2500 ohms. A PFL with an impedance of 800 ohms was designed and fabricated to match a 95 GHz millimeter wave magnetron.

The small size and ease of impedance matching of the helical PFL makes this device attractive for Darlington type voltage multiplication circuits. Such a circuit is shown in figure 8.

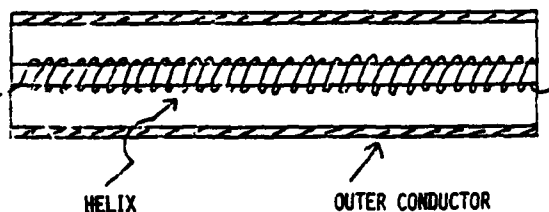


Fig. 1 Distributed PFL with helically wound center conductor

$$(1) L = \mu N^2 \pi^2 A^2 \times 10^{-7} H/M$$

A = MEAN DIAMETER OF SOLENOID (M)

N = TURNS PER METER

μ = RELATIVE PERMEABILITY

$$(2) C = \frac{2.4 \times 10^{-11} E}{\log(D/d)} \text{ F/M}$$

D = OUTER DIAMETER OF PFL

E = RELATIVE DIELECTRIC CONSTANT

d = OUTER DIAMETER OF SOLENOID (M)

$$(3) Z = \sqrt{\frac{L}{C}}$$

$$(4) T = 2\sqrt{LC}$$

Fig. 2 Inductance and capacitance formulas for helix PFL

LENGTH: 10.2 cm

HELIX DIA.: 0.64 cm (GROOVED BAKELITE ROD)

OUTER CONDUCTOR ID: 1.27 cm

OUTER CONDUCTOR OD: 1.43 cm

TOTAL # TURNS: 88

WIRE SIZE: #22HF

DIELECTRIC SLEEVE: STYCAST 12

Fig. 3 Helix PFL dimensions (200)

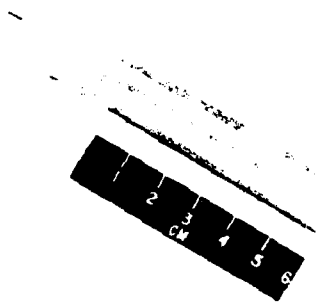


Fig. 4 Prototype helical pulse forming line

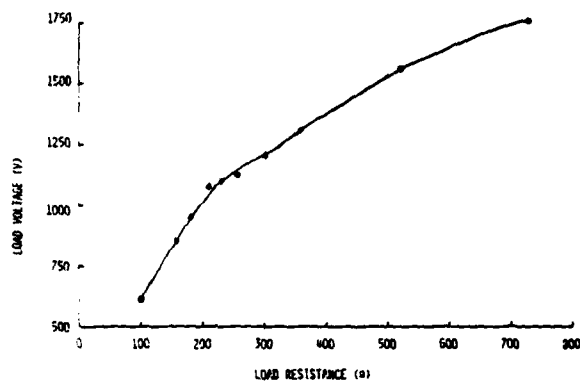


Fig. 7 Dependence of load voltage for helix PFL charge voltage, 2000 v

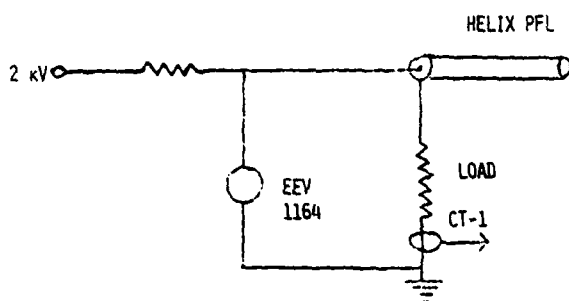


Fig. 5 Test circuit

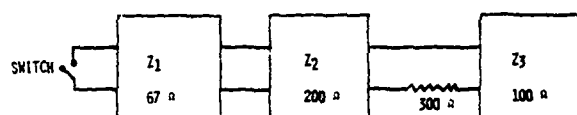


Fig. 8 Three-stage darlington

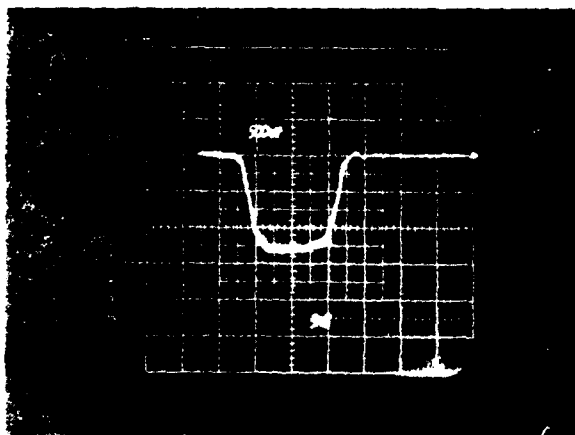


Fig. 6 Waveform of output pulse. Load, 180 ; charging voltage, 2 kv vertical, 360 v/cm; horizontal, 10 n sec/cm

PULSE CHARACTERISTICS OF XENON FLASHLAMPS

James P. O'Loughlin
Air Force Weapons Laboratory
Kirtland AFB, New Mexico

Summary

The efficient initiation of pulsed HF/DF lasers with uv light requires a source with high spectral intensity centered about 285 nm, a fast rise time (.5 μ sec), and a pulse width of about one microsecond. Xenon flashlamps are suitable for this purpose but require some special considerations for optimum performance. It has been determined by Lovo¹, Maynard and Smith¹ that xenon lamps are approximate black body radiators and a temperature of 13,365°K provides the maximum radiation efficiency of 26.18 percent through a fused quartz enclosure in the 250 nm to 400 nm band. Thus good performance would be expected from a lamp undergoing a temperature pulse to about 13,000°K in less than about .5 useconds and a width of about one microsecond. In order to accomplish this, power must be loaded into the lamp at a rate fast enough to overcome losses and raise the temperature to the target level within the .5 microsecond limit. To load power at this rate requires careful consideration and knowledge of the power source and the xenon lamp impedance characteristics.

Previous papers on xenon plasma impedance by Goncz² and Demenik et. al.³ are empirical and in poor agreement with each other. Also, no gas pressure, bore diameter or time-temperature characteristics are provided from the approximations. In both papers the resistivity is reported to be inversely proportional to the square root of the current density but the scaling factors differ from .22 (Goncz) to 1.13 (Demenik).

The approach taken in this paper models the resistivity of the plasma based on established physical characteristics, such as ionization rate, drift velocity, electron number density, fill pressure, bore diameter, specific heat, radiation loss, temperature and current density. Normally flashlamps are operated in a mode which is dominated by thermal ionization. When sufficiently high electric fields are forced upon flashlamps both thermal and electric field stress contribute to the ionization and the lamp will turn on (i.e. raise to high temperature) much more rapidly. In addition to more rapid turn on it has been experimentally observed that a large enhancement of ultraviolet radiation centered at about 300 nm occurs when the lamp is driven with high electric fields in the order of 150 Townsends.

Method of Approach

In order to gain a better understanding of the plasma impedance than that available from the empirical approach, a simple model based on established physical characteristics is used. Plasma resistivity is given by:

$$\rho = \frac{E}{j} = \frac{E}{eN_eV_d} \quad (1)$$

where: ρ = resistivity (ohm-cm)
 E = electric field (volts/cm)
 j = current density (amps/cm²)
 e = electron charge (1.602 E-19 coulombs)
 N_e = electron number density (#/cm³)
 V_d = electron drift velocity (cm/sec)

In addition to the usual assumption that the current is all electronic, the number density (N_e) is taken to be due to thermal ionization and the drift velocity is assumed to be proportional to E/N .

The degree of thermal ionization is given by Saha's equation⁴ as:

$$\frac{X^2}{1-X^2} = \frac{2.4E-4}{P_{Torr}} T^{2.5} \exp(-eV_i/kT) \approx Q \quad (2)$$

where: X = fraction of ionization ($N_e = XN$)
 P_{Torr} = lamp fill pressure (Torr)
 T = temperature °K
 V_i = ionization potential (12.08 volts for Xe)
 K = Boltzman's constant (1.38E-23 Joule/K°)
 $Q \approx X^2/(1-X^2)$

The linear approximation for the drift velocity⁵ is:

$$V_d = A(E/N) \text{ (cm/s)} \quad (3)$$

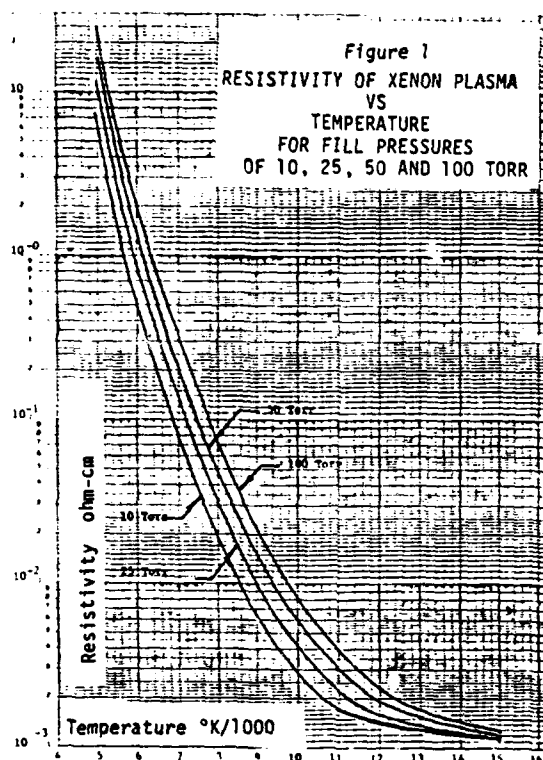
where: A for Xe $\approx 5.31E21$ (cm² volt-sec)
 N = molecular number density

Combining (1), (2), and (3) the resistivity as a function of temperature and fill pressure is:

$$\rho = \left(\frac{1+Q}{Q} \right)^{1/2} / eA \quad (4)$$

Equation (4) is, of course, valid only when thermal ionization dominates above about 3000°K, so for xenon lamps operating between 9000°K and 15,000°K it's a valid assumption. The second ionization potential of Xe is 32 volts and could be used to extend the temperature range above 15,000°K if one desired.

In figure 1 the calculated resistivity of Xe is shown as a function of temperature for fill pressures of 10, 25, 50, and 100 Torr.



If one assumes that the black body radiation from a cylindrical lamp is in equilibrium with the input electrical power the expression in (5) evolves.

$$j \sqrt{D} = \left(\frac{\sigma T^4}{\rho} \right)^{1/2} \quad (5)$$

where: D = lamp bore diameter (cm)
 σ = emissivity

The equilibrium condition exists for time spans greater than tens of microseconds. A reasonable agreement with data published by Avizonis⁶ for 200 microsecond pulses is shown in Table I. Also shown are the values of resistivity as predicted by Goncz and Demenik which are approximately an order of magnitude too low.

TABLE I

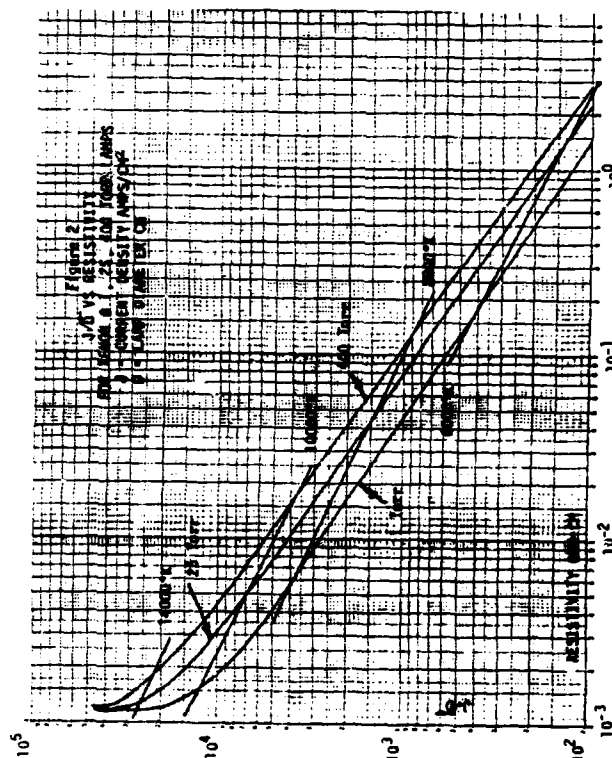
XENON RESISTIVITY DATA
Resistivity Values (ohm-cm)

Data No.	Measured by (6) Avizonis	Calculated per this paper	Calculated per (2) Goncz	Calculated per (3) Demenik
1	.0528	.042	.0021	.0110
2	.0480	.025	.0017	.0087
3	.0467	.038	.0018	.0052
4	.0460	.033	.0017	.0087

For the case of cylindrical lamps equations (4) and (5) can be combined to obtain a plot of $j \sqrt{D}$ (current density times root lamp diameter) vs ρ (resistivity). These curves for fill pressures of 1, 25, and 400 Torr are shown in figure 2. Notice the curves are relatively insensitive to pressure over the 400 to 1 range and that they converge to about .0012 ohm-cm at high temperatures ($\approx 14000^\circ K$).

The fact that the resistivity (and consequently the resistance) of a lamp is quite low in the desired operating temperature range implies that for efficient operation the characteristic impedance of the driver (usually a pulse forming network, PFN) must approximate a good match to the lamp over the major (low resistance) portion of the pulse.

If this is the case then the maximum voltage to which the network is initially charged is only on the order of twice the voltage when it is delivering power to the lamp at operating temperature. A check of the electric field E obtained from figure 2 shows a typical range on the order of 100 volts per centimeter corresponding to only 5.6 Townsends or about twice this amount, 11.2 Townsends as a maximum stress when the PFN first turns on into a cold gas. As the gas heats up the E field stress drops to much lower levels.



The point is that such low stress eliminates any possibility of electric field ionization therefore under these conditions the turn on time process of the lamp is entirely controlled by the development of thermal ionization.

If one is to speed up the rate at which the lamp raises its temperature to the desired operating level one must force it to accept energy at a faster rate. The logical thing to do is apply enough voltage to cause E field ionization in addition to the thermal ionization. This means raising the PFN or capacitor voltage to much higher levels but still maintaining a low characteristic impedance to insure an efficient overall energy transfer. The danger is too much energy will break the lamp. Empirically the explosion energy density is given by:

$$J_{\text{EXP}} = 18000 \sqrt{\tau/D} \text{ joules/cm}^3$$

where: J_{EXP} = explosion energy density (J/cm^3)
 τ = pulse width (sec)
 D = lamp diameter (cm)

To keep below the explosion limit one must reduce the capacitor size as the voltage is increased such that the explosion limit is not exceeded.

Experiments were made with 50 Torr lamps with stresses as high as 150 Townsends (2666 volts/cm). This is about equivalent to applying 40 kV/cm to atmospheric air.

Under these conditions the lamp of course turns on much faster but other things also happen. The current to the lamp shows a strong erratic behavior indicating streamers in the plasma, this both increases the rate of bulk temperature rise and enhances the output of ultraviolet light. A trace of lamp current showing the erratic behavior is shown in figure 3.

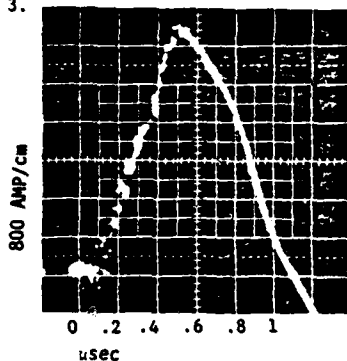


Figure 3
CURRENT PULSE 4 mm LAMP

A black body equilibrium between current density, resistivity and temperature assumed in figure 2 no longer holds. Of the total power input to the plasma only about 10-20 percent is accounted for by black body radiation, the rest is taken by the ionization of the gas, the excitation of metastable states, the raising of the bulk temperature, and other losses. Lamps of 4, 5, and 7 mm bore diameter at fill pressures of 50 Torr were tested. The observed current density and resistivity of a 5 mm is shown in figure 4. Also plotted in figure 4 is the resistivity based on the assumption of only thermal ionization. Since the time scale is much too short to even approach thermal equilibrium and the electric field strength is sufficiently high to contribute to the ionization and considerable discrepancy between the two resistivities is to be expected. The relative spectral intensity was measured at 1.3 kV/cm, 2.0 kV/cm, and 2.6 kV/cm and is shown in figure 5. The time waveform of the light pulse at 300 nm is shown in figure 6. The spectral intensity develops a very intense peak around 300 nm. This peak is far in excess of what would be expected from a black body radiator and is attributed to the ultraviolet radiation from the hot streamers which are assumed to be at a higher temperature than the bulk temperature of the gas. The 7 mm lamp produced a peak at about 250 nm whereas the 4 and 5 mm lamps peaked at about 300 nm. In any event the spectral peak is very desirable in frequency, intensity and time envelope for the efficient initiation of HF/DF chemical laser reactions.

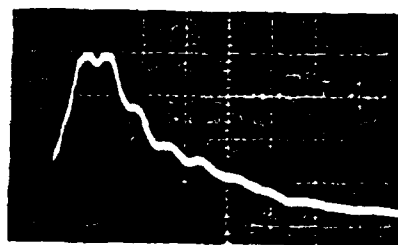
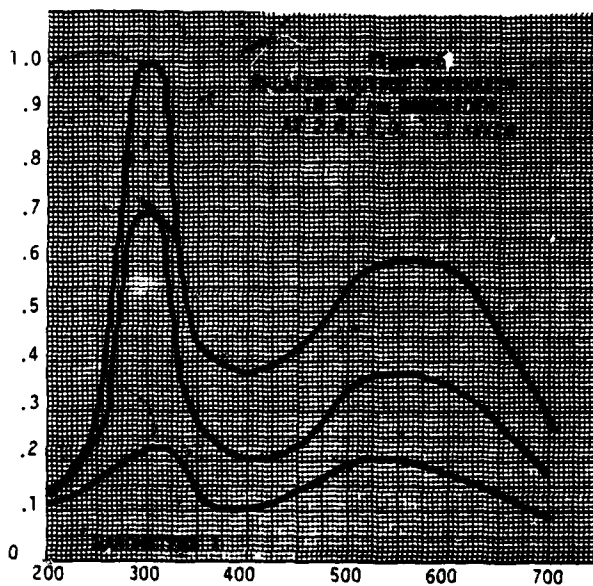
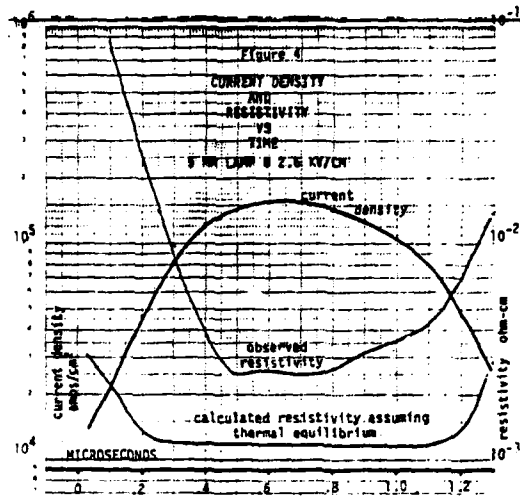


Figure 6
DETECTED LIGHT INTENSITY .5 us/cm
5 mm LAMP 155 kA/cm²
 $\lambda = 30 \text{ nm}$ $\Delta\lambda = 50 \text{ nm}$

Conclusions

The resistivity of xenon plasma may be calculated on the assumption of thermal (Saha) ionization and a linear approximation of electron drift velocity provided that the applied electric field is not sufficient to contribute to the ionization, i.e. less than about 40 Townsends. These calculations show a weak dependence of resistivity on the lamp fill pressure over a very wide range. The resistivity can be related to lamp current density, diameter, and fill pressure when black body radiation processes are near equilibrium. Very fast and intense ultraviolet output, in less than a microsecond, can be obtained when the lamp is driven with sufficiently high E field stress to produce electric field ionization streamers in addition to the thermal ionization process.

Acknowledgement

The assistance of Douglas Larson with instrumentation and experimental apparatus is greatly appreciated.

References

1. Lovoi, P.A., Maynard, R., and Smith, B., "Flashlamp efficiency for Photoinitiation in HF/DF Lasers," Proc. of the International Conference on Lasers '79.
2. Goncz, John H., "Resistivity of Xenon Plasma," Journal of Applied Physics, Vol. 16, No. 3, March 1965.
3. Demenik, I.V., et. al., "Resistance of Xenon Plasma in a Large Flashlamp," Soviet Physics, Vol. 13, No. 6, December 1968.
4. Cobine, J.D., "Gaseous Conductors," Dover Publication, 1958, p. 90ff.
5. Huxley, L.G.H., and Crompton, R.W., "The Diffusion and Drift of Electrons in Gases," John Wiley.
6. Avizonis, P.V., et. al., "Electrical and Spectrographic Study of a Double-Pulsed Flashtube as Applied to Laser Pumping," Journal of Applied Physics, Vol. 36, No. 10, October 1965.

BROAD-AREA DISPENSER CATHODES FOR HIGH POWER GAS LASERS

H. W. Friedman, J. E. Eninger, L. N. Litzenberger
Avco Everett Research Laboratory, Inc., Everett, MA 02149

Summary

We have demonstrated long life operation of dispenser cathodes in configurations applicable to high power gas lasers. Grid switched operation reduces pulse power requirements and the high repetition rate permits high average power operation. A 10 cm x 10 cm modular cathode has been scaled to a full 1 meter array. Operation for long duration pulses, in a magnetic field and at high repetition rates has been demonstrated.

Introduction

Dispenser cathodes have several properties which render them well suited for e-beam sources in high power gas laser systems.(1) The cathodes exhibit no diode closure effects even at high current density and for long pulse widths. The emission density is uniform and compatible with externally applied guide magnetic fields. The cathodes can be repetitively pulsed in either a diode or triode configuration and the useful lifetime can be thousands of hours.

The Avco Everett Research Laboratory has been developing these cathode arrays for laser applications and in a previous work(2) reported high current density e-beams in a guide magnetic field and under repetitively pulsed conditions. In this paper we report two continuing efforts; a lifetime test for a single 10 cm x 10 cm module and scale-up of ten such modules to a full 1 meter e-beam. The life test parameters are applicable to e-beam stabilized discharge lasers such as HgBr while the 1 meter array results are directed towards e-beam sustained discharge lasers such as CO₂, see Fig. 1.

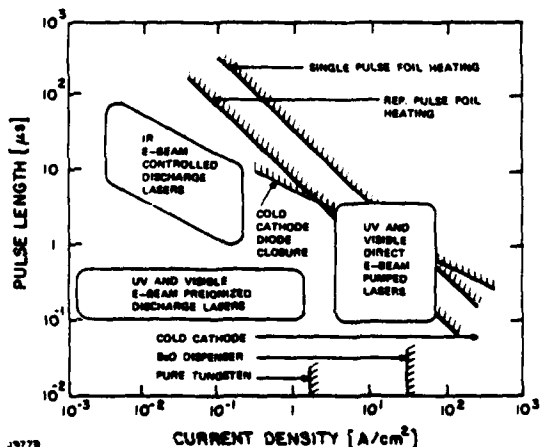


Fig. 1. E-Beam Source Requirements and Constraints for Several Classes of Lasers.

Table 1 summarizes the parameters of the two tests.

Table 1
Dispenser Cathode Development Tests

	LIFE TEST	1 METER TEST
CATHODE SIZE	10 x 10 cm	10 x 100 cm
GRID PULSE	10 kV	2 kV
ACCELERATION VOLTAGE	75-100 kV	120 kV
CURRENT DENSITY	1.6 A/cm ²	30 mA/cm ²
PULSE WIDTH	285 msec	20 μsec
REPETITION RATE	200 Hz (CONTINUOUS)	500 Hz (5 PULSE BURST)
MAGNETIC FIELD	N.A.	1 kG
FOIL	1 MH Ti (CONDUCTION COOLED)	1 MH Al (HEAT SUNK)

Cathode Life Test

The life test was carried out with a single 10 cm x 10 cm dispenser cathode module in a grid pulse mode with a d.c. applied accelerating voltage of up to 100 kV. A photograph of the grid portion of the high voltage terminal is shown in Fig. 2. A smoothly faired

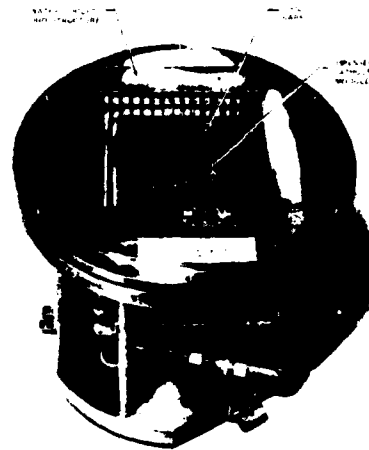


Fig. 2. 10 cm x 10 cm Dispenser Cathode Grid Structure.

cover fits around the grid with the grid bars flush with the surface. The grid structure is water cooled including the grid bars and the dispenser cathode module, shown in Fig. 3, is set 1.5 cm behind the bars. The heater structure consists of tungsten rods encased in alumina tubes which are inserted in holes drilled in the cathode block.

The grid pulse circuit, shown in Fig. 4, uses a step down transformer for the filament power and a thyatron switched Blumlein configuration for the grid pulse.

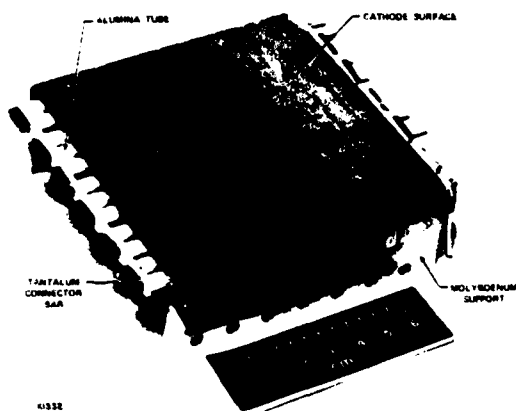


Fig. 3. 10 cm x 10 cm Dispenser Cathode Module with Tubular Heater Structure.

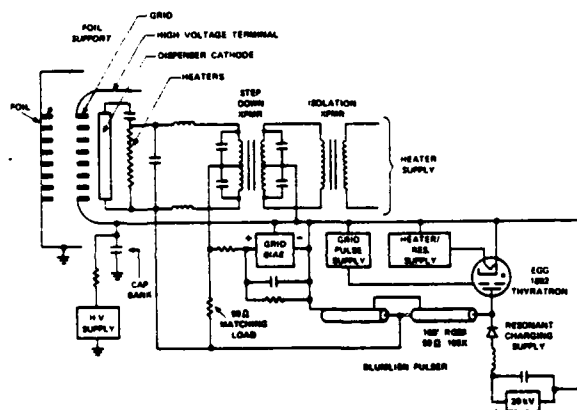


Fig. 4. Grid Pulse Circuit for Life Test Experiment.

The results of the life test are indicated in Fig. 5. An average emission current density of 1.6 A/cm^2 was obtained throughout the 70 hour test although slow variations about this average were observed during the day. These variations were caused by drifting charge voltage levels in the unregulated grid pulse power supply. No degradation of the cathode emission was noted during the 70 hours and the test was stopped for programmatic rather than technical reasons. The repetition rate was set at 200 Hz because of power dissipation in the grid pulse supply, however, repetition rates of 500 Hz were easily achieved for short bursts of ~ 1 sec duration.

One Meter Cathode Array

In the second test, ten of the 10 cm x 10 cm dispenser cathodes were arranged in line to demonstrate scaling to the 1 meter length level. The operating mode was again a triode configuration with an accelerating

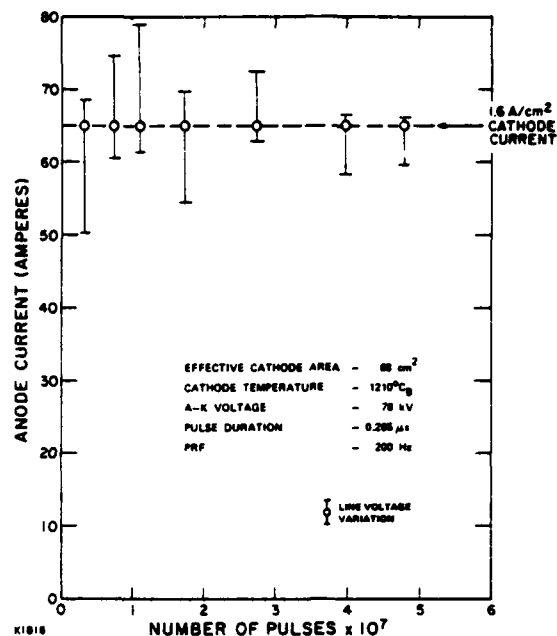


Fig. 5. 50-Million Shot E-Beam Test Results.

voltage of 120 kV. Pulse lengths of 20 μsec and current densities of 30 mA/cm^2 were representative of CO_2 laser operation, see Fig. 1. The repetition rate of 500 Hz was limited to bursts of 5 pulses for power supply considerations.

A photograph of the 10-module cathode array is shown in Fig. 6 with the filament structure, similar to that shown in Fig. 3, running longitudinally through the modules. A water cooled grid structure is placed 1.5 cm in front of the cathodes as shown in Fig. 7. The grid aperture has been masked down to 6 cm in



Fig. 6. 1 Meter Dispenser Cathode Array.

height for other purposes. A smoothly faired cover plate fits flush with the face of the grid structure to provide a high voltage terminal. The grid pulse circuit, Fig. 8, is similar to that of the life test with the short pulse thyatron modulator replaced by a hard-tube pulser. Thermal modeling calculations including radiation and conduction

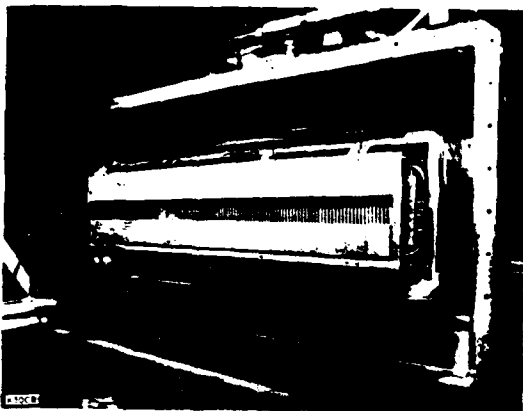


Fig. 7. 1 Meter Water Cooled Grid Structure.

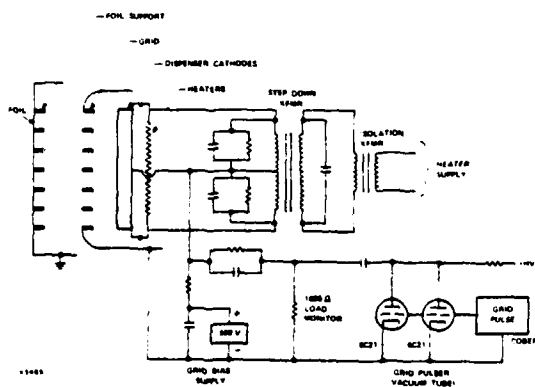
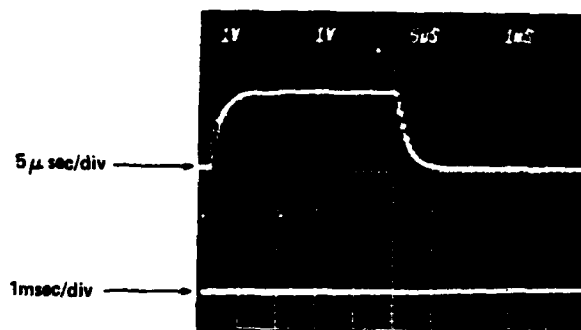


Fig. 8. Pulse Circuit for 1 Meter Array.

losses from the cathode structure agree with the filament power required to maintain the cathodes at the brightness temperature of 1200°C_B as is confirmed by direct pyrometer measurements.

The output waveshape for the e-gun current is shown in Fig. 9 for a 120 kV accelerating voltage and a 1 kG externally applied axial field. Two pulses were generated with a spacing of ~2 msec for an effective repetition rate of 500 Hz. The top trace is the overlay of the two pulses at a fast sweep speed and the bottom trace shows the pulses at a slower speed. The pulse-to-pulse reproducibility is excellent as is the case with an overlay of up to ten, 2 pulse runs. The rise and fall times have been purposefully extended to reduce the possibility of inductive "kicks" which could induce arcing for these long duration pulses. The natural rise time of the pulse is less than 100 nsec.



B = 1KG
BEAM ENERGY = 120 kV
2 PULSES AT 500 Hz

K4811

Fig. 9. E-Beam Current Pulse shape from the 1 Meter Array.

References

- (1) J. E. Eninger, "Broad Area on Beam Technology for Pulsed High Gas Lasers", 3rd IEEE Pulsed Power Conf., Albuquerque, N.M., June 1981, Paper 27.1, p. 499.
- (2) H. W. Friedman, J. E. Eninger, "Repetitive-ly Pulsed Dispenser Cathodes", 3rd IEEE Pulsed Power Conf., Albuquerque, N.M., June 1981, Paper 27.6, p. 519.

THYRATRON SWITCHED MARX GENERATOR¹

Craig L. Kimberlin, HQ Defense Nuclear Agency
Washington, D.C. 20305
Randy L. Lundberg, Lawrence Livermore National
Laboratories, Livermore, California 94550
William H. Wright, Jr., ET&D Laboratory, U.S.
Army ERADCOM, Ft. Monmouth, New Jersey 07708

Summary

Operation of a Marx generator using 8613 hydrogen thyratrons as switches and pulse-forming networks as energy storage elements, with the switches in the upper stages of the Marx being triggered by a signal derived from the lower stages (internal triggering), was investigated.

Timing requirements and erection diagnostics were determined using a two-stage Marx, with both stages triggered from separate external sources (manual triggering). It was found improper timing led to large voltage spikes on the last stage anode and a poor output pulse shape. Triggering the second (N+1) stage from a signal in the first (Nth) stage was unsuccessful.

A three-stage Marx was examined, with all stages triggered manually, to confirm timing requirements. Triggering the third (N+2) stage from a signal in the first (Nth) stage, with stages one and two externally triggered, was successful.

Triggering the N+2 stage from the Nth stage using a four-stage Marx (four from two and three from one) was very successful.

The investigation showed the amplitude of the voltage spike, on the last stage anode, and the output pulse shape to be a function of the trigger timing between stages. Output pulse risetime was almost twice as fast as the PFN's (pulse-forming network) risetime.

Introduction

Pulsed power supplies to drive loads such as high energy lasers, charged particle beam accelerators or electron beam guns often require repetitive operation in the kilohertz (kHz) range. Marx generators are commonly used to provide high energy pulses for various loads.

Basic Marx generators operate by charging capacitive energy storage elements arranged in parallel to a low or medium voltage level. Switches are used to electrically reconfigure (erect) the storage elements in series, producing an effective multiplication of the charging voltage.

The switching component normally used with the Marx, a high pressure spark gap, is severely limited in repetition frequency by the time required to recover its voltage holdoff capability for the next charging cycle. The thyatron, a low pressure, gas filled, hot cathode switch is inherently capable of much higher repetition frequencies. Since thyratrons are switched differently from spark gaps, they will not substitute directly for the spark gaps.

Thyratrons are normally switched on when a grid pulse is applied, but will also go into conduction if their forward breakdown voltage is exceeded. Conduction due to self-breakdown (overvoltage) is undesirable since it results in slower deionization times, decreased lifetimes at higher frequencies and a loss

of control over timing of the switching event. Proper operation of the thyatron requires the grid pulse be applied soon enough to allow the start of conduction before overvoltage occurs.

Marx operation imposes an additional requirement on the switching of the thyatron. A well-formed output pulse requires the Marx be erected in an orderly manner. A poorly formed output pulse results from applying the grid pulses too early or too late.

The use of thyratrons in a Marx has been prevented by the requirements to introduce a trigger signal and heater power to the thyatron at elevated voltage levels. Isolation of these inputs at high voltages is a difficult problem. Only the triggering problem was addressed in this experiment.

A logical method to obtain the properly timed grid pulses for the upper stage thyratrons would be to derive them from the lower stages of the Marx (internal triggering). Ewanizky examined this problem earlier.²

Two-Stage Marx Generator

A manually triggered, resonantly charged, negative output, two-stage Marx shown in Figure 1 was used. The switch tubes are 8613/HY1A triode hydrogen thyratrons and the stage isolating chokes (L) are 1.7 millihenry inductances. The trigger isolation pulse transformer T₁ has a 1:1 turns ratio, and the load consists of low inductance carborundum resistors with a total resistance of 94.4 ohms. Each PFN is a five-section, E-star, 50-ohm, 1-microsecond pulse width with a (IEEE) risetime of 175 nanoseconds. Time to major break is also 175 ns and is defined as the time from the 10% point (same as the 10% point on the 10-90% risetime) of the risetime to where the knee on the major rise occurs. This time is used to indicate the sharpness of the initial rise.

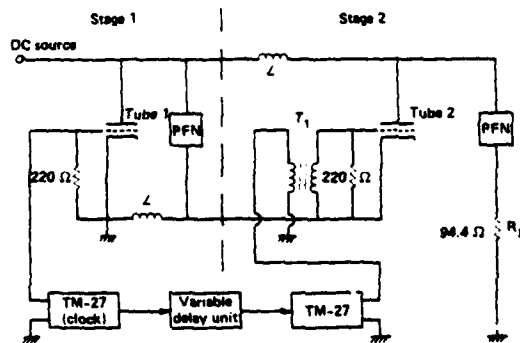


Figure 1. Manually Triggered Two-Stage Marx

A spike always appears on the anode voltage of whichever thyatron is firing last. Since a large voltage spike on the anode could cause the thyatron to overvolt, the spike amplitude was used as a figure of merit for the performance of the Marx.

Both thyratrons of the Marx were externally

triggered to determine the timing requirements necessary to prevent excessive anode voltage spikes and to observe output waveforms for various time delays between tubes one and two. The time difference between firings is measured from the anode voltage falls of the tubes.

When the firings of the tubes are brought closer together in time, the anode spike decreases in magnitude and the output voltage waveshape improves. This seemed to indicate that both tubes should be fired at the same time. Although anode voltage spikes were eliminated by firing the thyratrons simultaneously, the best output shape occurred when tube one was triggered approximately 35-40 ns before tube two. It is probable the lead time in triggering tube one is required to charge the stray capacitances present in the second stage of the Marx.

Table I shows the relationship between the spike on tube two's anode voltage and the time difference between triggering tubes one and two, which must be small if the anode spike is to be held down. This provides an excellent diagnostic tool for internal triggering.

TABLE I
Trigger Diagnostics

Time Difference Between Tube One and Two Anode Voltage Falls	Tube Two's Anode Voltage Spike Amplitude
35 ns	4 00 v
40 ns	1 000 v
50 ns	2 000 v
60 ns	3 000 v
70 ns	4 000 v

After the trigger timing requirements and diagnostics were established, experimentation to trigger tube two from an event in stage one began. Many trigger circuits and locations are possible, but the trigger circuit in Figure 2 offered an excellent chance for success. This trigger circuit was selected because it did not add inductance to the discharge path of the erected Marx. Energy for the trigger circuit comes from the power supply and not from the erected Marx.

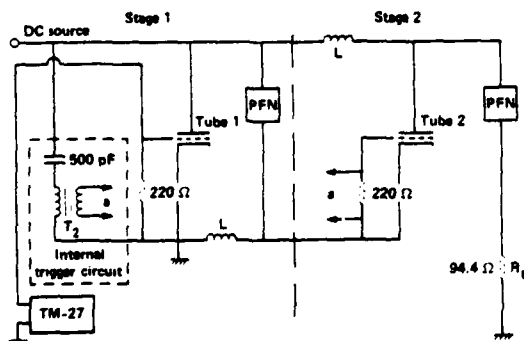


Figure 2. Internally Triggered Two-Stage Marx

The trigger circuit consists of a 500-picofarad (pF), 30-kV capacitor in series with the primary side of T_2 , a 1:1 hand-wound transformer. The capacitor was sized by determining the charge required to fire the thyatron.

Anode voltages of the internally triggered two-stage Marx are shown in Figure 3. The top trace is anode two voltage and the bottom trace is anode one voltage. The traces were separated vertically for clarity.

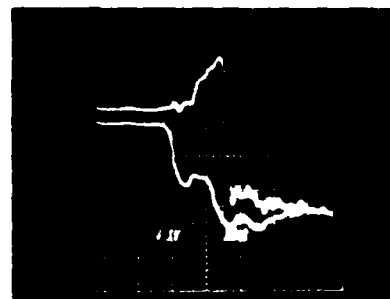


Figure 3. Anode Voltages of Internally Triggered Two-Stage Marx

Anode two had a voltage spike of 3000 volts, and there was a time difference of 65-70 ns between the two anode falls. This time difference corresponds closely with the time difference for a 3000-volt anode spike in Table I.

Tube two was being fired far too late and several changes to the circuit were made in an attempt to fire tube two sooner. All attempts to decrease the time difference were unsuccessful.

It was decided that triggering the $N+1$ stage from the N th stage was not possible, but triggering the $N+2$ stage from the N th stage had a high probability of success. This optimism was due to the fact that a 35-40 ns time difference between the anode falls gave a good output shape, when manually triggered, and internal triggering was giving a time difference of 65-70 ns between the anode falls.

Three-Stage Marx Generator

A third stage was added to the Marx and the load resistance was increased to 140 ohms. Trigger circuitry was set up so the three thyratrons could be fired in any order with any desired separation between the anode falls. This was done to verify the two-stage results.

It was found that the tubes could be fired in any order and still give an acceptable output pulse shape, with proper timing of the triggering. Best results, however, were obtained with a 1, 2, 3 firing order, as expected.

A good load pulse shape was obtained with tube one firing 20-30 ns before tube two, with tube three firing anywhere between 0 and 25-30 ns after tube two. Timing requirements for the three-stage Marx have become a little tighter, especially between the second and third stages. It is felt the significant decrease in time difference between the last two stages is due to the stray capacitances being partially charged when tube one is fired.

Next, the first and second stages were triggered

manually using TM-27's, with the third stage being triggered from the first. The trigger circuit for the third stage was the same as in the two-stage Marx.

Since timing for the three-stage Marx was still highly variable, it was decided to look at all three anode voltage falls equally spaced. Success of this case would imply the internal trigger method could be used for Marx generators having a larger number of stages. This time spacing did not provide the optimum output pulse, but still gave an acceptable load pulse shape. There were approximately 35 ns between the fall of each anode. Tube two and tube three both had anode spikes close to 1000 volts and, therefore, correspond very nicely to the values in Table I.

Four-Stage Marx Generator

A fourth stage was added to the Marx with stages one and two fired externally. Stage three was triggered from stage one and stage four was triggered from stage two. The internal trigger circuits are the same as in the two-stage circuit except the hand-wound transformers are wound as step-up transformers with a 1:2 turns ratio. The load was increased to 188 ohms. The firing of the second thyatron was delayed 30 ns from that of the first tube due to results of the two- and three-stage Marx experiments.

The anode voltages for all four thyatrons are shown in Figure 4. The time between each anode fall is 30-35 ns. While small anode spikes are present on the third and fourth thyatrons, they do not cause firing due to overvoltage. The traces are separated vertically for clarity.

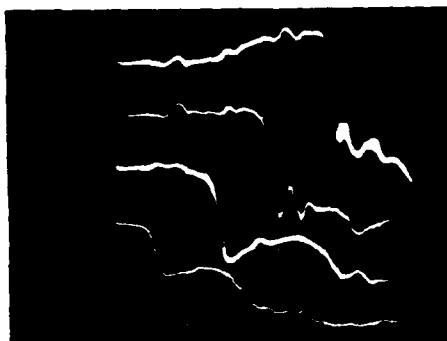


Figure 4. Anode Voltages for Four-Stage Marx, 100 Hz, $e_{py} = 6$ kV

Vertical - 1 kV/small div - all traces
Horizontal - 10 ns/small div - all traces
Top to Bottom - Tubes 4, 3, 2 and 1

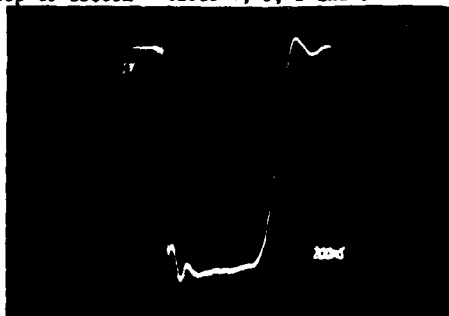


Figure 5. Load Voltage for Four-Stage Marx
Vertical - 1 kV/small div
Horizontal - 200 ns/small div

The load voltage output waveshape is presented in Figure 5. The waveform has a risetime (10-90%) of 100 ns and a small amount of ripple.

An interesting and significant result is the risetime of the load pulse. The load pulse has a 10-90% risetime of 100 ns with a time to major break of 70 ns. The PFN's times were 175 ns and 175 ns, which are considerably slower. This could possibly be caused by a sharpening effect from each stage. More work is needed in this area to determine the exact cause of output pulse sharpening.

To insure that the internal trigger circuits were actually responsible for firing the third and fourth thyatrons, several checks were made. First, the internal trigger circuit transformers were disconnected from only the third and fourth stage thyatrons. Then the transformers were reconnected to the third and fourth stages and disconnected from the first and second stages. Finally, the internal trigger circuits were completely removed from the Marx generator circuit. The Marx did not operate in an acceptable manner for any of these conditions.

In all three cases, the results were the same. Excessive anode voltage spikes characteristic of overvoltage appeared on tubes three and four. The output pulse waveshape had a ragged leading edge and a large amount of ripple on the top of the pulse. Only minimal control of the anode voltage spikes and the output waveshape could be achieved by varying the time delay between tubes one and two. No timing setting could reduce the anode voltage spikes to an acceptable level or return the output pulse waveshape to that shown in Figure 5. These results show that proper firing of tubes three and four is due to the internal trigger circuit and not capacitive division or inductive coupling effects.

Once the baseline data was collected, the peak anode voltage, e_{py} , and repetition rates were varied to the limits of the power supply and internal trigger circuit transformer insulation as seen in Table II. The output waveshapes remained constant with variations in repetition rate and charging voltage.

TABLE II

Circuit Capabilities

Frequency	Load Voltage	Limit
100 Hz	26.0 kV	Insulation of Internal Trigger Circuit Transformers
1000 Hz	12.5 kV	Power Supply
2000 Hz	6.0 kV	Power Supply

An important and encouraging effect of raising the charging voltage was observed on the anode voltage of the fourth tube. The anode voltage spike did not increase proportional to the increasing value of e_{py} . This means that e_{py} can be raised to nearly the voltage holdoff limit of the tube without firing due to an overvoltage caused by the spike.

There are two possible causes for this effect:

1. The increasing energy stored in the trigger circuit capacitor. This energy increases by the

square of e_{py} and could cause the tube to turn on faster.

2. The increasing anode voltage brings the tube nearer to its self breakdown voltage. The nearer the thyatron is to its breakdown voltage, the easier it is for the same grid signal to turn on the tube.

To determine if the internal trigger circuit could be used in a Marx that had more than four stages, internal trigger circuits with dummy loads were attached to tubes three and four. The operating conditions were the same as the basic four-stage Marx experiment. The output waveshape and tube four's anode voltage were compared with and without the dummy-loaded trigger circuits in stages three and four. There were no observable differences between the sets of waveforms. This indicates that a stage fired by an internal trigger circuit can fire another stage without adversely affecting Marx operation.

Conclusion and Recommendations

It is possible to use an internal triggering scheme to fire hydrogen thyatrons employed as switches in a Marx generator and achieve a well-formed output pulse.

Based on observations made during the investigation, the following recommendations are proposed for further study:

1. Although a workable triggering circuit was proven, more experiments should be conducted to

find a faster method of triggering.

2. Investigate what effect the number of stages in the Marx has on the risetime of the output pulse.

3. A five- or six-stage Marx should be constructed to prove that a stage fired by the internal trigger circuit can actually fire another stage as indicated by the experiment with trigger circuits attached to tubes three and four.

4. Replace the PFN's with lengths of coaxial cable to examine Marx operation with a fast risetime pulse. It is possible a fast pulse may require the time difference between anode falls to be very small in order to prevent excessive anode spikes.

Footnotes

¹ This work was done as partial fulfillment of a Masters Degree at the Air Force Institute of Technology by Capt Kimberlin and CPT Lundberg. It was jointly funded by the Defense Nuclear Agency and ET&D Laboratory, U.S. Army ERADCOM, Ft. Monmouth, New Jersey. The thesis was entitled "Internal Triggering Marx Generator Using Hydrogen Thyatrons." Mr. William Wright served as thesis advisor.

² EWANIZKY, THEODORE F., "High Repetition Rate Thyatron Marx Bank," IEEE Conference Record of 1980 Fourteenth Pulse Power Modulator Symposium, CH1573-5 191-194, IEEE Electron Devices Society, 1980.

LINE TYPE MODULATOR WITH PULSEWIDTH AGILITY

Edward M. Plechowiak, Edward H. Hooper, Ernest C. Farkas
Westinghouse Electric Corporation
Command and Control Divisions
P.O. Box 1897
Baltimore, MD 21203

Michael Lipka, Code 5331
Naval Research Laboratories
4555 Overlook Avenue, S.W.
Washington, D.C. 20375

Summary

A modular line-type modulator has been developed with design features that include variable pulsewidth and PRF, single shot and burst capability, and automatic fault isolation with switching to remove failed modules from the system while continuing operation at a reduced level of performance. The design addresses a requirement of 40 kW average power output, 7.5 MW peak power output, and 3, 6, and 12 second pulsewidths. The pulsewidth can be changed on a pulse-to-pulse basis by utilizing selective resonant charging in conjunction with PFNs that incorporate diode isolation between segments.

Modular construction is used in the inverter power supply, the charging system, and the modulator to facilitate maintainability and allow for automated graceful degradation. The modulator uses Reverse Blocking Diode Thyristors (RBDTs) for the discharge switches to offer instant-on capability with a high degree of reliability.

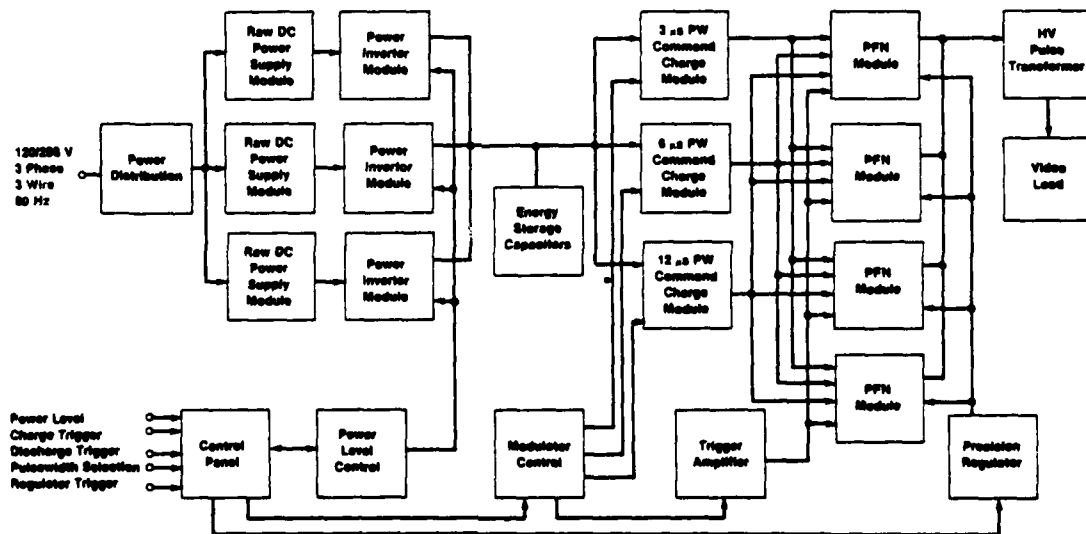
Two stages of regulation are incorporated to achieve pulse-to-pulse stability of the high voltage output. Inverter regulators provide the first stage of regulation followed by a precision solid-state regulator to accurately control the charge voltage amplitude on the PFNs.

Introduction

The program to develop the versatile solid-state modulator described herein was funded by the Naval Research Laboratories under contract N00173-78-C-0245. It was intended to extend the previous modular solid-state modulator technology development to include such key features as:

- Selectable pulsewidth on a pulse-to-pulse basis
- Variable pulse repetition frequency from 0 to 1500 pps average
- Single pulse or burst capability of up to 2000 pps
- Variable output voltage from 0 to 112 kV
- Automatic fault isolation with the capability to disconnect failed modules
- Pulse-to-pulse voltage regulation of at least 0.05 percent.

The basic block diagram of the modulator and the associated charging system is shown in figure 1. Modularity is used in the raw dc power supply, the power inverter, the selectable charging networks, and the pulse forming network modules which also contain the discharge switches. The power flow through the system starts with line rectification of the 120/208 volt, 3 phase input. The power inverter modules, which operate at a frequency of 10 kHz, step the unregulated dc up to



82-1433-V-2

Figure 1. Basic Block Diagram for Multiple Pulsewidth Solid-State Modulator

a maximum voltage of 1500 volts. The outputs from three power inverter modules are combined in three paralleled energy storage capacitors. Command resonant charging is accomplished by triggering the desired command charge module which determines the pulsewidth to be used for a particular PRT. Each of the three command charge modules feeds into four paralleled PFN modules, charging only those sections of the PFN that correspond to the selected pulsewidth. The trigger amplifier, after receiving a discharge signal, produces a common high voltage trigger with a rate of rise of 25 kV/microsecond that is applied to the four PFN modules. The PFN module outputs are combined in the primary of a high turns ratio pulse transformer to deliver the output pulse to the load. The precision regulator, shown in the lower right-hand corner of the diagram, is triggered on to perform its regulating function at a predetermined time before the discharge process begins. It provides a controlled bleed of the energy stored on the PFNs to give a pulse-to-pulse regulation of 0.05 percent. One other control signal applied to the modulator power system is the input that selects the amplitude of the voltage processed by the modulator. This control is accomplished by varying the on time of the power inverter modules. Figure 2 is a photograph of the system. The cabinet on the right contains the raw dc modules, storage capacitors, and regulator. The main modulator cabinet houses the three power inverters at the top, the four PFN modules and trigger amplifier in the center, and the three command charge modules and cooling blower at the bottom.



Figure 2. Prototype Modulator and Power Supply

Power Conditioning

Figure 3 shows the basic circuit used for generating the 1500-volt input to the command charge modules. Each of the three raw dc modules has a power contactor in its ac input, and each power inverter module is fed through an isolating diode at its output. These features provide the means to remove a failed unit from the operating system when a fault is detected. The raw dc module contains a three-phase bridge, step start circuitry to minimum in-rush current, and an LC filter. Approximately 5400 microfarads of capacitance are provided in each of the modules. The 280-volt output feeds into an inverter module that contains the basic SCR inverter which operates into a step up

transformer and single phase rectifier bridge to produce the 1500-volt output. The three paralleled outputs for the system provide over 45 kW of output power in normal operation. The reserve power capability of the inverter modules is such that the required 45 kW can be supplied by only two modules. Such would be the case when a faulty inverter module was disconnected from the system. The obvious penalty that is paid for this feature is a larger sized module. Figures 4 and 5 show the raw dc and inverter modules, respectively, and figure 6 shows the cabinet that houses the raw dc supplies and storage capacitors.

PFN Charging System

The charging system is shown in figure 7. The choke used for the resonant charging is an air core inductor divided into three sections, each having 0.22 mH of inductance. All three sections are used when charging the PFNs for the 12-microsecond pulsewidth, two sections for the 6-microsecond case, and only one section for the 3-microsecond pulse. Changes in inductance are required because of the different PFN capacitance at the various pulsewidths and the different PRF requirements at the various pulsewidths. The PRF and pulsewidth relationship is as follows:

Pulsewidth	PRF
3 microseconds	0 to 1680 pps
6 microseconds	0 to 920 pps
12 microseconds	0 to 420 pps

Each of the command charge modules contains five series SCRs which are triggered from a multiple secondary pulse transformer to provide adequate isolation between SCR triggers. Three diodes are also employed in series with the SCRs to improve the voltage hold-off capability of the string. The output of each of the modules is routed through a power contact to isolate it from any PFN module which may have failed. A photograph of a typical command charge module is shown in figure 8. The "L" shaped configuration is used in order to conveniently package the three command charge modules around the charging inductor, as shown in figure 9.

Pulse Forming Network Module

The basic building block of the modulator is the PFN module, which contains a pulse forming network, an RBDT switch assembly, a trigger circuit, monitoring circuitry, and minor auxiliary circuitry. A simplified schematic diagram of the PFN module in figure 10 can be used to illustrate the function of the module.

The pulse forming network has three charging terminals. Each terminal and the portion of the network that is charged through it is diode isolated from the sections to the right. Thus, application of voltage to terminal 1 results in only section 1 of the network being charged. When terminal 2 is used, both sections 1 and 2 are charged together. The network is an "E" type network, but there is only minimal mutual coupling between the three discrete pulsewidth sections of the PFN.

The switch used to discharge the PFN is a series string of five RBDTs packaged in an assembly that includes the trigger blocking diodes and the backswing diodes. The assembly includes finned heat-sinks between each of the semiconductors over which flows cooling air which is ducted to the PFN module. The RBDT stack is triggered by applying a high rate of rise voltage impulse across the RBDTs in the forward direction. This impulse is generated by dumping a trigger storage capacitor through a trigger transformer that is capacitively coupled across the RBDT stack. Dumping of all trigger storage capacitors to generate the trigger pulse is controlled by the trigger amplifier chassis located to the right of the PFN modules in the center shelf of the modulator cabinet. Various monitors are included in each PFN module, including charging current, discharge current, and stack voltage, which can be used to detect a failed RBDT. Since the voltage rating on the RBDT is a minimum of 800 volts per device, the hold-off voltage of the stack is at least 4000 volts. Operation of the circuit

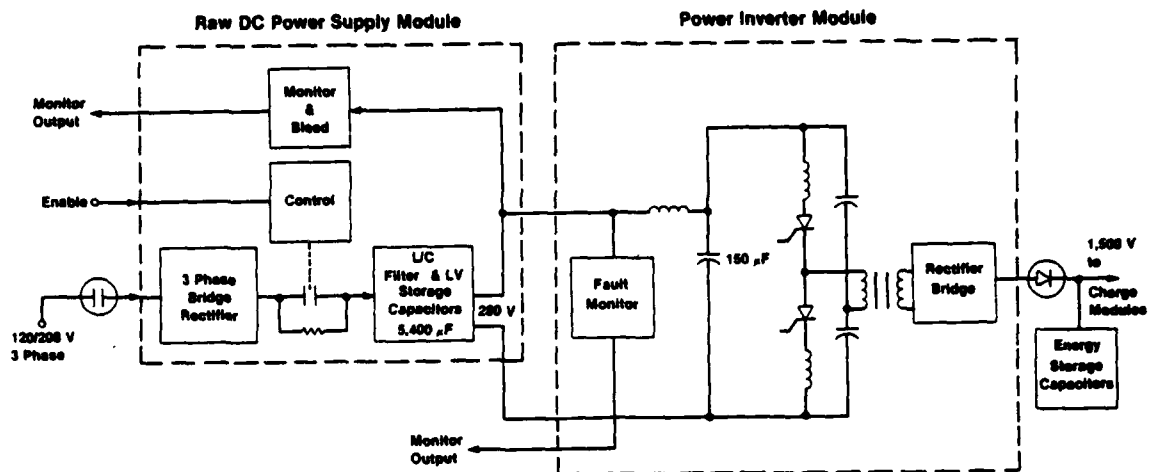


Figure 3. Power Conditioning Circuits

82-1433-B-4

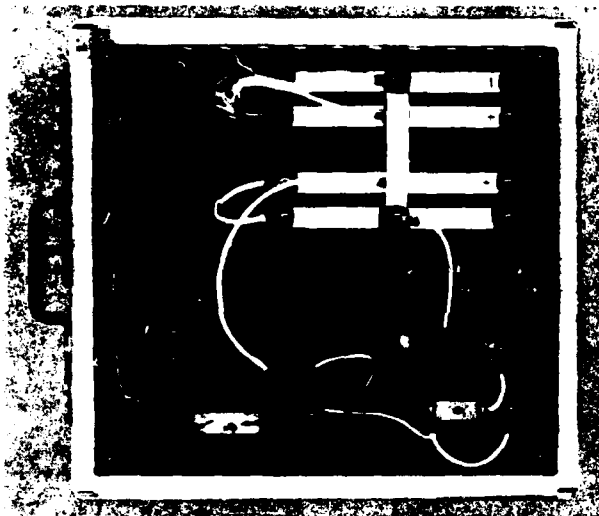


Figure 4. Raw dc Power Supply Module

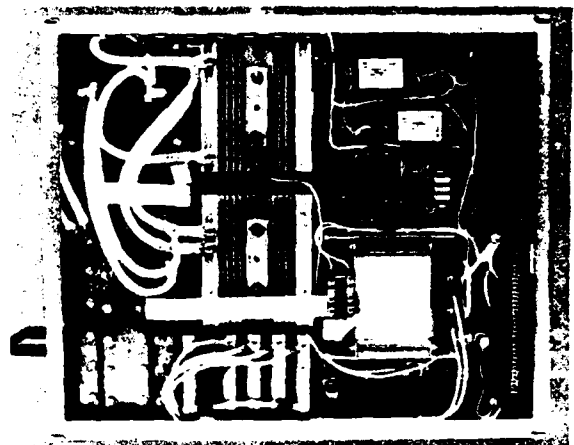


Figure 5. Power Inverter Module



Figure 6. Raw dc Power Supply and Regulator Cabinet

requires a maximum hold-off of only 3 kV. Since the mode of failure of an RBDT is too short, the circuit can continue to perform within specification with failed devices in the circuit. The voltage monitor for the stack is provided to give an indication that a device has failed. The relatively low voltage and high current levels employed when using RBDT switches result in low characteristic impedance for the PFNs in this type of modulator. In this instance, the PFN was selected to have a 1-ohm impedance per module. With four modules in a parallel bank, the total source impedance seen at the pulse transformer primary is only 0.25 ohm. This low source impedance places a strict limitation on the amount of stray inductance that may be introduced by the copper path between the PFN bank and the pulse transformer. This restriction can be overcome by proper selection of location of modules in the system and by the proper selection of the type of high current conductor used in the connections between the PFN modules and the input to the pulse transformer. Among the candidates used previously are multiple twisted pairs, coaxial cable, and copper conductor/dielectric sheets. In this particular application, twisted pairs of wire were used to facilitate connections made to the various contacts used to isolate modules. Because of the need to continue operation of the modulator when a PFN module has failed and been disconnected from the modulator, there is a need to consider what effects take place under those conditions. Figure 11 is the load line nomograph that can be used for such an analysis. The normal mode of operation is with four modules operating at a storage voltage on the PFN of 2375 volts. The load is a klystron with a beam microperveance of 2.0. If a PFN module is dropped from the modulator PFN bank, the output current decreases by about 10 amperes and the output voltage decreases by about 10 kV. In order to return to the original operating point, the

voltage on the PFN is increased to 2825 volts and full performance can be achieved with only three modules. Similarly, if the voltage is increased to 3 kV and the full complement of PFN modules is available, then operation is possible at up to 108 kV and 71 amperes with the capacity built into the modulator. The module characteristics under various conditions are summarized below:

	4-module Operation Normal Power	3-module Operation Normal Power	2-module Operation Reduced Power	4-module Operation Maximum Power
PFN Storage Voltage (V)	2375	2825	3000	3000
Pulse Current/ Module (A)	1188	1584	1978	1562
Pulse Power Out/ Module (MW)	1.22	1.62	1.63	1.92
Total Modulator Pulse Power Out (MW)	4.86	4.86	3.27	7.67

The PFNs that are used in the modules are constructed from dry reconstituted mica capacitors and coils made from rectangular cross-section conductors. The mechanical construction of the PFNs is such that the diodes that isolate each section are built into the network to minimize lead length. They are, however, easily removable through access holes in the framework of the PFN modules. The capacitance of the pulse forming network used in each module is 2.02, 3.42, and 5.99 microfarads, respectively, for the 3, 6, and 12 microsecond portions of the networks. Figure 12 shows the mechanical packaging of the pulse forming network module. The switch stack is located near the bottom and the PFN at the top. The backswing clipper circuit in the center of the module makes use of the diodes mounted in a compression fitting to the left of the noninductive resistors. Quick disconnect electrical connections capable of handling the high peak currents are located between a pair of guide pins that provide for proper alignment when inserting the PFN module into the cabinet.

Output Transformer and Load

The output transformer is a high turns ratio device (1:88) with a primary that uses copper sheet to combine the outputs from the four PFN modules. Insulation is provided by kraft paper and the unit is immersed in an oil tank. This same tank is used to provide the cooling and insulation for the load used during testing. A 1667-ohm woven resistor bank is immersed in the oil to provide the load on the transformer secondary. The heat transferred to the oil is removed by water cooling circulated through heat exchanger coils in the tank. The contacts that provide isolation between the transformer and the PFN modules in the event of module failure are located outside of the tank and are mounted to the modulator cabinet wall adjacent to the transformer/load tank location.

The transformer design is similar to that used on various production programs, such as the TPS-43G. Because of the high leakage inductance that high turns ratio transformers tend to have, special winding design is required. The leakage inductance referred to the primary is approximately 0.9 microhenries and the open circuit inductance referred to the primary is about 67 microhenries. Figure 13 depicts a typical transformer in this class.

Precision Regulator

There is some degree of regulation provided by the power inverter modules, typically 0.5 percent. In cases where added transmitter stability is required for applications like high performance MTI systems, a precision regulator is necessary. The approach selected for this application is one which operates directly on the charge that has been applied to the PFN. During each charge cycle, the PFN is overcharged by a small amount. The regulator is then turned on at a fixed time before the discharge of the network. Charge is then bled off of the PFN at a rate which is directly proportional to the difference between the PFN voltage sample and a reference voltage. The reference voltage is a level derived from the long-term average of samples taken from

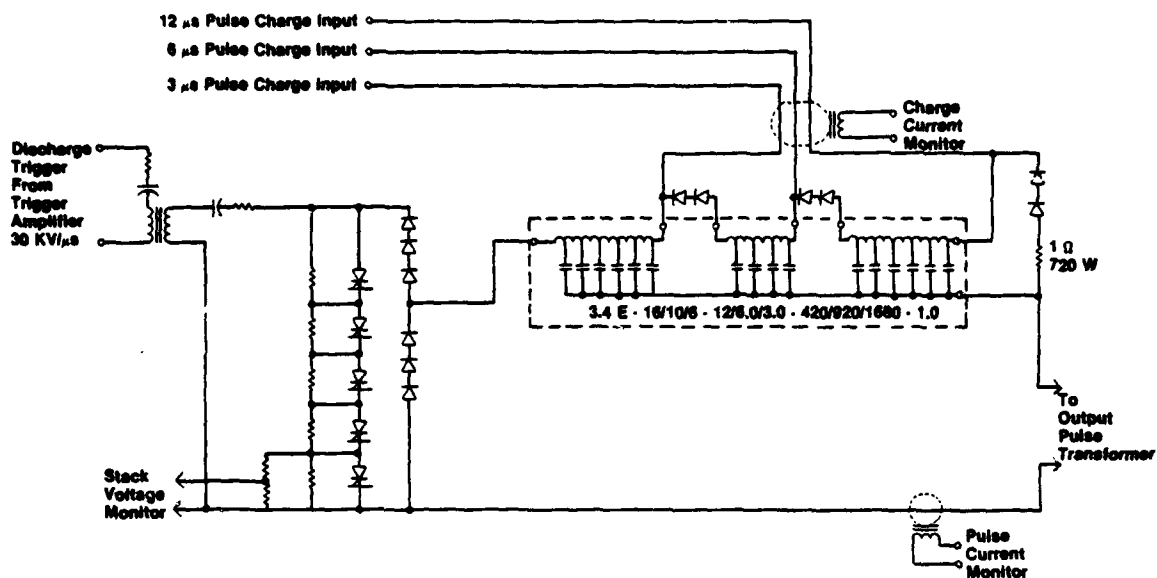


Figure 10. Pulse Forming Network Module

82-1433-B-11

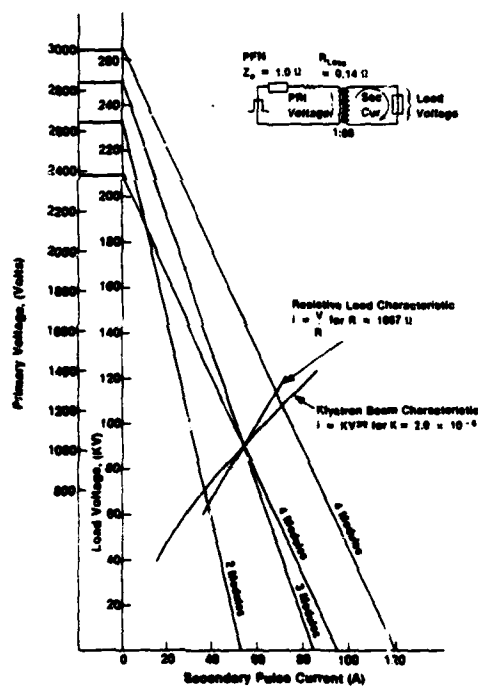


Figure 11. Load Line Nomograph

82-1433-B-16

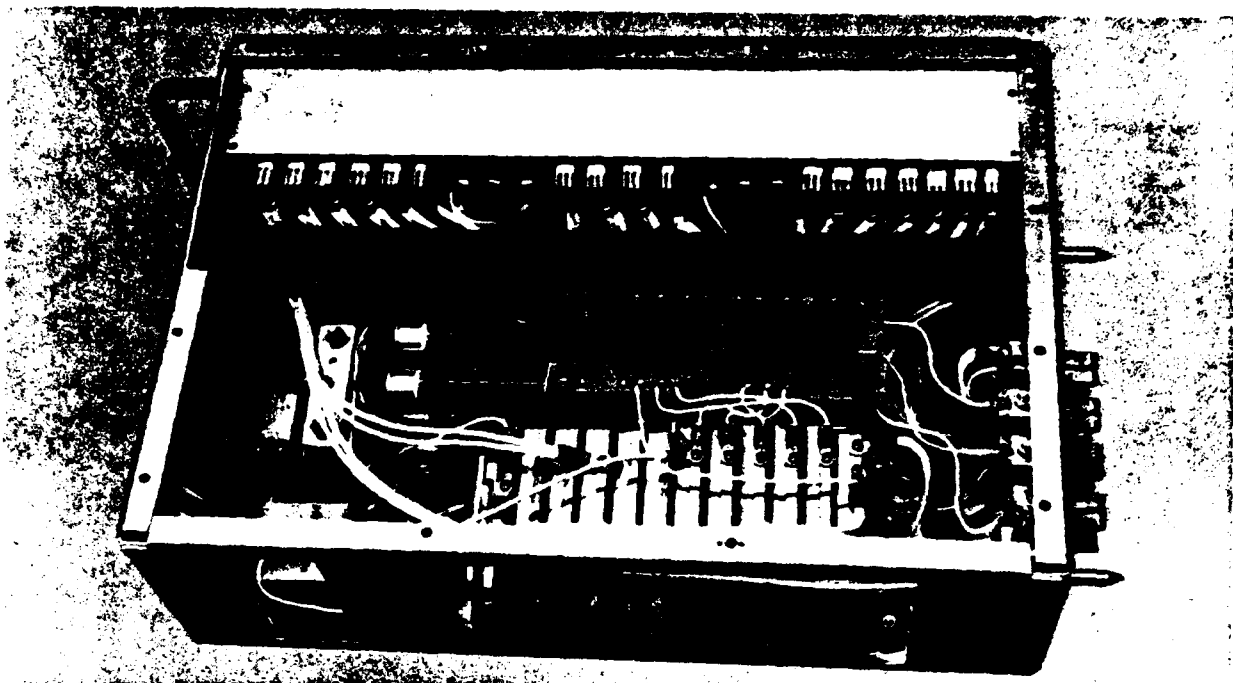


Figure 12. Pulse Forming Network Module

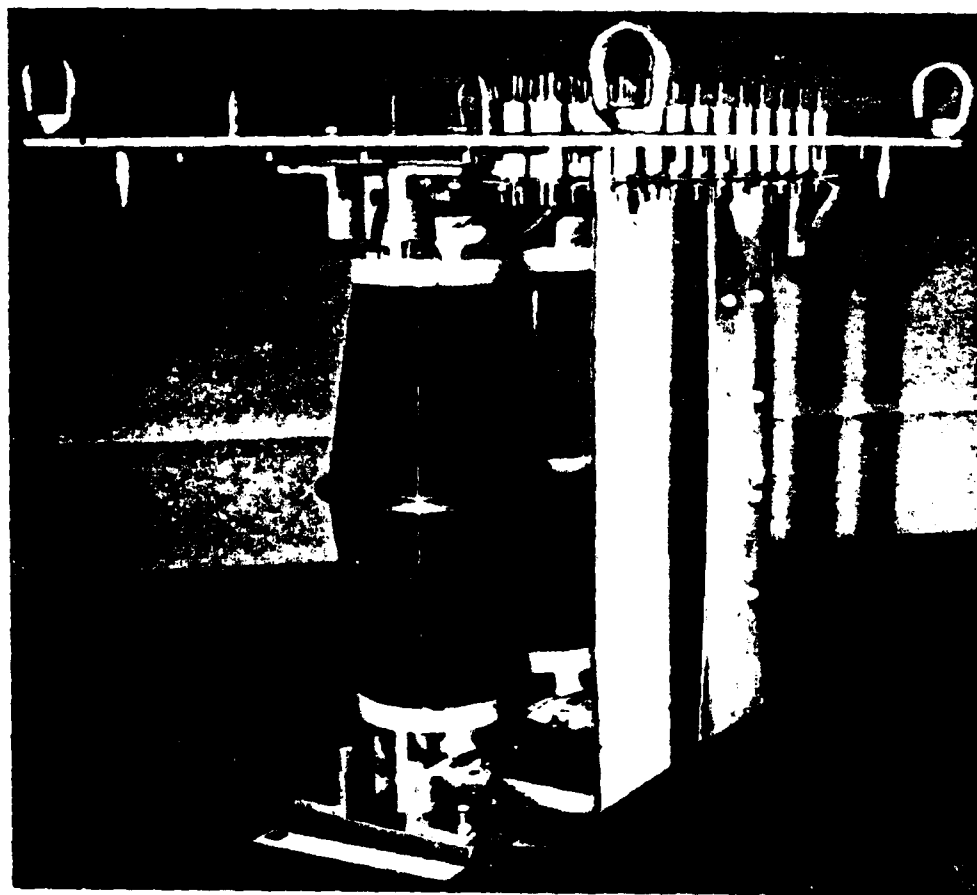


Figure 13. High Turns Ratio Pulse Transformer

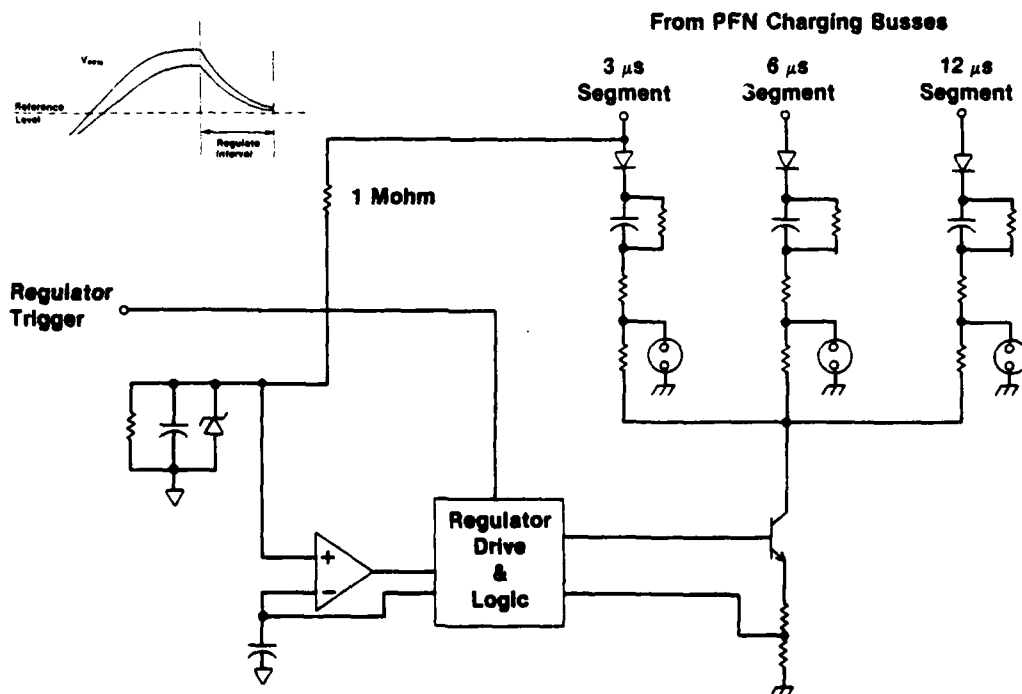
previous charge voltage samples. The result is that the reference, and therefore the PFN voltage, is free to float up and down with the high voltage power supply. The dissipation in the regulator is minimized, and the short-term stability required for the MTI system operation is maintained. Since coarse regulation is maintained by the power inverters to within one step of inverter operation, typically 12 volts, the precision regulator can then hold the pulse-to-pulse regulation of the PFN voltage to approximately 1 volt. The quality of regulation is also influenced by the amount of time that can be allowed for regulation operation, in this case, about 50 microseconds. The regulation period is determined by the PRF and by the amount of time required to charge the PFNs. Obviously, more time, and therefore better regulation, can be achieved by making the power inverters larger. Operation at higher inverter frequencies to minimize the inverter step size also helps to improve the regulation. Figure 14 is a simplified schematic of the regulator. For this application, where the PFN is divided into three separate pulsewidths, the sample of the voltage is taken from the 3-microsecond segment since it has voltage applied to it regardless of which of the pulsewidths is selected. The chassis housing the precision regulator is shown in figure 15.

The synchronization of the regulator with the other modulator triggers is shown in figure 16. The charge trigger input starts the appropriate command charge of the PFN modules. As the voltage on the storage capacitors falls, the power inverter modules turn on to replenish the energy withdrawn from the capacitors. When the regulator is triggered, current is conducted through the regulator in an exponentially decaying rate up until the time the discharge pulse is triggered. Because of the use of a staggered PRF, variations in interpulse period occur which are compensated for by varying the time between the pulse discharge and the time at which the command charge modules are turned on.

Test Data

Since a number of the features that can be achieved with solid-state RBDT modulators have been described in previous papers, we will address here those items which are peculiar to this program. First is

the maximum PRF of 2000 pps. Previous production modulators have operated in the 250 to 700 pps range using RBDTs. In this system, the use of power inverters to charge a capacitor bank which furnished the source for a command charge circuit was necessary. Prior techniques using inverters to directly charge the PFN modules did not allow sufficient time to charge the modules at this short interpulse period. By having a limitation on the operating frequency of the inverters, the size of the voltage steps necessary to charge the PFN in the interpulse period cause intolerable voltage ripple on a pulse-to-pulse basis. In addition, the command charge approach also offered a convenient way to incorporate the pulsewidth selection. Figure 17a, b, and c indicate the voltage pulse which is measured at the rear of the cabinet for the 3, 6, and 12 microsecond pulses. Of primary interest is the effect on pulse shape of the diodes inserted within the PFNs to isolate between the sections. A relatively flat pulse is achieved even with the diode discontinuities. A slight perturbation can be noted on the expanded scale in the upper trace of the 6 and 12 microsecond pulses. Figure 17 is a composite of the currents for the three pulsewidths taken at slightly different voltage levels on the PFN (100-volt dc variation). The rise and fall times of the pulses appear to be excessive, particularly for the short (3 microsecond) case. The reason for this is in the relatively long interconnecting cables that were required to mate the various modulator assemblies with the disconnect switches used for automatic fault removal. The problem was further compounded by the mechanical layout of the cabinet which was dictated for the program. The pulse transformer and load are located to the side of the modulator cabinet, rather than at the back where the PFN module output connections are located. Testing was done to verify that the automatic fault sensing and reconfiguration circuitry functioned as desired with good results. It seems, therefore, that the inclusion of this circuitry is a mixed blessing. Since further testing is scheduled for the modulator, one of the prime items will be a revamping of the interconnections to the oil tank from the modulator. There is every reason to believe that rise times on the order of 1 microsecond will be achieved based on the history noted in a variety of different production RBDT modulators.



82-1433-B-13

Figure 14. Precision Regulator

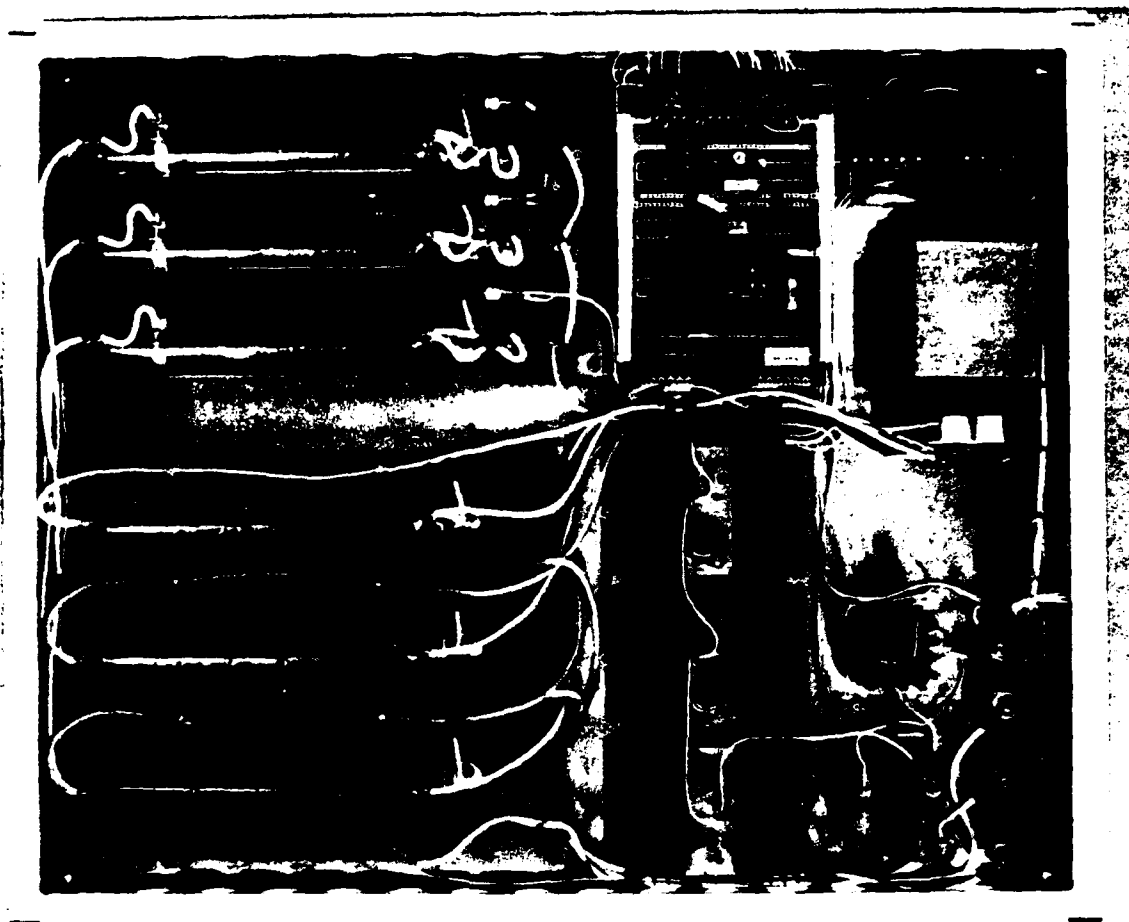
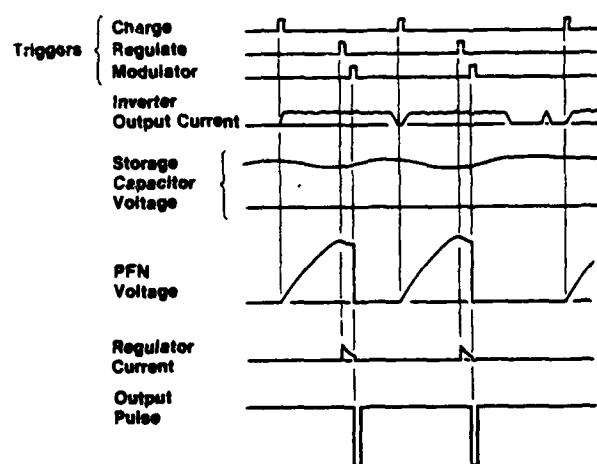
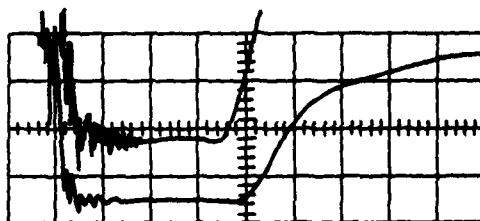


Figure 15. Precision Regulator Module

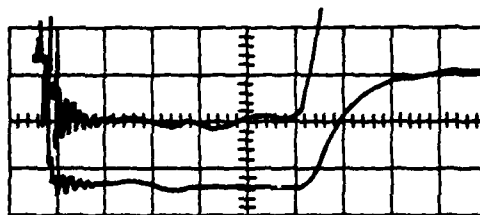


82-1433-B-17

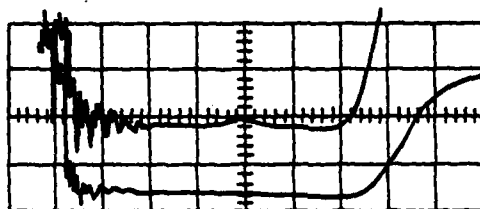
Figure 16. Modulator Timing and Waveform Diagram



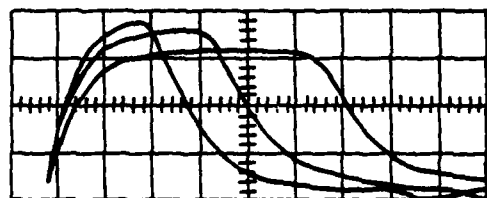
3 μ s Pulsewidth
1 μ s/Div
50 and 200 V/Div



12 μ s Pulse
2 μ s/Div



6 μ s Pulsewidth
1 μ s/Div



Load Current Pulses
With V_{DC} Reduced to
500 V at 12 μ s Pulse
600 V at 3 μ s Pulse
1200 A/Div 2 μ s/Div.

82-1433-B-15

Figure 17. Pulsewidth Selection

PRECISION PULSE REGULATOR FOR RADAR MODULATORS

Charles A. Corson
Westinghouse Electric Corporation
Baltimore, Maryland

SUMMARY

The transmitted RF in modern radar systems is required to have a high degree of phase stability. This in turn places a stringent requirement on the pulse to pulse repeatability of modulator systems that power the RF amplifiers in high performance transmitters. This paper describes how a single transistor has been used to control the pulse forming network (PFN) voltage in an 18.5 KW average power modulator to $\pm 0.001\%$ pulse to pulse. A 90 watt all solid state high voltage regulator controlled a 3000 volt PFN pulse voltage with less than 1/2% dissipated power loss. Staggered pulse repetition rate variations of $\pm 30\%$ were demonstrated.

HISTORICAL DEVELOPMENT

In the early 1970's, Westinghouse developed two different high voltage, high power shunt regulators to regulate PFN voltage in a transmitter modulator. One regulated a 5% pulse to pulse variation on a 25 KV PFN to $\pm 0.02\%$ and the other regulated a 4% pulse to pulse variation to $\pm 0.02\%$ on a 3 KV PFN. Both regulators dissipated about one thousand watts at a cost of about 5% of the total system power, and both regulators were designed using a vacuum tube as the dissipative shunt load. This was required because of the high voltages involved. In 1978 a new technique was developed which allowed the vacuum tube to be replaced with a solid state regulator. A regulator was designed for delivery in several radar systems for a foreign country. A 2 1/2% pulse to pulse variation on a 3 KV PFN was regulated down to $\pm 0.005\%$ and the power dissipated in the regulator was 4% of the modulator power. At the same time another design was being developed at Westinghouse to demonstrate $\pm 0.001\%$ regulation on a 2.5 KV PFN. This unit was used in conjunction with a Westinghouse developed charging technique that pre-regulated the PFN voltage to 0.4% pulse to pulse without any dissipative regulators. This solid state shunt regulator dissipated only 1% of the total modulator

power in an 11 KW average power modulator. The shunt regulator assembly was later modified to regulate the PFN voltage in an ARSR-3 radar transmitter modulator. The Westinghouse ARSR-3 radar is used by the FAA for air traffic control. The modified unit was designed to regulate the existing 0.05% pulse to pulse PFN voltage variation down to $\pm 0.001\%$ with a single transistor and dissipated only 90 watts out of the 18.5 KW in the modulator (99.5% efficiency). Figures 1 and 2 show the breadboard of this regulator.

REGULATOR CIRCUIT DESCRIPTION

Figure 3 is a schematic of the basic regulator. PFN voltage is sampled and compared against a reference. The error is amplified to drive the regulating transistor. Regulator current is sensed and fed back so that regulator current is proportional to PFN error voltage. This produces exponential current and error voltage which approach perfect regulation at the rate of the time constant of the regulator loop. R1 was chosen to pass slightly more than the maximum average current that would be needed to shunt regulate the PFN voltage based on expected performance without this regulator. C1 was chosen so that the pulse to pulse voltage variations across R1 would be considerably less than the zener (VR1) voltage rating, which is lower than the transistor (Q1) voltage rating. C1, Q1 and VR1 can be seen in Figure 1 and R1 is shown in Figure 2. Selecting these components was relatively easy. What could have been difficult was providing a stable reference. If a system were to produce 1% pulse to pulse PFN voltage, the regulator would then be required to bleed about 1% of the modulator power continuously. A slight drift in the reference or reference divider (say 1/2%) would throw the regulator out of control so that it was either turned on all the time or not turned on enough and not regulating all pulses. Therefore the absolute reference level must be held to a much tighter tolerance. An adjustment potentiometer would permit this but would not automatically adjust for major

changes in the PFN voltage level. Some applications allow a proportion of the output to be heavily filtered and adjusted with a potentiometer as the reference. This can be reasonably successful except for tight tolerance applications where temperature or long term drift may alter the relationship of the actual PFN voltage to the regulators' reference. This problem was overcome with a floating reference derived from the average current in R2 instead of the PFN voltage or a fixed reference.

Figure 4 shows how this reference was implemented. R2 senses regulator current. R3 and C3 filter out the pulsed characteristics of the regulator current. Amplifier A2 has a fixed gain of about 100. Because R4 and C4 are large values and R5 is small, the voltage on C4 does not change substantially from pulse to pulse but has a fixed ratio to the average regulator current. Because of the gain in A2, drift in the reference and part value tolerance effects were corrected by the gain of A2. When the PFN voltage is intentionally changed, the floating reference voltage on C4 adjusts itself in the same direction. Regulator current changes proportionally with PFN voltage. By controlling regulator current, regulator losses have been maintained very close to the minimum level required for perfect regulation, and excess power has not been thrown away to make up for parts tolerance and drift.

This regulator was designed to be adjusted to pass 80% of the bleed current in R1 through Q1 and 20% through VR1. In this way, changes in component values because of temperature drift or aging may change the 80%, but not so much as to require greater than 100% to pass through Q1 or to cause a small enough value that the transistor cannot maintain complete control of the regulation. This was made possible by the small value of C1 which bleeds about 90 volts from pulse to pulse. This bled down voltage must be recharged either through Q1 or VR1. Note that the peak PFN voltage was only varying about 1.5 volts (0.05%) before adding the regulator. The regulator actually discharges an average of 8 volts off of the PFN each pulse and therefore has plenty of range to fully regulate every charge cycle.

One other feature in this regulator is the small change in reference that is triggered a fixed time before modulator discharge. The reference is reduced about 0.1% during the last portion of the regulating

period which corresponds to regulating the 3 KV PFN voltage down another 3 volts. This helps to compensate for PFN droop caused by leakage and bleed currents. In a staggered pulse rate system, the regulator will complete its regulating function varying times before modulator discharge due to the variable interpulse periods. After this time, the PFN would continue to droop and would droop varying amounts because of the varying amounts of time left before discharge. By performing the second regulation step to a slightly lower level which is lower than the maximum expected droop, these errors are practically eliminated. The change in reference is triggered 100 microseconds before modulator discharge. This is about 20% of the total time available for regulation and more than adequate for the final precise regulation.

PERFORMANCE PARAMETERS

The ARSR-3 modulator being regulated had the following characteristics:

Video Pulsewidth	3 microseconds
Pulse repetition rate	330 PPS $\pm 30\%$ with a staggered variable interpulse period.
PFN voltage	3.1 KV maximum, linearly adjustable down to 2 KV.
PFN energy	55 joules per pulse
Average power	Up to 18.5 KW
Modulator pulse	135 KV @ 104 Amps, or 14 megawatts out of the step-up transformer

The PFN shunt regulator had the following performance:

Regulation	1.5 volts pulse to pulse disturbance was regulated to ± 30 millivolts, or ($\pm 0.001\%$)
Dissipated power	90 watts maximum (0.5%) by a single transistor on a convection cooled heat sink.

Note that due to the unique "floating reference" on C4, this regulator can also regulate at the reduced power level without adjustment when the PFN voltage is turned down.

Figure 5 shows the PFN voltage, reference change command and regulator current waveforms. Figure 6 shows a train of about 25 pulses with 1 volt/cm. sensitivity and the oscilloscope is offset about 3 KV. The top of the traces shows the unregulated voltage that is to be corrected. The bottom of the traces shows the final regulated level after discharge. Figure 7 shows a train of about 100 pulses with 0.1 volt/cm sensitivity. Modern high performance MTI radars only compare 3 or 4 adjacent pulses and so it is the variation from pulse to pulse that must be held constant.

CONCLUSION

The value and versatility of this regulating technique has been proved by its use in several different production systems. It is adaptable to PFN voltages from several hundred volts up to many thousand volts. It can upgrade the performance of a modulator in an existing transmitter to deliver high stability performance. MTI Improvement Factor limits of well over 60 dB are achievable. Because the regulating element consumes a small portion of the regulator power and only needs to be exposed to a portion of the PFN voltage, this technique can be applied to high voltage systems as a total solid state design.

Its outstanding features are its precision regulation and high efficiency. Its low loss allows a very small unit to accomplish very impressive performance, as shown above. The simplicity of this regulator provides a low parts count with very few power components. The low parts count and low power provide high reliability. Because the average regulating power is determined by the bleed resistor and capacitor (R1 and C1) this unit cannot be overloaded.

The precise regulating capability and versatility of this circuitry make it a very powerful tool that will undoubtedly be used extensively in the future.

REFERENCES

1. C. A. Corson, A Modular Modulator For An Air Defense Radar, Twelfth Modulator Symposium, February, 1976, New York, New York.
2. C. A. Corson, U.S. Patent No. 3,781,690 - "Improved PFN Voltage Regulator", (1973).



Figure 1 - Shunt Regulator Breadboard, Top View

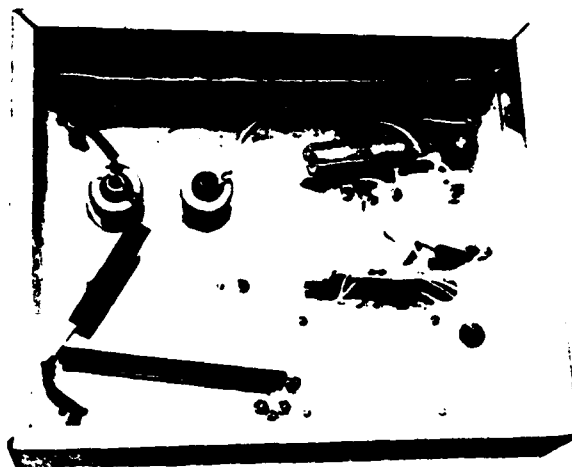


Figure 2 - Shunt Regulator Breadboard, Bottom View

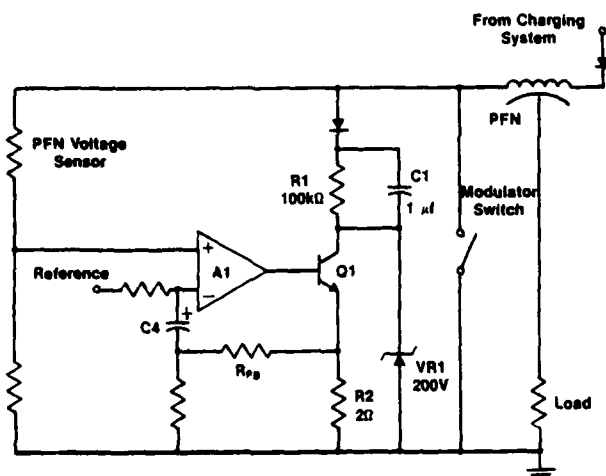


Figure 3 - Basic Regulator Schematic

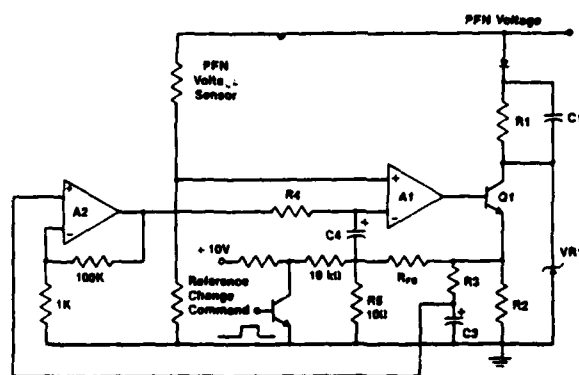


Figure 4 - Detailed Schematic

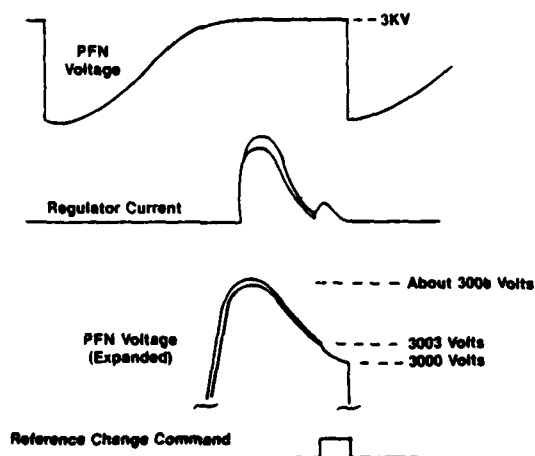


Figure 5 - Waveforms

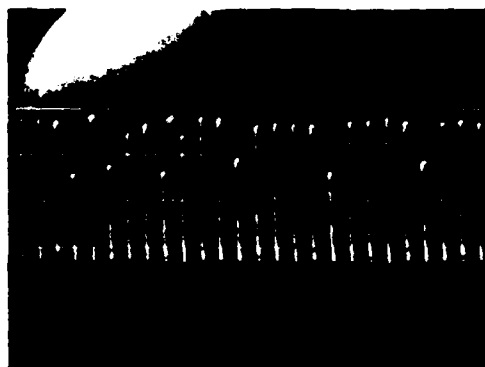


Figure 6 - Actual Performance



Figure 7 - Actual Performance

AN EVALUATION OF CHARGING TECHNIQUES FOR LINE TYPE MODULATORS

Edward H. Hooper
Westinghouse Electric Corporation
Command and Control Division
P.O. Box 1897
Baltimore, Md. 21203

Summary

Inverter and inductive flyback techniques for charging a pulse forming network in a line type modulator are compared with resonant charging techniques in an analysis which highlights the advantages of each approach. The bases for comparison include the per pulse energy transferred to the network, total voltage transformation ratio, internal energy storage requirements, and regulation and control of network storage voltage.

Each technique is defined and described, including performance characteristics and essential parameters. Resonant charging is carried through command charge control with de-Qing or post charge shunt regulation. Both the inverter type approaches and inductive flyback approaches are shown to eliminate the need for bulky and heavy high voltage transformers operating at power line frequency.

Introduction

The charging of a pulse forming network (PFN) in a line type modulator is a controlled transfer of energy from a source to the PFN within an allotted time interval. Figure 1 identifies the charging function in terms of its relationships with other parts of a modulator power chain. Primary processing and storage, with or without voltage transformation, establishes a DC voltage source for the charging system. The regulator function adds precision to PFN voltage control beyond that provided by the charging system by precisely diverting energy either during or following charging system operation.

Three methods of controlled energy transfer in the charging function are as follows:

1. Series inductive, as in conventional resonant charging, either free running or with command start.
2. Shunt inductive, as in inductive flyback transfer.
3. Inverter, in which both inductance and capacitance are employed in a multiple cycle energy transfer process.

Each has unique characteristics and its suitability to a given situation must be evaluated in terms of costs and benefits.

Cost, in this instance, is in terms of size, weight and complexity. A useful index of cost is the percentage of total energy placed on the PFN which is stored tempor-

arily within the charging system during the PFN charging interval. This will be called the storage factor (SF) of the system and is defined as follows:

$$SF = \frac{\text{Peak energy stored within the charging function}}{\text{Total energy placed on the PFN}} \times 100\%$$

As the percent energy storage factor increases, then the charging function will tend to become physically larger and heavier or more complex, or both for a given average power level of operation.

The benefits to be derived involve consideration of the charging system as a whole with respect to such factors as the following:

1. Regulator requirements on the basis of pulse-to-pulse voltage control achievable by the charging system.
2. Primary processing size and weight savings weighed in the context of charging system size and weight or complexity.
3. Reliability and maintainability gains.
4. Versatility in modulator performance which the charging system affords.

Series Inductive Charging

Series inductive charging is conventional resonant charging either through a charging diode or a triggered switch such as a thyatron or a thyristor. In this method, as illustrated with a triggered switch in Figure 2, energy transfer is affected through action of a series inductor between the source and PFN.

In the circuit in Figure 2, as illustrated by the waveforms, charge transfer from source to PFN begins with triggering of the switch and continues as a half-sine wave pulse of current. The source is assumed to be a voltage source of voltage E and the PFN is assumed to have no initial charge. The peak value of current is then $E/\sqrt{L/C_{PFN}}$ and the final voltage on the PFN is 2E volts. At the current peak, PFN voltage just equals E and the energy W_{PFN} in the PFN and the energy W_L in the inductor, are equal, or

$$W_L = \frac{1}{2} L I^2 = \frac{1}{2} L \left[\frac{E}{\sqrt{L/C_{PFN}}} \right]^2 = \frac{1}{2} C_{PFN} E^2 = W_{PFN}$$

In "charging" the inductor from the source an equal amount of energy has been placed on the PFN. In "discharging" the inductor during the remainder of the charging period, an additional equal quantity of energy is transferred from the source to the PFN with the results that at the end of the charging cycle, the inductor is empty and the PFN is charged to four times the energy that it contained at the midpoint of the charging cycle, or

$$W_{PFN} = \frac{1}{2} C_{PFN} [2E]^2 = 4 \left[\frac{1}{2} C_{PFN} E^2 \right] = 4 W'_{PFN}$$

The transfer of energy has been accomplished with an intermediate storage of only 25% of the total energy transferred.

In this method of charging, close cycle-to-cycle regulation can readily be achieved by dumping the inductively stored energy at any time after PFN voltage exceeds the source voltage. This is the common practice of de-Qing whereby inductor energy is either dissipated or returned to the source at which time all transfer of energy to the PFN is stopped. Figure 3 illustrates the action of a de-Qing path Q in which inductor current is diverted following the firing of switch SW₂ at any time T such that $\omega T = \frac{\pi}{2}$ and $\omega T = \pi$. Voltage placed on the network can be controlled closely over the range of from E to 2E on a pulse-to-pulse basis. The diverted current represents energy which may be dissipated or more desirably returned to the dc source. The price paid for this degree of control is an increased stored energy factor. In the extreme of maximum de-Qing in which $\omega T = \frac{\pi}{2}$, energy stored is equal to energy transferred and the energy storage factor increases from 25% to 100%.

Shunt Inductive Charging

Shunt inductor charging transfers energy from the source to the PFN by way of an inductor in which the entire amount of energy transferred is stored and then transferred to the PFN. This approach inherently has an energy storage factor of 100%. However, it offers the important advantage of incorporating voltage multiplication through circuit action.

Figure 4 illustrates the basic shunt inductor charging approach. Energy is transferred from the DC source to the inductor through a switch as a ramp up of current determined by source voltage and inductor inductance. Energy is transferred

to the PFN, which is in parallel with the inductor but isolated by a blocking diode, when the inductor charging switch is opened. Then the emf of the inductor reverses to keep current flowing, the diode conducts, and the energy stored in the inductor is transferred to the PFN.

The energy transferred by this method is a uniquely controlled parcel. The energy placed on the PFN is given by

$$W_{PFN} = \frac{1}{2} L I_T^2 = \frac{1}{2} C_{PFN} V_{PFN}^2$$

where

$$I_T = \frac{E}{L} t_{SW}$$

is the current in L at time T when the switch SW is opened. The voltage placed on the PFN is given by

$$V_{PFN} = \sqrt{\frac{L}{C_{PFN}}} I_T = \sqrt{\frac{T}{LC_{PFN}}} E$$

The ratio of voltage placed on the PFN to the source voltage is determined by the ratio of switch closure time T to the resonant frequency of L and C_{PFN}.

Figure 5 shows a variation of this approach in which the inductor voltage is clamped to the source voltage to relieve voltage stress on the switch devices. The inductor has taken on a secondary winding related to the primary or original winding by a ratio n. The diodes now clamp the voltage on the PFN to the transformed primary voltage nE in the manner illustrated in Figure 5. Note that when operated into the diode clamping range, some inductive energy is returned to the source so that more energy is stored than is placed on the PFN. In this case, the storage factor becomes greater than 100%.

Inverter Approach

In the inverter approach, energy is transferred to the PFN in multiple small parcels in repeated operations similar to either of the inductive transfer approaches above. Each charging cycle of the circuit places only a small portion of the required charge on the PFN. With shunt inductor operation transfer is affected with the same storage factor. However, with series inductive transfer an auxiliary capacitive storage element must be used and a significant amount of circulating energy must be handled by the inverter relative to the energy transferred to the PFN.

When multiple cycles of operation of a shunt inductor system are used to charge a PFN, the total energy placed on the PFN is first stored in the inductor and only portions of total energy are handled at a time. Implied in this form of operation is a lower inductance inductor than and would be used with a single step and a switching current which is higher. The net result is no gain in performance but an increase in control difficulty and possibly a physically larger inductor. The energy storage per total PFN charging cycle remains the same since the total energy placed on the PFN must first be stored in the inductor.

On the other hand, the use of series inductive transfer in an inverter configuration offers control of energy transfer and voltage transformation through high frequency transformers much smaller and lighter in weight than those required at primary power frequencies. Basic to this approach is transfer of energy within the inverter on each cycle which is high relative to that transferred to the PFN per inverter cycle.

Figure 6 is an example of an inverter charging approach using series inductive transfer. The circuit in figure 6 is a half bridge inverter with backswing diodes and triggers timed at $\frac{\pi}{2}$ radians into the backswing current. The waveforms in Figure 6 illustrate its operation. The maximum voltage to which the PFN can be charged by this circuit approaches $(nE)/2$ where n is the transformer turns ratio and E is the DC source voltage. This limitation is imposed by limiting the range of circuit operation to that which will cause current reversal through the SCR-diode combination and force SCR recovery. The maximum energy W_{PFN} which can be placed on the PFN is then

$$W_{PFN} = \frac{1}{2} C_{PFN} \left(\frac{nE}{2} \right)^2 = \frac{n^2 C_{PFN} E^2}{8}$$

For the limit to which the PFN can be charged, the average inverter half cycle charge transfer Q_{INV} is

$$Q_{INV} = C_{INV} \Delta V_{INV} = 25 C_{INV}$$

where the voltage swing on the inverter capacitor over the full PFN charging interval ranges from $3E$ at no PFN voltage to $2E$ at maximum PFN voltage. Also

$$Q_{INV} = \frac{n V_{PFN} C_{PFN}}{N} = \frac{n^2 C_{PFN} E}{2N}$$

where N is the number of inverter half cycles required to charge the PFN to the maximum voltage of $(nE)/2$. Equating the two,

$$C_{INV} = \frac{n^2}{5N} C_{PFN}$$

Energy transfer per half cycle in the inverter circuit ranges from $2.5 C_{INV} E^2$ with no voltage on the PFN to $1.5 C_{INV} E^2$ as the maximum charge is approached for a total average energy transfer of $2 C_{INV} E^2$ per step. The average energy transferred in the inverter per half cycle is then

$$W_{INV} = 2 C_{INV} E^2 = \frac{2n^2 C_{PFN} E^2}{5N} = \frac{32}{N} W_{PFN}$$

In terms of total energy transferred by the inverter circuit

$$\frac{W_{INV} \text{ TOTAL}}{W_{PFN}} = \frac{N W_{INV}}{W_{PFN}} = 32$$

The conclusion from this is that the total energy transferred within the inverter is 320% of that placed on the PFN while the maximum energy stored in the inverter is this same percentage divided by the number of steps required to charge the network.

Conclusion

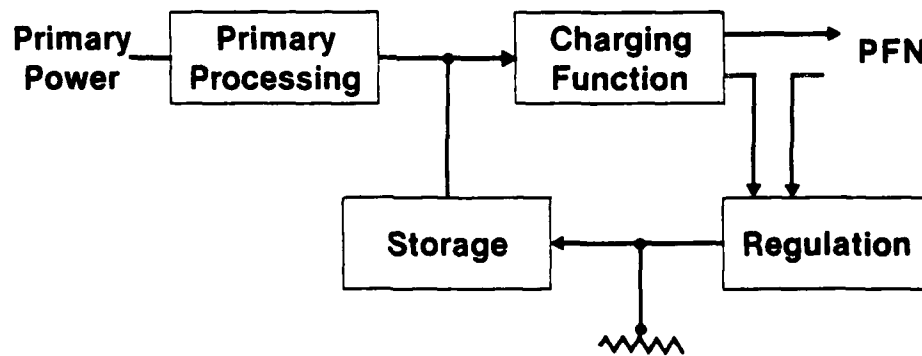
Table 1 summarizes the results of this discussion and characterizes the charging approaches on the basis of ideal operation right up to limiting conditions. The price paid in energy storage is lowest in most cases with an inverter type charging system. For example, with 50 step charging the maximum energy stored is 6.4% of the total energy placed on the PFN. At the same time the amount of energy which must be handled by the system's active devices is highest in the inverter. In overall terms, the inverter and the shunt inductor approaches offer the additional advantage of not requiring bulky and heavy transformers operating at primary power frequency to transform voltage.

All three approaches have been employed in radar transmitters of approximately the same power levels. Figure 7 shows a system employing command charging of the PFN's; Figure 8 has the same average power but uses the shunt inductive method of PFN charging and is a cabinet assembly of one-half the size. Figure 9 is a photograph of the modulator cabinet, including all power processing, for a tactical radar system of 50% greater average power using an inverter system. The impact on size (and weight by implication) is obvious. The use of the shunt diode approach and inverter approach resulted in a reduction in volume by one-third.

Table 1 Comparison of Three Basic Charging Approaches

	Primary Processing	Storage	Charging Function	
			Storage Factor	Transfer Factor
Series Inductive	Line Freq. Transformer and Rectifier	HV Capacitor	25%	100%
Shunt Inductive	Rectifier Only	Electrolytic Capacitors	100%	100%
Inverter	Rectifier Only	Electrolytic Capacitors	320/N%	320%

82-1625-BA-10



82-1625-BA-2

Figure 1 Basic Charging Model

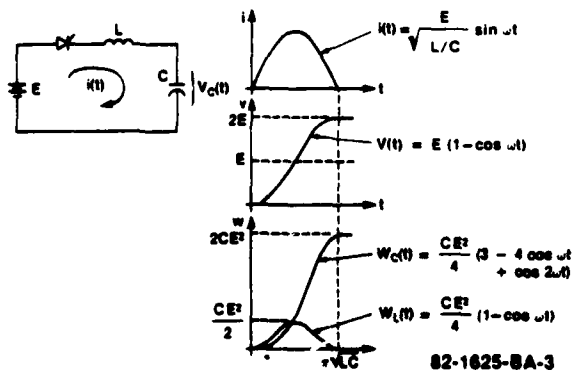


Figure 2 Series Inductance Charging

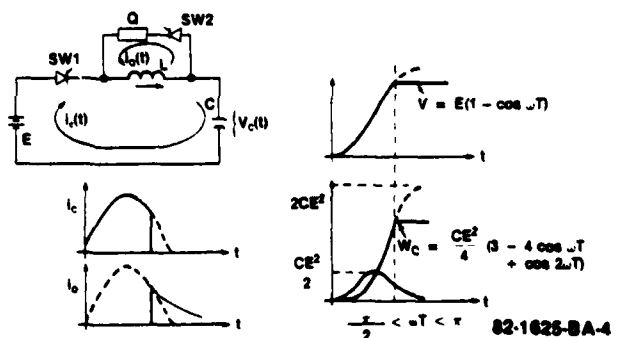


Figure 3 Series Inductance Charging with de-Qing

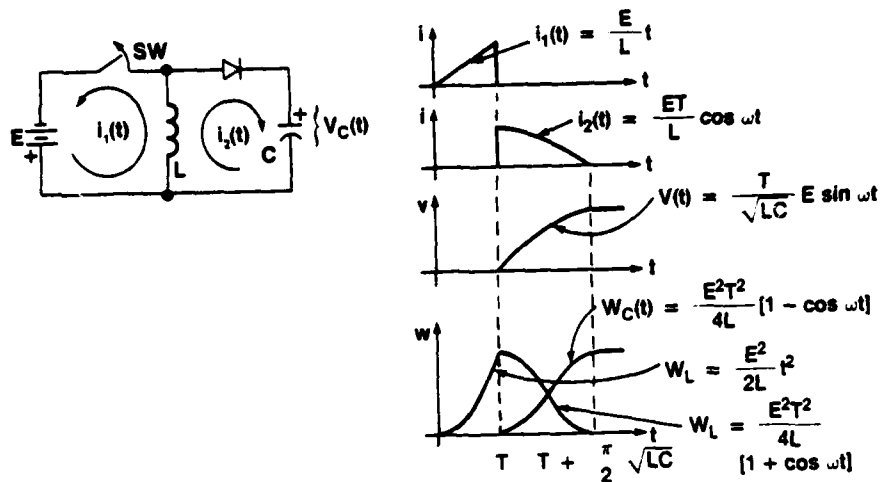


Figure 4 Parallel Inductance Charging

82-1625-V-5

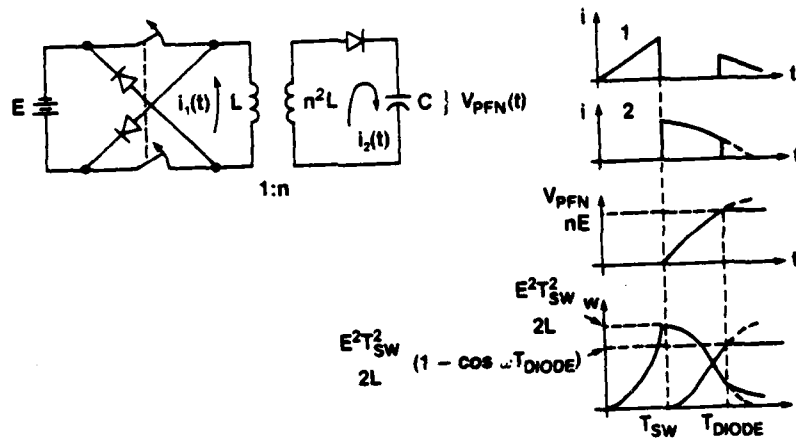


Figure 5 Parallel Inductance Charging With Switch Voltage Clamped

82-1625-V-6

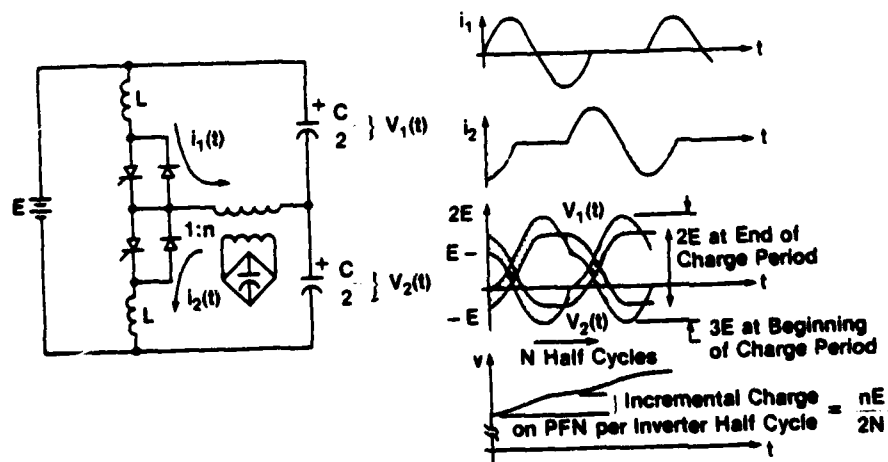


Figure 6 Inverter Charging with Half-Bridge Circuit

82-1625-V-7

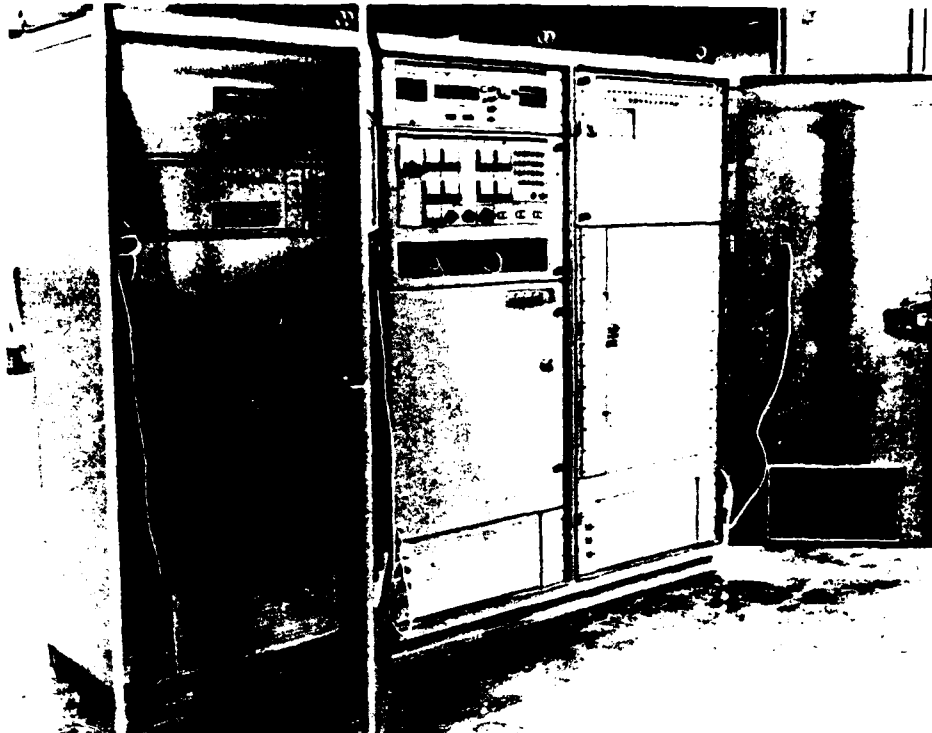


Figure 7 Transmitter with Resonant Charging and de Qing

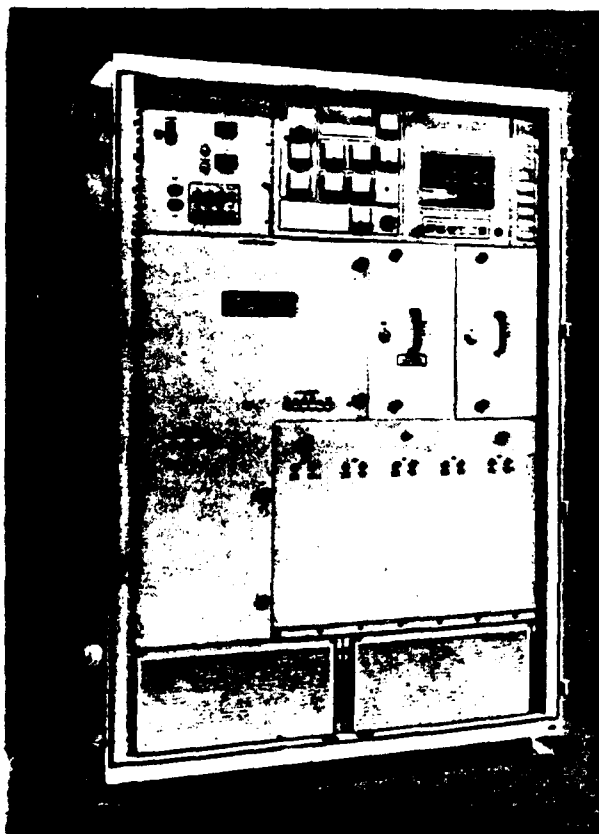


Figure 8 Transmitter with Shunt Inductive Charging

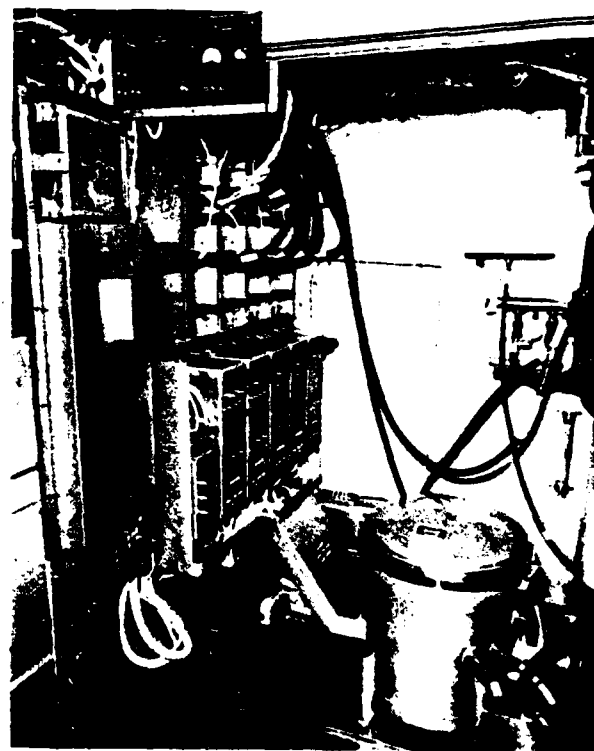


Figure 9 Tactical Radar Modulator with Inverter Charging

DEVELOPMENT AND EVALUATION OF SYSTEMS FOR CONTROLLING PARALLEL HIGH di/dt THYRATRONS

Allen Litton and Glen McDuff
University of California, Los Alamos National Laboratory
P. O. Box 1663, Los Alamos, New Mexico 87545

Abstract

Increasing numbers of high power, high repetition rate applications dictate the use of thyratrons in multiple or "hard parallel" configurations to achieve the required rate of current rise, di/dt . This in turn demands the development of systems to control parallel thyatron commutation with nano-second accuracy. Such systems must be capable of real-time, fully-automated control in multi-kilohertz applications while still remaining cost effective. This paper describes the evolution of such a control methodology and system.

Three techniques to control thyatron commutation have been examined and tested resulting in the development of a computer-controlled system. By proper correlation of trigger time and amplitude, three thyratrons have been operated in hard parallel with a common 10 Ω PFN and load up to 1500 pps. The discharge circuit and controls have operated over 10^8 shots without faults. Load current jitter has been maintained to ± 2 ns at the 25 kV 10 Ω operating point with little or no change in current sharing with changes in repetition rate. This characteristic lends itself to applications requiring forms of pulse modulation. The proposed control circuitry uses currently available off-the-shelf analog and digital components to keep system costs low.

Summary

As reported a year ago,¹ two low-inductance HY-3103 thyratrons were operated in "hard parallel" in a 25 Ω modulator circuit at repetition rates to 250 pps. This was accomplished by adjusting the negative grid bias (thus the anode delay time) to force the thyratrons to commute at the same time. This method allowed the use of a single source to trigger both tubes, thus reducing jitter. A common driver may also reduce the cost, particularly in a multiple-tube circuit.

Adjusting the negative-grid bias affects more than just the anode delay time, as recovery, anode falltime, and field grading within the tube also change. Controlling commutation in this manner proved possible but at high repetition rates these characteristics made operation very unstable and adjustments critical. A bias update rate of several times a second was found necessary to maintain control, requiring very high-speed analog and digital circuitry. It was decided to investigate the characteristics of each tube separately to see if any parameter could be identified as causing the instability before trying other control methods.

Tube Characterization

The first measurement made was dynamic breakdown voltage vs reservoir voltage (tube pressure) and the graphical results are shown in Fig. 1. Both thyratrons were new and operated in the same resonant charged modulator circuit when taking these data. At first glance, it appears that the tube pressures are different. Conversations with EG&G engineers revealed that hydrogen fill pressures have better

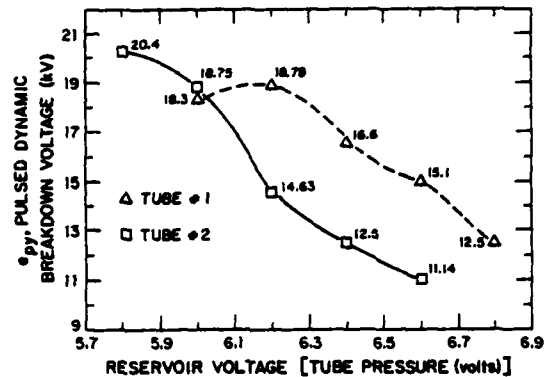


Fig. 1. Dynamic breakdown voltage vs reservoir voltage.

than 1% accuracy; however, the grid-anode spacing may vary up to $\pm 20\%$. Thus it is the "d" term of the Pd product causing the difference in breakdown voltages. The small difference between grid-anode spacing which may be acceptable in a single tube circuit has a drastic effect when thyratrons are operated in parallel. Further measurements were made to observe the differences in anode or commutation delay vs reservoir voltage between the tubes. As expected, the tubes were quite different in this respect, but the delay was linked loosely to the tube's dynamic breakdown.

The reservoir voltages for the two thyratrons were adjusted to closely match the commutation delays and the thyratrons were reconnected in parallel. This modification improved the circuit stability considerably, allowing operation of the modulator at up to 1000 pps at rated thyatron voltage. The requirement for frequent bias adjustments was found to be relaxed somewhat, reducing the need for high speed controls.

Even though the instabilities were reduced, the negative bias adjustment was still very critical, requiring an absolute accuracy of better than ± 250 mV. Further experiments with reservoir pressure, trigger amplitude, and bias control led to the conclusion that direct adjustments to the thyatron were too sensitive and affected too many of the tube characteristics to be of practical use.

Trigger Delay Control

The next method of commutation control investigated provided separate triggers with adjustable delays to each of the thyratrons. The dynamic breakdown voltages of two new HY-3013s was determined and the tubes were installed in the parallel tube discharge circuit. Circuit parameters such as drive voltage, drive impedance, bias, etc. were identical. The anode delays were measured at test conditions for each thyatron and the trigger delays were set so that the thyratrons would commute at the same time.

The thyratrons were brought up to rated voltage (25 kV resonant charge) and the tube currents were 250 amps peak each. Anode voltage was varied from 16 kV to 30 kV and the repetition rate from 100 pps to 1500 pps with less than 15% change in shared current amplitude. This method proved to be the most reliable and agile way of controlling parallel thyatron commutation. For a fixed anode voltage, the trigger delays would need adjusting a maximum of once an hour regardless of repetition rate. Continuous runs of 6 to 8 hours were common at rated thyatron voltage and 1000 pps.

All tests up to this point were done at a low peak current and thus low di/dt . Since good success was achieved with the individual trigger delay scheme, the next phase was to expand to three thyratrons and lower the discharge circuit impedance from 25 Ω to 10 Ω . A photo of the three-tube discharge circuit is shown in Fig. 2. Care was taken to reduce the discharge loop inductance and still limit the tube di/dt to 10^{11} amps/sec. It had been found previously that when the di/dt in the HY-3013 was in excess of 10^{11} amps/sec at 1000 pps, anode heating would cause the gas density (thus ion generation rate) to become sufficiently low to cause arcing in the grid-anode gap.²

A block diagram of the three-thyatron test circuit is seen in Fig. 3. Performance of the three-tube circuit was equal to or better than the two-tube circuit. Lowering the impedance from 25 Ω to 10 Ω did not affect the behavior of the thyratrons or the current-sharing stability. However, 10 Ω is still an order of magnitude higher than the impedance level ultimately needed. An oscillogram of the three tube currents and the load current is seen in Fig. 4. It should be noted that the load di/dt appears to be greater than the sum of the thyatron di/dt s. Because the effort of this program was to perfect a stand-alone system to operate thyratrons in hard parallel, the effect of di/dt enhancement was not investigated at this time. Current pulse parameters for both the two and three tube modulators are shown in Fig. 5.

Control Methodology

All development activities used Tektronix waveform digitizers to provide the nanosecond time resolution needed to control thyatron commutation. The thyratrons would current share if the commutation of

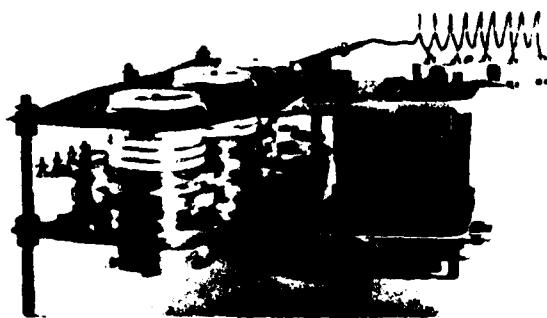


Fig. 2. Three parallel thyatron test circuit.

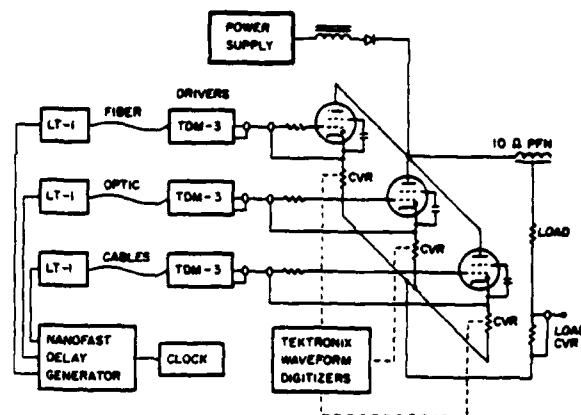


Fig. 3. A block diagram of the three-thyatron test circuit.

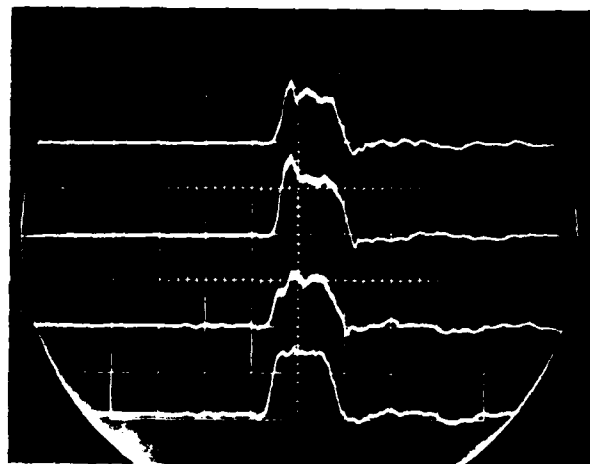


Fig. 4. Oscillogram of three tube current pulses. Top three traces - tube currents 200 A/div. Bottom trace - load current 500 A/div. Horiz - 100 ns/div.

TWO PARALLEL HY-3013 $e_{py} = 25$ kV $prr = 1000$ pps $Z = 25 \Omega$			
	di/dt	CURRENT RISETIME	PEAK CURRENT
TUBES	2.1×10^9 A/s	30 ns	500 A
LOAD	5.2×10^9 A/s	30 ns	1000 A
THREE PARALLEL HY-3013 $e_{py} = 25$ kV $prr = 1000$ pps $Z = 10 \Omega$			
	di/dt	CURRENT RISETIME	PEAK CURRENT
TUBES	1.8×10^{10} A/s	25 ns	400 A
LOAD	5.5×10^{10} A/s	20 ns	1200 A

Fig. 5. Current pulse parameters for both the two- and three-tube modulators.

all tubes was within a 2-4 ns window. Conventional counter-type measurement techniques can at best give 20-ns resolution, which is far from the nanosecond resolution needed. Sophisticated analog frequency shift techniques can give the real time resolution required, but are extremely involved and expensive. Using waveform digitizers with computer control is a viable solution but also expensive.

A block diagram of the system devised to control thyatron commutation is shown in Fig. 6. This control technique is based on charge transfer rather than real-time current measurements. The common energy store (PFN) is charged to voltage V and corresponding charge Q . With three thyratrons, each should pass $Q/3$ in the same amount of time if equal sharing is achieved. The output of the thyatron CVR is integrated (to give Q), amplified and fed to a sample-and-hold. The sample-and-hold is triggered at a predetermined time during the current pulse and the value of Q is stored. A low speed A/D converter translates the value of Q to an 8-bit digital word. The microprocessor averages all the values of Q and subtracts each Q from the average. If the difference between the average and the measured Q is within predetermined range, the microprocessor does nothing. If the difference is out of tolerance in the negative direction, that particular thyatron is commutating too early and the microprocessor adjusts the programmable delay accordingly. Likewise, if the difference is out of tolerance in the positive direction, the tube was fired too late. Experiments show that delay adjustments in two nanosecond steps is adequate to force current sharing. Hybrid programmable delay minicircuits are available that can increment in 1 ns steps from 1 ns to 255 ns and in 2 ns steps from 1 ns to 530 ns. These programmable delays interface directly with the 8-bit output of many microprocessors.

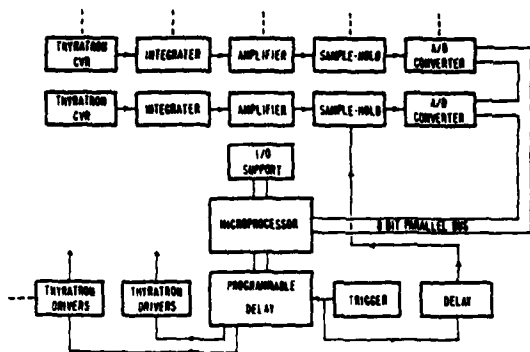


Fig. 6. Control system block diagram.

All development of the control circuitry has utilized the waveform digitizer for performing the integration, sample hold, and A/D functions and a PDP-11 has performed the microprocessor and programmable delay functions. The discrete integrator, sample-and-hold, and A/D portion of the control system has been built and tested but a complete system has not been completed.

Future Areas of Development

The successful operation of three hard parallel thyratrons makes the probability of using four or more tubes very good. Having reduced the impedance of the discharge circuit from 25 Ω (2 tubes) to 10 Ω (3 tubes) with no degradation in performance suggests development should be continued. Multiple uninterrupted 5-hour runs have proven the principle and stability of the system. Several characteristics of this system favor its use in applications where repetition rate and/or power agility are required as in high-energy laser systems or pulse-modulated power systems.

The next proposed step is to complete development of an integrated stand-alone control system for up to five parallel tubes. One suggested application involves construction of a fully-instrumented five-parallel thyatron-switched pulsed charged line in stripline geometry, possibly with an excimer laser load. Testing the system in an actual laser environment is most important to the development of a reliable control system.

Conclusion

Several methods for the control of hard-parallel thyratrons have been investigated and discussed. The most promising method of control developed so far seems to be accurate control of individual thyatron trigger timing. A method of using conventional analog and digital technology to implement a computer-controlled system is shown with hopes that a complete system can be demonstrated in the near future.

References

1. G. McDuff, "Parallel Operation of Thyratrons in Low Inductance Discharge Circuits," 3rd International Pulsed Power Conference, June 1981.
2. A. Litton, G. McDuff, "HY-3013 test data, unpublished, Los Alamos National Laboratory, 1981.

A NOVEL VOLTAGE MULTIPLICATION SCHEME USING TRANSMISSION LINES*

Ian D. Smith
Pulse Sciences Inc.
Oakland, California

Summary

The transmission line shown in Fig. 1, consisting of a series of sections with equal transit times and having impedances in the ratios shown, has a unique and surprising property. Consider that it is charged to a dc voltage V , and that a switch is then closed at the low impedance end. A voltage-cancellation pulse travels along the line, and its amplitude increases as it passes through the successive mismatches. Thus, it produces a voltage reversal that increases in the successive sections. At the eventual open circuit, voltage doubling occurs, further increasing the voltage reversal and changing the initial voltage V to an open circuit value $-NV$, where N is the number of sections, which is arbitrary. If at the time this voltage is created a matching load is connected to the line, for example by closing the switch S' , all of the energy that was stored anywhere in the line is immediately delivered to the load in a single rectangular pulse whose duration is only the double transit time of one section. This is true no matter how long the line. The pulse that travelled along the line accumulated all of the stored energy as it went, and delivered it promptly to the load. There are no reflections carrying energy back towards the switch S from the mismatches at the line junctions.

Voltage gain has been obtained as in the more familiar tapered-line transformer, but with one hundred percent efficiency.

In the following parts of this paper the properties of the transmission line, here named the cumulative wave line (CWL), are proved; the non-reflecting properties of the junctions are discussed; the incorporation of the CWL in circuits known as Darlington networks is described; it is explained how any CWL can be the basis of an air-cored accelerator stage; and some variations on these circuits are pointed out.

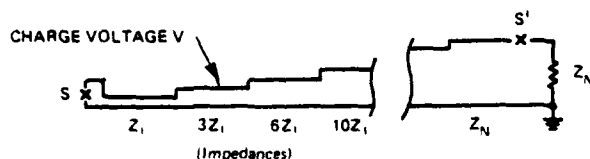


Figure 1. The cumulative wave line.

Proof Of The Properties Of The CWL

The cumulative wave line (CWL) consists of N connected sections of transmission line with equal transit times, Fig. 1. The long line so formed is charged to a voltage V , then shorted at one end by an ideal switch. The impedances of the line sections, as ratios to the impedance Z_1 of the first or switched section, are the successive sums of the natural integers; 1 , $1 + 2 = 3$, $1 + 2 + 3 = 6$, and so on. The final or N th section therefore has an impedance $N(N + 1)Z_1/2$.

* Work supported by Sandia National Laboratories, Albuquerque.

To calculate how the voltage cancellation pulse launched by the switch increases in amplitude as it travels along the line, we note that the impedances Z_n and Z_{n+1} of the n th and $(n + 1)$ th line sections are $n(n + 1)Z_1/2$ and $(n + 1)(n + 2)Z_1/2$. From the usual transmission line results it can readily be shown that between these sections the voltage cancellation pulse increases by a factor $(n + 2)/(n + 1)$. Therefore the voltage pulse entering the last or N th section is

$$-V \times \frac{3}{2} \times \frac{4}{3} \times \frac{5}{4} \dots \times \frac{N}{N-1} \times \frac{N+1}{N} \\ = -(N + 1)V/2$$

This voltage doubles at the open circuit; after the initial charge voltage is subtracted, the voltage produced is seen to be $-NV$. After the switch S' is closed, the voltage into the matched load is $-NV/2$. This remains constant for a time $2t$, where t is the single transit time of each section, since no reflections can reach the load in this time. The energy delivered is

$$(NV/2)^2 \times 2t/Z_N \\ = NV^2t/(N + 1)Z_1 \quad (1)$$

The capacitance of the n th section is

$$C_n = t/Z_n = 2t/n(n + 1)Z_1$$

and its stored energy is

$$1/2 C_n V^2 = V^2t/n(n + 1)Z_1$$

The total stored energy is therefore

$$\frac{V^2t}{Z_1} \sum_{n=1}^N \frac{1}{n(n+1)} = \frac{V^2t}{Z_1} \sum_{n=1}^N \left[\frac{1}{n} - \frac{1}{n+1} \right] \\ = \frac{V^2t}{Z_1} \left[1 - 1/2 + 1/2 - 1/3 \dots - \frac{1}{N+1} \right] \\ = \frac{V^2t}{Z_1} \left[1 - \frac{1}{N+1} \right] \\ = NV^2t/(N + 1)Z_1$$

This is equal to the delivered energy calculated in equation (1), so that the CWL is one hundred percent efficient.

The question arises why energy is not reflected back from the mismatches towards the switch S and thereby lost from the initial pulse. The answer is that when a pulse is incident on the junction between two transmission lines, an impedance match is the condition that maximum power be transmitted only when the lines are initially uncharged; otherwise, a particular mismatch is required. Figure 2 illustrates the general case. A voltage transient V travels in a line of impedance Z towards a junction with a line of impedance mZ , both lines being initially charged to a voltage $-fV$. The power delivered to the second line is easily calculated to be

$$P = \left[\frac{2m}{1+m} - f \right] \frac{2}{1+m} \frac{V^2}{Z}$$

This has its maximum when

$$m = \frac{2+f}{2-f} \quad (2)$$

which makes

$$P = (1 - f/2)^2 \frac{V^2}{Z}$$

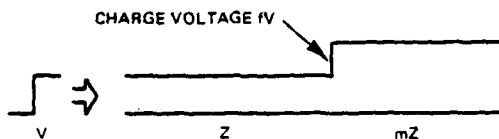


Figure 2. General case of voltage pulse incident on junction in a charged line.

This is the same as the power the first line could deliver if it was terminated in an open circuit and then connected to a matching load when the pulse arrived, i.e., it is all the power available.

If the two lines are uncharged, then $f = 0$, and the optimum value of m from equation (2) is unity - the lines should be matched in this familiar case. In the first line section of the CWL there is a charge voltage equal to the pulse voltage, that is $f = 1$; equation 2 now shows that $m = 3$ is needed for the first mismatch. In subsequent sections of the CWL the pulse amplitude gets progressively larger than the charge voltage, reducing f and consequently reducing the mismatch ratio needed in accordance with equation 2.

Darlington Networks

The circuit for these is shown in Figure 3. It employs a CWL whose final (Nth) section shares its charged conductor with another transmission line section of the same transit time as those composing the CWL. A resistive load R joins the ground conductors at the output ends of the two lines.



Figure 3. The Darlington network.

The single line section removes the need for the second switch S' in Figure 1. The resistive load sees no voltage until the pulse generated by the CWL arrives. This pulse reverses the sign of the voltage in the CWL so that the CWL and the single line begin to discharge into the load. The impedance Z' of the single line section is chosen so that its matched current $V/2Z'$ is the same as that of the CWL, i.e.,

$$V/2Z' = NV/N(N+1)Z_1$$

$$\text{or } Z' = (N+1)Z_1/2$$

The load resistance matches the sum of Z_1 and the CWL output impedance, i.e.,

$$R = (N+1)^2/2Z_1$$

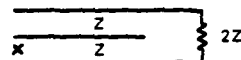
The open circuit voltage gain is $(N+1)$.

Note that the CWL "sees" an impedance

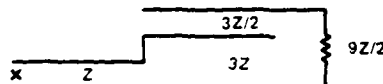
$$Z' + R = (N+1)(N+2)Z_1/2$$

which would be the impedance of the next CWL section if one were present; thus the CWL sees just the mismatch that it needs in order to be efficient.

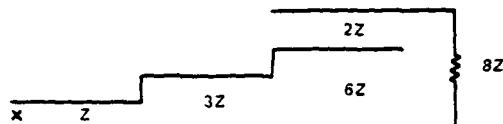
With $N = 1$ the circuit is that known as the Blumlein, Figure 4a. The circuits for $N = 2$ and $N = 3$ are illustrated in Figures 4b and 4c; they have matched gains of $3/2$ and 2 .



a. $N = 1$ (Blumlein)



b. $N = 2$



c. $N = 3$

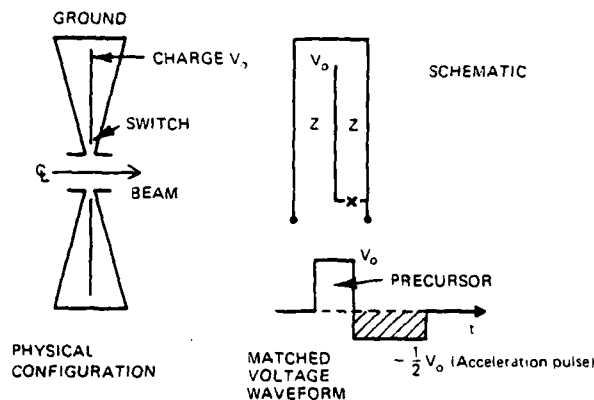
Figure 4. First three Darlington networks.

Induction Accelerator Circuits

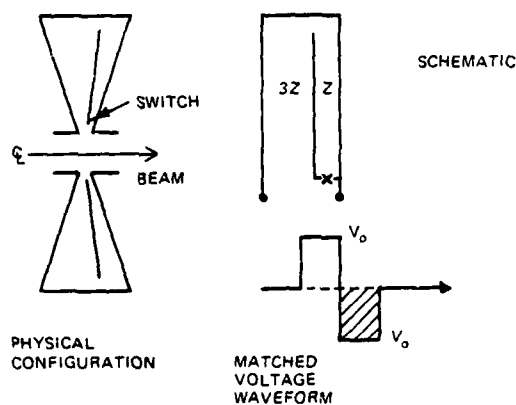
Several air-core linear induction accelerator circuits have been identified which can accelerate an electron beam with one hundred percent efficiency(1). Figure 5 shows two of these, in forms known as radial pulse lines (coaxial versions are possible, too). They each consist of an initially charged conductor in a grounded cavity that it divides into two radial transmission lines in which energy is stored. When the switch is closed the charge voltage appears across the accelerating gap, but no beam is present. When the pulse from the switch has travelled through both lines it reverses the sign of the voltage at the accelerating gap for a period during which the beam is passed through the gap and accelerated. If the beam current matches the line that feeds the gap, all the stored energy is extracted.

The circuit in Figure 5a is due to Pavlovskii(2), and forms the basis of his accelerator LIU 10(3). That of Figure 5b is due to Eccleshall and Temperley(4). Both circuits can be considered to be formed from a CWL, with one section in the case of Figure 5a and two sections in the case of Figure 5b. The CWLs are in effect folded about their midpoints, and the opposite ends of one conductor are connected together, to give the sections through the radial line cavities as shown in Figure 5.

It is now seen that CWLs with more than two sections give a infinite series of possible designs for inductive accelerator cavities, all of which are new. The next two designs in the series are shown schematically in Figure 6. The voltage gain increases through the series; a CWL of N sections gives a matched gain $N/2$.



a. Pavlovskii Design



b. Eccleshall-Temperley Design

Figure 5. Induction accelerator circuits.

In all such circuits the grounded cavity walls form a finite inductance connected across the accelerating gap. Therefore, if all the stored energy is to be extracted by the beam the voltage waveform at the end of the accelerating pulse must have a zero time-integral (5); otherwise, magnetic flux would remain in the cavity, and this would represent unused energy. Hence the waveform at the accelerating gap is necessarily bipolar, with a reverse voltage "precursor" before the accelerating pulse. The waveforms are illustrated in Figures 5 and 6.

In the Pavlovskii design the precursor voltage is twice the matched accelerator voltage, and in the Eccleshall design the two voltages are equal. In both cases the precursor can cause difficulty for the insulation in the accelerating gap and the nearby vacuum interface. Since the precursor voltage is always the charge voltage, the ratio of precursor voltage to accelerating voltage becomes progressively smaller as the number of sections in the CWL or cavity is increased, reducing the insulation problems. The precursor voltage is $2/N$ times the matched voltage. The zero time-integral of voltage is maintained because with more sections the precursor has a longer duration - the time needed for the switch pulse to traverse the CWL is clearly $N/2$ times the output pulse duration.

A second series of new induction cavity designs can be formed from CWLs of $N = 3$ or 7 or $11 \dots$

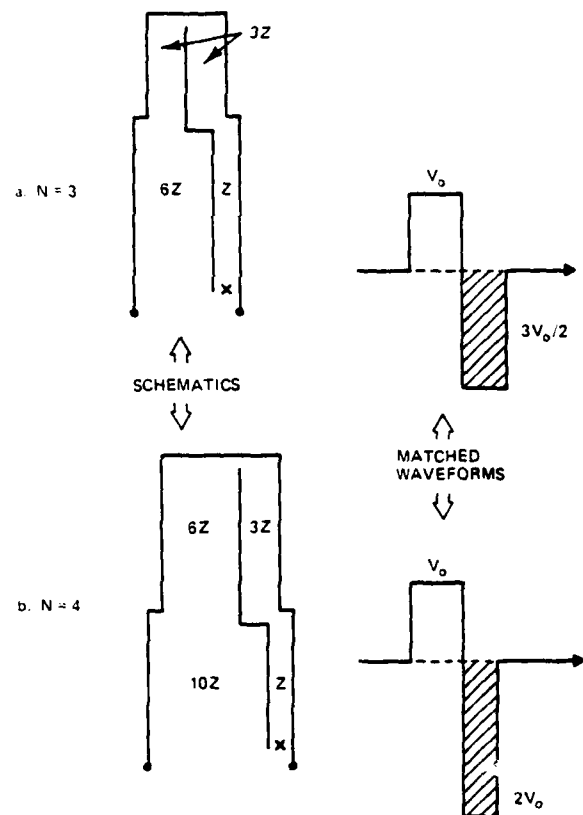


Figure 6. Induction accelerator circuits based on CWLs with $N=3$, $N=4$.

sections and a single line section placed between the switch and the accelerating gap. (Separation of the switch and gap may be desirable in a practical accelerator.) The first one in the series is shown in Figure 7. The matched gain is $(N + 1)/2$, and the precursor voltage is twice the charge voltage. Except in the first design of the series, the precursor is not steady but turns on and off periodically before the acceleration pulse.

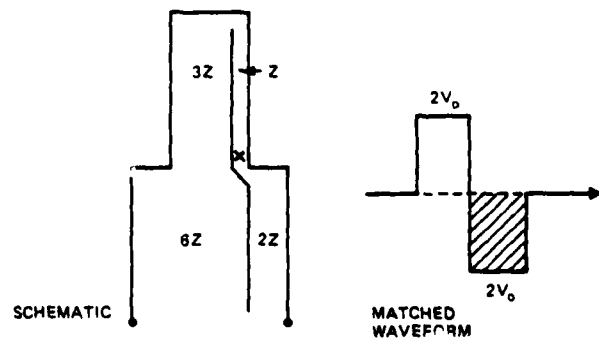


Figure 7. Induction cavity formed from CWL and one additional line (first of series).

Variations

Lumped Element Circuits

Figure 8 shows a crude lumped element version of the Darlington network with an $N = 4$ CWL. Each line section has been replaced by a single capacitor and inductor. This circuit bears the same relation to the ringing Marx or LC - inversion stage as the Darlington networks do to the Blumlein.

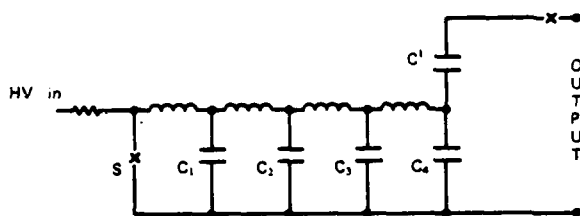


Figure 8. Simplified Darlington network

It is not likely that the circuit can be 100% efficient. In a brief empirical study, each capacitor was given a value inversely proportional to the corresponding line section impedance, and two out of the four inductors were varied to maximise the gain. The highest gain obtained was 4.7, compared with an ideal value of 5.0. About 88% of the initial stored energy was available in the series combination of C_4 and C' . Larger gains and efficiency may be possible by further optimisation.

Non-ideal Circuits

Higher voltage gains can be obtained from the transmission line circuits by departing from the impedances that give perfect efficiency when matched. For small impedance changes the loss of efficiency is small. This flexibility is greater the larger the number of sections N .

Figure 9 illustrates this for the Darlington network with $N = 3$ (matched gain 2). The graph shows the highest gain obtainable by adjusting the transmission line impedances (strictly their ratios to the load impedance) as a function of how far the

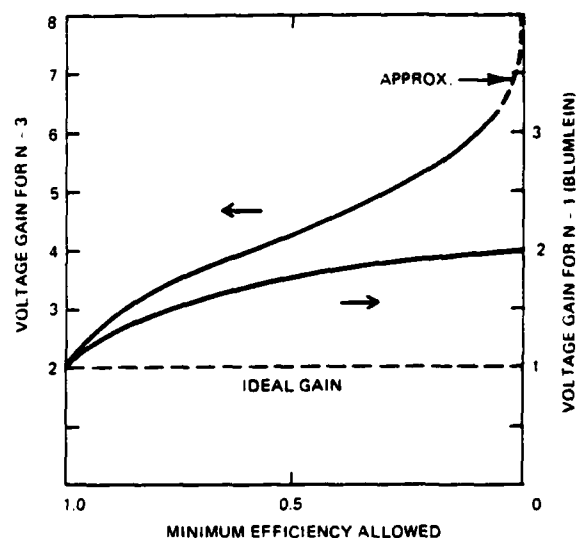


Figure 9. Gain of Darlington networks as a function of efficiency.

efficiency is allowed to decrease. Also shown is a similar curve for the standard Blumlein ($N = 1$) where the gain can only be increased by mismatching.

References

1. I. D. Smith, Rev. Sci Instrum 50 (6), 714, June 1979.
2. A. I. Pavlovskii, V. S. Bosaymkin, G. D. Kuleshov, A. I. Gerasimov, V. A. Tananakin, and A. P. Klementev, Sov. Phys.-Dokl. 20, 441 (1975).
3. A. I. Pavlovskii et al, DAN SSSR, V. 250, No. 5, 1980, p. 1118.
4. D. Eccleshall and J. K. Temperley, J. App. Phys. 49 (7) July 1978.
5. I. D. Smith, in "UltraRelativistic Electron Beam Sources for the ARA", PIFR-1103, Oct. 1978.

FAST, HIGH-POWERED TRIODE PULSE AMPLIFIERS

Stephen J. Davis
Pico Second Enterprises, Inc.
704 Whitney Street
San Leandro, CA 94577

Abstract

A line of commercially available, linear Planar Triode Pulse Amplifiers will be described. These amplifiers feature output peak powers to 2 MW, repetition rates in excess of 100 kHz, and 1 nanosecond rise and fall times for a variable duration pulse with a characteristic temporal stability on the order of 10 picoseconds.

The performance of the pulse amplifier as an electro-optic crystal driver will be discussed with an emphasis given to its extended capabilities for optical pulse selection, ASE isolation, cavity dumping, pulse carving and travelling wave modulation.

In addition, applications of the pulse amplifier in the fields of IFF radar detection and underground geological resource exploration will be presented.

Introduction

For the past two years, we at PSE have developed a product line of high peak power, fast rise and fall time pulse amplifiers based upon vacuum planar triodes. These amplifiers are characterized by nanosecond response times at 100:1 bandwidths and peak power levels exceeding 0.5 megawatts. The amplifiers are capable of average power levels greater than several kilowatts at burst mode frequencies exceeding tens of megahertz. Amplifier lifetime is primarily a function of cathode heater lifetime, not shot number.

Amplifier Description

These broadband amplifiers have an input to output gain greater than 70 db, and will produce 0.5 MW peak power pulses with nanosecond rise and fall times and less than 2% droop for 250 NS duration pulses. Amplifier average output power is limited to 75 watts by its plate supply.

As shown in Fig. 1, the amplifier consists of seven stages of gain, of which the first four are solid state while the latter three utilize planar triodes.

The first stage consists of a pair of 2 GHz bipolar linear power transistors which provides 8 W of peak drive power to stage two for 80 milliwatts of input power. After an impedance transformation of 4:1, this 8 W signal drives a single medium-sized FET in stage 2 to develop 32 watts, peak. The output of stage two also passes through a 4:1 impedance transformer and

and then drives two parallel FETs in stage 3. After an impedance transformation of 16:1 the 128 W peak power RF pulse from stage 3 is coupled into a repackaged power switching FET, stage 4. The drain of the stage 4 FET is directly connected to the cathode of stage 5's planar triode. Stage 5's 15 KW peak power output is impedance transformed (9:1) to drive stage 6. As in stage 5, stage six contains a single planar triode. The 57 KW output from stage 6 is impedance transformed (36:1) and is coupled into the cathodes of three parallel planar triodes. With 10 KV on the plates of the three parallel final stage tubes, the amplifier will deliver 5 KV into 50 Ohms, or 0.5 MW peak power.

These pulse amplifiers use 1 NS increment ECL delay generators for pulse width control to permit the amplifier to function as a pulse generator, producing a variable duration pulse from an input trigger.

Short term jitter and long term drift are minimized due to the very short transit times of the active gain elements in the amplifier. Throughput jitter is less than 30 picoseconds.

Since amplifier lifetime is primarily a function of the tube heater lifetime, the heater voltage is regulated at 6.0 VDC instead of 6.3 VDC. When failure of a triode tube occurs after more than 5,000 hours of operation, a new tube replaces the old tube without circuit adjustment. In addition, future amplifiers will be operated at approximately 100 microamps of DC cathode to plate current. This helps to clean and electron-polish the tubes.

When required, further gain stages can be added as above to increase amplifier peak power, and upgrading amplifier plate supply will allow for greater average power output.

The amplifier described above is contained in a 14" tall chassis of standard width having a 22" depth and an 85 lb. weight.

Technology Comparison

Other technologies having a similar dv/dt and peak/average power capabilities are:

- a) Spark gaps
- b) Krytrons
- c) Thyratrons
- d) Avalanche Transistors

Of these, only thyratrons have comparable

duty cycle and lifetime characteristics. None of these technologies produces an output with a spectral content as constant as the triode amplifiers. In addition, all of the above technologies are non-linear switches requiring pulse shaping PFNs at the output level. Since our triode amplifier uses linear gain elements throughout, pulse shaping is done at the input level. Our triode amplifiers can produce readily controllable pulse trains or pulse bursts without pulse to pulse recovery time requirements. Burst mode frequencies exceeding 100 MHz are possible. For a comparison of these technologies see Fig. 2.

Applications

The intensity of an optical signal can be modulated at high frequencies or for nanosecond time frames using the Pockels effect. By applying a voltage to a crystal of proper material, the polarization of an optical signal, often a laser, can be rotated. This is the Pockels effect. An optical gate is formed when a device using Pockels effect (i.e. a Pockels cell) is placed in a linearly polarized laser beam between polarization sensitive devices. One polarization is blocked while polarized signals 90° rotated pass.

Today's Pockels cells exhibit multi-megahertz upper end frequency responses while requiring drive into the megawatt peak power level.

Pockel cell applications generally fall into these categories: a) pulse selection, b) pulse carving, c) laser amplifier control or isolation.

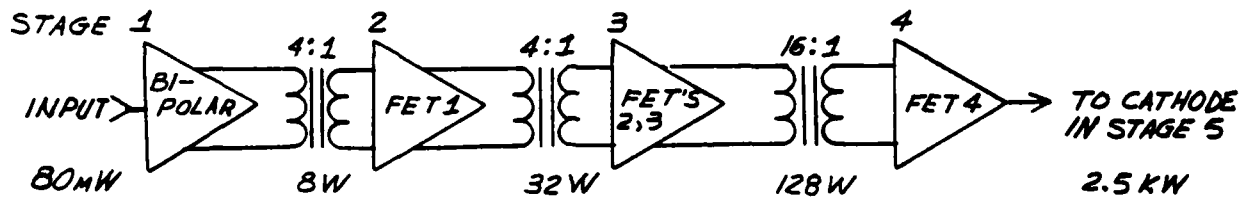
Pulse selection is often required when a laser oscillator is used to produce "mode locked" short duration pulses. In this case a train of pulses are emitted from which some are selected. (See Fig. 3, which depicts a typical pulse selection application.)

Pulse selection is also accomplished using a Pockels cell. In this case a portion of CW or long pulse laser light is allowed to pass through the cell gate for a pre-defined period at pre-defined signal levels.

Instantaneous Frequency Agile Transmitters

Since there are no tuned circuits in our triode amplifier, it can reproduce any RF signal input over its operating frequency range in real time. In class C mode, pulse code modulation is also possible as well as single sideband communications.

SOLID STATE STAGES



PLANAR TRIODE STAGES

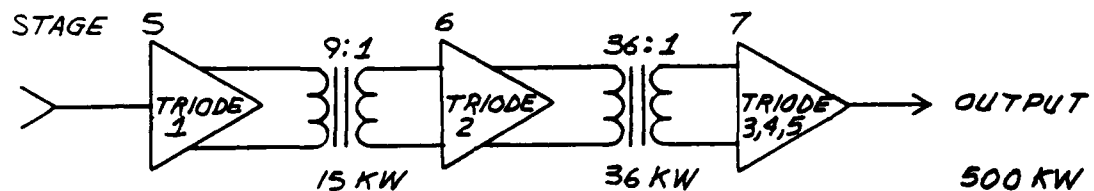


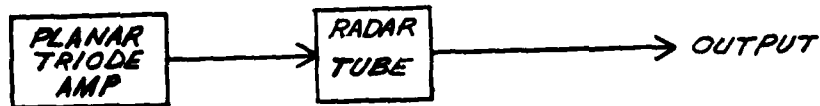
FIG. 1

FIG. 2

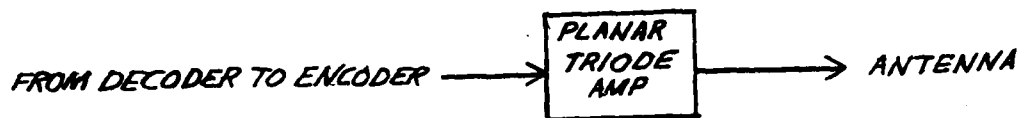
GAS SWITCH	RISE TIME	JITTER	HARMONIC CONTROL	RELIABILITY	BURST MODE CAPABILITY	DUTY CYCLE
SPARK GAP	1	3	3	3	3	3
KRYTRON	2	3	3	3	3	3
THYRATRON	3	2	2	2	3	1
SOLID STATE AVALANCHE SWITCH	2	1	2	1	3	3
VACUUM TRIODE	1	1	1	1	1	1
AUSTON SWITCH	1	1	3	3	3	3

1 - EXCELLENT
2 - MARGINAL
3 - POOR

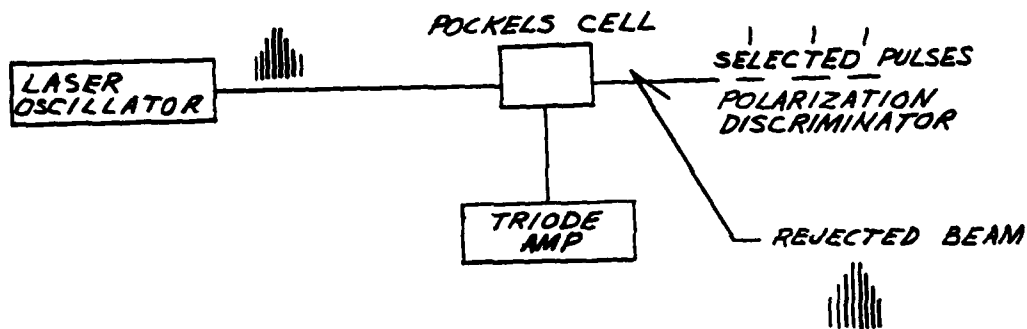
RADAR MODULATOR



JAMMING



LASER PULSE SELECTION



PULSE CARVING

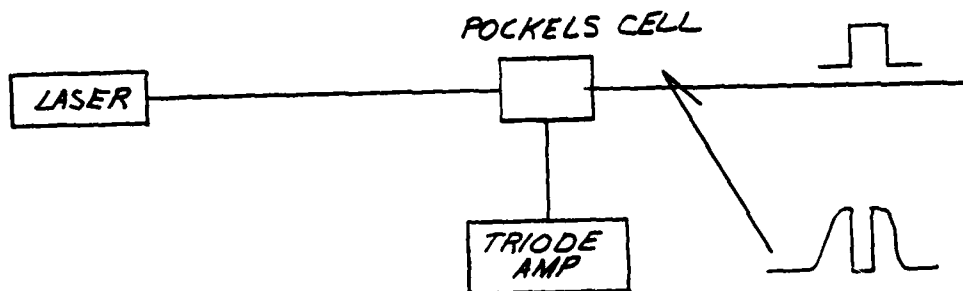


FIG. 3

A LOW POWER MODULATOR FOR A HIGH POWER PULSED E-BEAM

Rudolf Limpaecher, Rudolph Litte
Avco Everett Research Laboratory
Everett, Ma. 02149

Abstract

High power pulsed electric discharge lasers use wide area E-beams to ionize the lasing medium. The E-beam is gated with a pulse power system that must develop pulses having currents of hundreds of amperes and up to 10^4 volts.

The requirement for current density uniformity excludes the techniques commonly used in high power vacuum tubes to reduce the amount of "grid" power. This paper discusses a technique for modulating the E-beam with a pulser requiring a negligible amount of power. This is accomplished with a non intercepting electrode that develops a negative field around the filamentary cathode to hold the E-beam gun in a cut off state. When the voltage is removed from the non intercepting electrode a positive field from a second electrode acts on the cathode to extract a space charge limited current. Except for some small capacitive effects and small ion currents the non intercepting control electrode draws no current.

The concept was first reduced to practice in a small scale bell jar experiment. The concept was then scaled to a full size 250 kV E-beam operating up to 120 pps in the AERL program. This method of E-beam control proved to be successful in developing high repetition rate E-beam pulses of high current using a low power pulse generator.

The technique proved to be flexible and capable of very square pulses or other shapes as required, trapezoidal for example.

Back Plate Controlled Electron Beam Gun For Lasers

Introduction

The development of high power electric CW and pulsed electric lasers can be to a large part accredited to the existence of the vacuum tube technology. The use of this technology allowed the design and test of an easily controlled triode type E-beam gun for the first E-beam stabilized CO₂ laser. Subsequent scaling of the E-beam to cross section areas of 25 cm x 200 cm for the Big Bang and Humdinger devices with E-beam energies up to 180keV proved to be relatively straightforward. 1,2,3 For these and subsequent devices the electron gun and the electron acceleration were separated by enclosing the E-beam gun and its control electrodes in a Faraday cage, a screened aperture in the latter, serving as the anode of the gun.

Electrons exiting the gun through the screened aperture enter a region of uniform electric field. The field is of sufficient extent to impart enough energy to the electrons so that they pass through a foil vacuum barrier into a cavity filled with the lasing medium and there perform the ionizing function. Pulse control of these E-beams with conventional techniques require modulators having high peak power and in the case of high repetition rates high average power. A concept has been developed that can pulse modulate high power E-beams with negligible energy.

Background

The early laser E-beam guns consist of a filamentary cathode and control grid enclosed in a Faraday shield. A screened aperture in the Faraday shield allows the electrons to exit into the high voltage accelerating field. The screening factor in this aperture is high enough to prevent any significant penetration of the high voltage field. Because of this the analysis of the E-beam system can be simplified because the elements within the Faraday shield, often called the gun, can be considered separately from the analysis which is concerned with the acceleration aspects of the E-beam.

The analysis of the gun can be handled in the same manner as with a conventional vacuum tube triode. There is however one constraint on the E-beam gun that is not significant in a vacuum tube. That constraint is the need for uniformity in the electron density over the entire beam area.

In the early E-beam guns a planar control grid located between the filament and the anode (Faraday aperture screen) serves to control the electron beam current while a prescribed potential on the anode determines the density of the space charge limited current. For subsequent devices, as higher E-beam current densities were required, the control grid was removed and the anode to filament spacing reduced to take advantage of the distance squared effect to minimize the amplitude of the modulation voltage. Current control of this type of gun is achieved by pulsing the potential of filamentary cathode with respect to the anode. A positive bias potential, typically of the order of 500 volts, overcomes the high voltage penetration and work function energy of the electrons to maintain the gun in a cutoff condition. In the conduction mode negative pulse voltages in some cases as high as 15 kV applied to the filament produces current densities greater than one ampere per square centimeter out of the gun.

With the removal of the control grid the gun resembles a thermionic diode and although this simplified the gun it was at the expense of a high power pulser. High pulser power is required because the entire E-beam current, including a significant fraction intercepted by the Faraday cage aperture screen is supplied by the pulser. The peak power can amount to more than ten megawatts and at high repetition rates leads to significant average power. It was this power demand that motivated the development of a new type of E-beam control system that has a significant reduction of control power.

During the early periods of the vacuum tube development DeForest (1906) invented the Platon tube which subsequently appeared as the gammatron or gridless wonder. These tubes consisted of a row of filament wires between the grid and plate planes. Further experimental work on this concept is reported by H. Cohn⁽⁴⁾ in 1924. The latter work includes the performance of various contoured control plates.

To use the Platoon (also called the back plate) control configuration for high power pulsed lasers with anode voltage in the range of five to ten kilovolts and filament emissions to an ampere cm^{-2} theoretical as well as experimental work was required. This effort was further complicated by the requirement for a partially transparent anode as opposed to the solid plate anode of a conventional tube.

In a conventional tube spacial non uniformities in the electron current streaming to the anode are normally not important. In a laser electron beam uniformity of the electron density is of critical importance. In order that these various factors could be experimentally verified a short section of a full size gun with two filamentary cathodes was fabricated and tested.

The Electrostatic Field Of The Back Plate Gun

The potential within a plane configuration of the three electrodes shown in figure 1 in a manner developed by Spangenberg is given by:

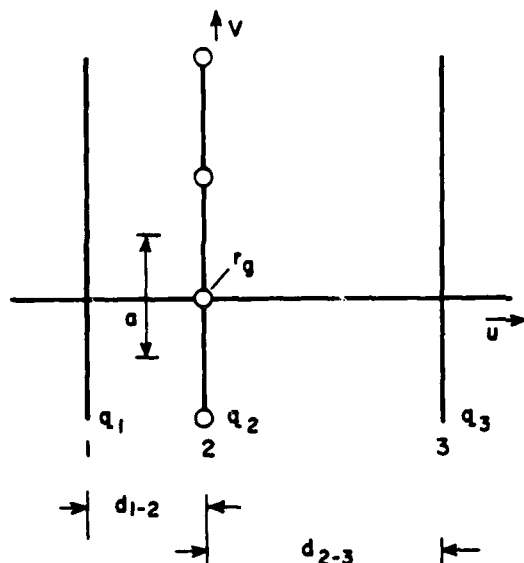


Figure 1. Electrostatic Field Coordinates

$$V_W = -\frac{q_2}{4\pi\epsilon_0} \ln \left(e \exp. \frac{4\pi u}{a} + 1 - 2 \left[e \exp. \frac{2\pi u}{a} \right] \cos \frac{2\pi v}{a} \right) - \frac{q_1}{4\pi\epsilon_0} \ln e \exp. \frac{4\pi u}{a} + C$$

This expression shows that the equipotential lines near the origin and near each electrode in the center plane are circles. For large values, both positive and negative, of u the equipotentials are planes parallel to electrodes 1 and 3.

When $u = +d_{2-3}$

$$V_3 = -\frac{d_{2-3}}{a\epsilon_0} (q_2 + q_1) + C$$

since $V = \frac{q}{C}$

When $u = -d_{1-2}$

$$V_1 = C + \frac{d_{1-2} q_1}{a\epsilon_0} + C$$

Since $r_2 \ll a$ potential at 0 ; r_2 and r_2'

are almost equal so for $u = 0$ and $V = r_2$

$$V_2 = -\frac{q_2}{4\pi\epsilon_0} \ln 2 \left(1 - \cos \frac{\pi r_2}{a} \right) + C$$

The potentials for the three planes have been established without regard to the function of each electrode. In a conventional triode electrodes 1, 2 and 3 are cathode, grid and plate respectively. In the back plate gun electrodes 1, 2 and 3 are back plate, filament and plate in that order.

The current from the E-beam gun is given by:

$$I = K \left(V_b + \frac{V_p}{u} \right)^{3/2}$$

At cutoff $I = 0$ and $V_b = -\frac{V_p}{u}$

Where u is the amplification factor which now can be determined

$$u = -\frac{V_p}{V_b} = \frac{V_3}{V_1}$$

$$u = \frac{\frac{d_{2-3}}{a\epsilon_0} (q_2 + q_1) + \frac{q_2}{2\pi\epsilon_0} \ln \left(\sin \frac{\pi r_2}{a} \right)}{\frac{d_{1-2}}{a\epsilon_0} q_1 + \frac{q_2}{2\pi\epsilon_0} \ln \left(\sin \frac{\pi r_2}{a} \right)}$$

Cutoff also means that the potential gradient at the filament and the charge q_2 are zero.

The expression for μ becomes very simple;

$$\mu = \frac{d_{2-3}}{d_{1-2}}$$

In practice this ratio is very small and the amplification factor typically is 2.

There are two means of illustrating the internal fields of the gun. The first is a contour representation which can be plots of the equipotential lines. The second is a potential profile representation which can be either along a line from the back plate to the anode through a filament and normal to the anode, or a parallel line between the filaments. Figures 2 and 3 show equipotential lines for cutoff and conduction conditions.

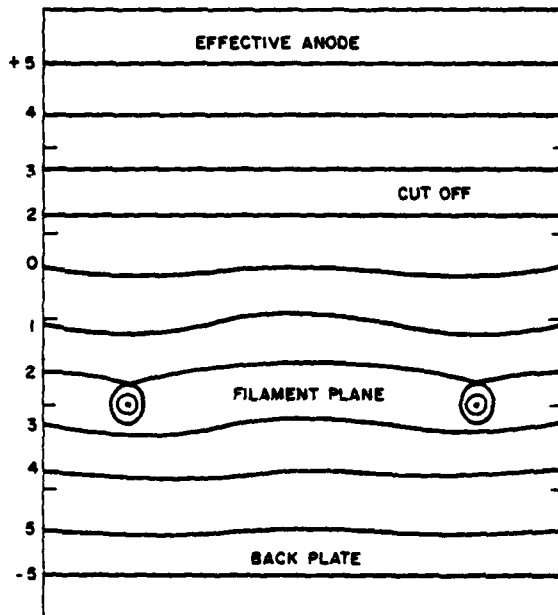


Figure 2. Equipotential Lines

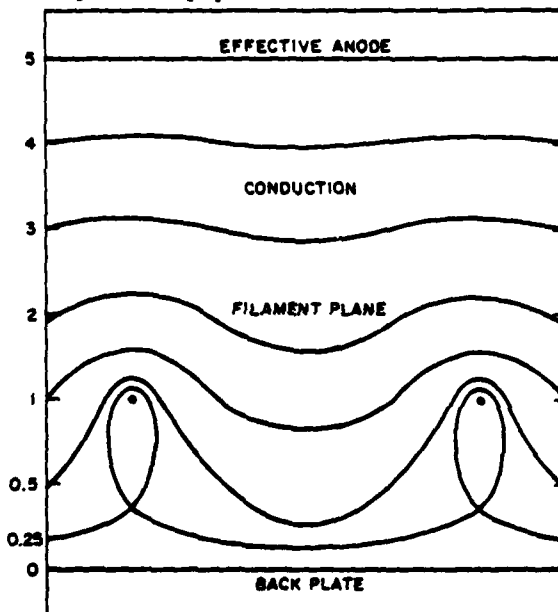


Figure 3. Equipotential Lines

Figures 4 and 5 show the same two conditions in the profile scheme.

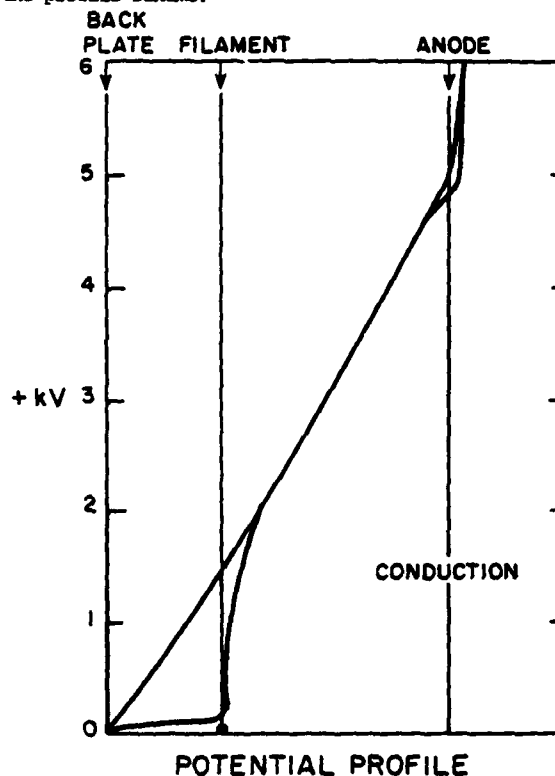


Figure 4. Potential Profile

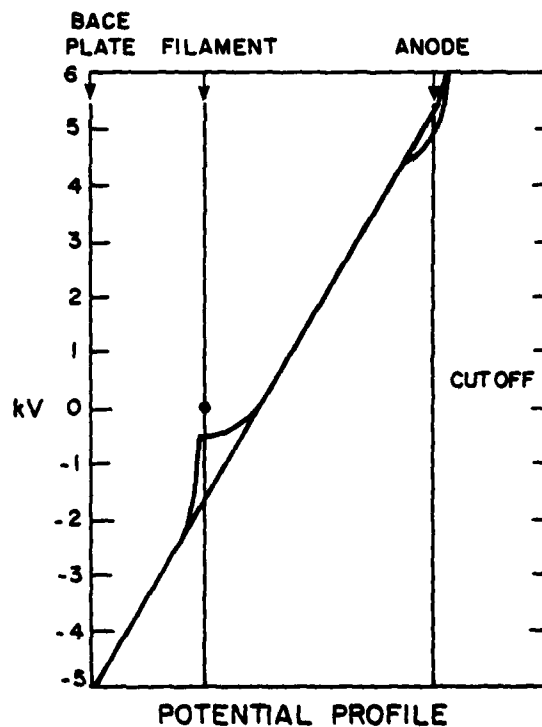


Figure 5. Potential Profile

Small Scale Experiment

A photograph of the test setup is shown in Fig. 6. The significant dimensions are shown in Table 1.

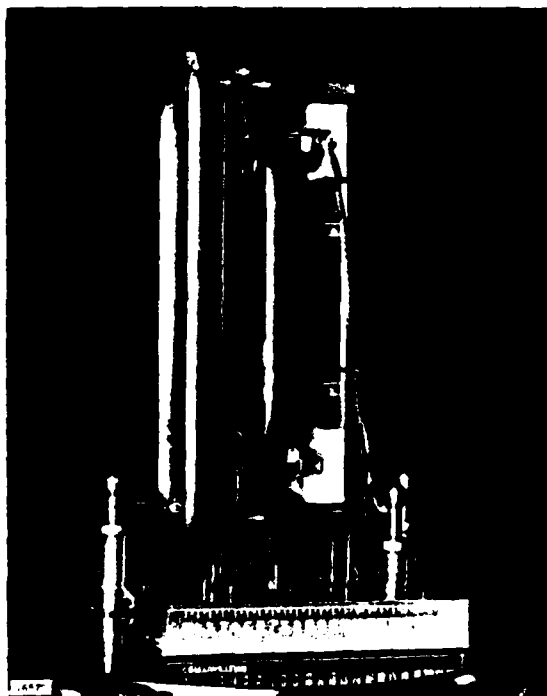


Figure 6. Small Scale Experiment

The experimental unit was assembled in a bell jar where a nominal pressure of 2×10^{-6} Torr was maintained. The level of the base pressure was not found to be critical and only slightly affected the control of plate current.

Electrical Circuits

Two types of pulsers were used to control the back plate voltage. A 1:2 pulse transformer stepped up the pulse voltage to 4.4 kV with pulse durations up to 50 μ sec. The capacitor C1 was charged sufficiently negative with respect to the filaments to assure complete E-beam current cut off in the absence of a pulse shown in Fig. 7.

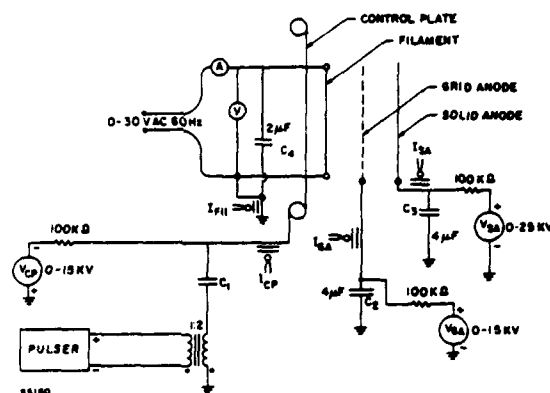


Figure 7. Electrical Control of E-Beam Test Set Up - Schematic

The second form of pulser was the R-C configuration shown in Fig. 8. A two uf capacitor was charged to the maximum desired control voltage and discharged through various resistors to obtain exponential decays with time constants ranging from 2 to 200 usec. In this manner a single oscillogram mapped out the E-beam current as a function of the back plate voltage for a given combination of grid and solid anode potentials.

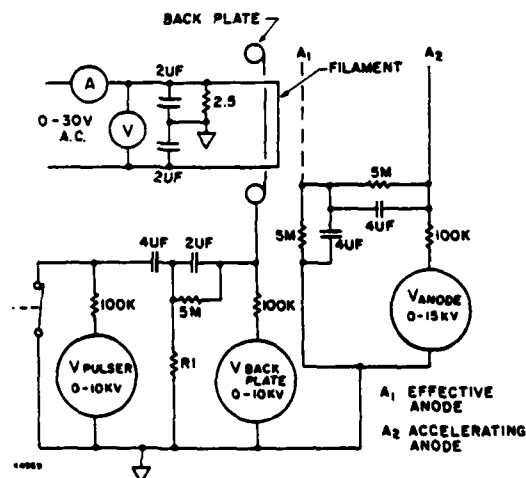


Figure 8.

Experimental Procedure

The filament temperature was adjusted so that space charge limited operation existed. This was accomplished by increasing the filament power slightly above the point where there was no further increase in E-beam current when the back plate was pulsed. Space charge limit operation is particularly important in E-beam gun operation because electron beam uniformity is then dictated by the interelectrode tolerances and not by temperature nonuniformities of the filaments.

The cut off potential was determined by reducing the back plate bias voltage to the value where a small E-beam current was emitted from the filaments. The back plate bias voltage was then increased by 10% to assure complete cut off.

The R-C type pulser was used to determine the gun control characteristics. Various fixed grid anode voltages were applied and for each voltage the E-beam current as a function of the control plate potential was displayed on the oscilloscope. A family of such curves is shown in Fig. 9.

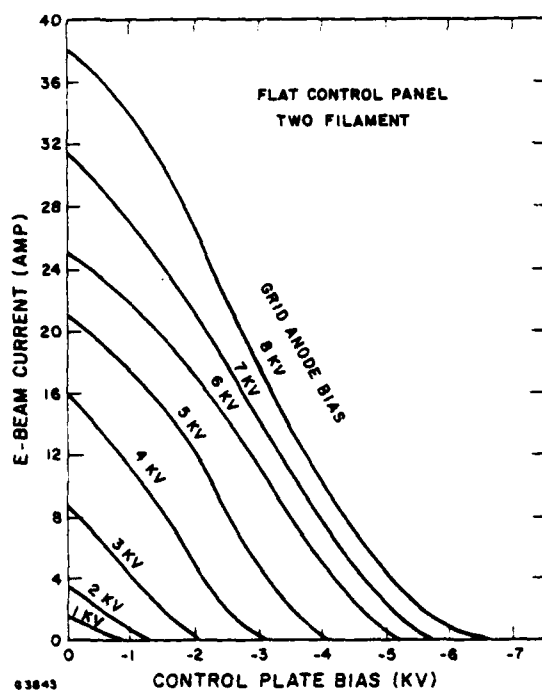


Figure 9. Control Plate Bias

The data is displayed in a format most useful for E-beam gun control application and not in the traditional form published for vacuum tubes. The typical tube parameters at an operational point of

$$V_p = -1.5 \text{KV and } \partial V_{ga} = 5 \text{KV are:}$$

$$\mu = \left(\frac{\partial V_{ga}}{\partial V_p} \right) I_{fil} = r_p g_m = 1.75$$

$$g_m = \left(\frac{\partial I_{fil}}{\partial V_{c_p}} \right) V_{ga} = 10.1 \text{ mmo}$$

$$r_p = \left(\frac{\partial V_{ga}}{\partial I_{fil}} \right) = 175 \text{ r}$$

Some of the characteristic curves were repeated using only one of the two filaments in order to predict the performance of a large gun with close to 100 filaments in parallel. The collected data indicate that the emission for a filament in an array is within 5% (lower) than emission of a single filament. This result was theoretically expected and is also in agreement with data collected from existing guns operated in diode mode.

The major incentive in development of the back plate controlled gun was to obtain a reduction of the control power requirements. As can be seen in Fig. 10 the control plate current, presumably ion and secondary electron emission, is orders of magnitude lower than E-beam current. The small back plate current permits E-beam control of even a full size gun with a ω power modulator.

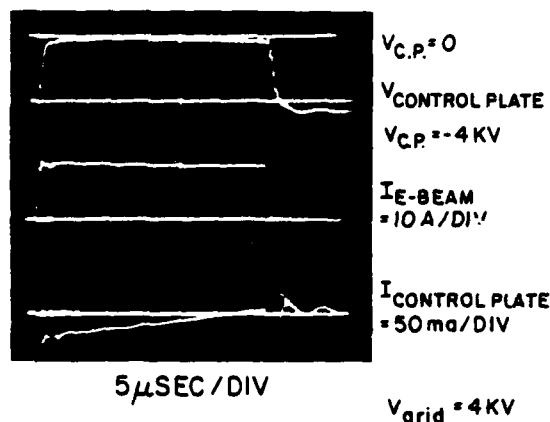


Figure 10. Pulsed Mode E-Beam Test

TABLE I
EXPERIMENTAL BACK PLATE GUN PARAMETERS

FILAMENT LENGTH	25cm
FILAMENT DIAMETER	0.05cm
NUMBER OF FILAMENTS	2
BACK PLATE TO FILAMENT (g)	1 cm
FILAMENT SPACING (S_f)	2.5cm
FILAMENT TO ANODE GRID (d-g)	2cm
ANODE GRID DIAMETER d_a	0.032cm
ANODE SPACING J_a	1.27cm
*A ANODE to ANODE S_{aa}	2.8cm

*Although the electrons exiting the gun were not accelerated to high energy levels in the test set up the field in the vicinity of the anode grid was consistent with that in the full scale unit.

FULL SCALE RESULTS

The data gathered in the small scale experiment was used to complete the design of a full scale gun. The performance of the full size E-beam agreed with the predictions obtained in the bell jar experiments. The only anomaly that was discovered was an instability that occurred in a particular operating regime. In concept a full range of E-beam current could be obtained by adjusting the magnitude of the pulse applied to the back plate. This was confirmed in the small scale experiment with a potential field just outside of the gun equivalent to the field in a full scale unit. In the large unit with the entire accelerating voltage present stable low current E-beams could not be obtained with a high gun anode voltage and low modulating pulse. However, there was no limit to the range of stable operations between maximum design value and zero if the gun anode voltage was varied. In any event the unstable region was concerned with E-beam current pulse levels much below the levels at which the gun is normally operated. It is reasonable to deduce that since the instability is a voltage effect and not a field effect the instability is brought about by ions penetrating into the gun and effecting the space region around the filament.

In the full scale unit the modulating pulse was obtained with a commercial hard tube pulse

generator. There was no practical limit to the pulse rate capability of the gun assuming of course that the power supplies for the high voltage and gun anode had the required capacity. The hard tube modulator was connected to the back plate through a 1:5 step up pulse transformer and even with the 25:1 impedance transformation there were no loading effects on the Oober. The high impedance characteristic of the back plate was further confirmed by connecting a high resistance in series with the back plate with no reduction in the output pulse amplitude. Figure 11 is an oscillogram of a single shot of a high current 40 μ sec E-beam pulse. Figure 12 shows 25 pulses taken at a high repetition rate. Amplitude spread is due to the dynamics of the high energy capacitor bank circuit and not because of a gun characteristic.

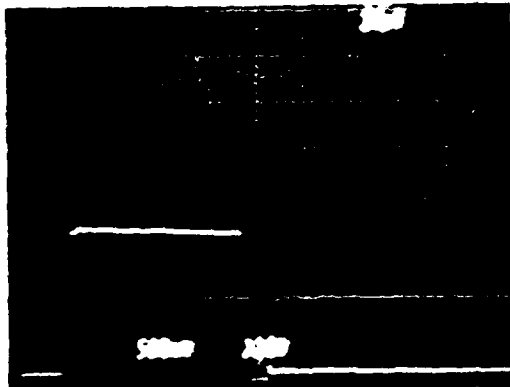


Figure 11.

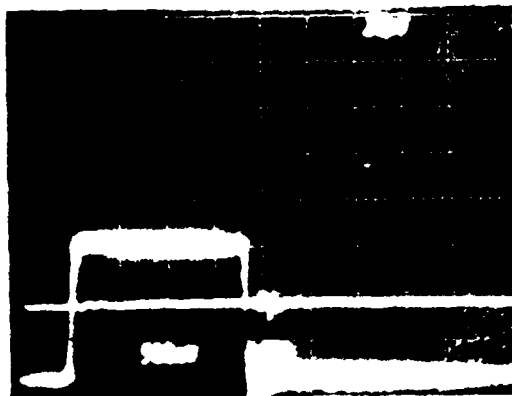


Figure 12.

Conclusion

A non-intercepting control electrode can pulse modulate a high power E-beam at high repetition rates. The control electrode has in effect a high impedance and requires little driving power.

References

1. J.D. Daugherty, E.R. Pugh, and Douglas-Hamilton
Bull. Am. Phys. Soc. 17, 399 (1972)
2. Big Bang Reports
3. Hunding Reports

MULTIMEGAWATT MODULATOR DESIGNS FOR MINIMUM WEIGHT AND VOLUME

J. J. Moriarty
A. M. Herling
P. A. Corbiere*
G. K. Simcox**

Raytheon Company
Missile Systems Division
Bedford, Massachusetts 01730

Summary

This paper describes the results of a study of sixty-five point designs of thyatron-switched modulators covering the parameter ranges:

Average Power: 0.5 to 30 MW
Energy Per Pulse: 10 to 100 kJ
Output Voltage: 20 kV
Pulse Duration: 5 to 40 μ sec
Pulse Repetition Frequency: 50 to 500 Hz
Maximum Burst Duration: 2 min

For the majority of the point designs, several thyatron modules were required, a feature which led easily to the concept of sequentially charging individual modules or groups of modules in order to smooth the load on the prime power. Both active and adiabatic cooling techniques were employed in the assumed environment of 10,000 ft. altitude and 20°C ambient temperature. Representative state-of-the-art components used in the designs were HY-7 thyatrons and 60 J/lb pulse capacitors. Conceptual designs of sixteen charging chokes were prepared to cover the range of parameters described above.

Graphical and tabular results describing the modulator weights and volumes are presented. Artist's concepts which illustrate the minimum weight and minimum volume approaches are also included.

This work was sponsored by the Aero Propulsion Laboratory, Air Force Wright Aeronautical Laboratories, Wright-Patterson AFB, Ohio 45433.

Introduction

This paper is based on the results of a design study of lightweight, low volume power conditioning subsystem in the range of 500 kW to 30 MW which has been undertaken as part of the Air Force exploratory development program in high power airborne electrical power supply technology. These designs are based on presently available component technology such as solid state switching devices, newly developed thyatrons and high energy density pulse capacitors.

Although these pulser subsystems are to be operated in the burst mode, active cooling concepts, rather than purely adiabatic thermal management, have been incorporated whenever they would offer an advantage in minimizing weight or volume. A simplifying assumption has been made that the environment is equivalent to an altitude of 10,000 ft and an ambient temperature of 20°C.

The designs which were prepared included all the elements of the well-known line-type modulator such as the command charge switch, pulse-forming line (PFL), discharge thyatron and its accessories. Pulse transformers were not considered. For the majority of the point designs several PFL-thyatron modules were required, a feature which combined readily with the concept of sequentially charging individual modules or groups of modules in order to smooth the load on the prime power source. The system interfaces and the basic circuit concept are further described in Figures 1 and 2.

A total of 65 design points were evaluated for both minimum weight and minimum volume resulting in 130 separate point designs. The parameter ranges used to generate the various design points are listed in Table 1.



Figure 1 - Block Diagram

* Present address, Consultant, 56 Bartlett St., Beverly, MA 01915

** Present address, Consultant, 199 Follen Rd., Lexington, MA 02173

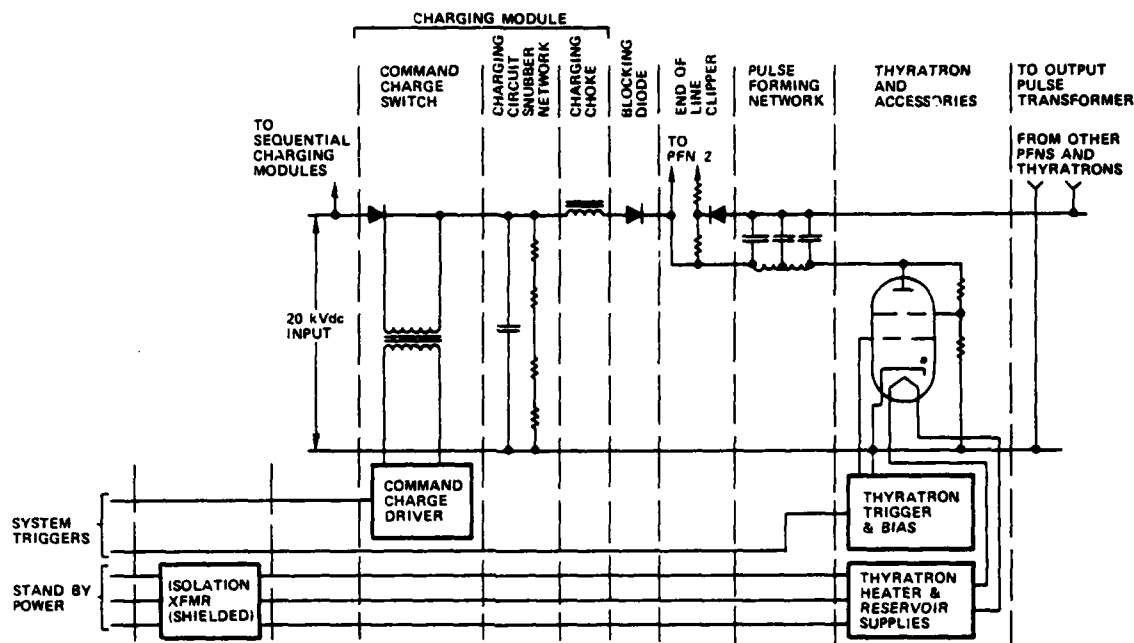


Figure 2 - Line Type Modulator Concept with Sequential Charging

TABLE 1
PARAMETER RANGES

Average Power	0.5 to 30 MW
Energy Per Pulse	10 to 100 kJ
Pulse Duration	5 to 40 μ sec
PRF	50 to 500 pps
Input Voltage	20 kVdc
Output Voltage	20 kV pulsed

Critical Components

The most influential components of the pulser design were the switches, pulse capacitors and charging chokes. Care was taken to stay within present device technology.

Output Switches

Because of the range of repetition rates considered it was straightforward to choose thyratrons as the output switches over alternatives such as spark gaps. The EG&G HPS-40 tube was selected as representative of the state-of-the-art in conventional thyratrons with a normal range of di/dt.

In order to minimize weight and volume it was found necessary to fully utilize the one-MW average power capability of the HY-7. This factor is illustrated by the nomograph in Figure 3.

There are both peak and average power limitations on the HY-7 thyatron. One purpose of the nomograph is to simplify analysis such that maximum system capability is achieved by using the switches at their maximum peak and average power capabilities simultaneously. An example which illustrates both the peak power (1000 MW) and average power (one MW) limitations is shown in the following paragraph.

HY-7 OPERATION

40 kV PEAK
50 kA PEAK
50A AVERAGE

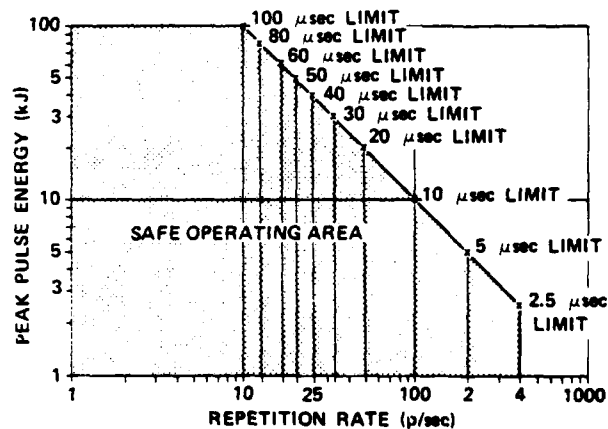


Figure 3 - Maximum HY-7 Thyatron Capability in PFN Module

For a 10- μ sec pulse width, for example, these limitations require:

$$\text{Peak Energy Per Pulse} = (1000 \text{ MW}) (10 \mu\text{sec}) = 10 \text{ kJ Maximum}$$

$$\text{Repetition Rate} = \frac{1 \text{ MW}}{(1000 \text{ MW}) (10 \mu\text{sec})} = 100 \text{ pps Maximum}$$

Note that the so-called safe operating area on the nomograph is based on using the HY-7 thyatron at its maximum peak and average power. That is, reduction of the peak pulse energy in the above example would, from average power considerations, allow a PRF of 200 pps. However, one can move along the limit line only in the direction of reduced peak energy per pulse.

The number of HY-7 thyatrons required for a given pulser design point may be determined by either peak or average power limitations of the HY-7.

Pulse Capacitors

Pulse capacitors for use in burst mode PFLs have been demonstrated (1,2) to operate with significant lifetime (10^5 to 10^6 shots) with energy storage densities of up to 80 J/lb. Although these data would indicate a lifetime of only a few hours at the repetition rates of interest, a nominal value of 70 J/lb was chosen for the designs. The capacitor size was determined by scaling a 60 J/lb, 0.84 μ F capacitor of known dimensions. (3) Because of the effects of case margins the actual densities ranged from 58 J/lb to 69 J/lb.

Charging Choke Designs

The charging choke designs selected were modified Brooks type air core inductors with an outer concentric core to confine and provide a return path for the magnetic flux.

Coil construction utilized a foil conductor and insulation sandwich type of winding on a cylindrical coil tube.

Adiabatic charging choke operation for the two minute duty cycle was assumed, with conductor current density selected for a temperature rise of 1.5°C/second or 180°C total temperature rise during operation. Core loss was a minor factor.

Charging choke Q and therefore charging circuit efficiency were dictated by minimum size and minimum weight constraints consistent with the adiabatic design described. Generally charging circuit losses were calculated to be $\sim 2\frac{1}{2}$ percent at the seven megawatt average power level, decreasing to half that at the highest average power levels studied.

Figure 4 entitled "Charging Choke Characteristics" represents the total charging choke core and coil weight in a given pulser. All data represent choke designs deployed into a four sequential charging module circuit configuration, with the operating frequency taken from the actual module resonant frequency. The dependence of total charging choke weight on equivalent operating frequency is striking. This effect is not caused by large changes in core weight as much as by increased charging choke energy storage in the coil air gap required by the higher peak energy pulsers, in order to maintain the uniform high voltage power supply (HVPS) current loading desired.

Referring again to Figure 4 total pulser charging choke minimum weight is achieved by utilizing the minimum number (4) required for the sequential charging modules selected. The use of 4 x 2 matrix of eight total chokes at 30 megawatts average power versus 4 x 3 matrix or 12 total chokes at 21 megawatts average power results in the apparent contradiction of higher total charging choke weight required for the 21 megawatt case. The actual number of charging chokes selected for a given pulser was dictated by the pulse forming network and thyatron module requirements.

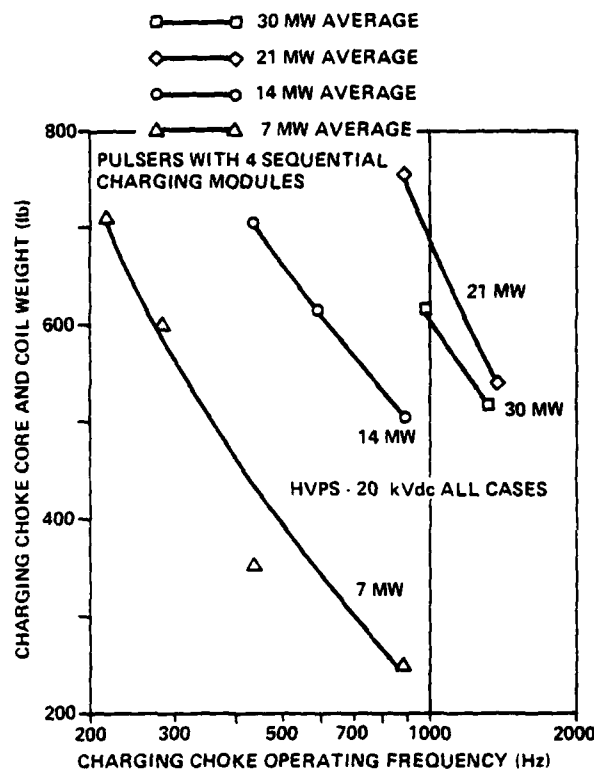


Figure 4 - Charging Choke Characteristics

Modularity And Configurations

In order to arrive at reasonable design matrices, account had to be taken of the general system requirements and the optimum use of critical components.

For the system, the basic considerations were for the operating environment, the duty cycle and the interface requirements for the PFN circuits at the power supply and load with an environment of air at 20°C ambient at 10,000 ft. altitude. It was decided to accept this as the general insulating medium for the minimum weight designs, after appropriate assignment of electrical stresses. Minimum volume designs would accept the weight penalties of a liquid medium.

The loading on the power supply was required to be uniform during the PFN operation, implying a low ratio of peak to average charging currents with consequent high power factor (0.8 - 0.9). To satisfy this requirement, the resonant charging of modules, or blocks of modules in sequence was adopted - a technique called "Sequential Charging".

Sequential Charging

In its simplest form sequential charging may be implemented through the use of separate charging circuits (modules) including a dedicated PFL and discharge thyatron equal to the number of sequential charging sections desired.

Since all PFL's are discharged simultaneously into a common load, the staggered command charge for each sequential section is timed from the PPC output pulse and may include a dead time to allow for thyatron recovery before any resonant charging is initiated.

Figure 5 graphically shows three module sequential charging currents (dotted lines) combined to represent the actual high voltage power supply current waveform (solid line). The hatched line shows a single charging module (and HVPS) current as in a conventional line type modulator design with a command charge feature.

In the case shown, the sequential charging waveforms are phased 120 degrees apart for τ/n sequential module charging time. Sequential charging frequency is $n/2\tau$ where τ is defined as the allotted charging period, rather than the interpulse period. Electrical degrees are given in terms of the sequential charging frequency.

A symmetrical HVPS current waveform top is derived from phasing the intersection of the sequential charging currents at 30 degrees and in the three sequential charging module case results in 13.4 percent peak-to-peak top ripple. The peak charging current in this example is 77.7 percent of that obtained in the single charging module case.

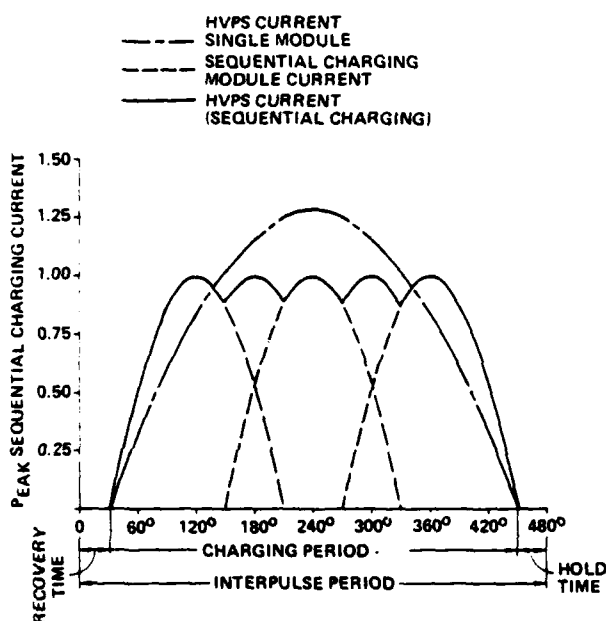


Figure 5 - Charging Current Waveforms

Power Supply Loading

High voltage power supply (HVPS) or prime power current loading is shown in Figure 6 entitled "Sequential Charging Current Characteristics" in which the pulser is charged continuously as shown in Figure 5, i.e., without recovery and hold times. The curves shown connect the realizable discrete points obtainable. Power factor in this case is presumed to be $I_{\text{average}}/I_{\text{peak}}$ which is the inverse of the upper $I_{\text{peak}}/I_{\text{average}}$ curve.

Should continuous HVPS and prime power loading be desired, the simplest approach is to use an additional sequential charging circuit module which is not fired simultaneously with the other modules. Thus the operating duty for each module becomes $(n-1/n)$ times the pulser duty where n is the total number of sequential modules employed.

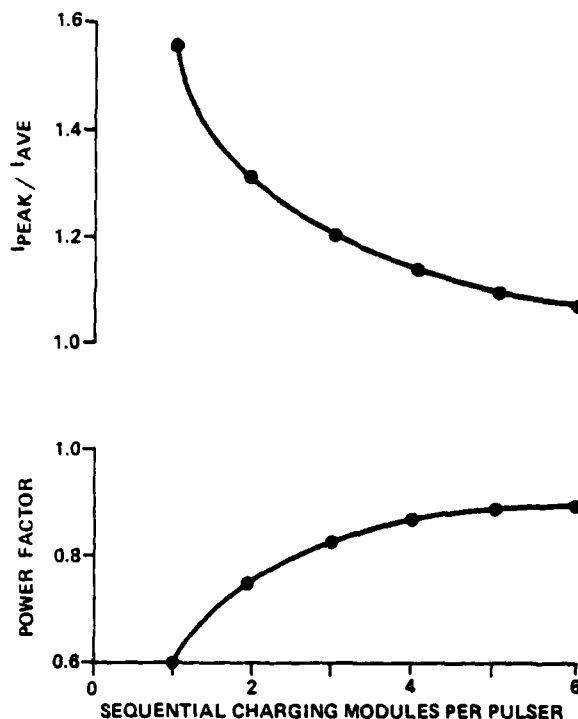


Figure 6 - Sequential Charging Current Characteristics

Combinations of Modules

It was apparent that PFL modularity was advantageous for the charging system and could also provide design alternatives at the output pulse transformer and load. The following illustrates the configurations adopted. The elementary module is that of an HY7 switch which is fully exploited at its average power rating of 1 MW. The configurations for this are shown in Figure 7 for a number of pulse durations, 5, 10, 20 - 40 μsec . Since the pulse risetime specifications were not difficult to achieve, the PFL modularity was, in the main, determined by the limitation of peak current imposed on the PFL capacitor unit, 10 k A.

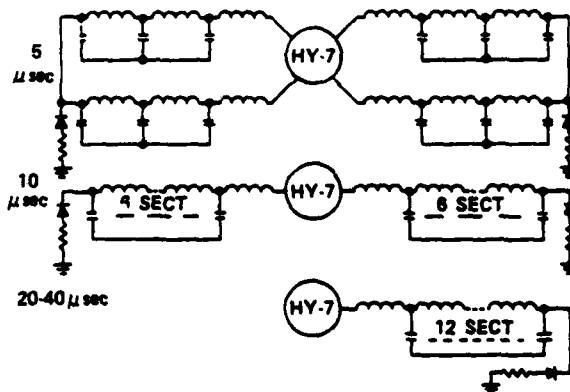


Figure 7 - Typical PFN Configurations

From the matrix of design parameters, standard PFL parameters were defined to aid the formation of module types. This is illustrated in Table 2.

TABLE 2
PFL CLASSIFICATION

PFL Type	Capacitor Value- μ F	Number of Capacitors	Energy Stored in PFL-kJ	Capacitor Density J/lb
a	0.25	12	2.4	58.5
b	0.33	12	3.13	62
c	0.45	12	4.32	66
d	0.50	12	4.80	67
e	0.66	12	6.25	69

Taking into account the range of average powers to be accommodated and the divisions of the systems necessary to apply sequential charging, a basic module containing two HY7 circuits rated for 1.75 MW average power was chosen. The mechanical configuration for this module is shown in Figure 8. This design ensures a low level of external fields due to the control of the discharge current paths. Provision is made for low impedance interconnections to other modules of the system and the module is self-contained with a compact arrangement of clipper and charging components.

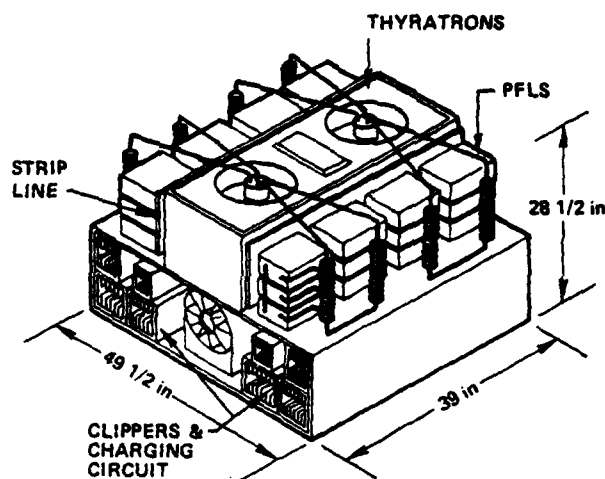


Figure 8 - Basic Module: Two Thyratrons with Charging Circuit

An accumulation of these modules to meet a 7 MW design is shown in schematic form in Figure 9 with the physical layout for a minimum weight concept in Figure 10.

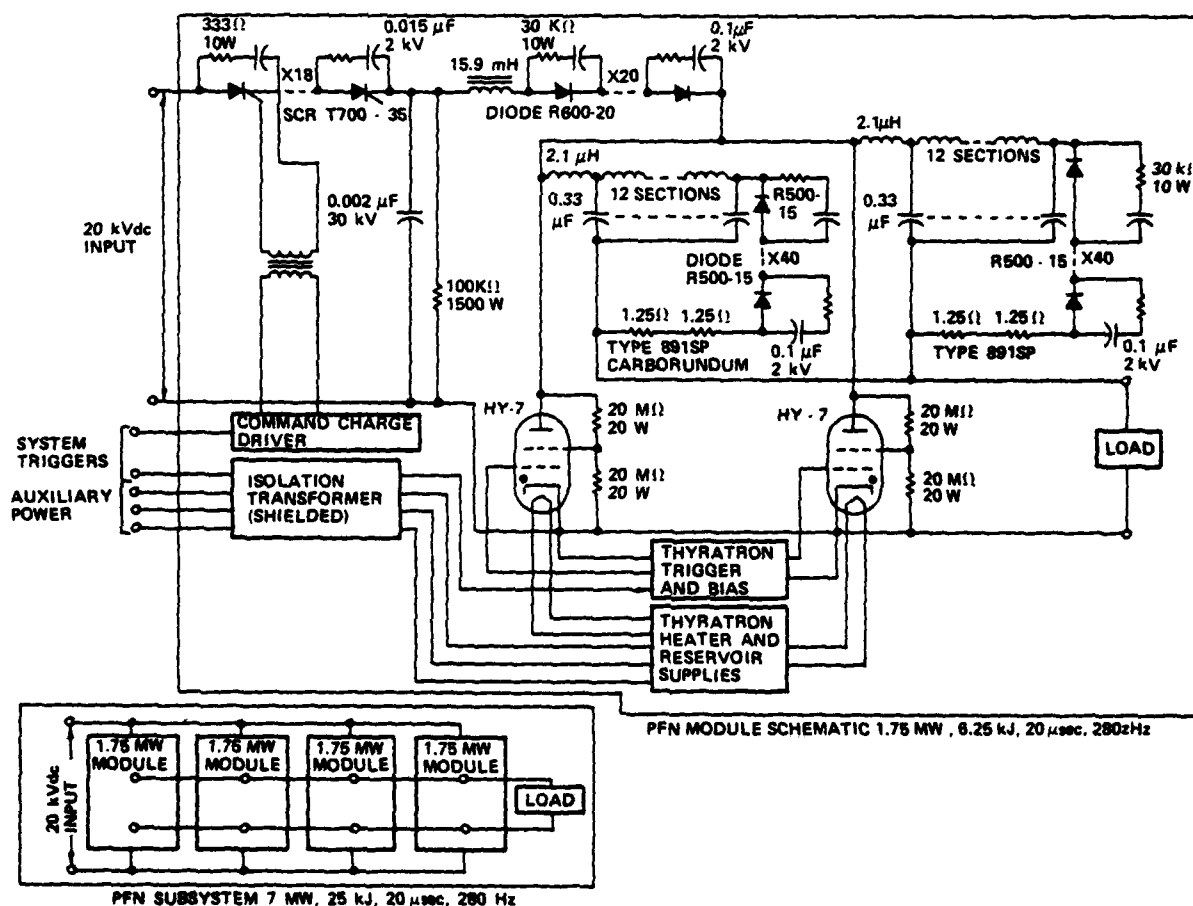


Figure 9 - PFN Schematic for 7 MW, 25 kJ, 20 μ sec, 280 Hz

This concept was used for extensions of average power to 30 MW with suitable modular divisions for the sequential charging. An artist concept of a 30 MW minimum volume design is shown in Figure 11.

Certain of the designs of the matrices could not be achieved with full exploitation of the HY-7 thyratrons; in these cases, penalties in size and weight were apparent. Examples of these occurred for two 14 MW designs at 100 kJ, 140 Jz, 5 μ sec and 50 kJ, 280 Hz, 5 μ sec respectively. In these cases, size and weight improvements could be made by future thyatron developments or by the choice of another switch type, such as a spark gap.

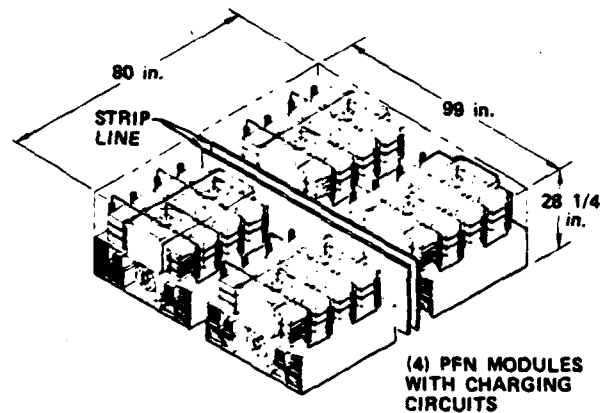


Figure 10 - PFN Minimum Weight Concept for 7 MW, 25 kJ, 20 usec, 280 Hz

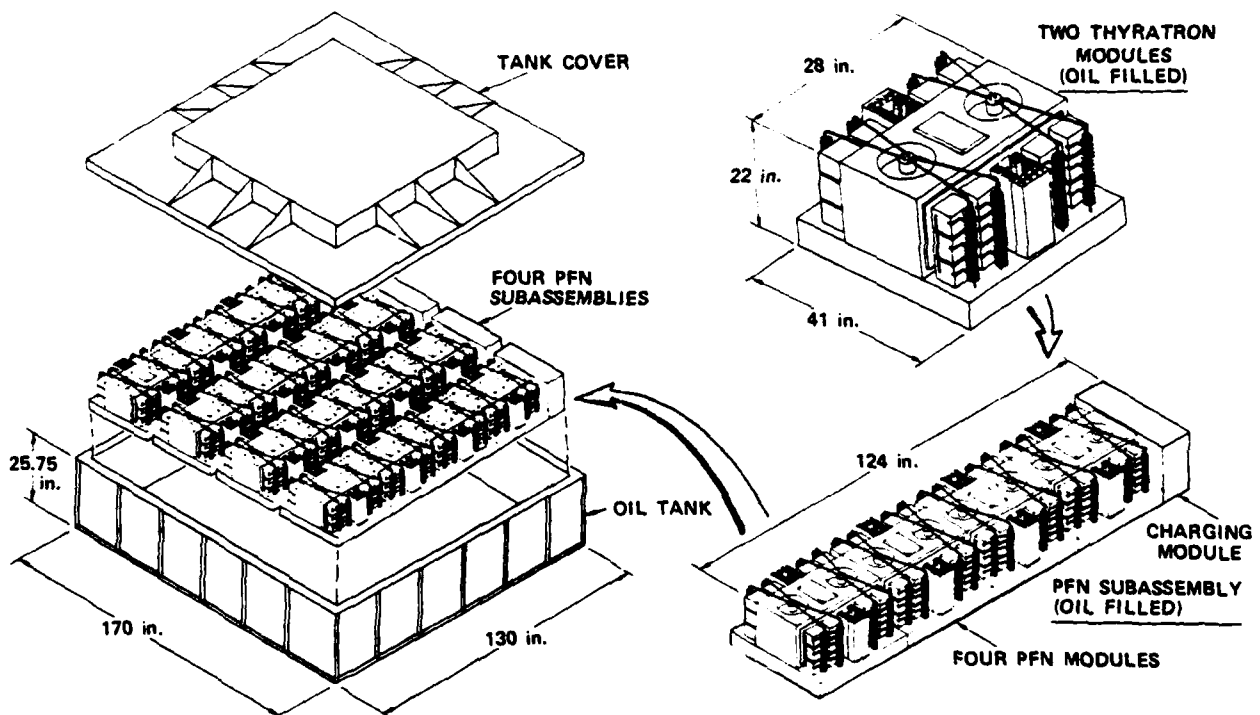


Figure 11 - PFN Minimum Volume Concept for 30 MW, 75 kJ, 5 usec, 400 Hz

Mechanical Design Consideration

The designs addressed the environment described earlier with particular guidelines depending on whether weight or volume was to be minimized. Minimum weight designs were air-insulated with the base at ground potential and the remaining surfaces containing exposed high voltage. Minimum volume designs, however, were oil-immersed and were therefore totally enclosed in a grounded metal container.

Component packaging utilized voltage grading techniques and current cancelling configurations to reduce EMI. Since the PFL capacitors were enclosed in insulating material, the internal construction and pad configuration was taken into account to achieve compact packaging.

Cooling techniques included natural and forced convection as well as water where necessary. Adiabatic absorption of heat during a burst was assumed to occur both in certain components and in the insulating oil. No circulating oil cooling was utilized in these designs. A summary of the cooling techniques used for various pulser components is given in Table 3.

In the minimum weight designs all the blocking diodes are air cooled except for the 30 MW design points 61 through 65. Similarly, all the command charge SCR stacks are air-cooled except for design points 41 through 65.

TABLE 3
PFN COMPONENT COOLING

Component	Cooling Technique	
	Min. Weight	Min. Volume
Thyratrons	Air	Oil
Pulse Capacitors	Adiabatic	Adiabatic
PFL Coils	Water	Oil
Clipper Diodes	Air	Oil
Clipper Resistors	Water	Water
Blocking Diodes	Air/Water	Oil
Command SCRs	Air/Water	Oil
Snubber Network	Air	Oil
Charging Choke	Adiabatic	Adiabatic

Results

The results of this design study are summarized in Table 4 and in the graphical presentations of Figures 12 through 18. The 500 kW design points were special cases which were not compatible with the sequential charging concept and did not fully utilize the HY-7 capabilities. Consequently these design points are not included in the graphical algorithms.

Figure 12 shows that the density remains fairly constant over the range of interest. Figures 13 through 18 show the dependence of weight on pulse energy for various pulse durations and average power levels. The volume dependence can be calculated directly from these curves and the density. Within the range of accuracy of the results the algorithms indicate an approximately linear dependence of weight and volume on energy.

Pulse capacitor energy density and thyatron peak power capabilities have a strong influence on the size and weight of pulse power conditioning systems. Of particular concern is the peak power limit of the HY-7 which results in a much larger number of thyratrons for short pulse systems having the same average power requirements as associated long pulse systems. This limitation could be ameliorated substantially by the development of such thyratrons as the HY-7160 with five-fold increased peak power capability. In addition, the development of so-called "quick-start" or "cold-cathode" thyratrons would eliminate the requirement for auxiliary power and filament transformers weighing about 30 lb each.

References

- (1) "Capacitors for Aircraft High Power", Final Report on Contract F33615-75-C-2021, by Hughes Aircraft Co., Culver City, CA (January 1980).
- (2) "High-Energy Density Pulse-Forming Network and Continued Capacitor Testing", Final Report on Contract DAAK40-77-C-0118, by Maxwell Laboratories, Inc. San Diego, CA (April 1980).
- (3) From Reference 2, p. 8

TABLE 4
PULSER DESIGN RESULTS

Design No.	Avg. Power (MW)	Energy (kJ/P)	Rep. Rate (Hz)	Pulse Width (μs)	Total Volume		Total Weight (Net)		Ref.
					Min. Vol. (ft ³)	Min. Wt. (lb)	Min. Vol. (ft ³)	Min. Wt. (lb)	
1	0.5	10	50	5	39.2	30.9	857	1800	99.7
2	0.5	10	50	10	30.3	23.9	710	1430	99.6
3	0.5	10	50	20	30.3	23.9	726	1450	99.8
4	0.5	10	50	30	11.5	24.9	676	1410	99.8
5	0.5	10	50	46	12.8	25.8	692	1460	99.8
6	7	25	280	5	129	89.2	2770	5770	94.1
7	7	25	280	10	129	89.2	2850	5850	94.6
8	7	25	280	20	129	89.2	2700	5690	94.7
9	7	25	280	30	135	92.8	2780	5910	94.7
10	7	25	280	40	140	96.4	2850	6130	94.7
11	7	50	140	5	194	122	4100	8220	93.8
12	7	50	140	10	180	113	3880	7690	94.5
13	7	50	140	20	180	113	3670	7480	94.6
14	7	50	140	30	163	102	3390	6780	94.6
15	7	50	140	40	170	106	3450	6990	94.6
16	7	75	93.3	5	291	182	5980	12450	93.6
17	7	75	93.3	10	221	138	4660	9390	93.2
18	7	75	93.3	20	206	129	4480	8990	93.6
19	7	75	93.3	30	214	134	4620	9320	93.6
20	7	75	93.3	40	222	139	4770	9660	93.6
21	7	100	70	5	415	267	7520	17350	92.4
22	7	100	70	10	295	190	6030	12880	93.2
23	7	100	70	20	290	187	5970	12680	93.4
24	7	100	70	30	240	154	5250	10720	93.4
25	7	100	70	40	249	160	5200	10860	93.4
26	14	50	280	5	277	175	5540	11700	94.3
27	14	50	280	10	277	175	5700	11860	94.7
28	14	50	280	20	277	175	5380	11540	94.8
29	14	50	280	30	288	183	5520	11990	94.8
30	14	50	280	40	299	189	5740	12420	94.8
31	14	75	186.6	5	300.72	193	6490	13400	94.1
32	14	75	186.6	10	294.94	190	6200	12940	94.7
33	14	75	186.6	20	294.94	190	5980	12720	94.8
34	14	75	186.6	30	307	197	6230	13140	94.8
35	14	75	186.6	40	319	205	6270	13570	94.8
36	14	100	140	5	423	267	8040	17810	94.0
37	14	100	140	10	386	256	7740	17030	94.7
38	14	100	140	20	386	256	7440	16730	94.8
39	14	100	140	30	327	210	6770	14240	94.8
40	14	100	140	40	339	218	6900	14670	94.8
41	21	50	420	5	384	247	7230	16100	94.7
42	21	50	420	10	384	247	7390	15950	95.1
43	21	50	420	20	384	247	6890	15450	95.1
44	21	50	420	30	399	257	7190	16420	95.1
45	21	50	420	40	415	267	7500	17100	95.2
46	21	75	280	5	388	251	7790	16770	94.2
47	21	75	280	10	388	251	8030	17010	94.6
48	21	75	280	20	388	251	7560	16520	94.7
49	21	75	280	30	404	262	7760	17180	94.7
50	21	75	280	40	420	271	8090	17820	94.7
51	21	100	210	5	415	267	8180	17790	94.2
52	21	100	210	10	415	267	8170	17780	94.6
53	21	100	210	20	415	267	7840	17440	94.8
54	21	100	210	30	432	278	8070	18080	94.9
55	21	100	210	40	449	289	8300	18710	94.9
56	30	75	400	5	512	329	9310	21290	94.3
57	30	75	400	10	512	329	9520	21490	94.6
58	30	75	400	20	512	329	9060	20930	94.7
59	30	75	400	30	532	343	9460	21640	94.7
60	30	75	400	40	553	356	9870	22740	94.7
61	30	100	300	5	516	331	9920	21860	94.6
62	30	100	300	10	510	331	10240	22180	95.0
63	30	100	300	20	510	331	9610	21550	95.1
64	30	100	300	30	539	344	9960	22400	95.1
65	30	100	300	40	560	357	10310	23260	95.1

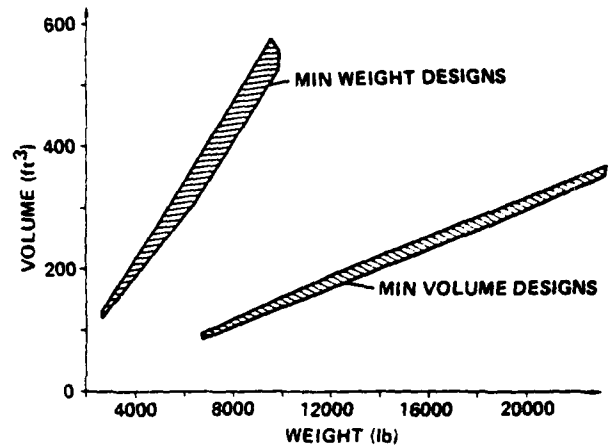


Figure 12 - Volume versus Weight for 7 MW to 30 MW Average Power Pulse Generators

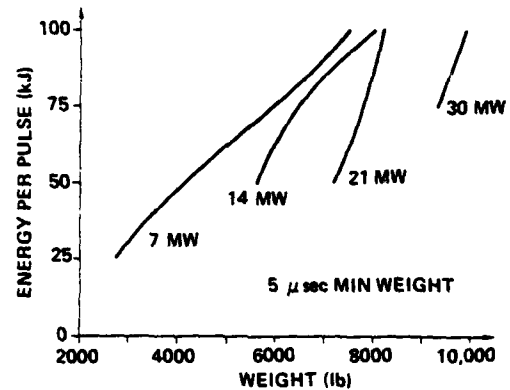


Figure 13 - Energy versus Weight for 5 μsec Minimum Weight Designs

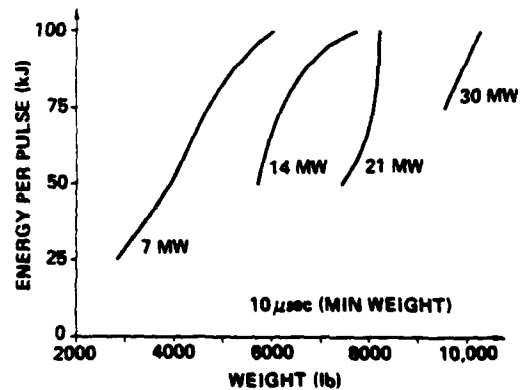


Figure 14 - Energy versus Weight for 10 μsec Minimum Weight Designs

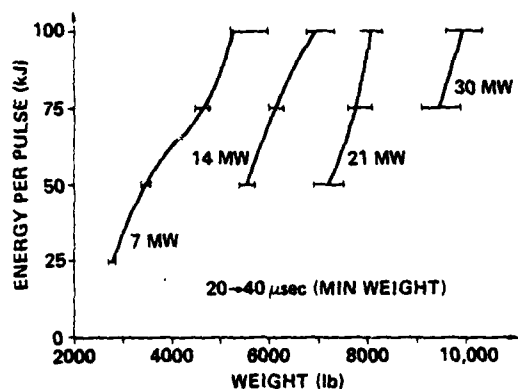


Figure 15 - Energy versus Weight for 20 μ sec - 40 μ sec Minimum Weight Designs

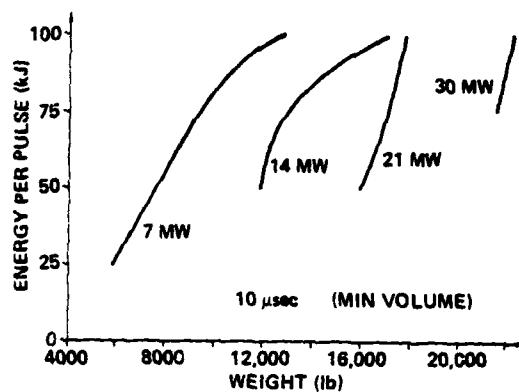


Figure 17 - Energy versus Weight for 10 μ sec Minimum Volume Designs

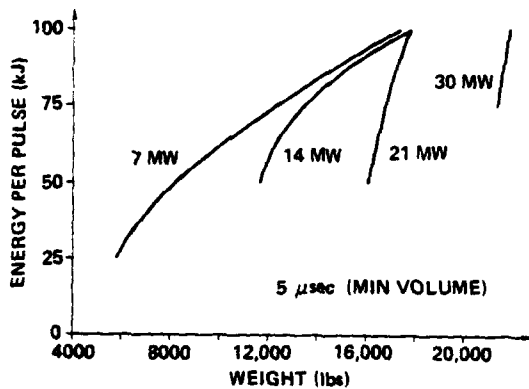


Figure 16 - Energy versus Weight for 5 μ sec Minimum Volume Designs

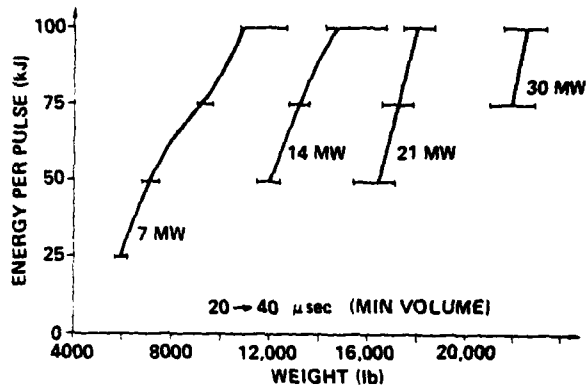


Figure 18 - Energy versus Weight for 20 μ sec - 40 μ sec Minimum Volume Designs

PULSE POWER CIRCUIT DIAGNOSTICS FOR THE NOVA LASER*

D. J. Christie, G. E. Dallum
D. G. Gritton, B. T. Merritt, K. Whitham
Lawrence Livermore National Laboratory
P.O. Box 5508, L-464
Livermore, CA 94550

L. W. Berkgigler
Los Alamos National Laboratory
Los Alamos, NM 87544

Summary

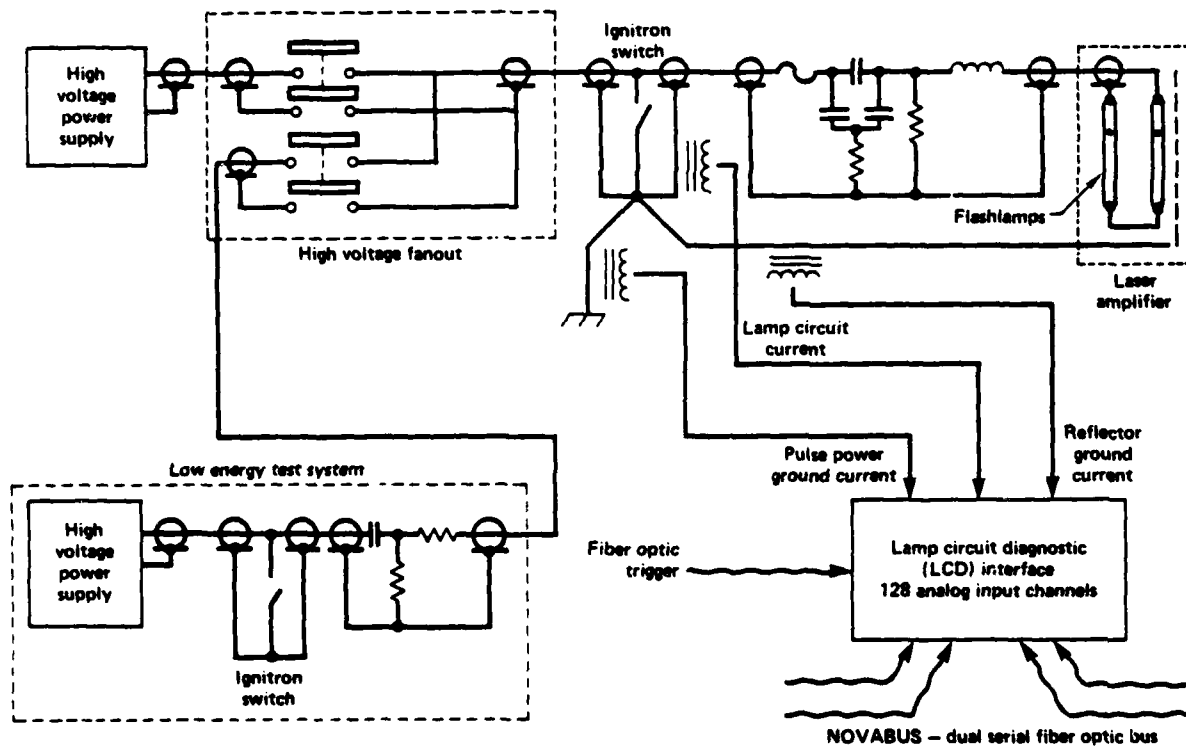
The Nova laser will have a large pulse power system for driving laser amplifiers, incorporating approximately 1,600 flashlamp circuits. An automated system has been designed for diagnosing the condition of these flashlamp circuits. It records digitized circuit current waveforms and detects current excursions above a given threshold. In addition, it is able to fire flashlamps at a low energy to ascertain the health of the system.

Data from this system can be plotted for inspection by the operator, analyzed by the computer system and archived for future reference.

Pulse Power System

The pulse power system is composed of about 1,600 circuits, several high voltage power supplies, ignitron switches and necessary control electronics and computer interfaces.

During normal operation, a capacitor is charged through a resistor by the high voltage power supply. The top supply in Figure 1 would be selected by the high voltage fanout in this case. At shot time, the capacitor is discharged into the flashlamps in the laser amplifier through an inductor. In a system of this size occasional failures are inevitable. These include a lamp that does not fire, a lamp which



PULSE POWER SYSTEM CONFIGURATION

FIGURE 1

*This work was performed under the auspices of the U.S. Department of Energy by the Lawrence Livermore National Laboratory under Contract No. W-7405-ENG-48.

breaks while firing, an arc from the flashlamps or their leads to the reflector, or an arc from the pulse power system to building ground. Because of the many failure modes, the pulse power circuitry has been instrumented to detect these kinds of failures. The current from building ground to the ignitron switch commons, the current from the amplifier reflectors to the switch commons, and the current in the return leg of the pulse power circuits are all monitored with current transformers.

The current transformers are physically located in the switch assembly. Data from the current transformers is recorded by the Lamp Circuit Diagnostics (LCD) interface. The LCD interface also has analog latches for determining whether the current exceeded a given level.

In addition to the normal firing circuitry, provision has been made for testing the pulse power system by firing the flashlamps at a very low energy. The bottom power supply in Figure 1 is used for this purpose. It charges a capacitor through a resistor. This capacitor is connected to the pulse power circuitry through the high voltage fanout (Figure 1) and the top power supply is disconnected. The switch fires, sending a pulse of approximately the same initial voltage but much lower energy to the laser amplifiers through the pulse power circuitry. Again, the current waveforms are monitored by the LCD interface to detect faults. This allows detection of ground faults, pulse power circuit failures, and broken or bad flashlamps before firing them at full energy. Firing into a bad flashlamp at full energy can result in a profoundly damaged laser amplifier, so testing flashlamps at low energy saves money and time by preventing unnecessary damage.

Lamp Circuit Diagnostic Interface

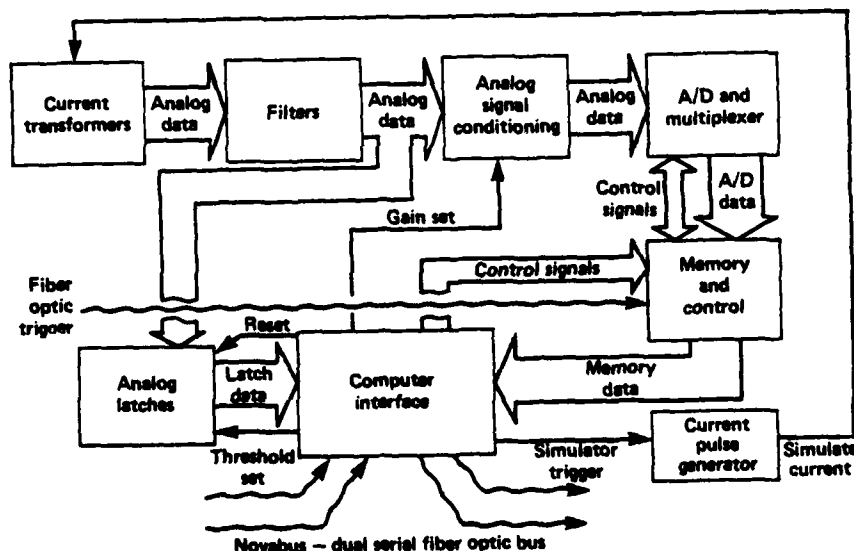
The LCD interface configuration is shown in Figure 2. Analog data is received from the current transformers and filtered. It is then processed in two ways. First, it is fed into analog latches which

detect excursions over a given threshold. There is a high and low threshold programmable through software. Latches are set when the inputs exceed the threshold and remain set until reset by the computer interface. The latch data is read directly as discrete inputs to a computer interface.

The analog data is also amplified by the analog signal conditioning circuitry. Then the analog channels are sequentially sampled by the A/D and multiplexer. The sampling process is initiated by either the fiber optic trigger or a software generated output from the computer interface. This data is recorded in a local memory for a period of approximately four milliseconds. This data is then transferred to the central computer system through the computer interface.

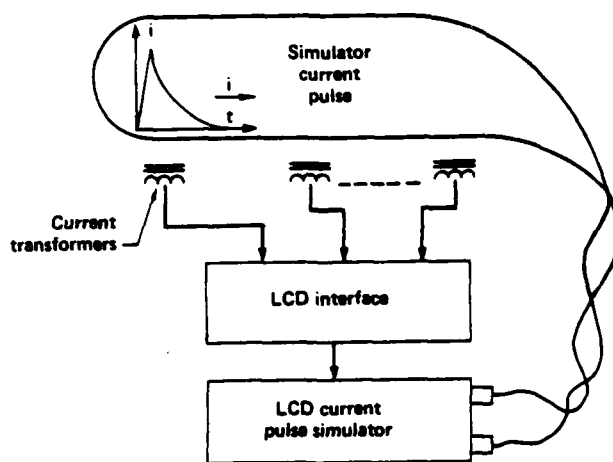
The LCD interface is composed of two identical 64 channel sections, providing a total of 128 input channels. The number of channels each of these sections samples is software programmable. The choices are 1, 8, 16, . . . 56, 64 channels. The A/D always samples at a 1 Mhz rate, so as more channels are selected, the slower the sample rate will be. For example, if one channel is sampled the rate is 1 Mhz, for 8 channels the rate is 125 KHz, and for 64 channels the rate is about 15.6 KHz. The fastest natural frequency for our pulsed power circuits is on the order of 2 KHz so even the slowest sampling rate is sufficient to diagnose them.

Self diagnostic capability is provided by a current pulse generator which sends a current pulse through all of the current transformers under computer control as shown in Figure 3. This is used to check the latches on low threshold and to check the data sampling and recording circuitry. It provides a pulse of amplitude and duration similar to the low energy flashlamp circuit current pulse generated in the preshot testing of the pulse power circuitry and flashlamp.



LCD INTERFACE CONFIGURATION

Figure 2



CURRENT PULSE SIMULATOR FOR SELF DIAGNOSTICS

Figure 3

The filtering and clamping circuitry is shown in Figure 4. Its major function is to protect the LCD interface from damage due to noise. This is important because the LCD interfaces are mounted in racks next to the ignitron switches, some of which switch currents on the order of 100 kA. The series resistors provide current limiting and the steering diodes direct the current limited noise to ground through a coupling capacitor. Our testing has shown this arrangement to be effective in preventing damage to the LCD interface.

Data Processing

Data is read back from the LCD interface to the central computer system. Here data will be handled in several ways. Current waveforms can be displayed

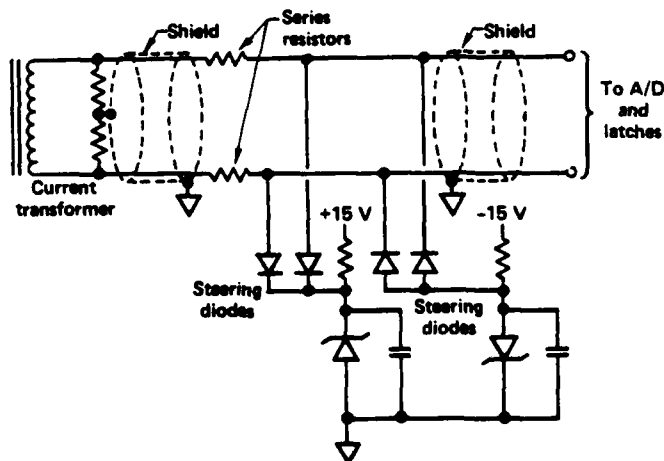
at the operator console for human inspection or analyzed by the computer. The lamp circuit current waveforms have a distinct characteristic shape, allowing an operator to easily recognize many typical problems with the pulse power system. The waveform analysis routine will determine whether the data is in limits or if it has changed since the last time it was sampled. The waveform data will also be placed in a file which can be archived if desired.

The latch data is used for a cursory inspection of the pulse power system. By reading the latches it can be determined whether the lamp circuits fired and whether there was significant current in the reflector ground or pulse power ground connection from the ignitron switch to earth ground. Waveform data will provide more detailed information if a problem is detected.

1. 1980 Laser Program Annual Report, LLNL, Nova Power Conditioning.
2. 1981 Laser Program Annual Report, LLNL, Nova Power Conditioning.

DISCLAIMER

This document was prepared as an account of work sponsored by an agency of the United States Government. Neither the United States Government nor the University of California nor any of their employees, makes any warranty, express or implied, or assumes any legal liability or responsibility for the accuracy, completeness, or usefulness of any information, apparatus, product, or process disclosed, or represents that its use would not infringe privately owned rights. Reference herein to any specific commercial products, process, or service by trade name, trademark, manufacturer, or otherwise, does not necessarily constitute or imply its endorsement, recommendation, or favoring by the United States Government or the University of California. The views and opinions of authors expressed herein do not necessarily state or reflect those of the United States Government thereof, and shall not be used for advertising or product endorsement purposes.



FILTERING AND CLAMPING CIRCUITRY

Figure 4

MAGNETRON FILAMENT CONTROL
by
PAUL NOCELLA
SPERRY CORPORATION
SPERRY DIVISION (GYROSCOPE)
MARCUS AVENUE AT LAKEVILLE ROAD
GREAT NECK, NEW YORK 11020

Summary

This paper describes the analysis and design of a DC power supply that automatically provides the correct filament voltage for any operating beam current in a magnetron. Accurate filament control is necessary since this determines the cathode operating temperature, and ultimately the cathode life of the tube.

Methods are described for filament modeling, bifilar resistance compensation, average beam current sensing, feedback control, and tube/power supply protection circuits.

Three power supplies were built and tested. Two are in constant use at transmitter test fixtures for acceptance testing of incoming magnetrons. The third is used in our transmitter laboratory.

Introduction

Control of cathode temperature is achieved by a DC power supply that monitors average beam current and produces a filament voltage in accordance with a prescribed heater schedule. This schedule will result in optimum cathode life.

The need for maintaining accurate cathode temperature in a magnetron will now be reviewed. Note that the following applies generally to all cross-field devices.

In stand-by operation the heater must bring the cathode temperature above a minimum value that will insure a space-charge limited region that can allow magnetron oscillation without arcing and possible cathode damage when high voltage is applied.¹ This stand-by temperature must at the same time be kept below the value that would cause excessive evaporation of oxide material from the cathode during long hours of stand-by operation.

When the magnetron is oscillating the cathode receives additional power that is from 2 to 10 percent of the average beam power due to back-bombardment. Since back-bombardment power and heater power are thermally equivalent the overall effect is to increase cathode temperature and cause increased oxide evaporation. The only control available that will restore the cathode to its proper temperature is to lower heater power in proportion to the increase in average beam power. Normal magnetron operation requires that the cathode furnish a space-charge limited current density. If the temperature is reduced too far, the space-charge region will be depleted. This results in a higher incidence of mode-skipping, poor spectrum, arcing and possible cathode damage. Therefore, optimum tube life and performance

requires accurate filament control. The degree of accuracy required depends on cathode material and design.

The task of providing a curve of filament voltage versus beam power belongs to the tube manufacturer.² The heater schedule should also indicate the output load conditions on the magnetron since the characteristics of the load affect tube performance. Magnetron beam power depends mainly on beam current since its V-I curve is similar to a biased diode. Thus, it is convenient to present the heater schedule in the form of filament voltage versus average beam current. The tube manufacturer obtains this curve by adjusting the filament voltage to achieve a specified cathode temperature (measured by an optical pyrometer) at a selected average beam current. A typical heater schedule for the magnetron used in our system is shown in Figure 1. The solid line represents nominal

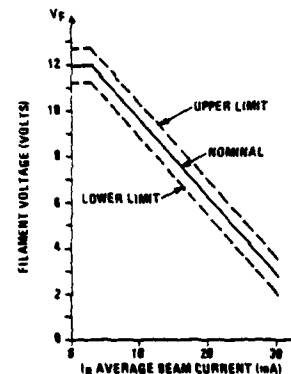


Figure 1. Magnetron Heater Schedule

values, and the dashed lines represent upper and lower tolerance limits of ± 0.75 volts. There are two regions in this curve. The first is a plateau section that keeps filament voltage constant at 12.0 volts from 0 to 2.96 mA of beam current. The second is a straight line segment with a slope of -0.3377 volts per mA and an intercept of 13.0 volts. This curve is described in equation form as:

V_F = voltage at filament terminals

I_B = average beam current

$$V_F = 12.0 \text{ volts} \pm 0.75 \text{ V} \quad 0 \leq I_B \leq 2.96 \text{ mA} \quad (1)$$

$$V_F = 13 - \frac{13}{38.5} I_B \quad 2.96 < I_B \leq 27.5 \text{ mA} \quad (2)$$

Compliance with the heater schedule must be at the magnetron filament terminals. Thus, verification requires floating a DC voltmeter since the filament is at a pulsed cathode voltage level of 20 to 25 KV. A floating measurement is necessary only during the design and validation phase.

Regulation, control and measurement of filament voltage is greatly simplified by choosing DC. Circuit implementation is straightforward and field maintenance is simple. The sections that follow describe the analysis and design of a DC supply that produces a filament voltage in accordance with Figure 1.

Design Considerations

The following areas were addressed in the design of this supply:

- Filament V-I modeling
- Bifilar resistance compensation
- Feedback control
- Beam current sensing
- Tube/supply protection
- Compliance with heater schedule
- Compatability with existing pulse tank package.

Power supply requirements that were met:

- Maintain filament voltage throughout a + or - 18% AC line input variation
- Provide accurate meter output indication of average beam current
- Provide a single field adjustment control to compensate for bifilar resistance and min/max filament tolerance
- Maintain low AC ripple output
- Provide filament voltage verification test points.

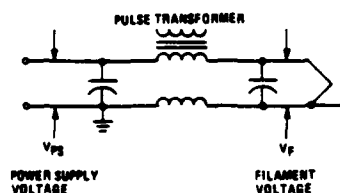


Figure 2. Filament Supply

Figure 2 shows the normal method of supplying filament voltage while simultaneously applying a cathode pulse of 20 to 25 KV through bifilar windings of a pulse transformer. This makes the task of complying with a heater schedule at the filament terminals difficult because of:

1. The bifilar winding resistance (R_B , 1.0 to 1.1 ohms cold, in our case) produces a considerable voltage drop.
2. The bifilar resistance increases due to the temperature rise of the pulse transformer during pulsed operation. (Up to 1.5 ohms in our case.)
3. The filament V-I curve in the region of operation cannot be interpreted as a single resistor.

An apparent solution to 1, 2 and 3 is to include the bifilar resistance inside a negative feedback loop. Feedback sensing would be at V_F , resulting in a highly stable filament voltage regardless of R_B or changes in filament V-I characteristics. However, direct feedback from V_F must provide 40 to 50 KV of isolation, remove the pulse voltage, and pass the DC filament voltage. Thus, direct feedback would be difficult to implement.

An alternate solution is to:

1. Mimic the characteristics of the bifilar winding and filament V-I curve. (i.e., set up a scaled circuit with a one-to-one correspondence between circuit elements and bifilar winding and filament model.)
2. Take feedback from the mimic circuit with the power supply feeding both mimic circuit and bifilar/filament in parallel.

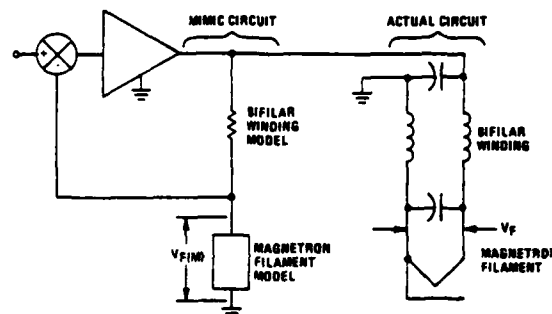


Figure 3. MIMIC Model

Refer to Figure 3. If scaling and modeling are done correctly, the voltage V_F at the filament will match $V_F(M)$, the voltage at the filament mimic model. The overwhelming advantage of this configuration is that no high voltage isolation is required, circuit simplicity is maintained, and all signals are directly referenced to ground.

Figure 4 is the functional block diagram of a complete filament power supply. The paragraphs that follow will describe the modeling, analysis and practical implementation of the design.

Filament Modeling

Eight magnetrons were used in the measurement of filament V-I characteristics. Data was taken with the magnetron beam power on and off over the filament range of 3 to 12 volts (standby). The beam on condition was done by operating at a selected beam

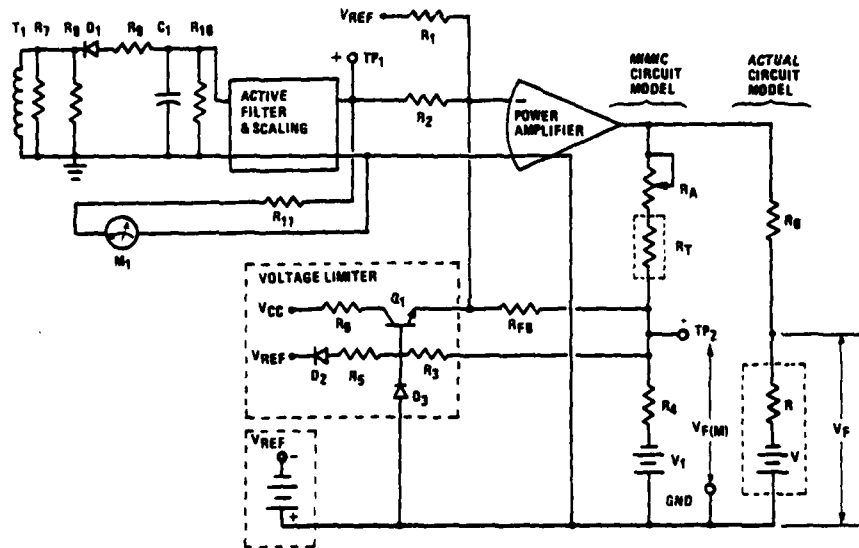


Figure 4. Power Supply Functional Diagram

current, measuring and adjusting for the correct filament voltage (V_F per Fig. 1) and recording filament current, I_F . The average is plotted in Figure 5.

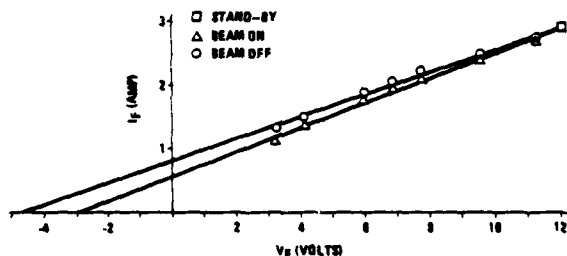


Figure 5. Filament V-I Curve

Three key items are immediately apparent.

1. Back-bombardment power also affects the filament V-I curve in this magnetron.
2. Over the operating range of 3 to 12 volts the data plot represents a good straight line.
3. The curve does not pass through the points $V_F = 0$, $I_F = 0$. This shows that an equivalent circuit cannot be only resistive.

A least-squares computer program was used to derive the intercept and slope of the best straight line fit to both sets of data. The result in equation form is:

$$I_F = 0.564 + 0.197 V_F \text{ (beam on)} \quad (3)$$

$$I_F = 0.808 + 0.177 V_F \text{ (beam off)} \quad (4)$$

These straight line equations may be interpreted in equivalent circuit form as a resistor in series with a voltage source. The slope of the straight line represents the reciprocal of the series resistor. The voltage source can be found by setting I_F to zero and solving for V_F .

Figure 6 shows the equivalent filament model. The equivalent circuit representing the "beam on" condition is used with the bifilar resistance model to make the mimic circuit.

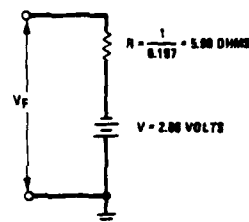


Figure 6. Filament Model

Bifilar Resistance Modeling

A single fixed resistor is not sufficient to model the bifilar winding resistance. Copper wire has a linear positive temperature coefficient of 0.393 percent per degree Celsius. A high winding resistance and a high temperature rise in the pulse transformer could cause an increased voltage drop which must be compensated in order to stay within heater schedule tolerance.

The pulse transformer in this discussion is contained in a small oil filled tank containing the pulse forming network and other components. The tank is a sealed unit and any temperature sensing must be done without internal additions or changes. Thus, any component used to sense and compensate for the resistance change with temperature must be mounted on the surface of the tank.

Temperature rise measurements of the bifilar winding and tank surface temperature (at the sensing component location) showed about a 2 to 1 ratio. Specifically, the surface temperature rise was about half the internal rise. Therefore, a network that has a linear temperature coefficient of twice that of copper is

required. This network, when mounted on the tank surface, will be used to track bifilar temperature changes.

The component selected for temperature compensation is a Texas Instruments "sensistor", a positive temperature coefficient silicon thermistor. Its coefficient of 0.7 percent per degree Celsius is so near the optimum value required that this component alone is all that is necessary for bifilar temperature compensation. Other coefficient values can be obtained by designing a suitable resistor-sensistor network.

The penalty for not being able to place a sensing element in direct contact with the pulse transformer is a time delay in complete temperature compensation. This is the result of the thermal time constant of the tank. The effect was measured and found not sufficient to cause an out-of-tolerance filament voltage. Implementation on other systems must be individually measured and analysed.

It is now possible to choose a resistance scale factor of 1:1000 between the bifilar filament and the mimic circuit. This value was selected because the bifilar resistance is 1.0 ohms at 25°C, and 1000 ohms at 250°C is a standard value sensistor. Furthermore, a 1.0K resistance level represents a good compromise between a high value that is susceptible to noise pick-up and a low value that is overly dissipative.

Feedback Control

Now that the mimic model components have been derived, we turn our efforts to circuit implementation. Equation 2 is the expression that must be followed for $I_B > 2.96$ mA. This straight line equation suggests the following:

- Convert the average beam current into a scaled voltage.
- Sum this scaled voltage (proportional to beam current) with a fixed stable reference at the summing junction of an operational amplifier.

By correctly choosing the scale factor and reference polarity, the op-amp output will be inversely proportional to beam current (V_{REF} negative, V_{TP1} positive). The plateau section of the heater schedule is produced by the active feedback limiter shown in Figure 4. Its action and design will be covered in subsequent paragraphs. Figure 4 shows the basic design whereby feedback is taken from the junction of the mimic components that represent the bifilar resistance and the filament. The voltage limiter resistor (R_3) and feedback resistor (R_{FB}) cause circuit loading so the output/input response of the circuit must be derived. The assumptions made are: The summing junction is at virtual ground; the voltage at the base of Q_1 is close to ground; and Q_1 is turned off ($I_B > 2.96$ mA). Only the necessary components for analysis are shown in Figure 7. By applying superposition it can be shown that the output response (V_{PS}) to each of the three inputs is:

$$\frac{V_{PS}}{V_{REF}} = - \left[\frac{R_{FB}}{R_1} + \frac{R_T'}{R_1} \left(1 + \frac{R_{FB}}{R_{TH}} \right) \right] \quad (5)$$

$$\frac{V_{PS}}{V_{TP1}} = - \left[\frac{R_{FB}}{R_2} + \frac{R_T'}{R_2} \left(1 + \frac{R_{FB}}{R_{TH}} \right) \right] \quad (6)$$

$$\frac{V_{PS}}{V_{TH}} = \frac{R_T'}{R_{TH}} \quad (7)$$

By selecting V_{REF} as a negative voltage and V_{TP1} as a positive voltage, the power supply output (V_{PS}) is found by combining equations (5), (6) and (7):

$$V_{PS} = V_{REF} \left[\frac{R_{FB}}{R_1} + \frac{R_T'}{R_1} \left(1 + \frac{R_{FB}}{R_{TH}} \right) \right] - V_{TP1} \left[\frac{R_{FB}}{R_2} + \frac{R_T'}{R_2} \left(1 + \frac{R_{FB}}{R_{TH}} \right) \right] + V_{TH} \frac{R_T'}{R_{TH}} \quad (8)$$

where V_{TH} is the Thevenin voltage at $V_F(M)$ produced by V_1 , R_3 and R_4 . R_{TH} is the parallel combination of R_3 and R_4 . R_T' is the series combination of the bifilar equivalent network (R_T) and a variable resistor (R_A) that allows a small adjustment range in output voltage. See appendix 1 for derivation of equations (5), (6), and (7).

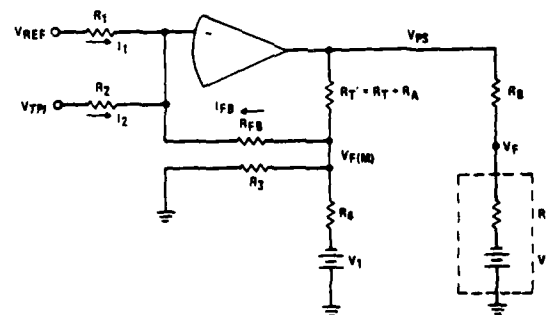


Figure 7. Feedback Design Model

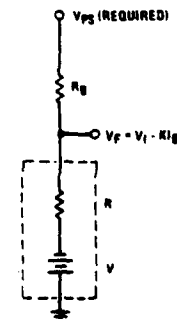


Figure 8. Bifilar and Filament Model

Based on knowing equation (2) must be satisfied at V_F , another expression can be derived that sets the requirements for V_{PS} .

$$\text{Let } V_F = 13 - \frac{13}{38.5} I_B = V_I - KI_B \quad (9)$$

so that V_I is the intercept voltage and K is the slope of the straight line. Equation (9) (the heater schedule) must be followed at the junction of the bifilar winding and the filament. Refer to Figure 8. By using superposition the power supply output (V_{PS}) required to follow equation (9) can be written as equation (10).

$$V_{PS} (\text{required}) = \frac{R_B + R}{R} (V_I - KI_B) + V \frac{R_B}{R} \quad (10)$$

Now coefficients may be equated and design values can be calculated.

(From (10)) (From (8))

$$V_I \frac{R_B}{R} = V_{REF} \left(1 + \frac{R_{FB}}{R_{TH}} \right) \frac{R_T'}{R_1} \quad (11)$$

$$KI_B \frac{R_B}{R} = V_{TP1} \frac{R_T'}{R_2} \left(1 + \frac{R_{FB}}{R_{TH}} \right) \quad (12)$$

$$V_I = V_{REF} \left(\frac{R_{FB}}{R_1} \right) \quad (13)$$

$$KI_B = V_{TP1} \frac{R_{FB}}{R_2} \quad (14)$$

$$V \frac{R_B}{R} = V_{TH} \frac{R_T'}{R_{TH}} \quad (15)$$

Multiplying and dividing the right-hand side of (15):

by $\frac{R_{FB}}{R_{TH} + R_{FB}}$, we have

$$V \frac{R_B}{R} = V_{TH} \frac{R_T'}{R_{TH}} = V_{TH} \frac{R_{FB}}{R_{TH} + R_{FB}} \frac{R_T'}{R_{TH} \frac{R_{FB}}{R_{TH} + R_{FB}}} \quad (16)$$

Thus, we now have the following design equations:

From (13)
$$V_I = V_{REF} \left(\frac{R_{FB}}{R_1} \right)$$

From (14)
$$KI_B = V_{TP1} \left(\frac{R_F}{R_2} \right)$$

From (16)
$$\frac{R_B}{R} = \frac{R_T'}{R_{TH} \frac{R_{FB}}{R_{TH} + R_{FB}}} \quad (17)$$

From (16)

$$V = V_{TH} \frac{R_{FB}}{R_{TH} + R_{FB}} \quad (18)$$

Voltage Feedback Limiter

The plateau section of the heater schedule is obtained by the action of the voltage limiter section shown in Figure 4. This circuit is used to independently set standby filament voltage, V_L ($I_B < 2.96$ mA). Q_1 starts conduction, and thus limiter operation, when the base voltage reaches the cutin value of 0.6 volts (V_{BE}) for a silicon transistor.³ Base voltage depends on V_{REF} , $V_{F(M)}$, and the values of R_3 , R_5 . Thus, the value at which limiting action begins can be set by V_{REF} and R_3 , R_5 . Filament mimic voltage ($V_{F(M)}$) becomes the controlled value. Actual filament voltage (V_F) is likewise controlled because of the correspondence between mimic and actual component values.

Diode D_3 protects the base-emitter junction of Q_1 from a high negative voltage. Diode D_2 is used to compensate for the temperature sensitivity of V_{BE} , and R_3 limits the current supplied to the summing junction. When Q_1 conducts, it supplies whatever current is required at the summing junction to keep $V_{F(M)}$ at the level set by V_{REF} , R_3 and R_5 . To simplify the analytical expression for the limiting voltage value, consider the equivalent input combination of V_{REF}/R_1 and V_{TP1}/R_2 to be an equivalent resistor R_{IN} and source V_{IN} .

Where
$$R_{IN} = \frac{R_1 R_2}{R_1 + R_2}$$

and
$$V_{IN} = R_{IN} \left(\frac{V_{TP1}}{R_2} + \frac{V_{REF}}{R_1} \right)$$

From Figure 4 it is possible to write by inspection:

$$V_{F(M)} = - \left(\frac{V_{IN}}{R_{IN}} R_{FB} + I_E R_{FB} \right) \quad (19)$$

I_E = emitter current of Q_1

$$I_E = \beta I_B \quad (20)$$

By solving for I_B and using equations (19) and (20) the voltage at the limit value is:

$$V_L = \frac{R_3}{R_3 + \beta R_{FB}} \left(- \frac{V_{IN}}{R_{IN}} R_{FB} \right) + V_{REF} \left(\frac{R_3}{R_5} \right) - \frac{R_3 V_D - R_3 V_{BE} - R_2 V_{BE}}{R_2} \quad (21)$$

where V_D is the voltage drop across D_2 . Equation (21) can be approximated to be:

$$V_L = V_{REF} \frac{R_3}{R_5} + V_{BE} \quad (22)$$

Hence, the plateau voltage can be set independently by proper choice of V_{REF} and the ratio R_3/R_5 . See appendix 2 for the derivation of V_L .

Beam Current Sensing

The function of converting beam current pulses into a low ripple, linear, scaled voltage at TP1 is performed by C1, D1, R9, R10, T1 and an active filter shown in Figure 4.

The purpose of each component is:

- T1 A current transformer with a one turn primary used around the two filament leads to measure beam current.
- D1 Used to pass only the negative output pulse from T1.
- R9 Limits peak diode current.
- C1 Bypass capacitor for AC component of pulse.
- R10 Equivalent input DC resistance of active filter. (See Figure 10 for schematic of active filter.)
- R7 Internal transformer shunt resistor. (Used to prevent high voltage across the secondary if external load is removed.)
- R8 External load. (Total external AC load on T1 is R8 in parallel with R9.)

The most important design consideration is the need for a linear voltage to beam current relationship. The equivalent input network is shown in Figure 9. A linear relationship among beam current, duty factor, and voltage across R10 is obtained by designing for a small DC voltage across R10. This is achieved by using a long charge time constant and a short discharge time constant. The small DC component of current flowing in Figure 9 must flow through R10. Referring to Figure 9, the peak diode current is:

$$I_D = \frac{V_{PK} - V_D}{R_9 + \frac{R_7 R_8}{R_7 + R_8}} \quad (23)$$

and the average DC current flowing through R10 is simply:

$$I_{AVG} = I_D \times D \quad (24)$$

D = pulse duty factor

R10 is made part of a conventional two pole low-pass active filter, shown in Figure 10. This configuration provides buffering and scaling to the next stage, as well as reducing the pulse repetition frequency (PRF) ripple at the output. Using the assumption of a virtual DC ground at the DC summing junction, it can be seen that I_{AVG} also must flow through R11. Therefore, the voltage at TP1 is:

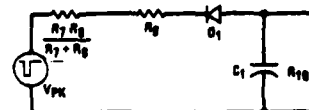
$$V_{TP1} = I_{AVG} R_{11} \quad (25)$$

I_{AVG} is related to I_B by:

$$I_{AVG} = \frac{\frac{I_B}{N} \frac{R_7 R_8}{R_7 + R_8} - V_D D}{R_9 + \frac{R_7 R_8}{R_7 + R_8}} \quad (26)$$

Hence, R11 can be selected for any scale factor desired. In this design 1 mA of average beam current will produce 0.1 volts at TP1. This convenient value also allows easy average beam current measurement with

a simple DC voltmeter at TP1.



$$V_{PK} = \frac{I_{PK} R_7 R_8}{N R_7 + R_8}$$

I_{PK} = PEAK BEAM CURRENT
 I_B = AVG BEAM CURRENT
 D = DUTY FACTOR
 $\tau_C = R_9 C_1$
 τ_C = CHARGE TIME CONSTANT
 $R_C = R_{10}$ IN PARALLEL WITH $R_9 + \frac{R_7 R_8}{R_7 + R_8}$
 $\tau_D = C_1 R_{10}$
 τ_D = DISCHARGE TIME CONSTANT

Figure 9. Diode Detector

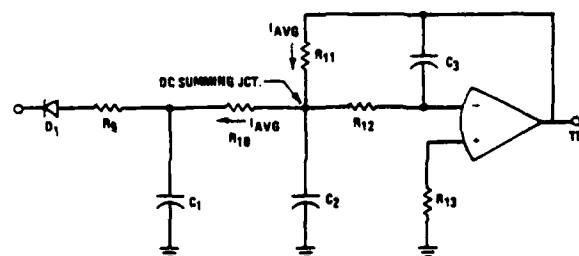


Figure 10. Active Filter

Tube/Supply Protection

The filament must be protected from high inrush currents at turn on and any over-voltage condition caused by a power supply failure. The power supply must be protected from any high amplitude short duration voltage spike arising from unbalance in the bifilar winding. Some unbalance is expected in normal operation, and the voltage spikes produced can upset normal DC feedback and regulation of the power supply if left unsuppressed.

Current Foldback Protection: Limiting the maximum output current is accomplished in this supply by a conventional foldback circuit. Its action is to allow normal output voltage up to a maximum specified current. Any attempt to draw more current (by lowering the load resistance) will cause the output voltage to decrease with a resultant decrease of output current. Figure 11 shows foldback action.

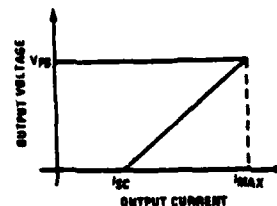


Figure 11. Foldback Current Limiting

The benefit of current foldback is reduced power dissipation in the output transistors under short circuit conditions. Power dissipation is limited to the product of unregulated supply voltage and short circuit current (I_{SC}). Short circuit current in this design was chosen to be 1/3 of the maximum limit value resulting in a 3 to 1 reduction in dissipation as compared to a simple current limit scheme. I_{SC} cannot be set too low. The inrush current will drive the supply into current foldback, and output voltage will fall.⁴ A stable point at a low filament voltage would occur unless I_{SC} supplies sufficient power to heat the filament and raise its resistance. Current foldback protects both the filament from high inrush currents and the power supply from short circuits. Power supply recovery from short circuits is immediate, no external reset is necessary.

A simple current foldback circuit is shown in Figure 12. Output current is sensed by resistor R_S . When in current limit, Q_1 diverts base current away from the pass transistor and thus reduces output current. Current limit (I_{MAX}) is reached when the base-emitter of Q_1 reaches the cutin value of 0.6 volts (V_{BE}). I_{MAX} should be selected from 1.3 to 1.5 times the maximum current requirement of the filament. This is necessary because regulation becomes degraded as I_{MAX} is approached. Under short circuit conditions the emitter of Q_1 becomes grounded and the voltage drop across R_S along with R_1 , R_2 determines the bias to Q_1 and the final foldback current I_{SC} .

Under short circuit conditions the voltage at the emitter of Q_1 is zero:

$$V_E = 0 \quad (27)$$

The open circuit voltage at the base (V_B) is:

$$V_B = \left(I_{SC} R_S \right) \frac{R_2}{R_1 + R_2} \quad (28)$$

by solving equation (27) and (28) for I_{SC} we have:

$$I_{SC} = \frac{V_{BE}}{R_S} \left(\frac{R_1 + R_2}{R_2} \right) \quad (29)$$

Under current limit conditions the voltage at the emitter of Q_1 is:

$$V_E = V_{PS} \quad (30)$$

(power supply output voltage) the open circuit voltage at the base of Q_1 is:

$$V_B = \left[V_{PS} + I_{MAX} R_S \right] \frac{R_2}{R_1 + R_2} \quad (31)$$

solving equation (30) and (31) for I_{MAX} we have:

$$I_{MAX} = \left(\frac{V_{BE}}{R_S} \frac{R_1 + R_2}{R_2} \right) + \frac{V_{PS}}{R_S} \frac{R_1}{R_2} \quad (32)$$

using equation (29) we can write equation (32) as:

$$I_{MAX} = I_{SC} + \frac{V_{PS}}{R_S} \frac{R_1}{R_2} \quad (33)$$

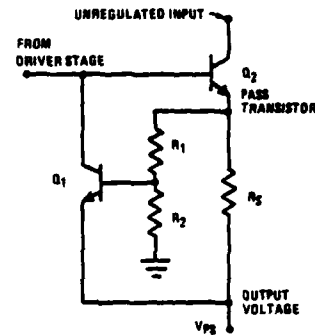


Figure 12. Overcurrent Protection

Overvoltage Protection: In the event of a short circuit between collector and emitter of the pass transistor, the filament would receive full unregulated voltage which could be twice the normal value. This will destroy the tube by rapidly evaporating oxide material from the cathode. Consequently, a circuit must be included that will monitor output voltage and eliminate overvoltage to the filament. If a false activation occurs, the circuit must automatically reset after a predetermined time.

A 555 integrated circuit⁵ is used for voltage monitoring and timing. When activated, the 555 turns on a transistor connected across the power supply output for a period of 10 seconds. If this is a false activation, the supply goes into foldback limiting. After 10 seconds, the transistor is turned off, the output voltage is monitored; and if it is less than the trip value, normal operation resumes. Otherwise, an actual pass transistor failure results in a fuse opening in the unregulated supply. A schematic is shown in Figure 13. The 555 is connected in a monostable mode. Quiescent conditions are: C_2 charged to V_{CC} ; pin 3 at V_{CC} ; Q_1 and Q_4 are off. The threshold for comparator #1 is set internally at 2/3 V_{CC} . Input above this value will reset the flip-flop; pin 3 will go low; Q_1 will turn on. C_2 will start to discharge through R_4 ; Q_4 will turn on and short the output. The input to comparator #1 is a fixed percentage of the output voltage determined by R_1 and R_2 . The overvoltage trip point (V_{OV}) can be expressed as:

$$V_{OV} = \frac{2}{3} V_{CC} \left(\frac{R_1 + R_2}{R_2} \right) \quad (34)$$

Capacitor C_2 continues to discharge until it reaches 1/3 V_{CC} , determined by the fixed internal trigger value of comparator #2. When the voltage across C_2 reaches 1/3 V_{CC} , the flip-flop is set, Q_1 and Q_4 turn off, and capacitor C_2 charges rapidly through D_1 . The time (τ) that Q_4 remains on is the time it takes for C_1 to go from V_{CC} to 1/3 V_{CC} and is approximately:

$$\tau = 1.1 R_4 C_2 \quad (35)$$

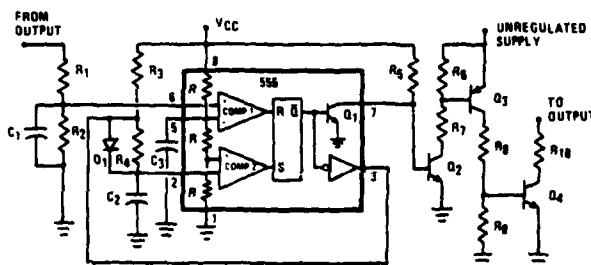


Figure 13. Overvoltage Protection

Additional Power Supply Protection: Other steps were taken to insure power supply survival. The first was to place a high value, high voltage capacitor directly across the power supply output terminals. This helps reduce any short duration high amplitude voltage spikes from upsetting the feedback loop. Across this capacitor is a General Semiconductor Industries "TransZorb". The breakdown of this transient voltage suppressor is selected to be higher than the over-voltage trip value. Its purpose is to limit the maximum voltage that can be allowed across the output terminals in the event of a high energy voltage spike. Finally a reverse biased diode is connected across the pass transistors, (cathode connected to unregulated input anode connected to power supply output). This prevents any possible reverse voltage from appearing across the pass transistors.

Compliance With Heater Schedule

The results of the previous sections can be used to determine component values. Some values are arbitrarily assigned and selection depends on design experience and component availability. The function of this supply is to satisfy equations (1) and (2) (a heater schedule) at the filament terminals of a tube. Listing the characteristics and requirements of the power supply/filament system, as shown below for our system, is the first step in achieving compliance.

- A) Bifilar resistance: $1.0 \text{ ohms at } 25^\circ\text{C},$
 $T_C + 0.393\%/^\circ\text{C}$
- B) Filament model: $R = 5.08 \text{ ohms}$
 $V = 2.86 \text{ volts}$
- C) Required scale factor at TP1:
 $V_{TP1} = 0.1 \text{ V/mA}$
- D) Current transformer turns ratio:
 $\frac{N_2}{N_1} = \frac{10}{1} = N$
- E) Heater Schedule: $V_F = 12.0 \text{ volts} \pm 0.75\text{V}$ (1)
For $0 \leq I_B \leq 2.96 \text{ mA}$
 $V_F = 13 - \frac{13}{38.5} I_B$ (2)
For $2.96 < I_B \leq 27.5 \text{ mA}$

- F) AC line input variation: $\pm 18\%$ from 115V
- G) External meter: $100 \mu\text{A}$ movement,
 1.33 K ohm meter resistance
- H) Adjustment range: Compensate up to 1.0 V
additional loss from power
supply to bifilar windings.

The equations in the feedback control and beam current sensing sections determine component values by matching required coefficients to circuit derived coefficients. An example will clarify the procedure:

Using requirement C and equation (14) at $I_B = 27.5 \text{ mA}$ we have:

$$V_{TP1} = 0.1 \frac{\text{V}}{\text{mA}} \times 27.5 \text{ mA} = 2.75 \text{ V}$$

$$K = \frac{13}{38.5} = 0.3377$$

(slope of heater schedule from equation (2))

Thus, from equation (14):

$$0.3377 \times 27.5 = 2.75 \frac{R_{FB}}{R_2}$$

R_{FB} can be arbitrarily chosen from standard values as 9.09 K ohms . Equation (14) is solved for R_2 , and equals 2.692 K ohms . This resistor can be the series combination of a standard value and a trimpot. Equations (13), (17), (18) are similarly used to compute R_1 , R_{TH} , V_{TH} . V_{REF} is arbitrary but should be selected from available temperature compensated values (6.2 V was used in this supply). R_T is made up of a sensistor (R_T) and a variable resistor (R_A). R_A allows a small adjustment in filament voltage. Equation (22) determines the plateau voltage and is used to meet requirement E, equation (1). If the active filter of figure 10 is used, then equations (25) and (26) can be used to find the DC feedback resistor, R_{11} . Short circuit and overvoltage protection can be implemented as shown in Figure 12 and 13 by using equations (29), (33), (34), (35).

Test Points and Metering: Two test points are used to determine the operation of the supply (TP1, TP2). The voltage at TP1 is proportional to average beam current. In this design the scale factor chosen is 0.1 V/mA . This value makes direct reading possible with a VOM (i.e. for average beam current equal to 20.0 mA the voltage at TP1 is 2.0 volts). A permanently installed microammeter is used in our system to monitor average beam current. As seen in Figure 4 TP1 is used to supply current to this meter. The full scale reading is $100 \mu\text{A}$. A suitable scale factor of $0.4 \text{ mA}/\mu\text{A}$ was chosen. Thus, at a meter reading of $60 \mu\text{A}$ the average beam current is $60 \mu\text{A} \times 0.4 \text{ mA}/\mu\text{A} = 24.0 \text{ mA}$, this corresponds to 2.40 volts at TP1. The total resistance necessary is $2.4 \text{ V}/60 \mu\text{A} = 40 \text{ K ohms}$. Since the meter resistance is 1.33 K ohms , an external 38.3 K ohm standard value resistor was selected. This meter is used to monitor average beam current without the need for an oscilloscope.

The voltage at TP2 is equal to the filament voltage. It can also be monitored with a $20,000 \text{ ohms/}$

volt VOM. This provides a convenient check of power supply operation and filament voltage monitoring.

A linear series-pass regulator design was chosen for the power amplifier section. The advantages are simple straightforward design, low EMI, elimination of thermal cycling in transistor junctions and high reliability. In order to meet the $\pm 18\%$ line variation requirement, while maintaining maximum output voltage and current without saturating the pass-transistor system, required an unregulated supply of almost twice the maximum output voltage. Efficiency was not a major concern for our application.

Conclusion

The design techniques discussed in this paper have been successfully implemented. Measurements taken with a floating DC voltmeter at the filament terminals indicate complete satisfaction of the heater schedule in Figure 1. This design has proven extremely useful in acceptance testing of magnetrons since it automatically supplies correct filament voltage for any beam current selected. Field use of this supply will increase tube life by continually supplying the optimum filament power for long cathode life over all conditions of line input voltage and beam current.

Appendix 1

Closed Loop DC Gain Of Power Amplifier Section

Refer to Figure 7. Replace R_3 , R_4 , V_1 with their Thevenin equivalent:

$$R_{TH} = \frac{R_3 R_4}{R_3 + R_4} \quad (A1.1)$$

$$V_{TH} = V_1 \frac{R_3}{R_3 + R_4} \quad (A1.2)$$

The power supply output voltage (V_{PS}) as a function of V_{REF} , V_{TP1} , V_{TH} and resistor elements will be derived. A virtual ground is assumed at the summing junction. Therefore, the sum of the currents at the summing junction must be zero:

$$I_1 + I_2 + I_{FB} = 0 \quad (A1.3)$$

$$I_{FB} = -(I_1 + I_2) \quad (A1.4)$$

$$I_1 = \frac{V_{REF}}{R_1} \quad (A1.5)$$

$$I_2 = \frac{V_{TP1}}{R_2} \quad (A1.6)$$

Superposition is used to find I_{FB} caused by V_{PS} and V_{TH} . (With V_{TH} set to zero.)

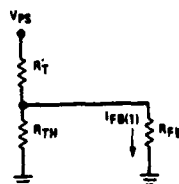


Figure A1.1.

$$I_{FB(1)} = \frac{V_{PS}}{R_{FB} R_{TH}} \frac{R_{TH}}{R_T' + \frac{R_{FB} R_{TH}}{R_{FB} + R_{TH}}} \quad (A1.7)$$

with V_{PS} set to zero.

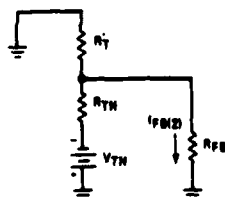


Figure A1.2.

$$I_{FB(2)} = - \frac{V_{TH}}{R_{TH} + \frac{R_{FB} R_T'}{R_{FB} + R_T'}} \frac{R_T'}{R_{FB} + R_T'} \quad (A1.8)$$

$$I_{FB} = I_{FB(1)} + I_{FB(2)} = -(I_1 + I_2) \quad (A1.9)$$

$$\left(\frac{V_{PS}}{R_T' + \frac{R_{FB} R_{TH}}{R_{FB} + R_{TH}}} \frac{R_{TH}}{R_{FB} + R_{TH}} \right) - \left(\frac{V_{TH}}{R_{TH} + \frac{R_{FB} R_T'}{R_{FB} + R_T'}} \frac{R_T'}{R_{FB} + R_T'} \right) = - \frac{V_{REF}}{R_1} - \frac{V_{TP1}}{R_2} \quad (A1.10)$$

$$\left(\frac{V_{PS}}{R_T' + \frac{R_{FB} R_{TH}}{R_{FB} + R_{TH}}} \frac{R_{TH}}{R_{FB} + R_{TH}} \right) - \left(\frac{V_{TH}}{R_{TH} + \frac{R_{FB} R_T'}{R_{FB} + R_T'}} \frac{R_T'}{R_{FB} + R_T'} \right) = - \frac{V_{REF}}{R_1} - \frac{V_{TP1}}{R_2} \quad (A1.11)$$

From (A1.11) the output due to V_{TH} ($V_{REF} = 0$, $V_{TP1} = 0$) is:

$$\frac{V_{PS}}{R_T' (R_{FB} + R_{TH}) + R_{FB} R_{TH}} R_{TH} = \quad (A1.12)$$

$$\frac{V_{TH}}{R_{TH} (R_{FB} + R_T') + R_{FB} R_T'} R_T' = \frac{V_{PS}}{V_{TH}} = \frac{R_T'}{R_{TH}} \quad (A1.13)$$

From (A1.11) the output due to V_{REF} ($V_{TH} = 0$, $V_{TP1} = 0$) is:

$$\frac{V_{PS}}{V_{REF}} = - \left[\frac{R_{FB}}{R_1} + \frac{R_T'}{R_1} \left(1 + \frac{R_{FB}}{R_{TH}} \right) \right] \quad (A1.14)$$

From (A1.11) the output due to V_{TP1} ($V_{REF} = 0$, $V_{TH} = 0$) is:

$$\frac{V_{PS}}{V_{TP1}} = - \left[\frac{R_{FB}}{R_2} + \frac{R_T'}{R_2} \left(1 + \frac{R_{FB}}{R_{TH}} \right) \right] \quad (A1.15)$$

Appendix 2

Feedback Voltage Limiter

Refer to Figure 4. Replace V_{REF}/R_1 and V_{TP1}/R_2 with:

$$R_{IN} = \frac{R_1 R_2}{R_1 + R_2} \quad \text{and} \quad (A2.1)$$

$$V_{IN} = R_{IN} \left(\frac{V_{TP1}}{R_2} + \frac{V_{REF}}{R_1} \right) \quad (A2.2)$$

The output voltage at $V_{F(M)}$ can be written by inspection:

$$V_{F(M)} = - \left(\frac{V_{IN}}{R_{IN}} R_{FB} + I_E R_{FB} \right) \quad (A2.3)$$

The following two approximations are used:

$$I_E \approx \beta I_B \quad (A2.4)$$

The summing junction is at virtual ground. I_B will be found and substituted in equation (A2.4) and (A2.3). Base current is calculated by solving for the Thevenin equivalent voltage and resistance presented to the base of Q1.

$$I_B = \frac{V_{TH} - V_{BE}}{R_{TH}} \quad (A2.5)$$

$$V_{TH} = \frac{V_{F(M)} + V_{REF} - V_D}{R_3 + R_5} R_5 + V_D - V_{REF} \quad (A2.6)$$

$$R_{TH} = \frac{R_3 R_5}{R_3 + R_5} \quad (A2.7)$$

Using (A2.7) and (A2.6) in equation (A2.5) gives:

$$I_B = \frac{\frac{V_{F(M)} + V_{REF} - V_D}{R_3 + R_5} R_5 + V_D - V_{REF} - V_{BE}}{\frac{R_3 R_5}{R_3 + R_5}} \quad (A2.8)$$

$$I_B = \frac{V_{F(M)}}{R_3} - \frac{V_{REF}}{R_5} + \frac{R_3 V_D - (R_3 + R_5) V_{BE}}{R_3 R_5} \quad (A2.9)$$

Using equations (2.4) and (2.3):

$$V_{F(M)} = - \frac{R_{FB}}{R_{IN}} V_{IN} - R_{FB} \beta \left[\frac{V_{F(M)}}{R_3} - \frac{V_{REF}}{R_5} + \frac{R_3 V_D - R_3 V_{BE} - R_5 V_{BE}}{R_3 R_5} \right] \quad (A2.10)$$

$$V_{F(M)} = \frac{R_3}{R_3 + \beta R_{FB}} \left(- \frac{R_{FB}}{R_{IN}} V_{IN} \right) + \frac{R_3}{R_3 + \beta R_{FB}} \beta \frac{R_{FB}}{R_5} V_{REF} - \frac{R_3}{R_3 + \beta R_{FB}} \beta R_{FB} \frac{R_3 V_D - R_3 V_{BE} - R_5 V_{BE}}{R_3 R_5} \quad (A2.11)$$

For β large and $V_D = V_{BE}$ (A2.11) becomes:

$$V_{F(M)} = V_{REF} \frac{R_3}{R_5} + V_{BE} \quad (A2.12)$$

Thus, $V_{F(M)}$ will have a maximum value given by (A2.12).

References

1. Collins, George B., Editor, "Microwave Magnetrons", MIT Rad. Lab. series, Vol. 6, McGraw-Hill, New York, 1948.
2. Ewell, George W., "Radar Transmitters", McGraw-Hill, New York, 1981.
3. Tobey, G.E., Graeme, J.G., Huelsman, L.P., "Operational Amplifiers", McGraw-Hill, New York, 1971.
4. Pressman, A.I., "Switching and Linear Power Supply, Power Converter Design", Hayden Book Company, New Jersey, 1977.
5. "Motorola Linear Integrated Circuits Data Book", Motorola Inc., Phoenix, Arizona, 1979.

Notice

This design has been proposed to the U.S. Navy for use in a FCS program. This does not imply approval, recommendation or support of magnetron filament control by the U.S. Navy in its programs.

A 95 GHz GRIDDED EIO TRANSMITTER WITH NANOSECOND PULSE WIDTHS

J. Bajda, S. Brody
Norden Systems, Inc., United Technologies Corporation
Norwalk, CT

Summary

This paper describes the requirements, design approach, and test results for a 95 GHz transmitter, using a Varian VKB2445T1 gridded Extended Interaction Oscillator (EIO). The transmitter is being developed for an airborne radar system application. To minimize RF losses, the EIO with its associated pulse circuitry will be mounted on a scanning antenna/microwave assembly.

A modulator, using a single planar triode driving a pulse transformer, has been designed, built, and integrated with the EIO. Clamp circuitry maintains grid pulse top flatness to minimize intrapulse and interpulse amplitude and frequency variations of the EIO RF output. The modulator provides the EIO with a 3kV grid pulse from a floating deck at a cathode potential of -20kV. Operation of the EIO at RF output pulses continuously adjustable from 10 nsec to 400 nsec at PRFs to 10 KHz and a peak output power of 1.4 kW at 95.0 GHz has been achieved. RF leading and trailing edge transition times were 4 nsec and 10 nsec respectively. No significant frequency spectrum degradation was observed for EIO RF output pulses of 80 nsec and 400 nsec. With a typical frequency sensitivity of 60 KHz/volt for the EIO cathode to body voltage, data is shown indicating the feasibility and limits for producing a frequency excursion of 60 MHz at 60 Hz rate by modulating the power supply providing this voltage.

Introduction

Table 1 summarizes requirements for the 95 GHz transmitter. The gridded EIO provides a peak output power in excess of 0.8 kW at a duty cycle of 0.005 over a mechanical tuning range from 93 GHz to 96 GHz. Peak output power at 95.0 GHz is 1.4 kW at a cathode voltage of -20.0 kV and a beam current of 0.64 amperes. An electronic tuning range of 200 MHz about 95.0 GHz can be obtained by varying the cathode voltage from -17.0 kV to -20.0 kV. Peak output power drops with a reduction of the cathode voltage from the maximum power point at -20.0 kV.

Table 1.

Frequency	95.0 ± 0.3 GHz
Output Power	1000 W minimum
Pulse Width	80 and 400 nsec
PRF	7.5 KHz
Spectrum Main Lobe Width	<1.1 (2/pulse width)
Spectrum First Sidelobe	-10 dB maximum
Frequency Agility	40 MHz minimum
Volume	60 Hz rate
Weight	130 cu. in. <10 lbs.

The EIO generates RF output when its aperture grid is pulsed from a -3 kV bias voltage (relative to cathode voltage) to cathode voltage. The leading edge of the EIO RF output is delayed relative to the leading edge of the grid pulse. The EIO generates RF output for approximately the top 40% of the trailing edge voltage excursion of the grid pulse. Although difficult to instrument accurately, observations on the trailing edge of the EIO RF output indicated appreciable frequency departure from the frequency corresponding to the flat top of the grid pulse. Grid capacitance is 25 pF.

Figure 1 shows a photograph of the antenna mounted assembly consisting of the gridded EIO, grid modulator, and cathode high voltage pulse components. Approximately half of the allocated 130 cubic inches is occupied by the EIO and the fan cooling the EIO collector. Weight of the assembly is 8 pounds. Voltages to the EIO and grid modulator are provided by a power supply assembly located off the antenna platform.

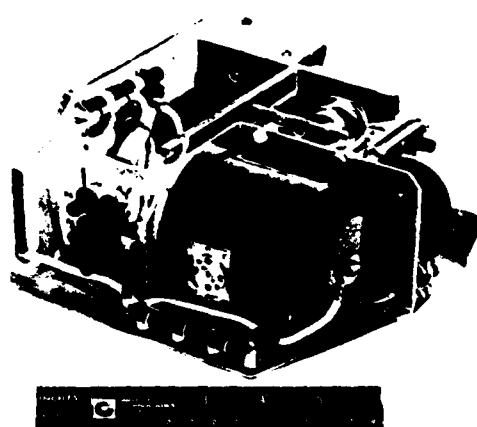


Figure 1. 95 GHz Gridded EIO Transmitter/Modulator

95 GHz Transmitter Design Approach

Presented in Figure 2 are details of the chosen design approach in order to meet the requirements listed in Table 1. High voltage, nanosecond pulses with a pulse amplitude of 3.0 kV are generated by gating the grid of an EIMAC 8940 triode V1 from a cutoff voltage of -100 volts to a grid drive voltage of +50 volts. Pulse width of the triode grid pulse determines EIO RF output pulse width. Grid pulses to the triode are provided by a simple FET drive circuit. Pulse transformer T1, having a 1:1 turns ratio, provides high voltage isolation, inverts, and couples the 3.0 kV pulse onto the floating deck at cathode

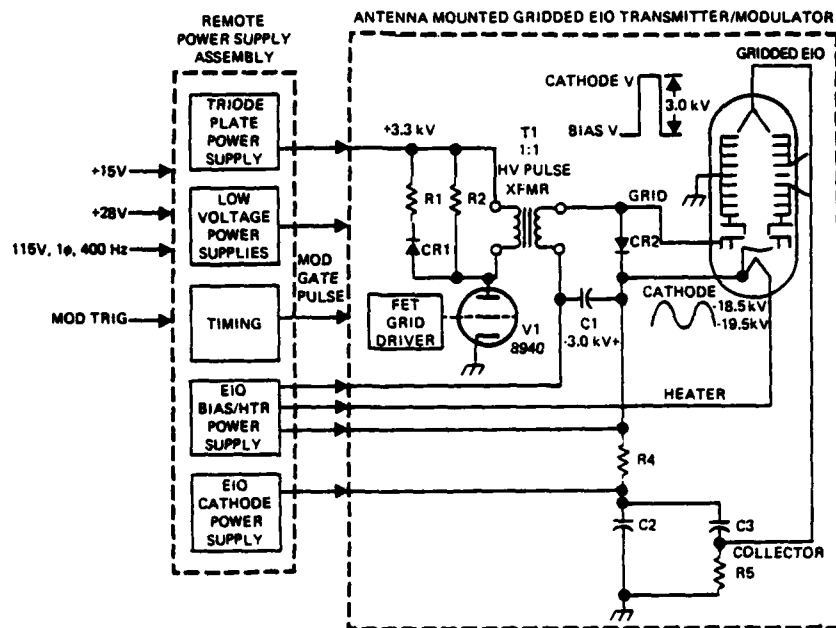


Figure 2. Gridded EIO Transmitter Design Approach

potential. During the interpulse period, -3 kV bias is provided to the EIO grid through the secondary winding of pulse transformer T1. High speed diode clamp CR2 shapes the natural oscillatory response introduced by the pulse transformer leakage inductance and the parallel combination of pulse transformer winding capacitance and EIO grid capacitance. Resistor R2 enhances grid pulse trailing edge transition time so as to obtain an acceptable trailing edge transition time on the EIO RF output without excessive power dissipation. Backswing voltage is limited by the series combination of diode CR1 and resistor R1.

The remote power supply assembly provides the EIO with cathode, grid bias, and heater voltages and the triode with plate voltage via a high voltage cable assembly. In addition, miscellaneous low voltages and a variable width modulator gate pulse are supplied to the grid modulator circuitry. The output of the EIO cathode power supply is capable of generating a voltage excursion of 1000 volts peak-to-peak at a 60 Hz rate when supplied with a low voltage programming input.

Beam current for the EIO is supplied by pulse capacitors C2 and C3. Capacitor C2 supplies body current and capacitor C3 supplies collector current with isolation provided by resistor R5. With a ratio of approximately 10 to 1 for collector to body current, voltage droop on the cathode-to-body voltage is reduced without the necessity of an increased value for cathode energy storage capacitance. Resistor R5 minimizes peak current and absorbs energy in case of an EIO arc or a breakdown in insulation of a component floating at cathode potential.

Grid Modulator Design

The effects of leakage inductance in the high voltage pulse transformer and stray capacitance in the high voltage pulse transformer and EIO grid are minimized in the design approach presented in Figure 2. A discussion of circuit parameters affecting the front edge, top of pulse, and trailing edge response of the grid modulator output pulse follows. (Ref. 1,2).

Figure 3 shows a simplified equivalent circuit of the parameters affecting the front edge response of the pulse. Parameters affecting the front edge response are triode plate resistance R_p , pulse transformer leakage inductance L_L , and the parallel capacitor combination C of pulse transformer winding capacitance and EIO grid capacitance. Presented in Figure 4 is a set of curves showing the output voltage versus oscillation period T of the circuit for different damping factors k where

$$L = 2\pi\sqrt{L_L C} \quad (1)$$

$$\text{and} \quad k = R_p / 2\sqrt{C/L_L} \quad (2)$$

Low damping factors k result in faster transitions to the steady state output voltage but with a more significant oscillation about this voltage. Clamping the output with diode CR2 results in an output pulse with a flat top when pulse amplitude reaches bias voltage. A fast leading edge transition is obtained for a circuit with low damping factor k . As can be seen by examining equation (2), higher values of pulse transformer leakage inductance (inherent in a transformer insulated to withstand 26 kV) result in a

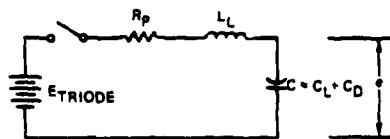


Figure 3. Simplified Circuit for Front Edge of Pulse Response

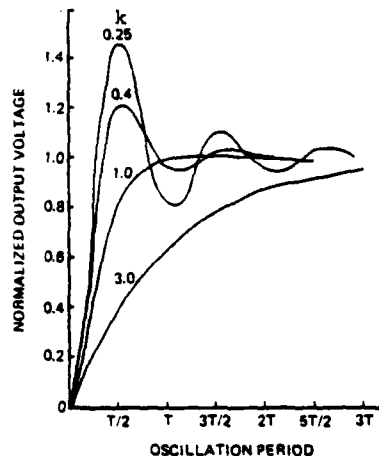


Figure 4. Front Edge of Pulse Response

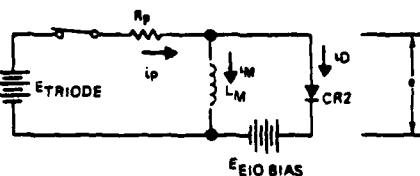


Figure 5. Simplified Circuit for Top of Pulse Response

lower damping factor k . Quicker transitions to the clamping voltage result.

Figure 5 shows a simplified equivalent circuit of the parameters affecting the top of the pulse performance. Triode plate voltage is set higher than EIO grid bias voltage so as to forward bias diode CR2. Triode plate current provides pulse transformer magnetizing current and forward bias current to diode CR2. A pulse with a flat top appears across the input of the pulse transformer. The modulator output is clamped to cathode voltage. Pulse amplitude is determined by EIO grid bias voltage. With the triode operated in the linear region, fluctuations in the triode plate voltage due to line, load, and ripple variations are attenuated by the divider action of the triode plate resistance R_p and the low resistance of forward biased diode CR2, shunting the output.

With approximate values of 200 ohms for the triode plate resistance, 20 μH for the pulse transformer leakage inductance, and 35 pF for total stray capacitance, unclamped oscillation period T and damping factor k are 170 nsec and 0.13 respectively for the modulator design of Figure 2 with EIO grid load. Clamping of the grid pulse occurs after a leading edge transition time of 40 nsec. This is consistent with information shown in Figure 4. Circuits with low damping factors k rise to a normalized output voltage of 1.0 in a quarter of the oscillation period T .

Figure 6 shows a simplified equivalent circuit of the parameters affecting the trailing edge response of the pulse. Discharge of the stray capacitance C occurs through the parallel combination of pulse transformer pulse inductance L_e (at the end of pulse) and resistor R_2 . Suitable EIO RF fall times were obtained with resistor R_2 dissipating 15 watts.

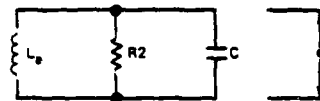


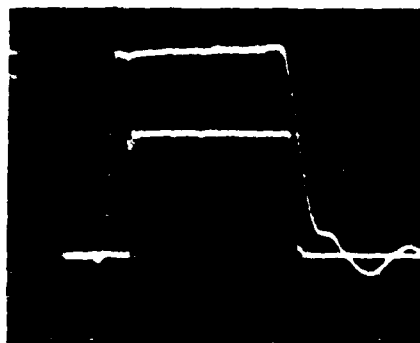
Figure 6. Simplified Circuit for Trailing Edge of Pulse Response

EIO Transmitter/Modulator Test Results

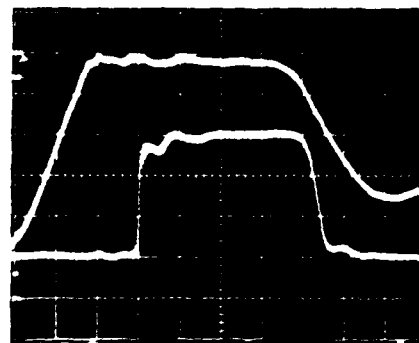
Presented in Figure 7 are photographs of the EIO grid-to-body voltage and the resulting detected RF output pulse at pulse widths of 80 nsec and 400 nsec for the modulator design of Figure 2. A slight tilt is discernible on the EIO grid-to-body voltage at the wide pulse width due to discharge of the cathode-to-body energy storage capacitor. The leading edge of the EIO RF output exhibits a 20 nsec delay after the grid has been clamped to cathode potential. RF leading edge transition time is less than 4 nsec. Leading edge jitter, inherent in the EIO, is on the order of 2 nsec peak-to-peak at a fixed cathode voltage. RF trailing edge transition time for the narrow pulse width is 10 nsec. EIO RF output pulses as narrow as 10 nsec were obtained by reducing the width of the grid pulse to the 8940 triode.

Spectrum measurements, using the setup of Figure 8, were conducted by mixing a sample of the EIO RF output pulse with the CW RF output from a mechanically tuneable oscillator. The tuneable oscillator was set so as to obtain a beat frequency in the order of 50 MHz at the output of the balanced mixer. The spectrum was displayed on a HP 8565A spectrum analyzer.

As shown in Figure 9, no significant degradation in main lobe width or sidelobe level was measured for the EIO RF output at pulse widths of 80 nsec and 400 nsec. Main lobe width was $2/(\text{pulse width})$ for both pulse widths. Maximum sidelobe level (first sidelobe) was 12 dB below the peak of the main lobe for the



HORIZONTAL = 100 NSEC/DIV



HORIZONTAL = 20 NSEC/DIV

UPPER TRACE: GRID PULSE VOLTAGE = 3.0 kV

LOWER TRACE: DETECTED RF PULSE

Figure 7. EIO Grid-to-Body Voltage and Detected RF Pulses

Frequency Agility Modulation Voltage

As shown in Figure 10, cathode power supply modulation is implemented by introducing a low level modulation input at the voltage reference port of the voltage error amplifier. A sine wave modulation input of 180 mV peak-to-peak at a 60 Hz rate results in an output voltage excursion of 1000 volts peak-to-peak with no significant distortion. Due to bandwidth limitations in the power supply, the output modulation lags the input by 25 degrees.

The EIO exhibits increasing RF leading edge delay as the cathode voltage approaches the value resulting in maximum output power. To minimize RF leading edge delay variation with frequency agility, the cathode voltage excursion of 1000 volts peak-to-peak is centered at a nominal voltage of -19.0 kV. A cathode voltage excursion from -18.5 kV to -19.5 kV produces a frequency excursion of 60 MHz, an output power variation of 1.3 dB, and an RF leading edge jitter of 9 nsec on the EIO RF output. Radar system requirements can tolerate this level of jitter in the frequency agile mode of operation.

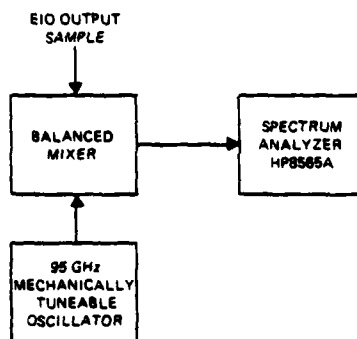


Figure 8. 95 GHz Pulsed RF Spectrum Measurement Setup

400 nsec pulse. Maximum sidelobe level (first sidelobe) was 11 dB below the peak of the main lobe for the 80 nsec pulse.

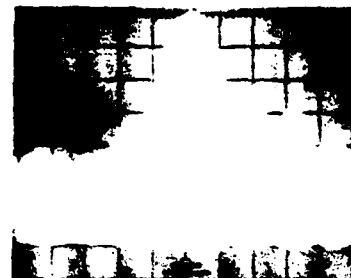


PULSE WIDTH = 400 NSEC

PRF = 8 kHz

VERTICAL = 5 dB/DIV

HORIZONTAL = 5 MHz/DIV



PULSE WIDTH = 80 NSEC

PRF = 8 kHz

VERTICAL = 5 dB/DIV

HORIZONTAL = 10 MHz/DIV

Figure 9. Gridded EIO RF Spectrum

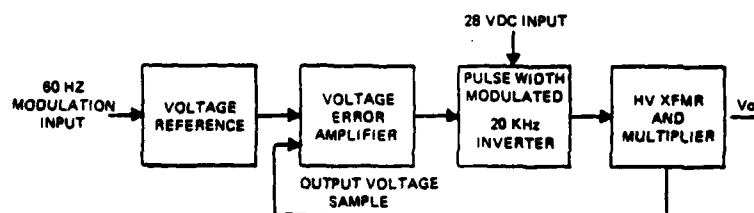


Figure 10. Cathode Power Supply Modulation

Conclusion

Simple circuit techniques have been utilized to design a modulator resulting in successful operation of a 95 GHz gridded EIO with nanosecond RF pulse widths. Pulsed RF spectrums of nanosecond pulses approaching a $\sin x/x$ shape have been measured. The limited size and weight of the EIO/modulator combination make it suitable for mounting on a scanning antenna platform. Sine wave voltage excursions of

1000 volts peak-to-peak at a 60 Hz rate have been obtained by supplying the EIO cathode power supply with a low voltage programming input at the same rate.

References

1. Reuben Lee, *Electronic Transformers and Circuits*, 1947, pp. 222-230.
2. George E. Ewell, *Radar Transmitters* 1981, pp. 144-150.

Impact of Electron Guns on Modulators for High Frequency, Mobile Platform Radar Systems

Bernard Smith
US Army Electronics Technology & Devices Laboratory (ERADCOM)
Fort Monmouth, NJ 07703

ABSTRACT

Modern millimeter wave radar and ECM systems require high power output pulses with rise times of the order of nanoseconds, thus imposing severe performance and size constraints on the modulator for mobile platform application. To meet these fast rise times at frequencies below I/J band various gridded gun designs are used. But for frequencies above I/J band high μ gun design using conventional gridded guns becomes difficult if not impossible. For high frequency, low voltage modulators, fast rise time applications, gridded gun designs can be achieved using a method in which the intercepting grid sets directly on the cathode surface supported by an insulator between the focus grid and the control grid. This method is called the bonded or integrated grid cathode technique.

The bonded grid cathode approach, because it operates at cathode temperature and also effectively shields a significant portion of the cathode area, places severe operating constraints on the cathode. The nature of these constraints and how they affect gridded gun design will be discussed. The advantages of the bonded grid gun design concept and various approaches to achieve a bonded grid electron gun is presented. The design of a bonded grid gun for a 95 GHz EIA is presented and the effect of the optimum grid design on modulator power requirements, size and weight are also presented. The factors that determine the optimum grid design such as grid-cathode interface, output power and cathode current density will also be discussed.

Introduction

Electronic counter measure (ECM) and advance surveillance and target acquisition radars for military system require high power output pulses with rise times of the order of nanoseconds. Rise times of the above magnitude impose severe performance requirements on both the modulator and the amplifier tube. To add to the modulator and tube designer's problems in many of these application such as mobile platform system there exist size and weight constraints which must be met. With state-of-the-art voltage modulation capabilities, fast risetimes are achieved in linear beam amplifiers by designing electron guns

with one or more grids. While the inclusion of these grids in electron guns have made the modulator design easier they have increased the design complexity of the tube, its overall cost due to reduced production yields and their susceptibility to damage (vs modulation by cathode pulsing) in system application.

Fabrication of high μ gridded guns at frequencies up to I/J band has become fairly routine. For frequencies above I/J band production fabrication of high μ guns is very difficult because of the small grid sizes and the tight tolerance required. At I/J band or above very few production tubes are fabricated with a shadow gridded gun because of the difficulty in building these guns at frequencies above ten GHz and maintaining the tight tolerances required for good beam optics.

Therefore at frequencies above I/J band if the μ required by the modulator to meet the size and weight constraint of mobile platform systems such as RPV's and tank radar systems are to be met conventional grid structures such as shadow grids are no longer adequate.

Since these guns will be used at millimeter wave frequencies in high power linear beam tubes they must not only be self-spacing but they must have a reasonably high μ to reduce the modulator voltage required for pulsed applications. To achieve the required μ these gridded guns must have a small enough mesh and grid size in addition to a smaller cathode to grid spacing. This would enable substantial reduction of the required grid voltage swings and attainment of the nanosecond switching speeds required for these system. In the proper design of these gridded gun structures a compromise between the best tube performance (beam optics) and modulator requirement must be made. When the proper choice of grid cell dimensions and grid sizes, as well as cathode grid spacings are made significant savings in modulator power requirement and therefore modulator size and weight can be made. Design consideration in the selection of the optimum choice of gridded gun will be discussed along with the impact of the cathode on the optimum bonded grid gun design. Modulators power requirements for state-of-the-art 95 GHz EIA will be compared to the modulator power requirements for a bonded grid EIA.

Design Consideration

The 95 GHz Extended Interaction Amplifier¹ (EIA) developed by Varion Canada is a cathode pulsed linear beam device. The relevant tube design specifications are given in table 1. The energy W required by the modulator to charge the cathode capacity is defined by the following equation:

$$W = \frac{1}{2} C V_p^2$$

where

W = Energy required to charge the cathode capacity

C = capacitance of device

V_p = pulse voltage

The energy required to charge the tube capacity after substituting the value in table 1 is 2.16×10^{-3} joules. At a pulse repetition rate of 2.5×10^5 PPS the power required from the modulator is 540 watts. Since the tube is only delivering power for only 2.6 kV of the 12 kV modulating pulse it is this 2.6 kV which must be covered in the specified rise time. Assuming a constant current source the current required by the modulator is given by:

$$I = \frac{C V_p}{t}$$

where

V = voltage

t = risetime

C = capacitance of EIA

substituting the values for C , V and t from table 1 into the equation we get a current of $I = 3.9A$ required from the modulator. Comparing these with the power requirements of the tube to produce RF power which is 126 watts and 0.6A it is apparent that approximately four times as much power is needed to switch the tube as is needed to actually produce RF power. The modulator must also be capable of delivering seven times as much current as the tube needs.

For mobile platform systems there is a size and weight constraint on the modulator of 2 Kg or less and a volume of 400 cm³. To achieve these size and weight constraints and meet the fast switching requirements of these tubes for high frequency applications is beyond the present state-of-the-art of modulator design. Looking at equation 1 the obvious solution is either to significantly reduce the charging capacitance which is difficult or reduce the switching voltage requirements which can be done if a gridded gun is used rather than a cathode pulsed gun. Fabrication of gridded guns at 95 GHz is extremely difficult because of the critical spacings and tolerance constraints. Because of the above constraints and the desire to make the gun a low

voltage non-intercepting gridded gun, approaches such as the modulating anode, center post control and negative grid approach are eliminated because they can not meet the criterias cited above. Shown in figure 1 is a set of four gridded gun approaches which could be considered. As previously stated the cathode control gun shown in figure 1 a requires a very high pulse voltage. The modified focus electrode control gun has a very low μ and requires pulse voltage of 3.0 kV or higher to modulate the beam in an EIA. The negative grid gun shown in figure 1-c is power limited, difficult to build and was primarily used in older gun designs. The shadow grid gun in figure 1-d is mechanically complex, difficult to align and space to the tolerances required at 95 GHz. For the above reason, all of the above guns would not be considered as viable candidates for the 95 GHz EIA.

Shown in figure II are three other types of gridded guns which I will discuss the merits of. The unigrid shown in figure II-a is a modified version of the shadow grid gun and is very difficult to fabricate at 95 GHz due to the required tight tolerances. Negative gridded guns shown in figure II-b may meet the requirements of beam control. Application of this gun at 95 GHz is considered marginal. The bonded or integrated grid gun shown in figure II-c is a metal-insulator metal grid which is mounted directly on the cathode surface. The major advantage of this design approach is that close tolerances required in grid to cathode spacing for electron guns at 95 GHz are easily obtained and maintained at cathode operating temperature. The bonded grid structure allows control of the beam current in the electron gun using a lower control voltage than the cathode to anode voltage. Therefore on the basis of the above the obvious choice of gridded gun for the 95 GHz EIA is a bonded grid gun.

Cathode Consideration

Because the bonded grid operates at or near cathode temperature the choice of cathode is critical to the development of bonded grid guns. In high power tubes at 95 GHz to achieve the desired output power a minimum beam current is specified. The beam current for the 95 GHz EIA is 0.5A. Based on this current loading and taken into account the design frequency and the screening factor of the grid a minimum current density of $8/cm^2$ is required. Because of the cathode screening factor and the cathode area chosen the convergence ratio of the bonded grid gun will be higher than for a cathode pulse gun to achieve the same beam current. At the current density cited the number of cathodes capable of delivering $3/cm^2$ at reasonable operating temperatures for long life is limited. Selection of the cathode is based on the ability of the cathode to deliver $3/cm^2$, space charge limited, at as low an operating temperature and sublimation rate as possible. The grid material selected must, (1) have high thermal and mechanical stability, (2) not adversely affect the emission characteristics of the cathode at elevated temperatures and (3) have very poor adherence for the evaporants evolved from the cathode. Pyrolytic boron nitride as the grid

insulator material, meets all of the above criteria. The importance of the above properties for the grid material can be seen from the following. For bonded grid cathodes operating temperature of 1000° C or higher grid currents occur due to, (1) bulk conductivity, (2) surface conductivity and (3) grid emission. At bias voltage the emission from the above sources can be described by the following equation⁽³⁾

$$J = A T^2 e^{-\phi/KT} + J_R$$

where

J = current density in A/cm²

A = constant = 120 A/cm² /°K

T = absolute temperature

ϕ = work function in eV

K = Boltzman's constant

J_R = leakage current

The total grid current for bonded grid guns to date have been on the order of several milliamp which is well within acceptable limits for gridded linear beam devices.

To minimize the effects of grid emission the grids are fabricated with a boron nitride coating. This coating acts as an emission suppressant since it has a very low sticking coefficient for Ba-BaO which is evolved from the cathode at operating temperatures. Figure 3 is a picture of a bonded grid cathode gun structure which was fabricated for ERADCOM. The gun shown was built for a C-band linear beam tube. The basic gun which is being developed for millimeter wave device is similar to the one shown in figure 1 but much more difficult to build because of the tight tolerances critical, spacings, and smaller grid cells to achieve low cut-off voltages.

Performance of Bonded Grid Gun

Development of a bonded grid electron gun is now in process under an ERADCOM contract. Preliminary design of the bonded grid electron gun indicates that the modulator voltage required to pulse the 95 GHz EIA is 500 volts. Using equation 1 and substituting 500 volts as the voltage required to pulse the tube we see that the power required by the modulator to switch the tube is 1.36 watts as compared to 540 watts in the cathode pulsed tube. The current required is less than 0.7A which is very close to the current requirements of the tube to deliver RF power. Shown in figure 4 is the grid transfer characteristics for a C-band bonded grid gun as compared to a standard gun. As can be seen the beam transmission from the bonded grid gun is significantly better than it is for the standard gun for this tube which used a unigrid. It is

anticipated that the performance achieved for the C-band tube can be achieved at 95 GHz in an EIA.

Conclusion

It has been shown that because in bonded grid guns the grid operates at cathode temperature proper choice of cathode is essential to minimize grid emission. Because of the high current requirement for high power linear beam devices a compromise must be made between cathode operating temperature, sublimation rate and the desired current density. State-of-the-art bonded grid gun used a M-cathode. For 95 GHz development of the cathode to be used in the EIA is being done on an ERADCOM contract.

By selecting a bonded gridded gun over other conventional gun types it has been shown that significant reduction in the modulator power requirements can be achieved. This reduction should make it easier for the modulator power supply engineer to design a package which will be compatible with the requirements of mobile platform systems especially at frequencies in the millimeter wave region.

References

1. Viant, M., "95 GHz Extended Interaction Amplifier A Development Program", ERADCOM Contract, DAAB07-78-C-0948, January 1981.
2. Smythe, William R. "Static and Dynamic Electricity", McGraw Hill (1950).
3. Ladd, D.S. and Butterworth, J.C. "Design Criteria For Compact Nanosecond Modulation for EIO's and EIA's", ERADCOM Contract No. DAA629-76-D-0100 Order No. 1458 (October 1980).
4. Miran, G. "Bonded Grid Technology For Convergent Guns", ERADCOM Contract No DAAB07-76-C-1379F (November 79).
5. Gewartowski, J.W. and Watson, H.A., "Principles of Electron Tubes", Van Nostrand, Inc. (1955).
6. Miran, G. and Viant, M. "Bonded Grid Electron Gun For 95 GHz EIA", ERADCOM Contract No DAAK20-81-C-0430.
7. Feinleib, M. "High Current Density Cathode for Microwave/Millimeter Wave Tubes", ERADCOM Contract DAAB07-81-C-0421.

Table I: Design Specifications of 95 GHz EIA.

BEAM VOLTAGE	21.0 KV
PULSE VOLTAGE	12.0 KV
BEAM CURRENT	0.6 A
CATHODE CAPACITY	15 PF
VOLTAGE CHANGE BETWEEN ZERO FULL RF POWER	2.5 KV
PULSE LENGTH	50 Ns
MAXIMUM RISE AND FALL TIMES	10 Ns
PULSE REPTION RATE	2.5×10^3 /sec
DUTY	0.01
FREQUENCY	95 GHz

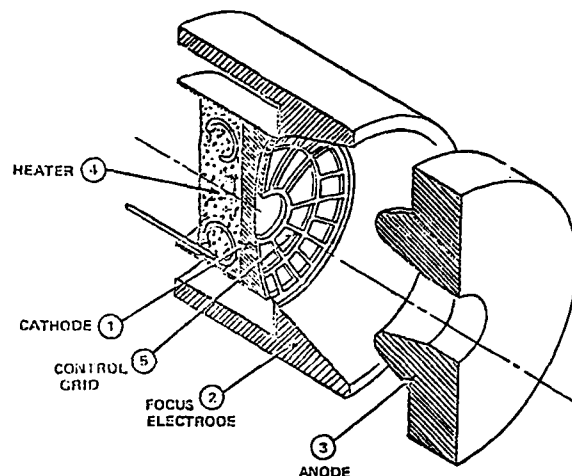


Figure 3: C-Band Bonded Grid Gun.

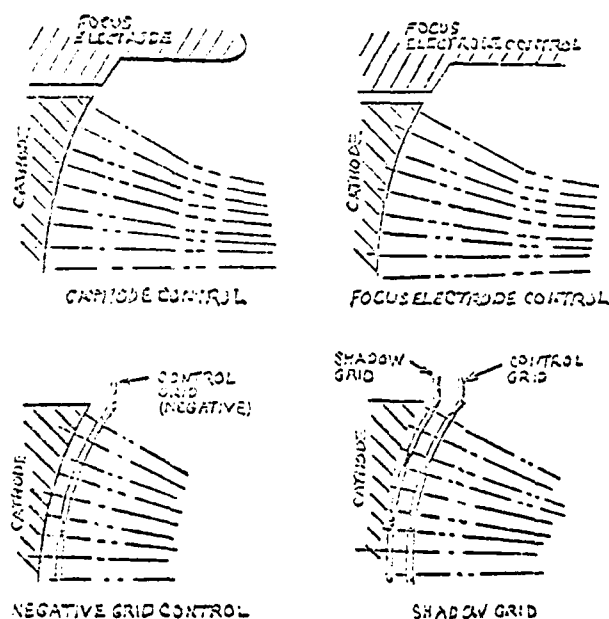


Figure 2: Gridded Electron Gun Designs.

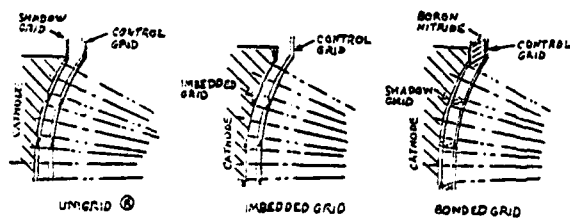


Figure 2: Gridded Electron Gun Designs.

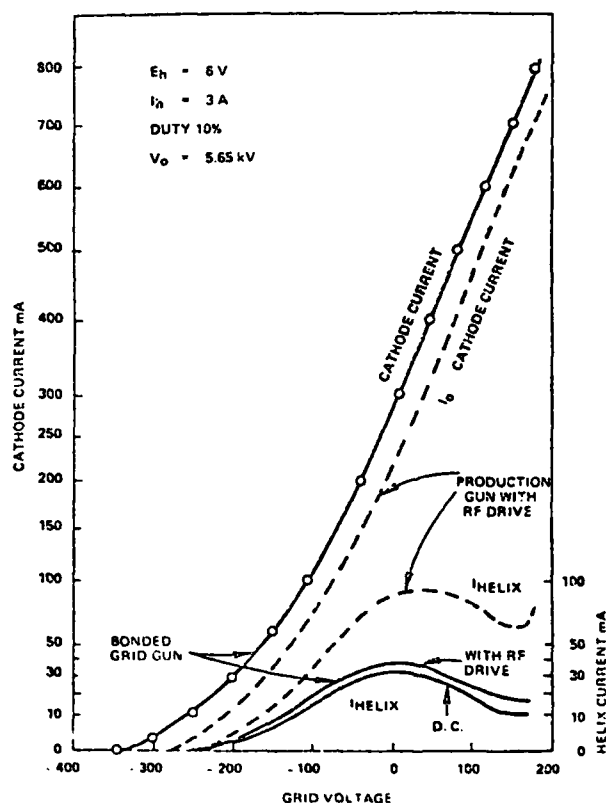


Figure 4: Grid Transfer Characteristics of a C-Band Bonded Grid Gun.

GRIDDED TRAVELING-WAVE TUBE MODULATOR TRADEOFFS

A. S. Zinkin, R. S. Boiles, R. F. McClanahan, and R. D. Washburn

Hughes Aircraft Company - Radar Systems Group

El Segundo, California

Abstract

This paper identifies three basic types of grid modulator circuits which can be used with gridded traveling-wave tube amplifiers in radar transmitters. Each modulator type has advantages and disadvantages, depending upon system requirements. The tradeoffs involved in the selection of a modulator are discussed, considering such factors as pulse repetition frequency and pulse width ranges, circuit reliability, power dissipation, and component count.

Introduction

In most modern airborne radar systems, the transmitter unit is based on a gridded traveling-wave tube (GTWT) which amplifies a microwave signal through interaction of the microwave field with a high-power electron beam. Figure 1 is a simplified block diagram of a GTWT transmitter. A high-voltage power supply is connected to the cathode and collector of the GTWT, providing power for the electron beam; the cathode voltage can be in the range from -5 kVDC to -100 kVDC depending on the particular GTWT. The electron beam (and thus the amplifier) is switched on and off at the radar pulse repetition frequency (PRF) by pulsing the GTWT grid. A positive grid-to-cathode voltage turns the amplifier on, while a negative voltage is required to turn the amplifier off; both the "on" and "cutoff" voltages can be in the range from 50 volts to 1000 volts.

The design of a grid modulator circuit for a radar transmitter is driven by several factors:

1. The modulator output circuitry must be referenced to the GTWT cathode voltage, which requires some means of low-voltage to high-voltage coupling.
2. GTWT performance is extremely sensitive to variations in the grid "on" voltage, which requires an accurate grid pulse amplitude (typically $\pm 2\%$) and very low grid ripple. For this reason, the transmitter generally includes two well-regulated low-ripple power supplies for the grid "on" and "cutoff" voltages, with the modulator providing a means for switching the GTWT grid between these voltages.
3. A modern pulse-doppler radar system seldom operates at a single fixed PRF and pulse width. In a multimode system, it is not uncommon to find a three-decade PRF range and a two-decade pulse width range.
4. Pulse rise and fall times must be kept to a minimum, since the GTWT RF circuit can be damaged by overheating if the transition times are excessive.

A large variety of modulator circuits have been designed with the above considerations in mind. Recent development work at Hughes Aircraft Company has concentrated on three basic types: the "floating deck"

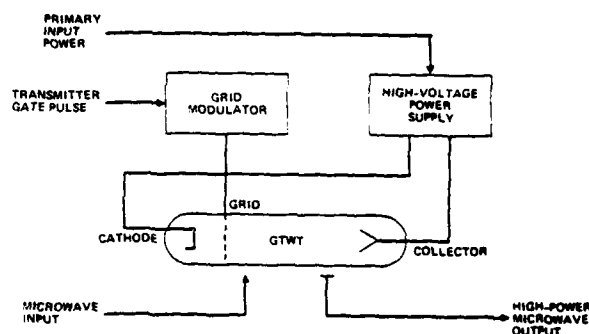


Figure 1. GTWT Transmitter Block Diagram

modulator, the pulse-transformer-coupled modulator, and the RF-transformer-coupled modulator.

Floating Deck Modulator

Figure 2 is a block diagram of a floating deck grid modulator, so named because it includes an active-circuit deck which "floats" at the GTWT cathode voltage. A logic-level transmitter gate pulse is first conditioned at ground potential, and is then coupled through some device which provides high-voltage isolation to two driver circuits, each of which controls a transistor switch. These transistors connect the GTWT grid alternately to a grid "on" ($B+$) or "cutoff" ($B-$) power supply.

The high-voltage coupling device is generally either a low-power pulse transformer or a fiber-optic link. Use of a transformer establishes an upper pulse width limit, and requires a tradeoff between pulse width and rise time. For this reason, the fiber-optic link is preferred for new designs; the maximum pulse width is unlimited, and the grid rise time is limited only by the switching speeds of semiconductor devices. The main drawback to the use of fiber-optics is the need for extra amplification on the output of the optical detector, resulting in a higher component count on the high-voltage deck.

Selection of the output switching transistors in a floating deck modulator requires careful consideration. The voltage seen by these devices is equal to the total GTWT grid voltage swing, which can exceed 600 volts for a high-power tube. Until recently, bipolar transistors were routinely chosen over field-effect transistors (FETs) for this application due to

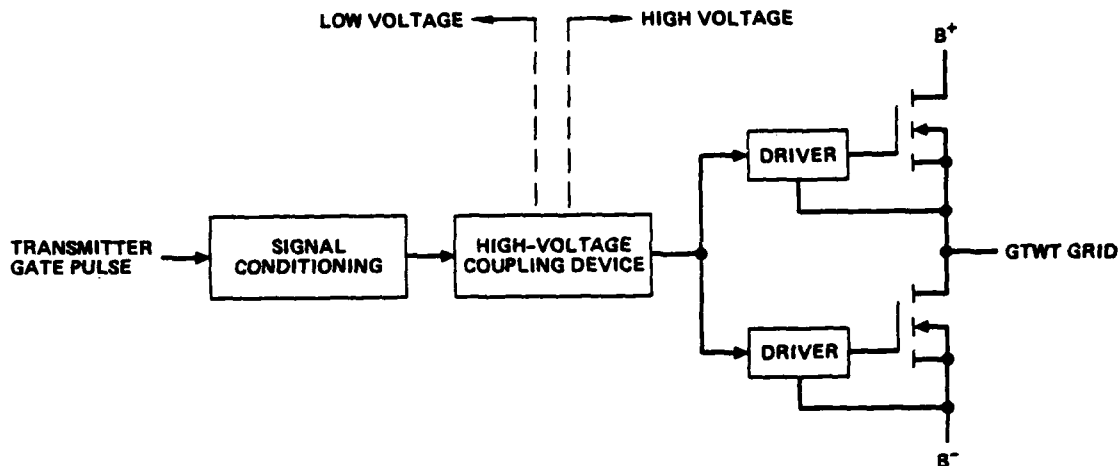


Figure 2. Floating Deck Grid Modulator

the higher voltage ratings of the bipolars. The availability of high-voltage metal-oxide-semiconductor FETs (MOSFETs) has eliminated the bipolar's voltage advantage; further, since MOSFETs are voltage-controlled devices, they will in general require less drive circuitry than a bipolar transistor. Some applications require voltage swings which exceed the capability of either transistor type, in which case it is necessary to cascade two or more devices to form each output switch.

The current-carrying capability of the output transistors also needs to be considered. The steady-state GTWT grid current is not a problem; grid current is generally about ten percent of the total GTWT beam current for a conventional grid, and is less than five milliamperes for the nonintercepting "shadow" grids used in most high-power tubes, so the steady-state transistor current is normally less than 100 milliamperes. However, the capacitive load being switched by each transistor (consisting of the GTWT grid-to-cathode capacitance plus the output capacitance of the opposite transistor) results in large surge currents, especially when the rise and fall times are very fast. For example, with a typical grid capacitance of 100 picofarads, a MOSFET output capacitance of 400 picofarads, a total grid voltage swing of 600 volts, and a transition time of 50 nanoseconds, the charging current can be approximated ($C \text{ times } dV/dt$) as 6 amperes. The initial turn-on surge current can be many times larger than this simple approximation, and must be suitably limited. For bipolar devices it is usually necessary to include a resistor in series with each switch; MOSFETs do not require this resistor due to their inherent current-limiting characteristic.

Pulse-Transformer-Coupled Modulator

Figure 3 is a block diagram of a pulse-transformer-coupled grid modulator. Unlike the floating deck modulator, which has most of its power amplification at high-voltage potential, the pulse-transformer-coupled modulator performs power amplification at ground potential and then uses a high-voltage power transformer for the low-voltage to high-voltage interface. A logic-level transmitter gate pulse is

connected to a driver circuit which controls a transistor switch (Q1). Q1 is held on during the gate pulse, thus coupling a high-power pulse through the transformer. The transformer output pulse is shaped by a passive network and is then clamped to the grid "on" ($B+$) power supply.

At the end of the gate pulse, a second transistor (Q2) is pulsed on to drive the transformer in the opposite polarity. This provides the falling edge of the grid pulse and resets the transformer's magnetic flux which prevents transformer saturation. A third transistor (Q3) is turned on whenever Q1 and Q2 are both off, so as to damp out any residual energy left in the transformer and thereby prevent interpulse ringing on the GTWT grid. Figure 4 illustrates a typical set of waveforms for a pulse-transformer-coupled grid modulator.

Some care must be taken when designing the transformer reset circuit. A fixed-width reset pulse is easy to generate and is thus very desirable, and can be used in low-duty-factor applications. We have successfully used this technique in a modulator with a maximum duty factor of 0.07 and a 20:1 pulse width range; the reset pulse width was fixed at the minimum grid pulse width. In most applications, however, it is necessary to vary the width of the reset pulse as a function of the grid pulse width. The ratio between these pulse widths, and therefore the modulator's maximum duty factor, is fixed by the need to maintain equal volts-seconds products on the two transformer primary windings. If both primaries are connected to the same input voltage (the normal case, as illustrated in Figure 3), and if the primaries have an equal number of turns, the reset and grid pulse widths will be equal and the maximum duty factor will be 0.50. Higher duty factors can be obtained by using two different power supplies or different turns ratios.

The pulse-transformer-coupled modulator also has limitations on minimum and maximum pulse width. Transistor switching speeds and the transformer rise time determine the minimum pulse width; with MOSFET switches a minimum pulse width of 400-500 nanoseconds can be realized. The maximum obtainable pulse width depends upon the rise and fall times needed, since wide-pulse

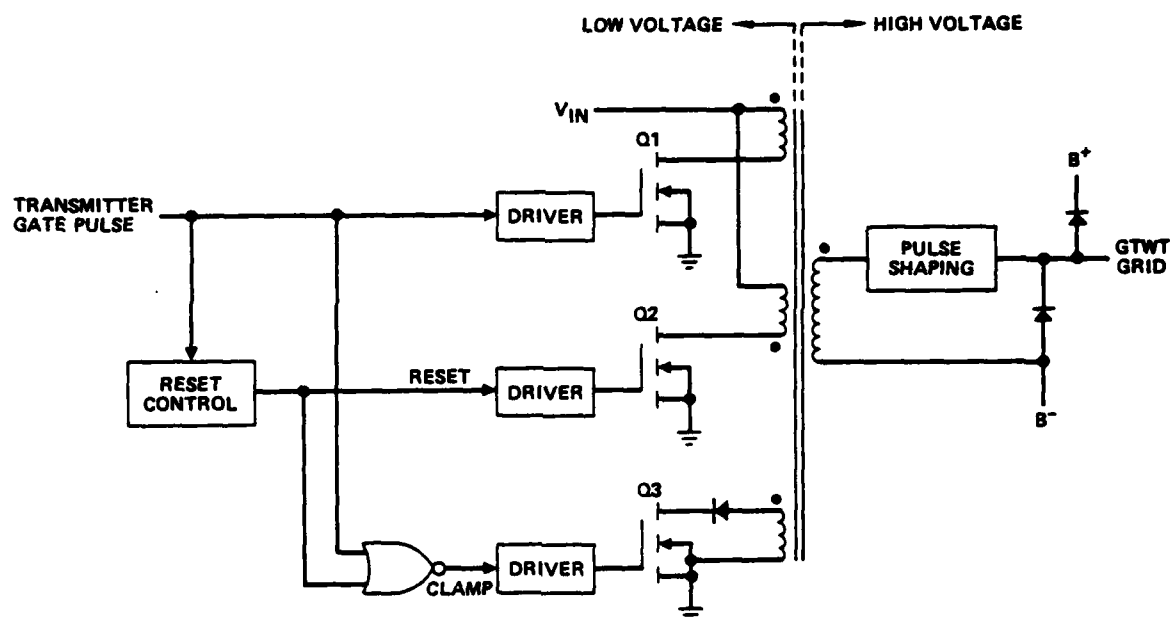


Figure 3. Pulse-Transformer-Coupled Grid Modulator

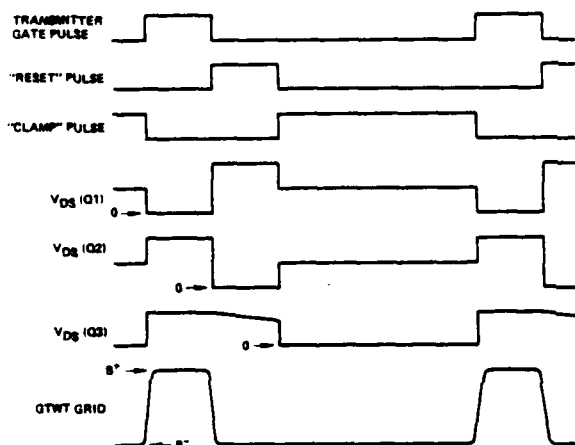


Figure 4. Pulse-Transformer-Coupled Modulator Waveforms

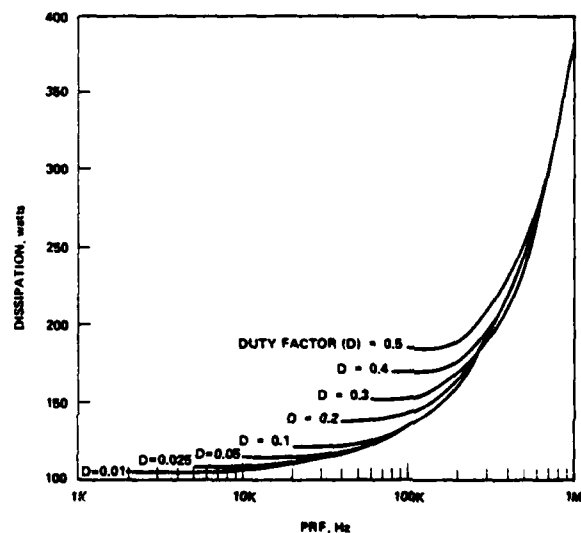


Figure 5. Typical Measured Power Dissipation for a Pulse-Transformer-Coupled Modulator

capability and fast rise time impose conflicting requirements on the design of the transformer. Rise and fall times of approximately 0.3 percent of the maximum pulse width are obtainable.

Power dissipation of a pulse-transformer-coupled modulator can be very large at high PRFs and duty factors. Switching losses in the transistor switches and output clamp circuit are proportional to the PRF; additional losses in the output circuit during the reset pulse are an exponential function of duty factor. Figure 5 shows the total power dissipation for a typical pulse-transformer-coupled modulator; this particular circuit was designed for high PRF and high-duty-factor operation, with a 500-volt grid swing and 50 nanosecond rise and fall times.

RF-Transformer-Coupled Modulator

Figure 6 is a block diagram of an RF-transformer-coupled grid modulator. A logic-level transmitter gate pulse is used to amplitude-modulate a 100 megahertz RF source. The resulting signal is amplified and then applied to a high-voltage isolation transformer (T1). In order to assure maximum RF power transfer, a passive impedance-matching network is connected to the transformer secondary. The output of the matching network is envelope-detected and is then clamped to either the grid "on" (B+) or "cutoff" (B-) power supply. A small filter removes ripple components at the carrier frequency and its harmonics. A bleeder resistor (R1) provides a steady-state path for cutoff bias.

The envelope detector is normally a full-wave bridge. Selection of the rectifiers for this bridge is critical to modulator performance. As previously noted, the typical GTWT grid voltage swing is several hundred volts; the rectifiers in the envelope detector must be rated at the full grid-swing voltage. Additionally, in order to obtain a good rectification efficiency at the high RF operating frequency, it is

necessary to use diodes with very fast forward and reverse recovery times (t_{fr} and t_{rr}) and with minimal junction (and package) capacitance. At the present time, single discrete diodes meeting all of the above requirements are not available. It is therefore necessary to use a number of Schottky or ion-implanted low-voltage rectifiers connected in series. It may also prove possible to use "synchronous rectification" techniques (where the rectifiers are replaced by synchronously-switched MOSFETs) in the envelope detector.

The response of the envelope detector alone yields unacceptable rise and fall times for nearly all applications; the rise time is limited by the load (grid-to-cathode) capacitance and the available RF input power, while the fall time is determined by the load capacitance and the bleeder resistance. In order to correct this problem, two "edge circuits" are added to the modulator to rapidly charge and discharge the load capacitance by means of relatively narrow pulses generated at the leading and trailing edges of the transmitter gate pulse. These edge pulses are coupled through transformers T2 and T3 to form the leading and trailing edges of the GTWT grid pulse. Due to the small pulse width for the edge transformers, grid pulse rise and fall times as small as 20 nanoseconds can be achieved.

Unlike the pulse-transformer-coupled modulator discussed earlier, the RF-transformer-coupled modulator has no significant resistive losses; power transfer is done reactively, and most of the dissipation is associated with the RF power amplifier and switching losses in the envelope detector. Another advantage of this reactive power transfer is the half-sinewave edges which are produced, which results in minimal far-out noise in the RF output spectrum.

This type of modulator does not have a maximum pulse width; the minimum pulse width is limited by the speed of the edge circuits, and is of the order of 250 nanoseconds. A comparable time period must be allowed between pulses, which results in a moderate duty cycle

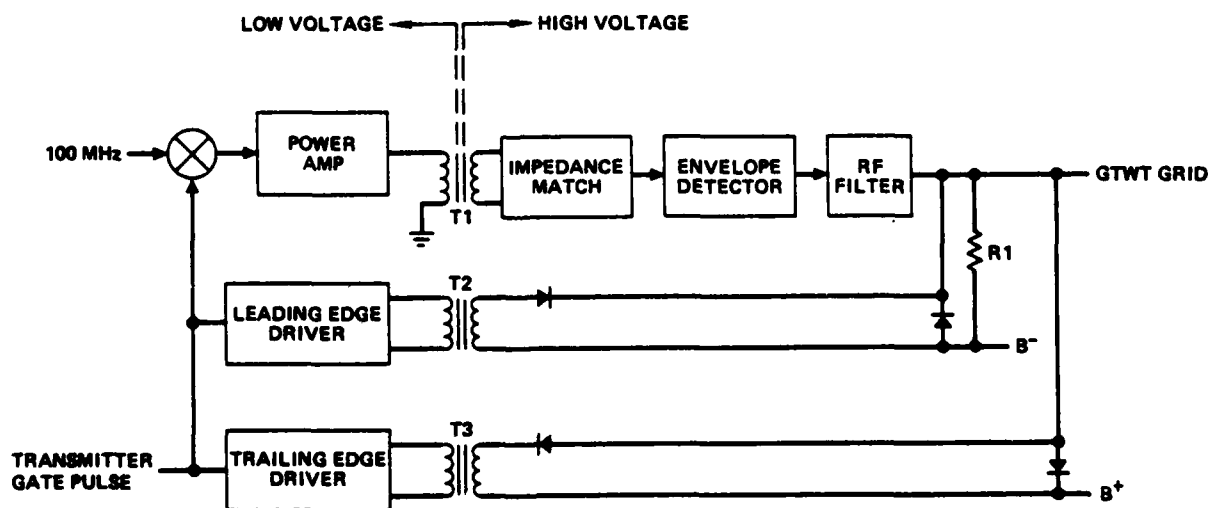


Figure 6. RF-Transformer-Coupled Grid Modulator

limitation at extremely high PRFs. We have successfully achieved a duty factor of 0.50 at a PRF of 2.25 megahertz with our present brassboard modulator.

Grid Bias Power Supplies

All three modulator types discussed in this paper require two grid bias ($B+$ and $B-$) power supplies, referenced to the GTWT cathode. As explained above, the grid bias supplies must be well regulated with minimal output ripple. Two basic types of power supply circuits can be employed, each using a transformer for power coupling and high-voltage isolation. The difference between these two approaches is in the location of the voltage regulator circuit.

In the first approach, an unregulated AC power form is connected to the transformer input; this input signal can be either a low-frequency (60 or 400 Hertz) sinusoidal power source, or a square wave generated by a switching-type power converter. Two transformer output signals are rectified and filtered, and then connected to a pair of active regulator circuits which generate the grid $B+$ and $B-$ voltages. This approach yields extremely accurate regulation ($\pm 0.5\%$ or better) but has two drawbacks: a number of active components must be "floated" at the high-voltage potential, and any grid-voltage adjustment must be done at high voltage.

Since most applications do not require this degree of regulation ($\pm 2\%$ is usually adequate), it is possible to locate the regulator circuit at low voltage in order to solve the problems stated above. This method is illustrated in Figure 7. A DC input power source is connected to a voltage regulator, whose output is connected to a DC-to-AC switching power converter. The converter drives a high-voltage isolation transformer, and the transformer's output signals are rectified and filtered to generate the grid "on" ($B+$) and "cutoff" ($B-$) voltages.

When a pulse-transformer-coupled modulator is used, the modulator switch bias voltage (V_{IN} on Figure 3) is often generated by adding a low-voltage secondary winding to the grid bias transformer. When the grid $B+$ voltage is decreased, the pulse transformer voltage swing is decreased by a corresponding amount; this results in less power dissipation in the grid clamp circuit at low grid voltages.

The values of the grid voltage bleeder resistors ($R1$ and $R2$ in Figure 7) depend upon the capacitance in the filter and upon the type of modulator used. A floating deck modulator does not have a clamped-type output and thus does not force current back into the bias supplies; in this case, $R1$ and $R2$ are selected at a nominal value to prevent peak-charging of the fil-

ters. The other two modulators, however, can force a significant amount of current into the bias supply output filters. This requires a relatively large bleed current through $R1$ and $R2$, and a correspondingly high power dissipation.

Modulator Comparisons

Table 1 presents a quantitative comparison of the three types of grid modulators discussed in this paper. Although most of the tabulated limitations could be exceeded under special conditions, we feel that the table represents the performance attainable in practical applications. For comparison purposes, we have used optical coupling in the floating deck modulator, and a pulse-transformer-coupled modulator designed for a 0.50 maximum duty factor.

It is difficult to define absolute mode limitations for the pulse-transformer-coupled modulator. If a relatively narrow pulse width range can be tolerated, it is possible to operate this type of circuit at PRFs up to one megahertz. However, with a pulse width range of a decade or more, it is necessary to limit the maximum PRF to a few hundred kilohertz to avoid an excessively large and complex pulse transformer. Also note that, although a 50 nanosecond rise time is readily achievable with this modulator, the maximum pulse width is approximately 300 times the rise time, or 15 microseconds; a wider pulse width will require a corresponding degradation in rise time.

The total component count in a modulator circuit is of interest since it is representative of the volume and weight required. The table also indicates the number of components which must be located at high-voltage potential, since these parts require special packaging techniques. Transient energy from arcs or other high-voltage phenomena can cause damage to these circuits, and in the case of the floating deck modulator can also cause noise-susceptibility problems. Although the floating deck modulator has a lower total component count than the other two types, this advantage is generally negated by the high-voltage component count.

The three modulators have different input power requirements. Those power forms referenced to ground are not a significant problem, because a typical radar transmitter includes a large variety of low-voltage power forms. The pulse-transformer-coupled modulator requires a significant amount of power from its transformer bias supply (V_{IN} on Figure 3), but as discussed above, this source can be added to the grid bias power supply. Power supplies referenced to a high-voltage potential are not difficult to design, but they do increase the high-voltage component count. The floating deck modulator requires two such supplies referenced to the GTWT grid and two referenced to the grid cutoff ($B-$) voltage. These four supplies are used by the output transistor drive circuits.

Power dissipation is one of the most notable differences between the three modulator types. We have tabulated the dissipations for three typical PRF/duty factor combinations. For comparison purposes, all numbers include the losses in the grid bias ($B+/B-$) bleeder resistors. Most of the dissipation in the floating deck modulator consists of switching losses in the output transistors; thus at higher PRFs the dissipation is a nearly linear function of PRF. As discussed above, the losses in the pulse-transformer-coupled modulator increase very rapidly as the PRF and duty factor increase; dissipation is the primary limitation of this modulator type. For the RF-trans-

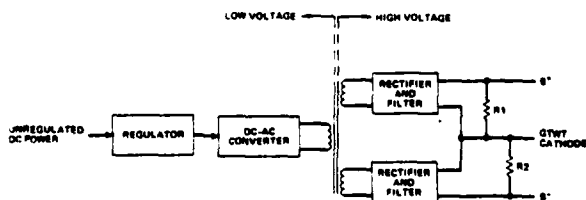


Figure 7. Grid Bias Power Supplies with Regulator at Low Voltage

Table 1. GTWT Modulator Comparisons

PARAMETER \ MODULATOR		FLOATING DECK	PULSE-TRANSFORMER COUPLED	RF-TRANSFORMER COUPLED
PRF	(MAXIMUM)	1 MHz	300 kHz*	2.5 MHz
PULSE WIDTH	(MINIMUM)	0.2 μ S	0.5 μ S	0.3 μ S
	(MAXIMUM)	DC	300 X (RISE TIME)	DC
RISE/FALL TIME		50 nS	50 nS	20 nS
COMPONENTS	AT LV	14	87	85
	AT HV	65	17	25
	TOTAL	79	104	110
POWER FORMS (EXCLUDES B ⁺ /B ⁻)	AT LV	1	2	3
	AT HV	4	0	0
DISSIPATION	MPRF (15 kHz, D = 0.2)	25 W	140 W	40 W
	HPRF (300 kHz, D = 0.5)	70 W	210 W	80 W
	EXTREME HPRF (1 MHz, D = 0.5)	220 W	390 W	120 W

*1 MHz ATTAINABLE WITH SEVERE PULSE WIDTH LIMITATIONS

former-coupled modulator, only the small amount of dissipation in the edge circuits is PRF-dependent, which results in a relatively low power loss even at high PRFs.

Conclusions

For general-purpose use in multimode radar systems, the floating deck modulator appears to be the best choice since it offers a wide PRF and pulse width range with minimal component count and power dissipation. The RF-transformer-coupled modulator is better suited to applications requiring an extremely

high PRF, due to its fast rise and fall times and low high-PRF losses. For low-cost applications with a maximum PRF of one or two hundred kilohertz and a maximum duty factor of 0.50, the pulse-transformer-coupled modulator is a good choice due to its relative simplicity and low number of high-voltage components.

Acknowledgements

The authors wish to thank W. B. Hwang, D. M. Kang, T. K. Lee, and M. Rosenfeld for their assistance in developing the modulator circuits described in this paper.

A UNIVERSAL MODULATOR FOR GRIDDED TRAVELING WAVE TUBES

Albert W. Mimms
Space Microwave Laboratories, Inc., Santa Rosa, California

and

Shandas Meppalli
Electronics and Radar Development Establishment - Bangalore, INDIA

Summary

General considerations in the design philosophy of a TWT grid modulator are outlined. The superiority of Power MOSFET devices over bipolar transistors in modulator switching applications has been emphasized. A grid modulator that is capable of switching the TWT grid from -600 volts to +600 volts within a few nanoseconds is described. These voltages are variable within the limits by simple circuit adjustments. The unit is built to provide up to 40 kilovolts isolation with respect to ground.

The modulator is capable of switching the TWT with various pulse programs. Some of the special features like the soft start and fault processing circuits are discussed. Test results are included to indicate the universality of the modulator.

Introduction

The traveling wave tube (TWT) is probably the most widely used microwave power amplifying device - be it for communication, electronic warfare or radar systems. The superiority of a TWT over any other class of tube in terms of bandwidth, duty cycle and gain makes it an ideal candidate for the latter two applications. These applications call for generation of high power RF pulses of varied repetition frequency, pulse widths and modulation programs. The control element to accomplish these pulse programs is the grid in the TWT. Normally this electrode is used to switch the tube ON or OFF at will depending on the application. It is biased negative with respect to the cathode to keep the tube at cutoff, and is driven to a pre-determined positive potential during the pulse period to make the tube conduct and amplify the RF output. The subsystem needed to do this switching - a universal modulator - is the topic of discussion of this paper.

General Considerations

The block diagram of the TWT power supply arrangement for a system with a depressed collector is shown in fig. (1). The solenoid supply required for tubes with electromagnets is omitted from this discussion. All the supplies are referenced to the cathode, and this makes it necessary for the grid modulator and heater supplies to float at cathode potential. The body supply is at the highest potential. The transmitter trigger signal is at ground level and normally in a TTL compatible pulse format. This needs to be coupled to the high voltage deck with sufficient isolation. Generally two methods of pulse coupling are used - transformer coupling and optical coupling. Selecting a method of coupling is mainly dependent on the system considerations in that factors like the voltage isolation needed, PRF, pulse width, amount of pulse power to be coupled, pulse fidelity, and environment are based on the system parameters. In the transformer coupling method the trigger pulse is processed at the low voltage level itself and coupled to the high voltage deck through the transformer.

The voltage isolation is provided by the transformer. The optical coupling uses optical fiber to isolate electrically the low voltage circuit from the high voltage deck, and the pulse processing is done at the high voltage deck.

The block indicated as 'Modulator Control' in the diagram consists of the pulse processing, interfacing, control and protection circuits of the modulator.

Negative grid bias (B_-) to keep the TWT at cutoff during the interpulse interval, B_+ supply for driving the grid positive according to the pulse command, the switching elements and the sensors for control and monitoring circuits are housed in the block "Grid Bias and Modulator". The output of this is a pulse, as shown in the diagram. The PRF and pulse width can vary in any format depending on the application. The modulator should be capable of responding to these changes. The shape of the output pulse from the modulator also is a very important aspect to be considered. The rise and fall times under loaded conditions have to be as short as possible - preferably a few nanoseconds - to ensure operation of the system under various pulse programs.

The amplitude perturbations at the top of the pulse are of great significance, especially in a Doppler radar system wherein information of phase on a pulse to pulse basis is extracted for detecting moving targets. This requires a highly stable radiated signal from the transmitter. Stability refers to only short term effects on a pulse-to-pulse basis. Factors contributing to the instability of the transmitted signal, apart from the spectral impurity of the source itself, are mainly the amplitude/phase modulation effects caused by the ripples in the various power supplies of the TWT amplifier. The tube manufacturers provide the information on the phase sensitivities of each electrode in terms of degrees/volt. The ripple rejection specifications for each power supply should be calculated from these figures taking into account the overall improvement factor needed.^{1,2} Even though the body supply is of primary importance here, the positive bias (B_+) which decides the amplitude of the grid pulse is also of considerable significance. Care should be taken to minimize instabilities in the B_+ supply and provide a flat-top pulse output from the modulator. This supply should have sufficient current capabilities to drive intercepting types of grids also.

Another important aspect to be considered is the interfacing of the modulator with the tube. The system design should take into account the probable faults in the power supply/modulator that can damage the tube and also provide adequate protection to the modulator if arcing occurs within the tube. The modulator has been considered as one of the weak links in terms of reliability in a radar or EW system by many system designers mainly because the failure of components within the modulator circuit disables the transmitter. As this unit is at the cathode

potential, any arcing in the tube could cause heavy current flow through the components in the modulator circuits. Many times the failure might have been due to this high current surge. Arrangements should be made to divert such a transient current from the sensitive elements in the modulator. The fault protection arrangement should be very reliable but it should not be so sensitive that it reduces the availability of the transmitter. Peak and average overcurrents, and an excessive duty cycle, are some of the major faults that need instantaneous circuit reaction to protect the system.

Basic Configurations

Two commonly used grid modulator schemes are shown in fig. (2) and fig. (3). Both have two power supplies, B- and B+, referenced to the cathode for providing the cutoff bias and the 'pulse-up' voltages. The transmitter trigger pulse after processing is given to the switch control circuit. In the grid modulator shown in fig. 2, the B- supply is connected to the grid of the TWT through the resistor R1. R2 is the short circuit current limiting resistor in the grid-modulator path. During the ON period of the pulse, switch S1 is closed by the control signal and the B+ supply is connected to the grid. As soon as the pulse is removed, S1 becomes open and R1 pulls the grid down to the B- voltage level. Since a resistor is used to pull down the grid to the cutoff level this circuit is known as a passive pull down circuit. The value of this resistor is a compromise between the power dissipation and the pulse fall time. This scheme is simple and can be used reliably in many systems requiring voltage swings up to 600 volts.

The active pull down scheme shown in fig. (3) utilizes one more switch, S2, which acts as a tail-biter. As in the previous case, S1 is closed during the pulse period. During this period S2 is open. At the end of the pulse, S1 is opened and S2 is closed for a short duration, and the grid is pulled down to B- level. Since R1 is connected in parallel to S2, this pull down switch need not be closed for long duration. The resistor R1 is much greater than the corresponding resistor that would be used in a passive pull down circuit. This scheme is better than the previous one because the fall time of the pulse is reduced and very little power is dissipated in the pull down device. But additional circuits are needed to provide the timing and control for the switching devices.

Power MOSFET as the Switching Device

The switches shown in fig. (2) and (3) are active elements and should have the following characteristics:

- a) fast switching;
- b) high frequency operation;
- c) high voltage capability;
- d) simple driving mechanism;
- e) very good reliability.

There are three main types of semiconductor devices available today for switching applications - Thyristors, bipolar transistors and MOS Field Effect Transistors (MOSFET). Out of these, thyristors are generally used for high current switching at fairly high voltages and do not find much use in TWT grid modulator applications because of their slow speed, frequency limitations and commutation problems. Bipolar transistors have been in extensive use but the circuits become very complex in many applications

requiring multiple pulse programs. MOSFET devices have been used in high speed switching circuits at low voltage and current levels. Analog switches for multiplexing, A/D converters and switch arrays are some of these applications. But it is only during the last five years that MOSFETs became available for use at higher power levels.^{3,4} Now Power MOSFETs have become very popular with power supply designers for use in high frequency switch regulators, inverters and converters. Some of the important features which make this device superior to bipolar transistors in grid modulator switching applications are given below:

Switching Time: Being a majority carrier semiconductor device, MOSFETs do not have the minority carrier delay times associated with bipolar transistors. The switching time is mainly controlled by the input capacitance, C_{iss} , between the gate and the source of the FET. This capacitance is in the range of 100 pf to 500 pf for the devices used in power switching applications. The switching time can be approximated to the time constant $C_{iss} \times R_{in}$ where R_{in} is the effective source impedance. It is possible to reduce this further by circuit techniques. When compared with a bipolar transistor of the same rating a Power MOSFET has an order of magnitude faster switching time.

Frequency of Operation: Power MOSFETs have much higher frequency operations capability than bipolar transistors. Because the switching time is very short, the power dissipated in the FET during switching is very low and this makes the FETs capable of switching at high frequencies. Pulse programs such as burst mode, stagger and multiple PRFs are easily achievable with Power MOSFETs as the switching devices.

Driving Mechanism: One of the chief differences between bipolar transistors and Power MOSFETs is in the drive requirements. Bipolar transistors are current operated devices and need a large base current to drive them into saturation. In the case of Power MOSFET a voltage is applied between the gate and the source terminals to produce a current flow in the drain. As the gate is electrically isolated from the source by a layer of silicon oxide, there is very little current flow into the gate. This makes the drive circuits very simple. The gate-source breakdown voltage of these FETs is about 20 volts and the drive level should be kept below this.

Voltage Capability: Power MOSFETs are available today with a voltage capability of 600 volts without any deterioration in their advantageous features. It is easy to connect these devices in series for higher voltage capability because of their simple driving requirements. This point is explained in detail later.

Reliability: The performance of a bipolar transistor is very much dependent on temperature. It is also susceptible to thermally induced breakdown. Power MOSFETs are much superior under the same environmental conditions. They have excellent gain and switching time stability with temperature changes. The switching time, as explained earlier, is dependent on the input capacitance - C_{iss} - which is not affected by temperature variations. The carrier mobility in a power MOSFET channel region decreases with temperature. If localized heating occurs, the carrier mobility decreases which in turn reduces the localized current. This mechanism forces overload currents to be uniformly distributed with the MOSFET. When localized hot spots are formed in a

bipolar transistor the effect is to reduce the impedance and to funnel the collector current through the small area and ultimately destroy the transistor.

Universal Modulator

When faced with a problem of developing TWT modulators for radar and EW systems operating in different frequency bands, we decided to examine the feasibility of combining the requirements and of designing a single unit with the capability of being adapted with minor adjustments to many systems. The modulator described here is the outcome of this design effort. The advantages of high frequency power supplies, such as reduction in size and weight and synchronization with the PRF of the main system, are made use of in the circuit. Important specifications of the modulator are listed below:

B+ and B- supplies : each variable from 100 volts to 600 volts

PRF : 1 kHz to 25 kHz (stagger mode also required)

Pulse Width : 100 nsec to 15 usec

Pulse Burst : 100 nsec 'ON' 100 nsec 'OFF' (pulse width and PRF limited by duty cycle)

Rise and Fall Time : less than 50 nsec

Ripple on Pulse Top : less than 5 millivolts

Voltage Isolation to Ground : 40 kilovolts

The block diagram of the modulator is shown in fig. (4). The prime power input is rectified and fed to a high frequency switch regulator. The output of the switch regulator is fairly well regulated. This regulated DC is applied to the high frequency inverter. In the absence of a synchronizing pulse, the switch regulator/inverter frequency is about 25 kHz. This could be phase locked to the system PRF if a synchronizing pulse derived from the PRF generator is given to the power supply control circuit. The inverter transformer T1 has four secondary windings for generating all the voltages needed. This transformer also provides the voltage isolation. It may be noted that the TWT heater supply is included in this unit. The advantages of integrating the TWT heater supply into this are:

- elimination of bulky low frequency transformer;
- easier implementation of heater supply with minimum circuit elements;
- reduction in AM/PM noise in the TWT by having a regulated DC heater supply.

All the DC voltages are well regulated and the outputs are adjustable. Low voltages needed for the protection circuits within the high voltage deck are also provided by this power supply unit. The B- supply is regulated by a simple Zener arrangement. B+ supply is a critical circuit derived by using a floating regulator arrangement with LM723 as the control element. Some additional features are incorporated in this power supply; for example, the soft start circuit shown in fig. (5). This circuit is used to ramp up the B+ slowly during the initial turn-on sequence. When the modulator is switched on after the warm-up delay, the B+ output will be at a

level decided by the setting of the resistor R2. As the tube starts drawing current, the current transformer (CT) provides a proportional pulse output voltage to the sample and hold circuit. The output of this circuit is fed to an error amplifier A1. The error amplifier has a reference voltage that is adjustable by R1. The output of the error amplifier is ramped up at a rate governed by the value of the capacitor C1. This ramp is applied to the summing amplifier A2 which has its output connected to the regulator error amplifier. Steady state condition is attained when the output of A1 reaches the peak value. The action of the two control loops - one formed by the regulator and A2 and the other comprising A1, A2 and the regulator - ensures the change of B+ level from a nominal voltage to the exact voltage at a pre-determined rate to avoid any beam surge currents during turn-on. It also acts as a beam current regulator in that the B+ level is brought down when the beam current exceeds the value for which R1 is adjusted. This decrease in the positive grid voltage causes a corresponding reduction in the beam current.

It may be seen from the block diagram of the modulator that an active pull down arrangement is used. The PRF trigger pulse is processed in the switch control circuit and coupled to the switching devices. Reliable protection circuits are used to safeguard the tube and the modulator. Switches S1 and S2 are strings of Power MOSFETs connected in series for the voltage swing required. R1 and R2 are the effective resistance across each switch. Fig. (6) shows the switching arrangement in more detail. Q1-Q8 are Power MOSFET devices. Q1 and Q2 are used to drive the two switches formed by the Power MOSFET series configurations Q3-Q5 and Q6-Q8. Pulse transformers T1 and T2 couple the drive pulse to each FET and also provide the voltage isolation between the low voltage deck and the high voltage deck. Resistors R7-R12 are used to ensure equal voltage sharing by the FETs. The gate of each FET is protected by Zener diodes. Transistor Q1 is used as the ON switch driver. This conducts for the duration of the pulse width needed, providing the gate drive to the ON switch, FETs Q3-Q5. The switch control circuit provides a narrow pulse - Pulse 2 - to Q2 which is the driver for the pull down switch transistors Q6-Q8. The timing relationship of Pulse 1 and Pulse 2 is such that the trailing edge of Pulse 1 coincides with leading edge of Pulse 2. There is a delay adjustment in the switch control circuit to ensure proper timing of these two pulses.

When both switches - Pull up and Pull down - are off, the B- supply is connected to the grid of the TWT through the resistors R10-R12 and the current limiting resistor R13, ensuring the tube is at cutoff. R10, R11 and R12 are equal in value but are much smaller than the resistor chain on the pull up switch R7-R9. When Pulse 1 is applied to Q1, the pull up switch transistors are driven into saturation by the coupled drive voltage and the B+ supply is connected to the grid. At the end of Pulse 1, transistor Q2 is turned on by Pulse 2 and the transistors Q6-Q8 are driven into saturation. This action pulls down the TWT grid to the B- supply level quickly. The pull up switch is open at this time. At the end of Pulse 2, transistors Q1 and Q2 are off and the grid remains at the B- level. Reset windings are provided in the pulse coupling transformers T1 and T2 to avoid saturation of the core. All the FETs used in the circuit are protected by connecting transient absorbing devices across them. This arrangement diverts the high transient energy during arcing away from the FETs.

Fault Protection and Monitor Circuits

The fault protection unit that includes the control functions, protection circuits and monitoring facilities is designed taking into account all the system aspects. For some of the faults occurring in the transmitter, redundant protection circuits may be required to ensure complete protection to the microwave tube and associated circuits. Monitoring of important parameters is necessary to identify any malfunction quickly. It is convenient to include many of these functions in the modulator unit since the control of the transmitter is easily accomplished by this.

Fault signals processed in the modulator unit and the parameters monitored are listed below:

<u>Faults</u>	<u>Monitor</u>
High Beam Current	Beam Current
Incorrect Grid Bias	Grid Bias Voltages
High Heater Voltage	Heater Voltage
Low Heater Current	Heater Current
Excess Duty Cycle	

With modern processing techniques in the manufacture of the TWT, the probability of arcing in the tube is considerably reduced. But still arcing takes place occasionally, especially after prolonged use of the tube. So it is essential to safeguard the tube and modulator against arcing. High voltage power supplies for the tube are designed to take care of this situation, but to protect the modulator additional circuits are needed. Beam current output is one of the convenient sensing parameters to detect any abnormalities and this is done here as indicated earlier in fig. (5). The current transformer output, apart from being used for the regulator control, is also made use of in triggering fast acting protection circuits. The output is compared with a pre-set reference in a comparator circuit. Whenever the comparator output changes its state due to the excess beam current, the modulator trigger is inhibited instantaneously and drives the tube to cutoff.

All the signals for triggering the fault protection circuits and the different voltages and currents to be monitored are coupled from the high voltage deck to low voltage deck via optical fibers. A block diagram of the signal conditioner circuit used for this is shown in fig. (7). Inputs from the various fault/monitor signal sensors are fed to the amplifier. The amplified voltage output is converted to a nominal frequency of 7 kHz in a voltage to frequency converter circuit. This frequency will vary according to the changes in the input voltage. The V/F converter output drives a light emitting diode. The light pulses are coupled to the low voltage deck using optical fibers. At the low voltage deck the light pulses are converted back to electrical pulses and, after amplification, are fed to a frequency to voltage converter. This voltage output is fed to the monitor circuit for indication of the parameter to be monitored. The signal is also fed to a comparator circuit wherein it is compared with a pre-set reference. In the event of any fault, the signal input to the comparator exceeds the reference causing a change of state at the output. This is latched in a logic circuit and the latched output is used to activate the protection circuits.

Packaging

Circuits used in the modulator are divided into small functional blocks and classified in two categories - essential and optional. Based on the system requirements the optional features could be added or deleted. Some of the features categorized as optional are monitoring circuits and the beam current regulator. By doing this it is possible to optimize the system for specific requirements. Packaging also varies to suit the system environment. For example, in one of the airborne applications, the modulator is housed in a leak proof aluminum container filled with flourinert liquid for providing good voltage isolation. This unit occupies a volume of less than 300 cubic inches and weighs approximately 15 pounds. This includes the weight of the dielectric fluid and the container. Another application needing a voltage isolation of only 20 kilovolts used an entirely different packaging. Flexibility in the engineering and packaging of this modulator is considered to be an advantageous point. Photographs of these units are shown in fig. (8) and (9).

Test Results

The modulator described above has been tested with various TWTs. The voltage swing levels and pulse programs were different in each case. Pulse widths ranging from 100 nanoseconds to 15 microseconds and PRFs varying from 1 kHz to 25 kHz were used in the testing program. Test results are shown in the figures (10) through (13).

Conclusion

The modulator described in this paper has been found to be useful in many systems in terms of performance and reliability. Because of the modularity in the design approach circuit configuration could be modified easily depending on the system requirements. Superiority of Power MOSFET devices over bipolar transistors in grid modulator switching applications has been established in this design. Even though this modulator was tested for PRFs up to 25 kHz only, the design is good for much higher frequency capability. The power supply arrangement for deriving the voltages needed for the modulator and heater has the advantage of easy adjustments to suit individual traveling wave tubes' requirements.

References

1. T.A. Barley and G.J. Rast, Jr., "Power Supply ripple effects on a near carrier transmitted spectrum". NTIS report number RE-75-11.
2. M.I. Skolnik, "Radar Handbook", McGraw Hill Book Company, New York.
3. "HEXFET Data book, Power MOSFET Application and Product Data"; HDB-1; International Rectifier, 233 Kansas Street, El Segundo, California.
4. R. Severns; "The Power MOSFET, A Breakthrough in Power Device Technology" Application Bulletin A 033, Intersil, Inc., 10710 N. Tantan Avenue, Cupertino, California 95014.

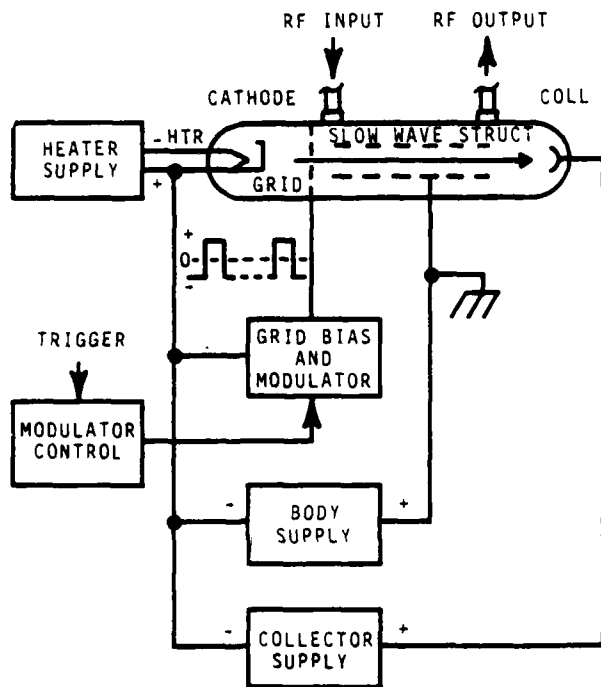


FIG. 1. TWT POWER SUPPLY/ MODULATOR ARRANGEMENT.

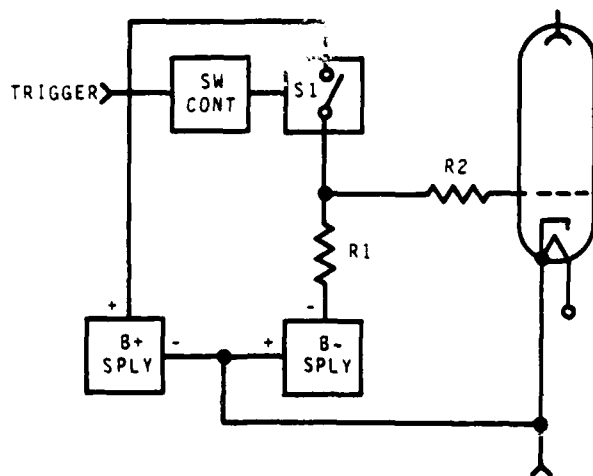


FIG. 2. GRID MODULATOR WITH PASSIVE PULL-DOWN.

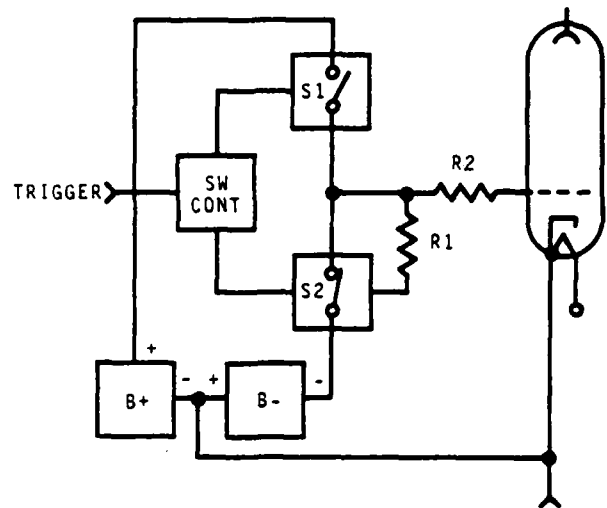


FIG. 3. GRID MODULATOR WITH ACTIVE PULL-DOWN.

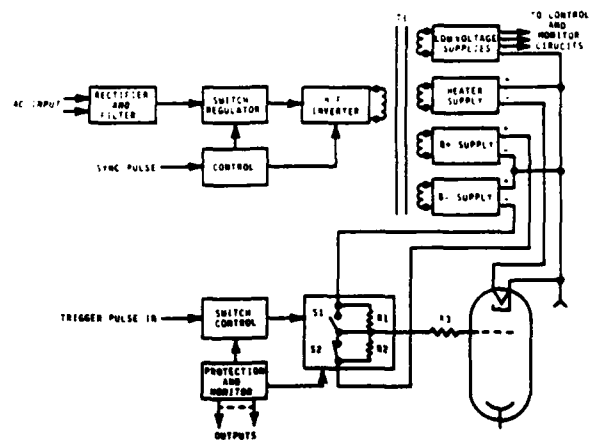


FIG. 4. BLOCK DIAGRAM OF UNIVERSAL MODULATOR.

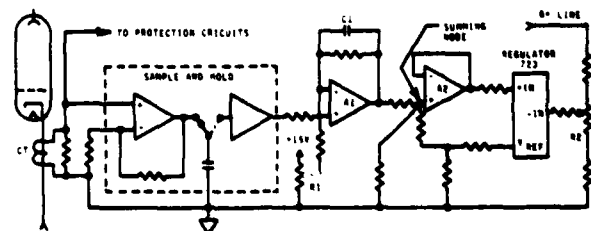


FIG. 5. SOFT START CIRCUIT.

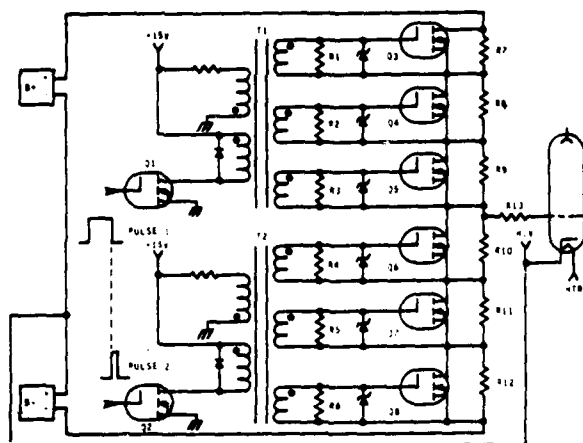


FIG. 6. SIMPLIFIED SCHEMATIC OF MODULATOR SWITCH ARRANGEMENT.

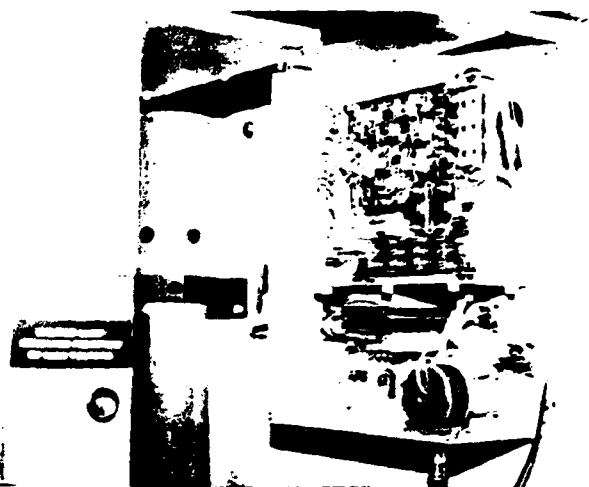


Fig. 9

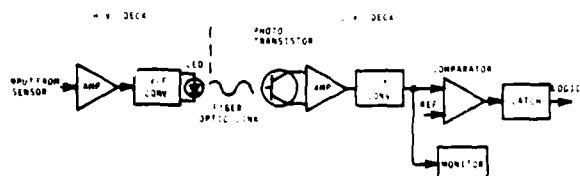


FIG. 7. SIGNAL CONDITIONER FOR FAULT PROTECTION CIRCUITS.

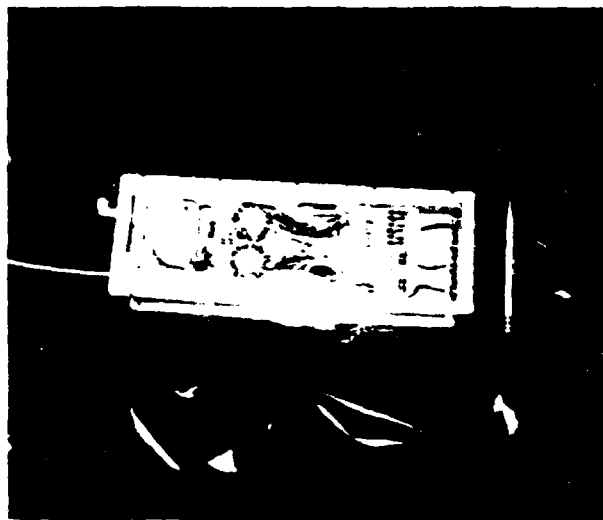


Fig. 8

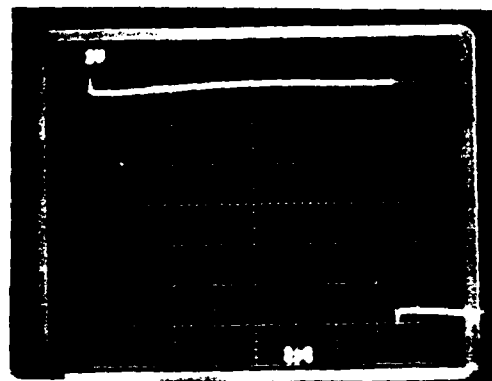


FIG. 10. MODULATOR OUTPUT PULSE

Pulsewidth : 15 μ sec.
PRF : 1 KHZ
Voltage Swing : \approx 1200 Volts

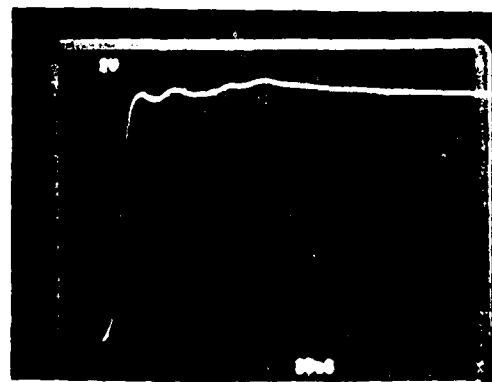


FIG. 11. LEADING EDGE CHARACTERISTICS

AD-A119 664

PALISADES INST FOR RESEARCH SERVICES INC NEW YORK
IEEE CONFERENCE RECORD OF 1982 FIFTEENTH POWER MODULATOR SYMPOS--ETC(U)
1982

F/G 9/5

UNCLASSIFIED

82-CH-1785-5

NL

4 4

4 4

4 4

4 4

4 4

4 4

4 4

4 4

4 4

4 4

4 4

4 4

4 4

4 4

4 4

4 4

4 4

4 4

4 4

4 4

4 4

4 4

4 4

4 4

4 4

4 4

4 4

4 4

4 4

4 4

4 4

4 4

4 4

4 4

4 4

4 4

4 4

4 4

4 4

4 4

4 4

4 4

4 4

4 4

4 4

4 4

4 4

4 4

4 4

4 4

4 4

4 4

4 4

4 4

4 4

4 4

4 4

4 4

4 4

4 4

4 4

4 4

END
DATE
FILMED
10.82
DTIC

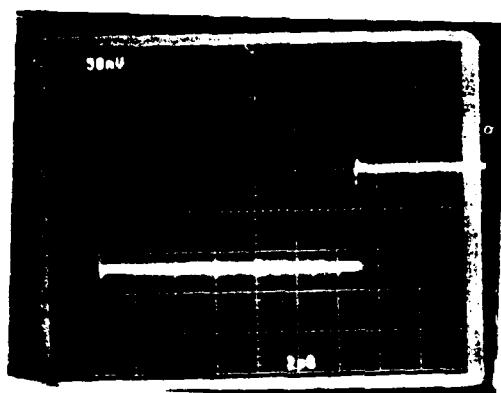


FIG. 12. DETECTED R.F. OUTPUT

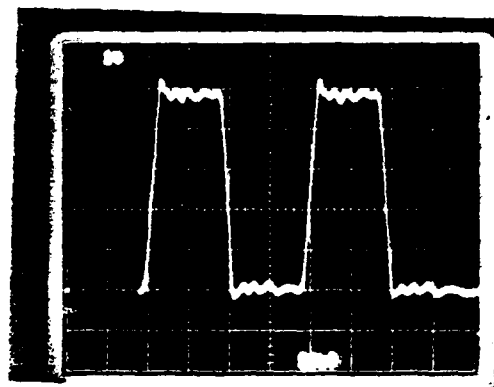


FIG. 13. PULSE BURST MODULATION

Pulsewidth : 100 nsec. on
 100 nsec. off

Duty Cycle : 1%

750 KW POWER SYSTEM
FOR
A SOLID STATE PULSED RF TRANSMITTER

Charles A. Corson & Howard S. Ginsberg
Westinghouse Electric Corporation
Baltimore, Maryland

SUMMARY

This paper describes a power and energy distribution and control system for the AN/SPS-40 transmitter which is a pulsed high power solid state radar transmitter recently developed by Westinghouse for the Navy. The solid state amplifier draws pulse currents of over 19,000 amperes at over 750 KW from a 40 VDC power supply system. The final stage includes over 100 RF amplifier modules. The entire system is regulated to better than 40 millivolts pulse to pulse in order to achieve excellent RF phase and amplitude stability even when variable pulse spacing is used. This modular amplifier system offers graceful degradation or soft failure, and improved on-line dependability.

DISTRIBUTION SYSTEM

The Final Amplifier stage of this transmitter includes 112 identical 2.5 KW solid state RF amplifier modules whose outputs are combined to produce over 200 KW peak output power at UHF. The individual modules draw up to 180 amperes at 40 volts DC during the RF pulse. Total requirements for the output stage are 19,000 amperes peak at 40 VDC. The duty of the 60 microsecond RF pulses is 1.8%, thereby requiring 13.5 KW average power. These large requirements are accomplished by dividing the amplifier system down into smaller units. The Final Amplifier is contained in two identical cabinets as depicted by the two right cabinets in Figure 1. Each cabinet contains 56 RF amplifier modules and 5 identical power supplies. Each power supply can power 12 RF modules, however all but one of the power supplies are only loaded with 11 amplifier modules. Because each power supply would have to deliver over 2000 ampere pulse currents, the output filter capacitors are distributed into each RF amplifier module close to the RF amplifier transistors. In this way each power supply only needs to deliver up to 40 amperes average current to recharge the distributed filter capacitors. Each module contains about 5000 microfarads which discharges two volts during each 60 microsecond pulse. The DC for each module is wired back to the power supply and all modules are recharged in parallel. After recharge, all modules on any power supply have the same DC voltage.

By distributing the amplifier system in this way, failures can be easily tolerated without shutting down the transmitter. A single RF module failure has no measurable impact on system performance and is reported to the operator by the automatic built in test features. A failure of a single power supply drops only 10% of the transmitter off line and the system continues to run using the remaining 90% of the amplifier. In the extreme case where an entire cabinet may have to be shut down, the radar system can still operate with reduced performance using the other operational half of the transmitter.

Each of the 10 power supplies are protected by an individual 3 phase, 440 VAC circuit breaker. This provides fault isolation so that the remaining 9 units stay on line. It also allows a defective unit to be depowered and replaced while the rest of the system continues to run. Each power supply contains its own self monitoring circuitry which reports to the transmitter system its status. An individual indicator for each power supply tells the operator which unit may have failed.

The RF Drive stage for the transmitter uses 12 more of the same RF modules and is powered by an 11th identical power supply. A 12th power supply is electrically connected to the Drive stage and is automatically powered up if the Driver power supply should fail. This same unit can be used as a spare for any of the 10 power supplies in the Final Amplifier cabinets.

CONTROL SYSTEM

The output of the Final stage of the amplifier can be controlled from zero to full output power in 5% steps. Each power supply accepts five different input commands. The first command is an on/off command which tells the supply to go to zero or the commanded voltage. The other four commands are a digital code which tells the power supply what voltage to produce. Those four inputs provide 16 possible voltages which are equally spaced in about one volt increments from 24 to 40 volts DC. By providing the same code to all 10 output power supplies, the entire 40 volt output system can be controlled from 40 volts down to 24 volts DC. This corresponds to approximately 5% steps of power reduction down to 40% of output power. Below this point, pairs of power supplies are commanded off-line pair by pair until the last pair (one in each cabinet) is delivering about 5% of the full transmitter power.

The digital power supply control also has another use in this transmitter. Because the Driver Amplifier does not require 40 volts DC to produce the required drive level, its power supply is normally commanded to a much lower output level. If one of the Drive amplifier modules should fail, an automatic control system senses the reduction in Drive power and commands a higher voltage for the remaining eleven modules to make up for the small power loss, and the Drive stage heals itself automatically. The failure information is detected and sent to the front panel display for operator corrective maintenance.

Figure 2 shows the Driver cabinet which contains all the transmitter control circuits and displays. The circuit breakers can be seen across the top of the cabinet. The RF modules can be seen in the bottom center with the two power supplies on the bottom left. The Control and Monitor Panel is just below the circuit breaker panel. It contains fault indicators

for all the power supplies and RF modules in the system as well as indicators for various cooling system degradations. A meter displays auxiliary power supply voltages and all key RF levels in the system. Switches are provided to control the total transmitter output power as well as all intermediate RF stages.

POWER SUPPLY DESCRIPTION

The power supply operates directly off of a standard three phase, 3 wire, 440 VAC L-L, 60 Hz power line without the need for a heavy high power 60 Hz step down transformer. It does this by utilizing a flyback switch configuration which recharges the pulse capacitors of the RF amplifiers in discrete steps during the radar interpulse period. Recharge accuracy is obtained by reducing the recharge step size as the power supply output voltage approaches the desired voltage as shown in Figure 3.

Figure 4 shows a block diagram of the power supply. The three phase AC input voltage is full wave rectified and filtered with a single section LC filter. The flyback switch drives the transformer primary of the inverter output transformer. The power train is completed with an output rectifier and output capacitors. These output capacitors, which are located in the power supply, are only a small portion of the total load capacitance.

An auxiliary bias transformer provides stepped-down AC voltage for an "inrush suppression" circuit and for the "auxiliary power supply" circuitry. The inrush suppression circuit includes an SCR, a small control circuit, and a resistor which limits the inrush current to the LC filter when AC power is first applied to the power supply. This helps to protect the input rectifier bridge and the capacitors of the input LC filter. The SCR is gated on and maintained on when the dc voltage on the LC filter output exceeds a set threshold. The auxiliary power supply circuitry provides regulated dc voltages for the power supply control circuitry. It also provides unregulated voltage which powers the driver circuitry for the power switching transistors of the flyback switch assembly.

The heart of the power supply is the control circuitry, which provides the drive, regulation, protection and monitoring functions. The control circuitry drives the inverter transformer on after which the duration of the inverter transformer secondary current is inversely proportional to the power supply output voltage. Therefore the time between drive pulses is made a function of power supply output voltage because the supply is programmable over a 24 to 40 volt range.

When the inverter transistors are driven on, the primary current in the inverter transformer rises and is monitored by a current transformer. When the output from this current transformer exceeds a reference, the drive pulses are terminated thus limiting the peak current in the inverter transistors under all conditions.

A four bit input command generates a programmed reference. A sample/hold circuit is used to sense the power supply output voltage when no current is being delivered to the output of the power supply, thereby avoiding the pulse output IR drops which would mask the true load voltage. The sample hold output is compared to the programmed reference to create an error signal which is used to determine which of two drive pulse widths will be selected. As the error approaches zero, the primary current limit is reduced

and this lowers the step size from the inverter. When the error signal reaches zero all inverter drive pulses are stopped.

The power supply is protected against low drive power and continuous output short circuits. It also protects the load from overvoltage by shutting down if an overvoltage is sensed. The power supply itself is inherently protected against instantaneous load short circuits. If the auxiliary drive dc voltage drops too low, all drive pulses are inhibited. This protects against weak drive to the inverter switch transistors. An overcurrent and overvoltage latch inhibit can only be reset by momentarily removing the AC input to the power supply.

A circuit monitors the power supply output voltage and gives a positive indication to the transmitter if the output voltage is within a window around its commanded voltage. The reference voltage for the window detector comes from the reference which was programmed by the 4 bit input command. The sensed input for the window detector is derived by peak detecting the power supply output. A peak detector is used because it is the peak load voltage that is of interest and not the charging voltage.

A positive signal on the remote ON/OFF input activates an optical coupler which allows inverter drive pulses. The absence of this input signal keeps the power supply off. A high speed optical coupler is used for this since this line is also used to blank the power supply during the radar RF pulse and therefore must have a fast response. Optical couplers are used on the remote ON/OFF input and each of the 4 bit voltage select inputs in order to eliminate noise.

Figures 5 and 6 show front and rear views respectively of the power supply. The unit is five inches wide, by eleven inches high, by eighteen inches deep and weighs 37 pounds. The power supply features blind plug-in connections with all input and output connections located at the rear of the unit.

Cooling of the power supply is accomplished by forced air convection with blowers located external to the power supply. This air supply is monitored in the cabinet for all power supplies. If the air supply becomes deficient, a built in back up blower is automatically energized. Air enters the power supply at the rear and exits at the front. A handle, located at the front of the power supply, is useful for inserting or withdrawing the power supply from its mating cabinet.

CONCLUSION

Solid state amplifiers operate at considerably lower voltages than the traditional vacuum tube and cavity amplifiers and this has caused a new spectrum of requirements for high current technology development. More and more high power radar systems are including solid state RF transmitter amplifiers. This trend has developed due to increased availability of reliable and affordable high power RF transistors. The equipment that has been described demonstrates that high power, low voltage DC can be distributed in an efficient and controlled manner. Shipboard installation of this equipment is planned during the next year.

ACKNOWLEDGEMENT

This work is being sponsored by Naval Research Labs under development Contract N00014-61-C-2039.

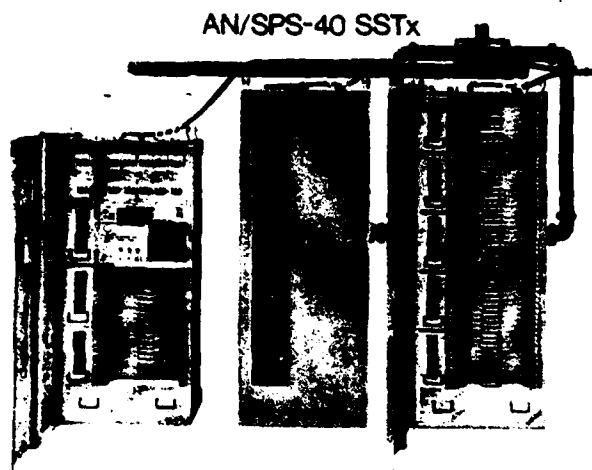


Figure 1
AN/SPS-40 TRANSMITTER

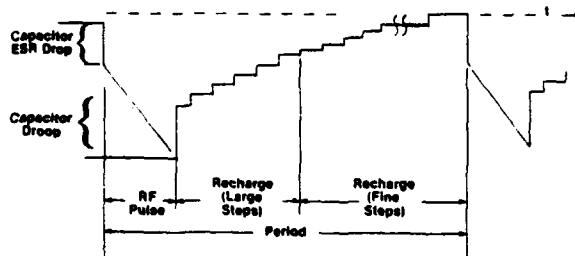


Figure 3
RECHARGE WAVEFORM

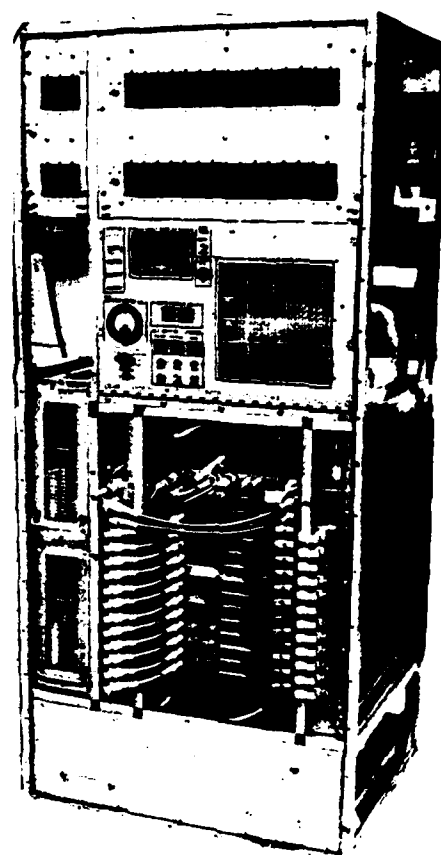


Figure 2
DRIVER CABINET

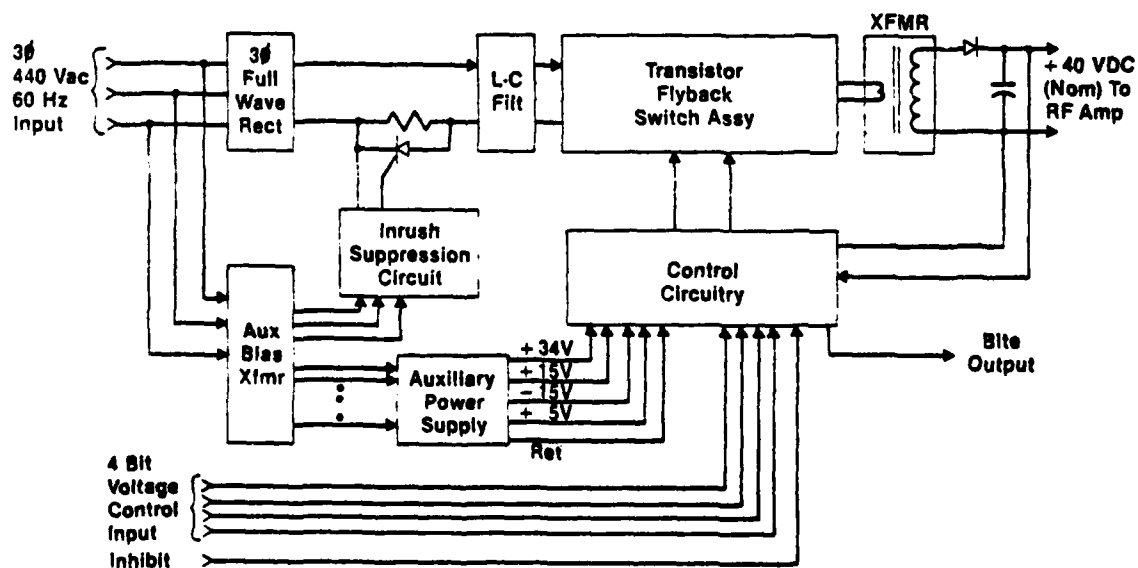


Figure 4
POWER SUPPLY BLOCK DIAGRAM

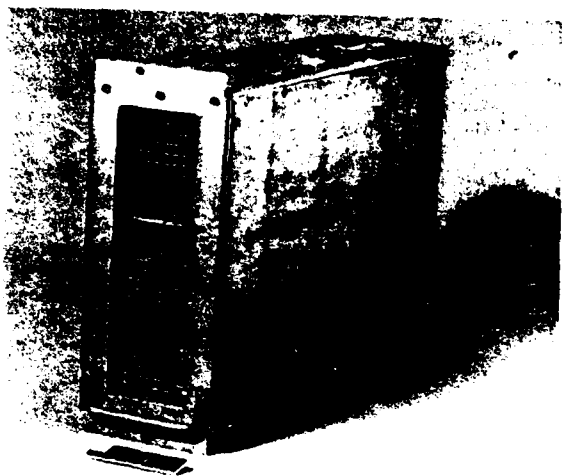


Figure 5
POWER SUPPLY FRONT VIEW

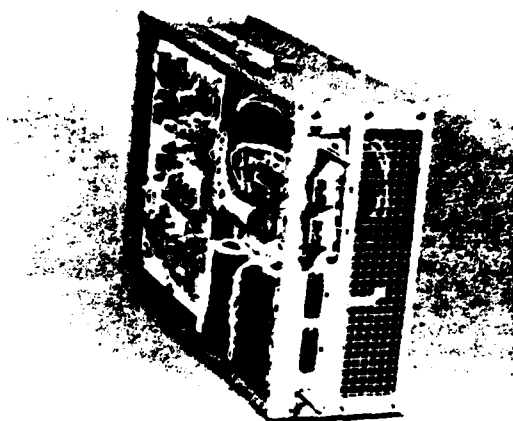


Figure 6
POWER SUPPLY REAR VIEW

UNIVERSAL ELECTRON TUBE CONTROL GRID MODULATOR

Daniel G. Miller

Westinghouse Electric Corporation
Systems Development Division
P.O. Box 746, MS 494
Baltimore, Maryland 21203

Abstract

Electron tubes require different modulator drives depending on their design and application. A shadow grid tube requires a low percentage of beam voltage on the grid electrode to control beam current, but it must swing positive with respect to cathode and will draw milliamps of current; while a focus control electrode tube will require a much higher control voltage, never go positive with respect to the cathode and draw much less than one milliamp of current. In addition, the application may require either pulse or CW operation, or some combination of both. Some pulse applications require very short delays from input to output in both rise and fall and most are critical as far as variations from one unit to the next. In the past, a new modulator design would be tailored for each application. However, the following modulator design addresses all of the above problems and is truly a universal design.

The following is an outline of the design capabilities of this universal modulator.

Pulsewidth:	0.2 μ s to CW
Pulse Swing:	800 volts achieved, 1500 volts believed possible divided between + and - supplies as required
PRR:	to 100 kHz
Isolation:	25 kV
Delay:	60 ns for both rise and fall
Size:	Possible to be packaged into power hybrid package

Schematics and timing diagrams will be shown and discussed for the above design.

Ref: Westinghouse Disclosure AA-80-040 Patent Application is being prepared by Wright Patterson Air Force Base

Background

Designers have long been striving, especially in ECM applications, to achieve a universal microwave power amplifier tube modulator. This modulator should have the following characteristics:

- Minimal delay plus rise time for repeater operation
- Long pulse and CW capability to allow the jammer to employ noise and various other jamming techniques
- Large voltage swing for modulating tubes employing focus anode control
- Reasonable current drive capability so that intercepting grid tubes, as well as shadow grid (nonintercepting) tubes, can be controlled

In the past, modulator designs have been tailored to the electron tube they were to drive. Typically, greater voltage swing capability resulted in slower rise and fall times and longer delays. Wide pulse capability also reduced the rise and fall time. Minimum pulsewidths were limited by storage times of bipolar transistors. CW operation extended rise, fall, and delay times into the microsecond range.

With the introduction of higher voltage Field Effect Transistors (FET), it is now possible to build a modulator with very good rise plus delay characteristics if special design techniques are used. FETs also make it possible to achieve very short pulsewidths to CW because they have no storage time and require very little power to maintain the ON condition.

New Design

The design presented in this paper makes use of FETs and special design techniques to provide minimum pulsewidths of 0.2 microseconds or less with no limit on the maximum pulsewidth. CW operation is achieved with the same rise, fall, and delays during transitions as is achieved for the mini-

mum pulsewidth. Total rise plus delay measures 60 nanoseconds for an 800-volt swing. Cathode voltage isolation to 25 kV and pulse repetition rates to 100 kHz can be achieved.

The above design is compatible with power hybrid packaging techniques, and approximately 8 cubic inches of volume is sufficient to package the entire modulator.

Design Details

The new design breaks down into three basic parts: the low voltage modulator, whose function is to generate ON and OFF triggers required for all possible drive conditions; the high voltage modulator, whose function is to transform the ON and OFF triggers into the high voltage pulse required to drive the tube grid; and the interconnecting transformers, which provide the voltage isolation required to float the high voltage modulator at the cathode voltage.

High Voltage Section of Modulator

Figure 1 is the schematic diagram for the high voltage section of the modulator. The circuit is push-pull using two high voltage N channel FETs. The gate drive circuitry makes use of the gate-to-source capacitance to maintain the drive during the ON condition. An ON trigger applied to terminals 1 & 2 and 5 & 6 will charge this capacitance of the ON switch Q1 and discharge it through Q3 for the OFF switch Q2. When an OFF trigger is applied to terminals 7 & 8 and 3 & 4, this capacitance will be charged for the OFF switch Q2 and discharged through Q4 for the ON switch Q1. The voltage is maintained on this capacitance while the switch is ON by the blocking action of CR1 and CR2. The value of the B+ and B- supplies is limited only by the maximum voltage capability of the switch FETs.

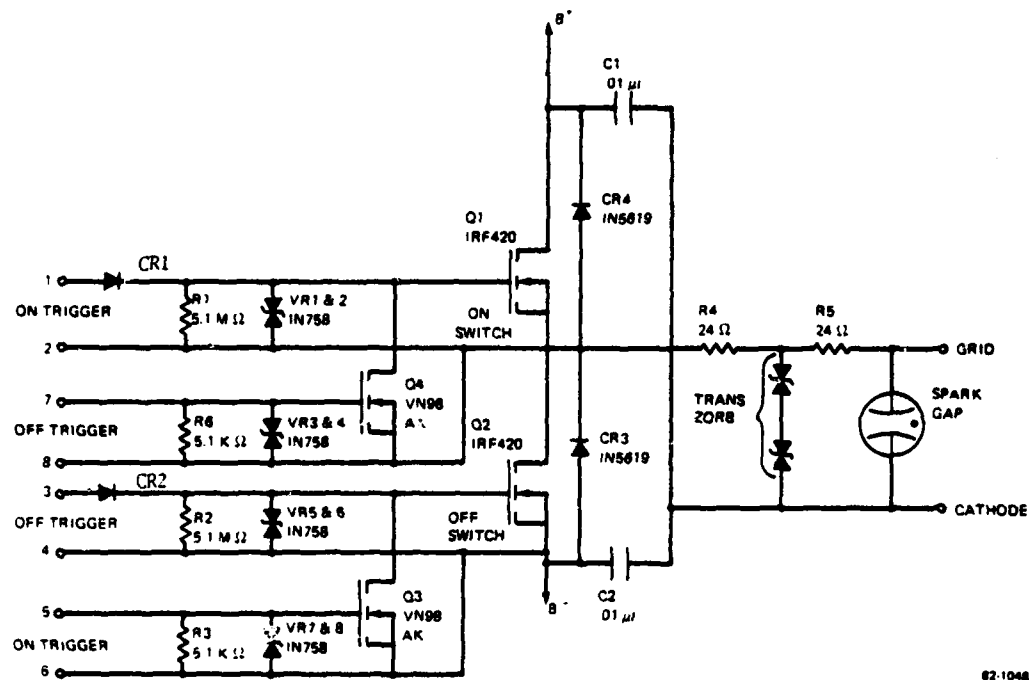
The circuitry is protected from the tube arcs by the spark gap and transzors shown on the schematic. Because of the more than adequate drive capability of the modulator, the additional capacitance loading of this circuit presents no problem.

Except for the spark gap, everything shown can be packaged in a power hybrid which greatly reduces the volume required.

Low Voltage Section of Modulator

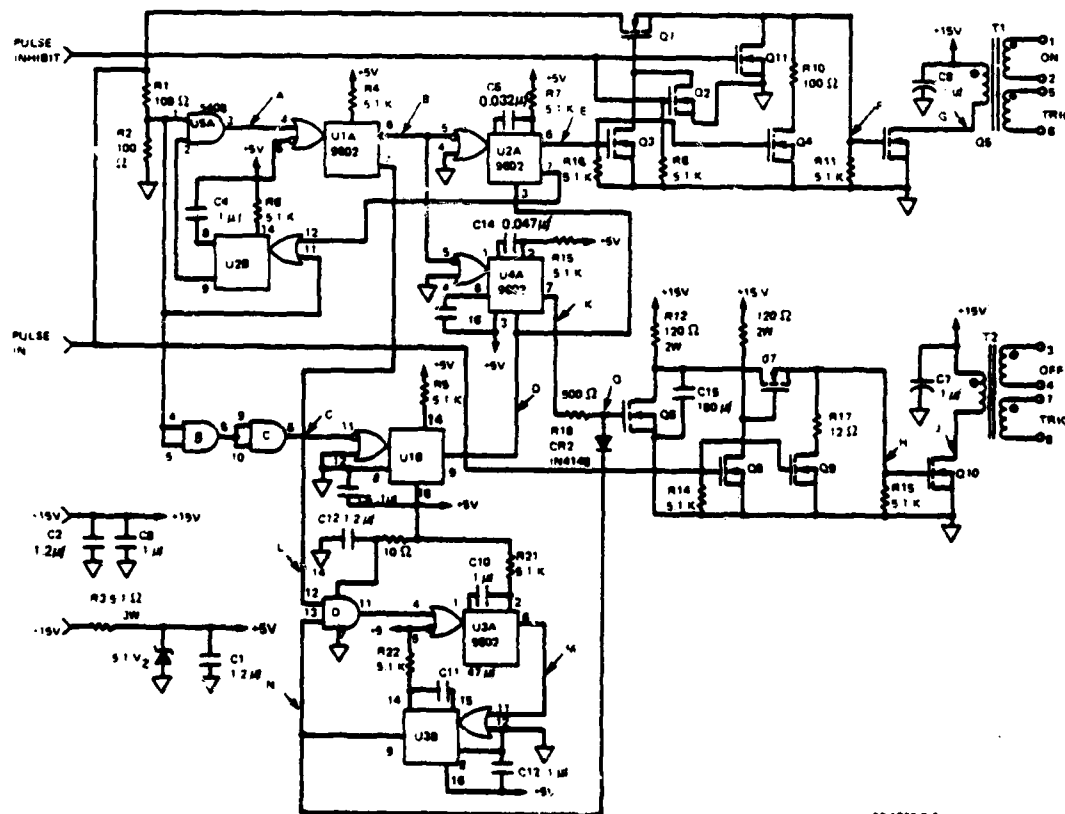
Figure 2 shows the schematic diagram for the low voltage section of the modulator, including the isolation transformers. The low voltage circuitry makes maximum use of FETs in order to maximize speed and minimize delay. The 9962 one-shots are used because of their high speed and short timing pulse capability. The following are the special design features of the low voltage section.

- One-shots U1A and U2A in conjunction with transistors Q1, Q3, and Q4 terminate the drive on Q5 approximately 150 nanoseconds after the input arrives to limit the bandwidth required for the pulse transformer T1.
- Likewise, one-shots U1A and U1B, and U4A, in conjunction with transistors Q6, Q7, and Q9 provide a similar narrow pulsewidth drive to Q10 to limit the required bandwidth for pulse transformer T2.
- One-shots U2A and U2B, in conjunction with and gate U5A, provide additional ON triggers if the incoming pulsewidth is longer than 60 microseconds. Additional ON trigger pulses are generated every 60 microseconds until the incoming pulse is terminated.
- One-shots U3A and U3B provide a similar function for the OFF trigger. If there is no input pulse within approximately 200 microseconds, another OFF trigger will be generated.
- Again, all the components used in the design are compatible with hybrid packaging, which greatly reduces the required volume.



82-1048-B-2

Figure 1. High Voltage Section



82-1048-B-3

Figure 2. Low Voltage Section

Isolation Pulse Transformers

These transformers are shown on the LV modulator schematic. The secondaries will be floating at cathode potential in actual circuit. Because of the narrow pulsewidths, only two turns are required to keep the magnetizing current to acceptable levels. This low number of turns improves leakage inductance to give a wide bandwidth transformer capable of nanosecond rise times. This is required to minimize delay and rise times.

In addition, the small number of turns allows HV wire to be used for one winding to provide the insulation between primary and secondary.

The combination of all of the above allows the size of the described transformers to be very small.

Detail Description of Circuit Operation

The timing diagram shown in figure 3 is for operation of the circuit for narrow and very wide pulses. The input pulse is shown on the top trace and all other traces are labeled by a letter which corresponds to the letters which appear on figure 2.

For pulsewidths between 0.2 and 60 μ s, the input pulse is reproduced at point (A) because input U5A/2 remains low for any pulse within this range. One-shot U1A is triggered by the rising edge of the (A) signal and the output pulse (B) is produced with the device minimum pulsewidth. The propagation delay for the 9602 is less than 50 ns. One-shot U2A is triggered on the trailing edge of U1A/6 output, and its output (E) then reproduces the input pulse with a delay of about 150 ns. This output, driving Q3 and Q4, terminates the drive to Q5 (F) which comes directly from the input, through Q1, with very little delay (less than 5 ns) and limits the maximum Q5 drive pulsewidth to approximately 150 ns.

Signal (C) is simply the input pulse delayed by the propagation of two AND gates, which is less than 25 ns. Signal (D), generated by one-shot U1/B, which is triggered on the trailing edge of (C), is used to reset one-shots U2A and U4A if the input pulse ends before the one-shot time is complete.

Signal (K) is generated by U4A one-shot from signal (B), the same as U2A; however, the one-shot time is longer than U2A. Signal (K) is used to enable the OFF drive circuitry so that when the input goes low, drive will be applied to Q10 through Q7 when Q8 and Q9 are turned off. The drive pulse will be terminated when signal (K) is reset by signal (D).

Signal (N) is generated by one-shots U3A and U3B, which act as an oscillator to produce a pulse every 200 μ s if no on trigger occurs within that period. The ON trigger is represented by signal (L).

Signal (O) is the OR'd combination of (K) and (N) and, since there is no input signal when the (N) portion is generated, a short OFF pulse drive will reach Q10 by way of Q6 and Q7.

In the high voltage circuitry shown in figure 1, the ON trigger charges the gate-to-source capacitance of Q1 to turn it ON through CR1, which blocks discharge through the transformer after the ON trigger terminates. It also turns on Q3, which discharges the gate-to-source capacitance of Q2 to turn it OFF.

When the OFF trigger is generated, the operation reverses. The OFF trigger charges the gate-to-source capacitance of Q2 to turn it ON through CR2, which blocks discharge through the transformer after the OFF pulse terminates. The OFF trigger also turns on Q4, which discharges the gate-to-source capacitance of Q1 and turns it OFF.

The spark gap and transzorb shown in the HV modulator schematic are used to protect the modulator during electron tube arcs. Capacitors C1 and C2 provide the peak currents required to charge the electron tube grid capacitance during the rapid rise and fall, and diodes CR3 and CR4 limit voltage transients which exceed B+.

For ON pulsewidths from 60 μ s up to and including CW operation, the following is a description of circuit operation.

Circuit operation is identical to that described above until one-shot U2A, which is set at 60 μ s, times out (signal (E)). This allows drive to reach Q5 (F) through Q1 when Q3 and Q4 are turned OFF. At the same time, U2B trig-

TIMING DIAGRAM LV MODULATOR

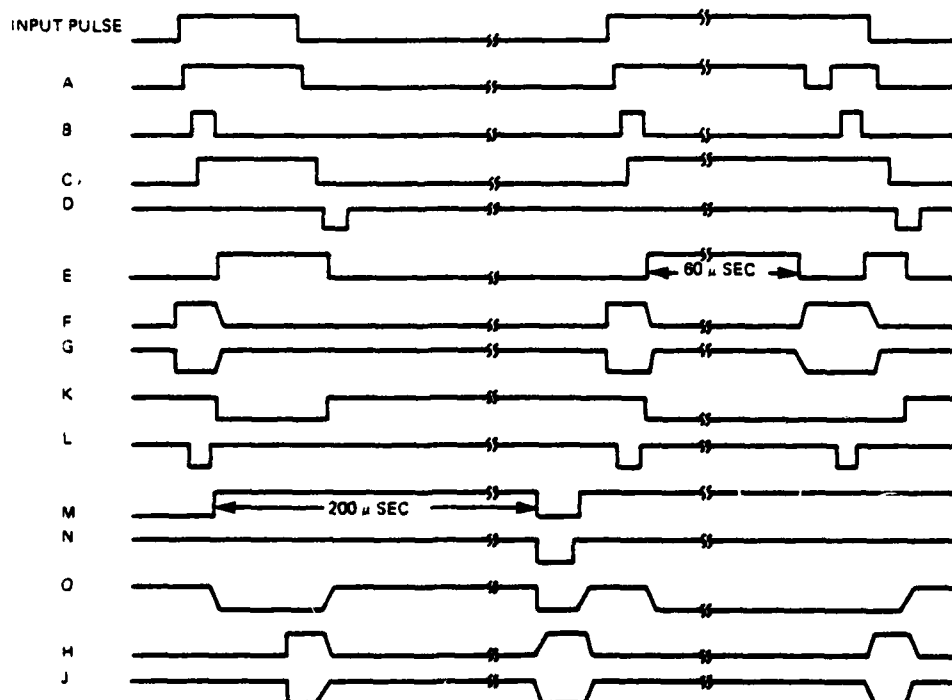


Figure 3. Timing Diagram

gers on this edge and completes a minimum one-shot timing cycle which removes the input from U5A/2 for the duration of this cycle.

When the input U5A/2 returns at the end of the cycle, it will cause one-shot U1A to retrigger, which in turn retriggers U2A to terminate the drive to Q5, [signal (F)] again. The time to complete this cycle is approximately 150 ns so that the retrigger pulses are the same width as the original.

U4A one-shot time is set longer than U2A so if the input terminates while another ON trigger is being generated, signal (K) is guaranteed to be low to allow generation of an OFF trigger.

The high voltage modulator operation is identical to the prior description. Multiple ON triggers will keep the gate of Q1 charged and the gate of Q2 discharged.

Summary of New Design Advantages

In general, the following is a summary of the design advantages which make this a truly universal design.

- Pulsewidth from 0.2 μ s to CW and large voltage swing capability allow the design to be used on a wide variety of pulse and CW transmitters for both radar and ECM applications. Voltage swing capability can be increased without redesign as higher voltage power FETs become available.
- The selection of circuit components is compatible with power hybrid packaging and requires very little volume.
- The delay times are very short and predictable, which is very important for both radar and ECM applications, and the design itself is simple and easy to build.

FAST PULSED MAGNET SYSTEMS FOR PROTON AND ANTIPROTON INJECTION INTO THE CERN 400 GeV PROTON SYNCHROTRON

E. Frick, H. Kuhn, M. Mayer, V. Rödel, G.H. Schröder, E. Vossenberg
CERN, Geneva, Switzerland

Summary

After transformation for its part time use as a pp collider, the CERN 400 GeV accelerator (SPS) is equipped with two new fast inflectors for protons and antiprotons.

The new proton inflector has been designed for injection energies up to 26 GeV and can fill the SPS with up to 5 proton batches for fixed target operation and with short proton bunches during collider operation. It consists of 12 delay line type kicker magnets of 0.7 m length each with parallel plate matching capacitors under vacuum. The magnets are powered in parallel pairs by pulses with a kick rise time of 145 ns, a duration of up to 12 μ s and a current amplitude of 2.4 kA. The pulses are generated in pulse forming networks charged to a voltage of 60 kV and discharged by double cathode thyatrons.

The antiproton inflector comprises 3 independent kicker systems which create a fast compensated bump for multiturn injection. The magnet modules are of the same design as the modules of the proton inflector. The generators consist of cable pulse forming networks of 400 ns electrical length and 2.4 kA current amplitude, each discharged by its own thyatron. The jitter of the timing is less than 5 ns over several weeks.

The design and the performances of both inflectors as well as the operational experience will be presented and discussed.

Introduction

The CERN 400 GeV proton synchrotron (SPS) has been transformed during a long shutdown in 1980/1981 for its part-time use as a proton-antiproton (pp) collider. Antiprotons at a momentum of 3.5 GeV/c are produced in a target by a high intensity proton beam which is extracted from a pre-accelerator (CPS) at a momentum of 26 GeV/c. The production efficiency is only about 10^{-6} . Therefore, more than 10^4 \bar{p} pulses are accumulated in a small storage ring for about one day to achieve sufficient intensity. Antiprotons are then pre-accelerated to 26 GeV/c in the CPS and sent to the SPS in 3 short high intensity bunches, each of 5 ns duration, via a specially built transfer line. In the SPS, which has already been filled with 3 bunches of counter rotating protons, all 6 bunches are accelerated to 270 GeV/c, the maximum energy which the SPS can achieve in d.c. operation. The particles collide then with a center of mass energy of 540 GeV at 6 interaction points of which 2 are equipped with sophisticated detectors for physics experiments¹⁾. The pp complex has been brought into operation in 1981 and its performance is now being actively developed. Experiments have been performed at a center of mass energy of 540 GeV using 2 p bunches and 1 \bar{p} bunch. Their respective intensities per bunch were $6 \cdot 10^{10}$ and $3 \cdot 10^9$ particles. The initial luminosity is about $10^{27} \text{ cm}^{-2} \text{ s}^{-1}$.

In addition to the transformation of the SPS into a pp collider, an intensity improvement program is being executed with the aim of increasing the beam intensity for fixed target operation²⁾. This program foresees to accelerate protons repeatedly in the CPS to 10 GeV/c and to place them successively around the circumference of the SPS, where they are circulating at injection

momentum until the ring is filled and the acceleration to 400 GeV/c can start. This scheme has been described in a previous report³⁾.

Apart from an antiproton inflector (MKA), these modifications and improvements of the SPS required also a new proton inflector (MKP) for two reasons:

- For pp operation, the injection momentum had to be raised from 10 GeV/c to 26 GeV/c, to avoid perturbing the short, high intensity proton bunches at transition.
- For the injection of up to 5 bunches for fixed target operation, a rise time of the magnetic field of less than 175 ns was required which is about 4 times shorter than that of the previous inflector.

This paper gives a general description of both inflector systems. Thereafter, the magnet modules and the pulse generators are discussed in more detail. Emphasis is put on the technical aspects, as the theoretical problems have been treated in a previous paper⁴⁾. Finally, the performance and the operational experience will be discussed.

System Description

The Proton Inflector

Performance requirements: The maximum required injection angle is about 5 mrad, corresponding to a kick strength of 0.43 Tm at maximum injection momentum (Table 1).

Table 1

Performance Requirements of Inflectors

	Inflector	
	Proton	Antiproton
Maximum injection momentum (GeV/c)	26	26
Deflection angle (mrad)	5	1
Kick strength (Tm)	0.43	0.087
Kick flat top duration (μ s)	1-12	0.2
	adjustable	fix
Kick rise time (ns)	175	600
Kick fall time (ns)	1300	600
Aperture (width x height, mm)		
type S	100 x 61	-
type L	140 x 54	140 x 54
Repetition rate	5 pulses, 0.65 s apart, within 12 s	2.4 s
Gas pressure in vacuum tank (Torr)	$2 \cdot 10^{-9}$	$2 \cdot 10^{-9}$

The pulse duration is determined by the different injection requirements: for fixed target operation, between 2 and 5 proton batches must be injected depending on the required intensity. Two batch injection requires a pulse duration of 11.5 μ s which must be reduced to 4.2 μ s for the injection of 5 batches. The

latter option determines the required rise time of the magnetic field integrated along the path of the protons, to about 175 ns. This latter parameter is called "kick rise time" in the following. For pp operation 3 bunches of 5 ns duration must be injected equidistantly around the SPS circumference at an energy of 26 GeV. This is done with pulses of about 1 μ s duration.

Main parameters: In view of the performance requirements given above, the main parameters of the system are chosen in the following way:

As for all other fast pulsed magnet systems at the SPS, the maximum voltage of the generators is limited to 60 kV. This level guarantees reliable operation of the thyatron switches at pulse durations exceeding 10 μ s. It allows furthermore the use of standard coaxial cables type RG 220/U, connected in parallel, as transmission line between the generators, located in an auxiliary building on the surface and the magnets, housed 60 m underground in the accelerator tunnel.

With aperture, voltage and strength of the magnetic field fixed, the system must be split into twelve independent magnet modules in order to achieve the required short kick rise time. Eight of the modules, with an aperture (vertical x horizontal) of 61 mm x 100 mm (type S), are used at the injection momenta of 10 GeV/c as well as 26 GeV/c. Their kick rise time is 145 ns. The remaining four modules which require for beam optical reasons an aperture of 54 mm x 140 mm (type L), are only required for injection at 26 GeV/c. For standardization reasons, all modules have the same magnetic length of 0.7 m. Because of the larger aperture ratio, the field rise time of the "L" modules is 220 ns.

The inductance of the magnet modules is matched to the characteristic impedance of the system by parallel plate capacitors inside the vacuum tank (delay line-type construction), in order to achieve a good pulse response with negligible reflections of the wave front. For similar reasons, a characteristic impedance of 12.5 Ω has been chosen for the magnet modules, the highest value which can be accommodated in the available space. The transmission lines are composed of 4 coaxial cables in parallel each with a characteristic impedance of 50 Ω .

The pulse generators are lumped element pulse forming networks, equipped with three switches, in order to produce pulses of adjustable duration and short fall time. For reasons of economy, two magnet modules are connected in parallel to one generator whose characteristic impedance is therefore 6.25 Ω . The parallel configuration is acceptable because the contribution of the generator to the kick rise time is small.

The electrical block diagram of one system is shown in Fig. 1. Table 2 summarizes the main parameters.

The Antiproton Inflector

Injection principle: The antiprotons are injected into the SPS through the channel which is normally used for the extraction of protons in opposite direction at an energy of 400 GeV. Before entering the first pair of kickers, (MKA 1,2, Fig. 2a), the antiprotons pass an electrostatic septum (ES) which provides a region of strong electrostatic field to deflect the incoming particles, adjacent to a region of vanishing field where the particles circulate after injection. The electrostatic field is generated between an array of wires of

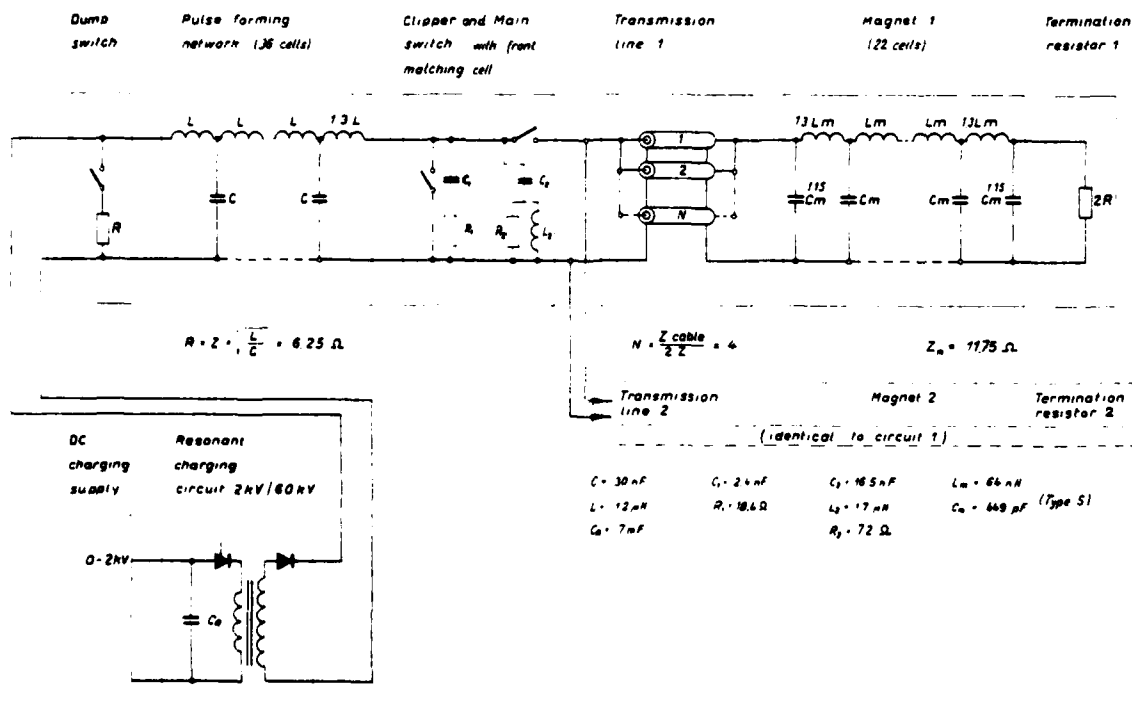


Fig 1 - Electrical block diagram of proton inflector

0.1 mm thickness (the septum itself) at earth potential and an h.t. electrode. For the injection of the first $3\bar{p}$ bunches which are equidistantly placed around the SPS circumference, only the first pair of kickers is excited.

Table 2

	Main Inflector Parameters	
	Proton	Antiproton
Maximum generator voltage (kV)	60	60
Characteristic impedance (Ω)		
generator	6.25	12.5
magnet	12.5	12.5
Current amplitude in generator (kA)	4.8	2.4
Number of magnet modules	12	5
Number of vacuum tanks	3	3
Magnetic length of module (m)	0.7	0.7
Kick rise time (2% - 98%) (ns)		
type S	145	-
type L	220	220
Kick fall time (98% - 2%) (ns)	690	220
System time jitter (ns)	< 5	< 5
Thyratron type (EEV)	CX1171B	CX1171A

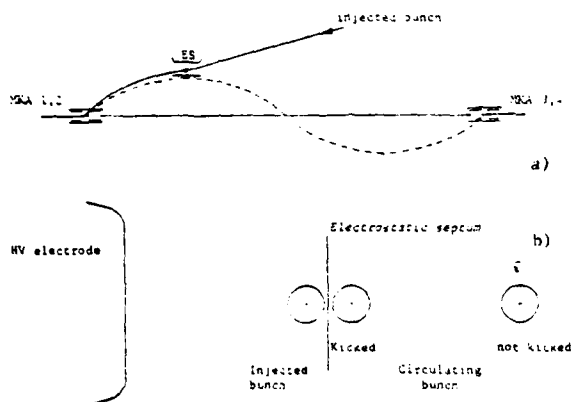


Fig. 2 - Injection of antiprotons (schematic)

- Layout
- Radial position of bunches in the electrostatic septum

To increase the particle intensity, it is foreseen to inject antiprotons up to 3 times into the same longitudinal SPS position (radial stacking). This is done in the following way: the second pair of kickers (MKA 3,4) deflects a circulating antiproton bunch and brings it in a coherent betatron oscillation near to the zero field side of the septum. The timing of the next injection is then arranged such, that at the same moment a new bunch arrives through the injection channel at the septum's high field side (Fig. 2b). Both bunches

whose centers are roughly 1 bunch diameter plus the septum thickness apart, travel then to the first kicker pair, one betatron wave length downstream from the second pair, where the oscillation is cancelled. A fifth kicker is necessary, when the wave length of betatron oscillation is not equal to the distance between the two pairs of kickers.

Main parameters: The pulse duration of the \bar{p} -inflector can in principle be very short, as the antiproton bunch length is only 5 ns. Nevertheless, a kick flat top duration of about 200 ns has been chosen to avoid deflection errors due to jitter or drift of the anode delay time of the electronic switches. As protons are injected prior to antiprotons, the kick rise and fall times must be shorter than 600 ns to avoid deflecting the counter rotating protons. The injection angle is about 1 mrad corresponding to a kick strength of 0.086 m Tm at an energy of 26 GeV (Table 1).

For standardization reasons, the design of the magnet modules is the same as for the modules of the proton inflector. Each module has its own cable pulse forming network with a characteristic impedance of 12.5 Ω , charged to a maximum voltage of 60 kV and discharged by a ceramic thyratron. The main parameters are listed in Table 2.

The Magnet Modules

Electrical Circuit

The electrical circuit of the magnet has been designed by means of computer modeling in order to obtain an optimum pulse response. Only circuits in which the inductance of the one-turn conductor is subdivided into several sections which are connected to capacitors to form a matched LC ladder network, give an acceptable pulse response⁴⁾. The adopted circuit is composed of 22 cells. This is a compromise between the requirements for pulse response and size of the capacitor plates.

Yoke configuration

For the yoke cross-section, a C-shape was chosen with shims at the edges of the pole profile near the open side of the gap, to improve the field quality in radial direction (Fig. 3). The return conductor is essentially inductance free and can be earthed at the magnets input and output. Compared to a window-frame magnet, the C-shaped cross-section allows therefore to use coaxial feedthroughs with earthed outer conductors. It avoids furthermore the risk of flash-over between the conductors along the ferrite surfaces.

Construction

The high rate of current rise calls for a high resistivity Ni-Zn ferrite as magnetic material. The Philips type 8C11 has been chosen because of its high saturation induction ($B > 0.3$ T at 100°C and 20°C) and its low coercitive force ($H_c < 0.25$ Oe). This material has furthermore excellent vacuum properties due to its low porosity ($\rho > 5.1$ g/cm³). It is manufactured in C-cores of overall dimensions 195 mm x 136 mm x 26 mm. Twenty-two of these bricks, interleaved with AlMg3 plates of about 40 cm x 50 cm area, form the h.t. part of the magnet module, with a length of about 0.7 m. On each side of these capacitor plates, at a distance of about 4 mm, similar AlMg3 plates are mounted as earth electrodes of the matching capacitors.

The characteristic impedance of the system is determined by adjusting individually the distance between the capacitor plates. A photograph of the magnet assembly is given in Fig. 4.

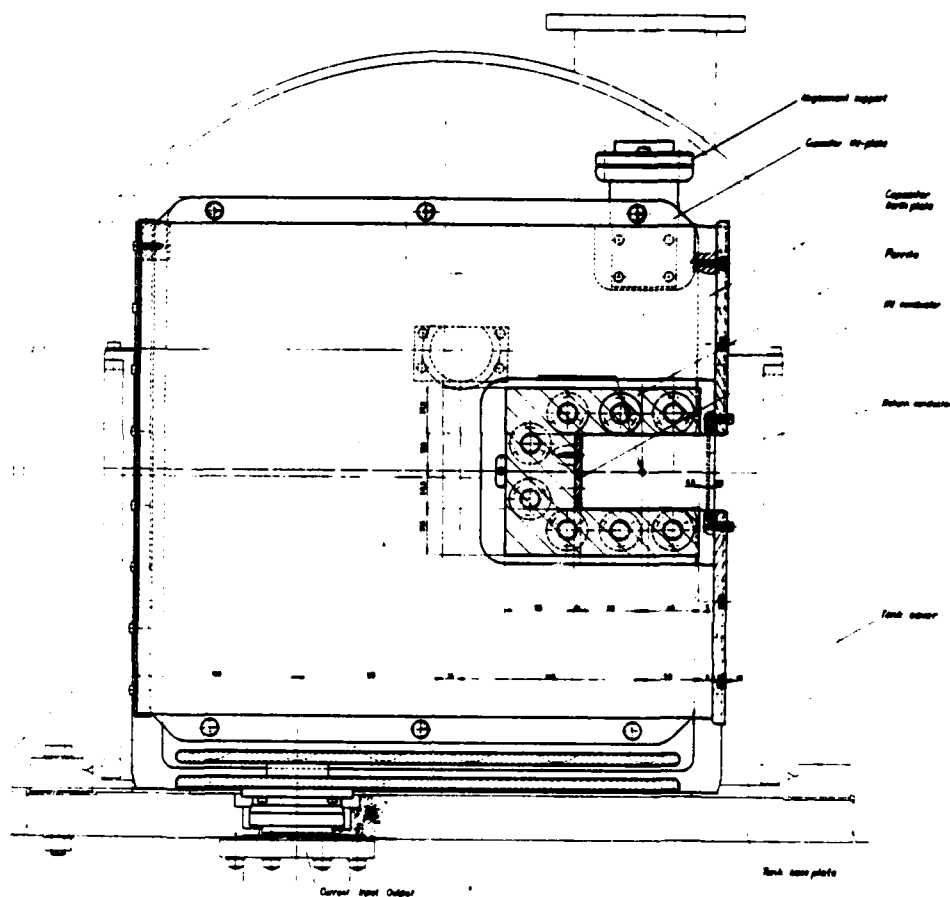


Fig. 3 - Cross-section of the magnet module type S in its vacuum tank

The magnet is excited by a one-turn high voltage conductor of 61 mm height and 5 mm width (type S), fixed tightly into the ferrite gap and providing the interconnections between the h.t. capacitor plates (Fig. 3). The earthed return conductor of 2,5 mm thickness is placed in front of the open side of the C cores at a distance of 6.5 mm from the ferrite. It is fixed to support-plates which form the base of the earth electrodes of the capacitors. In case of bad steering, the proton beam can hit the return conductor. To avoid damaging the magnet module, the return conductor is made of beryllium, into which, due to its low density, only a small amount of beam energy can be deposited.

The Vacuum Tank

All magnet modules are housed in vacuum tanks of omega cross-section. The 3 tanks of the proton inflector are each about 3.5 m long and contain 4 modules (Fig. 5), whereas 2 modules are housed in each of the 2 shorter tanks of the antiproton inflector. The modules are positioned and aligned in a common frame which poses at 3 points on the base plate of the tank. The omega shaped cover has the same diameter of 0.7 m for all tanks and is equipped with flanges for alignment-supports and connections to the adjacent vacuum chambers. An 8 m long aluminium gasket of diamond cross-section provides the vacuum tightness between base plate and cover.

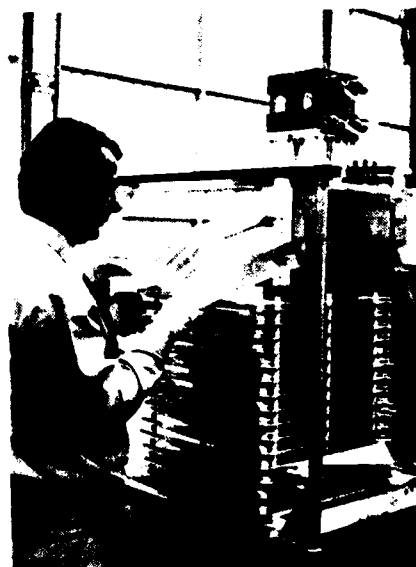


Fig. 4 - Assembly of a magnet module

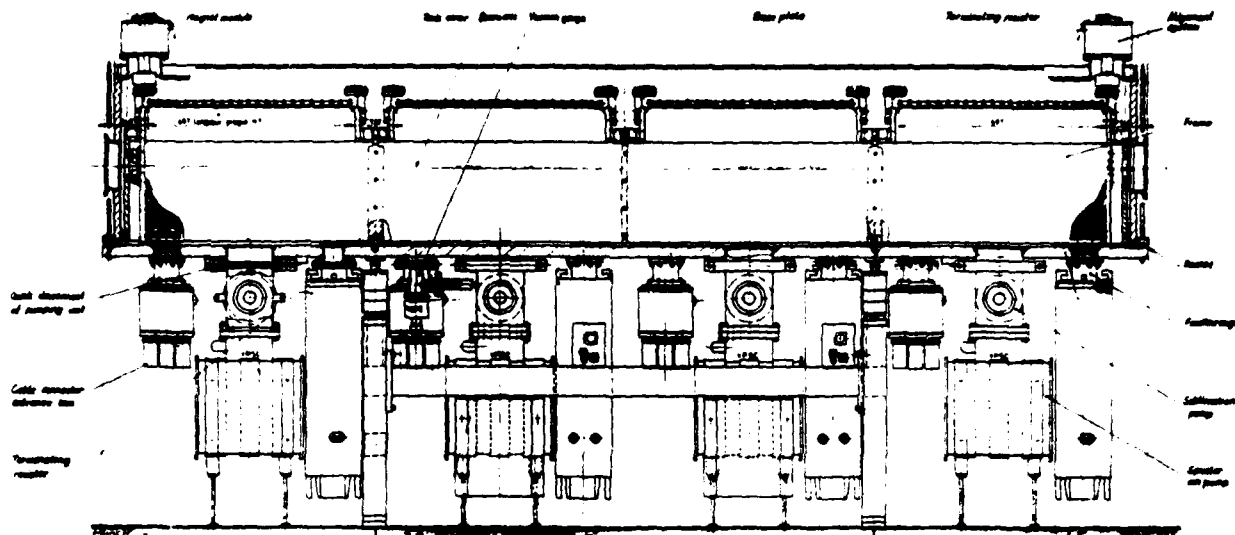


Fig. 5 - Longitudinal section through the vacuum tank of the proton inflector, showing 4 modules in their frame, terminating resistors and vacuum pumps

The tanks are made of electro-slag-refined stainless steel, type 304L, and despite their size have been stress relieved at a temperature of 960° C. The long tanks are equipped with 4 sputter ion pumps with a pumping speed of 360 l/s each. In addition, 4 titanium sublimation pumps are used to shorten the pump down time. For the smaller tanks, half the number of pumps provide about the same specific pumping speed. To achieve the design pressure of $2 \cdot 10^{-9}$ Torr, all metallic surfaces (about 100 m² per large tank) undergo a thorough chemical cleaning procedure. The ferrite blocks are backed at 400° C under vacuum prior to assembly. Fig. 6 shows the positioning of the modules into the frame of a large tank.



Fig. 4 - The 4 modules of the proton inflector on the base plate of the vacuum tank

Terminating Resistor

The first and last capacitor plate of the magnet are connected via short matched striplines to coaxial feedthroughs in the base plate of the vacuum tank. On the input side, a silicone insulated connector box with 4 coaxial h.t. sockets receives the cable connectors of the transmission line from the pulse generator. On the output side, a coaxial matched resistor has a particularly low stray inductance and is designed to hold a voltage of 30 kV. It is built up of 10 Allen-Bradley ceramic resistor discs, each 1 inch thick with 3 inches outer diameter and a central hole of 1.25 inches, mounted in a coaxial housing and insulated and cooled with silicone fluid. The discs are interleaved with flat metallic spirals which provide a good electrical contact and permit an efficient flow of the cooling liquid. A resistor of similar design has been described previously⁵⁾.

The Pulse Generators

The Proton Inflector

The requirements on the excitation pulse call for a lumped element pulse forming network (PFN) discharged by 3 switches: A "main" switch initiates the discharge, a "clipper" shortens the tail of the pulse and a "dump" switch discharges any residual energy of the pulse forming network. To achieve short rise and fall times, stray inductances between switch and pulse forming network must be minimised. Therefore, the switches are mounted directly on top of the PFN (Fig. 7). To avoid interference between them, all switches are housed in their own metallic tank (Fig. 8) and are branched through separate coaxial "plug-in" connections to the appropriate position of the PFN. This type of construction allows in addition a rapid exchange of switch tanks in case of thyatron faults.

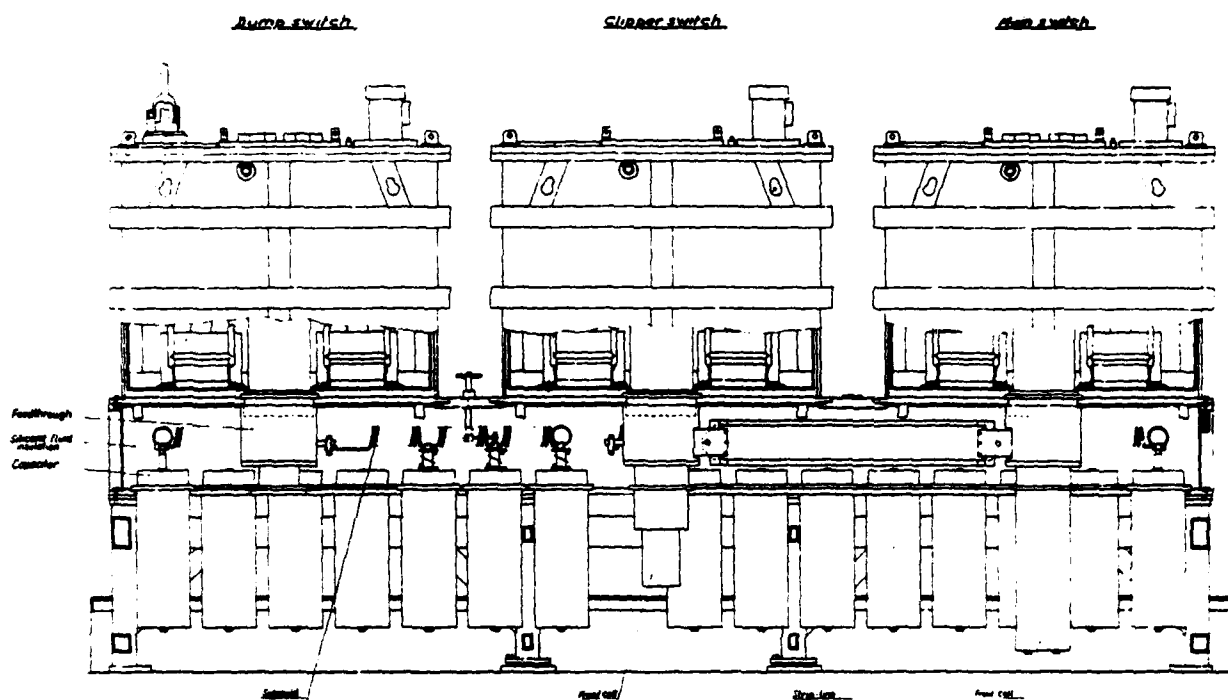


Fig. 7 - Mechanical assembly of the pulse generator of the proton inflector

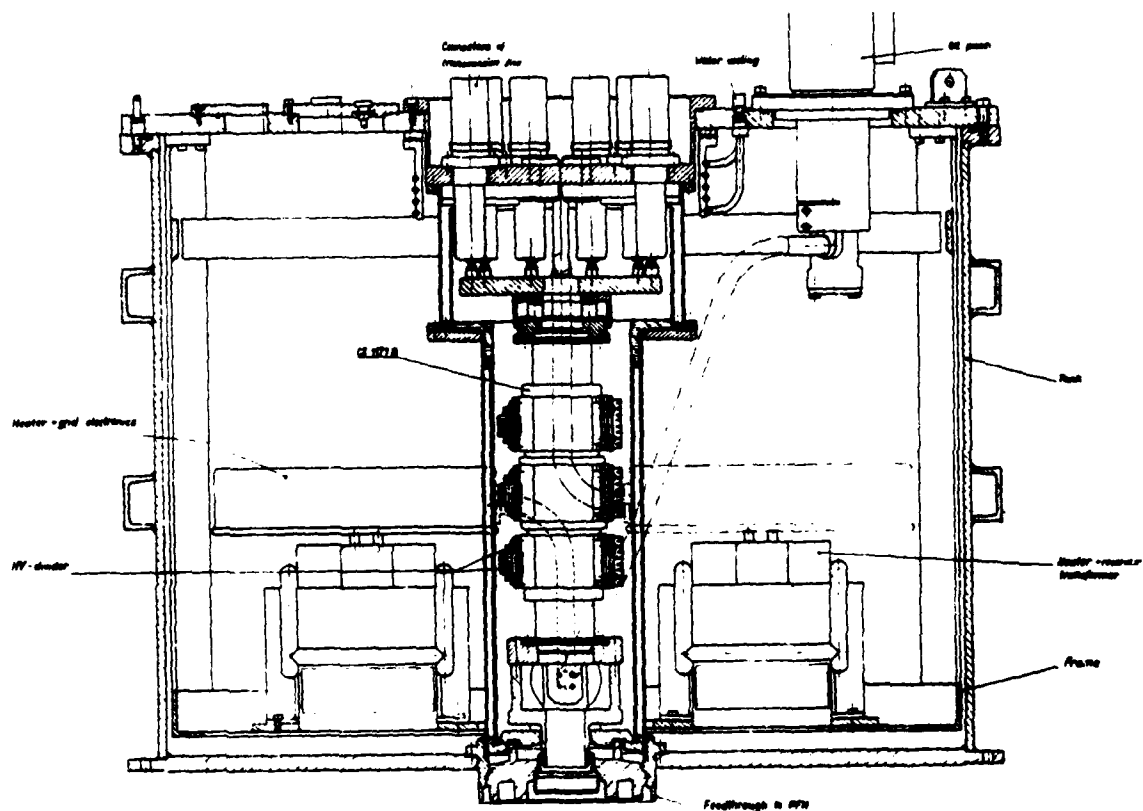


Fig. 8 - Assembly of a thyratron tank

The physical separation between the anodes of main and clipper switches introduces, however, an unwanted stray inductance which is suppressed by connecting both anodes via a matched stripline. The 36 cells of the PFN are arranged in 24 rows. They are composed of capacitors of 30 nF and solenoids of 1.17 μ H, giving a characteristic impedance of 6.25 Ω . The capacitors of cylindrical shape have an insulating outer case and are mounted over nine tenths of their length into metallic pots which are fixed vertically into the base plate of the PFN tank. Constructional details of the prototype generator have been reported previously³⁾.

The switches are three-stage ceramic deuterium filled thyratrons with 2 cathode assemblies, type EEV CX1171B. Double ended thyratrons are required because of the large product of flat top current and pulse duration (4.8 kA x 12 μ s) which cannot be handled by single ended tubes.

Two pulse generators are charged in parallel by one resonant charging power supply⁵⁾. The resonant charging allows to operate the thyratrons at a higher gas pressure. This measure decreases their plasma formation time and hence the rise time of the current pulse. It reduces furthermore the risk of quenching and prolongs therefore the lifetime.

The Antiproton Inflector

The short excitation pulse is generated in a cable pulse forming network of 40 m length, composed of 4 coaxial cables in parallel, each with a characteristic impedance of 50 Ω . This PFN is discharged through a three stage ceramic thyatron, type EEV CX1171A. The cable, manufactured by Felten & Guillaume, Cologne, has an outer diameter of 46 mm, an ionization inception voltage above 45 kV_{RMS} and an attenuation at 30 MHz of 1dB/100 m. Its solid inner copper conductor is fitted with a semi-conducting layer, over which the low density polyethylene insulation is extruded in one passage. A thin layer of brushed graphite is applied to the outer polyethylene surface, to improve the voltage holding. Two aluminium foils, one mounted axially, the other wrapped tangentially, form together with a tinned copper braid the outer conductor. Due to its comparably high impedance and its braided outer conductor, the cable has a bending radius of only 0.7 m which facilitates handling and installation.

The coaxial cable connector, designed for a withstand voltage of 60 kV, is a constructional element of particular interest. The connector socket on the tank has an epoxy insulator with a conical aperture, into which the cable plug is fitted under high axial pressure. To avoid breakdown via air gaps along the mating surfaces between socket and cable plug, a soft polyurethane layer is moulded onto the conically machined polyethylene insulation of the cable (Fig. 9). The same design is used for the smaller RG 220/U connectors. More than 600 of these connectors are in use in the SPS and their operational reliability is excellent.



Fig. 9 - Cable plug with polyurethane layer

For reasons of short pulse rise time, also the antiproton inflector is equipped with resonant charging power supplies.

Performance

Magnets

The kick of the magnetic field is measured at a voltage of 20 V by integrating the voltage difference between the first and last capacitor plate using a trapezoidal pulse with appropriate rise time. Complementary measurements are made with a matched stripline probe. The probe measurements are then repeated at high voltage. Fig. 10 shows the kick rise time of a proton inflector module (type S) at a generator voltage of 60 kV; Fig. 11 gives the kick signal of the \bar{p} inflector derived from low voltage measurements.

The non-uniformity of the magnetic field across the horizontal plane is determined in computer simulations and checked with a.c. probe measurements. Apart from a small region near the return conductor which cannot be occupied by the beam, the non-uniformity is negligibly small.

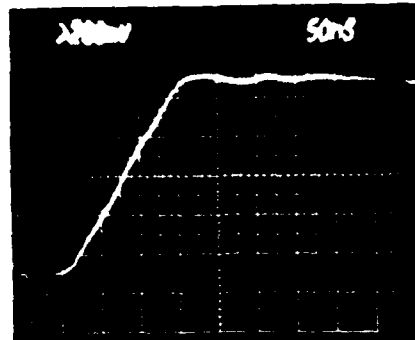


Fig. 10 - Kick rise time of the proton inflector (module S) measured at a generator voltage of 60 kV

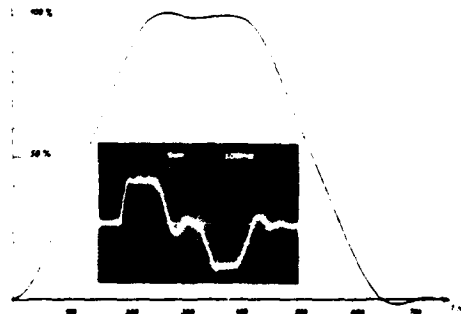


Fig. 11 - Kick signal of antiproton inflector, derived from low voltage probe measurements

The electrodes of the h.t. capacitors with a total area of 15 m^2 per module under an electrical stress of up to 75 kV/cm , are conditioned with d.c. rather than pulsed voltage. Because of the large electrode area and the correspondingly large predischage current at high voltages, the current is programmed to raise linearly, until a spark occurs or a present voltage of 35 kV , corresponding to a stress of 85 kV/cm , is reached. After each conditioning spark the current amplitude restarts at zero. Compared to a constant conditioning current, a raising current results in a more regular increase in voltage holding. This conditioning method has been found much faster and more efficient than the usually applied conditioning with a pulsed voltage.

Although tests on a full scale prototype module had shown excellent voltage holding at stresses up to 120 kV/cm , the withstand voltage of the final modules was initially insufficient due to magnesium oxide particles which stuck loosely to the AlMg3 electrode surface and were not removable with chemical cleaning methods. On the prototype plates which came from a different deliver batch, these particles had not been found. Etching away a layer of $20 \mu\text{m}$ thickness from the electrode surface in an aqueous solution of caustic soda cured this problem. Though the etching increased the surface roughness, all modules could be reliably conditioned at voltages exceeding 35 kV .

Pulse Generators

The flat top ripple of the long pulse of the proton inflector is minimised to less than $\pm 1\%$ by adjusting at low voltage the inductances of the solenoids while the pulse forming network is discharged with a mercury wetted relay. Prior to installation each pulse generator is tested at design voltage with 10^5 pulses. A typical oscillogram of the current in the termination resistor is shown in Fig. 12. Because of the large product of current amplitude and pulse duration, it is important that the main thyatron operates at a high reservoir voltage to avoid short current interruptions in the pulse flat top (quenching).

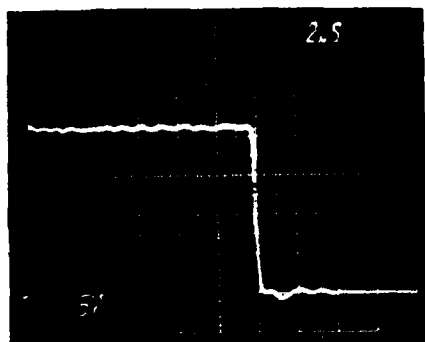


Fig. 12 - Current pulse of the proton inflector measured on the termination resistor

Fig. 13 shows the 6 pulse generators of the proton inflector installed in their auxiliary building.



Fig. 13 - The 6 pulse generators of the proton inflector system installed in the auxiliary building

Operational Experience

Both injection systems are in operation since June 1981 and work as anticipated. Thanks to the thorough life testing of all components prior to installation, the operational reliability of the complex systems, containing 23 ceramic thyatrons, 250 m^2 of h.t. electrodes and 26 racks of electronics, is excellent.

The inflectors are remotely controlled from the SPS control room via several sets of computer programs, written in the interactive language NODAL. One group of programs sets directly parameters of the inflectors, e.g. it turns on the mains, sets the charging voltage or the trigger instant and surveys the status of more than 50 interlocks. It gives alarms in case of faults. Other programs are written for a higher operation level, e.g. the operator chooses the type of injection required and the computer selects then the settings of the inflector system.

The oscillograms of the kicker signals can be displayed via BIOMATION transient recorders on the TV screens of the control room, together with signals of the beam current. This information is very useful for the detection of injection timing errors. A remotely controlled signal switching matrix connected to every transient recorder, allows to select 2 out of 16 signals for simultaneous display. The optimum BIOMATION display settings of each signal are stored in the computer together with the name of the signal and loaded into the transient recorder, when a specific signal is selected. This procedure ensures always a correct display of signals with different amplitudes, durations and trigger instants and facilitates substantially the operation of transient recorders. Fig. 14 shows a TV display of the standard two-batch injection scheme.

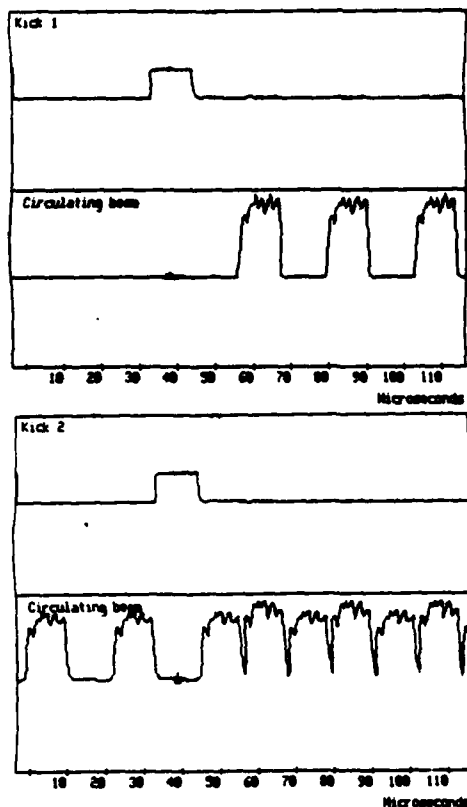


Fig. 14 - Two batch injection into the SPS
upper trace: magnetic field pulse of inflector
lower trace: proton beam intensity.

- a) injection of the 1st batch; half of the circumference is filled; 3 turns are displayed; (the delay of about 23 μ s between the signals of inflector and beam current meter is due to the time of flight between both elements).
- b) injection of the 2nd batch 1.2 s later.

References

- 1) J. Gareyte, The CERN P-F Complex, XIth Int. Conf. on High Energy Accelerators, CERN, 1980.
- 2) M.C. Crowley-Milling, B. de Raad, Proposal to Increase the Intensity of the SPS, CERN SPS/AC/77-12.
- 3) H. Kuhn, G.H. Schröder, High Power Pulse Generators for Fast Pulsed Magnets - Development and Operational Experience, 14th Pulse Power Modulator Symposium, Orlando, 1980.
- 4) H. Kuhn, G.H. Schröder, J-C. Soulié, SPS Inflector for Multibatch Injection, CERN/SPS/ABT/Int. 77-1.
- 5) P.E. Faugeras, E. Frick, C.G. Harrison, H. Kuhn, V. Rödel, G.H. Schröder, J-P. Zanasco, The SPS Fast Pulsed Magnet Systems, 12th Modulator Symposium, New York, 1976.

Acknowledgements

We would like to thank B. de Raad for many fruitful discussions and W.C. Middelkoop for his continuous support. We furthermore acknowledge particularly the contributions of J. Busetta, R. Chappuis, A. Lamouille, R. Oberli and R. Tröhler, who assembled, tested or installed the deflectors, J. Bonthond, J-L. Bretin and J-P. Zanasco, who designed and constructed the electronics and H. Verhagen who wrote the computer programs.

Finally, we wish to thank H. Menown and R. Snelling of English Electric Valve for their close collaboration.

H5 FAST KICKER MAGNET PULSER*

W. Frey, S. Ghoshroy and J.G. Cottingham

Brookhaven National Laboratory
Associated Universities, Inc.
Upton, New York 11973

Summary

The fast extraction kicker magnet for the AGS is powered by a novel pulse generator. A pulse forming network (PFN) is discharged into nearly 100 percent mismatched load. The pulser delivers a current pulse of 3000 amperes peak pulse with a 2 percent flat-top ripple into a 1.4 μ H single turn ferrite core magnet. The pulse is 2.8 μ sec wide with a 180 nsec rise time, at a 0.5 to 1.5 pps repetition rate. The pulse rise time is required to provide clean extraction of the 28 GeV proton beam by bringing the kicker magnet field up to 1.25 kG within the 220 nsec space between proton bunches in the machine.

The pulser is mounted adjacent to the kicker magnet in the AGS ring. The thyatron's characteristics are not affected by the ionizing radiation environment during operation of the AGS (Alternating Gradient Synchrotron).

Introduction

The fast extraction magnet for the AGS is a single-turn ferrite core magnet. The magnet must reach a field strength of 1.25 kG within the 220 nsec space between proton bunches in the machine. The pulser that drives the kicker magnet will have to have the following pulse parameters:

- 3000 A peak pulse current
- 2.8 μ sec pulse width
- 180 nsec rise-time (10% to 90%)
- 2% flat top ripple
- 0.5 to 1.5 pulses per second

The inductance of the kicker magnet is 1.4 μ H. Assuming 0.2 μ H stray lead inductance, the pulser will have to drive a load inductor of 1.6 μ H with dc resistance less than 1 milliohm. The minimum voltage step required to get the magnet current up to 3000 A in 160 nsec is:

$$V = L \frac{di}{dt} = 30 \text{ kV}$$

A standard matched load pulser with the same characteristic impedance would require a PFN voltage of 60 kV.

Figure 1 is a simplified schematic diagram of a typical kicker magnet pulser. The pulser of this design will have to be mounted outside the ring since ionizing radiation levels in the ring will degrade the dielectric properties of most dielectric fluids used as insulation.

However, since the magnet is a current device, the maximum current transfer from the PFN to the load inductance will occur when either the terminating resistor or the network impedance is reduced to zero. Hence we cannot reduce the network impedance to zero

we will reduce the terminating resistance to zero. In this mismatched mode, the current delivered by the PFN to the inductor is limited only by its characteristic impedance. Therefore, for a PFN voltage of 30 kV, a PFN characteristic impedance 10 Ω will deliver 3000 A into an inductor load. The PFN voltage will be approximately 30 kV so air can be used as an insulator for the PFN, and the PFN can be moved down into the ring next to the magnet. Since the switch and PFN can be mounted very close to the magnet, this configuration will have the least amount of stray inductance. The mismatched PFN will have a faster rise time than a matched line (see Appendix A). Figure 2 is a simplified schematic diagram of the mismatched pulser.

Design

Figure 3 is a simplified schematic of the H5 pulser. The network impedance of 9.7 Ω was selected to ensure a nominal 3000 A pulse with less than 30 kV on the network. The network is a Guillemin E type with a 0.005 μ F speed up capacitor at the input. The first section of the network is 1/2 delay section to aid in trimming the rise-time. Resistors are paralleled with the inductors to fine tune the top of the pulse.

The PFN was designed using the standard design equations to determine network capacitance and inductance, ($C_n = \frac{1}{2Z} = 0.144 \mu\text{F}$ and $L_n = \frac{1}{2Z} = 13.6 \mu\text{H}$). Since the magnet inductance is part of the solenoid inductance, the solenoid inductance is reduced to 12 μ H. Low-level testing indicated that a minimum of 10 sections would be needed to get the flat-top ripple down to 2%. Thus, a 12 section solenoid with 1 μ H/section and 0.011 μ F/section was selected.

The front end of the network was tailored to provide the maximum current rise-time through the magnet. The speed-up capacitor of 0.005 μ F is a compromise between discharge current and rise time.

A 1/2 time section was used to follow the speed-up capacitor to control the shape of the front of the pulse. Damping resistors in parallel with the inductors were used to get the ripple down to 2% after the inductances were adjusted.

The mismatched PFN will charge to $-100\% V_{\text{PFN}}$ unless an inverse diode and a line terminal resistor is used at the open end of the line. With the inverse circuit the capacitors can be rated for 50% voltage reversal instead of 100% voltage reversal. The inverse diode also limits the inverse voltage on the main switch tube at the end of the current pulse. The inverse diode is connected as shown to prevent inverse current flowing through the magnet. Tetrode thyatrons, CX1154, are used as the main switch and the inverse diode.

Due to space limitation, (the kicker is in a 3-foot straight section in the H superperiod of the AGS

*Work performed under the auspices of the U.S. Department of Energy.

ring), the PFN had to fold back on itself. Figure 4 is a photo of the prototype unit, and Figure 5 is a photo of the kicker mounted in the ring.

Performance

The prototype pulser has been in operation for several months. Figure 6 is typical current pulse and Fig. 7 shows the pulse rise time. Figure 8 illustrates the voltage across the magnet referenced to the current pulse. Figures 9 and 10 illustrate the voltage across the switch tube referenced to the pulse current.

The prototype unit received an estimated total radiation dose of 10^9 rads during operation at an estimated rate of 10^5 rad/hr. There was no noticeable degradation of thyratron performance during operation. The prototype used pulse capacitors with a mineral oil wetting agent. The capacitors failed as a result of radiation exposure. Radiation causes the mineral oil to change its physical and electrical properties. The capacitors failed mechanically before electrical failure. Radiation causes gases to be liberated from the oil and this eventually burst the phenolic case. Reconstituted mica pulse capacitors are being evaluated to determine whether there is any radiation effects on capacitor performance.

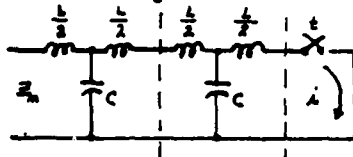
Acknowledgement

The authors wish to thank D. Warburton, and S. Bennett who built and tested the prototype. We also wish to thank J. Keane for his suggestions and support during the program.

Appendix 1

Comparison of Mismatched and Matched PFN Discharge Characters

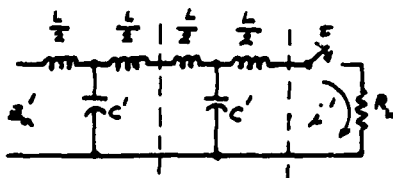
The artificial transmission line (PFN) can be represented by a ladder of T equivalent section of equal characteristic impedance. The rise time of the network is determined by the 1st section elements in the discharge



A. Mismatched Line

$$Z_n = (L/C)^{1/2}$$

$$i = \frac{V_{PFN}}{Z_n}$$



B. Terminated Line

$$Z' = R_L = (L'/C')^{1/2}$$

$$i' = \frac{V_{PFN}}{R_L + Z_n} = \frac{V_{PFN}}{2Z_n}$$

For the conditions of $L = L'$, $i = i'$ and $V_{PFN} = V'_{PFN}$ then

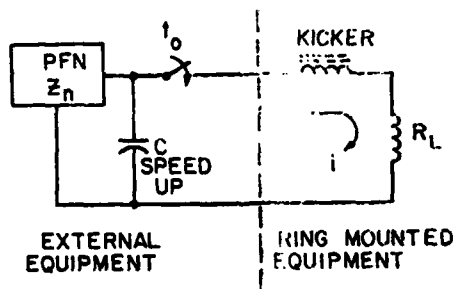
$$Z'_n = \frac{1}{2} Z_n$$

$$(L'/C')^{1/2} = \frac{1}{2} (L/C)^{1/2} \text{ but } L = L'$$

$$\frac{L}{C'} = \frac{L}{4C}$$

$$\Delta C' = 4C$$

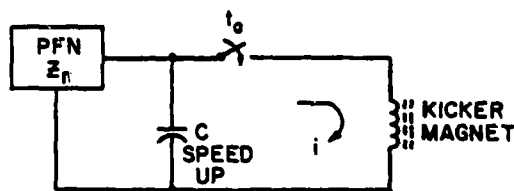
Measurements on several low impedance (about 10 to 15 ohms) indicate that the mismatched line will have a slightly faster rise than a matched line of 1/2 the characteristic impedance. The mismatch line rise time was 0.8 the rise time of a matched line of 1/2 the impedance.



$$R_L = Z_n$$

$$i = \frac{V_{PFN}}{R_L + Z_n}$$

Figure 1 - Typical Kicker Magnet Pulser



$$i = \frac{V_{PFN}}{Z_n}$$

Figure 2 - Mismatched Pulser

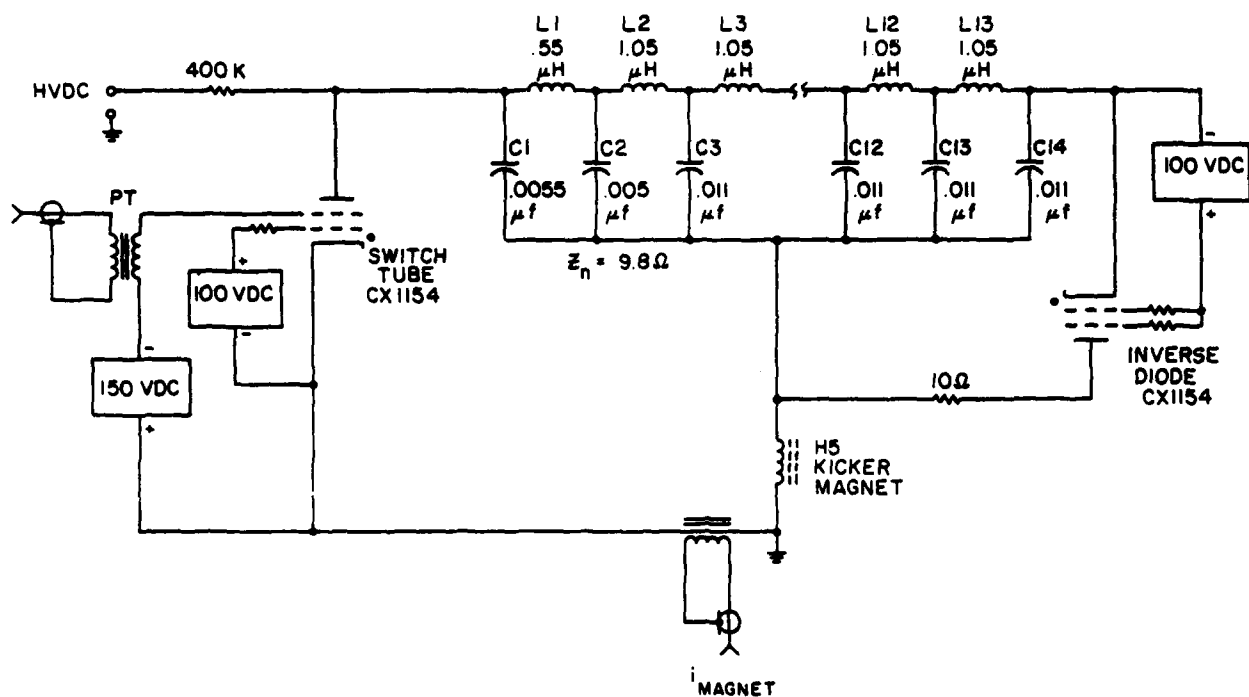


Figure 3 - Prototype H5 Kicker Magnet Pulser, Simplified Schematic

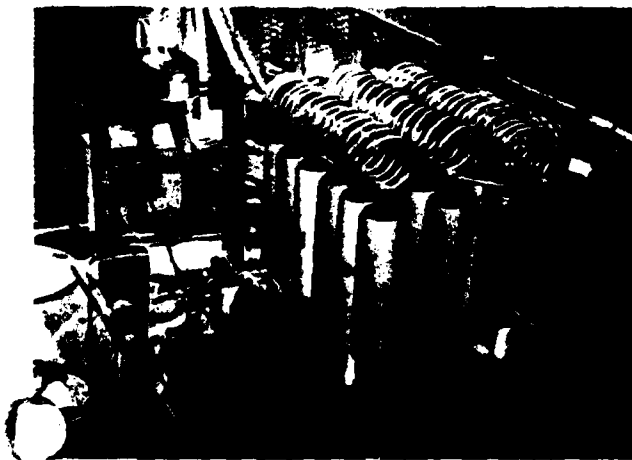


Figure 4 - Prototype H5 Pulsar

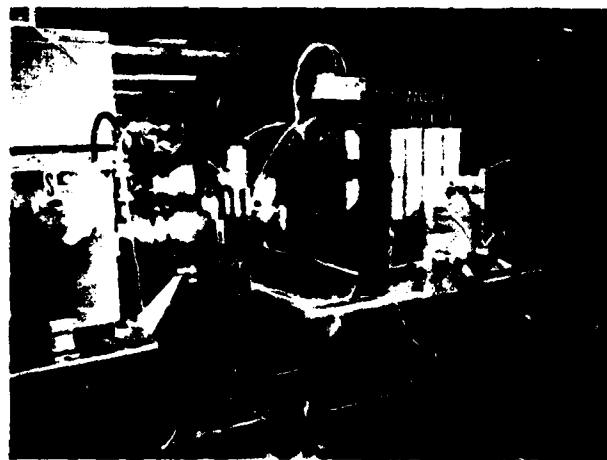


Figure 5 - Pulsar Mounted on H5 Kicker Magnet in AGS Ring

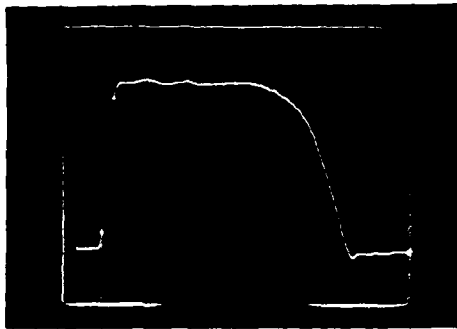


Figure 6 - Magnet Current Pulse; 3000A Peak, 500 nsec/cm

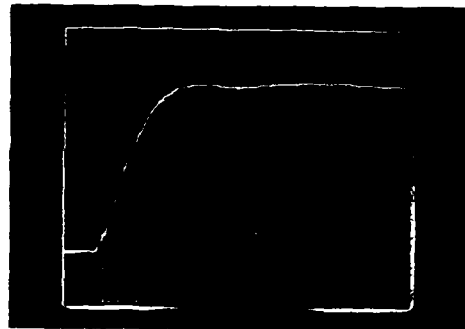


Figure 7 - Magnet Current Rise Time; 3000A Peak, 100 nsec/cm



Figure 8 - Upper Trace - Magnet Current
Lower Trace - Voltage Across HS Magnet
Time Base - 1 μ sec/cm

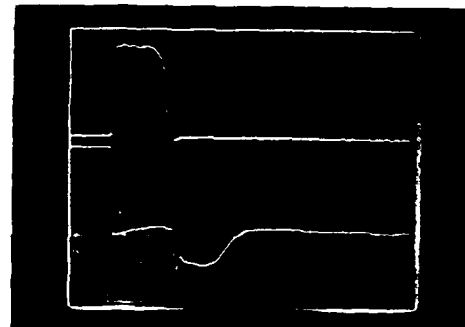


Figure 9 - Upper Trace - Magnet Current
Lower Trace - Voltage Across the Switch Tube
Time Base - 2 μ sec/cm

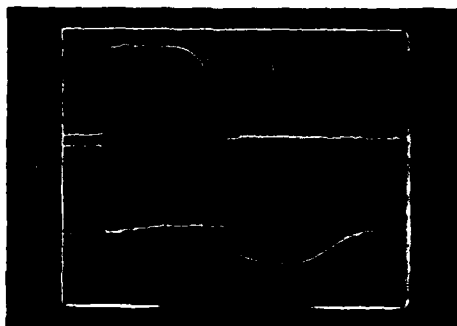


Figure 10 - Upper Trace - Magnet Current
Lower Trace - Voltage Across the Switch Tube

DESIGN OF A FAST-RISE SLOW-FALL MAGNET MODULATOR*

R.F. Lambiase

Brookhaven National Laboratory
Associated Universities, Inc.
Upton, New York 11973

Brookhaven National Laboratory is now in the process of expanding the capability of the AGS to include the acceleration of polarized protons.¹ One of the requirements to accomplish this is to pulse twelve quadrupole magnets to rapidly cross depolarizing resonances (see Figure 1). Having crossed the resonance, the field in the magnet must be maintained so as not to re-cross the resonance.

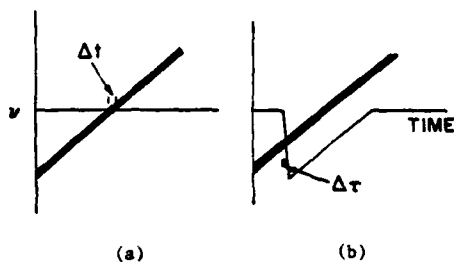


Fig. 1 - a) Normal resonance crossing
b) Rapid intrinsic resonance crossing by pulsing the vertical betatron frequency, ν

The parameters of the AGS require a magnet current pulse with a 2 μ s rise (dictated by the maximum permissible depolarization) and a 3 ms fall (determined by the rate of momentum change during acceleration). Eight of these pulses will be required during the acceleration of the protons. The first of these pulses will have a peak amplitude of +140 amps. Each succeeding pulse will be progressively larger and opposite in polarity of the preceding pulse, until the eighth pulse is generated with a -2,250 amps peak.

The problem is addressed with two mirror-image circuits, one to produce positive pulses, and the other negative. Each of these circuits are further divided into two sections, one to cause the rapid rise, and the other to maintain the slow fall.

The rapid rise is accomplished by discharging a 0.25 μ F capacitor into the 7 μ H, though approximately 17 kV is required to reach the maximum currents. One approach to the slow fall is to crowbar the high voltage capacitor with a large low voltage capacitor. This circuit is shown in Figure 2. The capacitor to ring with a quarter wavelength of three milliseconds would have a value of 0.6F, and would ideally be charged to exactly compensate for the arc drop of the thyatron switch tube. Since the 0.6F is such a large storage element as compared to the 7 μ H load, voltage mismatches between the thyatron arc drop and the voltage on the capacitor of less than one-half will result in unacceptable load current variations. In addition, the thyatron should be switched at a time where the anode voltage is less than 100 volts. It will not operate at this level.

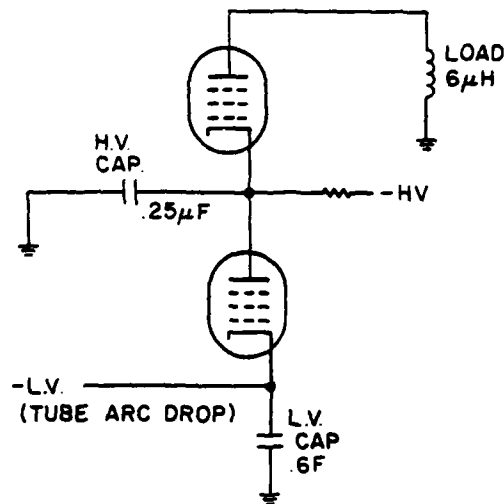


Fig. 2 - Capacitive slow-fall circuit

These drawbacks are overcome by using an inductor or as current source in the low voltage circuit. The simplified schematic of Figure 3 is used to demonstrate the operation of this circuit for one amplitude of a single polarity. The cycle starts by charging C1 to +200 volts. SCR1 discharges C1 in L1. When L1 is fully charged, SCR2 switches in C2 which has previously charged to -500 volts. This turns SCR1 off. As current continues to be drawn from C2, the voltage on V2's cathode drops rapidly. The current levels are programmed such that when the voltage at this point reaches -750 volts, the current in the inductor is at the desired peak current. Then V1 is fired discharging C4 in the load. When C4 is at zero volts (peak current) V2 is fired. Just prior to firing, there is 750 volts across V2, which is sufficient for reliable firing. When this tube turns on, the resulting voltage stop shuts off SCR2, and L1 maintains the current in the load. The C2-R2 combination balances any initial imbalance between the load current and the current in L1. The key waveforms are shown in Figure 4.

There are two very important design considerations to be mentioned here. First, the inductance of that portion of the circuit that is not carrying current at the time V2 is switched, must be kept low. Since 17 kV is used to cause a 2 μ s rise to full current in a 6 μ H load, it is clear that the V2 circuit with only 750 volts available must have low inductance in order to build up to full current in a small fraction of that 2 μ s. A coaxial configuration is being used to minimize the inductance in the V2 circuit.

*Work performed under the auspices of the U.S. Department of Energy.

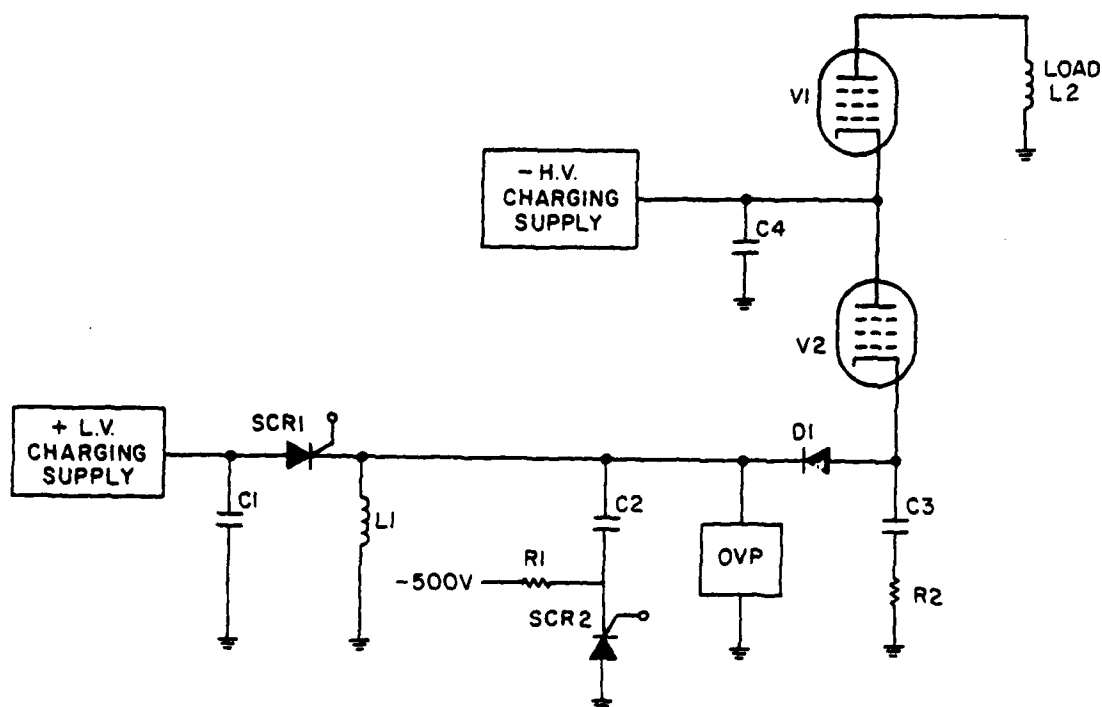


Fig. 3 - Inductive slow-fall circuit

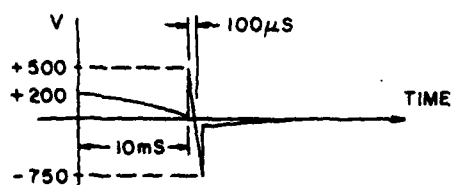
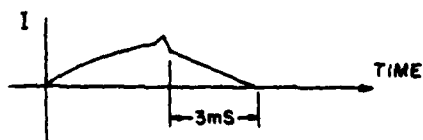


Fig. 4 - a) Voltage across L1



b) Current through L1



c) Current through the load (L2)

Secondly, the timing of the SCR's is a function of current set points. During the short interval that L1 is charging C2, L1 is effectively a constant current source. The slope of the voltage on C2 is proportional to this current, which implies that the time to reach -750 volts is also. Using the highest current pulse case as an example, a $\pm 20\%$ change in the current setting would result in V2 firing voltages from -520 volts to -982 volts if not corrected by changing the SCR firing times.

When the positive and negative halves are put together, the possibility for crossfiring exists. Figure 5 shows the portion of the circuit where this problem exists. Just prior to firing, each tube has an anode-to-cathode voltage on it of 17 kV. When one tube fires, the other will experience step increases to 34 kV with a rise time of only 60-70 ns. This strongly tries to cross-fire the tube. To ease this stress, an alternate circuit was developed² as shown in Figure 6. This circuit requires a bipolar high voltage power supply, but now the cross-firing stress is nearly eliminated.

An additional advantage of this circuit is that the maximum anode-to-cathode voltage is half that of the original circuit. This enables the use of ignitrons to be paralleled with the thyratrons to extend their life.

The full circuit is shown in Figure 7. Separate charging circuits are used for each resonance to reduce the charging power requirements.

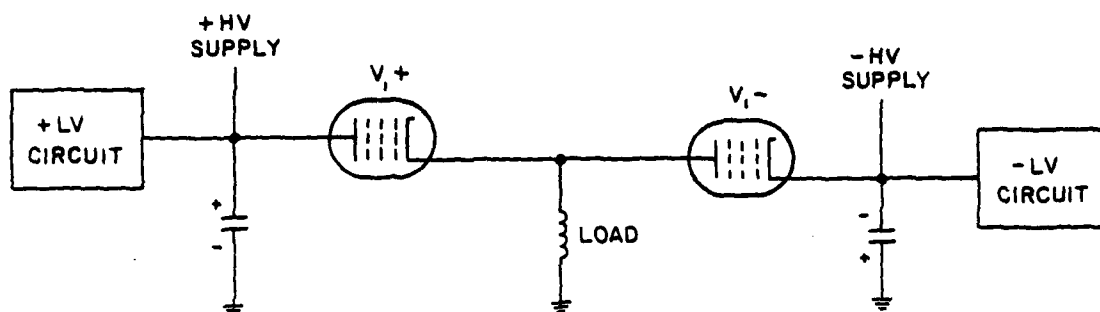


Fig. 5 - Original high voltage switching

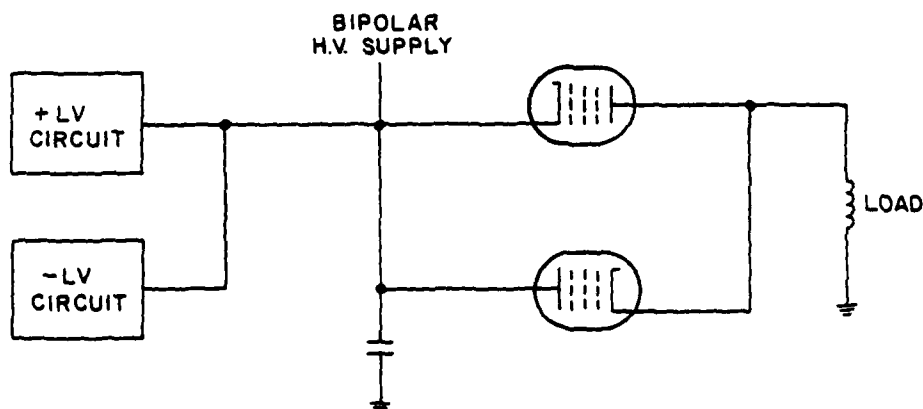


Fig. 6 - Alternate high voltage switching

A microcomputer will be used to control all twelve systems. Typical functions include d.c. power supply settings, timing pulses, and mode controls. The microcomputer will monitor system performance, and detect equipment malfunctions. In addition, the microcomputer provides an interface to the larger computer system that integrates all the components in the AGS.

Conclusion

The use of an auxiliary inductor is proposed as an effective method of producing a slow current fall in a fast rise magnet modulator. The current source operation of the inductor results in stable operation of the supply as parameters in the high voltage switch devices vary.

References

1. K.M. Terwilliger, D.G. Crabb, A.D. Krisch, M. Fujisaki, J.A. Bywater, R.J. Lari, L.G. Ratner, E.D. Courant, A. Feltman, R. Lambiase, Y.Y. Lee, R.D. Ruth and L.W. Smith. Acceleration of polarized protons in the Brookhaven AGS; IEEE Trans. on Nucl. Sci., NS-28, No. 3, June 1981.
2. H. Menown, B. Newton and R.F. Lambiase. A high power, triple grid thyatron and its test circuit; submitted to the 1982 Fifteenth Power Modulator Symposium, Baltimore, Maryland, June 14-16, 1982.

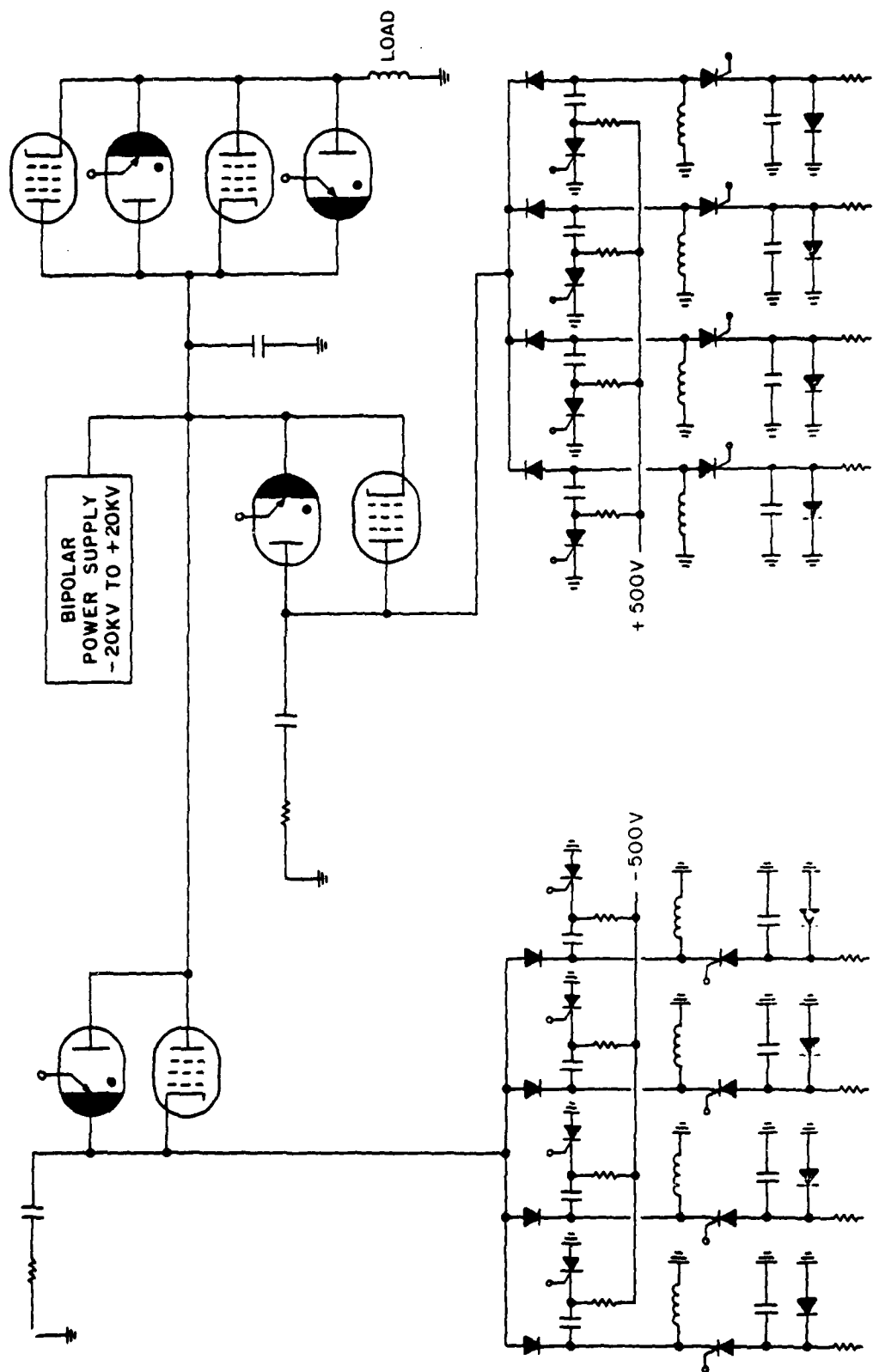


Fig. 7 - Circuit for generating eight pulses of alternating polarity

INITIAL PERFORMANCE PARAMETERS ON FXR*

B. Kulke, T. Innes, R. Kihara, R. Scarpetti

Lawrence Livermore National Laboratory
P.O. Box 808, Livermore, California 94550

Summary

Construction of the new flash x-ray induction LINAC (FXR) at Lawrence Livermore National Laboratory has been completed. Initial tuning of the machine has produced stable current pulses in excess of 2 kA at the design energy of 20 MeV, with an 80 ns FWHM pulse width, producing single-pulse radiation doses near 500 Roentgen at one meter from the target. The electronic spot size on the bremsstrahlung target is estimated at 3 - 5 mm. In this paper we will discuss the basic FXR design; running-in and tuning of the machine; emittance measurements; beam stability; switch gap synchronization; and measurements of the radiation dose and angular distribution.

Introduction

The FXR machine is a high-current, linear-induction, electron accelerator for flash radiography that was designed and built at the Lawrence Livermore National Laboratory. This facility has been commissioned by the U.S. Department of Energy in March 1982, and is currently in its running-in phase. The nominal beam parameters are 20 MeV, 4 kA, 60 ns FWHM, for an x-ray dose of 500 - 1,000 Roentgen at 1 m. For tuning purposes, the machine can be pulsed at 1/3 Hz. The machine design and some test results from component subsystems have been reported previously;¹⁻⁴ in this paper, we will present primarily the overall test results that led to acceptance and commissioning of the machine.

A view along the beam line is shown in Fig. 1, seen from the injector end. Acceleration takes place through 48 elements that are each driven to 400 kV for a 90 ns FWHM pulse. Each element contains a 10 ohm, water-insulated, Blumlein pulse forming line that energizes a 45 mm wide accelerating gap in the 146 mm dia. beam tunnel. Each gap in turn forms part of a 1 m diameter, evacuated, stainless steel cavity that contains sufficient ferrite to prevent premature shorting of the applied voltage pulse along the cavity walls. A built-in focusing solenoid is capable of generating up to 2 kG on axis. Both the ferrite discs and the symmetrically placed, coaxial feed terminals are housed in an oil-filled chamber that is separated from the evacuated part of the cavity through an epoxy diaphragm. Symmetrical, 40 ohm columns of recirculated copper sulfate solution act as ballast loads. The Blumleins are resonant-charged in groups of four from 12 Marx banks which in turn are energized from bipolar, +35 kV DC power supplies. The Blumleins are switched through coaxial, midplane spark gaps that are pressurized to 55 psi with recirculating SF₆ gas. Synchronization is derived through calibrated cable lengths from two master switch gaps that trigger the Marx banks and the Blumlein switches, respectively.

The injector uses six accelerator elements acting in tandem as a 1.5 MeV voltage source driving a planar diode. The 90 mm diameter, foil spiral cathode is supported by a 2.5 m long hollow steel stem that threads through four 250 kV gaps and so sums their

voltage contributions. Similarly, a hollow anode stem threads through two voltage modules. The tungsten mesh anode is backed by an adjustable collimator (typically, 40 mm ID) which selects the central, 4 kA portion of the 10 - 20 kA, emitted beam for further acceleration.

Beam confinement over the 34 m long beam tunnel is through a near-continuous array of solenoids that are positioned both internal and external to the accelerating elements. Beam transport from the last accelerating cavity to the bremsstrahlung target is achieved with discrete solenoid lenses. The target consists of a rotatable array of 0.75 mm thick, tungsten platelets. When focused to its nominal 6 mm spot size, the electron beam will visibly damage the target in a single pulse. CAMAC-based electronics provide computer-assisted monitoring and control of the FXR machine parameters, as well as rapid analysis of performance data.

Beam Transport and Emittance

The beam envelope was modeled using the TRANSPORT code, assuming a shielded cathode, a nominal 40 mm, injected beam diameter and a 65 mr-cm emittance, based on measurements reported earlier.² In tuning the machine, we followed the progress of the beam from readings on the Resistive Beam Monitors (RBM's) that measure the total beam current and transverse position of the beam centroid after each block of four cavities. Beginning with a complete set of focus coil settings derived from TRANSPORT code runs, we observed the effect of small changes in field strength of the group of solenoids immediately preceding each RBM. In maximizing the beam transmission, we generally gave preference to good pulse shape rather than to perfect centering of the beam, as indicated by the RBM. The beam position can be adjusted through steering coils that are positioned after every four cavities; in general, we tried to minimize the external steering.

Fig. 2 shows an axial B field profile that optimized the transmission for a 2.5 kA injected beam, and Fig. 3 gives the corresponding TRANSPORT model of the beam envelope. For reference, the Brillouin field profile is also shown for 2 cm and 4 cm diameter beams. The initial beam diameter is nominally 4 cm. Clearly, the empirical tune produced focusing fields far in excess of the 4 cm Brillouin tune, resulting in much smaller average beam diameters and strong scalloping of the beam. Note that the range shown represents the field ripple which has been minimized for the first 12 accelerator cavities through special solenoid design but is allowed to increase thereafter. As shown in Fig. 2, the measured transmission is better than 90 percent through most of the machine, although more beam is lost beyond the last accelerator cavity. Higher-current injected beams (3.5 kA) appeared to be more difficult to tune for maximum transmission, and for this reason we initially concentrated on developing tunes for a 2.5 kA beam.

*Work performed under the auspices of the U.S. Department of Energy by the Lawrence Livermore National Laboratory under contract number W-7405-ENG-48.

Typical signals from the RBMs for a well-centered beam are shown in Fig. 4 for two positions along the beam line, i.e., near the injector and 24 m downstream, just ahead of cavity No. 37. The four signals shown correspond to the four quadrants of the RBM; when the beam wanders off center, the signals become unequal and the beam centroid displacement can then

be calculated approximately as $\frac{\Delta r}{r} = \frac{1}{2} \frac{V_+ - V_-}{V_+ + V_-}$

where V_+ and V_- represent the sum and difference of opposite quadrant signals, respectively.⁵ For a well centered beam, the current amplitude repeated within 5 - 10 percent from shot to shot; with the beam off-center, repeatability was degraded rapidly. Beam steering with 200 - 300 Gauss-cm of transverse magnetic field was applied primarily within the first two blocks of 16 accelerator cavities, as marked by asterisks in Fig. 2. The beam was kept nominally centered within a few millimeters, wherever possible. In certain locations, however, the beam pulse shape began to be degraded when steering fields were applied, and in those cases we simply tuned for maximum transmission.

Emittance measurements have been reported earlier (Refs. 2, 3) where we used a 1 mm thick brass plate, perforated with 1 mm diameter holes, as a shadow mask and measured the expansion and the lateral divergence of the resulting beamlets. The same apparatus was used again to characterize the beam after acceleration through 16 gaps. For measuring the emittance after acceleration through all 48 gaps, we changed the shadow mask to a 15 mm thick brass plate with 2 mm diameter holes. The results are summarized in Table I. Note that there is some variation in injector voltage and beam current which may have had some effect on the emittance. The measured emittance is uniformly higher than the value obtained by scaling inversely with the beam energy, corresponding to a normalized emittance growth of about 3 percent per cavity.

Table I. Measured emittance at three points in the FXR beam line.

Emittance Measured	At Injector	After Gap #16	After Gap #48
Shot No.	#1336	#778	#1121
Injector diode voltage	1.5 MV	1.3 MV	1.3 MV
Calculated beam energy	1.5 MeV	7.1 MeV	19.8 MeV
Beam current	3.4 kA	2.3 kA	2.1 kA
Approx. beam diameter at shadow mask	7.0 cm	4.0 cm	8.0 cm
Measured emittance	65 mr-cm	24 mr-cm	17 mr-cm
Scaled emittance	65 mr-cm	17 mr-cm	6.4 mr-cm

Beam Stability

Transverse beam oscillations of the beam breakup (BBU) variety have long been recognized as a limitation to successful beam transport in very long or high-current linear accelerators, including FXR.⁶ A beam propagating slightly off-center through an accelerating cavity may excite microwave resonances with transversely directed magnetic field components

that in turn tend to increase the beam displacement, finally leading to complete loss of the beam to the walls. Using swept-frequency and field-mapping techniques we have measured f_0 and the unloaded Q factor for the five lowest BBU modes that can be excited in an FXR accelerating cavity (Table II). Termination of the feedline and ballast load ports reduces Q somewhat; the TM₁₁₀ mode had $Q_0 = 33$ in the loaded condition, compared to $Q_0 = 50$ before. All the observed modes can be damped much more, to values of $Q_1 \leq 7$, by placing a modest amount of ferrite loading (modified common mode chokes) on the feedline and ballast load terminals inside the cavity, although this modification has not yet been implemented on the machine.⁷ As seen from the typical signal traces shown in Fig. 4, the beam appeared to be stable at the 2 - 2.5 kA level. B probe signals taken after the last cavity did show some ringing but at a frequency (160 MHz) that did not correspond to any BBU mode. However, the need for strong focusing in order to ensure good beam transmission (Fig. 2), may have been due to incipient beam instabilities that were reduced by the magnetic focusing field.

Table II. Measured resonant frequencies and unloaded Q's for the five lowest TM_{1,m,0} modes in the FXR cavity.

TM Mode	f_0 MHz	Q_0
110	261	50
120	420	10
130	650	13
140	860	24
150	1050	≤ 7

Switch Gap Synchronization

Our computer-based data acquisition system provides real-time recording and display of firing delays for all spark-gap switches that control the timing of the accelerating voltage pulses. This enables us both to assess the machine performance after each shot and to accumulate statistics over multishot samples. Table III gives jitter data for a 20-shot sample taken on the first block of 4 cavities, following the injector. Spark gap J10 is an intermediate switch triggering the four Blumlein switches J11, 12, 13, and 14 which in turn energize individual cavities. The 1.5 ns jitter is acceptable in the context of our 90 ns accelerating pulse length, although we expect to reduce it to $\sigma \leq 1$ ns through further optimization.

Table III. 4-cavity group firing delays, 20 shot sample.

Switch Gap	Standard Deviation, σ , ns
J10	1.5
J11	1.4
J12	1.4
J13	1.2
J14	1.5

A more difficult problem is the equalization of average firing delays between different switch gaps which is necessary for the correct stepping of the voltage pulses along the beam line. For example, for

the first group of 16 cavities following the injector we find the intermediate gaps deviating by up to 4 ns from their nominal 8 ns spacing, on the average.

Such deviations in effect add to the energy spread near the beginning and near the end of the accelerated beam pulse.

Radiation Dose and Spot Size

The nominal design goal for FXR was to produce a single-shot dose of 500 Roentgen at a distance of 1 m from the bremsstrahlung target, with an electronic spot size of 3 - 6 mm. Using an array of thermoluminescent detectors (TLDs) we measured a dose of 480 R at 1 m, (Shot #2416) by letting a 1.6 kA beam impinge on a temporary target consisting of two 0.5 mm tungsten discs sandwiched together. The nominal beam energy for this shot was 18 MeV. From the width of the burn mark that was left on the aluminum flange supporting the tungsten discs we inferred an electronic spot size of approximately 5 mm. Combining this with the measured emittance of 17 mr-cm and assuming a uniform distribution of electron angles yields a mean electron angle of 2.6 degrees. The effective thickness of the tungsten target was 1.9 g/cm². Using available measured curves for the angular distribution of bremsstrahlung from 15 MeV, paraxial electrons impinging on a 4.5 g/cm² tungsten target one finds a FWHM beam width of 10 degrees.⁸ Assuming this same number to hold for our beam, and performing a geometric addition of the mean electron angle and the half-beam width of the bremsstrahlung

distribution yields a total effective beam width of 11.3 degrees, FWHM. The observed x-ray beam width, as derived from TLD readings (Shot #2415, 460 R at 1 m, on axis), is shown in Fig. 5, i.e., 8.3 degrees FWHM in the vertical plane and 9.5 degrees FWHM in the horizontal plane, in reasonable agreement with the calculated estimate.

Further radiation measurements were taken with the beam directed at the 0.75 mm thick tungsten platelets that form part of the rotatable, permanent target assembly. Because of machine problems at the time the charge deposited on target was less than before and the observed dose was only 180 R at 1 m. Some target platelets are shown in Fig. 6; the arrangement shown corresponds roughly to the target wheel. A single beam pulse struck the gap between two platelets grazing both and leaving visible burn marks; the holes punched through the other two platelets probably are each due to more than one beam pulse. The size of the witness marks appears to be compatible with an electronic spot size on the order of 3-6 mm.

Conclusion

Preliminary measurements (over 3,000 pulses) on FXR have produced satisfactory single-pulse x-ray doses of up to 480 R at 1 m, although the machine has not yet been run at the full design current of 4 kA. The measured emittance for a 20 MeV, 2 kA beam is less than 20 mr-cm, yielding a narrow radiation cone while maintaining a small spot size.

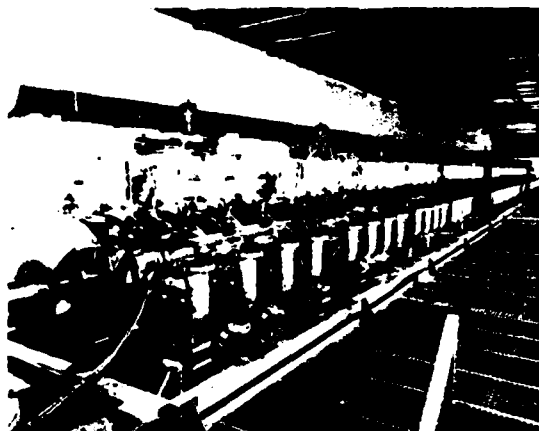


Figure 1. View along the FXR beamline, seen from high-energy end.

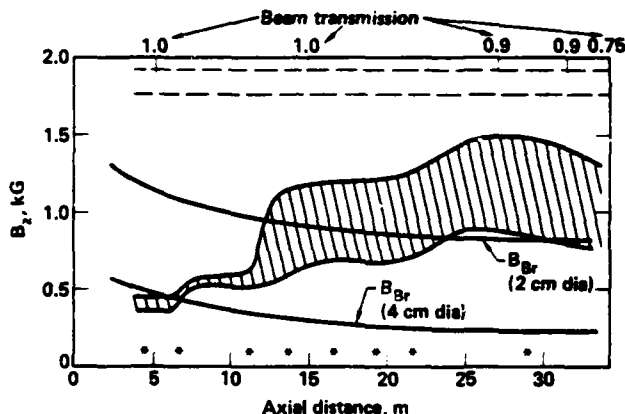


Figure 2. Calculated B_z profile of actual tune used, showing the range between maxima and minima of the rippling field. Also shown are the Brillouin field profiles for a 2 cm and a 4 cm dia beam, and the measured transmission of the 2.5 kA beam. Injector voltage is 1.3 MeV, accelerating potential 354 kV/gap, final beam energy 18.3 MeV. The asterisks mark locations where 200-300 gauss-cm of transverse beam steering was applied.

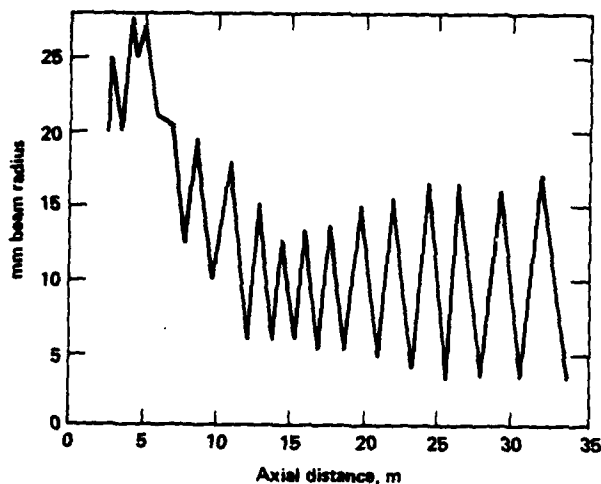


Figure 3. Calculated beam envelope (TRANSPORT code), based on the calculated B_z profile from the actual tune. Beam parameters, same as in Fig. 2; the emittance at injection was assumed to be 65 $\text{mr}\cdot\text{cm}$.

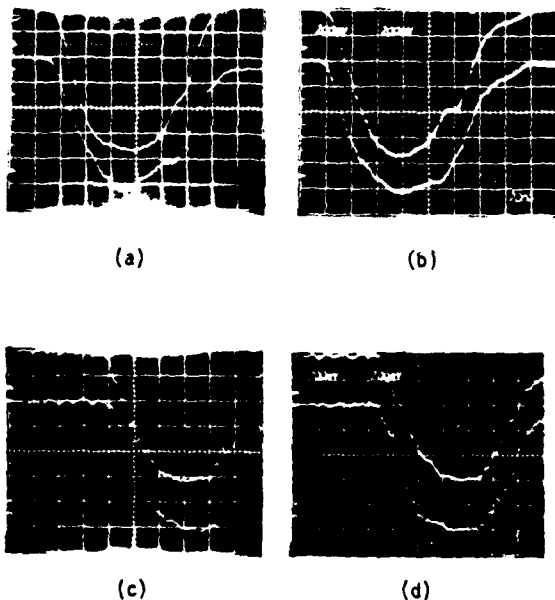


Figure 4. Beam monitor signals for a well-centered beam, at two different positions along the beamline. Figures (a) and (b) show the four quadrant signals preceding the first accelerator cavity (2.45 kA peak, 1.3 MeV). Figures (c) and (d) show similar signals 24 m downstream, preceding cavity No. 37 (2.25 kA peak, 14. MeV). The time scale is 20 ns/div.

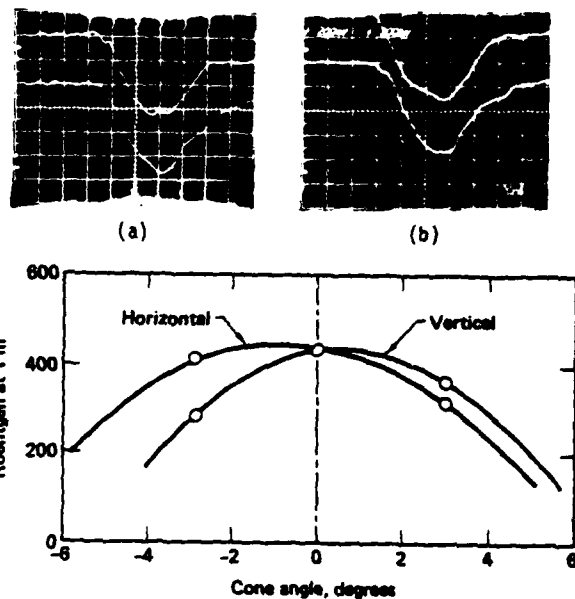


Figure 5. Beam current and measured radiation pattern for Shot #2415. Traces (a) and (b) show the four quadrant signals for the beam current monitor immediately preceding the target, with 20 ns, 450 A/div. The radiation pattern was estimated from a five-TLD array mounted on axis. The average beam width is 9° FWHM.

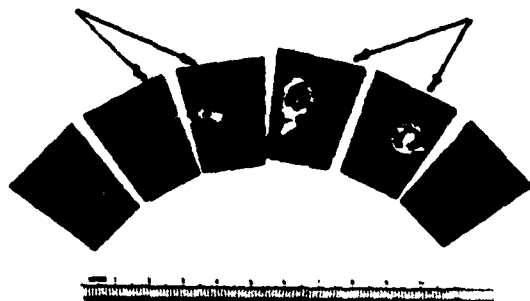


Figure 6. Damage to tungsten target platelets, shown approximately as mounted on the FXR rotatable target array. The larger holes were probably made by more than one pulse.

References

1. B. Kulke, et al., Design of a 20 MeV, 4 kA Linear Induction Accelerator for Flash Radiography, UCID-18939, Lawrence Livermore National Laboratory (1981).
2. B. Kulke, R. Kihara, D. Ravenscroft, R. Scarpetti and G. Vogtlin, Beam Tests on the 4 kA, 1.5 MeV Injector for FXR, Proc. 4th Int. Topical Conference Electron and Ion Beam Research and Technology, Palaiseau, France, pp. 821-828 (1981).
3. B. Kulke, D. S. Ravenscroft and G. E. Vogtlin, Design and Performance of the 1.5 MeV Injector for FXR, Trans. IEEE NS-28, 2882-2884 (1981).
4. R. D. Scarpetti, C. D. Parkison, Switching System for the FXR Accelerator, 14th Pulse Power Symposium, Orlando, Florida, June 1980.
5. T. J. Fessenden, B. W. Stallard and G. G. Berg, Beam Current and Position Monitor for the Astron Accelerator, Rev. Sci. Inst. 43, 1789-1792 (1972).
6. V. K. Neil, L. S. Hall and R. K. Cooper, Further Theoretical Studies of the Beam Breakup Instability, Particle Accelerators 9, 213-222 (1979).
7. B. Kulke and R. Kihara, Lawrence Livermore National Laboratory internal note FXR 1321 (November 1980).
8. Ian Smith, Lawrence Livermore National Laboratory internal note FXR 1082 (July 1978).

DISCLAIMER

This document was prepared as an account of work sponsored by an agency of the United States Government. Neither the United States Government nor the University of California nor any of their employees, makes any warranty, express or implied, or assumes any legal liability or responsibility for the accuracy, completeness, or usefulness of any information, apparatus, product, or process disclosed, or represents that its use would not infringe privately owned rights. Reference herein to any specific commercial products, process, or service by trade name, trademark, manufacturer, or otherwise, does not necessarily constitute or imply its endorsement, recommendation, or favoring by the United States Government or the University of California. The views and opinions of authors expressed herein do not necessarily state or reflect those of the United States Government thereof, and shall not be used for advertising or product endorsement purposes.

VARIABLE FREQUENCY INVERTERS FOR HT SUPPLY FOR PULSED RADAR TRANSMITTERS

J McCafferty
Marconi Radar Systems Ltd

and

N S Nicholls
Royal Signals and Radar Establishment

Summary

Radar transmitters employing gridded-gun microwave tubes require a voltage-stabilised HT supply system capable of supplying a relatively large pulsed current load. Conventionally, the supply is provided by a transistor inverter operating at a few tens of kHz, followed by a transformer, rectifiers and a relatively large reservoir capacitor. Voltage stabilisation may be implemented by on/off control of the inverter.

One problem which must be addressed in the design of such systems is the close to short-circuit load condition experienced by the inverter during the early stages of charging of the reservoir capacitor or when the HT transformer core is inadvertently saturated. In the scheme described, the inverter transistor peak and average current may be kept constant under all conditions by the use of a series inductor in the AC part of the circuit, whose reactance is varied by varying the inverter frequency.

Advantages of the scheme described are that capacitor charging time is minimized, short-circuit protection is inherent, and a very high accuracy of voltage control may be achieved by raising the inverter frequency as the desired capacitor voltage is approached. Within cycle turn off may be used. A substantially reduced component count is thus achieved at the expense of a more severe transistor turn-off condition, but one which is within the capability of available FET's.

1. Introduction

A growing proportion of medium powered pulsed radar transmitters employ gridded-gun linear-beam microwave amplifier tubes. Apart from the added freedom which this gives to microwave tube designers, other obvious advantages are flexibility in pulse duration and timing and good within-pulse phase-stability, the latter due to the within-pulse voltage stability made possible by the use of a large reservoir capacitor on the DC HT supply.

The HT supply system for such a transmitter must generate a high DC voltage with an absolute DC voltage accuracy of (typically) $\pm 0.5\%$ and a pulse-to-pulse tolerance of 1 in 10^4 or better is often needed. This must be achieved for average load currents fluctuating between zero and maximum rating and for supply voltage fluctuations of typically $\pm 10\%$ or more. It must tolerate unforeseen load short-circuits without risk of damage and must achieve the specified HT voltage with a minimum of delay both at switch-on and after a temporary load short circuit.

Small size and high reliability are usually prime requirements. To achieve a high predicted reliability under MIL STD 217C rules it is necessary to use only correctly rated qualified components and also to achieve a low component count. High efficiency and low cost are not usually prime requirements, but high

efficiency is likely to be helpful in the achievement of small size coupled with high reliability.

It is often found that the best form of HT supply system for this type of transmitter is to use a DC link inverter arrangement. By using an inverter operating at a frequency considerably above that of the prime power source advantages may be gained in two areas. The size of the HT transformer may be significantly reduced. Also, if the inverter frequency is much higher than the prf, no HT smoothing is needed apart from the reservoir capacitor required to supply the current pulses drawn by the load. At the same time, compensation for the effect on the HT voltage of load current and supply voltage variations may be effected more rapidly. However, too high a frequency may give rise to various problems with inversion and rectification and also with transformer design. A frequency above the audible range is usually preferred.

When using inverter designs where complete half-cycles must be generated, the resulting "quantum" of HT voltage will typically be a few tenths of a percent. Since pulse-pulse voltage fluctuations of this magnitude are seldom admissible, it is usually necessary in such cases to add a further analogue type voltage stabiliser in the HT circuit, with consequent increase of component count and power loss. If the inverter transistors could be tuned off at any point in the cycle, voltage control would be improved, but current would still continue to flow for a short time due to the inevitable inductance of the AC circuit. This will lead to a voltage overshoot dependent on the current flowing at the instant of shut-off and also affected to a lesser extent by the instantaneous voltage of the incoming DC supply. For cases where this still leads to unacceptable pulse to pulse voltage fluctuation, further improvement of the voltage control performance would be possible without any significant increase in component count if it were feasible to reduce the peak inverter current as the target voltage is approached. This will be discussed later in the paper.

For the case which will be considered here as an example, prime power is 200 V AC 3 phase 400 Hz and in accordance with usual practice this is rectified directly without the use of a 400 Hz transformer. Whilst dispensing with a large component, this dictates the DC supply voltage to the inverter and also means that neither side of the supply is grounded. Inverter designs must therefore be compatible with these requirements.

Any inverter control scheme designed to maintain a constant HT voltage without precise advance knowledge of the time of arrival of the next pulse must lead to intermittent operation of the inverter. After each transmitter pulse, the inverter will need to operate at full available power until the reservoir capacitor voltage is restored to a state of readiness, after which it will typically remain inoperative until the next transmitter pulse occurs. Changes in pulse duration will only affect the duration of each burst of inverter operation.

Because sufficiently fast semi-conductor inverting devices have restricted voltage-withstand capabilities and are very vulnerable to over-voltages, simple capacitors are the preferred method of filtering the DC supply at inverter frequency. Preferably, no significant filtering at input rectifier ripple frequency is provided. In this way no large inductors are involved which could lead to serious voltage surges being generated on the input DC supply as a result of the intermittent current demand of the inverter, while the form factor of the AC line current is better than would be obtained when using a large input reservoir capacitor.

Although other inverter circuits are possible, we will confine ourselves to those circuits where the transistor voltage does not exceed the DC supply voltage. The basic circuit having this property is the bridge inverter with reverse diodes across the transistors (fig 1).

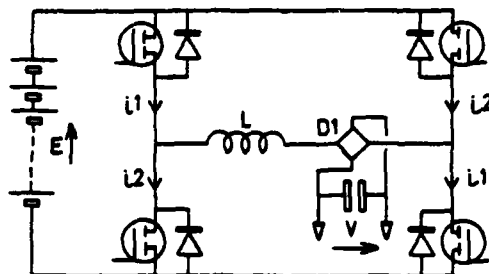


Fig 1. Bridge inverter

The box marked X in fig 1 is a reactance network part of which is parasitic (the leakage inductance of the HT transformer) but which normally has to be augmented to limit the current or at least the rate of rise of current, at switch-on or when a load-fault occurs. When using bipolar transistors, a popular practice is to use for X a series-resonant LC circuit tuned to the inverter fundamental frequency (which must therefore be approximately constant). This causes the switch current to be of the form of half-sine waves, so that the current is small at the time of switch opening, thus avoiding the risk of second breakdown problems. The large build-up of voltage in the resonant circuit which would occur under short-circuit conditions, with associated very large switch current, is prevented by the fitting of clamping diodes.

When using MOSFETs as the inverter switches, there are no turn-off problems provided that the transistors are turned off rapidly, even if the devices are simultaneously subjected to maximum voltage and maximum current. This makes it possible to employ a simple inductor for X. Then the inverter frequency may be allowed to vary in order to control the current. Also, the inverter may be switched-off at any point in the cycle. In what follows it is shown that these attributes may be used to make unnecessary an additional series stabiliser for most applications, while at the same time achieving a true constant current characteristic for the inverter. This makes the inverter inherently safe in the presence of load short-circuits or if the HT transformer core saturates, and allows the desired rapid charging of the HT reservoir capacitor from start-up, without added components.

2. The Characteristics of the Inductive Output Inverter Loaded by a Rectifier with Capacitor Input Filter

2.1. The Waveforms

To understand the waveforms it is convenient to analyse the operation of a full-bridge. The equivalent is shown in fig 2. In this, the HT transformer has

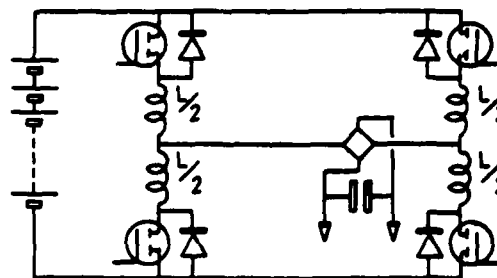


Fig 2. Inductive inverter

been eliminated by referring the secondary circuit values to the primary in the usual way. We will suppose that the base-drive to the FET's is controlled in such a way that when the magnitude of the peak current (irrespective of direction) reaches a prescribed level, the transistors which are on are turned off and the other ones are turned on. The transistor current rises at a rate $(E - V)/L$ (neglecting transistor and transformer resistance, which are relatively small) and the diode current falls at a rate $(E + V)/L$. Since, to a good approximation, the voltages are constant during each half cycle, the current-waveforms are built up from triangles, as shown. The frequency of operation is determined by the circuit conditions and will vary with load and supply voltages. Fig 3 shows the resulting waveforms both with zero output voltage and for the more typical case when the DC output voltage (referred to the primary of the HT transformer) is about 80% of the supply voltage. In both cases the transistor turn-off threshold is fixed at the same level. The following points may be noted:-

2.1.1. For a fixed peak current, the rectified DC output current is constant (at half the peak current) irrespective of the voltage on the reservoir capacitor or the supply voltage.

2.1.2. The average current in each transistor rises with output voltage, from one eighth of the peak current on short circuit to approaching one quarter of the peak current at the maximum output voltage. The DC supply current is then approaching one half of the peak transistor current.

2.1.3. The inverter frequency drops as the load-voltage rises. An output voltage equal to the supply voltage would give zero frequency. The maximum ratio output voltage/supply voltage which can be allowed is restricted by the ratio of highest to lowest frequency which can be accepted. Switching losses in the transistors and rectifier are possible factors limiting this.

2.1.4. In any limb of the bridge, transistor current is always immediately preceded by diode current. Thus the transistors are always turned on at zero voltage. Turn-off, however, always occurs at maximum current, and maximum transistor voltage. Hence this circuit is only economical for use with MOSFETs, where there is no problem with second breakdown.

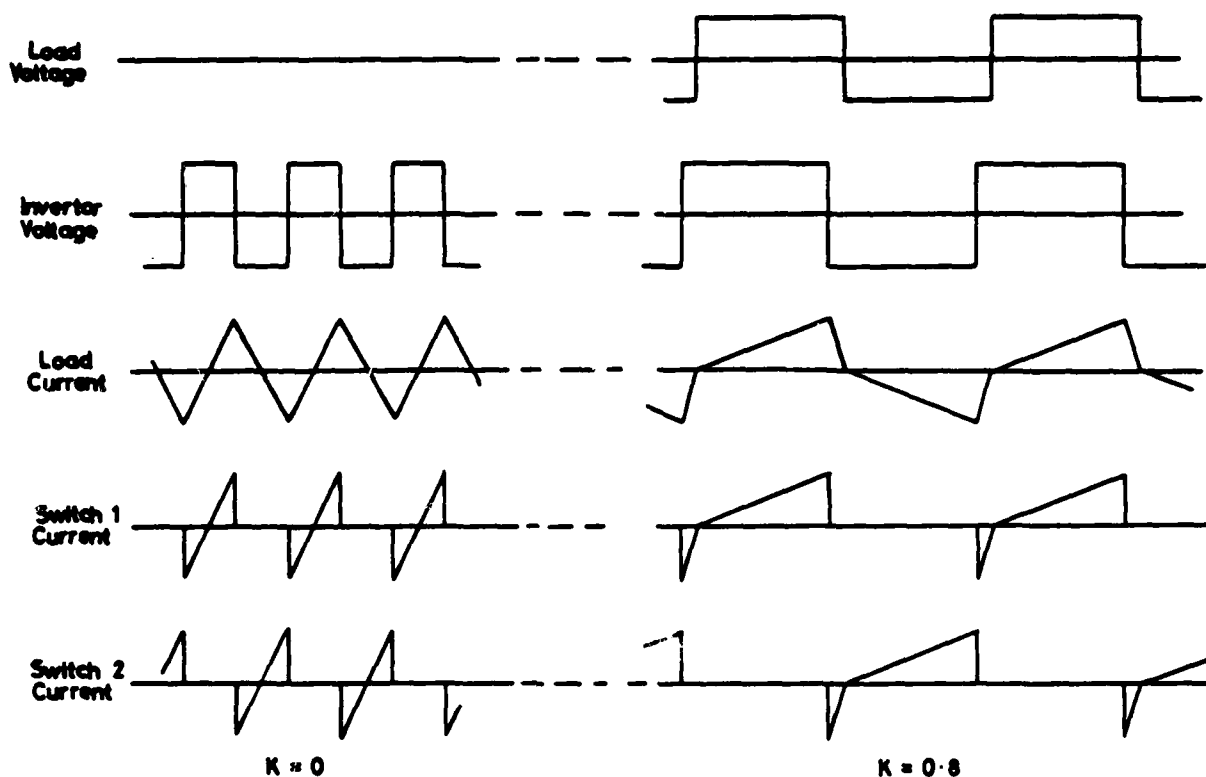


Fig 3. Idealized waveforms of inductive inverter

2.1.5. If the drive to the transistors were removed while current is flowing, there would still be a significant further charge delivered to the load reservoir due to the diode current, which is sustained by the energy stored in the circuit inductance.

2.2. Overall Characteristics

Neglecting resistance, the overall characteristics of the inverter may readily be expressed in terms of the following parameters:-

- I is peak transistor current
- L is the total AC circuit inductance
- E is the DC supply voltage
- V is the output DC voltage
- K is the ratio E/V

Then if t_1 and t_2 are the durations of transistor and diode conduction:-

$$t_1 = LI/(E - V)$$

$$t_2 = LI/(E + V)$$

Whence

$$t_1/t_2 = (1 + K)/(1 - K)$$

The average current in each transistor

$$= I(1 + K)/8$$

The average current in each diode

$$= I(1 - K)/8$$

The RMS current in each transistor

$$= I\sqrt{(1 + K)/6}$$

The average output DC current

$$= I/2$$

The average supply current

$$= KI/2$$

The frequency of operation with $V = 0$,

$$f_0 = E/4LI$$

The operating frequency

$$f = f_0(1 - K^2)$$

An important characteristic is the charge per cycle passing through each diode, because this charge will be passed on to the reservoir capacitor after all the transistors have been turned off, if the latter occurs when the current is at its peak value. It will therefore determine the maximum voltage error which can occur on the recharged output reservoir capacitor.

The diode charge per cycle

$$= \frac{1}{2} I_{r2} = q_0 / (1 + K)$$

where

$$q_0 = LI^2 / 2E$$

is the diode charge during short-circuit operation.

The dependence of various quantities on K for this idealized model is shown in fig 4.

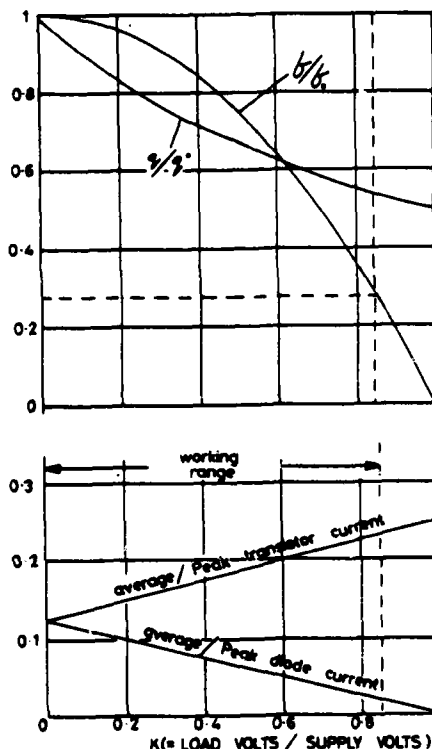


Fig 4. Overall characteristics of idealized inductive inverter

2.3. Protection Against Corruption of the Base Drive by Interference

If the transistor drive-circuits operate incorrectly in such a way as to cause even brief conduction of both pairs of switches simultaneously, then an abnormally large current will flow through the transistors which could lead to deterioration. A similar risk would exist if a transistor were turned on again very soon after it had turned off. Then the diode between it and the opposite supply rail would be in heavy conduction and would be able to pass a large reverse current for a short time due to stored carriers. The sensitive wide-band voltage comparator which is needed in the HT voltage-control system would tend to be vulnerable to interference, so that there is a risk that this situation will arise unless precautions are taken.

The method of tackling this problem is by the insertion of a time block in the drive circuits to prevent the interval between change-overs falling below a pre-determined minimum. Also the turn-on of each transistor should be delayed a small amount after the

turn-off of the other to guarantee against overlap.

If such provisions were deemed inadequate in a particular case, the inductor could be split into four inductors, each part being placed directly in series with each transistor-diode combination (fig 5). Then

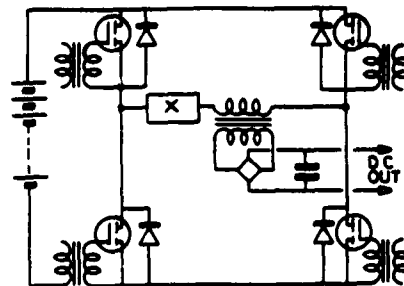


Fig 5. Inverter with split inductors

the rate rise of current could not be very high in any circumstances, and brief conduction overlaps between the transistors will therefore produce very little change of current. However, to ensure good matching of durations of the two half-periods during normal operation, the inductance values for each diagonal pair would have to be accurately matched at all values of current.

3. The Performance of a Typical Design

The idealized analysis of section 2 is significantly modified when a realistic value for the MOSFET on-resistance is inserted.

The following figures for a typical design for a full bridge (4 transistors) are based on a more accurate analysis:-

Min. instantaneous supply voltage	220 V
Referred load voltage	180 V
Peak transistor current	20 A
Transistor resistance (each device)	0.3 Ω
Minimum frequency	20 kHz
Maximum frequency (V = 0)	73 kHz
Circuit inductance	37 μ H
Inverter power output (continuous operation)	1.9 kW
Transistor loss (4 devices, 20 kHz)	100 W
Inverter efficiency	95%

The maximum output voltage quantum, with 1 millifarad referred reservoir capacitance, is about 1 part in 10^4 with the current limit set at 20 A. If the current limit were reduced to say 7 A, whenever the output HT voltage approaches within 1 part in 10^4 of its target value, the maximum voltage quantum would be reduced to 1 part in 10^5 at the expense of an additional delay not exceeding 20 μ s in the reservoir recharging time between each pulse. Much further improvement in voltage accuracy is likely to be prevented by noise in the wide-band voltage comparator required to control the inverter, unless the terminal charging rate is further reduced, so as to reduce the bandwidth required, which would involve further extension of the complete recharging cycle.

4. Conclusions

We have seen how a bridge converter circuit in which the only significant impedance is an inductor in series with the AC output has particularly useful characteristics for HT supply in pulsed radar transmitters using gridded-gun microwave tubes.

By arranging that transistor switching is controlled by the instantaneous value of the current, the DC output is given a constant current characteristic which imparts an immediate safe reaction to load short-circuits while at the same time giving rapid charging of the output reservoir capacitor at start-up. The frequency of operation of the inverter varies over a range of up to about 4:1 over the range of load conditions which are encountered in such cases.

A penalty is that transistor turn-off takes place at maximum current, so that MOSFETS may have to be used to avoid second breakdown problems. Also the peak transistor current is 27% higher for a given power-flow than the series resonant inverter, though the transistor RMS current is only about the same. Advantage is, however, taken of the high switching-speed of MOSFETS to achieve a very fine control of output DC voltage. This is done by the use of within-cycle turn-off and will often render further means of voltage stabilisation unnecessary. This yields a substantial overall reduction in component count and hopefully, confers a significant advantage in size and reliability over conventional HT supply systems.

THE TAP CONVERTER
An Alternative VSCF Converter

by

Melvin Sandler

and

Marivaz Wrzesniewski

The Cooper Union
Cooper Square
New York, NY 10003

Abstract

An alternative frequency conversion technique is examined theoretically and on the basis of laboratory tests. The circuit relies on switching between taps to produce the desired frequency conversion of an output waveshape, and is therefore referred to as a tap converter. The operation of the tap converter has been examined with a view to its usefulness in VSCF (variable speed-constant frequency) generating systems. A single phase tap converter has been built and tested to facilitate the comparison with conventional frequency changing circuitry.

Introduction

It is clear that a great deal of attention must be paid to studying electronic power conversion for the remainder of this century. New and alternative sources of energy such as wind power generation will not necessarily match the requirements of existing grids. Similar problems will occur in aircraft rators and when new energy storage devices and cems are tied to existing power grids. Finally, electric motor drives must be improved if high speed ground transportation and the electric car are to become more than just a feasibility demonstration or an oddity. The problems of designing an electric vehicle, a flywheel storage system, or a compatible wind power generator are very similar. However, the following discussion will be concerned with the extraction of energy from a variable speed generator. This limiting is done for purposes of clarity and focus. The technology developed can be applied if not directly, then with modification to similar systems.

Net cost plays a decisive role in all realistic systems. Any device proposed to improve existing frequency conversion technology must be compared to rotating mechanical frequency changers, to cycloconverters, and to rectifier/inverter combinations. In addition, capital investment must be a minor fraction of a typical wind generator or power plant cost based upon a cost per kilowatt capacity. Therefore, if a capital investment cost of \$2000 per kw is used, the total cost per kilowatt capacity of the electronic conversion technique must be small compared to \$2000. Five percent or \$100 is reasonable per kilowatt rate. There is an exception: for the most part current electric utility rates are tied to both capital investment and to fuel cost. However, if the energy is free, or in military applications, investment costs even above \$2000 per kilowatt may be justifiable.

Frequency changing techniques which are not electronic may be classified into two groups: mechanical speed reducers and motor generator sets. Both techniques are expensive. The mechanical speed reducer is especially costly and expensive when there is a significant variation in driver speed. Furthermore, there is general agreement that these techniques will not be popular in the future. Rectifier and inverter combinations tend

to be expensive and suffer commutation problems because of the inverter stage. Cycloconverters can be used to replace the rectifier/inverter combinations when frequency reduction is greater than three-to-one. However, the waveforms are of poor quality and like the inverter produce waveshapes with a high harmonic content. The harmonics are parasitic to the operation of electro-mechanical loads and cause a great deal of electromagnetic interference. In addition, the cycloconverter requires a greater number of thyristor switches. Capital investment costs from \$10 to \$50 per kilowatt are generally quoted for the electronic conversion. The \$10 figure (which seems futuristic) was quoted by Exxon in a news release dated May 17, 1979. The news release described the use of high power transistors to perform the inversion. When power transistor inverters are employed, commutation and waveshaping problems are non-existent. However, there are still limitations on power levels and while transistor price is low, circuitry cost establishes price. As a result, Exxon announced it was abandoning its original design. (News release -- dated April 14, 1981.) The techniques described below are in competition with the transistor inverter and must always be compared to this device.

A competing, albeit potentially more versatile technique, involving tap changing, is described in the next section. The tap converter offers significant improvements in VSCF generator output waveshapes and in motor speed control. Harmonic content is reduced and the waveshapes are continuous. Frequency reduction limits of less than three-to-one are possible. Therefore, unlike cycloconverters, tap converters need not be operated in an "inverter mode" at slower machine speeds.

Tap Converters

A typical tap converter circuit design is shown in Figure 1. The circuit shown utilizes twelve SCR switches. The minimum number which would allow for both voltage and frequency reductions is eight. In a tap changer mode of operation (i.e., where only voltage stepdown is required) precisely one-half of the switches may be eliminated. Therefore, the minimum number of SCR switches required in a tap changer mode is four. Four possible modes of operation are shown in Figure 1 along with the resulting output waveshapes. Mode one or full voltage operation is produced by firing sequence: 3, -3, 3-3...etc. Mode two or tap changer sequence is produced by firing the SCR switches at a lower level, for example: 2, -2, 2-2...or, 1, -1, 1-1...etc. The full tap conversion possibilities are accomplished by firing sequences such as 2, 2', -2', -2, 2, 2'...etc. or 1, 1', 1, -1', -1, -1'...etc. Finally the circuit may be operated in cycloconverter and cycloconverter/tap converter modes by merely delaying the firing times.

Both tap converters and cycloconverters have the

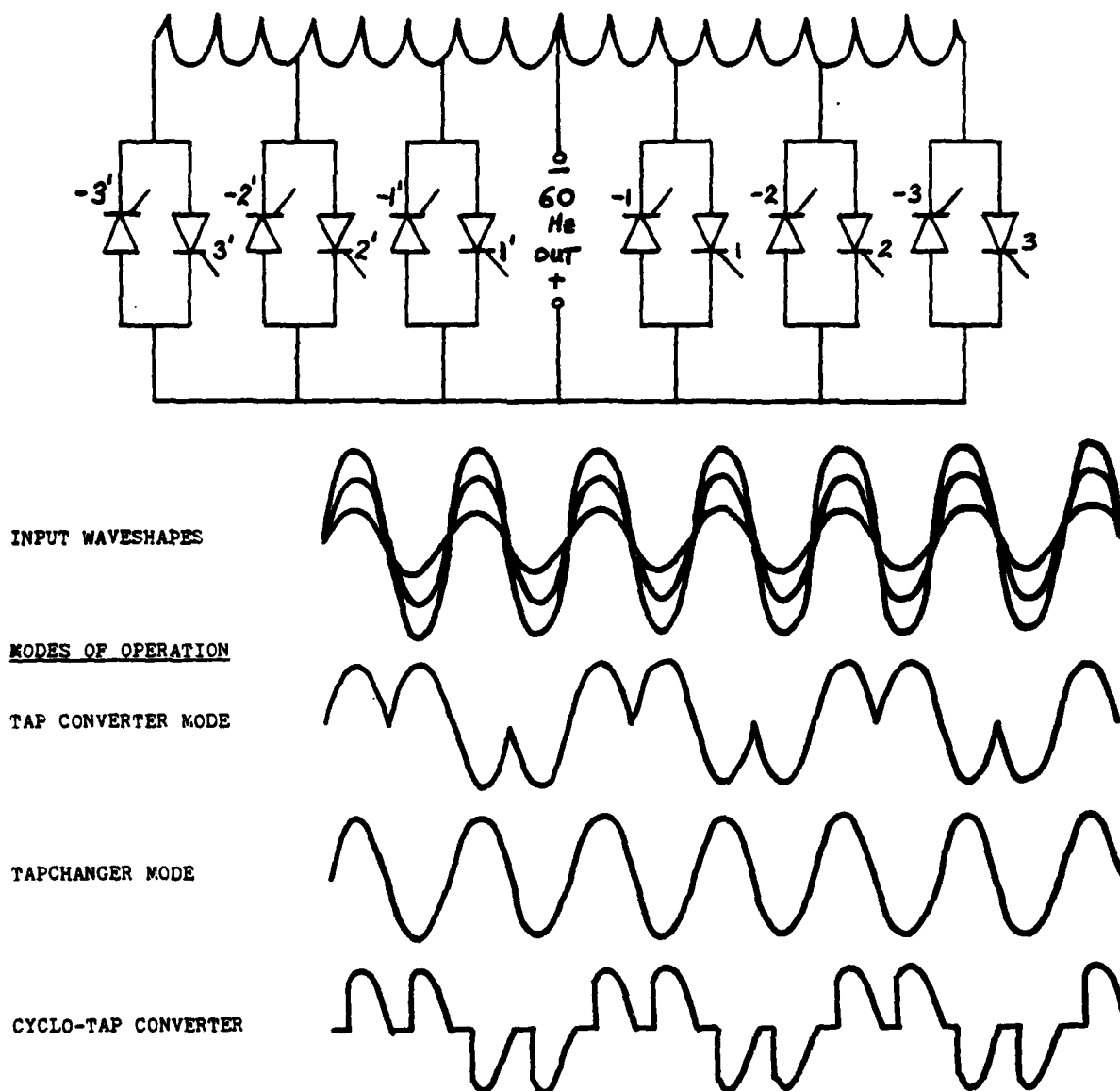


Figure 1. A three-step, two-way, single phase tap converter circuit

advantage when compared to a rectifier/inverter combination because they rely on supply voltage commutation. The rectifier/inverter combination requires either external circuitry or operation into a leading power factor load. The leading power factor forces commutation by sending a reverse current to the previously conducting SCR. The disadvantages of the cycloconverter are: minimum frequency reduction of three-to-one and choppy waveforms. A solution to both problems is shown in Figure 1.

The technique of changing both voltage and frequency by switching between taps is a new addition to the current alternative methods of inversion and cycloconversion. A single phase version of the output is shown in Figure 2. The full advantages of tap changing circuits are realized in multiphase operation. (Figure 3.) Consider the two waveshapes shown in Figures 2 and 3. As in the case of the cycloconverter, com-

mutation is accomplished because of changes in the supply voltage. The cycloconversion technique has been improved upon by creating stepped variation in the amplitude of the input waveshape. The result is smoother output wave with less destructive harmonic content. The number of SCR switches required increases with the number of taps. Finally, the cost of the system does not increase directly with the number of SCR switches required by the designer. For example, the 1 unit amplitude tap in a 1234 tap converter carries only one-fourth the current of the four-unit tap and so on. Therefore, maximum current ratings and cost are significantly reduced.

Tap converter gating sequences must include provisions which avoid shorting transformer coils. Consider a step up from point (a) to point (b) in Figures 2 or 3. Switch SCR#K commutates SCR#K+1 and step up is completed. A similar combination of events occurs,

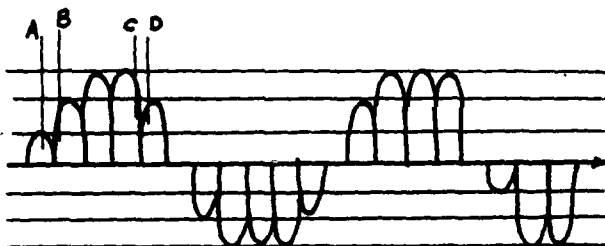


Figure 2. Single phase tap converter output showing 5.6 to 1 frequency reduction



Figure 3. Multiphase (2) tap converter output showing 5.6 to 1 frequency reduction

respectively, when a step down from point C to point D is required. Switch SCR#K commutates SCR#K'-1 when the lower tap voltage rises above the higher tap voltage (in multiphase circuits), or when the current passes through zero. If the load on the tap converter has a lagging power factor, a triggering signal may cause a tap short circuit and loss of load power. A short circuit would result, for example, when as SCR#1 is still conducting the voltage waveshape changes polarity. This calls for a triggering of SCR#1' or SCR#2' if a step down is called for. Similar shorts can occur through a variety of paths and are eliminated by logic circuits that control the gate drive circuitry. To prevent tap shorting, the control circuit must place a gate drive on a subsequent tap, only when the previous tap switch has been extinguished. In other words, the gate control circuitry must tap change in accordance with the existing load power factor. Consider the waveshapes and the firing order shown in Figures 2 and 3. Waveshapes are smooth, approximately sinusoidal and are lower in harmonic content than the waveform of the competing cycloconverter or rectifier/inverter. Finally, where cycloconversion is employed, the cycloconverter must be operated as an inverter at frequencies which are above one-third of the supply frequency. This restriction does not apply in the case of the tap converter. A wide variety of algorithms are available for tap converter programs. Optimum programs may be developed to control specific undesirable harmonics, depending upon application.

The major drawback of using tapped generator windings to achieve the desired modulation, is the increased number of required thyristor switches. This, of course, raises the total cost and weight of the converter. It is not, however, unreasonable to assume that the cost of the silicon-controlled rectifiers will continue to decrease in the coming years. More importantly, the required voltage and current rating of the additional thyristors required for taps are much lower

and, as previously stated, the total thyristor price might less than double, even if more than two taps are used.

In single-phase applications the tap converter is many ways superior to the cycloconverter.

In the tap converter, the input displacement factor is very close to one given a unity displacement factor load, since phase delay modulation is not necessary. Also, the output voltage waveform is much smoother - and its instantaneous deviation from the wanted component is on the average much smaller than that of the cycloconverter. In addition, savings can be made in the cost of protective SCR circuitry required since voltage transients (dv/dt) are significantly reduced, compared with the single phase cycloconverter.

The tap converter mode of operation introduces quantization error which is highly dependent on the number of taps. Operation in the tapped cycloconverter mode can eliminate this error. However, some of the advantages of the tap converter are then lost (or reduced).

A multiphase comparison requires laboratory tests and computer simulations to make the trade-offs more definite. However, input displacement factor improvement and smoother output waveforms are also the main advantages of the multiphase tap converter.

It is clear that a multiphase tap converter will produce sinusoidal waveshapes with the least harmonic content. A design for a two-phase, four-pulse tap converter employing a Scott transformer for three to two phase conversion was considered. This type of converter, while it achieves a smooth and relatively harmonic-free output voltage waveshape, has only a slightly higher thyristor cost than the conventional three-phase, six-pulse cycloconverter. However, because of time and budget considerations, a single-phase tap converter circuit was used in the experimental evaluation.

Experimental Test Results - Single-Phase Design

An experimental version of the three-step, two-way single-phase tap converter is shown in Figure 4, where the gate control has been designed to produce the following prearranged firing sequence of thyristors: 1, 2', 3, 3', 2, 1'-1, 2, -3', -3, -2'-1; or 1', 2, 3', 3, 2', 1, -1, -2', -3, 3'-2, -1', depending on the phase of the input voltage at the starting point. This circuit is therefore designed to produce a six-to-one frequency reduction with a unity displacement factor load. Figure 5 shows the voltage waveform appearing across a purely resistive load. The effect of an inductive load on the output voltage and current waveforms of the three-step tap converter circuit illustrated in Figure 4 is shown in Figure 6, (a)-(d). Each successive photograph corresponds to a more reactive load than the previous one. The firing arrangement is the same as for the purely resistive load. However, due to the inductive nature of the load, and to the particular firing scheme, the given bank is always switched on one-half of the input cycle later than in the resistive case. For example, if thyristor "1" is the last one fired before the negative bank is switched on, thyristor "-1" is to receive the triggering pulse at the beginning of the next input voltage half-cycle. However, with an inductive load, the current stays positive past the voltage zero-crossing, and thus SCR "1" is still conducting when "-1" receives the triggering pulse. Thyristor "-1" is therefore prevented from turning on. If the inductive load is such that the delay in the current zero-crossing does not exceed the duration of the input voltage half-cycle, circulating current-free operation is achieved. No detection of current zero-crossings is required; but a slight amount of distortion must then be tolerated. Figures 6, (a)-(c) illustrate such cases.

The possibility of shorts occurring with more inductive loads is demonstrated in Figure 6, (d). This can

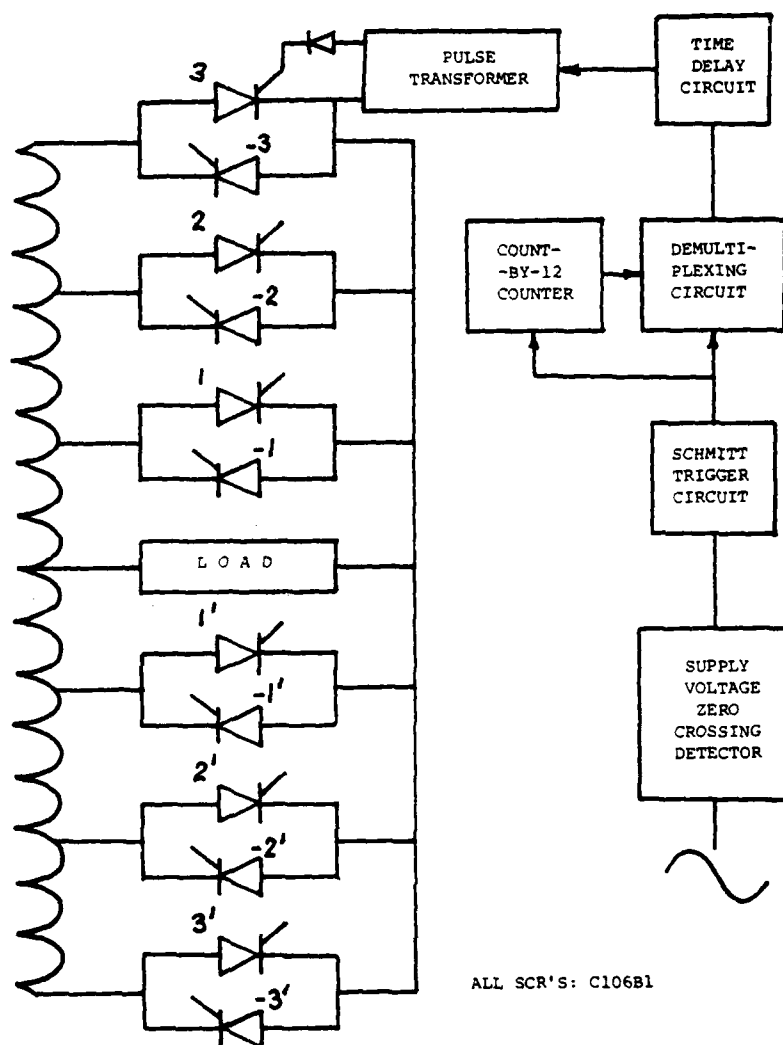


Figure 4. Experimental version of a single phase tap converter. The control circuitry for a prearranged firing pattern is shown in block diagram form.

$R_L = 50 \text{ ohms}$
frequency stepdown 60/10 Hz

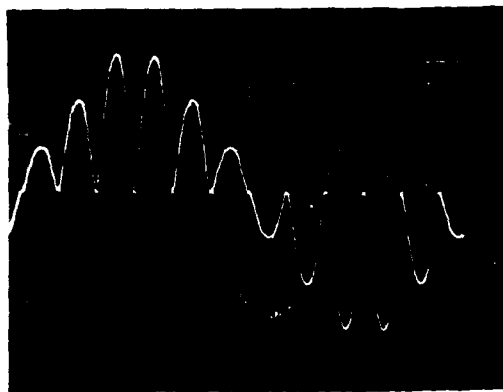


Figure 5. The voltage across the load of the single phase tap coverter operating into a resistive load.

cause damage to the generator winding or thyristors as the circuit does not include (for economic reasons) circulating current reactors.

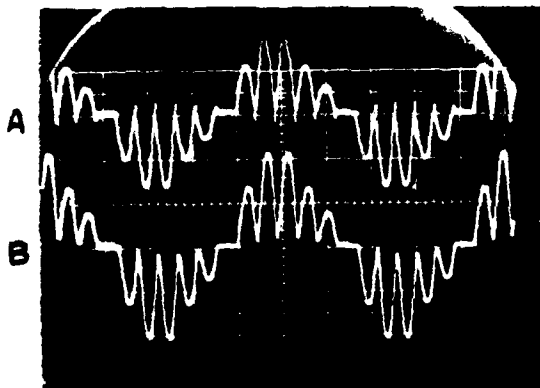
The tap converter can perform reliably if operated in either the circulating current-free mode (using the current-sensing circuitry, or in the circulating current mode. However, some additional departure from the expected output voltage waveshape takes place when the tap converter is feeding an inductive load. This departure may be seen by examining Figure 6, (c) and (d). The distortion occurs especially in the beginning of each output voltage half-cycle, where the rate of change of current is by far the highest. This is the result of $L \frac{di}{dt}$ type voltage fluctuations across the inductive load, and occurs because the voltage impressed on the load at a given time is not "rigid"; that is because the conducting thyristor has some impedance. This problem is common to all modes of operation, and can be countered only by introducing closed-loop control of the output voltage to supplement the algorithm.

Conclusions

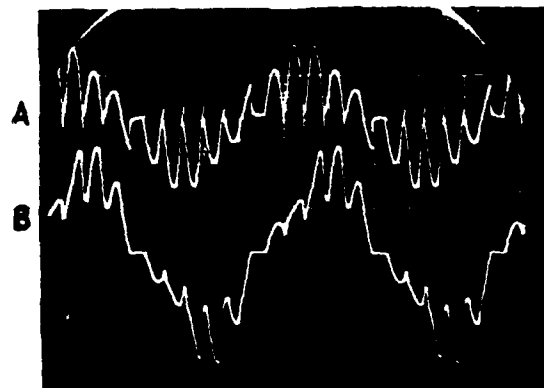
The operation of the tap converter has been examined with a view to its usefulness in VSCF generation systems. A single-phase tap converter has been built and tested to facilitate the comparison with the conventional frequency changing devices. The tap converter relies on AC supply commutation, acts as a favorable load on the input AC system, and is capable of operation into any type of load. Therefore, the tap converter offers, in many respects, a significant improvement over the alternative methods of frequency conversion. The absence of cycloconverter discontinuities in the load voltage results in a very smooth output waveshape, especially in multiphase operation. The tap converter is well suited for use in wind-powered VSCF systems. Unlike the cycloconverter, it can perform voltage regulation over a wider range without deterioration of the input power factor. Feedback regulation of the alternator field current is not necessarily required. It can, therefore, be concluded that the tap converter represents an attractive alternative to the conventional frequency changing techniques.

Bibliography

1. H.J. Allison, R. Ramakumar, and W.L. Hughes, "A Field Modulated Frequency Down Conversion Power System", IEEE Transactions on Industry Applications, vol. 1A-9, No. 2, March/April 1973, pp 220-226.
2. General Electric Co., General SCR manual, 5th ed., Electronics Park, Syracuse, NY, 1972.
3. W. McMurray, "The Theory and Design of Cycloconverters", The MIT Press, Massachusetts, 1972.
4. E.W. Kimbark, "Direct Current Transmission", vol. 1, John Wiley and Sons, Inc., New York, 1971.
5. Pelly, B.R., "Thyristor Phase - Controlled Converters and Cycloconverters", John Wiley and Sons, Inc., New York, 1971.
6. Westinghouse Electric Corp., Westinghouse SCR Designers Handbook, 2nd ed., Youngwood, Pa., 1970.
7. K.M. Chirwin, "A Variable-Speed Constant-Frequency Generating System for a Supersonic Transport", Supplement to IEEE Transactions on Aerospace, June 1965, pp 387-392.
8. D.L. Plette and H.G. Carlson, "Performance of a Variable-Speed Constant-Frequency Electrical System", IEEE Transactions on Aerospace, vol. 2, April 1964, pp 957-970.
9. A.F. Puchstein, T.C. Lloyd and A.G. Conrad, "Alternating-Current Machines", 3rd ed., John Wiley and Sons, Inc., New York, 1954.

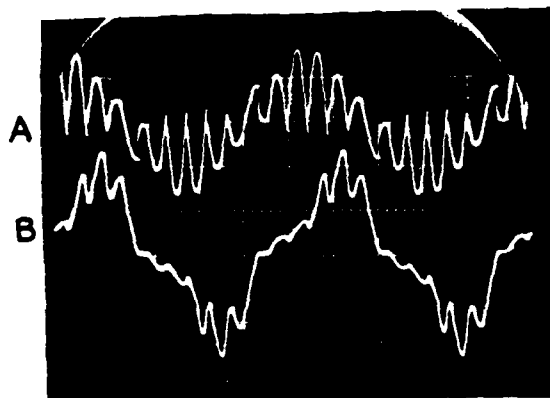


(a) $R_L = 155$ ohms, $L_L = 95$ mH

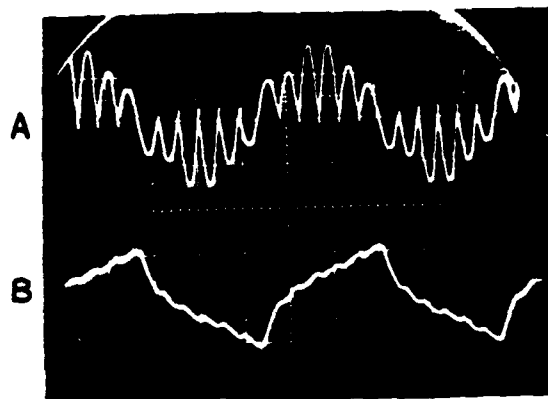


(b) $R_L = 153$ ohms, $L_L = 153$ mH

Figure 6. The load voltage and current of a single phase tap converter operating into an inductive load; trace A- voltage, trace B- current, stepdown 60/10 Hz



(c) $R_L = 70 \text{ ohms}$, $L_L = 153 \text{ mH}$



(d) $R_L = 110 \text{ ohms}$, $L_L = 0.77 \text{ H}$

Figure 6 (cont.) The load voltage and current of a single phase tap converter operating into an inductive load; trace A- voltage, trace B- current, stepdown 60/10 Hz

THE ROTARY FLUX COMPRESSOR - A NEW HIGH POWER COMPACT ENERGY STORE*

Bruce Carder and David Eimerl
University of California
Lawrence Livermore National Laboratory
Livermore, CA 94550

William Bird
Center for Electromechanics
The University of Texas at Austin
Austin, TX 78712

Abstract

Capacitors and explosives are the only devices that are traditionally used for storing energy for long periods of time when the need exists to release this energy very rapidly, at very high powers. Rotary energy stores, e.g., flywheels, are also capable of storing energy for reasonably long times (i.e., tens of minutes), but until recently, the minimum discharge times for these stores have been the order of a tenth of a second.

This paper discusses a new rotational energy store, the rotary flux compressor, that has produced high power electrical discharges of less than one millisecond in duration. Computer codes have shown the feasibility of machines that will deliver up to 15 megajoules in single or multiple sub-millisecond impulses.

Several types of rotary flux compressors exist, including the Compulsator, the Active Rotary Flux Compressor (ARFC), and the Brushless Rotary Flux Compressor. The ARFC is currently under development at LLNL and the University of Texas. It requires startup energy (via a capacitor), but tests to date demonstrate 15 times more energy delivered by the machine than is stored by the startup capacitor. This paper discusses the conclusions drawn from these tests.

Summary

The results of tests with an 8-inch rotor ARFC have proven conclusively that rotary flux compression is feasible. The machine has produced peak output current of 25 kA, with a ratio of peak to startup current as high as 17 and pulsewidth as low as 590 usec (FWHM). The ratio of energy delivered to initial energy stored in the startup capacitor was 15 at the highest rotor speeds of 5600-plus rpm. We noted that this ratio is independent of startup energy, but it increases with machine speed. Thus one can deliver any desired energy from the machine by the simple expedient of varying the voltage on the startup capacitor.

A computer code predicts this machine's output current with reasonable accuracy. An additional feature of the code allows machines to be optimized from the many variables.

The results of the work to date indicate that machines of the present design are feasible up to a maximum rotor diameter of 42 inches. This dimension is established by the maximum available width of transformer-grade silicon-steel sheet stock. Larger

machines will suffer from the reduced performance expected from segmented rotors. A size scaling factor will also degrade the specific power output of very large ARFC's: i.e., the mass scales as r^3 whereas the maximum available power scales as r^2 (r = the rotor radius).

Machines with this 42-inch rotor diameter dimension have been optimized for flashlamp loads. Our code indicates that feasible ARFC's of this size can deliver up to 15 megajoules in a one millisecond pulse. Such a machine will weigh approximately 50 metric tons, and its overall dimensions will be 1.6 m diameter by about 4 m long. At \$30/kg, machines of this size, would cost roughly \$1.5 M, or 10¢/Joule, excluding engineering costs. A competitive capacitive energy store, including power supplies, switches, mountings and connections, and other peripheral hardware that is replaceable by the ARFC presently costs \$3M for 15 megajoules, or 20¢/Joule.

Introduction

The rotation of massive cylinders is an attractive means of storing energy because of its compactness and low cost. This method presents problems for pulsed power applications however, because of the difficulty of rapidly releasing energy from the store. Usual methods of converting mechanical rotational energy to electrical power provide discharge times no better than about a tenth of a second. We present here, test and calculational results from a new inertial energy store, the rotary flux compressor (RFC) that has demonstrated an electrical pulse discharge time of 590 microseconds.

The RFC lends itself well to either single or multiple pulsing, and the energy retrieved during each pulse can be as small or as large as desired, up to virtually 100% of that stored. The machine will match rather high impedance loads, with terminal voltages in excess of 10 kilovolts available. Our initial purpose in developing the RFC was to provide an alternative means to drive flashlamps for large lasers, replacing the presently used bulky (and expensive) systems of capacitor bank modules.

Rotary Flux Compressors

Three basic types of rotary flux compressors have been tested in the program: the compulsator, the active rotary flux compressor (ARFC), and the brushless rotary flux compressor (BRFC), Figure 1. The ARFC is expected to be the most cost effective machine for use with flashlamp circuits because it is smaller than the compulsator and more efficient than the BRFC. Also, it will not require a fast recovering output switch to prevent multiple pulsing. This problem is inherent with the

*Work performed under the auspices of the U.S. Department of Energy by the Lawrence Livermore National Laboratory under contract number W-7405-ENG-48.

TABLE 1. Summary of Test Results with the 8-Inch ARFC

Run No.	Initial Speed (RPM)	Final Speed (RPM)	Inertial Stored Energy (kJ)	Startup Capacitor Energy* (J)	Energy Out of Machine (kJ)	Peak Current (kA)	Current Pulse FWHM (msec)	Ratio: Peak to Startup Current	Energy Gain	$\frac{AR^2}{B+R^2}$ **
25	2143	1925	12.3	363	2.4	5.1	1.93	7.3	7.5	7.6
26	3109	2885	25.9	363	3.6	8.3	1.15	11.2	10.9	10.9
27	3077	2600	25.3	738	7.2	11.3	1.30	10.3	10.8	10.8
28	3133	2400	26.3	1124	10.9	13.0	1.45	9.4	10.7	11.0
29	3158	2080	26.7	1508	15.1	13.6	1.53	8.3	11.0	11.0
30	3846	2878	39.6	1508	17.4	17.2	1.10	9.6	12.6	12.6
31	4124	3175	45.6	1508	18.5	18.2	1.12	10.9	13.3	13.1
32	4545	4348	55.3	363	4.7	12.0	0.73	15.4	13.9	13.8
33	5381	5217	77.5	363	4.7	13.6	0.60	15.4	13.8	14.7
34	5607	5333	84.1	568 ^a	8.0	17.1	0.59	17.0	15.1	15.0
35	5671	5280	86.1	818 ^b	11.5	19.5	0.67	15.1	15.0	15.0
36	5682	4856	86.4	1660 ^b	23.3	25.6	0.79	14.1	15.0	15.0

*Capacitors charged to 2.0 kV, except:

a = 2.5 kV

b = 3.0 kV

**A = 17.92

B = 6.23

R = $\frac{\text{Initial RPM}}{1000}$

compulsator unless a large fraction of the energy is removed with the first pulse.

The ARFC requires a startup capacitor that will store roughly 10% of the total energy delivered to the load. The compulsator has somewhat of an advantage in this regard because it generates its own startup current. This advantage is also a liability, however, since repeated rotation through the field will cause eddy current heating in the windings and core losses in the laminated iron. Thus the compulsator will require a larger sustaining motor than the ARFC. The compulsator also needs external startup energy to be efficient, but it only requires about half that of an ARFC.

The BRFC is an interesting machine because it is the simplest of the rotary flux compressors. It can only be used for fast pulse operation, however, because of current diffusion in the rotor. It also suffers from inefficiency that reduces the available power output. Because of its limitations this machine is not currently being considered as a candidate to drive flashlamps.

The 8-Inch Model ARFC

Because of the advantages inherent with the ARFC, a test machine was constructed with an 8-inch diameter rotor, 24 inches long. The rotor mass and inertia were 98 kg and 0.488 kg·m² respectively. This machine has been previously described^{1,2}, and preliminary test results have been given.³ Further results of our analyses are presented here.

The final twelve runs with the machine are listed in Table 1. The initial and final speeds of the rotor, before and after the pulse are given. These speeds are provided by a monitor on the shaft that marks the time at each revolution. The inertial energy stored in the rotor and the energy stored in the capacitor just prior to the pulse are presented. The energy out of the machine is

calculated by subtracting the inertial energy in the rotor after the pulse from that before the pulse. Note that up to 56.6% of the energy was removed from the rotor during the discharge (run number 29).

The current pulse was monitored with a Pearson 301X current transformer. The peak current, current pulse halfwidth (full-width at half-maximum), and ratio of peak to startup current are also given for each run in Table 1.

The energy gain given in the table is calculated by dividing the total energy removed from the system by the initial energy stored in the capacitor. The energy removed includes both the change in rotor energy and the initial energy in the capacitor. We note that this energy gain coefficient G is independent of the energy in the capacitor: it appears to be dependent only upon the initial machine speed, increasing with speed according to the relationship

$$G = \frac{AR^2}{B+R^2} \quad (1)$$

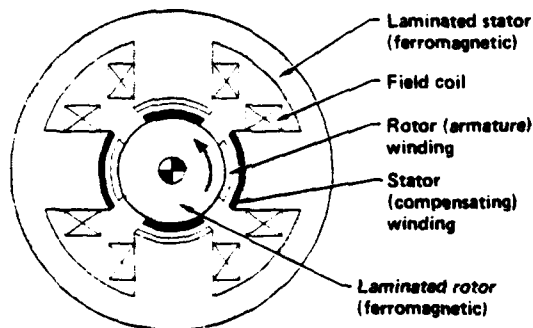
where R is the initial speed (thousands of RPM), and A and B are found to be 17.92 and 6.23 respectively. The final column lists this empirical result, to show how closely it fits the actual gain measurement. Energy gain vs RPM is plotted in Figure 2.

The results of this test with the 8-inch ARFC indicate that an arbitrary large fraction of the energy stored inertially in machines of this type can be removed in a single pulse. In fact, we believe the rotor can be stopped, if need be. The results also show that the energy gain is machine speed dependent, but independent of the initial energy in the startup capacitor. At a given RPM, therefore, the energy delivered is just the gain factor (at that RPM) times the energy in the startup capacitor.

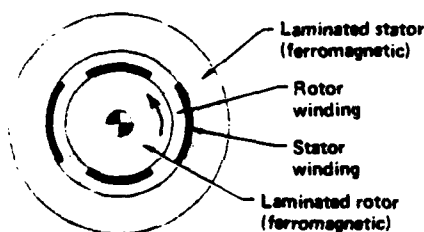
In our tests, gain factors to 15 were observed. With these tests, the ARFC was driving a very low impedance load (1.2 mΩ, 0.66 μH), and most of the energy was dissipated in the machine windings. As machines become larger than our model, and with fewer turns per pole, an ARFC will better drive external loads. (The 8-inch ARFC was a four pole device with 12 turns per pole.) The model performed better than expected, however, and it verified our computational code. As a result, we have confidence in the ability of the code to predict the performance of large ARFC's driving actual flashlamp loads.

References

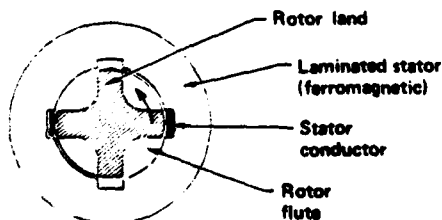
1. M. L. Spann, et.al., "The Design, Assembly, and Testing of an Active Rotary Flux Compressor", 3rd IEEE Pulsed Power Conference, Digest of Technical Papers, June 1981, pp 300-303.
2. W. L. Bird, "The Continued Testing and Evaluation of the Engineering Prototype Compulsator", LLNL Final Report, March 1981.
3. B. Carder, et.al., "Testing and Optimizing Active Rotary Flux Compressors", 3rd IEEE Pulsed Power Conference, pp 304-307.



STATIONARY FIELD COMPULSATOR



ACTIVE ROTARY FLUX COMPRESSOR



BRUSHLESS ROTARY FLUX COMPRESSOR

Figure 1. Basic Types of Rotary Flux Compressors. Laminated sheet steel provides the necessary magnetic circuit for high flux compression.

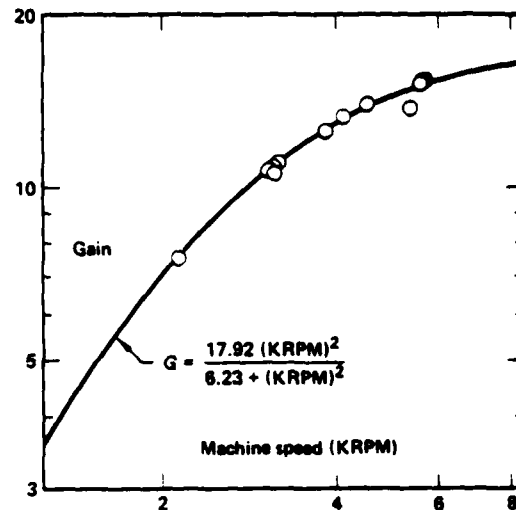


Figure 2. Energy gain versus machine speed for 8-inch ARFC THE ROTARY FLUX COMPRESSOR FAMILY

The Compulsator is a three-winding rotary flux compressor. Voltage is produced across the armature winding as it rotates through a magnetic field created by the field winding. When the circuit is closed, current is generated that is forced to flow back through the compensating winding. This latter winding is as nearly identical to the armature winding as possible, but it is wound on the member containing the field winding (i.e., the stator if the armature rotates, or the rotor if the armature is stationary). The armature, compensating winding, and load are all in series, connected via brushes and slip-rings, and an external switch. The switch is closed when the inductance in the armature/compensating circuit is high. The generated voltage starts current to flow that is amplified by flux compression as the two windings rotate into their lowest inductance position.

The Active Rotary Flux Compressor, ARFC, has two-windings. The field winding is omitted, so the machine cannot generate its own current. Startup current is supplied from an external capacitor bank when the rotor is in the high inductance position. Flux compression provides a high current output pulse as the machine rotates to the low inductance position. The stator and rotor windings are connected in series via brushes and slip rings to the external circuit comprising a startup current source and the load.

The Brushless Rotary Flux Compressor, BRFC, has only one winding and that is on the stator. Startup current is also required in this machine, but the startup and load circuits are only connected to the stator winding and no slip rings or brushes are used. The rotor surface is effectively a shorted winding; current is induced in this "winding" when the startup circuit is pulsed. As the rotor turns, this induced current in the rotor opposes the current in the stator, and flux is compressed, generating a high current output pulse.

DISCLAIMER

This document was prepared as an account of work sponsored by an agency of the United States Government. Neither the United States Government nor the University of California nor any of their employees, makes any warranty, express or implied, or assumes any legal liability or responsibility for the accuracy, completeness, or usefulness of any information, apparatus, product, or process disclosed, or represents that its use would not infringe privately owned rights. Reference herein to any specific commercial products, process, or service by trade name, trademark, manufacturer, or otherwise, does not necessarily constitute or imply its endorsement, recommendation, or favoring by the United States Government or the University of California. The views and opinions of authors expressed herein do not necessarily state or reflect those of the United States Government thereof, and shall not be used for advertising or product endorsement purposes.

A COMPACT SEMI-CONDUCTOR AC SWITCH WITH HIGH INTERRUPTING CAPACITY

D E Creech

Marconi Electronic Devices Ltd, UK

and

P R Pearson and N S Nicholls

Royal Signals and Radar Establishment, UK

Summary

An AC contactor with a high interrupting capability is required in some types of power electronic equipment, particularly where vacuum or gas-filled tubes or spark-gaps are involved. In some severe environments, a semi-conductor switch may be preferred to an electromechanical relay because it is little affected by altitude, climate and acceleration, and it is more compact when a convenient heat sink is available. It will also withstand large inrush currents on closure.

Thyristors connected in inverse-parallel are preferred to triacs because of the superior electrical characteristics attainable. Driving the additional gate involved is shown to be a small penalty.

The PS25N module consists of two specially passivated square thyristor chips in a flat base assembly with internal insulation and plastic encapsulation. It is rated to interrupt 330 A peak in a low power-factor circuit on 200 V 400 Hz supplies. Life is at least 10,000 operations at maximum fault level, with a 25 A rms continuous rating at 90°C heat-sink temperature. It has been qualified to a full military specification in accordance with BS9000.

Special automatic test facilities have been built which simulate every aspect of AC system faults while monitoring device behaviour. Many millions of full power fault condition tests have been carried out in the course of the development.

1. Introduction

Semi-conductor AC switches are often preferred to electromechanical relays where a very large number of operations is required, in severe mechanical environments or for use at high altitudes. It is the object of this paper to show how, with suitable design, they may also be preferable on grounds of compactness where severe current surges are encountered during opening or closing.

A drawback of the semi-conductor AC switch is that, due to the voltage drop, there is an appreciable dissipation associated with the passage of load current, and some form of heat-sink will generally be required. In electronic equipment this is not usually too serious because some form of cooling system is likely to be needed for other components. The penalty may be minimized by design of the device package for a low overall thermal resistance.

The switch to be described was developed to control the supply to a 5 kW transformer and rectifier in a transmitter. The main requirement was to be able to safely interrupt the 3 phase 200 V 400 Hz AC supply under repeated short-circuits on the DC side. In section 2 the circuit is analysed to determine the switch requirements.

The design of the PS25N inverse-parallel thyristor module to meet these requirements with minimum size and

weight is described in section 3. A full military climatic specification was required, with heat-sink temperatures between -55°C and 90°C.

The gate drive required is small, but it must be electrically isolated. Hardware devised to provide this is described in section 4.

Section 5 describes special automatic test equipment which has been developed for reliability testing of the devices under circuit-breaking conditions at up to 350 A peak current. The results from these and other tests designed to establish reliability in the military environment are given.

2. Analysis of the Switch Requirements

2.1 Blocking Voltage and dv/dt Requirements

The blocking-voltage requirements on the switch were found to be dictated by stray voltage spikes. Surges generated by the switch during circuit-breaking are relatively small because the cut-off current is quite small (no more than 0.3 A under the worst conditions). Snubbing components will be needed across each switch to limit the rate of rise of voltage both during circuit-breaking and in the presence of steep voltage spikes on the supply lines. To minimize their size, a high dv/dt rating is required for the switches. A rating of 500 V/μsec was adopted, and a 22 nF capacitor in series with a 47 Ω resistor was found to be generously adequate for snubbing in the presence of the transformer impedance. Under these conditions a surge blocking rating of 750 V was found to be adequate for the switches.

2.2 Current Rating Required

To supply the required load power of 5 kW at minimum continuous supply voltage of 194 V rms the switch in each line must be rated for at least 15 A rms continuous, with the maximum heat-sink temperature of 90°C. A continuous rating of 25 A rms at this temperature was eventually adopted.

When working under these conditions, the switches are also required to act as a circuit breaker for short-circuits on the DC output. This means that they must retain their forward and reverse blocking capability immediately after passing the current surge which results from a symmetrical short-circuit abruptly applied to the transformer secondary with the supply voltage at its maximum surge value of 220 V rms. It was established that the effective impedance under these conditions is 0.43 Ω resistive and 0.47 Ω inductive (at 400 Hz) in series with each line. When a short-circuit is applied abruptly under these conditions, the waveforms of the three line currents depend on the phase of the supply voltage at the instant of its application. A method for calculating the fault currents is given in the Appendix. To predict which will be the worst case, possible failure mechanisms for the device must be considered. The risk of deterioration of the structure will increase with the peak silicon temperature, and this will depend on the

magnitude and duration of the current surge. It turns out that both the magnitude and duration peak at the same value of phase. The corresponding current waveforms for the three switches are shown in fig 1a. It was assumed that the gate-drives are shut off immediately after the fault, and that each switch blocks at the first current zero thereafter. Because it is a three-wire system, the sum of the currents will be equal to zero. The peak current is 265 A and the duration, defined as the duration of a $\frac{1}{2}$ sine wave of equal i^2t value, is about 1.3 msec.

Another possible failure mechanism is temporary loss of forward blocking due to excessive silicon temperature, possibly locally within the chip. Because the thermal time-constant of the silicon to the surrounding metal parts is estimated to be below 1 msec, the risk of forward blocking failure was thought to be greatest when the duration of the inverse voltage was shortest. The switch voltage waveforms for the case of fig 1a are given in fig 1b, and this was thought to be close to the worst case (for switch No 2). However, even if a switch does fail to block forward voltage, the element of redundancy inherent in a 3 wire, 3 switch arrangement ensures that the circuit will be interrupted. The waveforms for this case are shown by dashed lines in fig 1.

If the most probable failure mode for a semiconductor switch is a permanent short circuit, then there will be effective redundancy from the reliability standpoint provided that the switches are adequately rated for the more severe conditions which can arise in this case. This has been investigated with the

result shown in fig 2a and b. The forward current is more severe with a peak value of 305 A and the equivalent duration of 1.6 msec.

3. Power Device Design

A pair of thyristors connected in inverse-parallel were chosen for this switch in preference to a triac because the thyristor pair offered higher dv/dt and repetitive surge capabilities owing to the electrical and thermal separation of opposite electrical quadrant device areas.

The choice of a flat base plastic encapsulation was made because it had a number of significant advantages. For example, the flat base provided excellent thermal contact with the heatsink and all electrical contacts were conveniently made on the same side of the unit which could therefore be mounted directly on to a cooled enclosure surface. Internal electrical isolation was considered essential since it was more efficient and reliable than external insulation which is vulnerable to minor errors of assembly. The adoption of a plastic encapsulation also enabled the assembly to be kept very compact although it did not provide a truly hermetic environment for the thyristor pellets.

These advantages were sufficiently attractive to provide the incentive to tackle the severe requirements imposed by the non-hermetic plastic on the thyristor passivation system. High electric fields occur at the periphery of the thyristor pellets where the blocking junctions are terminated. For reliable operation the passivation layers applied to these high

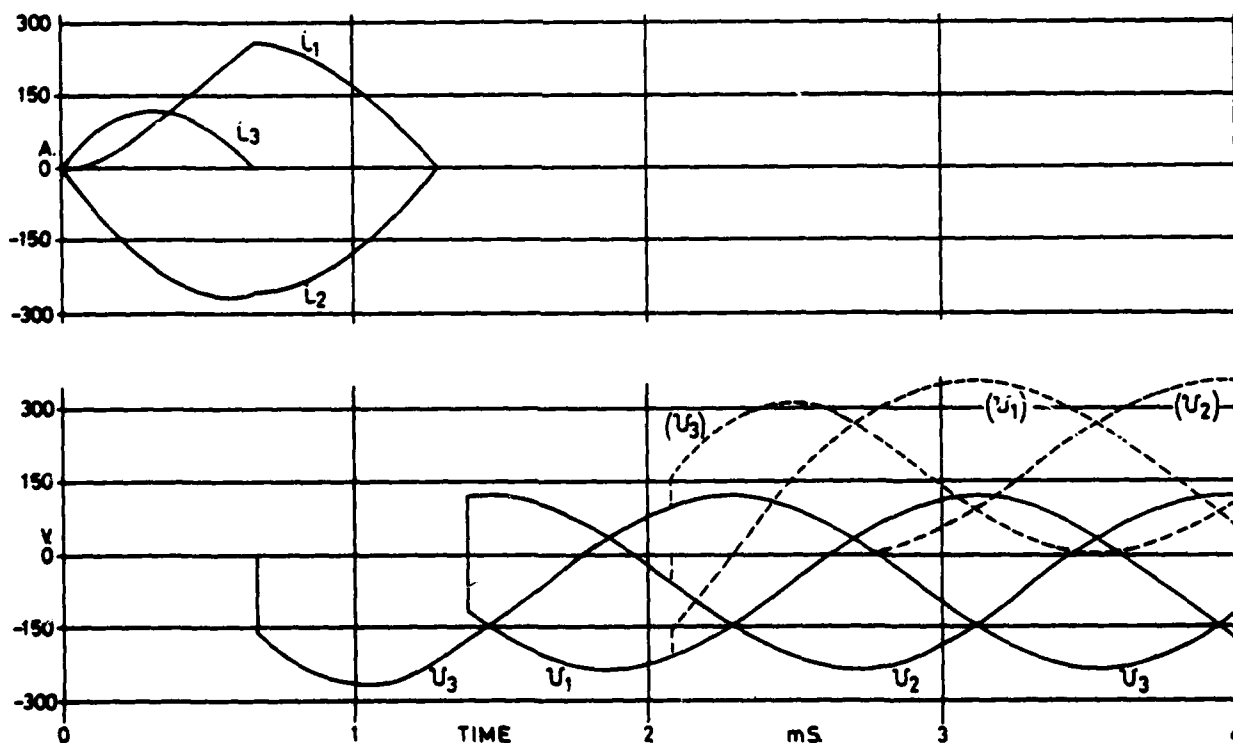


Figure 1

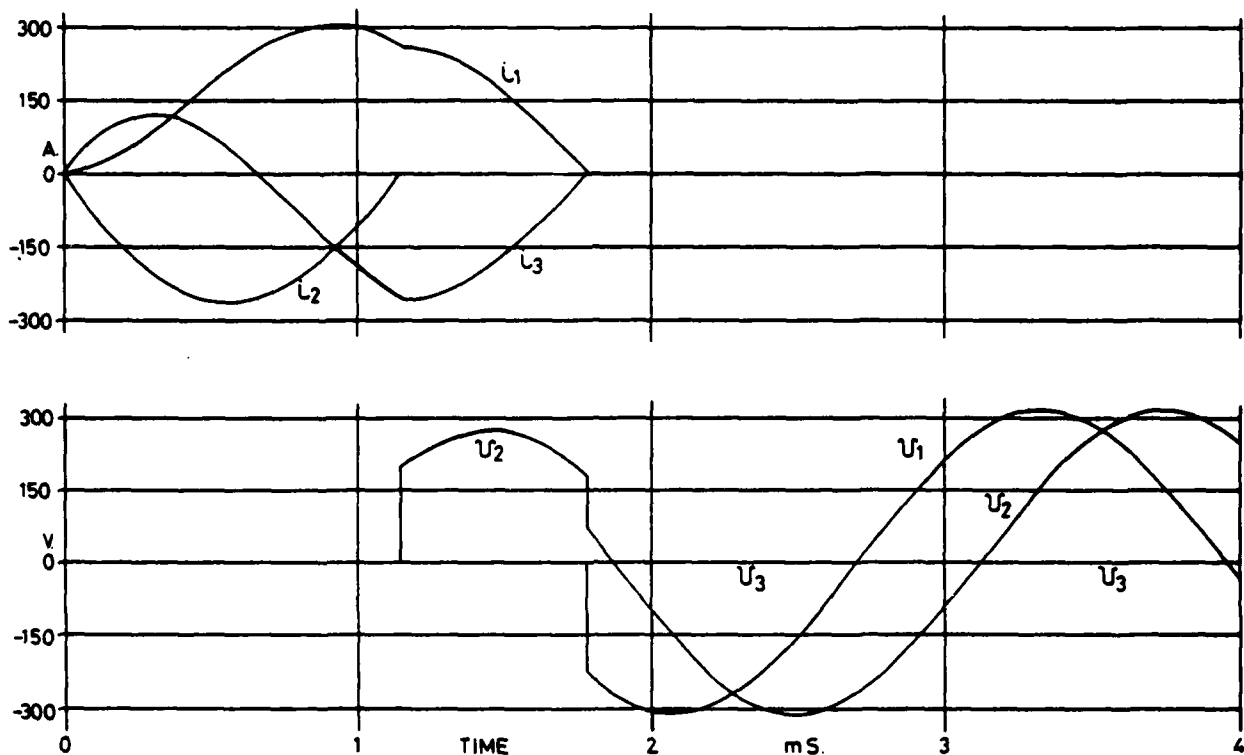


Figure 2

field regions must provide adequate dielectric strength coupled with protection from ionic contamination.

The solution adopted for the PS25N is shown in fig 3. It differed from conventional glass passivation by the additional thin HVOX layer interposed between the silicon and glass surfaces. This HVOX layer, which was formed by low pressure chemical vapour deposition (LPCVD) of polysilicon, acted to neutralise the effects of surface charges on the underlying silicon while the thick outer glass layer provided the required additional dielectric strength.

Internal isolation of the thyristor chips and their contacts from the copper base was achieved via metallised alumina preforms. Considerable differences in expansion coefficient between the various materials in the assembly were inevitable and contact materials were therefore chosen with care in order to achieve reliable operation over a wide range of temperatures. The thyristor chip was mounted onto a silver plated molybdenum disc chosen for its close expansion match to silicon and fatigue resistant multicomponent solders were used for all the joints. Components were also dimensioned to balance thermal and fatigue resistances.

During the development of this assembly it was found essential to prevent direct contact of the plastic filler material with the silicon chip and its immediate contacts in order to prevent mechanical damage by the plastic when operating at temperatures below -35°C . This separation was achieved in practice by placing a PTFE cap over each thyristor pellet before filling the assembly case as shown in fig 4.

The high repetitive surge current rating, rather than the average current requirement, dictated the

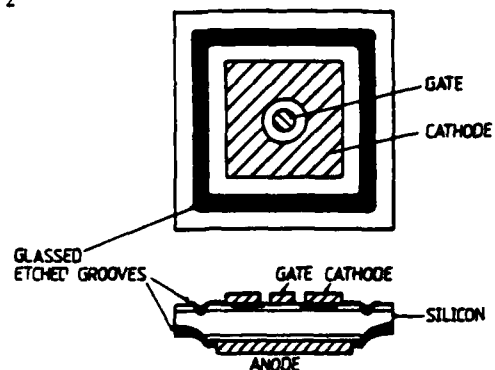


FIGURE 3a Glass Passivated Thyristor Chip

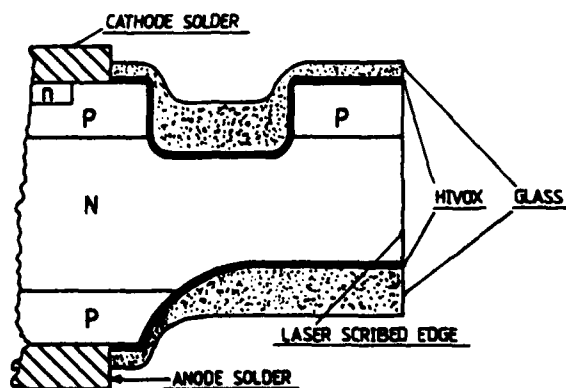


FIGURE 3b Detail of HVOX + Glass Passivation

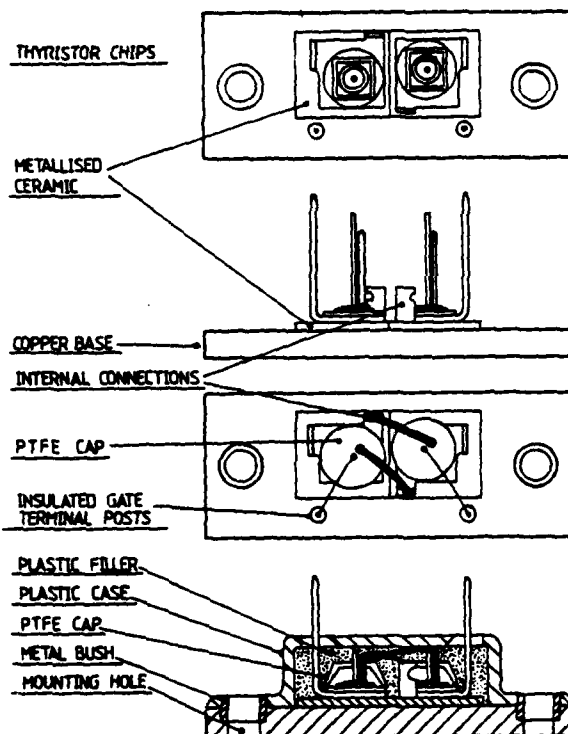


Figure 4 Final Assembly Design

dimensions of the silicon chips and internal contacts. The cathode contact, particularly, was designed to provide a maximum of contact area to the diffused thyristor cathode region and strict processing controls were implemented to ensure uniform high quality joints.

4. Gate Driving Circuits for the PS25N

4.1 Gate Drive Requirements

The PS25N is rated for DC gate drive, provided that the drive is applied and removed simultaneously on both gates of the device. DC gate drive may be preferred on grounds of simplicity, since no synchronization is involved, and versatility, since there is no requirement on the load to pass current continuously during each conduction period.

For satisfactory triggering throughout the rated temperature range while eliminating the risk of damage due to excessive inverse current in the thyristors, the DC gate drive must lie in the range 50 mA to 100 mA. The gate-cathode voltage will lie between 0.5 V and 2.5 V. Due to the provision of localized internal gate-cathode short-circuits, the impedance of the external gate circuit is not important to the blocking and dv/dt characteristics.

4.2 DC Gate Drive Circuits

A suitable circuit for driving one gate of the PS25N would have an emf of $9 \text{ V} \pm 0.5 \text{ V}$ DC with an impedance of $100 \Omega \pm 5\%$. Six isolated gate drive circuits are required for a 3-phase switch, with insulation for 2000 V peak test to ground and between

circuits. A convenient way to obtain the isolation and also to satisfy the simultaneous switching requirements is to use a single transformer having six secondary windings, the primary being fed with a high-frequency square-wave from a low impedance source. Such a transformer for operation at 100 kHz need occupy no more than one cubic inch. Each secondary would be fitted with a bridge rectifier and a current limiting resistor. Shottky rectifiers such as the IN5818 may be preferred on grounds of efficiency. The total power consumption of the driver in the operating state would be about 7 watts. In the off state, it would be negligible. A possible circuit for operation from low-voltage DC is shown in fig 5.

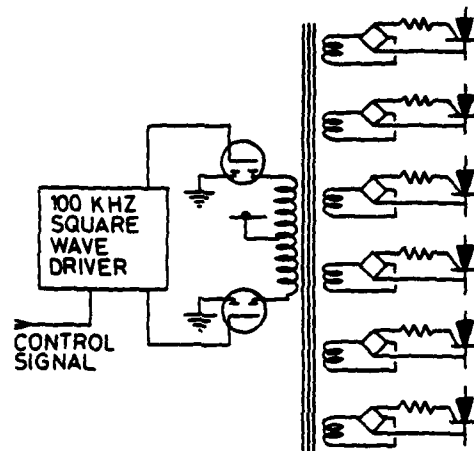


Figure 5 Drive Circuit for 3-Phase Switch

5. Testing and Test Results

5.1 Reliability Testing Results

The tests of specific interest for this plastic encapsulated unit were as follows:

- Electrical endurance for which eight units were subjected to 2000 hrs blocking at maximum repetitive voltage, VRM, and maximum junction temperature. No failures were observed.
- Rapid change of temperature plus damp heat cyclic for which eight units were subjected to five cycles of -55°C to $+90^\circ\text{C}$ followed by six 24 hr cycles of damp heat to BS2011 Part 2.1 Da. One allowable failure was observed.

The overall result was that all BS9000 tests were successfully passed.

5.2 Equipment for Testing Under Circuit-Breaking Conditions

In the interests of economy and silence, it was decided to generate the waveforms using inductors and capacitors rather than an alternator. This only enables the fault current to be simulated, the effect of the normal full-load current is simulated by pre-heating the whole package to a temperature somewhat above the estimated maximum silicon temperature which could arise under the continuous ratings.

The high power part of the circuit is shown in fig 6. The capacitor bank totalling about 440 μF is pre-charged by a controlled rectifier to a pre-determined voltage in the vicinity of 450 V. The device under test (DUT) then discharges this through an

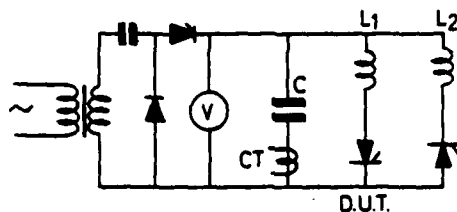


Figure 6 Test Circuit

inductor, which swings the capacitor voltage to about -350 V, in the process passing a current of half-sinewave shape with peak current up to 350 A and duration 1.6 msec. When the current ceases, the capacitor voltage appears as inverse voltage across the DUT (see fig 7). After a selected interval, an

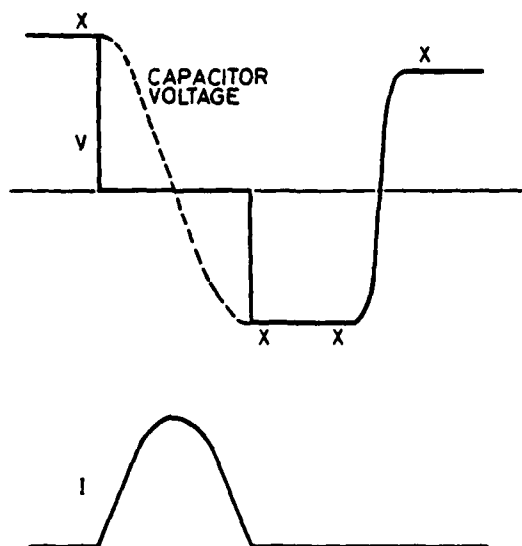


Figure 7 Test Waveforms

auxiliary thyristor is triggered and recharges the capacitors to about + 320 V through a second inductor. The capacitors are then recharged by the controlled rectifier to the initial voltage and after a suitable interval the cycle is repeated. The voltage is monitored at the parts marked X on the waveform. If the initial capacitor voltage falls outside a tolerance of $\pm 1\%$ of the target value, the test is aborted and the fault indicated. If the subsequent voltages or the peak current are too small the fault is indicated and the test is stopped at the end of the cycle. The device leakage currents are monitored at the points X and the values displayed.

5.3 Test Results Under Circuit-Breaking Conditions

The bulk of the special surge testing was carried out under particularly severe conditions with junction temperatures in the range 125°C to 135°C as compared to a maximum operating junction temperature of 125°C .

The results are presented in fig 8 and show only one failure at less than the required 5000 shots.

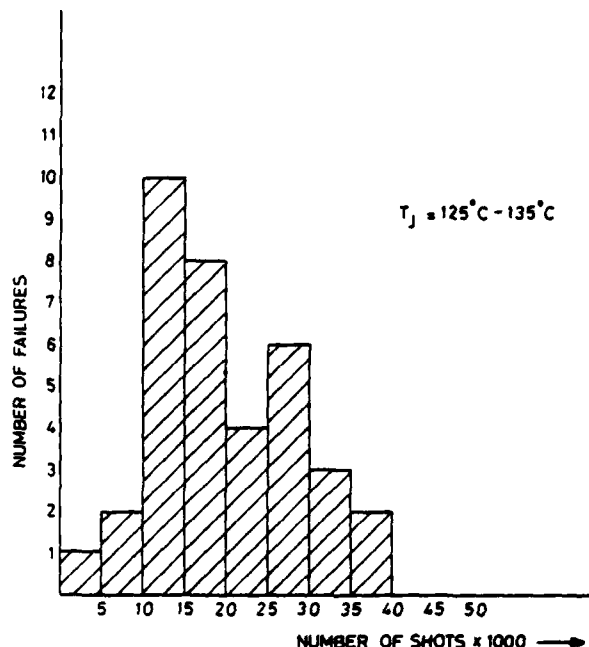


Figure 8 Test Results

Additional testing was carried out with device junction temperatures of $110-112^{\circ}\text{C}$. No failures occurred at less than 20,000 shots and the mean number of shots to failure was in excess of 54,000.

These results demonstrate a very satisfactory performance under worst conditions and the device has been qualified to a full military specification in accordance with BS9000.

Appendix - Calculation of the Switch Currents in a Symmetrical 3-Phase Circuit Assuming Switches Open at Zero Current

A1 The Method

We shall first obtain a general analytical solution for the single-phase circuit using the Laplace Transformation.

We shall then show that the solution suffices for the calculation the the switch currents in the 3-phase case provided that the initial currents in the 3 lines are balanced.

A2 Fault Current in Single-Phase AC Circuit with Arbitrary Initial Current

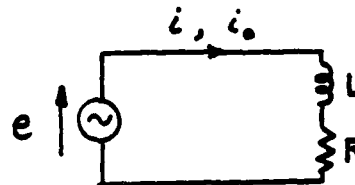


Figure A1

The circuit to be analysed is shown in fig A1. The generator EMF is given by:-

$$e = E \sin(\omega t + \phi) \cdot U(t) \quad (1)$$

where:-

E is the peak voltage of the AC source
 ω is the angular frequency of the AC source
 ϕ is the initial phase
 $U(t)$ is the unit step function

Then if

\bar{I} is the Laplace Transform of the current i
 i_0 is the initial current
 \bar{e} is the Laplace Transform of e
 p is the Laplace Operator

$$L(p\bar{I} - i_0) = \bar{e} \quad (2)$$

By evaluating \bar{e} from equation (1) and writing:-

$$\alpha = R/L$$

$$I = E/\sqrt{R^2 + \omega^2 L^2} \quad (\text{the peak steady state current})$$

we may obtain from equation (2) an expression for \bar{I} . Taking Inverse Laplace Transforms then yields:-

$$i = I/\sqrt{\omega^2 + \alpha^2} \left[A \sin \omega t + B(\cos \omega t - e^{-\alpha t}) \right] + i_0 e^{-\alpha t} \quad (3)$$

where:-

$$A = \omega \sin \phi + \alpha \cos \phi \quad (4)$$

$$B = \alpha \sin \phi - \omega \cos \phi \quad (5)$$

A3 Fault Currents in a Symmetrical 3-Phase Circuit with Balanced Initial Currents

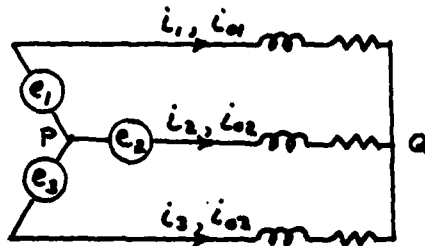


Figure A2

$$i_{01} + i_{02} + i_{03} = 0 \quad (6)$$

where i_{01} , i_{02} , i_{03} are the initial currents and also the three emf's e_1 , e_2 and e_3 differ only in regard to phase, thus:-

$$\left. \begin{aligned} \phi_2 &= \phi_1 - \frac{2\pi}{3} \\ \phi_3 &= \phi_1 + \frac{2\pi}{3} \end{aligned} \right\} \quad (7)$$

We shall postulate that there is no voltage between P and Q at any time and show that under these conditions the sum of the three currents will be zero at all times.

With no voltage between P and Q, the currents i_1 , i_2 and i_3 may be calculated using equation (3).

Substituting from (7) in equation (4) gives:

$$A_1 + A_2 + A_3 = 0 \quad (8)$$

Likewise, substituting from (7) in equation (5) gives

$$B_1 + B_2 + B_3 = 0 \quad (9)$$

Hence, taking equations (3), (6), (8) and (9) together:-

$$i_1 + i_2 + i_3 = 0 \quad \text{at all times.}$$

A4 Calculation of Switch Currents in a Symmetrical 3-Phase Circuit

We have shown that while all three switches remain conducting, the current in each switch may be calculated separately using equation (3). If it is assumed that switch conduction ceases when the current is zero, then at the instant when the first switch opens, the current in the remaining two switches is equal and opposite. Current continues in these remaining switches as a single-phase fault and may also be calculated using equation (3) with the emf appropriately changed in magnitude and phase.

THE POWER CONDITIONING SYSTEM FOR THE ADVANCED TEST ACCELERATOR

M. A. Newton, M. E. Smith, D. L. Birx, D. R. Brannum
E. G. Cook, R. L. Copp, F. D. Lee, L. L. Reginato, D. Rogers, and G. C. Speckert

Lawrence Livermore National Laboratory
P. O. Box 808
Livermore, CA. 94550

Introduction

The Advanced Test Accelerator (ATA) is a pulsed, linear induction, electron accelerator currently under construction and nearing completion at Lawrence Livermore National Laboratory's Site 300 near Livermore, California. The ATA is a 50 MeV, 10 kA machine capable of generating electron beam pulses at a 1 kHz rate in a 10 pulse burst, 5 pps average, with a pulse width of 70 ns FWHM. Ten 18 kV power supplies are used to charge 25 capacitor banks with a total energy storage of 8 megajoules. Energy is transferred from the capacitor banks in 500 microsecond pulses through 25 Command Resonant Charge units (CRC) to 233 Thyatron Switch Chassis. Each Thyatron Switch Chassis contains a 2.5 microfarad capacitor and is charged to 25 kV (780 joules) with voltage regulation of $\pm .05\%$. These capacitors are switched into 10:1 step-up resonant transformers to charge 233 Blumleins to 250 kV in 20 microseconds. A magnetic modulator is used instead of a Blumlein to drive the grid of the injector (see Figure 1).

system was also used for the development and testing of the electronic control circuits for the power conditioning system.

Overall Power Conditioning System

There are three separate power conditioning systems in ATA which are identical except for output power level (Figure 1). The largest power conditioning system is used to drive the 190 accelerator cells while the other two systems separately drive the 10 injector cells and the trigger system. The power conditioning was arranged in this manner to allow the accelerator to operate at different levels than the injector since the spark gap gas systems are separate. The injector and trigger systems, however, are tied to a common gas system and their output levels cannot vary by more than 20% before jitter begins to be intolerable. A block diagram of the basic power conditioning system is shown in Figure 2.

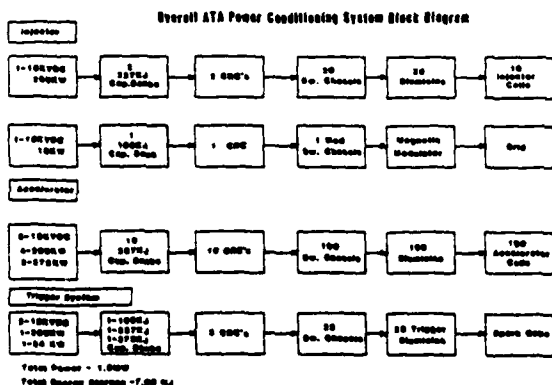


Figure 1

The Experimental Test Accelerator (ETA) has served as a technology base for all of the major components of the Power Conditioning System for the ATA, although many changes have been incorporated into the ATA system to improve reliability and performance. A prototype test stand incorporating all major power conditioning components was constructed and used for development work and testing of the major components for millions of shots. Another test system was built to test all 233 Thyatron Switch Chassis for at least 100,000 shots at full voltage (25 kV) and current (10 kA). This

*Lawrence Livermore National Laboratory is operated by the University of California for the Department of Energy under contract No. W-7405-Eng-48.

This work is performed by LLNL for the Department of Defense under DARPA (DOD) ARPA Order No. 3717, Amendment 41 monitored by NSMC under contract #N60921-81-LT-W0043, and DARPA (DOD) ARPA Order No. 4395 A#1.

This abstract is submitted to the Fifteenth Power Modulator Symposium, June 14-16, 1982, Baltimore, Maryland.

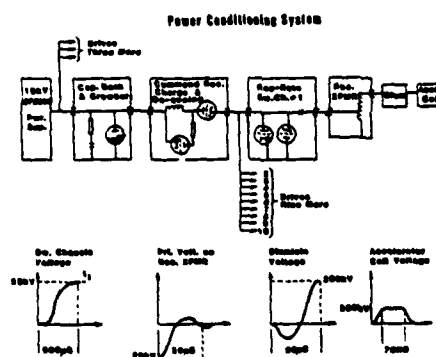


Figure 2

Power Supplies

There are ten power supplies in the system of four different ratings. Except for component sizes, they are essentially identical. The basic schematic is shown in Figure 3. SCR phase control is used in the primary to vary the output voltage level. The output current level is sensed by current transformers in the primary. These signals are rectified and compared to a dc reference to limit the power supply output current. As the output voltage nears the requested level, the voltage feedback loop takes over and stops the charging of the capacitor bank at the requested voltage. The

loop gain of both feedback loops is about fifty, which provides more than adequate regulation for the purpose. The only unusual feature of these power supplies is the inclusion of resistance and reactance in the primary circuit. This is required to limit fault currents to a reasonable level when the system is crowbarred. The rectifier transformers are actually power-distribution pole transformers purchased for another application but never used. The impedance of these units is about 2%, so additional impedance had to be added.

Basic Schematic of 270 kW Power Supply

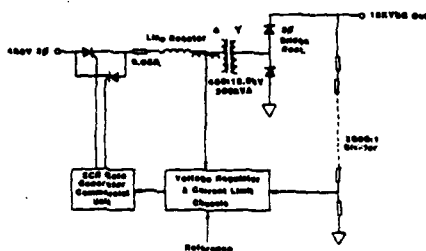


Figure 3

Capacitor Banks

The ATA design requirements for ten pulses at one kilohertz with 5 Hz average, dictated that the peak power of a few hundred megawatts during a burst be derived from capacitor banks. The schematic of the basic capacitor bank is shown in Figure 4. It consists of forty 50 μ F, 18 kV capacitors. Each capacitor has an energy limiting fuse and a 12.5 ohm resistor in series with it. The resistor limits the crowbar current to a reasonable value (58,000 A). The fuses are required to prevent rupture of a capacitor case if it breaks down inside. Two ground switches are included to discharge the bank on normal shutdown. The soft-ground switch closes first and the stored energy is dissipated in 144-660 watt glow-coil heaters. About one second later, the hard-ground switch closes. The delay is provided by energy stored in a capacitor connected in parallel with the solenoid. Since several banks are connected to a single power supply, a diode is provided on the input of each bank to prevent discharging several banks through one crowbar or grounding switch.

Basic Schematic of Capacitor Bank

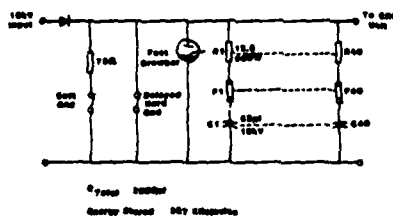


Figure 4

Command Resonant Charge Unit

Each CRC charges 10 switch chassis or 25 microfarads. The mean charge time is approximately 500 microseconds with a peak current of 1500 amps in a single pulse mode (5 pps) and 1600 amps in a

regulated burst mode (1 kHz). Droop in the capacitor bank voltage (~16% for ten pulses) during a burst would cause a decrease in the switch chassis voltage, and ultimately the accelerating potential, on each successive pulse, if unregulated. Therefore it is necessary to regulate the charge voltage on each switch chassis. Regulation is obtained by de-queuing or resistive clipping. The CRC Unit is shown in Figure 5. It contains six parallel EEV CX-1538 hydrogen thyratron tubes for the series switch (V1-V6) and four parallel CX-1538R tubes for the de-queuing switch (V7-V10). Six tubes in parallel were used for the series switch in order to keep the RMS current through the tubes approximately the same as the RMS current in the switch chassis tubes. The series resistors insure current sharing. Four tubes were used in parallel for the de-queuing switch for the same reason. The resistors in series with each of the de-queuing tubes were chosen to limit the RMS current through the tubes and yet dissipate as little energy as possible, since the de-que current commutates back to the capacitive load.

Command Resonant Charge Unit

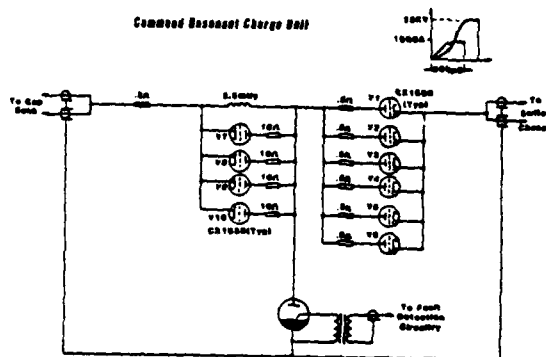


Figure 5

If the de-queuing tubes are triggered at the correct time, the voltage to which each switch chassis is charged during each pulse will be constant. The triggering of these tubes is controlled by the circuit in Figure 6. The circuit, which consists primarily of a comparator and a burst amplifier, compares the voltage waveform from a fairly low-impedance divider (50 k Ω) to a 0 - 10 VDC reference. A trigger pulse is generated when these two voltages are equal. There is an unavoidable delay time, τ_D , from the time the correct voltage is sensed to the time V7-V10 begin conduction. Because of the inherent τ_D , which is typically a couple of microseconds, the best regulation that could possibly be obtained is several tenths of a percent depending on the capacitor bank droop and τ_D . Figure 7A shows the exaggerated effect of firing time delay. In order to compensate for this time delay, it is necessary for the voltage from the voltage divider to be slightly ahead in time with reference to the actual switch chassis voltage so that at a time τ_D after the voltage divider signal reaches V_{REF} , the actual switch chassis voltage is equal to V_{REF} as shown in Figure 7B. On ATA, this is accomplished very simply by placing the voltage divider on the CRC side of the current limiting resistors in series with each switch chassis as shown in Figure 6; this output phase lag corresponds to shifting ahead the comparator signal. Since this phase difference is considerably larger than that which is required to offset τ_D , the signal from the voltage divider

must also be phase shifted later in time. This is accomplished with R_1 and C_1 . Using R_1 as fine-tuning, voltage regulation of $+ .025\%$ has been obtained in burst operation (See Figure 8).

The ignitron in Figure 5 is used to dump any energy stored in the CRC in the event of a fault. The trigger signal originates from a CMOS logic circuit designed to detect any abnormal current or voltage waveforms. If an abnormal waveform is detected, a trigger pulse is sent to the ignitron in the CRC as well as the one in the capacitor banks. The CRC ignitron prevents excessive current in the series tubes in the event of a short on the output of the CRC, such as the prefire of a switch chassis.

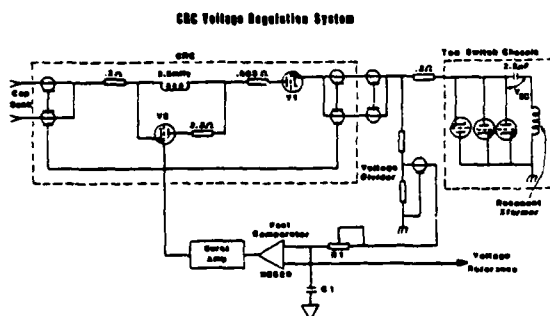


Figure 6

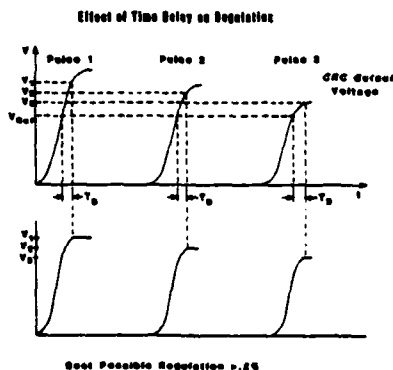


Figure 7A

Compensating for T_0

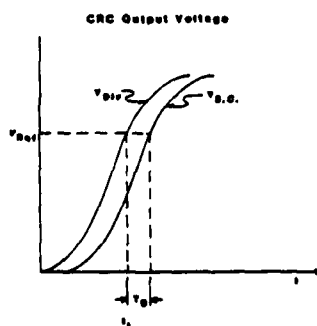
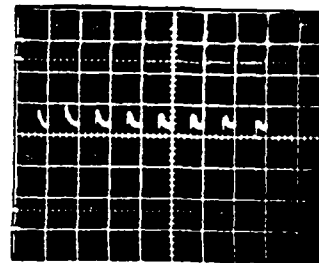


Figure 7B

6 Pulse Burst
18kV

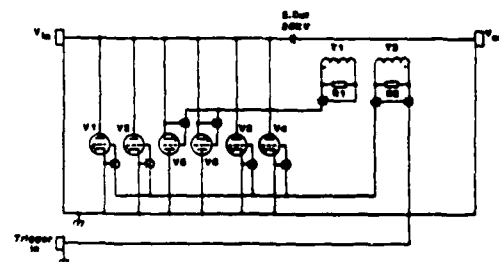


50V/div
1ms/div

Figure 8. Regulated CRC Output

Switch Chassis

Each Thyatron Switch Chassis contains 6 EEV CX-1538 hydrogen thyatron tubes which are used to switch the energy stored in the 2.5 microfarad, 25 kV capacitor into the primary of the resonant transformer. The CX-1538 thyatrons were developed by English Electric Valve Company to meet LLNL specifications in a competitive development program. They were specifically developed for use in the ATA switch chassis. The switch chassis will run at 1 kHz, 10 kA peak (2.5 kA/tube) at 25 kV. A schematic of the switch chassis is shown in Figure 9.



ATA Thyatron Switch Chassis Schematic

Figure 9

The switch chassis contains a bi-directional switch with 4 parallel tubes (V1-V4) conducting current during the first half cycle (forward direction) of the Blumlein charge cycle and 2 parallel tubes (V5, V6) conducting current during the second half cycle (reverse direction). Tubes V5 and V6 are automatically triggered using a small, saturating, iron-core pulse transformer (T1), which uses the output cable as a primary and has an air gap so the generated pulse occurs just prior to the zero crossing as shown in Figure 10. The same basic pulse transformer (T2) is used in series with the thyatron grid trigger for the 'forward' tubes in order to trigger all four tubes in the event that one of the thyatrons prefires (see Figure 10). The negative pulses are diode clipped so that the thyatron grids only see a positive pulse.

Switch Chassis Pulse Transformer Waveforms

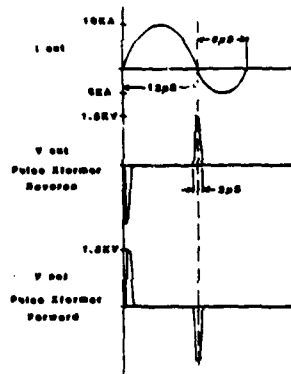


Figure 10

Resonant Transformer

The 12 Ω , 14 nF Blumleins are charged by using a 10:1 step-up, air-core, dual-resonant transformer. A resonant transformer is a very efficient way of charging a capacitive load such as a Blumlein. An optimum mode of charging with a resonant transformer is with the coefficient of coupling, $k = .6$, and with the primary and secondary tuned to the same frequency. With this configuration, the primary voltage and current and the secondary current are equal to zero at the same time the secondary voltage is at its peak (see Figure 11). Theoretically this is a condition for 100% energy transfer although in practice, because of transformer and switch losses, the efficiency drops to less than 90%.² An additional benefit of this charging mode is that spark gap recovery time is enhanced as there is no energy remaining in the transformer to maintain the arc.³



Figure 11. Resonant Transformer Waveforms

This mode of operation requires a bi-directional switch in each Thyatron Switch Chassis because the primary current in the resonant transformer reverses polarity before the secondary voltage reaches its peak as seen in Figure 11. This is the reason that each switch chassis has 'forward' conducting tubes and 'reverse' conducting tubes.

Control System

A multiprocessor control and monitor system is used to facilitate the control and monitor requirements of the Power Conditioning System as well as all other ATA systems. The control and monitor systems consists of dual DEC VAX 11/750 minicomputers, five DEC LSI 11/23 microprocessors, four Modicon 584 programmable controller systems (PCs), and a CAMAC data acquisition system (see Figure 12). The computers and programmable controllers are organized as a dual hierarchical network. The

function of the minicomputer is to act as the operator interface, make high-level decisions, and do data archival and retrieval. The microprocessors are the interface between the minicomputer and the PCs. The PCs, with its remote I/O structure, are the interface between the equipment and the computer system. The PCs are used to collect data, effect control commands, and make low-level decisions. The operator interface to the control system is through a color graphics system for information display, transparent touch panels, digital knobs and a few switches for command inputs.

ATA Computer System

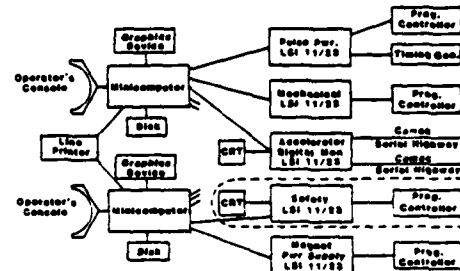


Figure 12

The programmable controllers are programmed in a symbolic language known as ladder logic, the microprocessors and minicomputers use mostly Pascal, with some assembly language. Standard vendor operating systems and network communications packages are being used. A data driven software architecture provides the flexibility and expandability necessary for this experimental system. Utilization of graphically defined controls and displays allow the operator complete freedom to interact with the machine in a convenient fashion.

Present Status of ATA

ATA is scheduled for completion in October of 1982. Testing and check-out of the power conditioning systems has already begun and will continue to October. An upgrade of ATA to a burst rate of 10 kHz is already under study. Photographs of the power conditioning equipment for ATA are shown in Figures 13-15.

FOOTNOTES

1. Overview of the ETA/ATA Pulse Power by L. L. Reginato and R. E. Hester, Fourteenth Pulse Power Modulator Symposium, Orlando, Florida, 1980.
2. Off-Resonance Transformer Charging for 250kV Water Blumlein by E. G. Cook and L. L. Reginato, IEEE Transactions on Electron Devices, Volume ED-26, No. 10, October 1979.
3. Advanced Test Accelerator (ATA) Pulse Power Technology Development by L. L. Reginato, et al. IEEE Transactions on Nuclear Science, Vol. NS-28, No. 3, June 1981.



Figure 13
ATA Power Conditioning Area

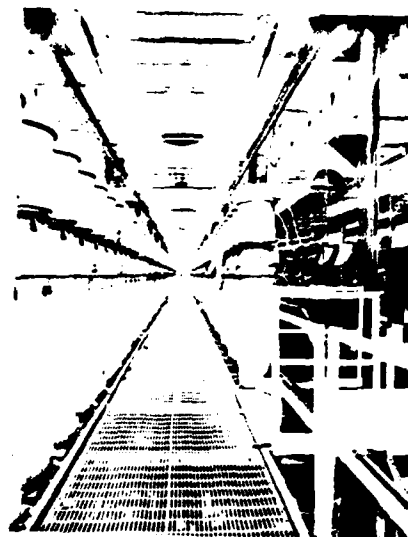


Figure 15
ATA Blumlein Assemblies



Figure 14
ATA Switch Chassis Bay

DISCLAIMER

This document was prepared as an account of work sponsored by an agency of the United States Government. Neither the United States Government nor the University of California nor any of their employees, makes any warranty, express or implied, or assumes any legal liability or responsibility for the accuracy, completeness, or usefulness of any information, apparatus, product, or process disclosed, or represents that its use would not infringe privately owned rights. Reference herein to any specific commercial products, process, or service by trade name, trademark, manufacturer, or otherwise, does not necessarily constitute or imply its endorsement, recommendation, or favoring by the United States Government or the University of California. The views and opinions of authors expressed herein do not necessarily state or reflect those of the United States Government thereof, and shall not be used for advertising or product endorsement purposes.

SOLVING THE LOW-FIRST-PULSE PROBLEM

BY

WILLIAM H. WRIGHT, JR.
US Army Electronics Technology & Devices Laboratory, ERADCOM
Fort Monmouth, NJ 07703, Phone (201) 544-5404

SUMMARY:

A simplified voltage-doubler circuit is described capable of charging a PFN to its full voltage prior to the first pulse to avoid the low-first-pulse problem. Design considerations, equations for choosing component values, and a sample calculation are given.

INTRODUCTION:

Typical resonantly-charged line-type modulators operate with the fast energy store, usually a lumped-element PFN, charged to approximately twice the power supply/filter capacitor voltage level. However, as the system is turned on and the filter capacitor is charged slowly from the main power supply, there is no resonance and the PFN charges slowly through the charging diode to the same voltage as the power supply/filter capacitor voltage. This factor of two can create problems for the load, such as the transmission foil on an e-beam pumped laser wherein the foil absorption increases for lower electron energies, or for the discharge switch which often has less than a two-to-one operating range between no-fire and pre-fire. This switch range problem is especially bothersome on a modulator used for switch development, where switch performance may be particularly intractable. For nonlinear loads whose impedance varies with voltage, the load match presented to the PFN varies with PFN voltage. It may, then, take many pulses before operation settles down to its steady-state condition.

While other techniques have been used previously to solve this problem, such as manually-controlled separate power supplies connected on the PFN side of the charging diode, or a high voltage contactor closed manually after the filter capacitor has been fully charged, it is felt that the circuit presented here, which requires neither attention nor moving parts, offers the simplest, cheapest, and most reliable solution. One of the most attractive features is that the boost circuit's output automatically tracks with the main power supply.

THE BOOST CIRCUIT:

Starting from the widely used three-phase full-wave rectifier circuit shown in Figure 1(a), any power supply drawing its power from one or more phases of the plate transformer, or from separate windings on the transformer core, and totally isolated by diodes in the output and return lines, as shown in Figure 1(b) would provide the necessary voltage and self-tracking features. The logical choices for the boost circuit power supply are the transformerless voltage doublers, the half-wave and full-wave, shown in Figures 2 and 3 respectively. The half-wave can be simplified still further by recognizing in Figure 2(a) that the isolating diode D1 is in series with the doubler diode D2 and can be eliminated, and isolating diode D3 is in parallel with the rectifier diode D4 and the line containing D3 can be eliminated. In Figure 3(a), the return isolating diode D1 may be unnecessary if the impedances through the doubler circuit are high, in which case doubler diode D2 is in parallel with rectifier diode D5 and can be eliminated. In any event, the circuit in Figure 3 has two capacitors, which are the largest and most expensive components used. The simplified half-wave circuit in Figure 2(b) is the one studied and described here.

CIRCUIT REQUIREMENTS:

For optimum results, the boost circuit should charge the capacitance of the PFN in a few seconds prior to the first pulse, have no effect on the modulator after the first pulse, and be self-protecting from all foreseeable fault modes. By properly choosing component values, the half-wave doubler circuit can do all of this. By adjusting the voltage to which the boost circuit charges the PFN to be slightly less than the resonant recharge voltage, the boost circuit output diode will be reverse biased at all times except prior to the first pulse and during the recharge interval. It will therefore spend most of its time

open-circuited and be invisible to the rest of the modulator circuit. If the boost circuit unloaded voltage were higher than the resonant recharge voltage, there would be a voltage "creep" and the PFN voltage would depend undesirably on the interpulse period.

The low impedance main power supply will charge the PFN through the charging diode to the filter capacitor voltage as the power supply is raised. The boost circuit, with a high Thevenin-equivalent impedance, R_{eq} , will act as a topper with a $R_{eq}C_{PFN}$ time constant on the order of one second.

The discharge transients of the PFN are kept off the boost circuit by connecting it to the filter capacitor side of the charging inductance.

CIRCUIT DESIGN AND COMPONENT CONSIDERATIONS:

By analyzing the boost circuit in the limiting cases of PFN voltage higher than the boost circuit voltage (open-circuit case) and PFN shorted, component values can be determined which will survive the worst-case conditions. All calculations will be referenced to V_{pk} , the peak value of the AC voltage across one side of the delta-connected transformer.

$$V_{pk} = 2 V_{rms} = 1/2 V_{\text{peak-to-peak}}$$

If the transformer is wye-connected, then

$$V_{pk} = 3 \times 2 V_{rms, \text{phase-to-neutral}}$$

V_{pk} will be approximately half the peak charging voltage on the PFN.

Figure 4(a) shows the boost circuit with its load, C , being the capacitance of the PFN, R , the total leakage resistance across the PFN, and D_{in} is the diode in the rectifier bank, D_{out} in Figure 2(a), through which the boost circuit finds its return path. In the open-circuit case, Figure 4(b), the boost circuit looks like an unloaded half-wave rectifier in which the coupling capacitor, C_c , charges to V_{pk} , the peak inverse voltage on D_{in} goes to $2 V_{pk}$, and the current flow and dissipation in the resistor R_{in} are essentially zero. In this condition, the peak inverse voltage across D_{out} is V_{pk} . However, if the AC is removed from the boost circuit, the voltage on D_{out} briefly goes about 20% higher. Figure 4(c) shows the short-circuit condition with AC power on, which would apply to a turn-on with a shorting stick accidentally left in place. The peak current through either diode is:

$$I_{pk} = V_{pk} / X_c^2 R^2$$

where $X_c = 1 / 2 \pi f C_c$, the AC reactance of the coupling capacitor

and R the value of either R_{in} or R_{out} . The average current through each diode is

$$I_{avg} = I_{pk} / 2$$

If $R_{in} = R_{out}$, the currents may be calculated separately; R_{in} only affects the peak and average current through D_{in} and R_{out} only through D_{out} . In practice, X_c , R , and the choice of C_c controls I_{pk} .

Figure 4 (d) shows the equivalent circuit for the case where the load shorts and the AC to the power supply is turned off quickly while the coupling capacitor is fully charged, as in the case of a kick-out resulting from a load fault. For the worst case of the transformer coil looking like a short, the surge current through D_{out} is

$$I_{surge} = V_{pk} / R_{out}$$

and a reasonable value to use for tolerable surge current is 25 times the average current rating of the diodes chosen. This criterion will normally drive the choice of R_{out} . The transformer coil, shown here as a short, is still inductive and the surge current will ring back through D_{in} , limited by R_{in} .

The value of C_c is chosen to give the voltage gain desired, which in turn is controlled by the ratio of filter capacitance, C_p , and the PFN capacitance, C_p . To a first approximation

$$V_p / V_f = 2 / 1 C_p / C_f$$

although losses in the charging inductance and charging diode reduce the voltage gain. It should be remembered that a stiff transformer-rectifier combination, particularly in conjunction with a long resonant time, partially recharge the filter capacitor during the resonant time and give the effect of a much larger C_p . Inverse voltage left on the PFN will increase the voltage gain, but a well-matched load or an inverse clipper circuit will minimize this effect. A gain of 1.8 is generally indicative of a good resonant charging circuit. The voltage to which the transformer-rectifier charges the filter capacitor varies with the loading on the power supply from V_{pk} at light loading to .95 V_{pk} at heavy loading. Combining these effects, the voltage on the PFN can be expected to be approximately 1.75 V_{pk} .

The leakage resistance across the PFN, R , in Figure 4(a), has a large effect on choice of C_c . Previous analyses have assumed equal values for the coupling and load capacitors, which leads to the erroneous conclusion that the RC product of the load controls the voltage gain of a doubler. The charge coupled into the circuit through C_c and bled out through R , the R/X_c ratio, controls the circuit response. Changing the load capacitance over three orders of magnitude had less than 1% effect on voltage gain. The total leakage paths across the PFN load—the internal leakage of capacitors, the voltage diagnostics, the diode end-of-line clipper circuit, and the balancing resistors for a multigap thyatron, are in the order of 1 Megohm.

The voltage gain through the circuit depends on the leakage across the PFM, R_p , the resistance in series with the diodes, $R_{in} = R_{out} = R_d$, and the coupling capacitor C_c . From Ref. 1, the allowable R_d for a given voltage gain, R_p , and large value of C_c , can be found to be

$$R_d = \frac{K}{\sin^{-1} \left(\frac{K}{2} \right)} \frac{1 - (K/2)^2 - (K/4)}{2}$$

where $K = V_p / V_{pk}$.

For the assumed 1.75 voltage gain, this allows $R_d/R_p = .76\%$, but only for large C_c . Since the capacitor is the largest and most expensive component used, reducing R_d to allow a smaller C_c is advantageous.

For charging-time considerations, an equivalent voltage source impedance, R_{eq} , can be used with the capacitance of the load, C_c , to give an $R_{eq} C_c$ charging time constant. For the circuits investigated, the value of R_{eq} was approximately $3 X_c$.

SAMPLE DESIGN

A boost circuit was designed and fabricated for the following conditions:

PFM charging voltage, $V_p = 40$ kV

PFM capacitance, $C_p = 9.0$ uF

PFM leakage, $R_p = .67$ Megohm

Filter capacitor, $C_f = 47$ uF

The expected resonant voltage gain was

$$\frac{V_p / V_f = 2 C_f / (C_f C_p)}{(47 \text{ } 9)P = 1.68} = (2 \times 47)$$

The measured gain was 1.57, for a drop of 6.5% in the charging inductor and diode. The required filter voltage for 40 kV on the PFM was

$$V_f = 40 \text{ kV} / 1.57 = 25.5 \text{ kV}$$

The transformer rectifier produced a filter voltage of $0.97 V_{pk}$, requiring a peak AC voltage of

$$V_{pk} = V_f / .97 = 25.5 \text{ kV} / .97 = 26.3 \text{ kV}$$

and the desired voltage gain from the boost circuit was $V_p/V_{pk} = 40 \text{ kV}/26.3 \text{ kV} = 1.52$.

The price of high voltage diode stacks is nearly constant up to 750 ma average current and rises rapidly above that, making the 750 ma diode a logical choice for the circuit. The surge rating, at 25 times the average rating, is 18.8 amps. From the considerations discussed in Figure 4(d), with C_c charged to $V_{pk} = 26.3$ kV

$$R_d = 26.3 \text{ kV} / 18.8 \text{ A} = 1.4 \text{ k}$$

The ratio of R_d/R_p was $1.4 \text{ k} / .67 \text{ M} = .21\%$. The limiting ratio for a gain of 1.52 is

$$R_d/R_p = \frac{1.52}{\sin^{-1}(.76)} = \frac{1 - (.76)^2}{.38} = 2$$

or $R_d/R_p = 2.4\%$ for the large C_c case. There is obviously room for increasing R_d for diode safety or reducing C_c for a size and cost saving. From Figure 5, for $.25\% R_d/R_p$ and $V_p/V_{pk} = 1.52$, $R_p/X_c = 16$,

$$X_c = R_p / 16 = .67 \text{ M} / 16 = 41.9 \text{ k} = 1 / 260 C_c \text{ and}$$

$$C_c = 1 / 41.9 \times 10^3 \times 377 = .063 \text{ uF}$$

Checking the shorted load, AC-on fault mode, the impedance is dominated by X_c , and $I_{pk} = V_{pk}/X_c = 26.3 \text{ kV} / 41.9 \text{ k} = .63$ amp with the average current per diode

$$I_{avg} = I_{pk} / 2 = .63 / 2 = .22 \text{ amp}$$

which is well within the .75 amp rating. The I^2R dissipation in the R_d resistors is 68 watts, assuming a shutdown in ten cycles the energy into each R_d is 11 joules, and the peak voltage across each R_d is $.63 \times 1400 = 880$ volts. A string of a few 2 watt carbon resistors is more than adequate for the voltage and energy considerations.

The minimum component values for the above circuit are

$$C_c: .063 \text{ uF}, 26.3 \text{ kV}$$

$$R_{in} = R_{out} = R_d: 1.4 \text{ k}, 880 \text{ volts peak, 11 joules}$$

$$D_{in}: 220 \text{ ma average current} \\ 18.8 \text{ amp surge current} \\ 52.6 \text{ kV PIV}$$

$$D_{out}: 220 \text{ ma average current} \\ 18.8 \text{ amp surge current} \\ 26.3 \text{ kV PIV}$$

Choosing $C_c = .1$ uF for convenience, for $X_c = 26.5 \text{ k}$ and $R_c/X_c = 25.3$ allows increasing R_d/R_p to 1.75%, from Figure 5,

$$R_d = .0175 \times 670 \text{ k} = 11.7 \text{ k}$$

$$I_{surge} = 26.3 \text{ kV} / 11.7 \text{ k} = 2.2 \text{ amps}$$

$$I_{pk} = 26.3 \text{ kV} / ((11.7 \text{ k})^2 (26.5)^2) = 26.3 / 290 = .91 \text{ amp}$$

$$I_{avg} = .91 / 2 = .32 \text{ amp}$$

for even greater diode safety.

When varying R_{in} and/or R_{out} to adjust V_p/V_{pk} to be slightly less than the resonant voltage gain, experimentation has shown that for small C_c , where X_c

dominates R_{in} , R_{out} is about twice as effective as R_{in} for varying the voltage gain. For large C_c , R_{in} is more effective.

Using the approximation of $R_{in} = 26.5 k \times 2 = 53 k$, and $C_p = 9 \mu f$, the estimated time constant was $\tau_p = .72$ sec. The observed exponential time constant for the actual circuit charging $C_p = 9 \mu f$ was .95 sec.

CONCLUSIONS:

A simple, cheap circuit has been demonstrated which can charge the PFN of a resonantly charged modulator prior to the first pulse to avoid the low-first pulse problem. The circuit requires no attention and has no adverse effect on the rest of the modulator.

REFERENCES:

- 1: D. L. Waldelich and C. L. Shackelford, "Characteristics of Voltage-Multiplying Rectifiers", Proceedings of the I.R.E., vol. 32, pp. 470-476, August 1944.
- 2: O. H. Schade, "Analysis of Rectifier Operation", Proc. I.R.E., vol. 31, pp. 341-361, July 1943.

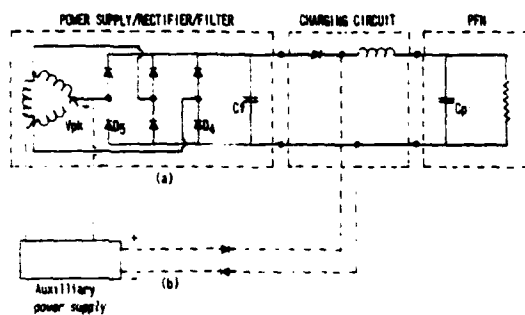


Fig 1 Three phase full wave rectifier, charging circuit, and PFM with arbitrary auxiliary power supply.

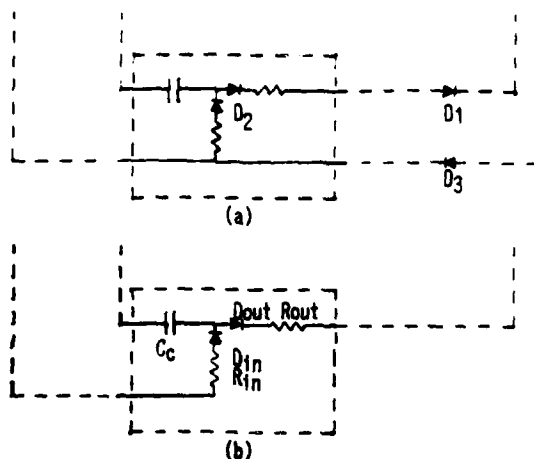


Fig 2(a) Half-wave voltage doubler
(b) Simplified half-wave doubler

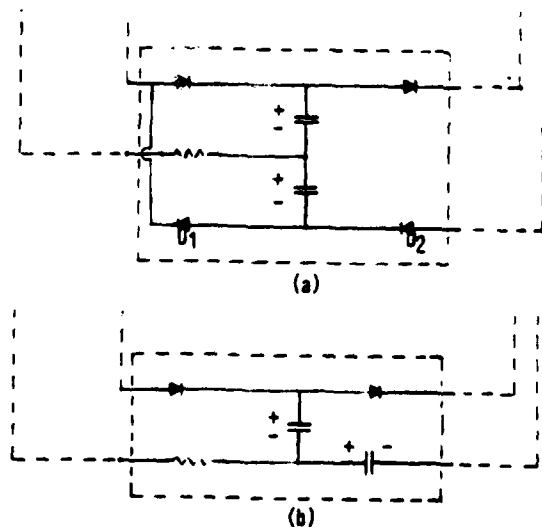


Fig 3(a) Full-wave voltage doubler
(b) Simplified full-wave doubler

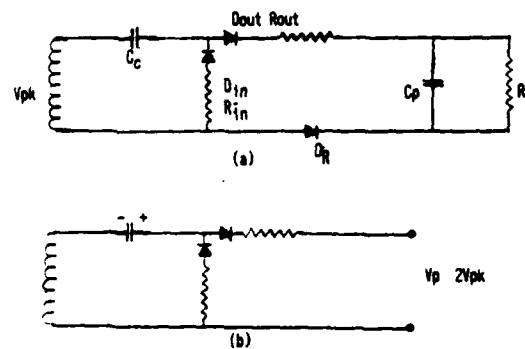


Fig 4 Half-wave boost circuit in operating and fault modes.

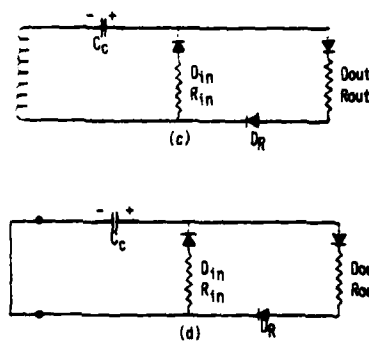


Fig 4 (cont) Half-wave boost circuit in operating and fault modes.

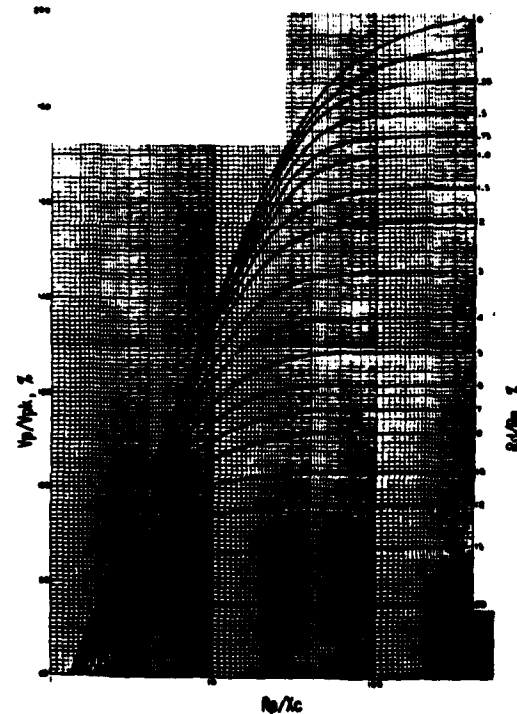


Fig 5 Boost Circuit Gain
(adapted from Schade, Ref. 2)

LIST OF ATTENDEES

1982 FIFTEENTH POWER MODULATOR SYMPOSIUM

Richard G. Adams	Sandia National Laboratories
C. S. Ashman	MEL Phillips, U.K.
Ken Baile	Naval Surface Weapons Center
Joseph Bajda	Norden Systems
Howard J. Baker	University of Hull, U.K.
Edwin D. Ball	Naval Surface Weapons Center
Susan Ball	Physics International Co.
John P. Barber	IAP Research, Inc.
David M. Barrett	Old Dominion University
Jack W. Beal	General Atomic Co.
Tom L. Bekker	Naval Ship Weapon Systems Engineering Station
Baruch Berman	Rockwell International
Willi Bette	Kraftwerkunion AG, W. Germany
K. James Bickford	Los Alamos National Laboratory
John Bless	TRW Systems
Daniel L. Birs	Lawrence Livermore National Laboratory
George Blaszczyński	Elsint, Inc.
Laird P. Bradley	Lawrence Livermore National Laboratory
Howard M. Brady	Electron Technology
Donald A. Brichta	Northrop Corp.
Alan Bromborsky	Harry Diamond Labs, U.S. Army ERADCOM
Charles Bruno	Commissariat à l'Energie Atomique, France
Mel Buchblinder	Sperry Gyroscope
Jacques Buchet	Commissariat à l'Energie Atomique, France
Tom R. Burkes	T.R.B., Inc.
Scott C. Barkhart	Lawrence Livermore National Laboratory
R. Burnham	Naval Research Laboratory
Edward P. Burns	Hughes Aircraft Co.
Joseph K. Burton	Sachs/Freeman
J. M. Butner	Naval Surface Weapons Center
Malcolm Buttram	Sandia National Laboratories
James E. Calpin	Westinghouse Electric Corp.

LIST OF ATTENDEES

Hugh A. Calvin	Beta Development Corp.
Thomas A. Campbell	Grumman Aerospace Corp.
Bruce Carder	Lawrence Livermore National Laboratory
Robert Caristi	EG&G, Inc.
Herbert J. Carper, Jr.	Texas Tech University
Peter H. Castine	Los Alamos National Laboratory
Matija B. Cenanovic	Ontario Hydro Research Laboratory
Y. G. Chen	Maxwell Laboratories, Inc.
Paul Christensen	BDM Corp.
David J. Christie	Lawrence Livermore National Laboratory
Ed Chu	Maxwell Laboratories, Inc.
Gerald Clark	EG&G, Inc.
David Cohn	Northrop Corporation
Dominick Conte	R&D Associates
Ed Cook	Lawrence Livermore National Laboratory
Chatham M. Cooke	MIT
Paul A. Corbiere	Raytheon Co.
Charles A. Corson	Westinghouse Electric Corp.
Carl R. Crager	Litton Industries
Walter Crewson	Universal Voltronics
David B. Cummings	Physics International Co.
Ashok N. Datar	Allied Corporation
Stephen J. Davis	Pico Second Enterprises, Inc.
Frank DeLurgio	Emerson Electric Co.
Robert DeWitt	Naval Surface Weapons Center
A. Stuart Denholm	Hipotronics, Inc.
Anthony Donaldson	Texas Tech University
Robert L. Druce	Air Force Weapons Laboratory
Jackie N. Elkins	United Technologies Research Center
Jan Eninger	AVCO Everett Research Laboratory, Inc.
George W. Ewell	Georgia Tech, Engineering Experiment Station
Edward A. Farrell	Rel, Inc.
David B. Fenneman	Naval Surface Weapons Center

LIST OF ATTENDEES

Bill Fox	Maxwell Laboratories, Inc.
George Frazier	Physics International Co.
Walter W. Frey	Brookhaven National Laboratory
Steven Friedman	EG&G, Inc.
Hayden Gallagher	Hughes Research Laboratories
Robert A. Gardenghi	Westinghouse Electric Corp.
Woo Fee Gee	Lawrence Livermore National Laboratory
Victor H. Gehman, Jr.	Naval Surface Weapons Center
Ezra Gershgoren	Space Microwave Laboratories, Inc.
Antonio Giacometti	Contraves Italiana, Italy
Robert E. Gibson	Siemens Medical Laboratories
A. S. Gilmour, Jr.	State Univ. of New York at Buffalo
Howard S. Ginsberg	Westinghouse Electric Corp.
Jerry A. Goldlust	Dielectric Sciences
Robert A. Goodman	
A. E. Gordon	ITT Electron Tube Div.
Lloyd B. Gordon	Lawrence Livermore National Laboratory
Bob Gray	Rome Air Development Center
Ronald Gripshover	Naval Surface Weapons Center
Henry C. Gruenwald	ITT Electron Tube Div.
Arthur H. Guenther	Air Force Weapons Laboratory
Shekhar Guha	University of Southern California
Martin Gundersen	University of Southern California
Marion Hagler	Texas Tech University
J. R. Hall	Rockwell International
Jed Hammon	Physics International Co.
Kenneth W. Hanks	Los Alamos National Laboratory
Leonard W. Hardesty, Jr.	Naval Surface Weapons Center
C. J. Harrison	English Electric Valve Co., Ltd., U.K.
D. Kurt Haskell	Maxwell Laboratories
Bob Hathaway	Allied Corporation
H. Hayes, Jr.	Maxwell Laboratories
R. E. Hebner	National Bureau of Standards

LIST OF ATTENDEES

Alvin Herting	Raytheon Co.
Phillip Herren	Air Force Wright Avionics Laboratory
Stuart Hesselson	EEV, Inc.
Robert A. Hill	Westinghouse Electric Corp.
James V. Hill	Lawrence Livermore National Laboratory
Wayne W. Hofer	Lawrence Livermore National Laboratory
Ronald W. Holloway	Lawrence Livermore National Laboratory
Emanuel M. Honig	Los Alamos National Laboratory
Edward H. Hooper	Westinghouse Electric Corp.
Gerald Hughes	Lawrence Livermore National Laboratory
Thomas Innes	Lawrence Livermore National Laboratory
Yasuaki Ito	Keio University, Japan
Douglas James	Lumonics, Inc.
Hansjorg Jansen	Los Alamos National Laboratory
B. Jennis	English Electric Valve Co., Ltd., U.K.
John P. Kennedy	
J. C. Keyes	Pico Second Enterprises, Inc.
Ronald Kihara	Lawrence Livermore National Laboratory
Craig L. Kimberlin	Defense Nuclear Agency
Clifford King	Elsint, Inc.
Hugh C. Kirbie	Old Dominion University
Gregory F. Knapp	Old Dominion University
R. Kremens	U.S. Army Ballistics Research Laboratory
Bernhard Kulke	Lawrence Livermore National Laboratory
Robert F. Lambase	Brookhaven National Laboratory
James Laudenslager	Jet Propulsion Laboratory
E. J. Lauer	Lawrence Livermore National Laboratory
Norman Lee	
G. L. Legate	Los Alamos National Laboratory
Jeffrey I. Levatter	Hellonetics, Inc.
Stephen Levy	ET&D Laboratory, U.S. Army ERADCOM
Rudy Limpacher	AVCO Everett Research Laboratory
Michael Lipka	Naval Research Laboratory

LIST OF ATTENDEES

Rudolph Litte.....	AVCO Everett Research Laboratory
Allen B. Litton.....	Los Alamos National Laboratory
Robert Lockey.....	Brookhaven National Laboratory
Gary K. Loda.....	Beta Development Corp.
Lawrence H. Luessen.....	Naval Surface Weapons Center
Randy Lundberg.....	Lawrence Livermore National Laboratory
Phil Mace.....	Los Alamos National Laboratory
P. N. D. Maggs.....	English Electric Valve Co., Ltd., U.K.
V. Nicholas Martin.....	AVCO Everett Metalworking Laser
Thomas H. Martin.....	Sandia National Laboratories
Donald A. Masqueller.....	Lawrence Livermore National Laboratory
Bart Mass.....	XMR, Inc.
M. L. Matnick.....	Axel Electronics, Inc.
J. D. McCarthy.....	Fermilab
H. Bruce McFarlane.....	Lawrence Livermore National Laboratory
Ronald H. McKnight.....	National Bureau of Standards
Erline McNees.....	EIMAC Div. of Varian
Hugh Menown.....	English Electric Valve Co., Ltd., U.K.
Shandas Meppalli.....	Electronics & Radar Dev. Establishment, India
Bernard T. Merritt.....	Lawrence Livermore National Laboratory
Spencer Merz.....	Lambda Physics
Raffee Mgrdechian.....	Axel Electronics, Inc.
Bob A. Michalak.....	Del Electronics Corp.
Louise Miles.....	Naval Surface Weapons Center
Daniel G. Miller.....	Westinghouse Electric Corp.
Albert W. Mimms.....	Space Microwave Laboratories, Inc.
Stuart L. Moran.....	Naval Surface Weapons Center
John J. Moriarty.....	Raytheon Company
Tapas Mikutmoni.....	Hughes Aircraft Co.
John J. Mulrey.....	EG&G, Inc.
Jacques Murachver.....	EG&G, Inc.
P. Yawrocky.....	Brookhaven National Laboratory
C. Neale.....	English Electric Valve Co., Ltd., U.K.

LIST OF ATTENDEES

Mark Newton	Lawrence Livermore National Laboratory
Nigel S. Nicholls	Royal Signals & Radar Establishment, U.K.
Paul Nocella	Sperry Gyroscope
Eugene Notling	Naval Surface Weapons Center
W. C. Nunnally	Los Alamos National Laboratory
R. F. Nylander	Los Alamos National Laboratory
Joseph C. O'Connell	ET&D Laboratory, U.S. Army ERADCOM
J. P. O'Donnell	Axel Electronics, Inc.
James O'Loughlin	Air Force Weapons Laboratory
Minoru Obara	Keio University, Japan
R. Oberholtzer	Fermilab
Henry B. Odom, III	Naval Surface Weapons Center
Jeffrey A. Oicles	Lawrence Livermore National Laboratory
Robert A. Olson	Systems Research Laboratories
Walter Orsulak	Naval Surface Weapons Center
Thomas J. Pacala	Jet Propulsion Laboratory
S. T. Pai	Opto-Electronics, Ltd.
Mark Parsons	Los Alamos National Laboratory
Charles Parsons	Naval Surface Weapons Center
P. R. Pearson	Royal Signals & Radar Establishment, U.K.
Ronald James Pederson	Texas Tech University
Rodney Petr	Math Sciences, N.W.
Edward M. Piechowiak	Westinghouse Electric Corp.
Charles T. Pike	AVCO Everett Research Laboratory
James R. Pollard	Naval Surface Weapons Center
John F. Power	Los Alamos National Laboratory
Mark S. Pronko	Old Dominion University
D. L. Pruitt	RCA
Allen Ramrus	Maxwell Laboratories
Mark Rand	Allied Corp.
William A. Reas	Los Alamos National Laboratory
Lou Reginato	Lawrence Livermore National Laboratory
Nicholas Reinhardt	Impulse Electronics, Inc.

LIST OF ATTENDEES

Doug Remsen General Atomic Co.

Barry Ressler Universal Voltronics

Benjamin G. Rice ITT Electron Tube Div.

Larry Rinehart Naval Surface Weapons Center

Kenneth N. Rinker Litton Industries

Doyle Rogers Lawrence Livermore National Laboratory

Gerald J. Rohwein Sandia National Laboratories

M. Frank Rose Naval Surface Weapons Center

Jay Samuels Los Alamos National Laboratory

Melvin Sandler The Cooper Union

George Santamaria Lucidyne, Inc.

W. J. Sarjeant State Univ. of New York at Buffalo

Victor E. Scherrer Naval Research Laboratory

Roger Schirmer Naval Research Weapons Center

Winfried Schmidt Kernforschungszentrum Karlsruhe, W. Germany

John Schmidt Lawrence Livermore National Laboratory

Sol Schneider

Gerhard Schroper CERN, France

Adolf J. Schwab University of Karlsruhe, W. Germany

Alexander Shpilman University of Maryland

Hal Silverman.....

Gordon K. Simcox G.K.S. Associates

Timothy L. Skvarenina Air Force Institute of Technology

Kenneth M. Smalley Raytheon Co.

Bernard Smith ET&D Laboratory, U.S. Army ERADCOM

Carl H. Smith Allied Corp., Metglas Products

Ian Smith Pulse Sciences, Inc.

Mark E. Smith Lawrence Livermore National Laboratory

Richard J. Sojka GTE Sylvania

Willard Souza Lawrence Livermore National Laboratory

Louis W. Springer General Electric Co.

Alexander Stewart Harry Diamond Laboratories, U.S. Army ERADCOM

Joe V. Stover Hughes Aircraft Co.

LIST OF ATTENDEES

J. E. Sunderlin	Westinghouse Electric Corp.
P. J. Swan	Thorn EMI Varian Ltd., U.K.
Leonard Swisher	Lawrence Livermore National Laboratory
Rod S. Taylor	NRC of Canada
Jim Thompson	University of South Carolina
P. B. Tole	Tata Institute of Fundamental Research, India
Gary Tripoli	Ion Physics Co.
David V. Turnquist	Impulse Electronics, Inc.
Vance I. Valencia	Maxwell Laboratories
Fred Van Haaften	Los Alamos National Laboratory
Ihor M. Vitkovitsky	Naval Research Laboratory
Roy E. Voghall	Westinghouse Electric Corp.
Michael L. Wardlaw	Naval Surface Weapons Center
Oren A. Wasson	National Bureau of Standards
Robert Weeks	Lumonics, Inc.
E. F. Weinberg	Raytheon Co.
Maurice Weiner	RT&D Laboratory, U.S. Army ERADCOM
William Weiss	Lawrence Livermore National Laboratory
Kenneth Whitham	Lawrence Livermore National Laboratory
Norman H. Williams	Varian Associates
Walter Willis	Los Alamos National Laboratory
Mark A. D. Wilson	National Bureau of Standards
P. S. Wise	ITT Gilfillan
George R. Wisner	United Technologies Research Center
Joe R. Woodworth	Sandia National Laboratories
William H. Wright, Jr.	ET&D Laboratory, U.S. Army ERADCOM
Arthur S. Zinkin	Hughes Aircraft Co.
Thomas Znotins	Math Sciences Northwest

AUTHOR INDEX

NAME—SESSION NO.—PAPER

PAGE

NAME—SESSION NO.—PAPER

PAGE

Adams, R.G.—II-3	79
Bajda, J.—VII-2	260
Berkbigler, L.W.—VI-10	246
Bernhardt, T.—I-6	32
Bickford, K.J.—II-5	89
Bird, W.—IX-3	323
Birx, D.L.—I-1, I-2, I-3, I-8, IX-5	4, 10, 15, 47, 333
Boiles, R.S.—VII-4	269
Branum, D.R.—IX-5	333
Brody, S.—VII-2	260
Burke, T.—IV-4	164
Buttram, M.T.—V-1	168
Carder, B.—IX-3	323
Carper, H.J.—II-8	105
Carter, J.—IV-4, V-4	164, 186
Christie, D.J.—VI-10	246
Chu, E.Y.—I-6	32
Cole, H.—III-1	119
Colne, E.—III-4	133
Commisso, R.J.—IV-1	146
Cook, E.G.—I-2, I-3, IX-5	10, 15, 333
Cooper, R.A.—V-3	181
Copp, R.L.—IX-5	333
Corbiere, P.A.—VI-9	237
Corson, C.A.—VI-3, VII-6	210, 282
Cottingham, J.G.—VIII-2	299
Crees, D.E.—IX-4	327
Dallum, G.E.—VI-10	246
Davis, S.J.—VI-7	227
DeWitt, R.N.—II-7	99
Donaldson, A.L.—II-4	84
Druce, R.L.	1
Eimerl, D.—IX-3	323
Elkins, J.N.—II-6	93
Eninger, J.E.—V-6	193
Farkas, E.C.—VI-2	200
Fenneman, D.B.—V-2	174
Fernsler, R.F.—IV-1	146
Frey, W.—VIII-2	299
Frick, E.—VIII-1	290
Friedman, H.W.—V-6	193
Friedman, S.—II-6, III-3	93, 127
Frost, C.A.—II-3	79
Fujioka, T.—II-9	110
Fulkerson, E.S.—I-9	51
Ghoshroy, S.—VIII-2	299
Gilmour, A.S., Jr.—I-10	55
Ginsberg, H.S.—VII-6	282
Gripshover, R.J.—V-2	174
Gritton, D.G.—VI-10	246
Guenther, A.H.	1
Guha, S.—III-1	119
Gundersen, M.A.—III-1	119
Hagler, M.O.—II-4	84
Hanks, K.W.—I-5, II-5	28, 89

Haskell, D.K.—V-3	181
Haumesser, R.L.—I-10	55
Hawkins, S.—I-3	15
Herling, A.M.—VI-9	237
Hofmann, G.—I-6	32
Hooper, E.H.—VI-2, VI-3	200, 214
Innes, T.—VIII-4	307
Itoh, Y.—II-9	110
Kent, H.—I-6	32
Kihara, R.—VIII-4	307
Kimberlin, G.L.—VI-1	196
Kitchin, H.D.—III-4	133
Kristiansen, M.—II-4	1, 84
Kuhn, H.—VIII-1	290
Kulke, B.—VIII-4	307
Kunc, J.—III-1	119
Kunitomo, K.—II-9	110
Lambiase, R.F.—III-2, VIII-3	123, 303
Lauer, E.J.—I-8	47
Lauer, G.—IV-3	160
Lee, F.D.—IX-5	333
Leopold, K.E.—II-10	113
Levine, M.—IV-3	160
Limpaecher, R.—II-2, VI-8	75, 231
Lipka, M.—VI-2	200
Litte, R.—VI-8	231
Litton, A.—I-5, VI-5	28, 220
Litzenberger, L.N.—V-6	193
Lockwood, D.L.—I-10	55
Lundberg, R.L.—VI-1	196
Mace, P.N.—I-5	28
Marton, J.P.—IV-2	153
Mayer, M.—VIII-1	290
McCafferty, J.—IX-1	312
McClanahan, R.F.—VII-4	269
McDuff, G.—VI-5	220
McGowan, J.—III-3	127
Menown, H.—III-2	123
Meppalli, S.—VII-5	275
Merritt, B.T.—VI-10	246
Meyers, A.—I-3	15
Miller, D.G.—VII-7	286
Mimms, A.W.—VII-5	275
Moran, S.L.—II-7	99
Moriarty, J.J.—VI-9	237
Ness, R.—II-4	84
Newton, B.—III-2	123
Newton, M.A.—IX-5	333
Nicholls, N.S.—IX-1, IX-4	312, 327
Nocella, P.—VII-1	249
Nunnally, W.C.—I-5	28
Obara, M.—II-9	110
O'Connell, J.—I-10, III-3	55, 127
Oicles, J.A.—I-9	51
O'Loughlin, J.P.—V-5	189

AUTHOR INDEX

NAME—SESSION NO.—PAPER	PAGE	NAME—SESSION NO.—PAPER	PAGE
Pai, S.T.—IV-2	153	Smith, I.—IV-3	160
Pearson, P.R.—IX-4	327	Smith, I.D.—VI-6	223
Pederson, R.J.—II-8	105	Smith, M.E.—IX-5	333
Pereira, N.R.—II-1	67	Smith, M.W.—I-2, I-3	10, 15
Petr, R.—III-3	127	Speckert, G.C.—IX-5	333
Piechowiak, E.M.—VI-2	200	Springer, T.E.—I-5	28
Power, J.—I-5	28		
		Taylor, R.S.—II-10	113
Ramrus, A.—II-1	67		
Reginato, L.L.—I-1, I-2, I-3, IX-5	4, 10, 15, 333	Valencia, V.—V-3	181
Rinehart, L.F.—II-7	99	Vitkovitsky, I.M.—IV-1	146
Rodei, V.—VIII-1	290	Vossenber, E.—VIII-1	290
Rogers, D.—IX-5	333		
		Washburn, R.D.—VII-4	269
Salome, J.M.—III-4	153	Weiner, M.—II-6, IV-4	93, 164
Sandler, M.—IX-2	317	Whitham, K.—VI-10	246
Scarpetti, R.—VIII-4	307	Willis, W.L.—II-5	89
Scherrer, V.E.—IV-1	146	Woodworth, J.R.—II-3	79
Schmidt, J.A.—I-1, I-2, I-3	4, 10, 15	Wright, W.H., Jr.—III-5, VI-1, IX-6	141, 196, 338
Schneider, R.—II-2	75	Wrzesniewski, M.—IX-2	317
Schneider, S.—I-7	37		
Schröder, G.H.—VIII-1	290	Youmans, R.—IV-4	164
Simcox, G.K.—VI-9	237	Zinkin, A.S.—VII-4	269
Smith, B.—VII-3	265		
Smith, C.H.—I-4	22		

FILME
0-8